

University of Alberta

U-Pb dating of Paleoproterozoic mafic dyke swarms of the South Indian Shield:
Implications for paleocontinental reconstructions and identifying ancient mantle plume
events

by

Jason Edward French



A thesis submitted to the Faculty of Graduate Studies and Research in partial fulfillment
of the requirements for the degree of Doctor of Philosophy

Department of Earth and Atmospheric Sciences

Edmonton, Alberta
Fall, 2007



Library and
Archives Canada

Bibliothèque et
Archives Canada

Published Heritage
Branch

Direction du
Patrimoine de l'édition

395 Wellington Street
Ottawa ON K1A 0N4
Canada

395, rue Wellington
Ottawa ON K1A 0N4
Canada

Your file *Votre référence*
ISBN: 978-0-494-32957-3
Our file *Notre référence*
ISBN: 978-0-494-32957-3

NOTICE:

The author has granted a non-exclusive license allowing Library and Archives Canada to reproduce, publish, archive, preserve, conserve, communicate to the public by telecommunication or on the Internet, loan, distribute and sell theses worldwide, for commercial or non-commercial purposes, in microform, paper, electronic and/or any other formats.

The author retains copyright ownership and moral rights in this thesis. Neither the thesis nor substantial extracts from it may be printed or otherwise reproduced without the author's permission.

AVIS:

L'auteur a accordé une licence non exclusive permettant à la Bibliothèque et Archives Canada de reproduire, publier, archiver, sauvegarder, conserver, transmettre au public par télécommunication ou par l'Internet, prêter, distribuer et vendre des thèses partout dans le monde, à des fins commerciales ou autres, sur support microforme, papier, électronique et/ou autres formats.

L'auteur conserve la propriété du droit d'auteur et des droits moraux qui protègent cette thèse. Ni la thèse ni des extraits substantiels de celle-ci ne doivent être imprimés ou autrement reproduits sans son autorisation.

In compliance with the Canadian Privacy Act some supporting forms may have been removed from this thesis.

Conformément à la loi canadienne sur la protection de la vie privée, quelques formulaires secondaires ont été enlevés de cette thèse.

While these forms may be included in the document page count, their removal does not represent any loss of content from the thesis.

Bien que ces formulaires aient inclus dans la pagination, il n'y aura aucun contenu manquant.


Canada

“In ancient days two aviators procured to themselves wings. Daedalus flew safely through the middle air and was duly honoured on his landing. Icarus soared upwards to the sun till the wax melted which bound his wings and his flight ended in fiasco....The classical authorities tell us, of course, that he was only ‘doing a stunt’; but I prefer to think of him as the man who brought to light a serious constructional defect in the flying machines of his day.

So, too, in science. Cautious Daedalus will apply his theories where he feels confident they will safely go; but by his excess of caution their hidden weaknesses remain undiscovered. Icarus will strain his theories to the breaking-point till the weak joints gape. For the mere adventure? Perhaps partly, that is human nature. But if he is destined not yet to reach the sun and solve finally the riddle of its construction, we may at least hope to learn from his journey some hints to build a better machine.”

- From *Stars and Atoms*, by Sir Arthur Eddington
(Oxford University Press, 1927, p.41)

“Study nature, not books.”

- Louis Agassiz

ABSTRACT

A multi-technique geochronological study of Paleoproterozoic mafic dyke swarm emplacement in the south Indian shield is presented. Radiometric ages constrain the timing of emplacement of numerous mafic dykes from the Dharwar and Bastar cratons, including high precision U-Pb isotope dilution thermal ionization mass spectrometry (IDTIMS), and high spatial resolution electron microprobe (EM) chemical U-Th-total Pb age determinations.

U-Pb IDTIMS ages determined on baddeleyite and zircon from mafic dykes spanning a vast tract of the Dharwar craton define a punctuated record of mafic magmatism throughout much of the Paleoproterozoic era. Emplacement of the giant radiating Bangalore and Northern Dharwar mafic dyke swarms took place at 2.37 Ga and 2.18 Ga, respectively. Similar ages of 2.21 Ga were determined for a NW-SE trending picrite and a N-S trending sub-alkali basaltic dyke south of the Cuddapah basin. U-Pb IDTIMS ages on baddeleyite and zircon for two NW-SE trending dykes from the BD2 mafic dyke swarm, southern Bastar craton, and the Pulivendla mafic sill from the Cuddapah basin, Dharwar craton, range from 1891 to 1883 Ma, and indicate the existence of a large igneous province within the south Indian shield that is genetically associated with rifting and basin development.

For the first time, rigid time correlations are made between Paleoproterozoic mafic magmatism in southern India and the record preserved in other Archean cratons worldwide. On the basis of high precision geochronology, the emerging Paleoproterozoic record of punctuated and catastrophic mafic magmatic activity

preserved in the south Indian shield bears strong resemblance to the record preserved in the Superior and Slave cratons of North America. These correlations indicate that the paleocontinents Ur and Kenorland may have broken up at the same time, and provide new evidence suggesting that these paleocontinents could have been part of a single larger Paleoproterozoic continent or supercontinent called Kurnorland. This study also has implications for defining enhanced periods of global mantle plume activity at 2.2 Ga and 1.9 Ga, or alternatively, the identification of global mafic magmatism at these times in association with widespread asthenospheric upwelling not associated with mantle plumes.

ACKNOWLEDGEMENTS

Completing this thesis has been without question the most staggeringly difficult but life-enriching experience of my life. The unwavering encouragement, love, and support provided by my family, friends, and colleagues while I carried out this monumental task made it continually seem far less impossible.

First I would like to thank my supervisor Larry Heaman for his guidance, support, friendship, and care throughout the course of this project. I would also like to thank Tom Chacko for his invaluable guidance and support during our forays into the world of electron microprobe chemical dating, and without whose limitless enthusiasm and encouragement I would not have come close to completing this thesis.

Were it not for the encouragement, love, and support provided by my family throughout the course of this thesis, I think that completing it would have been more than astoundingly harder. I would like to thank my parents Alice and Brian French, my sister Janine Woronuk (and her husband Mark Woronuk), and my brother Jonathan French for always being there for me when I needed them, but most importantly for always believing in me and providing the encouragement that helped me through the most difficult times. I would also like to thank my aunt Cynthia and late uncle Christian Graefe for their encouragement and love during my thesis, and for helping to spark my interest in geology and the outdoors when I was a boy.

My close friends have not only been there to encourage and support me during my thesis (or distract me with climbing road trips), but some have shared the grad school adventure. Mathew Mylod: Mat, thank you for your friendship, love, and encouragement during fieldwork in India and throughout the entirety of my thesis, for coaxing me up rock faces and ice falls, and for our many stimulating conversations about science and beyond. Shahin Dashtgard: Shaw, thanks for your friendship, moral support, sharing your enthusiasm for geology with me, and especially for those peaceful, serene moments atop Rocky Mountains when I needed them most during my thesis. Paul Glombick: Paul, thanks for your friendship and camaraderie during our grad school adventures, and for many exciting times at school, at the house, in the field, on the wall, or simply snoozing on a gravel bar. Ralf Tappert: Ralf, thanks for your friendship and kindness, and for many great times as office mates, roommates, and especially as compadres on our geological and camping excursions. Trevor MacHattie: Trevor, thanks for your friendship and scholarly companionship, and for many great times, enthusiastic geological discussions, and high-octane squash. Sarah Gleeson: Sarah, thanks for your friendship and encouragement, for many great laughs, and above all, for our peaceful Alberta wilderness retreats and your uncanny ability to predict wild animal sightings before they happen. I would also like to thank many other friends of mine whose love, encouragement, and laughter helped to lighten the thesis load over the years including Stephanie Ross, Brigid Mylod, Jeannie Bertrand, Jan Heaman, Jason Frank, Ian Armitage, Micheal Schultz, and Rajeev Nair.

There are many other colleagues in geology whose help, advice, and discussions over the years have contributed to my thesis in positive and constructive ways and enabled me to succeed in various aspects of the project, and these include Stacey Hagen, Sergei Matveev, Lang Shi, Benoit Rivard, Barbara Böhm, Antonio Simonetti Rajesh K. Srivastava, R.K. Singh, and Jonathan Patchett.

TABLE OF CONTENTS

CHAPTER 1

Introduction

Background on Mafic Dyke Swarms.....	1
Origin and Tectonic Significance of Mafic Dyke Swarms.....	2
Mafic Dyke Swarms and Paleoproterozoic Earth.....	5
Paleoproterozoic Continents and India.....	6
Study Areas in Southern India.....	8
Strategies and Methodology in U-Pb Dating of Mafic Dyke Samples.....	9
Presentation.....	12
References.....	13

CHAPTER 2

Feasibility of chemical U-Th-total Pb baddeleyite dating by electron microprobe

INTRODUCTION.....	25
Background on Baddeleyite Dating.....	27
U-Pb IDTIMS Results.....	27
<i>Phalaborwa Carbonatite, S. Africa (IN1)</i>	29
<i>Faber Lake Gabbro Sheet, Great Bear Magmatic Zone, N.W.T (GFA92-567)</i>	30
<i>Moore's Lake Gabbro, Churchill Province, Saskatchewan (9009)</i>	30
<i>Muskox Feldspathic Pyroxenite, Slave craton, N.W.T. (3101)</i>	31
<i>Binneringie Gabbro Dyke, Yilgarn craton, Australia (LH97-18)</i>	32
EM sample preparation and analytical procedure.....	33
<i>Sample preparation</i>	33
<i>Analytical procedure</i>	33
Age determination and data presentation.....	37
<i>Age calculation</i>	38
Results.....	40
Fields of Application.....	44
Summary and Conclusions.....	48
Acknowledgements.....	49
References.....	49

CHAPTER 3

1891-1883 Ma Southern Bastar-Cuddapah Mafic Igneous Events, India: A Newly Recognized Large Igneous Province

INTRODUCTION.....	70
GEOLOGICAL SETTING.....	72
Bastar craton.....	72
Extent and Nature of Mafic Dyke Swarms in the Bastar craton.....	74
The Cuddapah Basin, Dharwar craton.....	76
PETROGRAPHY.....	78
BD2 mafic dyke swarm, Bastar craton.....	79
<i>U- and Th-bearing accessory minerals</i>	80
HMD metamorphosed mafic dyke, Bastar craton.....	81
Pulivendla sill, Dharwar craton.....	82
ANALYTICAL METHODS.....	83
EM Chemical Monazite Dating.....	83
U-Pb LA-MC-ICP-MS monazite dating.....	84
U-Pb IDTIMS Geochronology.....	84
<i>Mineral Separation</i>	85
<i>SAMPLE JEF-00-36</i>	85
<i>SAMPLE JEF-00-30</i>	86
<i>SAMPLE JEF-00-14</i>	88
<i>SAMPLE JEF-99-9</i>	88
<i>U-Pb IDTIMS Analysis</i>	88
RESULTS.....	91
U-Pb IDTIMS Data.....	91
<i>BD2 mafic dyke swarm, Bastar craton</i>	91
<i>HMD metamorphosed mafic dyke, Bastar craton</i>	94
<i>Pulivendla sill, Dharwar craton</i>	94
Monazite dating.....	95
<i>EM chemical U-Th-total Pb monazite dating</i>	95
<i>LA-MC-ICP-MS monazite dating</i>	97
DISCUSSION.....	97
The timing, duration, and extent of Southern Bastar-Cuddapah Magmatic Events.....	98
Implications for Paleoproterozoic crustal evolution of the Dharwar protocontinent.....	100
Worldwide distribution of 1.9 Ga continental mafic igneous provinces.....	104
SUMMARY AND CONCLUSIONS.....	110
REFERENCES.....	111

CHAPTER 4

U-Pb IDTIMS ages for Paleoproterozoic mafic dyke swarms of the Dharwar craton, South India: Implications for an Ur-Kenorland connection

INTRODUCTION.....	138
GEOLOGICAL SETTING.....	140
Archean geology of the Dharwar craton.....	140
<i>Western Dharwar craton</i>	141
<i>Eastern Dharwar craton</i>	144
Proterozoic mafic dyke swarms of the Dharwar craton.....	148
<i>Previous geochronology of Proterozoic mafic dykes of the Dharwar craton</i>	150
DYKE SWARM SAMPLING AND PETROGRAPHY.....	154
The Bangalore dyke swarm.....	154
<i>Harohalli dyke (JEF-99-1): 12° 38.92' N; 77° 29.80' E</i>	154
<i>Penukonda dyke (JEF-99-6): 14° 08.06' N; 77° 36.03' E</i>	154
<i>Chennekottapalle dyke (JEF-99-7): 14° 15.06' N; 77° 37.33' E</i>	155
NW-SE trending dyke swarm, south-eastern Dharwar craton.....	156
<i>Somala dyke (JEF-99-11): 13° 29.29' N; 78° 49.86' E</i>	156
N-S trending dyke swarm, south-eastern Dharwar craton.....	157
<i>Kandlamadugu dyke (JEF-00-55): 13° 40.20' N; 78° 25.78' E</i>	157
E-W trending dyke swarm, north-eastern Dharwar craton.....	158
<i>Bandepalem dyke (JEF-00-43): 17° 08.63' N; 79° 27.50' E</i>	158
NW-SE trending swarm, Western Dharwar craton.....	159
<i>Dandeli dyke (JEF-00-1): 15° 19.49' N; 74° 36.06' E</i>	159
GEOCHEMICAL CLASSIFICATION OF DHARWAR MAFIC DYKES.....	159
MINERAL SEPARATION AND ANALYTICAL TECHNIQUES.....	162
Conventional mineral separation.....	162
Water-based baddeleyite mineral separation.....	163
U-Pb IDTIMS analysis.....	165
RESULTS.....	165
Harohalli dyke (JEF-99-1).....	165
Chennekottapalle dyke (JEF-99-7).....	168
Penukonda dyke (JEF-99-6).....	169
Dandeli dyke (JEF-00-1).....	170
Bandepalem dyke (JEF-00-43).....	172
Somala dyke (JEF-99-11).....	174
Kandlamadugu dyke (JEF-00-55).....	174
DISCUSSION.....	175
Regional extent and timing of emplacement of the Bangalore dyke swarm.....	176
U-Pb evidence for ~2.2 Ga pan-Dharwar mafic magmatism.....	179
Tectonic Implications.....	183
SUMMARY AND CONCLUSIONS.....	201
REFERENCES.....	202

CHAPTER 5

Conclusions

Summary.....	254
EM Dating of Mafic Dykes: Exploration of New Applications and Geochronometers.....	255
The Paleoproterozoic record of mafic dyke swarm emplacement in the south Indian shield: New high precision age constraints from U-Pb IDTIMS dating of baddeleyite and zircon.....	259
Implications for Paleoproterozoic crustal evolution of the south Indian shield.....	260
<i>Tectonic Significance of the 1.9 Ga Southern Bastar-Cuddapah LIP.....</i>	<i>260</i>
<i>New Regional Time-Markers and Paleo-Stress Indicators for the South Indian Shield.....</i>	<i>262</i>
Global correlation of Paleoproterozoic mafic magmatic events: Implications for paleocontinental reconstructions involving the Dharwar and Bastar cratons and identifying ancient superplume events.....	265
References.....	267

APPENDIX A

Morphological and geochemical characterization, and electron microprobe chemical U-Th-total Pb dating of zircon from the BD2 mafic dyke swarm, Bastar craton, India

Summary.....	277
Analytical set-up during electron microprobe analysis of zircon.....	277
ZIRCON MORPHOLOGIES.....	279
Polyhedral zircon.....	280
Bladed zircon.....	281
Dendritic zircon.....	281
ZIRCON GEOCHEMISTRY AND IN-SITU CHEMICAL DATING.....	283
References.....	290

APPENDIX B

Modelling of dendritic zircon formation by deterministic volume filling fractal growth

Modelling of dendritic zircon formation by deterministic volume filling fractal growth.....	306
References.....	313

APPENDIX C

Electron microprobe chemical U-Th-total Pb dating of baddeleyite (ZrO₂) and zircon (ZrSiO₄) from mafic dyke swarms of the south Indian shield

Summary.....	321
Analytical set-up during EM baddeleyite dating.....	322
EM baddeleyite dating: Southern Bastar-Cuddapah Large Igneous Province (LIP).....	323
References.....	328

APPENDIX D

Whole rock geochemistry (major, trace, and rare earth elements) for representative samples of the BD2 and HMD dyke swarms, Bastar craton

Summary.....	339
Geochemical comparisons of the BD1, BD2, HMD, and BK dyke swarms.....	340
References.....	342

APPENDIX E

Electron microprobe chemical U-Th-total Pb dating of zirconolite (CaZrTi₂O₇)

Summary.....	347
Analytical set-up during EM zirconolite dating.....	348
EM dating of <i>in situ</i> zirconolite and baddeleyite: Duck Lake sill, Slave craton.....	349
EM dating of <i>in situ</i> zirconolite: Phalaborwa carbonatite, South Africa.....	352
References.....	354
Abstract: Electron Microprobe dating of mafic to ultramafic igneous rocks.....	354

APPENDIX F

Description of samples collected during fieldwork in south India (Dec. 7, 1999 to March 5, 2000), and included in the thesis collection for this project

LIST OF TABLES

CHAPTER 2

Table 2-1. A comparison of reference isotopic ages, new IDTIMS ages, and new EM ages for baddeleyite.....	55
Table 2-2. U-Pb baddeleyite/zircon results for reference samples.....	56
Table 2-3. Chemical composition of baddeleyite samples.....	57

CHAPTER 3

Table 3-1. Summary of radiometric ages for rocks of the Cuddapah basin.....	123
Table 3-2. U-Pb IDTIMS and LA-ICP-MS data for mafic dykes from the Bastar craton and the Pulivendla mafic sill, Dharwar craton.....	124
Table 3-3. Chemical composition of monazite in BD2 dyke sample JEF-00-30.....	125

CHAPTER 4

Table 4-1. Major and trace element geochemistry for mafic dykes of the Dharwar craton dated by U-Pb in this study.....	221
Table 4-2. U-Pb IDTIMS baddeleyite/zircon results for mafic dykes of the Dharwar craton.....	222
Table 4-3. Summary chart of available high precision U-Pb baddeleyite/zircon ages for Paleoproterozoic mafic magmatic events on Earth.....	223
Table 4-4. Summary of previously determined paleomagnetic data for Dharwar mafic dyke swarms dated by U-Pb baddeleyite in this study.....	226

APPENDIX A

Table A-1. Chemical data for zircon from sample JEF-00-36 of the BD2 mafic dyke swarm (Bastar craton), determined by electron microprobe WDS spot analysis.....	292
Table A-2. Chemical data for zircon from sample JEF-00-39 of the BD2 mafic dyke swarm (Bastar craton), determined by electron microprobe WDS spot analysis.....	294
Table A-3. Chemical data for zircon from sample JEF-00-37 of the BD2 mafic dyke swarm (Bastar craton), determined by electron microprobe WDS spot analysis.....	296

APPENDIX D

Table D-1. Major and trace element geochemistry for representative mafic dykes from the BD2 and HMD dyke swarms, Bastar craton.....	343
--	-----

APPENDIX E

Table E-1. Electron Microprobe data for baddeleyite and zirconolite from sample JA HD-07 of the Duck Lake (Hayduck) sill, Slave craton - Analytical session 1.....	357
Table E-2. Electron Microprobe data for zirconolite from sample JA HD-07 of the Duck Lake (Hayduck) sill, Slave craton - Analytical session 2.....	359
Table E-3. Electron Microprobe chemical data for zirconolite from the Phalaborwa carbonatite, South Africa.....	360

APPENDIX F

Table F-1. Samples collected by the author during fieldwork in south India (Dec. 7, 1999 to March 5, 2000), comprising the thesis collection for this project.....	371
---	-----

LIST OF FIGURES

CHAPTER 1

- Figure 1-1.** Distribution of mafic dyke swarms and inferred mantle plume centres associated with opening of the Atlantic and Iapetus Oceans.....21
- Figure 1-2.** The principle tectonic elements of the Indian shield including Archean cratons and major Proterozoic mafic dyke swarms.....22
- Figure 1-3.** Geological map of the Dharwar craton showing the distribution of Proterozoic mafic dykes and the locations of mafic dykes and sills sampled for U-Pb dating in this study.....23
- Figure 1-4.** Geological map of the southern Bastar craton depicting the locations of mafic igneous rocks sampled for U-Pb dating in this study.....24

CHAPTER 2

- Figure 2-1.** Weighted average diagram constructed from $^{207}\text{Pb}/^{206}\text{Pb}$ ages of baddeleyite fragments from the Phalaborwa carbonatite.....58
- Figure 2-2.** Concordia diagrams showing U-Pb results for baddeleyite and zircon fractions from the Faber Lake gabbro, Moores Lake gabbro, Muskox feldspathic pyroxenite, and Binneringie dyke.....59
- Figure 2-3.** PbO content versus crystallization age for baddeleyite of various UO_2 concentrations.....60
- Figure 2-4.** A plot of Pb content versus Th^* in monazite and U^* in baddeleyite showing the typical range of values encountered during an EM chemical U-Th-total Pb analysis of each mineral.....61
- Figure 2-5.** Plot of PbO vs. UO_2^* for baddeleyite from the Phalaborwa carbonatite...62
- Figure 2-6.** BSE images of feldspathic pyroxenite sample 3101 from the Muskox intrusion showing the petrographic positions of baddeleyite crystals analysed in this study.....63
- Figure 2-7.** Close-up BSE images of the *in situ* crystals of baddeleyite analysed from sample 3101 of the Muskox intrusion, showing the context of WDS spot analyses and contour diagrams of U and Pb concentrations.....64
- Figure 2-8.** Plots of PbO vs. UO_2^* for *in situ* baddeleyite crystals from the Muskox intrusion.....65
- Figure 2-9.** Plot of PbO vs. UO_2^* for baddeleyite from the Moores Lake gabbro.....66
- Figure 2-10.** Plot of PbO vs. UO_2^* for baddeleyite from the Faber Lake gabbro.....67
- Figure 2-11.** Plot of PbO vs. UO_2^* for baddeleyite from the Binneringie dyke.....68
- Figure 2-12.** Comparison of chemical (EM) ages with isotopic (IDTIMS) ages for the five baddeleyite reference samples analysed in this study.....69

CHAPTER 3

Figure 3-1. Overview map of the principle geologic and tectonic elements of the Indian shield.....	126
Figure 3-2. Geological map of east-central peninsular India, highlighting the locations of U-Pb geochronology samples of mafic igneous rocks.....	128
Figure 3-3. Geological maps of the southern Bastar craton shown to scale and relative position and orientation, and depicting the locations of mafic dykes sampled for isotopic and chemical dating.....	129
Figure 3-4. Geological map of the southwest Cuddapah basin showing the location of the Pulivendla dolerite sill sampled for U-Pb dating.....	130
Figure 3-5. Thin section photomicrographs (plain light) showing petrographic textures of mafic dykes from the southern Bastar craton.....	131
Figure 3-6. Photomicrographs of baddeleyite grains with zircon overgrowth isolated from sample JEF-00-36.....	132
Figure 3-7. Concordia diagrams showing U-Pb isotopic data for baddeleyite, zircon, and rutile from mafic dykes of the southern Bastar craton.....	133
Figure 3-8. Concordia diagram, showing U-Pb IDTIMS isotopic data for baddeleyite from Pulivendla dolerite sill sample JEF-99-9.....	134
Figure 3-9. EM BSE images, photomicrograph, and scanning electron microscope secondary electron image of monazite in polished thin section of BD2 dyke sample JEF-00-30 dated by EM and LA-MC-ICP-MS.....	135
Figure 3-10. Trace element geochemistry of igneous monazite from BD2 dyke JEF-00-30.....	136
Figure 3-11. Plot of $\Sigma(\text{La}+\text{Ce}+\text{Pr})$ in atomic% REE versus La/Nd for igneous monazite from BD2 dyke JEF-00-30.....	137

CHAPTER 4

Figure 4-1. The principle tectonic elements of the Indian shield including Archean cratons and major Proterozoic mafic dyke swarms.....	227
Figure 4-2. Geological map of the Dharwar craton showing the distribution of Proterozoic mafic dykes and the locations of mafic dykes sampled for U-Pb dating in this study.....	228
Figure 4-3. Summary chart of previously determined isotopic ages for mafic dykes intruding Archean basement rocks of the Dharwar craton.....	229
Figure 4-4. Geological map of the Harohalli area showing the location of gabbro dyke sample JEF-99-1.....	230
Figure 4-5. Photographic and Landsat7 imagery of mafic dykes from the Bangalore dyke swarm of South India.....	231
Figure 4-6. Panchromatic Landsat7 image highlighting a prominent outcropping of the Bangalore dyke swarm.....	232
Figure 4-7. Lineament map interpreted from the Landsat7 image from Fig. 4-6.....	233
Figure 4-8. Geological map of the region north of the Cuddapah basin where gabbro sample JEF-00-43 of the Bandepalem dyke was collected.....	234

Figure 4-9. Geological map of the northern Shimoga supracrustal belt where sample JEF-00-1 of the Dandeli gabbro dyke was collected.....	235
Figure 4-10. Plots of major element geochemical data for mafic dykes of the Dharwar and Slave cratons, including a total alkalis versus silica diagram, a ternary (Na ₂ O+K ₂ O)-(FeO+0.8998Fe ₂ O ₃)-MgO diagram, and a diagram showing CIPW normative mineralogy plotted on the basalt tetrahedron.....	236
Figure 4-11. Mid Ocean Ridge Basalt (MORB)-normalized Pearce (1982) plot and a chondrite-normalized REE diagram for Dharwar mafic dykes analysed in this study, in addition to the average data for Proterozoic dyke swarms of the Slave craton.....	237
Figure 4-12. Photomicrographs and scanning electron microscope secondary electron images of baddeleyite crystals isolated from Dharwar mafic dyke samples.....	238
Figure 4-13. Concordia diagram showing U-Pb IDTIMS data for baddeleyite isolated from the Harohalli dyke (JEF-99-1).	239
Figure 4-14. Concordia diagrams showing U-Pb IDTIMS data for baddeleyite isolated from the Chennekottapalle (JEF-99-7) and Penukonda (JEF-99-6) dykes.....	240
Figure 4-15. Photomicrographs of representative zircon crystals isolated from the Bandepalem (JEF-00-43) and Dandeli (JEF-00-1) dykes.....	241
Figure 4-16. Concordia diagrams showing U-Pb IDTIMS data for baddeleyite and zircon isolated from the Dandeli dyke (JEF-00-1).....	242
Figure 4-17. Concordia diagram showing U-Pb IDTIMS data for baddeleyite and zircon isolated from the Bandepalem dyke (JEF-00-43).....	243
Figure 4-18. Concordia diagrams showing U-Pb IDTIMS data for baddeleyite isolated from the Somala (JEF-99-11) and Kandlamadugu (JEF-00-55) dykes.....	244
Figure 4-19. Overview of the Dharwar craton showing an interpretation of the plausible regional extent of mafic dyke swarms dated by U-Pb in this study.....	245
Figure 4-20. Concordia diagram showing a composite regression based on U-Pb IDTIMS baddeleyite data for three dykes from the Bangalore mafic dyke swarm....	246
Figure 4-21. Correlation chart of U-Pb ages for Paleoproterozoic mafic igneous provinces from Archean provinces worldwide.....	248
Figure 4-22. Overview of the three Archean provinces sharing the most similar records of Paleoproterozoic mafic magmatism on the basis of global correlation of U-Pb ages.....	249
Figure 4-23. Paleocontinental reconstruction involving the Dharwar, Superior, and Slave cratons at ~2.2 Ga.....	250
Figure 4-24. Paleocontinental reconstruction involving the Dharwar, Superior, and Slave cratons at ~2.2 Ga.....	251
Figure 4-25. Paleocontinental reconstruction of Kurnorland showing break-up in two separate stages at 2.5-2.37 and 2.23-2.17 Ga.....	253

CHAPTER 5

- Figure 5-1.** Overview of Paleoproterozoic mafic igneous provinces of the south Indian shield dated by U-Pb IDTIMS in this study.....272
- Figure 5-2.** Comparison of electron microprobe (EM) chemical ages with isotopic (IDTIMS) ages for fourteen baddeleyite samples analysed in this study.....273
- Figure 5-3.** Global correlation of U-Pb ages for mafic magmatism in the Paleoproterozoic.....274
- Figure 5-4.** Palecontinental reconstruction of Kurnorland showing break-up in two separate stages at 2.5-2.37 Ga, and 2.23-2.17 Ga.....275

APPENDIX A

- Figure A-1.** BSE images and photomicrograph of igneous zircon in polished thin sections of BD2 mafic dykes, Bastar craton.....297
- Figure A-2.** Close-up BSE images of zircon from polished thin sections of BD2 dyke samples, highlighting three morphological types of igneous zircon and showing the petrographic context of individual EM age determinations.....298
- Figure A-3.** Plots of CaO (wt%) versus apparent age (*t*) for zircon spot analyses determined by electron microprobe (WDS) from BD2 mafic dykes.....299
- Figure A-4.** High contrast BSE images of baddeleyite and zircon from BD2 dykes showing overgrowth relationships of zircon on baddeleyite and the context of individual EM age determinations.....300
- Figure A-5.** Selected plots of geochemical data for zircon from BD2 mafic dykes....301

APPENDIX B

- Figure B-1.** BSE images of igneous zircon from BD2 dyke sample JEF-00-36.....316
- Figure B-2.** Three successive iterations of deterministic volume filling fractal growth, simulating rapid crystallization of zircon.....317
- Figure B-3.** Deterministic volume filling fractal tree simulating rapid zircon crystallization, and interpreted to represent a reasonable first approximation of the three-dimensional structure of dendritic zircon in BD2 dyke sample JEF-00-36.....318
- Figure B-4.** Comparison of natural dendritic zircon to the fractal growth model.....319

APPENDIX C

- Figure C-1.** Geological map of the Dharwar craton showing the locations of mafic dyke samples dated by electron microprobe chemical U-Th-total Pb baddeleyite and zircon analysis.....329
- Figure C-2.** UO₂* versus PbO diagrams, showing EM chemical data for baddeleyite from Southern Bastar - Cuddapah LIP.....330

Figure C-3. Plots of Nb ₂ O ₅ concentration in baddeleyite, versus apparent age (<i>t</i>) and background intensity at the upper background position for PbM α	331
Figure C-4. UO ₂ * versus PbO diagrams for baddeleyite and zircon from mafic dykes of the Dharwar craton, south India.....	332
Figure C-5. BSE images of zircon from mafic dyke sample JEF-00-1, Dharwar craton, showing spatial context of electron microprobe chemical ages.....	337

APPENDIX D

Figure D-1. Total alkalis versus silica diagram (Le Maitre, 2002) showing geochemical data for mafic dyke swarms of the Bastar craton.....	344
Figure D-2. Three representative variation diagrams showing geochemical data for mafic dyke swarms of the Bastar craton.....	345

APPENDIX E

Figure E-1. Context of EM apparent ages determined on zirconolite from the Duck Lake sill (JA HD-07) during analytical session 1.....	361
Figure E-2. BSE images of zirconolite and baddeleyite from sample JA HD-07 of the Duck Lake sill.....	362
Figure E-3. BSE images of baddeleyite from sample JA HD-07 of the Duck Lake sill, showing the locations of WDS spot analyses used in EM chemical dating.....	363
Figure E-4. Chemical isochron plot showing EM baddeleyite data for the Duck Lake sill.....	364
Figure E-5. Chemical isochron plot showing EM zirconolite data (session 1) for the Duck Lake sill.....	365
Figure E-6. Chemical isochron (errorchron) plot showing all EM zirconolite data (session 1) for zirconolite Grain of the Duck Lake sill.....	366
Figure E-7. Chemical isochron plot showing EM zirconolite data (session 2) for the Duck Lake sill.....	367
Figure E-8. Context of EM apparent ages determined on zirconolite from the Phalaborwa carbonatite, south Africa.....	368
Figure E-9. Probability density plot for electron microprobe chemical U-Th-total Pb ages for zirconolite from the Phalaborwa carbonatite, South Africa.....	369

LIST OF ABBREVIATIONS USED IN THE TEXT

BD1 – A >2.1 Ga set of metamorphosed mafic dykes, southern Bastar craton
BD2 – A 1891-1883 Ma set of dolerite dykes, southern Bastar craton
BK – Bhanupratappur-Keskal
BS – Bijapur-Sukma
BSE – Backscattered electron
CFB – Continental flood basalt
CHIME – Chemical isochron method
CIPW – (initials of four petrologists who devised the ‘CIPW’ normative classification)
CITZ – Central Indian Tectonic Zone
DLA – Diffusion-Limited Aggregation
EDC – Eastern Dharwar craton
EDS – Energy-dispersive spectrometer
EGB – Eastern Ghats Belt
EM – Electron microprobe
GSI – Geological Survey of India
GT – Gidam-Tongpal
HFSE – High field-strength elements
HMD – >2.1 Ga metamorphosed high-Mg boninite dykes, southern Bastar craton
ICP-MS – Inductively coupled plasma – mass spectrometry
IDTIMS – Isotope dilution thermal ionization mass spectrometry
LA-ICP-MS – Laser ablation – inductively coupled plasma – mass spectrometry
LA-MC-ICP-MS – Laser ablation – multi-collector – inductively coupled plasma – mass spectrometry
LIP – Large Igneous Province
MORB – Mid Ocean Ridge Basalt
MSWD – Mean Squared Weighted Deviation
NK – Narainpur-Kondagaon
REE – Rare Earth elements
SBC – Southern Bastar craton
SEM – Scanning electron microscope
SHRIMP – Sensitive high-resolution ion microprobe
SIMS – secondary ion mass spectrometry
SNC – Shergottites-Nakhlites-Chassigny
TAS – Total-alkalis versus silica
ThO₂* – measured ThO₂ concentration combined with the equivalent amount of fictive ThO₂ necessary to account for radiogenic Pb production from U decay
TTG – Tonalite-Trondhjemite-Granodiorite
UO₂* – measured UO₂ concentration combined with the equivalent amount of fictive UO₂ necessary to account for radiogenic Pb production from Th decay
WDC – Western Dharwar craton
WDS – Wavelength-dispersive spectrometer

CHAPTER 1

Introduction

Background on Mafic Dyke Swarms

Pioneering work on mafic dyke swarms late in the 20th century revealed their potentially enormous size and tectonic significance, and outlined how studying the nature of mafic dyke swarms through space and time is critical in understanding many important aspects of Earth evolution (Fahrig and Jones, 1969; Halls, 1982; Fahrig and West, 1986; Fahrig, 1987). It has now become clear that emplacement of mafic dyke swarms can be genetically linked with many other major geodynamic processes including eruption of continental flood basalt provinces (for which the dykes represent feeder systems), mantle plume activity, development of intracontinental sedimentary rift basins, ocean opening, and supercontinent break-up (Kamo et al., 1989; LeCheminant and Heaman, 1989; Ernst et al., 1995a; Ernst et al., 1995b; Courtillot et al., 1999). Advancements in U-Pb dating of mafic dykes (e.g.: Krogh et al., 1987; Heaman and Machado, 1992; Heaman and LeCheminant, 1993; Wingate et al., 1998; Wingate and Compston, 2000; Söderlund and Johansson, 2002) have enabled the acquisition of a substantial database of high precision age information on mafic magmatism through time (compiled in Ernst and Buchan, 2001a). Detailed case studies indicate that mafic dyke swarms may be emplaced over incredibly vast regions of the continental crust within geologically short time spans of less than five million years (e.g. 1267 Ma Mackenzie igneous events: LeCheminant and Heaman, 1989; Heaman and LeCheminant, 1993; Schwab et al., 2004; 780 Ma Gunbarrel magmatic event: Harlan et

al., 2003). Such short duration, large volume mafic magmatic events (formation of large igneous provinces) are commonly produced by mantle plumes, and have been tied to massive climate change and mass extinctions in the Phanerozoic (e.g.: Campbell et al., 1992), and may generate ore deposits of great economic importance (Schissel and Smail, 2001).

Origin and Tectonic Significance of Mafic Dyke Swarms

The process of mafic dyke emplacement within continents is ultimately a consequence of melt generation in the underlying mantle and extension in the continental crust (Hoek and Seitz, 1995). Dyke propagation may occur vertically above the mantle source region of the magma, and also laterally away from this source region for distances of up to ~2100 km along a level of neutral buoyancy in the crust (Ernst and Baragar, 1992; Ernst et al., 1995b). In the formation of continental flood basalt provinces (and associated continental mafic dyke swarms), magma generation may occur through decompression melting as anomalously hot asthenosphere (up to ~200° hotter than ambient mantle temperatures) rises buoyantly into lithosphere thinned and stretched above a mantle plume (White and Mackenzie, 1989). Voluminous mafic magmatism associated with continental break-up above a mantle plume, may also involve an initial stage of melt generation derived from decompression melting of the mantle lithosphere (Hawkesworth et al., 2000).

Although there is some evidence to suggest that mantle plumes and associated continental flood basalt provinces may play an active role in continental break-up (Courtilot et al., 1999), they are not a requirement and do not always lead to break-up. For example, rifting of Australia and Antarctica during the break-up of Gondwanaland

was not associated with major continental flood basalt volcanism or mantle plume activity (Storey, 1995), and eruption of the mantle plume-related ~16 Ma Columbia River flood basalt province in the north-western United States (Takahashi et al., 1998) did not result in continental break-up. Although subduction-plate boundary forces may be the principal cause for continental break-up (Storey et al., 1992), mantle plumes may to some degree control the sites of break-up and ocean opening (Storey, 1995; Courtillot et al., 1999). This was the case during opening of the Atlantic Ocean, which was guided by impingement of three separate mantle plumes and associated continental large igneous provinces. Remnants of these provinces can be found today on both sides of the Atlantic (Fig. 1-1a) (Courtillot et al., 1999). Opening of the central Atlantic Ocean followed closely formation of the ~200 Ma Central Atlantic Magmatic Province (Courtillot et al., 1999) which includes a giant radiating mafic dyke swarm (central Atlantic reconstructed swarm, Ernst et al., 1995b) that spans much of northwest Africa, northeast South America, and southwest North America (Fig. 1-1a). Such radiating dyke swarms reflect radial extension in the continental crust during buoyant up-lift above an arriving mantle plume head. Accordingly, the focal point of a giant radiating mafic dyke swarm may be used to identify ancient mantle plume centers and magma source regions, and where associated with a break-up margin provides an ideal piercing point for paleocontinental reconstructions (Heaman, 1997; Ernst and Buchan, 2001b). Mafic dykes emplaced perpendicular to a newly forming break-up margin can penetrate deep into a continental interior and may be associated with development of a failed-arm rift (Fahrig, 1987). Because of their excellent preservation potential, such dykes, which may represent part of a giant radiating swarm, provide especially valuable piercing

points in ancient Precambrian paleocontinental reconstructions because associated volcanic provinces and coast parallel dykes may have been destroyed by erosion or tectonic processes such as continent-continent collisions. A good example of this is shown by the 590 Ma Grenville dyke swarm, which formed in association with development of the Ottawa graben and opening of the Iapetus Ocean (Fig. 1-1b), and remains intact after closure of the Iapetus during the Appalachian orogeny (Kamo et al., 1995; St. Seymour and Kumarapeli, 1995).

The 1267 Ma Mackenzie dyke swarm, which spans ~ 2.7 million km² of the Canadian Shield and radiates through $\sim 150^\circ$ of arc (including the Bear River extension into Yukon: Schwab et al., 2004) is the largest mafic dyke swarm on Earth (Fahrig, 1987; Ernst et al., 1995b). High precision U-Pb dating of several mafic dykes spanning a wide distribution of sampling sites, indicates that this giant dyke swarm was emplaced in a geologically short time span of < 5 m.y. (LeCheminant and Heaman, 1989; Heaman and LeCheminant, 1993; Schwab et al., 2004). A growing number of additional U-Pb geochronological datasets for giant mafic dyke swarms including the 723 Ma Franklin and 780 Ma Gunbarrel magmatic events, demonstrate how determining precise U-Pb ages for a limited number of dyke samples in a Precambrian terrain provides a very powerful regional time marker that is useful (through cross-cutting relationships with country rocks) in elucidating crustal evolution over a large geographic area (Heaman et al., 1992; Harlan et al., 2003). In addition to providing excellent regional time markers, piercing points for paleocontinental reconstructions, and potentially a record of mantle plume activity and continental break-up, the geometry of mafic dyke swarms of known ages may be used to constrain regional paleo-stress fields in the continental crust

through space and time (Halls, 1982; Féraud et al., 1987; Ernst et al., 1995b).

Mafic dyke swarms and Paleoproterozoic Earth

A number of fundamental changes in Earth evolution took place immediately following the Archean-Proterozoic boundary (2.5 Ga), including a massive change in global climate at ~2.4 Ga resulting in global glaciation or “snowball Earth” conditions (Kirschvink et al., 2000), the first proliferation of Superior-type banded iron formation at ~2.45-2.4 Ga (Barley et al., 1997; Abbott and Isley, 2001), a change in the sulfur cycle at 2.45-2.09 Ga (Farquhar et al., 2000), oxygenation of the atmosphere at ~2.3 Ga during the “Great Oxidation Event” (Holland, 2002), a major increase in the $^{87}\text{Sr}/^{86}\text{Sr}$ signature of seawater (Veizer, 1976), a large increase in the $\delta^{13}\text{C}$ values of marine carbonates at 2.22-2.06 Ga (Holland, 2002), possible collapse of the stable density stratification in the core at ~2.5 Ga (Kumazawa et al., 1994), and nucleation of the solid inner core of Earth by ~2.5 Ga (Smirnov et al., 2003). Many of these drastic changes to major Earth systems were synchronous with a sudden proliferation of continental mafic magmatism at 2.5-2.4 Ga that also shows a global coincidence in timing with high-grade metamorphism (Heaman, 1997; Heaman, 2002). There may have been a direct genetic link between 2.45 Ga mafic magmatism and some of these other geological events including deposition of banded iron formation (Barley et al., 1997), global high-grade metamorphism (Heaman, 2002), and core processes (Heaman, 1997). Many changes taking place in the early Paleoproterozoic atmosphere and oceans were interrelated including the rise of oxygen and changes in the Sulfur cycle (Farquhar et al., 2000), and may have been directly linked with changes in volcanic out-gassing (Holland, 2002). Constraining the changing configuration of the continents through the Paleoproterozoic

(aided by U-Pb dating of mafic dyke swarms) is critical in understanding global climate change during this time, because it has been proposed that a preponderance of continents in the middle to low latitudes could have set the stage for a snowball Earth event at this time (Hoffman and Schrag, 2002).

Paleoproterozoic Continents and India

Probably the most accurate piercing points being used to reconstruct continents in the early Paleoproterozoic are large igneous provinces associated with continental break-up events for which high precision U-Pb ages and paleomagnetic data are available (e.g.: juxtaposition of the Superior and Karelian cratons at ~2.45 Ga: Heaman, 1997; Mertanen et al., 1999; Pesonen et al., 2003). But the configuration of continental blocks (and potentially a supercontinent) in the early Paleoproterozoic is currently not very well constrained, and paleocontinental reconstructions older than Rodinia (~1.0 Ga) are to a large degree premature and inferred from very indirect evidence (Rogers, 1996). The current database of geochronological and paleomagnetic information suggests that a large continental landmass called Kenorland existed in equatorial regions at ~2.45 Ga. Kenorland which included at least Laurentia, Baltica, Australia, and the Kalahari craton, appears to have undergone a protracted period of break-up from ~2.45-2.10 Ga (Pesonen et al., 2003). Another large continent thought to have been in existence as early as ~3.0 Ga is the original continent Ur proposed by Rogers (1993, 1996) which included much of the Indian shield (Dharwar, Bastar, and Singhbhum cratons), the Kaapvaal craton of south Africa, the Pilbara craton of northwest Australia and parts of eastern Madagascar and Antarctica. The principal geological argument for the inclusion of most of these Archean provinces within Ur is the ubiquity of old (3.0-2.8 Ga) shallow-water

supracrustal sequences coupled with the proximity of these provinces within Gondwanaland (Rogers, 1996). A recent paleomagnetic study of rocks from the south Indian granulite terrain provides additional support for the existence of Ur between ~2900-2200 Ma (Piper et al., 2003). Potential geographic links between Ur and Kenorland at 2.45 Ga (i.e.: the existence of a supercontinent) are currently sparse, but include the possible connection of the Kalahari craton (which includes the Kaapvaal craton) to Kenorland at 2.45 Ga (Pesonen et al., 2003). By inference, this connection may include the rest of Zimvaalbara, another large continental landmass that has been proposed to have coexisted with Kenorland at ~2.45 Ga (Aspler and Chiarenzelli, 1998). Zimvaalbara comprises the Zimbabwe, Kaapvaal, and Pilbara cratons, and possibly the São Francisco craton in addition to continental blocks in India. The Dharwar, Bastar, and Singhbhum cratons of southern India (Fig. 1-2) are central to many proposed reconstructions of Proterozoic supercontinents including 3.0-2.2 Ga Ur (Rogers, 1993; Rogers, 1996; Piper et al., 2003), ~1.7 Ga Capricornia (Krapez, 1999), and ~1.5 Ga Columbia (Rogers and Santosh, 2002), and these cratons (especially the Dharwar) are transected by numerous Proterozoic mafic dyke swarms (Halls, 1982; Murty et al., 1987; Murthy, 1995) for which there is currently an almost complete lack of accurate age information. In light of the relevance of the south Indian shield to early Precambrian plate reconstructions and the apparently dominant role of mafic dyke swarm emplacement in the Paleoproterozoic crustal evolution of this region, one of the principal goals of this study is to obtain, for the first time, accurate, high-precision U-Pb isotopic ages for a number of mafic dyke swarms of the Dharwar and Bastar cratons.

Study Areas in Southern India

An enormous amount of previous research has been carried out on Proterozoic mafic magmatism in south India (see Chapter's 3 and 4), and indicates that a very protracted and complex history of mafic dyke swarm emplacement took place in the Dharwar craton from ~2.5 Ga to ~0.65 Ga (e.g.: Murty et al., 1987; Mallikarjuna Rao et al., 1995; Murthy, 1995), and that at least three episodes of Paleoproterozoic mafic dyke swarm emplacement took place in the Bastar craton (Ramakrishnan, 1990; Srivastava et al., 1996; Srivastava et al., 2000; Srivastava and Singh, 2003; Srivastava and Singh, 2004). The present research project, which is focused on U-Pb dating of mafic dyke swarms in the Dharwar and Bastar cratons, aims to build upon these pioneering studies, of which more detailed summaries may be found in Chapters 3 and 4.

The project commenced with a three-month field excursion by the author to south central India starting in December 1999, and support and technical assistance in the field was provided by Dr. Larry Heaman of the University of Alberta, Drs. Rajesh K. Srivastava and R.K. Singh of the Banaras Hindu University, and colleague Mathew Mylod. Fieldwork was focused primarily on reconnaissance geochron sampling of mafic dyke swarms from the Dharwar and Bastar cratons, but also included sampling of a variety of other basement rocks as well. Strategies for U-Pb geochron sampling of igneous rocks generally included carefully collecting 10-20 kg samples of suitably coarse grained and fresh (i.e.: non- to minimally weathered) material. Where possible samples were obtained from active rock quarries. In total, 79 rock samples were collected including 47 mafic igneous rocks (41 mafic dyke samples, 3 mafic volcanic rocks from the Bastar craton, and 3 mafic sills from the Cuddapah basin) comprising a

representative sampling of a large number of the major Precambrian mafic dyke swarms in the Dharwar (Fig. 1-3) and Bastar (Fig. 1-4) cratons. A variety of other country rock samples were also collected (see Appendix F). The densest concentration of mafic dyke swarms in southern India occurs in the eastern block of the Dharwar craton around the Proterozoic Cuddapah basin, where numerous crosscutting, crustal scale mafic dyke swarms of various orientations occur and potentially represent as many as 18 separate Proterozoic swarms (Halls, 1982; Murty et al., 1987; Mallikarjuna Rao et al., 1995). Geochron sampling in the Dharwar craton was focussed primarily on mafic dyke swarms of different orientations around the Cuddapah basin, in addition to mafic sills within the basin (Fig. 1-3). Particular focus was placed on sampling a prominent E-W trending dyke swarm from the southeastern Dharwar craton because of its apparently large size (Halls, 1982) and early Paleoproterozoic Rb-Sr age of ca. 2.4 Ga (Ikramuddin and Stueber, 1976). This swarm has also been the subject of numerous paleomagnetic investigations (Kumar and Bhall, 1983; Dawson and Hargraves, 1994; Prasad et al., 1999). Dyke swarm sampling in the Bastar craton was focussed in a 40 by 25 km region of the southern Bastar craton (Fig. 1-4) in collaboration with Dr. Rajesh K. Srivastava (Banaras Hindu University), where at least three geochemically and petrographically distinct mafic dyke swarms of approximately Paleoproterozoic age are known to occur (Srivastava et al., 1996; Srivastava et al., 2000; Srivastava and Singh, 2003; Srivastava and Singh, 2004).

Strategies and Methodology in U-Pb Dating of Mafic Dyke Samples

A number of late-crystallizing U- and Th-bearing accessory minerals may potentially be used as geochronometers in determining the timing of emplacement of

mafic dykes by U-Pb isotopic dating, including baddeleyite (ZrO_2), zircon (ZrSiO_4), rutile (TiO_2), zirconolite ($\text{CaZrTi}_2\text{O}_7$), and monazite ($\text{Ce,La,Nd,Th} \text{PO}_4$) (Krogh et al., 1987; Heaman and LeCheminant, 1993; Oberthür et al., 2002; Rasmussen and Fletcher, 2004; Chapter 3, this thesis). Of these possible candidates for U-Pb dating, baddeleyite is the mineral of choice because of its relatively common occurrence in mafic dykes, high U content, low common Pb content, high estimated closure temperature and resistance to Pb-loss, and ability to retain crystallization ages during partial decomposition to zircon during metamorphism (Heaman and LeCheminant, 1993). As such, for the mafic dyke swarms of southern India under investigation in this study, the primary objective has been to determine high precision U-Pb IDTIMS (Isotope Dilution Thermal Ionization Mass Spectrometry) ages on baddeleyite (\pm igneous zircon) crystals isolated from dyke samples by mechanical mineral separation techniques. On account of its elongate bladed habit, conventional mineral separation commonly results in poor baddeleyite recovery (Söderlund and Johansson, 2002). Accordingly, U-Pb dating can be difficult because even very large dyke samples (e.g.: 49 kg) processed by this technique may still yield an extremely low number of baddeleyite grains (Heaman, 1997). Although conventional mineral separation was successful in isolating ample baddeleyite for some mafic dyke samples in this study, the overall success rate was quite low, particularly for samples with relatively fine-grained baddeleyite ($<30 \mu\text{m}$). To mitigate this problem, I employed the water-based method of baddeleyite separation recently developed by Söderlund and Johansson (2002).

In contextural dating studies of miniscule monazite crystals (or crystal domains) in polished thin section, the electron microprobe chemical U-Th-total Pb (EM) dating

technique is now routinely used, and enables determination of rapid textural age information with a spatial resolution of $\sim 1\mu\text{m}$ (Suzuki and Adachi, 1991; Montel et al., 1996; Cocherie et al., 1998; Williams et al., 1999). As an additional effort to determine baddeleyite crystallization ages for mafic dykes with fine-grained baddeleyite in this study, one aspect of this research project has been to explore the feasibility of U-Th-total Pb chemical baddeleyite dating by electron microprobe (French et al., 2002; Chapter 2). Additional EM dating studies were carried out on a variety of accessory minerals in mafic dykes from south India including zircon (Appendix A), baddeleyite (Appendix C), monazite (Chapter 3), and zirconolite (Appendix E). A comprehensive EM study of the chemical and morphological characteristics of igneous zircon from the BD2 mafic dyke swarm is presented in Appendix A, and the 3-dimensional structure of the dendritic variety of zircon is estimated using a model of deterministic volume-filling fractal growth (Appendix B).

All rock crushing, mineral separation, and U-Pb IDTIMS analysis (employing a VG354 mass spectrometer) was carried out by the author at the Radiogenic Isotope Facility in the Department of Earth and Atmospheric Sciences at the University of Alberta, with the guidance and technical support of Dr. Larry Heaman and Stacey Hagen. Electron Microprobe analysis was also carried out by the author in this Department on a JEOL 8900 Electron Microprobe equipped with five wavelength-dispersive spectrometers and one energy-dispersive spectrometer, with guidance and technical support of Dr. Tom Chacko, Dr. Lang Shi, and Dr. Sergei Matveev. In-situ dating of monazite in one polished petrographic thin section (sample JEF-00-30, Chapter 3) by LA-MC-ICP-MS (Laser Ablation – Multi Collector - Inductively Coupled Plasma

– Mass Spectrometry) was carried out by Dr. Antonio Simonetti employing a Nu Plasma MC-ICP-MS coupled to a Nd:YAG laser ablation system ($\lambda=213\text{nm}$). Additional help and advice during data acquisition for this sample was provided by Dr. Tom Chacko. All U-Pb isotopic ages were calculated by the author using an in-house program and version Ex/3.00 of the Isoplot program (Ludwig, 2003). Chemical U-Th-total Pb age calculations were carried out by the author after the method of Suzuki and Adachi (1991), and facilitated by a spreadsheet designed by Dr. Tom Chacko.

Presentation

A paper format was chosen for this thesis and so the research results are presented as three separate papers (Chapters 2 to 4) in a fashion similar to how they would appear in a scientific journal. Chapter 2 presents the results of a feasibility study aimed at applying the Electron Microprobe chemical U-Th-total Pb dating technique to the mineral baddeleyite, and is essentially as it appears in the published version in the journal *Chemical Geology* (French et al., 2002). The results of U-Pb radiometric dating of mafic dyke swarms from southern India are presented as two separate papers (Chapters 3 and 4). Chapter 3 focuses on U-Pb dating of a late Paleoproterozoic (~1.88 Ga) large igneous province that has been identified in this project. This LIP, which bridges the Godavari Rift (Fig. 1-2), occurs as a mafic dyke swarm in the southern Bastar craton and a mafic sill province within the Cuddapah basin of the Dharwar craton. The implications for late Paleoproterozoic crustal evolution of the Dharwar protocontinent are discussed, as well as possible links with concurrent geological events taking place elsewhere in Ur and other Archean cratons worldwide. Chapter 4 presents the results of a U-Pb IDTIMS baddeleyite (\pm zircon) dating study of seven mafic dykes

from the Dharwar craton, defining major episodes of Paleoproterozoic mafic dyke swarm emplacement at 2.37 Ga, 2.21 Ga, and 2.18 Ga. The Paleoproterozoic mafic magmatic record for southern India defined in this project by U-Pb dating of baddeleyite and zircon, is compared to the available database of U-Pb ages for Paleoproterozoic mafic igneous provinces in Archean cratons worldwide. The implications for Paleoproterozoic continental reconstructions are considered in light of these new age data. Chapter 5 presents a summary of the research conducted in this thesis, providing an overview of the major conclusions to be drawn in addition to suggestions for future research directions.

References

- Abbott, D. & Isley, A. (2001). Oceanic upwelling and mantle-plume activity: Paleomagnetic tests of ideas on the source of the Fe in early Precambrian iron formations. In: *Ernst, R.E. & Buchan, K.L., (eds.), Mantle Plumes: Their Identification Through Time – Geological Society of America Special Paper 352*, 323-339.
- Aspler, L.B. & Chiarenzelli, J.R. (1998). Two Neoproterozoic supercontinents? Evidence from the Paleoproterozoic. *Sedimentary Geology* **120**, 75-104.
- Barley, M.E., Pickard, A.L., & Sylvester, P.J. (1997). Emplacement of a large igneous province as a possible cause of banded iron formation 2.45 billion years ago. *Nature* **385**, 55-58.
- Campbell, I.H., Czamanske, G.K., Fedorenko, V.A., Hill, R.I., & Stepanov, V. (1992). Synchronism of the Siberian Traps and the Permian-Triassic Boundary. *Science* **258**, 1760-1763.
- Cocherie, A., Legendre, O., Peucat, J. J., Kouamelan, A. N. (1998). Geochronology of polygenetic monazites constrained by in situ electron microprobe Th-U-total lead determination: Implications for lead behaviour in monazite. *Geochimica et Cosmochimica Acta* **62**, 2475-2497.
- Courtillot, V., Jaupart, C., Manighetti, I., Tapponnier, P., & Besse, J. (1999). On causal links between flood basalts and continental breakup. *Earth and Planetary Science Letters* **166**, 177-195.
- Crookshank, H. (1963). Geology of southern Bastar and Jeypore from the Bailadila

range to the Eastern Ghats. *Memoirs of the Geological Survey of India* **87**, 149p.

Dawson, E.M. & Hargraves, R.B. (1994). Paleomagnetism of Precambrian dike swarms in the Harohalli area, south of Bangalore, India. *Precambrian Research* **69**, 157-167.

Ernst, R.E. & Baragar, W.R.A. (1992). Evidence from magnetic fabric for the flow pattern of magma in the Mackenzie giant radiating dyke swarm. *Nature* **356**, 511-513.

Ernst, R.E., Buchan, K.L., & Palmer, H.C. (1995a). Giant dyke swarms: Characteristics, distribution and geotectonic applications. In: *Baer & Heimann (eds.), Physics and Chemistry of Dykes*, 3-21.

Ernst, R.E., Head, J.W., Parfitt, E., Grosfils, E., & Wilson, L. (1995b). Giant radiating dyke swarms on Earth and Venus. *Earth-Science Reviews* **39**, 1-58.

Ernst, R.E. & Buchan, K.L. (2001a). Large mafic magmatic events through time and links to mantle-plume heads. In: *Ernst, R.E. & Buchan, K.L., (eds.), Mantle Plumes: Their Identification Through Time – Geological Society of America Special Paper 352*, 483-566.

Ernst, R.E. & Buchan, K.L. (2001b). The use of mafic dike swarms in identifying and locating mantle plumes. In: *Ernst, R.E. & Buchan, K.L., (eds.), Mantle Plumes: Their Identification Through Time – Geological Society of America Special Paper 352*, 247-265.

Fahrig, W.F. & Jones, D.L. (1969). Paleomagnetic Evidence for the Extent of Mackenzie Igneous Events. *Canadian Journal of Earth Sciences* **6**, 679-688.

Fahrig, W.F. & West, T.D. (1986). Diabase Dyke Swarms of the Canadian Shield: Geological Survey of Canada Map 1627A.

Fahrig, W.F. (1987). The tectonic settings of continental mafic dyke swarms: failed arm and early passive margin. In: *Halls, H.C. and Fahrig, W.F., (eds.), Mafic Dyke Swarms, Geological Association of Canada Special Paper 34*, 331-348.

Farquhar, J., Bao H., & Thiemans, M.H. (2000). Atmospheric influence of Earth's earliest sulfur cycle. *Science* **289**, 756-759.

Féraud, G., Giannérini, G., & Campredon. (1987). Dyke Swarms as Paleostress Indicators in Areas Adjacent to Continental Collision Zones: Examples from the European and Northwest Arabian Plates. In: *Halls, H.C. and Fahrig, W.F., (eds.), Mafic Dyke Swarms, Geological Association of Canada Special Paper 34*, 273-278.

French, J.E., Heaman, L.M., & Chacko, T. (2002). Feasibility of chemical U-Th-total Pb baddeleyite dating by Electron Microprobe. *Chemical Geology* **188**, 85-104.

- GSI. (1998). Geological Map of India, 1:2,000,000 scale. Geological Survey of India, Hyderabad.
- Halls, H.C. (1982). The importance and potential of mafic dyke swarms in studies of geodynamic processes. *Geoscience Canada* **9**, 145-153.
- Harlan, S.S., Heaman, L., LeCheminant, A.N., & Premo, W.R. (2003). Gunbarrel mafic magmatic event: A key 780 Ma time marker for Rodinia plate reconstructions. *Geology* **31**, 1053-1056.
- Hawkesworth, C.J., Gallagher, K., Kirstein, L., Mantovani, M.S.M., Peate, D.W., & Turner, S.P. (2000). Tectonic controls on magmatism associated with continental break-up: an example from the Paraná-Etendeka Province. *Earth and Planetary Science Letters* **179**, 335-349.
- Heaman, L.M. (1997). Global mafic magmatism at 2.45 Ga: Remnants of an ancient large igneous province? *Geology* **25**, 299-302.
- Heaman, L.M. (2002). Musings on 2.45 Ga Earth: The temporal link between global mafic magmatism and high grade metamorphism. *GAC/MAC Abstracts Volume 27*, 48.
- Heaman, L.M. & Machado, N. (1992). Timing and origin of midcontinent rift alkaline magmatism, North America: evidence from the Coldwell Complex. *Contributions to Mineralogy and Petrology* **110**, 289-303.
- Heaman, L.M., LeCheminant, A.N., & Rainbird, R.H. (1992). Nature and timing of Franklin igneous events, Canada: Implications for a Late Proterozoic mantle plume and the break-up of Laurentia. *Earth and Planetary Science Letters* **109**, 117-131.
- Heaman, L.M. & LeCheminant, A.N. (1993). Paragenesis and U-Pb systematics of baddeleyite (ZrO₂). *Chemical Geology* **110**, 95-126.
- Hoek, J.D. & Seitz, H.-M. (1995). Continental mafic dyke swarms as tectonic indicators: an example from the Vestfold Hills, East Antarctica. *Precambrian Research* **75**, 121-139.
- Hoffman, P.F. & Schrag, D.P. (2002). The snowball Earth hypothesis: testing the limits of global change. *Terra Nova* **14**, 129-155.
- Holland, H.D. (2002). Volcanic gases, black smokers, and the Great Oxidation Event. *Geochimica et Cosmochimica Acta* **66**, 3811-3826.
- Ikramuddin, M. & Stueber, A.M. (1976). Rb-Sr ages of Precambrian dolerite and alkaline dikes, southeast Mysore State, India. *Lithos* **9**, 235-241.
- Kamo, S.L., Gower, C.F., & Krogh, T.E. (1989). Birthdate for the Iapetus Ocean? A

precise U-Pb zircon and baddeleyite age for the Long Range dikes, southeast Labrador. *Geology* **17**, 602-605.

Kamo, S.L., Krogh, T.E., & Kumarapeli, P.S. (1995). Age of the Grenville dyke swarm, Ontario-Quebec: implications for the timing of Iapetan rifting. *Canadian Journal of Earth Sciences* **32**, 273-280.

Kirschvink, J.L., Gaidos, E.J., Bertani, L.E., Beukes, N.J., Gutzmer, J., Maepa, L.N., & Steinberger, R.E. (2000). Paleoproterozoic snowball Earth: Extreme climatic and geochemical global change and its biological consequences. *PNAS* **97**, 1400-1405.

Krapez, B. (1999). Stratigraphic record of an Atlantic-type global tectonic cycle in the Palaeoproterozoic Ashburton Province of Western Australia. *Australian Journal of Earth Sciences* **46**, 71-87.

Krogh, T.E., Corfu, F., Davis, D.W., Dunning, G.R., Heaman, L.M., Kamo, S.L., Machado, N., Greenough, J.D., & Nakamura, E. (1987). Precise U-Pb isotopic ages of diabase dykes and mafic to ultramafic rocks using trace amounts of baddeleyite and zircon. In: Halls, H.C. and Fahrig, W.F., eds., *Mafic Dyke Swarms*, Geological Association of Canada Special Paper **34**, 147-152.

Kumar, A. & Bhall, M.S. (1983). Palaeomagnetism and igneous activity of the area adjoining the south-western margin of the Cuddapah basin, India. *Geophysical Journal of the Royal Astronomical Society* **73**, 27-37.

Kumazawa, M., Yoshida, S., Ito, T., & Yoshioka, H. (1994). Archaean-Proterozoic boundary interpreted as a catastrophic collapse of the stable density stratification in the core. *Journal of the Geological Society of Japan* **100**, 50-59.

LeCheminant, A.N. & Heaman, L.M. (1989). Mackenzie igneous events, Canada: Middle Proterozoic hotspot magmatism associated with ocean opening. *Earth and Planetary Science Letters* **96**, 38-48.

Ludwig, K. R. (2003). ISOPLOT a plotting and regression program for radiogenic isotope data, version Ex/3.00.

Mallikarjuna Rao, J., Bhattacharji, S., Rao, M.N., & Hermes, O.D. (1995). ^{40}Ar - ^{39}Ar Ages and Geochemical Characteristics of Dolerite Dykes Around the Proterozoic Cuddapah Basin, South India. In: Devaraju, T.C., ed., *Mafic Dyke Swarms of Peninsular India*, Geological Society of India Memoir **33**, 307-328.

Mertanen, S., Halls, H.C., Vuollo, J.I., Pesonen, L.J., & Stepanov, V.S. (1999). Paleomagnetism of 2.44 Ga mafic dykes in Russian Karelia, eastern Fennoscandian Shield – implications for continental reconstructions. *Precambrian Research* **98**, 197-221.

Mishra, D.C., Singh, B., Tiwari, V.M., Gupta, S.B., & Rao, M.B.S.V. (2000). Two cases of continental collisions and related tectonics during the Proterozoic period in India – insights from gravity modelling constrained by seismic and magnetotelluric studies. *Precambrian Research* **99**, 149-169.

Montel, J.-M., Foret, S., Veschambre, M., Nicollet, C., & Provost, A. (1996). Electron Microprobe dating of monazite. *Chemical Geology* **131**, 37-53.

Moyen, J.-F., Nédélec, A., Martin, H., & Jayananda, M. (2003). Syntectonic granite emplacement at different structural levels: the Closepet granite, South India. *Journal of Structural Geology* **25**, 611-631.

Murthy, N.G.K. (1995). Proterozoic mafic dykes in southern peninsular India: A review. In: Devaraju, T.C., ed., *Mafic Dyke Swarms of Peninsular India*, Geological Society of India Memoir **33**, 81-98.

Murty, Y.G.K., Babu Rao, V., Guptasarma, D., Rao, J.M., Rao, M.N., & Bhattacharji, S. (1987). Tectonic, petrochemical and geophysical studies of mafic dyke swarms around the Proterozoic Cuddapah basin, South India. In: Halls, H.C. & Fahrig, W.F., eds., *Mafic Dyke Swarms*, Geological Association of Canada Special Paper **34**, p.303-316.

Nagaraja Rao, B.K., Rajurkar, S.T., Ramalingaswamy, G., & Ravindra Babu, B. (1987). Stratigraphy, Structure and Evolution of the Cuddapah Basin. In: *Purāna Basins of Peninsular India (Middle to Late Proterozoic)*, Geological Society of India Memoir **6**, 33-86.

Naqvi, S.M. & Rogers, J.J.W. (1987). Precambrian Geology of India, *Oxford monographs on geology and geophysics* **6**, 233p.

Oberthür, T., Davis, D.W., Blenkinsop, T.G., & Höhndorf, A. (2002). Precise U-Pb mineral ages, Rb-Sr and Sm-Nd systematics for the Great Dyke, Zimbabwe-constraints on late Archean events in the Zimbabwe craton and Limpopo belt. *Precambrian Research* **113**, 293-305.

Pandey, B.K., Gupta, J.N., Sarma, K.J., & Sastry, C.A. (1997). Sm-Nd, Pb-Pb and Rb-Sr geochronology and petrogenesis of the mafic dyke swarm of Mahbubnagar, South India: implications for Paleoproterozoic crustal evolution of the Eastern Dharwar Craton. *Precambrian Research* **84**, 181-196.

Pesonen, L.J., Elming, S.-Å., Mertanen, S., Pisarevsky, S., D'Agrella-Filho, M.S., Meert, J.G., Schmidt, P.W., Abrahamsen, N. & Bylund, G. (2003). Paleomagnetic configuration of continents during the Proterozoic. *Tectonophysics* **375**, 289-324.

Piper, J.D.A., Basu Mallik, S., Bandyopadhyay, G., Mondal, S., & Das, A.K. (2003). Paleomagnetic and rock magnetic study of a deeply exposed continental section in the Charnockite Belt of southern India: implications to crustal magnetisation and

paleoproterozoic continental nuclei. *Precambrian Research* **121**, 185-219.

Prasad, J.N., Satyanarayana, K.V.V., & Gawali, P.B. (1999). Paleomagnetic and Low-Field AMS Studies of Proterozoic Dykes and their Basement Rocks Around Harohalli, South India. *Journal of the Geological Society of India* **54**, 57-67.

Radhakrishna, T. & Joseph, M. (1998). Geochemistry and petrogenesis of the Proterozoic dykes in Tamil Nadu, southern India: another example of the Archaean lithospheric mantle source. *International Journal of Earth Sciences* **87**, 268-282.

Ramakrishnan, M. (1990). Crustal development in southern Bastar central Indian craton. Geological Survey of India Special Publication 28, 44-66.

Rao, J.M., Rao, G.V.S.P., & Patil, S.K. (1990). Geochemical and paleomagnetic studies on the Middle Proterozoic Karimnagar mafic dyke swarm, India. In: Parker, Rickwood & Tucker, eds., *Mafic Dykes and Emplacement Mechanisms*, 373-382.

Rasmussen, B. & Fletcher, I.R. (2004). Zirconolite: A new U-Pb geochronometer for mafic igneous rocks. *Geology* **32**(9), 785-788.

Rogers, J.J.W. (1993). India and Ur. *Journal of the Geological Society of India* **42**, 217-222.

Rogers, J.J.W. (1996). A history of continents in the past three billion years. *The Journal of Geology* **104**, 91-107.

Rogers, J.J.W & Santosh, M. (2002). Configuration of Columbia, a Mesoproterozoic supercontinent. *Gondwana Research* **5**, 5-22.

Schissel, D. & Smail, R. (2001). Deep-mantle plumes and ore deposits. In: Ernst, R.E. & Buchan, K.L., eds., *Mantle Plumes: Their Identification Through Time – Geological Society of America Special Publication* **352**, 291-322.

Schwab, D.L., Thorkelson, D.J., Mortensen, J.K., Creaser, R.A., & Abbott, J.G. (2004). The Bear River dykes (1265-1269 Ma): westward continuation of the Mackenzie dyke swarm into Yukon, Canada. *Precambrian Research* **133**, 175-186.

Smirnov, A.V., Tarduno, J.A., & Pisakin, B.N. (2003). Paleointensity of the early geodynamo (2.45 Ga) as recorded in Karelia: A single-crystal approach. *Geology* **31**, 415-418.

Söderlund, U. & Johansson, L. (2002). A simple way to extract baddeleyite (ZrO₂). *Geochemistry Geophysics Geosystems* **3**(2), 1-7.

Srivastava, R.K., Hall, R.P., Verma, R., & Singh, R.K. (1996). Contrasting Precambrian mafic dykes of the Bastar craton, central India: petrological and geochemical

characteristics. *Journal of the Geological Society of India* **48**, 537-546.

Srivastava, R.K., Heaman, L.M., French, J.E., & Singh, R.K. (2000). 1.8 Ga old dolerite dyke swarm from the southern Bastar craton, central India: implications on east Gondwanaland reconstruction. *Abstracts of Papers: The National Symposium on Milestones in Petrology & Annual Convention of Geological Society of India, Varanasi*. 50.

Srivastava, R.K., & Singh, R.K. (2003). Geochemistry of high-Mg mafic dykes from the Bastar craton: evidence of late Archean boninite-like rocks in an intracratonic setting. *Current Science* **85**, 808-812.

Srivastava, R.K. & Singh, R.K. (2004). Trace element geochemistry and genesis of Precambrian sub-alkaline mafic dikes from the central Indian craton: evidence for mantle metasomatism. *Journal of Asian Earth Sciences* **23**, 373-389.

Storey, B.C., Alabaster, T., Hole, M.J., Pankhurst, R.J., & Wever, H.E. (1992). Role of subduction-plate boundary forces during the initial stages of Gondwana break-up: evidence from the proto-Pacific margin of Antarctica. In: Storey, B.C., Alabaster, T. & Pankhurst, R.J. (eds.), *Magmatism and the Causes of Continental Break-up, Geological Society Special Publication* **68**, 149-163.

Storey, B.C. (1995). The role of mantle plumes in continental break-up: case histories from Gondwanaland. *Nature* **377**, 301-308.

St. Seymour, K. & Kumarapeli, P.S. (1995). Geochemistry of the Grenville dyke swarm: role of plume-source mantle in magma genesis. *Contributions to Mineralogy and Petrology* **120**, 29-41.

Suzuki, K. & Adachi, M. (1991). Precambrian provenance and Silurian metamorphism of the Tsubonosawa paragneiss in the South Kitakami terrane, Northeast Japan, revealed by the chemical Th-U-total Pb isochron ages of monazite, zircon, and xenotime. *Geochemical Journal* **25**, 357-376.

Takahashi, E., Nakajima, K., & Wright, T.L. (1998). Origin of the Columbia River basalts: melting model of a heterogeneous plume head. *Earth and Planetary Science Letters* **162**, 63-80.

Veizer, J. (1976). $^{87}\text{Sr}/^{86}\text{Sr}$ evolution of seawater during geologic history and its significance as an index of crustal evolution. In: Windley, B.F. (ed.), *The Early History of the Earth*, Wiley, London, 569-578.

White, R. & McKenzie, D. (1989). Magmatism at Rift Zones: The Generation of Volcanic Continental Margins and Flood Basalts. *Journal of Geophysical Research* **94**, No. B6, 7685-7729.

Williams, M. L., Jercinovic, M. J., Terry, M. P. 1999. Age mapping and dating of monazite on the electron microprobe: Deconvoluting multistage tectonic histories. *Geology* **27**, 1023-1026.

Wingate, M. T. D., Compston, W. 2000. Crystal orientation effects during ion microprobe U-Pb analysis of baddeleyite. *Chemical Geology* **168**, 75-97.

Wingate, M. T. D., Campbell, I. H., Compston, W., Gibson, G. M. 1998. Ion microprobe U-Pb ages for Neoproterozoic basaltic magmatism in south-central Australia and implications for the breakup of Rodinia. *Precambrian Research* **87**, 135-159.

Zhao, G., Sun, M., & Wilde, S. (2003). Correlations between the eastern block of the North China craton and the South Indian block of the Indian shield: an Archean to Paleoproterozoic link. *Precambrian Research* **122**, 201-233.

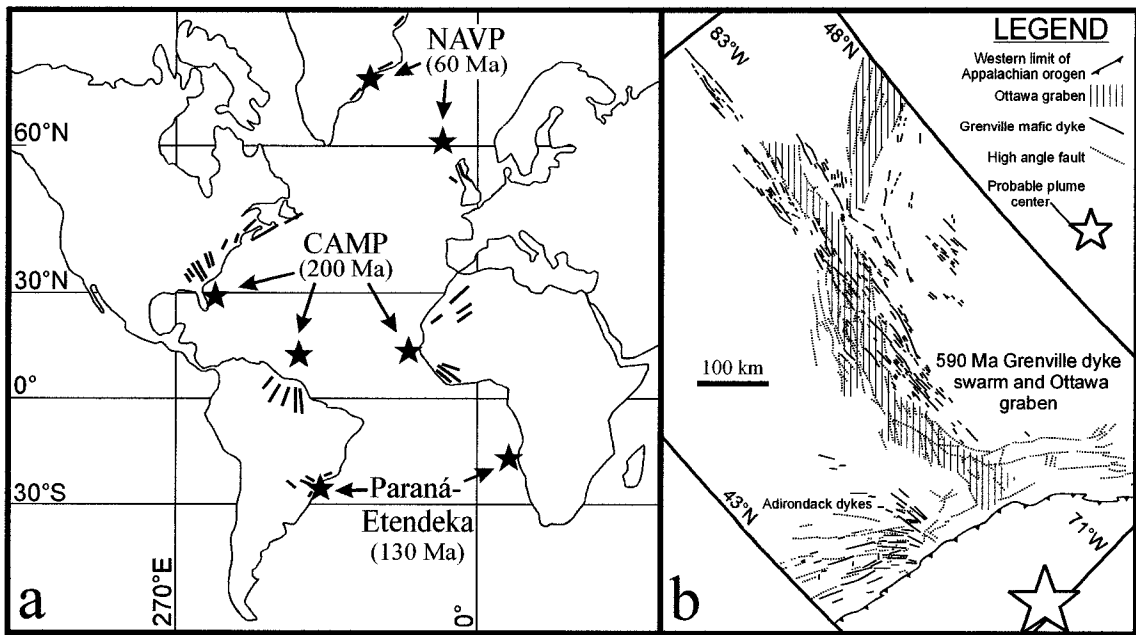


Fig. 1-1. a) Distribution of mafic dyke swarms and inferred mantle plume centres associated with opening of the Atlantic Ocean. Abbreviations: CAMP Central Atlantic magmatic province; NAVP North Atlantic volcanic province. (Modified from: Ernst and Buchan, 2001b). b) Geological map of the 590 Ma Grenville dyke swarm and Ottawa graben associated with opening of the Iapetus Ocean. (Geology modified from: Kamo et al., 1995; probable mantle plume center from: St. Seymour and Kumarapeli, 1995).

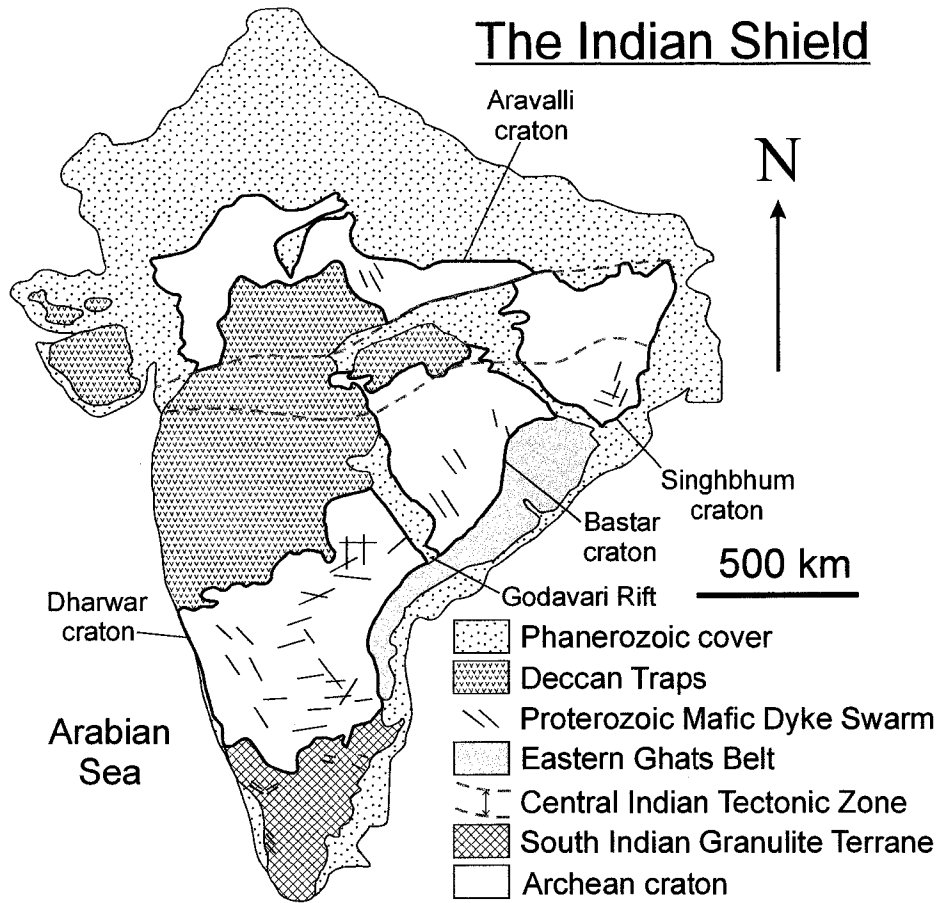


Fig. 1-2. The principle tectonic elements of the Indian shield including Archean cratons and major Proterozoic mafic dyke swarms. (Geology modified from: Naqvi and Rogers, 1987; Murthy, 1995; GSI, 1998; Mishra et al., 2000; Zhao et al., 2003).

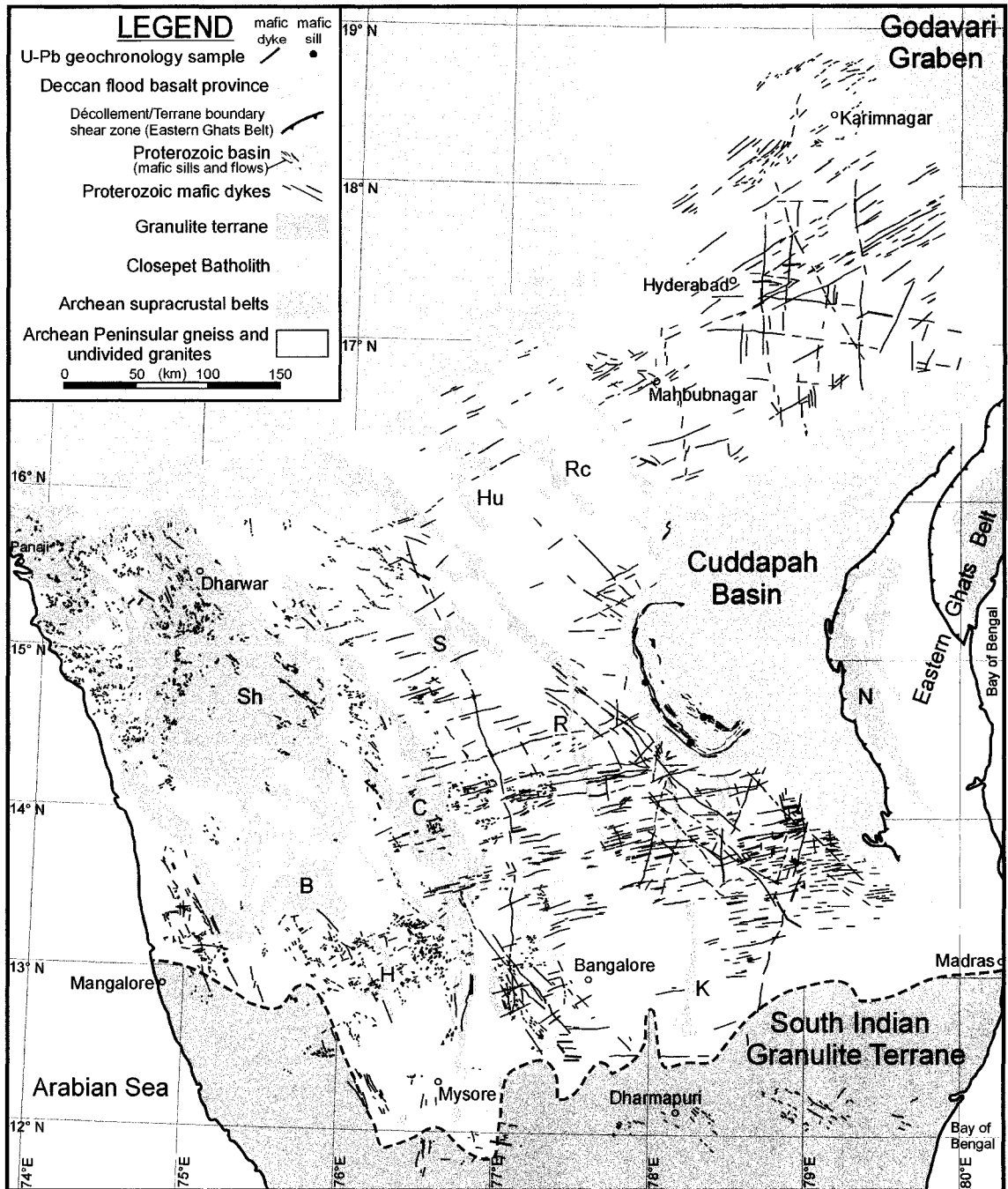


Fig. 1-3. Geological map of the Dharwar craton showing the distribution of Proterozoic mafic dykes and the locations of mafic dykes and sills sampled for U-Pb dating in this study. Greenstone belts: B Bababudan; C Chitradurga; H Holenarsipur; Hu Hutti; K Kolar; N Nellore; R Ramagiri; Rc Raichur; S Sandur; Sh Shimoga. (Geology modified from: GSI, 1981; Halls, 1982; Nagaraja Rao et al., 1987; Murty et al., 1987; Rao et al., 1990; Pandey et al., 1997; GSI, 1998; Radhakrishna and Joseph, 1998; Moyen et al., 2003).

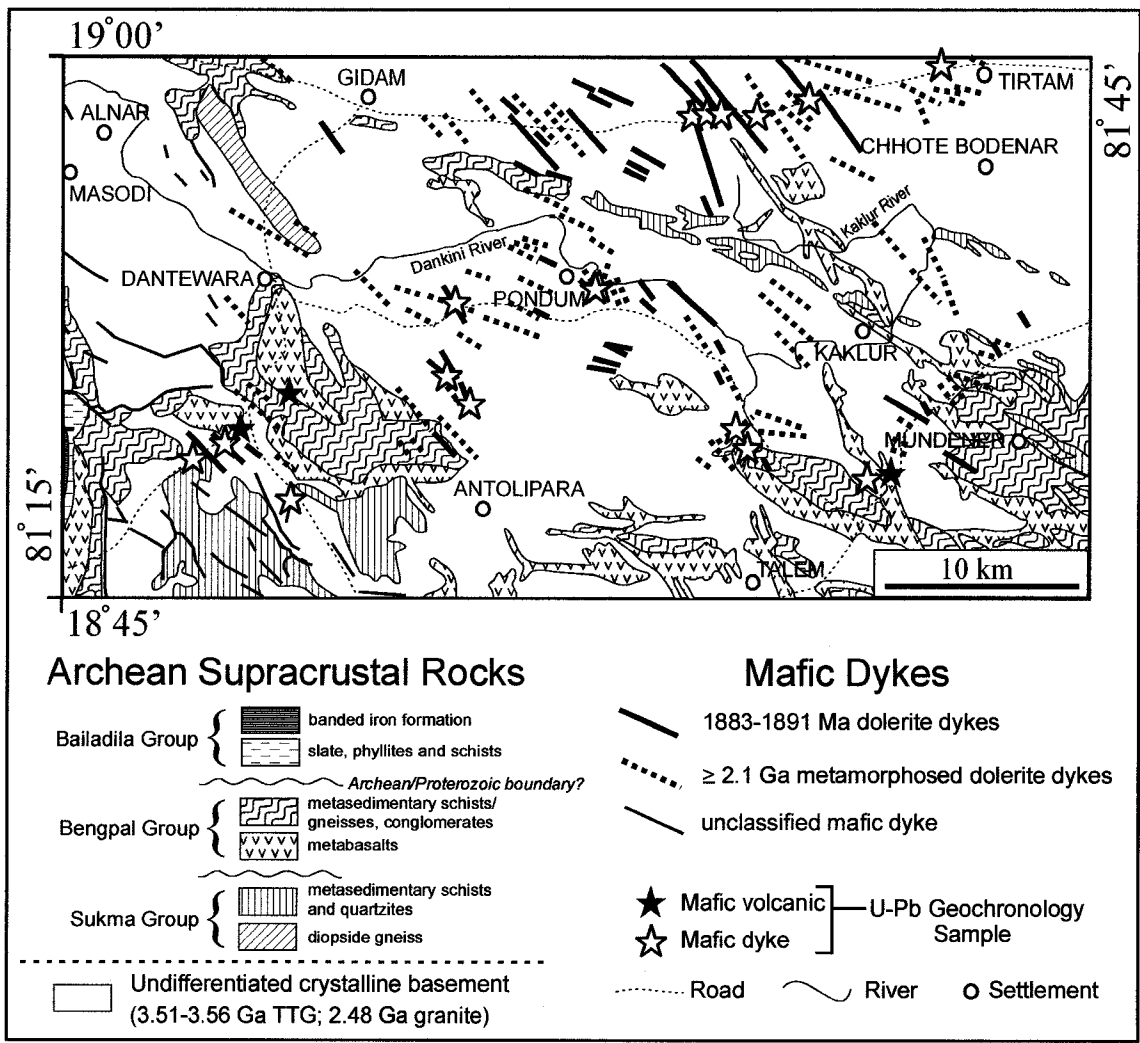


Fig. 1-4. Geological map of the southern Bastar craton depicting the locations of mafic igneous rocks sampled for U-Pb dating in this study. (Geology modified from: Crookshank, 1963; Naqvi and Rogers, 1987; Ramakrishnan, 1990; Srivastava and Singh, 2003).

CHAPTER 2

Feasibility of chemical U-Th-total Pb baddeleyite dating by electron microprobe

Jason E. French, Larry M. Heaman, and Thomas Chacko

Department of Earth and Atmospheric Sciences, University of Alberta, Edmonton, AB, Canada, T6G 2E3

Note: The paper presented in this chapter was published in the journal *Chemical Geology* in 2002 (Vol. 188, p.85-104)

INTRODUCTION

The Electron Microprobe (EM) chemical dating technique has become increasingly popular over the past ten years (Suzuki and Adachi, 1991; Suzuki et al., 1991; Montel et al., 1996; Cocherie et al., 1998; Williams et al., 1999; Crowley and Ghent, 1999; Scherrer et al., 2000). Most EM chemical dating studies utilize minerals with high Th and or U contents (typically > 10,000 ppm) and low common Pb contents. Although many studies have focused on chemical dating of monazite, the technique has also been applied to other accessory phases such as xenotime and zircon (Suzuki and Adachi, 1991; Geisler and Schleicher, 2000). In light of the diversity of U-bearing accessory phases that can be dated isotopically by U-Pb isotope methods, there potentially remain a number of other minerals to which EM chemical dating could also be applied.

The mineral baddeleyite (ZrO₂) is a U-bearing accessory phase that occurs in many mafic and ultramafic rocks, and has been used extensively for U-Pb dating of mafic magmatic events (e.g., Krogh et al., 1987; Heaman and LeCheminant, 1993).

Baddeleyite is an ideal geochronometer for mafic igneous rocks because it has relatively high concentrations of uranium (200-1000 ppm), negligible common lead, and is highly resistant to lead loss (Heaman and LeCheminant, 1993). Currently, separated baddeleyite crystals $>20\ \mu\text{m}$ in size are required for all isotopic techniques including Isotope Dilution Thermal Ionization Mass Spectrometry (IDTIMS), Sensitive High Resolution Ion MicroProbe (SHRIMP) and Laser Ablation – Inductively Coupled Plasma – Mass Spectrometry (LA-ICP-MS) grain mount studies. This limits significantly the number of mafic dyke samples that can be dated, because many dykes are fine-grained and typically contain baddeleyite crystals smaller than $20\ \mu\text{m}$. In addition, there are certain physical limitations to in-situ LA-ICP-MS studies as baddeleyite crystals in mafic rocks are typically quite thin ($<10\ \mu\text{m}$). The excellent spatial resolution that is possible with EM chemical dating ($\sim 1\ \mu\text{m}$) represents one important reason why this technique could have a large impact in reconnaissance geochronological studies of mafic rocks. A limited number of U-Pb isotopic age determinations, coupled with a larger number of EM ages, could provide more rigorous comprehensive age constraints than IDTIMS age determinations alone.

In this paper we evaluate the feasibility of applying the EM U-Th-total Pb chemical dating technique to the mineral baddeleyite. We report EM ages from a selection of baddeleyite-bearing reference samples for which accurate and precise IDTIMS ages are available in the literature or have been determined in this study (Table 2-1). Baddeleyite from four mafic igneous rocks and one carbonatite were chosen to cover a broad spectrum of ages (2400-800 Ma). The EM analyses were carried out on in-situ baddeleyite grains in polished thin section, or physically separated baddeleyite

fractions embedded in epoxy grain-mounts.

Background on Baddeleyite Dating

Because of the widespread occurrence of baddeleyite in mafic to ultramafic rocks (e.g., Keil and Fricker, 1974; Siivola, 1977), and its marked suitability for U-Pb geochronology, baddeleyite has become an accessory phase that is commonly used to obtain the precise and accurate emplacement age of mafic dykes and sills (e.g., Krogh et al., 1987; LeCheminant and Heaman, 1989; Dunning and Hodych, 1990; Heaman, 1997) and layered mafic intrusions (e.g., Amelin et al., 1995) using IDTIMS. Recent investigations have also demonstrated the ability to obtain relatively precise $^{207}\text{Pb}/^{206}\text{Pb}$ ages for mafic rocks by SHRIMP analysis of baddeleyite crystals (Wingate et al., 1998; Nemchin and Pidgeon, 1998; Wingate, 1999). In addition to studies of mafic rocks, baddeleyite has also been used in IDTIMS geochronological investigations of felsic-intermediate alkaline plutonism (Corriveau et al., 1990; Heaman and Machado, 1992), xenocrystic mantle baddeleyite in kimberlites (Scharer et al., 1997; Heaman and LeCheminant, 2000), carbonatites (Heaman and LeCheminant, 1993), and anorthosites (Scoates and Chamberlain, 1995). However, because baddeleyite is relatively rare in these rock types compared to its abundance in mafic rocks, this study focused primarily on the application of the EM chemical dating technique to baddeleyite-bearing mafic rocks.

U-Pb IDTIMS Results

In order to test the accuracy of baddeleyite chemical dating by EM, five samples were selected for an IDTIMS study to span the most prolific period of mafic dyke swarm emplacement in the Precambrian (ca. 2400-800 Ma). The reference samples include the

Faber Lake gabbro, a NE-striking sheet-like intrusion in the Great Bear magmatic zone, N.W.T. (GFA92-567), the Moores Lake gabbro, Churchill Province, Saskatchewan (9009), a feldspathic pyroxenite from the Muskox intrusion, Slave craton, N.W.T. (3101), a single baddeleyite crystal from the Phalaborwa carbonatite, S. Africa (IN1), and a gabbro sample from the Binneringie dyke, Yilgarn craton, Australia (LH97-18). The U-Pb results for all samples except for the Phalaborwa carbonatite are presented in Table 2-2. All data are new except for the Muskox intrusion, where we re-interpret the data of LeCheminant and Heaman (1989).

The mafic samples were pulverized using standard equipment (jaw crusher and disk mill). Heavy mineral concentrates were obtained with a Wilfley Table and baddeleyite and zircon grains were isolated using a series of magnetic (Frantz Isodynamic Separator) and density (methylene iodide) separation techniques. All grains were hand picked using a binocular microscope with the aim of selecting only the best quality crystals devoid of inclusions, fractures and turbidity. The selected grains were washed in nitric acid (2N), weighed using an ultra-microbalance and dissolved in TFE digestion capsules in a solution of 48%HF: 7N HNO₃ (5:1). A measured amount of a ²⁰⁵Pb/²³⁵U tracer solution was added to each sample prior to dissolution. Uranium and lead were purified from each fraction using anion exchange chromatography, and following closely the procedure of Heaman and Machado (1992). The isotopic compositions of U and Pb were determined either on a VG354 or S54 thermal ionization mass spectrometer operating in single collector mode. All atomic ratios were corrected for spike addition, initial common Pb (Stacey and Kramers, 1975) and mass discrimination: VG354 (Pb-0.088%/amu; U-0.155%/amu) and S54 (Pb-0.153%/amu; U-

0.137%/amu). The uranium decay constants used are those determined by Jaffey et al. (1971): $^{238}\text{U}=1.55125\times 10^{-10}\text{ yr}^{-1}$; $^{235}\text{U}=9.8485\times 10^{-10}\text{ yr}^{-1}$. All age calculations were determined using Isoplot (Ludwig, 1998) and age uncertainties are reported at the two sigma level.

Phalaborwa Carbonatite, S. Africa (IN1)

The Phalaborwa carbonatite is well known for its large baddeleyite crystals (up to several centimetres in length) and has been the subject of numerous U-Pb dating studies (e.g., Eriksson, 1984; Heaman and LeCheminant, 1993; Reischmann 1995; Horn et al., 2000; Wingate and Compston, 2000). The ages from all U-Pb dating techniques are similar: $2059.8\pm 0.8\text{ Ma}$ (IDTIMS, Heaman and LeCheminant, 1993), $2060.6\pm 0.5\text{ Ma}$ (IDTIMS, Reischmann, 1995), $2057\pm 8\text{ Ma}$ (LA-ICPMS, Horn et al., 2000) and $2057.1\pm 2.6\text{ Ma}$ (SHRIMP, Wingate and Compston, 2000).

A large baddeleyite crystal from the Phalaborwa carbonatite was obtained originally from the Royal Ontario Museum to evaluate whether this material might make a suitable mineral standard for U-Pb studies. After this crystal was comminuted and sized, the first U-Pb age determinations were conducted at the Royal Ontario Museum (Heaman and LeCheminant, 1993). Some of this material has been distributed to other laboratories for testing by other U-Pb dating techniques as well (e.g., Horn et al., 2000). A portion of this material has been used as an internal U-Pb mineral standard at the University of Alberta Radiogenic Isotope Facility for the past five years. During this time a total of 22 aliquots of differing amounts have been analysed. A summary of these results are presented here (Fig. 2-1). The weighted average $^{207}\text{Pb}/^{206}\text{Pb}$ date for these 22 analyses is $2059.6\pm 0.4\text{ Ma}$ (MSWD=1.05); identical to the results obtained at the Royal

Ontario Museum (see above). Other chemical features of this internal standard include rather variable U contents between 205-1943 ppm (mean: 595 ± 387 ppm), low Th contents between 1.9-24.2 ppm, (mean: 8.0 ± 6.7 ppm), low Th/U between 0.007-0.038 (mean: 0.013 ± 0.008) and low total common Pb between 4-26 pg (mean: 14 ± 7 pg).

Faber Lake Gabbro Sheet, Great Bear Magmatic Zone, N.W.T. (GFA92-567)

The Faber Lake gabbro is a poorly mapped sheet that extends 30 km across the Great Bear magmatic zone and disappears beneath Paleozoic cover to the southwest. It forms part of the Gunbarrel Igneous Events in western North America as defined by LeCheminant and Heaman (1994). The U-Pb results for two baddeleyite fractions from this Gunbarrel sill are reported in Table 2-2 and displayed on a concordia diagram in Fig. 2-2a. Baddeleyite in this sample has moderate uranium contents (1158-1323 ppm) and similar $^{207}\text{Pb}/^{206}\text{Pb}$ dates of 779.2 and 779.9 Ma, respectively. A reference line constructed to pass through these two analyses yields an upper intercept date of $784 \pm 10 / -4$ Ma. Our preferred estimate of the baddeleyite crystallization age is 779.5 ± 1.5 Ma (MSWD=0.22), the weighted average of the $^{207}\text{Pb}/^{206}\text{Pb}$ dates.

Moores Lake Gabbro, Churchill Province, Saskatchewan (9009)

This gabbro phase of the Moores Lake intrusion was obtained from drill hole DDH 307-79-5 (51.65-52.40 meters) and was provided by David MacDougall of the Saskatchewan Geological Survey. A modest number of baddeleyite and zircon shards were recovered. The U-Pb results for two baddeleyite (#3 and #4) and two zircon (#5 and #6) fractions are reported in Table 2-2 and displayed on a concordia diagram in Fig. 2-2b. A feature common to the Moores Lake sample and other mafic rocks in general (see Muskox data below) is the more discordant nature of zircon compared to

baddeleyite from the same sample. Baddeleyite in this sample shows the typical low Th content and Th/U common for baddeleyite crystallizing from mafic magmas. Zircon fraction #5 is typical of zircon crystallizing directly from a mafic magma with quite high Th contents and Th/U (>1). The data taken together are not collinear and there is a range in $^{207}\text{Pb}/^{206}\text{Pb}$ dates between 1096 and 1111 Ma. A reference line through the two baddeleyite analyses (3,4) and the more discordant zircon analysis (6) yields an upper intercept date of 1113.5 ± 3.4 Ma (MSWD=0.4). This could be a good estimate of the gabbro emplacement age. However, considering the similarity in the two more concordant baddeleyite analyses, our preferred estimate for the emplacement age is 1108.8 ± 2.4 Ma, the weighted average $^{207}\text{Pb}/^{206}\text{Pb}$ baddeleyite dates. This age is identical to the timing of Midcontinent Rift mafic magmatism in the Lake Superior region (e.g., Davis and Sutcliffe, 1985). The existence of Midcontinent Rift mafic magmatism more than a thousand kilometres northwest of the Lake Superior region was first suggested by Armstrong and Ramaekers (1985) based on relatively imprecise Rb-Sr dates for diabase dykes in the Athabasca Basin, Saskatchewan. The U-Pb age of 1108.8 Ma reported here provides unequivocal evidence that Midcontinent Rift mafic magmatism is much more widespread than previously recognized.

Muskox Feldspathic Pyroxenite, Slave craton, N.W.T. (3101)

The U-Pb results for two baddeleyite and one zircon fraction from the Muskox intrusion are those reported by LeCheminant and Heaman (1989) and are reproduced here in Table 2-2 and Fig. 2-2c. The reason for reporting the data again is that a pattern has been observed in several samples in which the combination of nearly concordant baddeleyite analyses with quite discordant zircon analyses from the same sample leads

to unusually old upper intercept projections. This may be the case for the Moores Lake gabbro above and could apply to the MuskoX data, as the zircon analysis (#8) is much more discordant (8%) than the baddeleyite results. We interpret the weighted average $^{207}\text{Pb}/^{206}\text{Pb}$ date of 1269.4 ± 1.1 Ma as a better estimate of the baddeleyite crystallization age. This is a slight revision of the previously reported date of 1270 ± 4 Ma, but does not affect the interpretations of LeCheminant and Heaman (1989).

Binneringie Gabbro Dyke, Yilgarn craton, Australia (LH97-18)

Abundant baddeleyite was recovered from a Binneringie gabbro dyke sample collected at Binaronca Rocks. Baddeleyite occurs in two populations: 1) euhedral light brown blades and 2) light brown blades with incipient development of zircon on crystal faces. Fractions containing grains with zircon coatings are more discordant (#12 and #14). Polycrystalline zircon coatings on baddeleyite are a common feature of metamorphosed mafic rocks (e.g., Heaman and LeCheminant, 1993), but the Binneringie dyke is generally not metamorphosed. The origin of these zircon coatings is unclear, but could be related to a younger low temperature hydrothermal overprint. The U-Pb results for five baddeleyite fractions are reported in Table 2-2 and displayed on a concordia diagram in Fig. 2-2d. Baddeleyite in this Binneringie sample has moderate U contents (521-868 ppm) and $^{207}\text{Pb}/^{206}\text{Pb}$ dates between 2366 to 2409 Ma. A regression line calculated using all analyses yields an upper intercept of 2412.4 ± 6.1 Ma (MSWD=5.6). The more precise upper intercept of 2410.3 ± 2.1 Ma (MSWD=0.07) using analyses 11, 13 and 14 is interpreted to be a better estimate of the baddeleyite crystallization age in this sample. The lower intercept of 581 ± 32 Ma is interpreted to be close to the time of formation of the zircon coatings. To our knowledge, there is no other known evidence

for Eocambrian or Paleozoic hydrothermal activity in this region. The 2410.3 Ma U-Pb baddeleyite age obtained here is similar to but slightly younger than the IDTIMS (2418±3 Ma) and SHRIMP (2420±7 Ma) dates reported by Nemchin and Pidgeon (1998) for a sample of this dyke collected to the west.

EM sample preparation and analytical procedure

Sample preparation

Baddeleyite crystals to be epoxy-mounted for EM analysis were hand picked using a binocular microscope from the same mineral fractions described in the previous section. All grain mounts were prepared by enveloping the selected baddeleyite crystals in epoxy-resin (Petropoxy 154) and then cured blocks were ground down to expose baddeleyite and polished using 0.5 and 0.25 μm diamond powder to ensure a flat surface. Polished thin sections and grain mounts were cleaned ultrasonically in millipore water and then dried overnight prior to carbon coating.

Analytical procedure

Locating baddeleyite crystals in thin section using optical techniques can be difficult, especially for grains less than 50 μm in their longest dimension. EM back-scattered electron (BSE) images are used commonly to locate tiny monazites in thin section by adjusting the contrast of the image and then verified using energy dispersive spectrometry (e.g., Montel et al., 1996; Scherrer et al., 2000). This method is also very efficient for locating baddeleyite crystals in polished thin sections. Baddeleyite in mafic rocks occurs commonly in association with other accessory minerals including apatite, ilmenite, zircon, and zirconolite (Heaman and LeCheminant, 1993), but can be distinguished readily from these minerals because its higher average atomic number

makes it appear brighter on a BSE image.

EM chemical dating of baddeleyite presents an analytical challenge in that many Precambrian baddeleyite crystals have Pb contents only slightly above detection limit of the instrument. The U content of baddeleyite in mafic rocks is typically between 200 and 1000 ppm (Heaman and LeCheminant, 1993), such that the total accumulated radiogenic Pb ranges from below detection limit of the EM (0.015 wt.% PbO in this study) or substantially high (e.g. 0.050 wt.% PbO) depending on the age of the sample (Fig. 2-3). EM chemical dating of baddeleyite is clearly best suited for Mesoproterozoic and older samples, but in cases where the U content is much higher (>2000 ppm; e.g., Heaman and Machado, 1992) the technique could potentially be applied to reconnaissance dating of baddeleyite-bearing rocks as young as 500 Ma.

The EM used in this study is a JEOL 8900 equipped with 5 wavelength dispersive spectrometers (WDS) and one energy dispersive spectrometer (EDS). During WDS analysis, the accelerating voltage was set at 20 kV, the beam current at 150 nA, and the beam diameter at 1-2 μm . The average concentrations of UO_2 and PbO measured from baddeleyite samples in this study varied between 0.064-0.158 wt.% and 0.010-0.030 wt.%, respectively (Table 2-3), which are an order of magnitude lower than those measured typically in an EM monazite analysis (Fig. 2-4: e.g., Suzuki et al., 1991; Montel et al., 1996; Cocherie et al., 1998; Scherrer et al., 2000). As such, the final precision of an EM baddeleyite age should in general be lower than that of a typical EM monazite age. Baddeleyite characteristically contains Th concentrations less than 20 ppm and has correspondingly low Th/U ratios (<0.05) (Heaman and LeCheminant, 1993). The average concentrations of ThO_2 in the baddeleyite samples analysed in this

study were 0.002-0.007 wt.% (Table 2-3). However, because some localized regions of the crystals had ThO₂ concentrations as high as 0.02 wt.%, Th content was considered in all of the age calculations in this study, despite it usually having a small effect on the final age (5-10 m.y.). Count times were maximized for measurement of UO₂, PbO, and ThO₂ contents at 400, 400, and 250s, respectively, and corresponding background count times were 200, 200, and 120s. In order to evaluate the reliability and accuracy of the analyses, it was also necessary to analyse for other major and trace elements including Zr, Hf, and Si. Count times for these elements were 20 and 10s for peak and background measurements, respectively. The total analysis time for each WDS spot analysis was approximately 14 minutes, and typically at least 40-50 analyses were carried out on each sample. Determining the concentrations of a variety of major and trace elements is particularly important when obtaining EM chemical ages of baddeleyite in thin section. Monoclinic baddeleyite commonly forms as elongate, tabular blades and needles that can be vanishingly thin (approaching 1 μm). This can lead potentially to a problem during WDS analysis of in-situ baddeleyite because there is the possibility of exciting foreign material beneath the baddeleyite crystal. For example, a {100} pinacoid section of baddeleyite from a polished thin section may have dimensions of 5 x 30 μm, but only be 2 μm thick. During a WDS spot analysis at high accelerating voltage, the total excitation volume is >2 μm³, resulting potentially in contamination from underlying minerals. Because baddeleyite in mafic to ultramafic rocks is found most commonly within or associated with late crystallizing silicate minerals such as amphibole, biotite, chlorite, and K-feldspar-quartz granophyre (Heaman and LeCheminant, 1993), analysing for SiO₂ is one potential monitor of

contamination from adjacent minerals.

The Pb standard used in this study was natural galena (PbS), although during the course of this work it was discovered that calibration using a Pb-silicate glass (NBS-K 456) yielded comparable results. The glass represents a slightly more appropriate Pb standard than galena because interference of S on Pb can be avoided (Scherrer et al., 2000), and like baddeleyite, is an oxide. Synthetic oxide standards were used for U, Th and Zr calibration, and Si and Hf were calibrated using a natural zircon standard. UO₂, ThO₂ and PbO contents were determined simultaneously with three separate PET crystals using the UMβ, ThMα, and PbMα X-ray lines.

In EM dating of monazite, a correction must be made for the interference of the YLα X-ray line on the PbMα peak in Y-rich monazites (e.g., Suzuki and Adachi, 1991). Although substantially higher concentrations of Y (1.27-1.47 wt.%) have been reported from trace-element analyses of lunar baddeleyite (Haggerty, 1973), terrestrial baddeleyite characteristically has low Y contents (0.04-0.28 wt.%) (Heaman and LeCheminant, 1993). Interference of the YLα X-ray line on the PbMα peak is therefore not expected to have a significant impact in EM chemical dating of most terrestrial baddeleyite samples, so a Y correction was not applied in this study. As a precautionary measure, Y content was monitored for each sample with a representative number of WDS spot analyses on the grains analysed, and found to be negligible in all cases (<0.17 wt.% Y₂O₃). Although negligible in most terrestrial baddeleyite samples (0.05-0.38 wt.%; Heaman and LeCheminant, 1993), the Nb₂O₅ content of some lunar baddeleyite crystals exceeds 1.0 wt.% (Haggerty, 1973). High Nb contents could lead to an analytical problem in EM chemical dating of baddeleyite in that the NbKβ peak

coincides closely with a range of typical PbM α *positive* background positions (e.g., 170-171 mm). WDS analysis of baddeleyite with Nb₂O₅ concentrations greater than ~1.0 wt.% could potentially incorporate a significant background over-subtraction on the PbM α peak, resulting in erroneously young EM chemical ages. To verify that this was not a problem in our study, Nb₂O₅ was also monitored and found to be negligible in all cases (0.04-0.62 wt.%). We recommend that any intensive EM chemical dating study of baddeleyite (particularly during analysis of extraterrestrial samples) be preceded by a survey of the Y and Nb contents of the analysed grains.

Age determination and data presentation

The accuracy of ages obtained with EM chemical dating of baddeleyite is tied strongly to the assumptions that the mineral has remained closed to the migration of U, Pb, Th and all intermediate daughter products throughout its history, and that the proportion of common Pb is negligible. Conventional IDTIMS studies of baddeleyite from mafic to ultramafic rocks and carbonatites typically yield concordant results (i.e. 98-100% concordancy) and insignificant common lead (e.g., Krogh et al., 1987; Heaman and LeCheminant, 1993). In these respects, baddeleyite is ideally suited for EM chemical dating.

The U content of baddeleyite can vary by a factor of 2 to 10 from grain to grain within a single sample, such that in some cases the Pb content of a number of crystals may be substantially high (e.g., 0.050 wt.% PbO), whereas others from the same sample are below detection limit (<0.015 wt.% PbO). For this reason, a successful EM survey of a population of baddeleyite crystals typically requires the WDS chemical analysis of more than 40-50 spots on a variety of different grains to locate crystals with sufficiently

high Pb contents for reliable geochronological analysis. In turn, this requires the additional assumption that all crystals analysed are a part of a single age population, which is reasonable because the occurrence of xenocrystic baddeleyite in mafic rocks is very unlikely (Heaman and LeCheminant, 1993). Owing to the variability in U and Pb concentrations within each sample, a useful strategy is to obtain a few preliminary points on each grain in order to focus on the baddeleyite grains with Pb contents above detection limit. This can be difficult for baddeleyite crystals in polished thin sections that have a grain size conducive to only a few chemical analyses (i.e. 5-10 μm in length), in which case analysis of a large number of crystals may be required.

The functional detection limit for PbO in this study was exclusively chosen to discriminate analyses for which the relative precision on the background-corrected peak-intensity (Reed, 1996: p. 159) was greater than 40%, which under these operating conditions corresponded to a PbO content of 0.015 wt.%. Therefore, analyses that yielded PbO contents below 0.015 wt.% were not included in the age calculations. In addition, analyses with poor oxide totals (<95 wt.%) and/or high silica content (>1 wt.% SiO_2) possibly reflecting contamination from adjacent minerals were also discarded. The arithmetic mean age was calculated for each sample and all $>2\sigma$ outliers (typically only one or two data points considered to represent instrumental artefacts) were excluded from the isochron plots and weighted-mean diagrams described below.

Age calculation:

Age calculations were carried out following the chemical isochron method (CHIME) of Suzuki and Adachi (1991). As a first step, the UO_2 , ThO_2 , and PbO contents measured in each spot analysis were used to calculate an apparent age t for each

spot by iteratively solving the equation:

$$\frac{\text{PbO}}{W_{\text{Pb}}} = \frac{\text{ThO}_2}{W_{\text{Th}}} [\exp(\lambda_{232}t) - 1] + \frac{\text{UO}_2}{W_{\text{U}}} \left[\frac{\exp(\lambda_{235}t) + 138\exp(\lambda_{238}t)}{139} - 1 \right] \quad (\text{Eq.1})$$

where W_{Pb} , W_{U} , and W_{Th} are the molecular weights of PbO (222), UO₂ (270), and ThO₂ (264), and λ_{232} , λ_{235} , and λ_{238} are the decay constants of ²³²Th, ²³⁵U, and ²³⁸U, respectively (Jaffey et al., 1971). Then the equation:

$$\text{UO}_2^* = \text{UO}_2 + \left[\frac{139\text{ThO}_2 \cdot W_{\text{U}} [\exp(\lambda_{232}t) - 1]}{W_{\text{Th}} [\exp(\lambda_{235}t) + 138\exp(\lambda_{238}t) - 139]} \right] \quad (\text{Eq.2})$$

was used to calculate UO₂*, which represents the measured UO₂ concentration combined with the equivalent amount of fictive UO₂ necessary to account for radiogenic Pb production from Th decay.

The computer program Isoplot (Ludwig, 1998) was used to construct chemical U-Th-total Pb isochron diagrams similar to the PbO versus UO₂* plots from Suzuki and Adachi (1991). In contrast to that study, however, all regressions were forced through the origin (c.f. Cocherie et al., 1998). This was done by including one imaginary analysis with UO₂* and PbO concentrations of zero, but with no associated data point errors. The procedure usually resulted in a significant improvement on the final age (particularly for samples where a relatively small number of analyses were carried out). The rationale for anchoring each regression to the origin is tied to the observation that IDTIMS analysis of all five baddeleyite reference samples measured insignificant common Pb (much lower than 1 ppm) and yielded concordant results (<2% discordancy for all pure baddeleyite analyses: Table 2), which indicates that the y-intercept on PbO

vs. UO_2^* diagrams for these baddeleyite samples should effectively be zero. Uncertainties on each data point are reported at the 2σ confidence level and were calculated individually from the equation (Reed, 1996):

$$\sigma_{\text{P-B}} = [(n_{\text{P}}/t_{\text{P}}^2) + (n_{\text{B}}/t_{\text{B}}^2)]^{0.5} \quad (\text{Eq.3})$$

This equation assumes that X-ray counts follow the Poisson Distribution Law (Reed, 1996), where $\sigma_{\text{P-B}}$ is the standard deviation of the background-corrected peak intensity, n_{P} and n_{B} are the number of counts measured on the peak and background, respectively, and t_{P} and t_{B} are the count times for the peak and background measurements, respectively.

Finally, the regressed slope m from the PbO versus UO_2^* diagram was used to estimate the age of crystallization of each sample by solving the equation:

$$m = \left[\frac{W_{\text{Pb}}}{W_{\text{U}}} \right] \times \left[\frac{\exp(\lambda_{235}T) + 138 \exp(\lambda_{238}T)}{139} - 1 \right] \quad (\text{Eq.4})$$

for T . Because the Th content is negligible in most baddeleyite crystals, the first age estimate T cannot be improved upon iteratively using the method of Suzuki and Adachi (1991), and as such the first approximation of T is usually the best estimate for the age of crystallization of baddeleyite by the CHIME method. Errors on the slope are reported at the 2σ level and were propagated numerically through equation 4 to get the final error on the age.

Results

The $>500 \mu\text{m}$ shard of baddeleyite (originating from a $>4 \text{ cm}$ long crystal) from the Phalaborwa carbonatite was by far the largest grain analysed in this study, and consequently all 63 WDS spot analyses used in the age calculation of the Phalaborwa

sample were from that single baddeleyite fragment. Many of the spot analyses from the Phalaborwa baddeleyite yielded PbO contents only slightly above detection limit of the EM (0.015 wt%), but some were up to 0.040 wt%. The UO_2^* versus PbO plot (Fig. 2-5) yielded a crystallization age of $2026 \pm 46/-47$ Ma, which overlaps within error of all of the previously determined ages (Table 2-1). These data demonstrate that EM chemical dating of baddeleyite containing typical UO_2 concentrations (0.050-0.110 wt%) is feasible on Paleoproterozoic samples.

Another goal of this study was to evaluate whether EM chemical dating could be conducted on baddeleyite crystals in thin section. A polished thin section of feldspathic pyroxenite sample 3101 from the MuskoX intrusion was analysed for this purpose. Baddeleyite is spatially associated with late crystallizing interstitial quartz, alkali feldspar, and biotite (Fig. 2-6). Both crystals measured approximately 30 μm in their longest dimension, large enough to allow for multiple analyses on each grain (Fig. 2-7). U and Pb contents varied significantly and systematically at the micron scale in both crystals, which allowed chemical isochron diagrams to be constructed for each crystal. Grains A and B yielded EM chemical ages (Fig. 2-8) that overlap within error of each other and with the previously determined IDTIMS age of 1270 ± 4 Ma (LeCheminant and Heaman, 1989) and the revised age of 1269.4 ± 1.1 Ma (baddeleyite only) reported above. The age derived from the PbO versus UO_2^* diagram (Fig. 2-8) for grain A of $1363 \pm 202/-213$ Ma was much less precise than that determined for grain B $1308 \pm 79/-80$ Ma. Combining data from both grains yielded an age estimate of $1329 \pm 84/-86$ Ma (Fig. 2-8). These results demonstrate that useful reconnaissance age information can be obtained from individual crystals of baddeleyite from polished thin section using the EM dating

technique.

Baddeleyite from the Moores Lake gabbro (sample 9009) was chosen in part because it is only ~160 m.y. younger in age than the Muskox intrusion and thus represents a good opportunity to test the resolution of the dating technique. Although more than 30 spot analyses were carried out on this sample, many of the grains analysed yielded PbO contents below 0.015 wt%. Fortunately, isolated regions on some of the grains had relatively high UO₂ contents (0.100-0.200 wt%) and consequently measurable amounts of total Pb. It was therefore possible to construct a ten-point PbO versus UO₂* diagram (Fig. 2-9) from those U- and Pb-rich regions, which yielded a U-Th-total Pb chemical isochron age of 1132 +134/-139 Ma that overlaps within error of the IDTIMS age of 1108.8±2.4 Ma reported above. Comparison of the EM chemical age of this sample with that of the Muskox intrusion (1329 +84/-86 Ma) indicates that these samples are at the limit of the age resolution of the technique (~150-200 m.y. for typical baddeleyite) in that the error envelope of the two samples slightly overlap.

The youngest baddeleyite reference sample analysed in this study was from the 780 Ma Faber Lake gabbro sheet (sample GFA92-567). Of all samples, baddeleyite from this gabbro displayed the most scatter in terms of the ages of individual data points. Although low precision and accuracy should generally be expected in EM dating of young baddeleyite, this was not expected to be much of a problem for the Faber Lake sample because some of the crystals analysed have U contents in excess of 2000 ppm. The resulting PbO versus UO₂* diagram (Fig. 2-10) yielded an EM chemical age of 921±29 Ma, which is older than the IDTIMS age of 779.5±1.5 Ma reported above. The pronounced scatter of the analyses and relatively poor accuracy on the EM chemical

baddeleyite age of the Faber Lake gabbro are difficult to explain. Although heterogeneously distributed common Pb at the micron scale could contribute to some scattering on the ages of individual data points, this is not likely because the common Pb content in all five samples analysed by IDTIMS in this study is negligible.

The UO_2^* versus PbO diagram for baddeleyite from Binneringie dyke sample LH97-18 (Fig. 2-11) yielded an age of $2548 \pm 35/-36$ Ma, which is older than the IDTIMS age of 2410.3 ± 2.1 Ma. Interestingly, data from LH97-18 form a more, well-defined isochron than the EM results from the Faber Lake gabbro, which is reflected in the superior MSWD of 1.3 for the Binneringie sample. In light of the systematically old ages for the Faber Lake gabbro and Binneringie dyke, a detailed analysis of Y_2O_3 content in baddeleyite from both samples was carried out and determined to be negligible in terms of potential for any significant overlap of the $\text{YL}\alpha$ x-ray line on the $\text{PbM}\alpha$ peak (Binneringie dyke: 0.019 wt% Y_2O_3 [$n=30$]; Faber Lake gabbro: 0.033 wt% Y_2O_3 [$n=61$]).

It has been well documented recently that crystal orientation effects during ion microprobe analysis of baddeleyite can play a role in producing erroneous U-Pb ages (Wingate et al., 1998; Wingate and Compston, 2000). SHRIMP measurements of $^{206}\text{Pb}/^{238}\text{U}$ ratios from a multi-grain population of monoclinic baddeleyite fragments and in some cases within a single polysynthetically twinned baddeleyite grain, can vary systematically by $\pm 10\%$ depending on the relative orientations of the baddeleyite crystal lattice and the primary ion beam (Wingate and Compston, 2000). The two baddeleyite samples that yielded systematically old EM chemical ages in this study both comprised multi-grain populations in which the crystallographic orientation of each

fragment was not characterized. Although crystal orientation effects during SHRIMP analysis of baddeleyite in part, might be attributed to channelling of primary ions, anisotropic emission of secondary ions, and/or preferential ionization of secondary species (Wingate and Compston, 2000), these are not problems which relate to EM analysis. The possibility that crystal orientation could also affect EM chemical dating of baddeleyite cannot be ruled out but is considered difficult to evaluate given the larger age uncertainties inherent in the technique, and is beyond the scope of this study.

Figure 2-12 compares the EM baddeleyite ages determined in this study with IDTIMS ages for the same samples. Three of the EM ages are within 2σ uncertainty of the corresponding IDTIMS ages and are accurate to within ~30-60 m.y., and two EM ages are too old by ~140 m.y.. The discrepancies for those samples remain to be explained, but do not detract from the overall conclusion that the EM technique is capable of providing reasonable first-order age information for typical Precambrian baddeleyite.

Fields of Application

Determining the timing of emplacement of Precambrian mafic dyke swarms can be challenging (Black et al., 1991), and ideally involves determination of the crystallization ages of a large number of dykes. The Mackenzie dyke swarm represents the largest preserved radiating mafic dyke swarm on Earth, and spans ~2.7 million km² of the Canadian Shield (Ernst et al., 1995). Conventional U-Pb IDTIMS dating of multiple mafic dykes and sills sampled from across that swarm yielded remarkably consistent ages clustering at 1267 Ma, demonstrating that the entire swarm was probably emplaced in a relatively short time span of about 5 m.y. (Heaman and LeCheminant,

1993). Geochronological investigations of crustal-scale mafic dyke swarms such as the Mackenzie swarm could benefit greatly from EM chemical dating. Isolating baddeleyite crystals from mafic dykes for IDTIMS studies typically requires obtaining 20-30 kg samples of each dyke. Mineral separation can be quite costly and time consuming and is not always successful. In contrast, EM chemical dating demands a much smaller sample size and mineral separation is not necessary. This greatly facilitates field logistics in that sampling of a much higher number of mafic dykes could be done in a more efficient manner, allowing for collection of a more representative sample inventory of a given mafic dyke swarm. A large number of EM chemical (baddeleyite) ages, coupled with a limited number of IDTIMS analyses, could then be used to obtain a more robust estimate on the timing of emplacement of a vast number of dykes. In addition, EM chemical dating could also be carried out on fine-grained mafic dykes that have a baddeleyite grain size that is not currently conducive to mineral separation and IDTIMS analysis.

Mafic dyke swarms with a more complex history of emplacement present an even greater challenge to U-Pb geochronologists, particularly when multiple parallel mafic dykes of differing age exist in the same region, such as in the Scourie dyke swarm of Scotland. On the basis of petrological and geochemical criteria, at least four distinct, sub-parallel dyke suites can be recognized in the Scourie area and IDTIMS baddeleyite data define at least two ages of emplacement of 2418 and 1992 Ma (Heaman and Tarney, 1989). Questions remain as to the relative abundance of dykes belonging to each swarm, and whether dykes of other ages are also present. As the U and Pb contents in baddeleyite from the Scourie dykes average 1900 and 800 ppm, respectively, for the older dykes, and 1600 and 600 ppm, respectively, for the younger dykes (Heaman and

Tarney, 1989), EM dating could potentially be carried out on polished thin sections of a number of mafic dykes from that swarm. This would allow more accurate estimates to be made of the relative abundance of each age component in the swarm. These data could also have a significant impact on petrogenetic modelling of the Scourie swarm as samples from different dykes are sometimes used in the modelling process without definitive geochronological evidence that all the samples are of the same age. Many Scourie dykes contain small (~20 μm) baddeleyite crystals that have thin (1-10 μm) polycrystalline zircon rims that are extremely difficult to separate for discrete IDTIMS analysis, so EM dating of the baddeleyite cores might be quite useful. Geochronological investigations of mafic dyke swarms in parts of the world where there is a lack of age information for any mafic dykes, and where possibly multiple ages of dykes separated by at least 200 m.y. in age exist in the same region would be greatly facilitated by EM dating. By performing an EM geochronological survey of a given sample inventory, which can be done in a matter of hours (for each sample), prioritization of samples for more precise and accurate IDTIMS studies can be done in a highly efficient manner.

Baddeleyite is also known to occur in many extraterrestrial materials including lunar dust, basalts and norites returned during the Apollo missions (e.g., Agrell et al., 1970; Ramdohr and El Goresy, 1970; El Goresy et al., 1971; Anderson and Hinthorne, 1972; Haggerty, 1973; Smith and Steele, 1976) and in SNC (Shergottites-Nakhlites-Chassigny) achondrites (e.g., Smith and Hervig, 1979; Lundberg et al., 1988). Although the grain size of baddeleyite in at least one lunar basalt allowed for determination of a low precision $^{207}\text{Pb}/^{206}\text{Pb}$ age of ~4.2 Ga by ion microprobe (Anderson and Hinthorne, 1972), baddeleyite in most lunar basalts is quite small (<20 μm). Despite the relatively

small grain size, EM dating could conceivably be carried out on many of the lunar samples, particularly in light of the great antiquity (e.g., >4.0 Ga) of many lunar igneous rocks (Nyquist and Shih, 1992). The baddeleyite crystals identified in the Shergotty meteorite are exceptionally tiny ($\sim 1 \mu\text{m}$) (Smith and Hervig, 1979) and are likely too small to obtain useful EM chemical age information. Because SNC achondrites are thought to have a Martian origin (Smith and Hervig, 1979; Stoffler et al., 1986; Lundberg et al., 1988), the observation that baddeleyite occurs in at least some SNC meteorites is important. The abundant evidence for basaltic volcanism on Mars (e.g., Lucchitta, 1987; Cattermole, 1990; Plescia, 1994) is an indication that some of the material collected during a Mars sample return mission will likely be basalt. As the amount of material returned from such a mission will probably be quite small, EM U-Th-total Pb baddeleyite dating represents the ideal geochronological tool for analysis of returned Martian basaltic samples because of its excellent spatial resolution ($\sim 1 \mu\text{m}$) and non-destructive nature.

Although baddeleyite occurs in terrestrial extrusive mafic igneous rocks such as Hawaiian alkalic basalts (Keil and Fricker, 1974), the grain size can generally be anticipated to be small ($< 20 \mu\text{m}$) for such rocks, and so baddeleyite cannot easily be isolated from terrestrial basalts for IDTIMS studies by standard mineral separation techniques. The high spatial resolution of the EM therefore offers a new method of obtaining reconnaissance age information for Precambrian terrestrial basalts. EM baddeleyite dating is clearly suited for reconnaissance geochronological investigations of mafic rocks, but has potential to be applied to geochronological problems involving other rock types that are known to contain trace amounts of baddeleyite. These include

metacarbonates (Purtscheller and Tessadri, 1985), alkaline syenites (Corriveau et al., 1990; Heaman and Machado, 1992), carbonatites (Eriksson, 1984), and baddeleyite schlieren from impact glasses (El Goresy, 1965). Mantle-derived baddeleyite can also be found in kimberlites as reaction rims on zircon megacrysts (Heaman and LeCheminant, 1993), as mantle megacrysts (Schärer et al., 1997), and as inclusions within large titanomagnetite crystals (Heaman and LeCheminant, 2000). EM chemical dating is probably not feasible on these materials because most kimberlites tend to be Phanerozoic in age (Smith et al., 1994; Heaman and Kjarsgaard, 2000) and such young grains generally have not accumulated sufficient radiogenic Pb to be measurable by the EM.

Summary and Conclusions

We assessed the feasibility of EM chemical U-Th-total Pb dating of baddeleyite by obtaining EM chemical ages for five baddeleyite reference samples for which IDTIMS information is available or was determined in this study. Three of the five baddeleyite samples yielded EM chemical ages that overlap within error of the IDTIMS ages, and that are accurate to within ~30-60 m.y.. Although it is not clear why two of the samples yielded ages that are systematically old by ~140 m.y., these data demonstrate that EM chemical dating provides reliable first-order age information for typical Precambrian baddeleyite. The excellent spatial resolution of the technique allows for determination of useful reconnaissance age information from individual crystals of baddeleyite in polished thin section. As many mafic dyke samples contain baddeleyite with a grain size too small for isolation and IDTIMS dating but large enough for EM chemical dating (i.e.: 5-20 μm), application of the EM chemical dating technique

to the mineral baddeleyite provides a dramatic increase in the number of samples from which reconnaissance age information can be obtained. EM dating of baddeleyite represents a time efficient, cost effective, contextual geochronological tool which, used in combination with conventional isotopic methods, could greatly enhance geochronological investigations of mafic magmatic events, ultimately facilitating reconstruction of Precambrian supercontinents.

Acknowledgements

We greatly appreciate the constructive comments of reviewers J.L. Crowley and M.T.D. Wingate. We would like to thank Lang Shi for his extensive support and technical advice during operation of the Electron Microprobe in the Department of Earth and Atmospheric Sciences at the University of Alberta. Special thanks to A.N. LeCheminant for his helpful comments and for providing polished thin sections of sample 3101 from the Muskox Intrusion. We would also like to acknowledge the assistance of Scott Doehler, Stacey Hagen, Laura Raynor, and Stephanie Ross for their contributions to IDTIMS analysis of some of the reference baddeleyite samples, Geoff Fraser for donating the materials for preparation of grain mounts and Don Resultay for his help with sample preparation. This work was funded by NSERC Research grants to LMH and TC.

References

- Agrell, S. O., Scoon, J. H., Muir, I. D., Long, J. V. P., McConnell, J. D. C., & Peckett, A. (1970). Observations on the chemistry, mineralogy, and petrology of some Apollo 11 lunar samples. *Proceedings of the 11th Lunar Science Conference* 1, 93-128.
- Amelin, Y. V., Heaman, L. M., & Semenov, V. S. (1995). U-Pb geochronology of layered mafic intrusions in the eastern Baltic Shield: Implications for the timing and duration of Paleoproterozoic continental rifting. *Precambrian Research* 75, 31-46.

- Anderson, C. A. & Hinthorne, J. R. (1972). U, Th, Pb and REE abundances and $^{207}\text{Pb}/^{206}\text{Pb}$ ages of individual minerals in returned lunar material by ion microprobe mass analysis. *Earth and Planetary Science Letters* **14**, 195-200.
- Armstrong, R. L. & Ramaekers, P. (1985). Sr isotopic study of Helikian sediment and diabase dikes in the Athabasca Basin, northern Saskatchewan. *Canadian Journal of Earth Sciences* **22**, 399-407.
- Black, L. P., Kinny, P. D., & Sheraton, J. W. (1991). The difficulties of dating mafic dykes: an Antarctic example. *Contributions to Mineralogy and Petrology* **109**, 183-194.
- Cattermole, P. (1990). Volcanic Flow Development at Alba Patera, Mars. *Icarus* **83**, 453-493.
- Cocherie, A., Legendre, O., Peucat, J. J., & Kouamelan, A. N. (1998). Geochronology of polygenetic monazites constrained by in situ electron microprobe Th-U-total lead determination: Implications for lead behaviour in monazite. *Geochimica et Cosmochimica Acta* **62**, 2475-2497.
- Corriveau, L., Heaman, L. M., Marcantonio, F., & van Breeman, O. (1990). 1.1 Ga K-rich alkaline plutonism in the SW Grenville Province. *Contributions to Mineralogy and Petrology* **105**, 473-485.
- Crowley, J. L. & Ghent, E. D. (1999). An electron microprobe study of the U-Th-Pb systematics of metamorphosed monazite: role of Pb diffusion versus overgrowth and recrystallization. *Chemical Geology* **157**, 285-302.
- Davis, D. W. & Sutcliffe, R. H. (1985). U-Pb ages from the Nipigon plate and northern Lake Superior. *Geological Society of America Bulletin* **96**, 1572-1579.
- Dunning, G. R. & Hodych, J. P. (1990). U/Pb zircon and baddeleyite ages for the Palisades and Gettysburg sills of the northeastern United States: Implications for the age of the Triassic/Jurassic boundary. *Geology* **18**, 795-798.
- El Goresy, A. (1965). Baddeleyite and its significance in impact glasses. *Journal of Geophysical Research* **70**, 3453-3456.
- El Goresy, A., Ramdohr, P. & Taylor, L. A. (1971). The geochemistry of the opaque minerals in Apollo 14 crystalline rocks. *Earth and Planetary Science Letters* **13**, 121-129.
- Eriksson, S. C. (1984). Age of carbonatite and phoscorite magmatism of the Phalaborwa Complex (South Africa). *Isotope Geoscience* **2**, 291-299.
- Ernst, R. E., Head, J. W., Parfitt, E., Grosfils, E. & Wilson, L. (1995). Giant radiating dyke swarms on Earth and Venus. *Earth Science Reviews* **39**, 1-58.

- Geisler, T. & Schleicher, H. (2000). Improved U-Th-total Pb dating of zircons by electron microprobe using a simple new background modelling procedure and Ca as a chemical criterion of fluid-induced U-Th-Pb discordance in zircon. *Chemical Geology* **163**, 269-285.
- Haggerty, S. E. (1973). Armacolite and genetically associated opaque minerals in the lunar samples. *Geochimica et Cosmochimica Acta* **4**, 777-797.
- Heaman, L. M. (1997). Global mafic magmatism at 2.45 Ga: Remnants of an ancient large igneous province? *Geology* **25**, 299-302.
- Heaman, L. M. & Kjarsgaard, B. A. (2000). Timing of eastern North American kimberlite magmatism: continental extension of the Great Meteor hotspot track? *Earth and Planetary Science Letters* **178**, 253-268.
- Heaman, L. M. & LeCheminant, A. N. (1993). Paragenesis and U-Pb systematics of baddeleyite (ZrO₂). *Chemical Geology* **110**, 95-126.
- Heaman, L. M. & LeCheminant, A. N. (2000). Anomalous U-Pb systematics in mantle-derived baddeleyite xenocrysts from Ile Bizard: evidence for high temperature radon diffusion? *Chemical Geology* **172**, 77-93.
- Heaman, L. M. & Machado, N. (1992). Timing and origin of mid-continent rift alkaline magmatism, North America: evidence from the Coldwell Complex. *Contributions to Mineralogy and Petrology* **110**, 289-303.
- Heaman, L. M. & Tarney, J. (1989). U-Pb baddeleyite ages for the Scourie dike swarm, Scotland: Evidence for two distinct intrusion events. *Nature* **340**, 705-708.
- Horn, I., Rudnick, R. L. & McDonough, W. F. (2000). Precise elemental and isotope ratio determination by simultaneous solution nebulization and laser ablation ICP-MS: application to U-Pb geochronology. *Chemical Geology* **167**, 405-425.
- Jaffey, A. H., Flynn, K. F., Glendenin, L. E., Bentley, W. C. & Essling, A. M. (1971). Precision measurement of half-lives and specific activities of ²³⁵U and ²³⁸U. *Physical Review C* **4**, 1889-1906.
- Keil, K. & Fricker, P. E. (1974). Baddeleyite (ZrO₂) in gabbroic rocks from Axel Heiberg Island, Canadian Arctic Archipelago. *American Mineralogist* **59**, 249-253.
- Krogh, T.E., Corfu, F., Davis, D.W., Dunning, G.R., Heaman, L.M., Kamo, S.L., Machado, N., Greenough, J.D., & Nakamura, E. (1987). Precise U-Pb isotopic ages of diabase dykes and mafic to ultramafic rocks using trace amounts of baddeleyite and zircon. In: Halls, H.C. and Fahrig, W.F., eds., *Mafic Dyke Swarms, Geological Association of Canada Special Paper* **34**, 147-152.

- LeCheminant, A. N. & Heaman, L. M. (1989). Mackenzie igneous events, Canada: Middle Proterozoic hotspot magmatism associated with ocean opening. *Earth and Planetary Science Letters* **96**, 38-48.
- LeCheminant, A. N. & Heaman, L. M. (1994). 779 Ma mafic magmatism in the Northwestern Canadian Shield and Northern Cordillera: A new regional time marker. *Abstracts, 8th International Conference on Geochronology, Cosmochronology and Isotope Geology – USGS Circular 1107*, 187.
- Lucchitta, B. K. (1987). Recent Mafic Volcanism on Mars. *Science* **235**, 565-567.
- Ludwig, K. R. (1998). ISOPLOT: a plotting and regression program for radiogenic isotope data, version 1.00a.
- Lundberg, L. L., Crozaz, G., McKay, G. & Zinner, E. (1988). Rare earth element carriers in the Shergotty meteorite and implications for its chronology. *Geochimica et Cosmochimica Acta* **52**, 2147-2163.
- Montel, J.-M., Foret, S., Veschambre, M., Nicollet, C. & Provost, A. (1996). Electron Microprobe dating of monazite. *Chemical Geology* **131**, 37-53.
- Nemchin, A. A. & Pidgeon, R. T. (1998). Precise conventional and SHRIMP baddeleyite U-Pb age for the Binneringie Dyke, near Narrogin, Western Australia. *Australian Journal of Earth Sciences* **45**, 673-675.
- Nyquist, L. E. & Shih, C. Y. (1992). The isotopic record of lunar volcanism. *Geochimica et Cosmochimica Acta* **56**, 2213-2234.
- Plescia, J. B. (1994). Geology of the Small Tharsis Volcanoes: Jovis Tholus, Ulysses Patera, Biblis Patera, Mars. *Icarus* **111**, 246-269.
- Purtscheller, F. & Tessadri, R. (1985). Zirconolite and baddeleyite from metacarbonates of the Oetztal-Stubai complex (northern Tyrol, Austria). *Mineralogical Magazine* **49**, 523-529.
- Ramdohr, P. & El Goresy, A. E. (1970). Opaque Minerals of the Lunar Rocks and Dust from Mare Tranquillitatis. *Science* **167**, 615-618.
- Reed, S. J. B. (1996). *Electron Microprobe analysis and scanning electron microscopy in geology*. Cambridge University Press, Cambridge.
- Reischmann, T. (1995). Precise U/Pb age determination with baddeleyite (ZrO₂), a case study from the Phalaborwa Igneous Complex, South Africa. *South African Journal of Geology* **98**, 1-4.

- Schärer, U., Corfu, F. & Demaiffe, D. (1997). U-Pb and Lu-Hf isotopes in baddeleyite and zircon megacrysts from the Mbuji-Mayi kimberlite: constraints on the subcontinental mantle. *Chemical Geology* **143**, 1-16.
- Scherrer, N. C., Engi, M., Gnos, E., Jakob, V. & Liechti, A. (2000). Monazite analysis; from sample preparation to microprobe age dating and REE quantification. *Swiss Bulletin of Mineralogy and Petrology* **80**, 93-105.
- Scoates, J. S. & Chamberlain, K. R. (1995). Baddeleyite (ZrO₂) and zircon (ZrSiO₄) from anorthositic rocks of the Laramie anorthosite complex, Wyoming: Petrologic consequences and U-Pb ages. *American Mineralogist* **80**, 1317-1327.
- Siivola, J. (1977). Baddeleyite – ZrO₂ – from Lovasjarvi diabase, southeastern Finland. *Bulletin of the Geological Society of Finland* **49**, 59-64.
- Smith, J. V. & Steele, I. M. (1976). Lunar mineralogy: a heavenly detective story. Part II. *American Mineralogist* **61**, 1059-1116.
- Smith, J. V. & Hervig, R. L. (1979). Shergotty meteorite: mineralogy, petrography and minor elements. *Meteoritics* **14**, 121-141.
- Smith, C. B., Clark, T. C., Barton, E. A. & Bristow, J. W. (1994). Emplacement ages of kimberlite occurrences in the Prieska region, southwest border of the Kaapvaal Craton, South Africa. *Chemical Geology* **113**, 149-169.
- Stacey, J. S. & Kramers, J. D. (1975). Approximation of terrestrial lead isotope evolution by a two-stage model. *Earth and Planetary Science Letters* **29**, 207-221.
- Stoffler, D., Ostertag, R., Jammes, C. & Pfannschmidt, G. (1986). Shock metamorphism and petrography of the Shergotty achondrite. *Geochimica et Cosmochimica Acta* **50**, 889-903.
- Suzuki, K. & Adachi, M. (1991). Precambrian provenance and Silurian metamorphism of the Tsubonosawa paragneiss in the South Kitakami terrane, Northeast Japan, revealed by the chemical Th-U-total Pb isochron ages of monazite, zircon and xenotime. *Geochemical Journal* **25**, 357-376.
- Suzuki, K., Adachi, M. & Tanaka, T. (1991). Middle Precambrian provenance of Jurassic sandstone in the Mino Terrane, central Japan: Th-U-total Pb evidence from an electron microprobe monazite study. *Sedimentary Geology* **75**, 141-147.
- Williams, M. L., Jercinovic, M. J. & Terry, M. P. (1999). Age mapping and dating of monazite on the electron microprobe: Deconvoluting multistage tectonic histories. *Geology* **27**, 1023-1026.

Wingate, M. T. D. (1999). Ion microprobe baddeleyite and zircon ages for Late Archaean mafic dykes of the Pilbara Craton, Western Australia. *Australian Journal of Earth Sciences* **46**, 493-500.

Wingate, M. T. D., Campbell, I. H., Compston, W. & Gibson, G. M. (1998). Ion microprobe U-Pb ages for Neoproterozoic basaltic magmatism in south-central Australia and implications for the breakup of Rodinia. *Precambrian Research* **87**, 135-159.

Wingate, M. T. D. & Compston, W. (2000). Crystal orientation effects during ion microprobe U-Pb analysis of baddeleyite. *Chemical Geology* **168**, 75-97.

Table 2-1. A comparison of reference isotopic ages, new IDTIMS ages, and new EM ages for baddeleyite.

Source	Rock Type	IDTIMS age (this work)	EM age (this work)	Previous Geochronology	Reference
Binneringie dyke (Yilgarn craton)	gabbro	2410.3 ± 2.1 Ma	2548 +35/-36 Ma	2418 ± 3 Ma (IDTIMS: B); 2420 ± 7 Ma (SHRIMP: B)	[1] [1]
Phalaborwa igneous complex (S. Africa)	carbonatite	2059.6 ± 0.4 Ma	2026 +46/-47 Ma	2059.8 ± 0.8 Ma (IDTIMS: B)	[2]
				2060.6 ± 0.5 Ma (IDTIMS: B)	[3]
				2057 ± 8 Ma (LA-ICP-MS: B)	[4]
				2057.1 ± 2.6 Ma (SHRIMP: B)	[5]
Muskox intrusion (Slave craton)	feldspathic pyroxenite	*1269.4 ± 1.1 Ma	1329 +84/-86 Ma	1270 ± 4 Ma (IDTIMS: B+Z)	[6]
Moores Lake intrusion (Churchill Province)	gabbro	1108.8 ± 2.4 Ma	1132 +134/-139 Ma	-	-
Faber Lake sill (Great Bear magmatic zone)	gabbro	779.5 ± 1.5 Ma	921±29 Ma	-	-

Mineral analysed: B - baddeleyite; Z - zircon

References: [1] = Nemchin and Pidgeon (1998); [2] = Heaman and LeCheminant (1993); [3] = Reischman (1995); [4] = Horn et al. (2000); [5] = Wingate and Compston (2000); [6] = LeCheminant and Heaman (1989)

* data re-interpreted from LeCheminant and Heaman (1989)

Table 2-2. U-Pb baddeleyite/zircon results for reference samples.

	Weight (μg)	U (ppm)	Th (ppm)	Pb (ppm)	Th/U	TCPb (pg)	$^{206}\text{Pb}/$ ^{204}Pb	$^{206}\text{Pb}/$ ^{238}U	$^{207}\text{Pb}/$ ^{235}U	$^{207}\text{Pb}/$ ^{206}Pb	Model Ages (Ma)			%Disc
											$^{206}\text{Pb}/$ ^{238}U	$^{207}\text{Pb}/$ ^{235}U	$^{207}\text{Pb}/$ ^{206}Pb	
<i>GFA92-567 Faber Lake Gabbro Sheet, Canada</i> (64° 07' N; 116°40'W)														
1 B [95]	42	1158	81	137	0.07	19	20065	0.1262±2	1.133±2	0.06515±3	765.9±1.0	769.3±0.8	779.2±1.0	1.8
2 B [74]	42	1323	56	157	0.042	37	12083	0.1272±1	1.143±1	0.06517±3	771.7±0.8	773.8±0.7	779.9±1.0	1.1
<i>9009 Moores Lake Gabbro, Canada</i>														
*3 B [23]	8	482	48	86	0.10	11	4113	0.1857±4	1.960±4	0.07653±5	1098.2±1.9	1101.8±1.4	1108.9±1.4	1.1
*4 B [43]	14	216	17	40	0.08	30	1201	0.1857±4	1.959±5	0.07652±9	1098.0±1.9	1101.6±1.6	1108.7±2.4	1.0
5 Z [11]	8	874	2026	251	2.32	35	2404	0.1829±4	1.931±5	0.07659±8	1082.6±2.0	1091.9±1.6	1110.6±2.1	2.7
6 Z [80]	18	292	86	54	0.30	39	1534	0.1786±4	1.873±4	0.07605±8	1059.4±1.9	1071.5±1.6	1096.4±2.2	3.7
<i>3101 Muskox Feldspathic Pyroxenite, Canada</i> (67°05'N, 115°11'W)														
7 B [70]	24	1363	33	280	0.02	47	9499	0.2182±4	2.497±4	0.08300±5	1272.5±1.9	1271.2±1.2	1269.1±1.3	-0.3
8 Z [50]	20	1412	2181	381	1.54	218	1602	0.1951±3	2.205±4	0.08198±9	1148.9±1.7	1182.7±1.3	1244.9±2.1	8.4
9 B [38]	11	828	19	168	0.02	11	11308	0.2159±3	2.472±4	0.08301±6	1260.5±1.8	1263.8±1.2	1269.5±1.4	0.8
<i>LH97-18 Binneringie Gabbro Dyke, Australia</i> (31°42'05"S, 121°41'32"E)														
10 B [9]	9	554	28	251	0.05	27	5174	0.4449±12	9.551±27	0.15569±11	2372.7±5.5	2392.5±2.6	2409.4±1.2	1.8
11 B [43]	41	521	23	234	0.04	41	14618	0.4463±12	9.560±28	0.15534±8	2378.9±5.5	2393.3±2.7	2405.6±0.9	1.3
12 B [43]	71	868	72	369	0.08	484	3299	0.4135±10	8.763±22	0.15371±9	2230.7±4.4	2313.6±2.3	2387.7±1.0	7.8
13 B [4]	18	661	22	300	0.03	36	9410	0.4498±13	9.650±28	0.15560±10	2394.5±5.5	2402.0±2.7	2408.4±1.0	0.7
14 B [44]	32	525	41	211	0.08	149	2786	0.3907±10	8.173±23	0.15173±9	2125.9±4.7	2250.3±2.5	2365.5±1.0	11.9

Notes:

Mineral Analysed: B - baddeleyite; Z - zircon; number of grains per fraction in: []

Th concentration estimated from abundance of ^{208}Pb and corresponding $^{207}\text{Pb}/^{206}\text{Pb}$ ages

TCPb refers to the total amount of common Pb in picograms measured in the analysis

Atomic ratios are corrected for fractionation, blank, spike and common Pb (Stacey and Kramers, 1975)

 $^{206}\text{Pb}/^{204}\text{Pb}$ ratios are corrected for fractionation and spike only

All errors quoted in this table are 1 sigma uncertainties

* Fractions analysed using the S54. All other analyses determined using a VG354

Data for Muskox feldspathic pyroxenite (3101) are reproduced from LeCheminant and Heaman (1989)

Table 2-3. Chemical composition of baddeleyite samples.

	Binneringie dyke (LH97-18)	Phalaborwa complex (IN1)	Muskox intrusion (3101)	Moore's Lake intrusion (9009)	Faber Lake sill (GFA 92-567)
	<i>g.m.</i>	<i>g.m.</i>	<i>t.s.</i>	<i>g.m.</i>	<i>g.m.</i>
ZrO ₂	98.08	100.06	100.99	98.08	98.02
HfO ₂	0.56	0.49	0.47	0.49	0.58
SiO ₂	0.01	0.00	0.02	0.01	0.01
UO ₂	0.064	0.080	0.144	0.066	0.158
PbO	0.029	0.027	0.030	0.010	0.021
ThO ₂	0.004	0.002	0.004	0.007	0.007
Total	98.75	100.66	101.66	98.66	98.80
<i>n</i>	140	75	17	35	138
<i>g</i>	13	1	2	12	19

g.m. refers to polished grain mount; *t.s.* refers to polished thin section; *n*=number of WDS point analyses; *g*=number of grains investigated

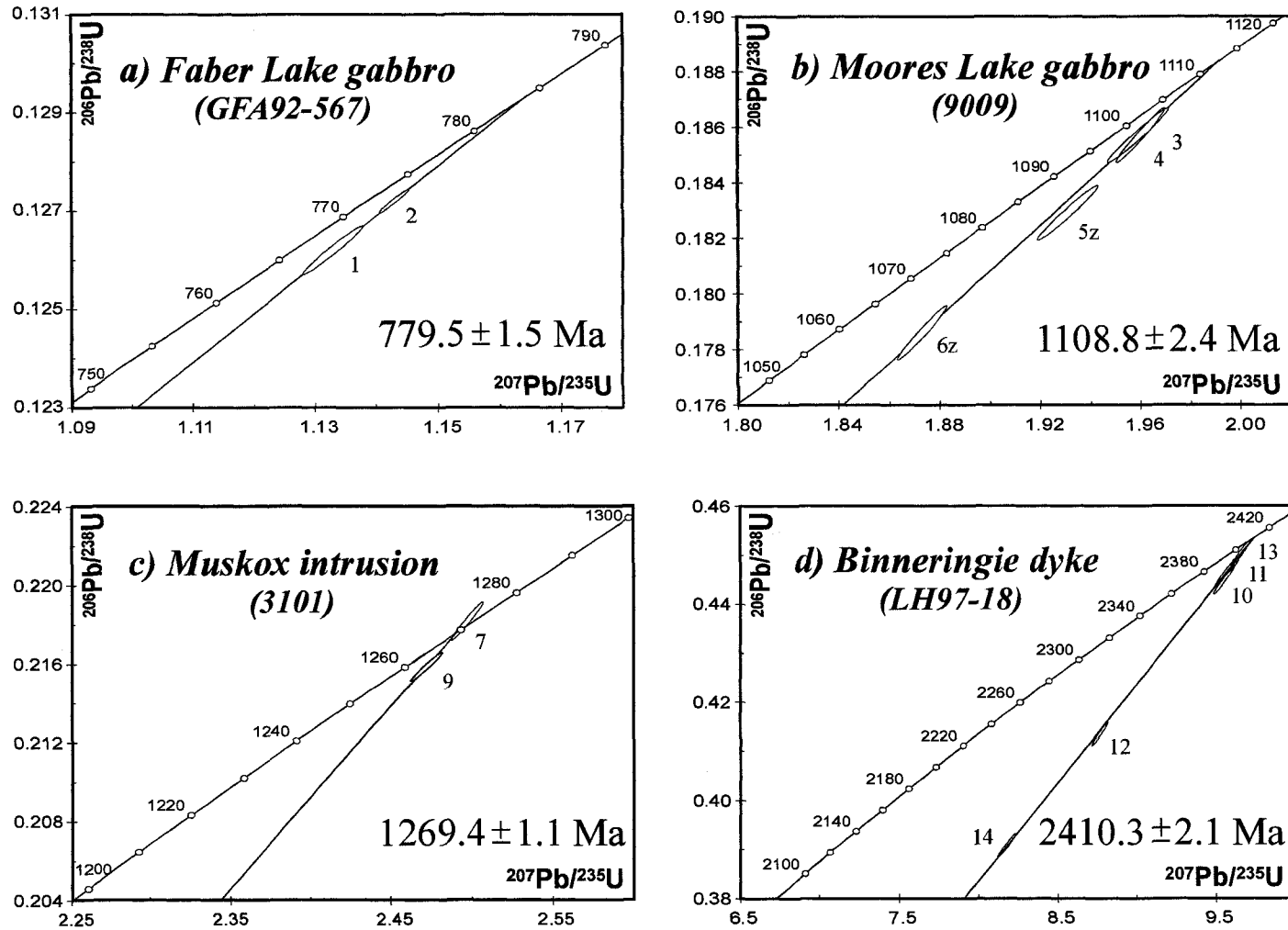


Fig. 2-2. Concordia diagrams showing U-Pb results for baddeleyite and zircon fractions from the Faber Lake gabbro (a), Moores Lake gabbro (b), Muskox feldspathic pyroxenite (c), and Binneringie dyke (d). Data for the Muskox feldspathic pyroxenite are from LeCheminant and Heaman (1989).

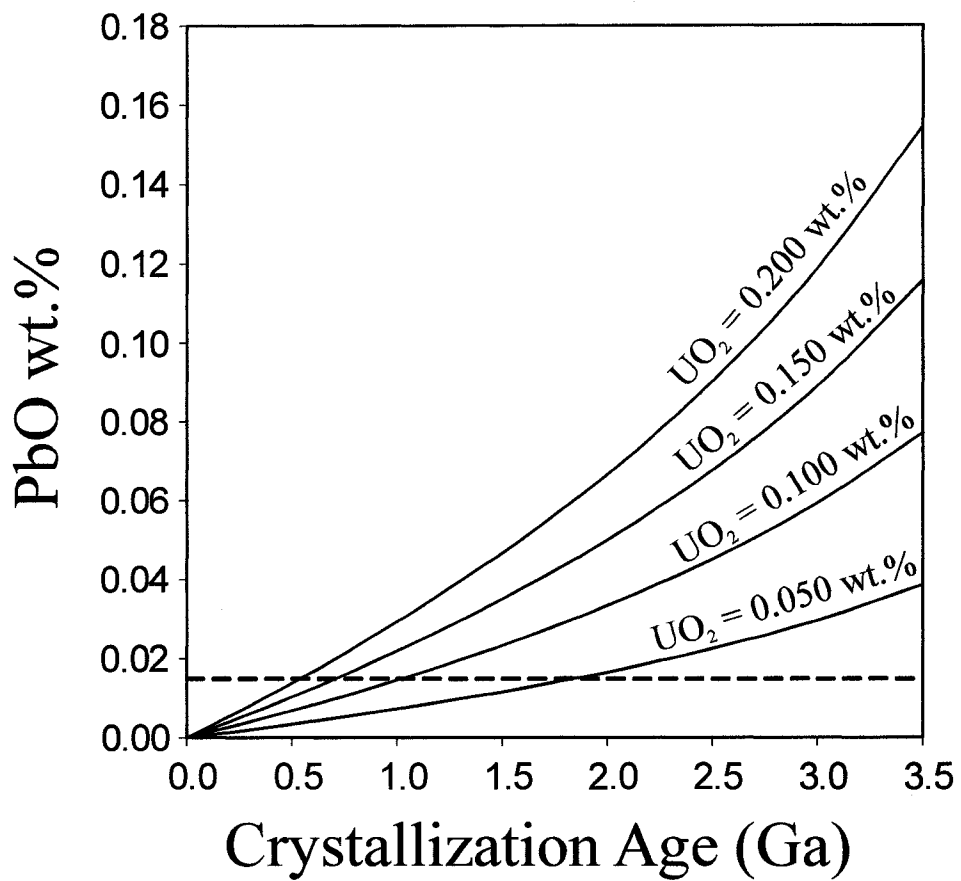


Fig. 2-3. PbO content versus crystallization age for baddeleyite of various UO₂ concentrations. The dashed line represents the functional detection limit of PbO in this study, and the intersection of that line with a given U-Pb concentration curve defines the minimum age of baddeleyite to which the EM U-Th-total Pb chemical dating technique is applicable.

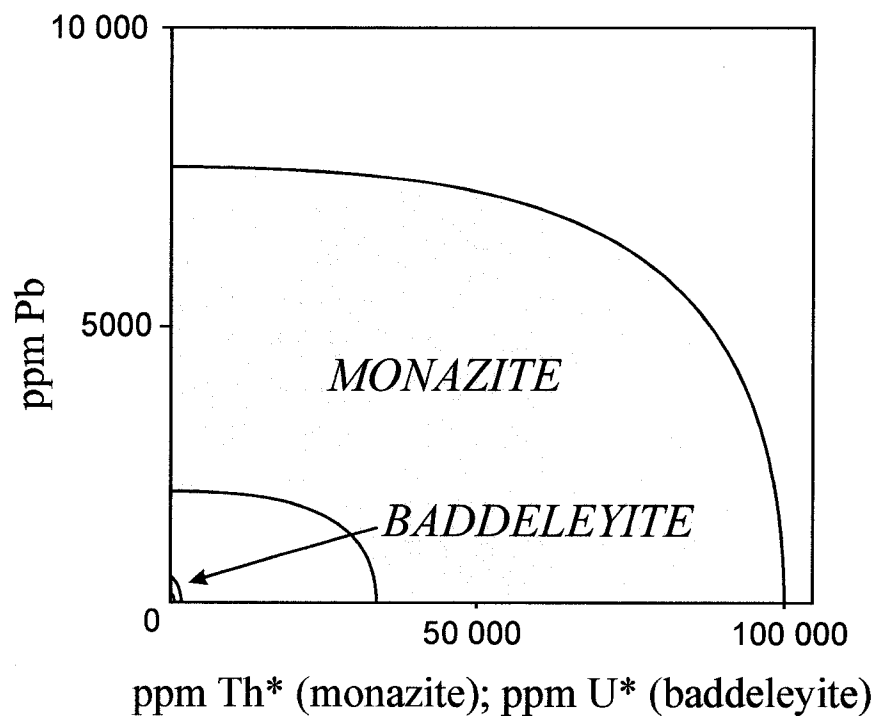


Fig. 2-4. A plot of Pb content versus Th* in monazite and U* in baddeleyite showing the typical range of values encountered during an EM chemical U-Th-total Pb analysis of each mineral. Th* represents Th content corrected for U contribution to radiogenic Pb, and vice versa for U*.

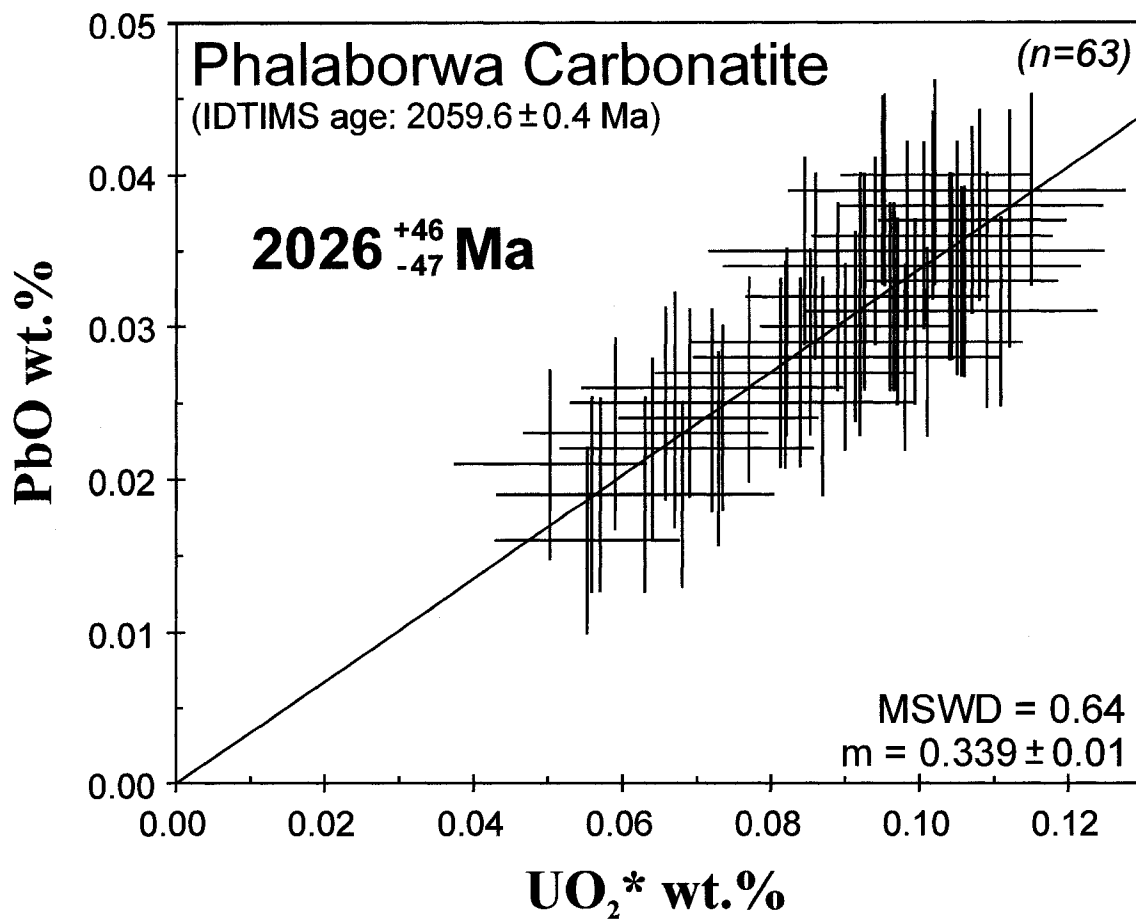


Fig. 2-5. Plot of PbO vs. UO₂* for baddeleyite from the Phalaborwa carbonatite. Individual error crosses represent 2σ analytical uncertainties; errors on the regressed slope and final age are at the 2σ level.

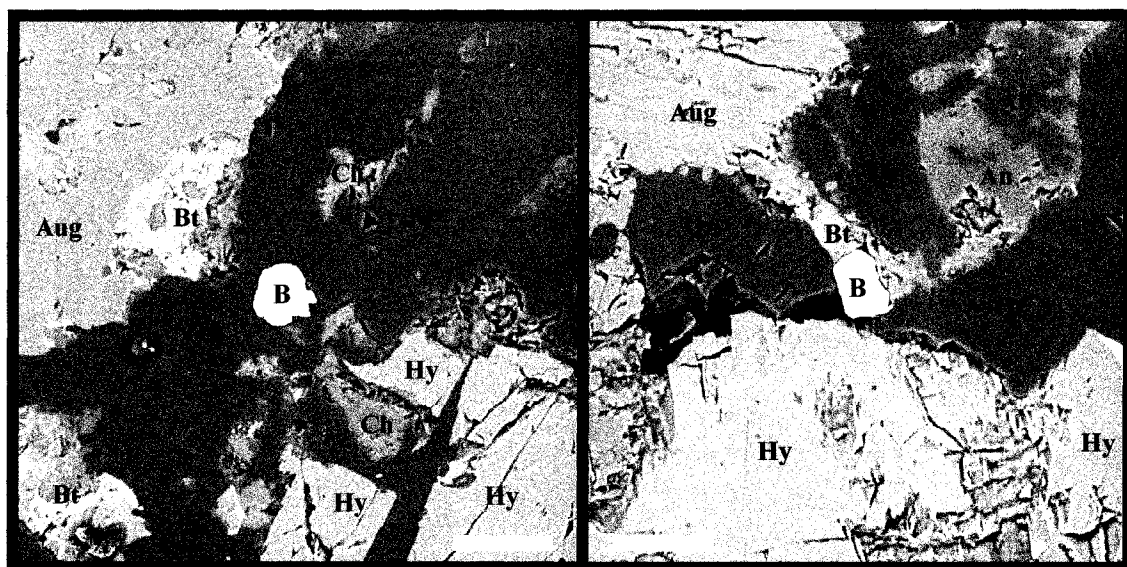


Fig. 2-6. BSE images of feldspathic pyroxenite sample 3101 from the MuskoX intrusion showing the petrographic positions of baddeleyite crystals analysed in this study (baddeleyite crystals referred to in the text as grains A and B are shown in the left and right BSE images respectively). Mineral abbreviations are as follows: Ab - albite, An - anorthoclase, Aug - augite, B - baddeleyite, Bt - biotite, Ch - chlorite, Hy - hypersthene, Qz - quartz. Scale bars are 50 μm .

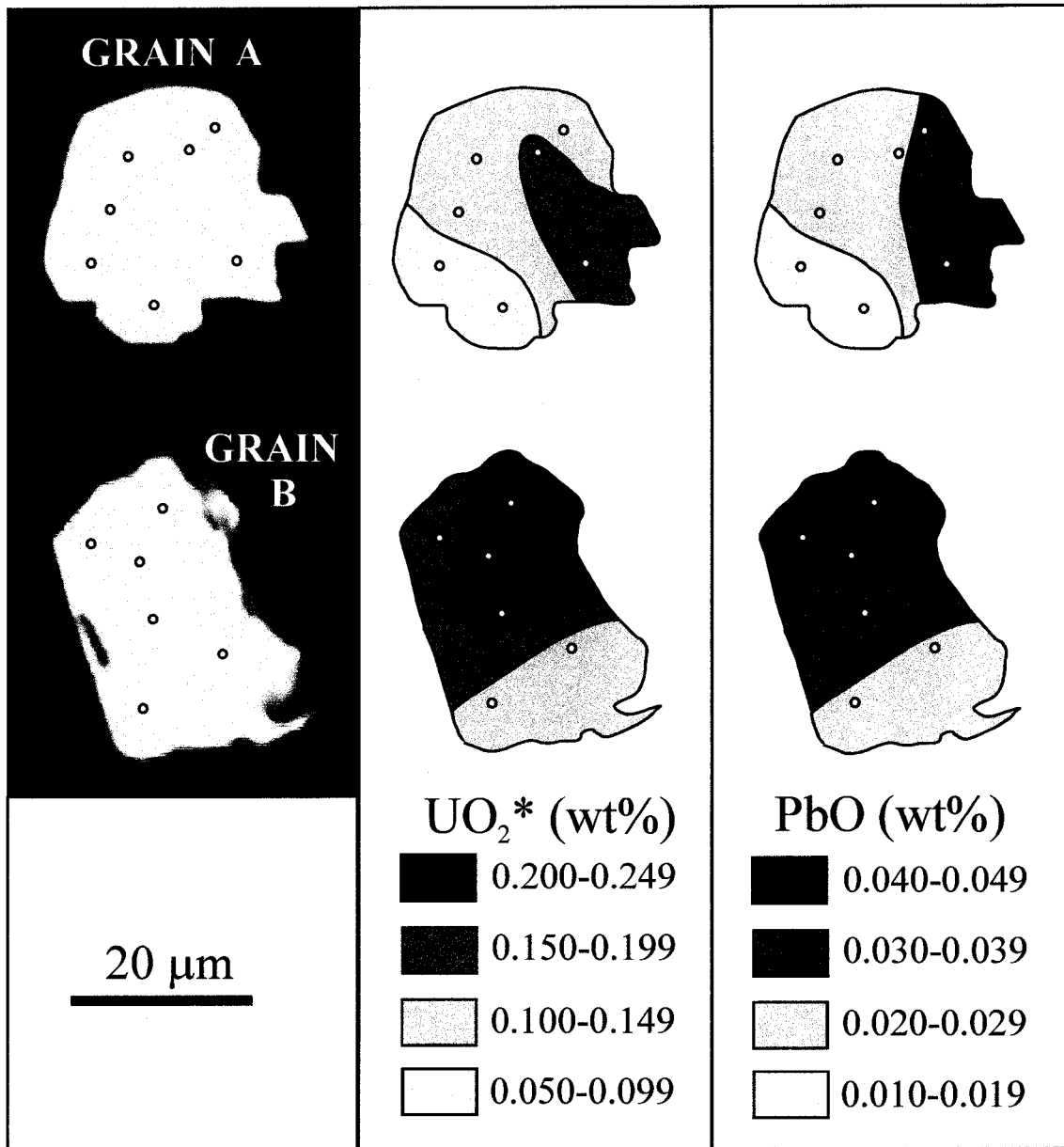


Fig. 2-7. Close-up BSE images (left) of the *in situ* crystals of baddeleyite analysed from sample 3101 of the Muskox intrusion, showing the locations of WDS spot analyses used in the EM chemical age determinations. The contour diagrams (right) display marked systematic variations in U and Pb content at the micron scale in baddeleyite.

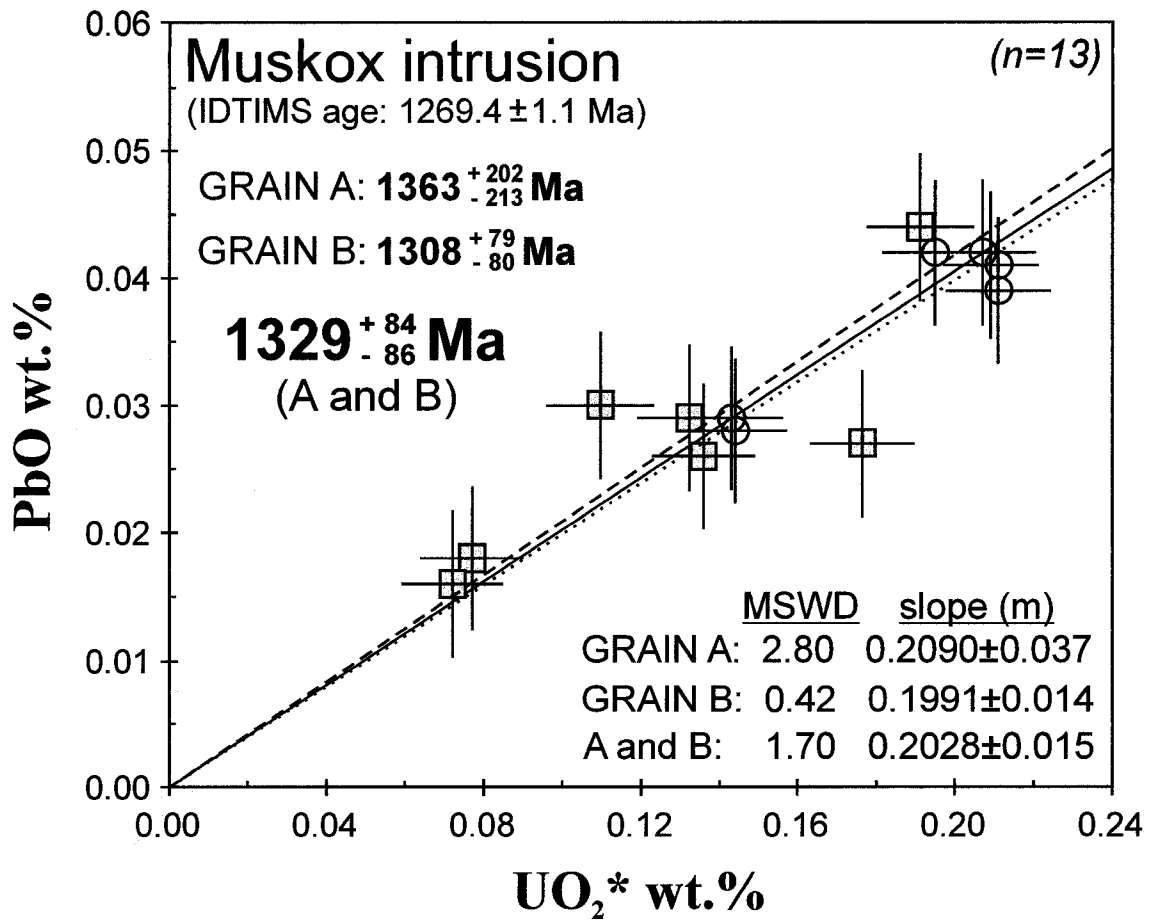


Fig. 2-8. Plots of PbO vs. UO_2^* for *in situ* baddeleyite crystals from the Muskox intrusion (feldspathic pyroxenite sample 3101) including grain A (shaded squares; dashed line), grain B (open circles; dotted line), and both grains together (solid line). Explanation of errors is the same as for Fig. 2-5.

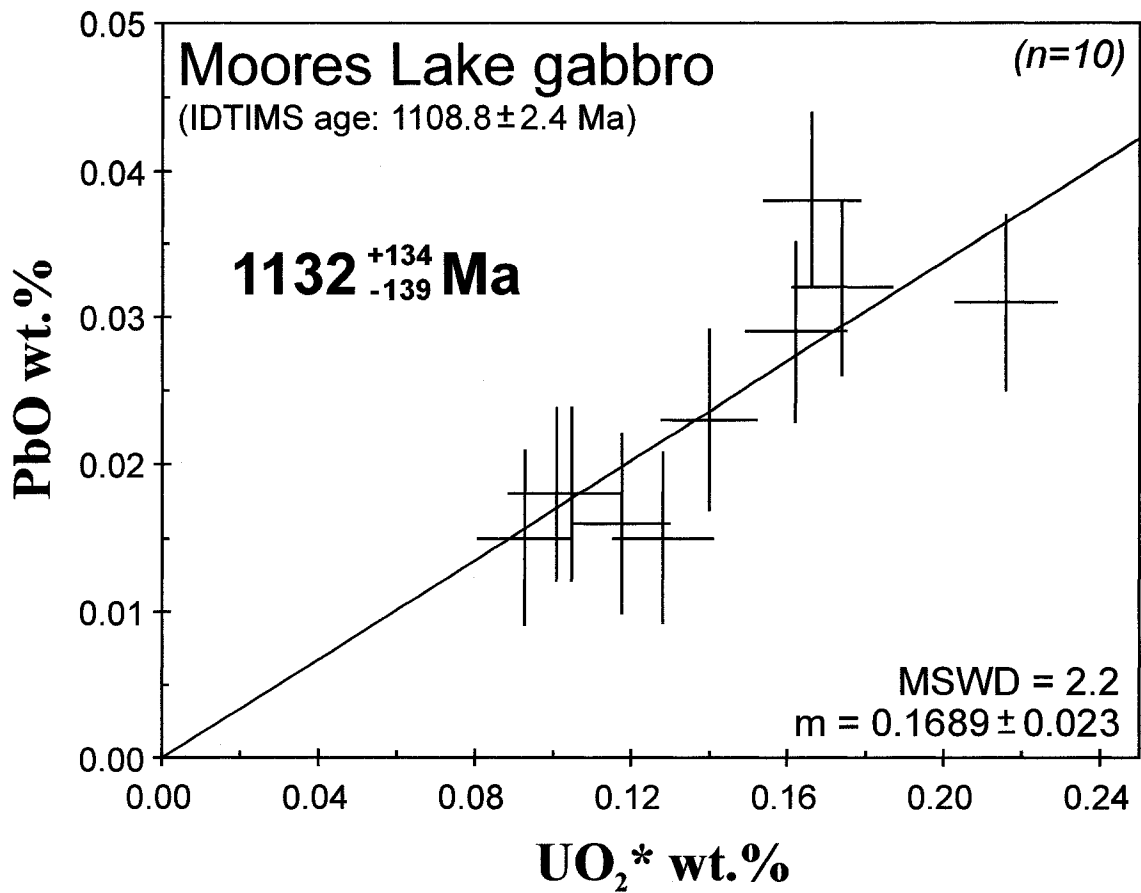


Fig. 2-9. Plot of PbO vs. UO₂* for baddeleyite from the Moores Lake gabbro dyke (sample 9009). Explanation of errors is the same as for Fig. 2-5.

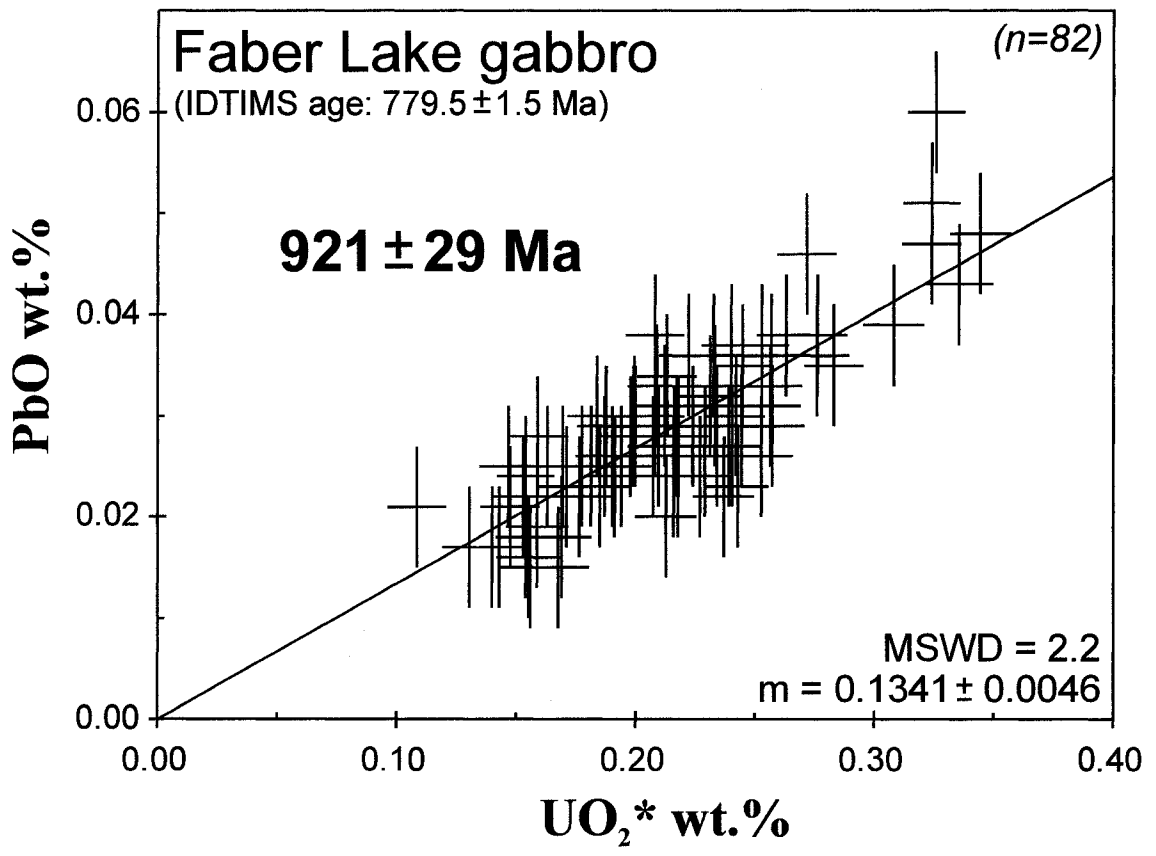


Fig. 2-10. Plot of PbO vs. UO₂* for baddeleyite from the Faber Lake gabbro sheet (sample GFA92-567). Explanation of errors is the same as for Fig. 2-5.

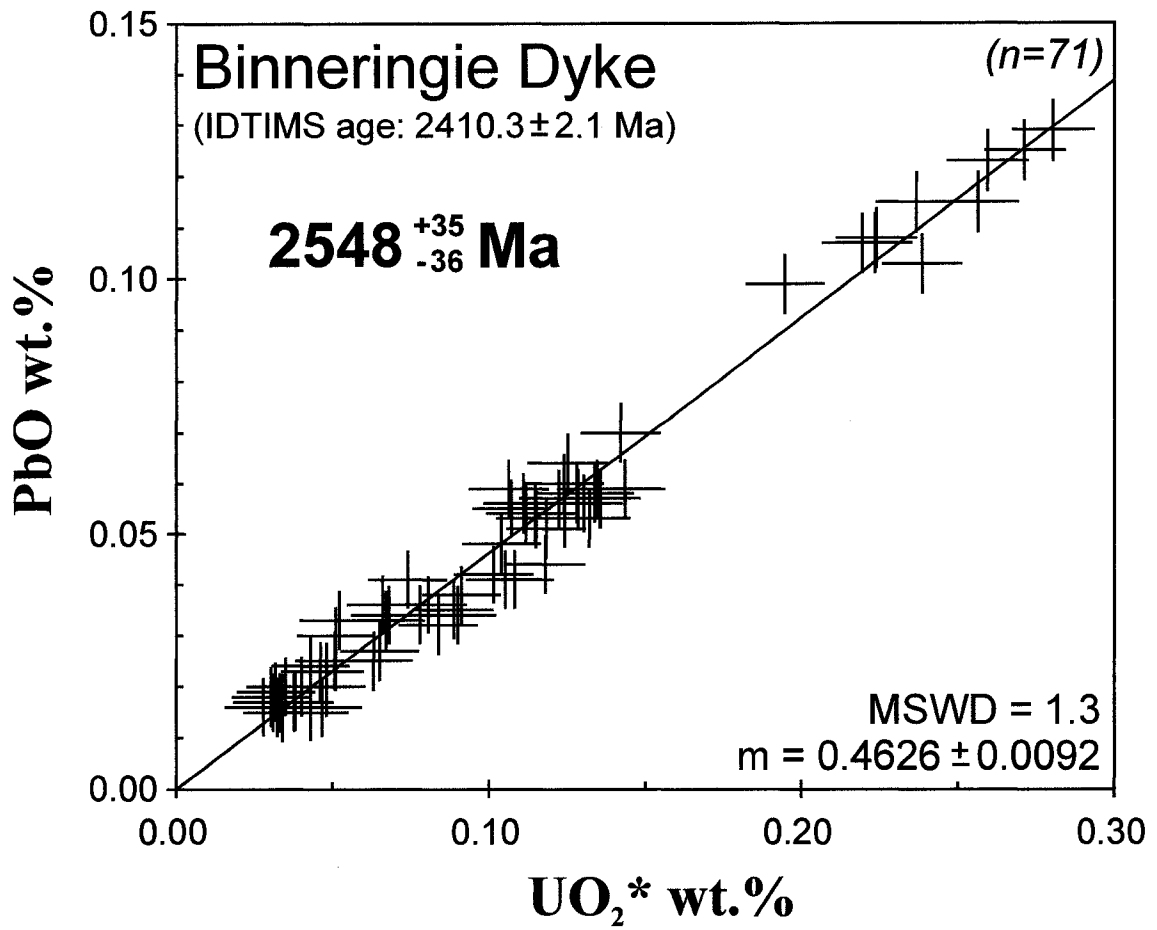


Fig. 2-11. Plot of PbO vs. UO₂* for baddeleyite from the Binneringie gabbro dyke (sample LH97-18). Explanation of errors is the same as for Fig. 2-5.

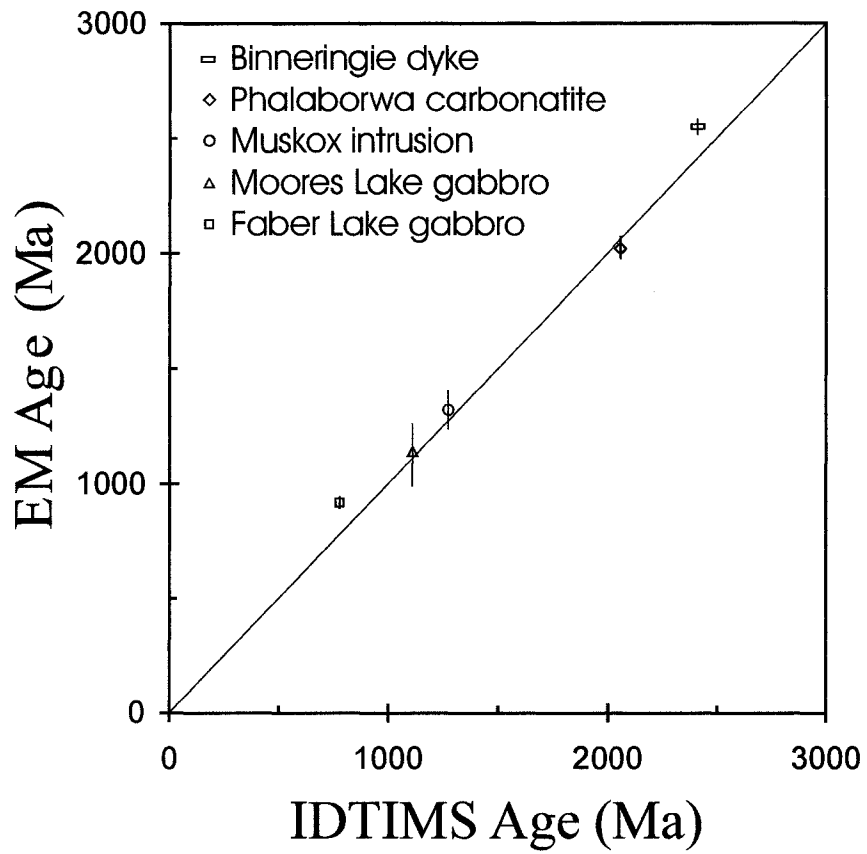


Fig. 2-12. Comparison of chemical (EM) ages with isotopic (IDTIMS) ages for the five baddeleyite reference samples analysed in this study. The line represents 1:1 correspondence in ages obtained with the two techniques.

CHAPTER 3

1891-1883 Ma Southern Bastar-Cuddapah Mafic Igneous Events, India: A Newly Recognized Large Igneous Province

Jason E. French^{a,*}, Larry M. Heaman^a, Thomas Chacko^a, and Rajesh K.
Srivastava^b

^a *Department of Earth and Atmospheric Sciences, University of Alberta, 1-26 Earth
Sciences Building, Edmonton, AB, Canada, T6G 2E3*

^b *Department of Geology, Banaras Hindu University, Varanasi 221 005, India*

INTRODUCTION

Giant mafic dyke swarms are preserved in many Archean cratons worldwide and are often interpreted to represent the erosional remnants of continental large igneous provinces (LIPs). They may represent feeders to continental flood basalts (CFBs) temporally linked to mantle plume activity and may be associated with major episodes of crustal extension that can lead to continental rifting and supercontinent break-up (Fahrig, 1987; LeCheminant and Heaman, 1989; Ernst and Buchan, 2001). Establishing the exact timing of emplacement of mafic dyke swarms is critical to unravelling crustal evolution because they represent excellent regional time markers (Fahrig, 1987; LeCheminant and Heaman, 1989; Harlan et al., 2003). Mafic dykes can also be used to constrain apparent polar wander paths (e.g.: Halls and Heaman, 2000; Wingate and Giddings, 2000), and can provide robust piercing points that enhance the veracity of paleocontinental reconstructions (e.g.: Heaman 1997; Wingate et al., 1998; Mertanen et al., 1999; Harlan et al., 2003; Hanson et al. 2004a).

The Indian shield is transected by numerous, crosscutting Precambrian mafic dyke swarms (Fig. 3-1; Drury, 1984; Murthy, 1987; Murthy, 1995; Ramachandra et al.,

1995). The southern part of the Bastar (Bhandara) craton alone is transected by a minimum of three geochemically and petrographically distinct Precambrian mafic dyke swarms (Srivastava et al., 1996; Srivastava and Singh, 2003; Srivastava and Singh, 2004). Currently there is a complete lack of robust geochronological information available for the age of emplacement of any mafic dyke swarm in this area, but field relationships and preliminary U-Pb results indicate that a prominent NW-SE trending dolerite dyke swarm was emplaced in the Paleoproterozoic (Srivastava et al., 2000). There is also compelling geochronological evidence which suggests that a record of late Paleoproterozoic (~1.9 Ga) extension and prolific mafic magmatic activity also exists in the Cuddapah basin of the adjacent Dharwar craton (Bhaskar Rao et al., 1995; Anand et al., 2003).

The Dharwar and Bastar cratons of peninsular India are central to many proposed reconstructions of ancient Precambrian supercontinents including Ur at ~3.0 Ga (Rogers, 1996), Capricornia at ~1.7 Ga (Krapez, 1999), Columbia (also known as Hudsonland) at ~1.5 Ga (Rogers and Santosh, 2002; Zhao et al., 2002), and possible juxtaposition of the southern block of the Indian shield with the eastern block of the North China craton at ~2.5 Ga (Zhao et al., 2003). Obtaining precise and accurate U-Pb ages for southern Bastar and Cuddapah mafic igneous rocks is critical for evaluating Paleoproterozoic continental reconstructions, and enables temporal correlation with LIPs in other cratons worldwide. In this paper, we present the results of a multidisciplinary geochronological investigation of a suite of mafic dykes from the southern Bastar craton (SBC), and one dolerite sill from the Cuddapah basin. We present ages obtained by conventional high precision U-Pb isotope dilution thermal ionization mass spectrometry (IDTIMS) dating

of zircon, baddeleyite, and rutile, and high spatial resolution dating of monazite in polished thin section using electron microprobe (EM) and laser ablation multi-collector inductively coupled plasma mass spectrometry (LA-MC-ICP-MS). Together, these new ages for mafic magmatism in the SBC and Cuddapah basin document the remnants of an extensive 1.9 Ga LIP. Furthermore, we show that 1.9 Ga mafic magmatism is preserved in several Precambrian cratons worldwide and discuss the possible origins of this global mafic magmatism.

GEOLOGICAL SETTING

The Precambrian shield of south India is transected by a >200 x ~1600 km long, ENE-WSW trending mobile belt known as the Central Indian Tectonic Zone (CITZ). The CITZ divides the shield into two major crustal blocks (Fig. 3-1), both of which are transected by Precambrian mafic dyke swarms (Drury, 1984; Murthy, 1987; Murthy, 1995; Ramachandra et al., 1995; Stein et al., 2004). The northern block is known as the Aravalli protocontinent and includes the Aravalli-Delhi Belt, Bundelkhand massif, and Vindhyan basin (Naqvi et al., 1974). The southern block is referred to as the Dharwar protocontinent and includes the Dharwar craton and South Indian granulite terrane (Dravidian shield of Rogers, 1986), and the Bastar and Singhbhum cratons (Singhbhum protocontinent of Naqvi et al., 1974; Rogers, 1986; Rao and Reddy, 2002; Zhao et al., 2003; Stein et al., 2004).

Bastar craton

U-Pb zircon ages of basement gneisses of $3509 \pm 14/-7$ Ma (Sarkar et al., 1993) and 3561 ± 11 Ma (Ghosh, 2004) indicate that the Bastar craton was an important component in the earliest stages of nucleation of the Indian shield. Sarkar et al. (1990;

1993) reported a U-Pb zircon date of 2480 ± 3 Ma for typical granite from the SBC, located at Markampara, and a Pb-Pb isochron age of 2573 ± 139 Ma for granite from Sukma. In addition, Re-Os molybdenite dating from mineralization associated with calc-alkaline plutonic rocks from Malanjkhanda at the north-western margin of the Bastar craton yielded an age of 2490 ± 8 Ma (Stein et al., 2004), which hints that the widespread granitoid plutonism at ~ 2.5 Ga in the eastern Dharwar (Jayananda et al., 2000) and Aravalli cratons (Wiedenbeck et al., 1996) is also present across much of the Bastar craton.

The Bastar craton is a $\sim 500 \times 500$ km, four-sided crustal block that is bounded by two mobile belts, the Central Indian Tectonic Zone (CITZ) to the northwest and the Eastern Ghats Belt (EGB) to the southeast, and by two rifts, the Mahanadi rift to the northeast and the Godavari rift to the southwest (Fig. 3-1). The CITZ is proposed to have formed through oblique collision between the Dharwar and Aravalli protocontinents beginning at ~ 2.5 Ga (Stein et al., 2004), but may also have been reactivated during later-stage events from ~ 2.2 - 0.9 Ga (Roy and Prasad, 2003). The EGB is interpreted to be the product of a multistage continent-continent collision involving the Dharwar protocontinent and continental crust presently in east Antarctica (Rogers, 1996). Parts of the EGB west of the Godavari rift experienced metamorphism at ca. 1.6 Ga whereas metamorphism in most of the EGB is Grenvillian (ca. 1.0 Ga) in age (Mezger and Cosca, 1999; Rickers et al., 2001).

Initiation of sedimentation in the Godavari rift is thought to have occurred as early as 1500-1600 Ma, with a minimum age constrained by a K-Ar date of 1330 ± 53 Ma reported for glauconitic minerals from Godavari Supergroup sediments (Chaudhuri et

al., 2002). On the basis of stratigraphic correlations with sedimentary rocks within the Vindhyan basin that yield K/Ar ages as old as 1.2 Ga, Rogers and Santosh (2002) suggested that some component of Mahanadi rifting may have been contemporaneous with early Godavari rifting. Recent U-Pb zircon dating and Sr isotope data from the lower Vindhyan Supergroup indicate that the lowest units have a minimum age of 1631 Ma (Ray et al., 2002), which in turn suggests that rifting along the pre-existing suture occurred by this time.

A number of other intracratonic basins were apparently also forming during the Meso- to Neoproterozoic in the Bastar craton, of which the most aerially extensive are the Chattisgarh and Indravati basins (Chaudhuri et al., 2002; Deb and Chaudhuri, 2002). Reactivation of the Godavari rift and concomitant development of the Mahanadi rift occurred in Permo-Triassic times during the break-up of Gondwanaland, and the final stages of rifting and sedimentation occurred in the Early Cretaceous, culminating with late uplift and erosion linked with arrival of the Deccan mantle plume and associated outpouring of voluminous flood basalts at the Cretaceous/Tertiary boundary (Courtilot et al., 1986; Allègre et al., 1999; Mishra et al., 1999; Biswas, 2003; Sengupta, 2003).

Extent and Nature of Precambrian Mafic Dyke Swarms in the Bastar craton

Precambrian mafic dyke swarms transect much of the SBC (Fig. 3-2) and semi-continuously span a minimum area of $\sim 17,000 \text{ km}^2$. These swarms predominantly trend NW-SE to WNW-ESE (Crookshank, 1963; Ramachandra et al., 1995), with subordinate ENE-WSW, and N-S orientations (Mishra et al., 1988; Ramakrishnan, 1990). Individual swarms may extend along strike for up to 150 km (Ramachandra et al., 1995). Mapped dyke abundance varies along a NE to SW transect and four relatively dense

concentrations of NW-SE trending mafic dykes have been identified (Ramachandra et al., 1995). NW-SE trending mafic dykes occur at least as far north as the southernmost extension of the N-S trending Kotri linear belt, where they are truncated by ~2.5 Ga continental rift-related rocks of the Kotri (Dongargarh) Supergroup (Ghosh, 2004).

Most mafic dykes in the SBC are parallel to the NW-SE trending Godavari rift and to spatially associated NW-SE trending lineaments identifiable in satellite imagery (Ramanamurthy and Parthasarathy, 1988; Rajurkar et al., 1990). Crookshank (1963) suggested that some dykes in the SBC may have been emplaced along pre-existing faults and that they are roughly parallel to the structural grain of older gneisses. Towards the north-eastern part of the craton, north of the Khariar basin (Fig. 3-2), the main trend of dolerite dykes is NNW-SSE, oblique to the trend of the Mahanadi rift further to the northeast (Biswal and Sinha, 2003). At the north-western edge of the Bastar craton, inter- and post-mineralization dolerite dykes associated with the porphyry Cu-Mo-Au deposit at Malanjkhand may have been emplaced close to 2490 ± 8 Ma (Re-Os molybdenite), the primary age of mineralization (Stein et al., 2004).

The first geological reports on the Bastar craton mafic dykes identified at least two ages of mafic magmatism based on the occurrence of both metamorphosed and unmetamorphosed dykes (Crookshank, 1963, Chatterjee, 1970; Ghosh et al., 1977; Ramakrishnan, 1990). Ramachandra et al. (1995), studied a suite of dolerite dykes from the NW-SE trending Bhanupratappur-Keskal (BK) mafic dyke swarm south of the Chattisgarh basin, and classified them as predominantly sub-alkaline basalts, ranging from quartz-normative tholeiites, with subordinate olivine-normative tholeiites and nepheline-normative calc-alkaline rocks. The BK swarm occurs in close spatial

association with the N-S trending bimodal belt of the Kotri Supergroup, but a temporal relationship is unclear (Ramachandra et al., 1995). Three other secondary dyke swarms, delineated mainly on the basis of frequency maxima of dyke abundances in different areas (Fig. 3-2), have also been recognized in the region; the Narainpur-Kondagaon (NK) swarm, the Gidam-Tongpal (GT) swarm, and the Bijapur-Sukma (BS) swarm (Ramachandra et al., 1995).

In the Bastar study area (Fig. 3-2 inset and Fig. 3-3), individual mafic dykes are typically 20- to 30-m-wide (ranging up to 200-m-wide) with strike lengths that can be traced from hundreds of meters to ~20 km. These dykes coincide with the GT swarm of Ramachandra et al. (1995) and were first studied in detail by Srivastava et al. (1996). On the basis of field, petrographic and geochemical characteristics they were classified into two petrogenetically distinct NW-SE to WNW-ESE-trending dyke swarms including an older metamorphosed swarm of amphibolite dykes (BD1 swarm) and a younger swarm of fresh to variably altered dolerite dykes (BD2 swarm). A third suite of geochemically and petrographically distinct metamorphosed high-Mg boninite dykes (HMD) has also been recognized in the region, and also trend NW-SE to WNW-ESE with subordinate NE-SW dykes (Srivastava and Singh, 2003). The BD1, BD2, and HMD dyke swarms outcrop over a minimum area of ~1000 km² (Fig. 3-3), but possible genetic and temporal relationships with mafic dykes in the BK, NK, and BS regions could greatly extend the dimensions of the swarms.

The Cuddapah basin, Dharwar craton

The crescent-shaped, Proterozoic Cuddapah basin ("C" in Fig. 3-1) spans ~44,500 km² within the eastern Dharwar craton and comprises a quartzite-pelite-

carbonate succession that is variably intercalated with volcanic flows and sills (predominantly mafic) with subordinate alkaline and felsic volcanoclastic rocks and intrusions. The basin has a total stratigraphic thickness of >12 km (Nagaraja Rao et al., 1987; Ramam and Murty, 1997; Singh and Mishra, 2002). The lowermost succession (the Cuddapah Supergroup) nonconformably overlies basement rocks of the Dharwar craton including Archean TTG (Peninsular) gneisses and greenstone belts, and numerous Paleoproterozoic mafic dyke swarms (Nagaraja Rao et al, 1987; Murty et al, 1987). The lower two thirds consists primarily of clastic and chemical sedimentary rock with minor intercalations of alkali to sub-alkali basaltic flows, mafic sills and ashfall tuffs (Nagaraja Rao et al, 1987; Chatterjee and Bhattacharji, 2001; Anand et al, 2003). The upper third of the Cuddapah Supergroup, is characterized by a much larger proportion of basaltic to picritic lava flows and sills, ignimbrites and ashfall tuffs (Nagaraja Rao et al, 1987; Ramam and Murty, 1997; Chatterjee and Bhattacharji, 2001).

The present study focuses on mafic igneous rocks of the Tadpatri Formation (Fig. 3-4). These rocks are predominantly intrusive in nature (Srikantia, 1984; Anand et al. 2003) but lava flows including pillow lavas have also been reported (Reddy, 1988). Geophysical investigations of the Cuddapah basin including magnetic, gravity, and seismic methods indicate the presence of a large (up to 4-5 km thick) asymmetrical, lopolithic mafic intrusion along the base of the basin, which is interpreted to have formed contemporaneously with mafic intrusions of the lower stratigraphy (Tewari and Rao, 1987; Mishra et al., 1987a; Singh and Mishra, 2002).

There have been a number of previous geochronological investigations of rocks from the Cuddapah basin employing a range of chronometers ($^{40}\text{Ar}/^{39}\text{Ar}$, K-Ar, Pb-Pb,

Rb-Sr; Table 3-1), including mafic lava flows and sills, a lampröite dyke at Chelima, and U-mineralized stromatolitic dolomites (Aswathanarayana, 1964; Crawford and Compston, 1973; Murty et al., 1987; Bhaskar Rao et al., 1995; Chalapathi Rao et al., 1996; Chalapathi Rao et al., 1999; Zachariah et al., 1999; Anand et al., 2003). On the basis of K-Ar and $^{40}\text{Ar}/^{39}\text{Ar}$ ages for the Chelima lampröite (Murty et al., 1987; Chalapathi Rao et al., 1996; Chalapathi Rao et al., 1999), sedimentation in the Nallamalai sub-basin commenced prior to ~ 1.4 Ga. Estimates for the timing of Cuddapah Supergroup deposition and magmatism are based on the timing of intrusion of mafic sills or U-mineralizing events and varies by more than a billion years, ranging from ~ 0.6 Ga to ~ 1.9 Ga (Table 3-1). Currently the most robust radiometric age constraints for the timing of intrusion of mafic sills within the Tadpatri Formation comprise two identical ages of 1899 ± 20 Ma for disparate (>100 km apart) mafic sills determined by ^{40}Ar - ^{39}Ar laser fusion dating of phlogopite separates (Anand et al., 2003). The data indicate that an early phase of extension and mafic volcanism occurred within the Cuddapah basin at ~ 1.9 Ga (Anand et al., 2003). However, the exact timing, duration, origin, and geographic extent of this ~ 1.9 Ga mafic magmatic province within the Dharwar protocontinent remain unclear.

PETROGRAPHY

Detailed petrographic descriptions, discriminating geochemical features, and petrogenetic interpretations of the BD1, HMD, and BD2 dyke swarms can be found in Srivastava et al. (1996), Srivastava and Singh (2003), and Srivastava and Singh (2004), and whole rock geochemical data for the dykes dated by U-Pb in this study are presented in Appendix D.

BD2 mafic dyke swarm, Bastar craton

In accordance with the three subgroups of BD2 dykes outlined by Srivastava and Singh (2004), the samples in this study (including samples dated by EM chemical baddeleyite and zircon: Appendices A and C) have been classified as fresh dolerite (JEF-00-18; JEF-00-30; JEF-00-37), hornblende dolerite (JEF-00-34), and altered dolerite (JEF-00-36; JEF-00-39). The major primary minerals in the fresh BD2 dykes in this study are clinopyroxene (30-40%), plagioclase (35-55%), quartz (5-20%), and lesser amounts of opaques (3-5%), and apatite (1-3%). The samples show ophitic to sub-ophitic texture, with clinopyroxene predominantly interstitial to the plagioclase. Primary U- and Th-bearing accessory minerals include a significant amount of zircon, and trace amounts of baddeleyite, zirconolite, and monazite, and in one case all four were discovered in the same thin section (JEF-00-30). Plagioclase commonly exhibits polysynthetic twinning, and to a lesser extent weak oscillatory zoning.

The 'altered' and 'hornblende' BD2 dykes also contain significant amounts of hornblende, biotite, chlorite, stilpnomelane, \pm prehnite, epidote (locally intergrown with allanite), and disseminated opaques. The degree of alteration of plagioclase ranges from ~20% in the fresh dolerite to ~90% in the most altered sample (JEF-00-36). Plagioclase is altered to an assemblage of predominantly sericite, with lesser amounts of chlorite and stilpnomelane. Clinopyroxene is variably altered from sample to sample, ranging from very minor (~5%) alteration restricted to grain boundaries and cleavage traces, to complete replacement by secondary minerals. Sample JEF-00-34 represents an intermediate example of the alteration styles observed in the BD2 dykes, and has ~25% relict clinopyroxene. This sample exhibits a corona texture, whereby clinopyroxene is

rimmed and pseudomorphed by hornblende. The two minerals are almost invariably separated by a fine-grained assemblage of chlorite \pm tiny disseminated opaques \pm stilpnomelane, which we interpret to have formed during preferential breakdown of clinopyroxene during later-stage sericitic alteration. Biotite is commonly associated with hornblende, and almost invariably associated with late crystallizing quartz, apatite, and opaques. In some dykes, biotite is partially altered to (particularly along cleavage planes) and pseudomorphed by prehnite \pm chlorite. The stilpnomelane is commonly associated with abundant iron-stained orange fractures, which in some cases exhibit thin alteration halos in hornblende, whereby the hornblende has been altered to chlorite along the orange coloured fractures. Particularly along grain boundaries and cleavage traces, hornblende is variably altered to felted fibrous mats of blue-green amphibole (uralite) that impart a colour zonation to most of the grains from brown or green-brown to blue-green (Fig. 3-5a), with associated zoned birefringence patterns.

U- and Th-bearing accessory minerals

Zircon is most abundant in hornblende- and biotite-rich samples, which supports the idea that these minerals formed during the latter stages of magma crystallization. In some cases several hundred zircons, typically $\sim 60 \mu\text{m}$ in length (but up to $400 \mu\text{m}$) are present in a single thin section and commonly occur in dense clusters of cross-shaped grains that tend to be equally spaced, oriented in the same way, and aligned in parallel rows (Fig. 3-5a; see Appendix A for detailed petrographic descriptions and geochemical characterization of zircon from BD2 mafic dykes). Each cluster of similarly oriented cross-shaped zircons probably represents a cross section through an individual zircon dendrite with many branches (Appendix B). Strong pleochroic haloes occur around

zircon where it has caused radiation damage within hornblende, biotite, chlorite, uraltite, and stilpnomelane, and visibly corroded zones within large euhedral, blocky zircon crystals are stained orange (Fig. 3-5a; also see Appendix A). Zircon is also common in late quartz pockets. Baddeleyite is most commonly observed within late quartz, potassium feldspar, and albite, but is also hosted by hornblende, clinopyroxene, biotite, chlorite, and plagioclase, and occurs as elongate, euhedral, and sometimes inter-grown blades ranging from $\sim 5 \mu\text{m}$ to $150 \mu\text{m}$ long. The baddeleyite crystals are typically pristine unaltered blades in all host minerals, but occasionally exhibit zircon overgrowths (Fig. 3-6a). Up to two generations of zircon overgrowth may be present including late-stage magmatic alteration of baddeleyite to zircon during emplacement of the dyke and relatively minor development of incipient zircon by hydrothermal alteration (Appendix A). Zirconolite blades ($30\text{-}50 \mu\text{m}$ long by $8 \mu\text{m}$ wide) identified in sample JEF-00-30 have a mottled appearance in back-scattered electron images and one blade was enveloped by a $\sim 5 \mu\text{m}$ thick rind of secondary zircon, in contrast to baddeleyite from that sample which was essentially pristine.

HMD metamorphosed mafic dyke, Bastar craton

One sample of a $\sim 25\text{-m}$ -wide NE-SW trending metamorphosed dyke from the HMD swarm was selected for a geochronological study, and contains a lower-greenschist facies mineral assemblage of $\sim 40\%$ actinolite, $\sim 20\%$ chlorite, $\sim 35\%$ sericitized zones with minor relict patches of plagioclase exhibiting polysynthetic albite twinning, and lesser amounts of quartz, epidote, and rutile. Late quartz \pm epidote stringers also occur. Actinolite occurs as subhedral elongate blades and exhibits a decussate texture over a range of grain sizes from medium grained $\sim 5 \text{ mm}$ blades to very

tiny <100 µm needles, and imparts a medium grained massive texture to the rock, which has a greenish-grey colour in hand sample. Chlorite occurs as fine-grained radiating arrays in thin section which either envelope the actinolite or progressively grade into it. Relict plagioclase and late quartz pockets are surrounded and penetrated by randomly oriented fine-grained needles of actinolite. Rutile exhibits two distinct morphologies: 1) trains and aggregates of equant to somewhat elongate rods (up to ~5:1 aspect ratio) that are yellow-orange to dark red-brown in colour, heavily striated, subhedral grains (Fig. 3-5b); and 2) highly elongate (as high as 20:1 aspect ratio observed), perfectly euhedral, isolated, randomly oriented needles and thin blades, ranging in colour from light orange to dark brown (Fig. 3-5c). The second type of rutile commonly shows elbow-shaped contact twins and is typically fully enveloped by the largest actinolite crystals. Granoblastic polygonal textures only occur very locally and along grain boundaries between type 1 rutile aggregates, actinolite, and quartz. We interpret the type 1 rutile to be the result of prograde metamorphism, and suggest that it was probably formed by the breakdown of titanite or ilmenite, Ti-rich biotite or hornblende (Zack et al., 2004), or Ti-rich clinopyroxene. Elongate needles of rutile occurring as inclusions within Ti-rich garnet have been described as forming by exsolution during cooling (see Fig.'s 2d of Zhang et al., 2003 and 2c of Zack et al., 2004), and it is this type of retrograde origin we attribute to type 2 morphology of rutile observed within large actinolite crystals from this study.

Pulivendla sill, Dharwar craton

One sample of a gabbro sill (JEF-99-9) intrusive to the Tadpatri formation of the Cuddapah Supergroup was collected ~2 km to the northwest of Pulivendla (Fig. 3-4),

and appears to be the same sill that was previously dated by Rb-Sr (Bhaskar Rao et al., 1995) and $^{40}\text{Ar}/^{39}\text{Ar}$ (Anand et al., 2003). The Pulivendla sill is a highly differentiated igneous body with a coarse-grained ultramafic cumulate base, which grades upwards into a medium-grained leucocratic gabbro (Anand et al., 2003). Sample JEF-99-9 is a moderately weathered coarse-grained dolerite comprising predominantly plagioclase (40%), calcic-clinopyroxene (30%), and orthopyroxene (30%), in addition to ~1% opaques, and trace apatite and baddeleyite (typically <30 μm equant to slightly elongate grains in thin section). The sample was collected from near the top of the sill and its petrographic characteristics are consistent with the description provided by Anand et al. (2003) for a high level sample of this intrusion. The sample shows an intergranular texture, with pyroxenes predominantly interstitial to randomly oriented plagioclase laths, and with the smaller plagioclase laths commonly occurring as inclusions within relatively larger pyroxenes (subordinate sub-ophitic to poikilitic texture). Plagioclase is ~60% saussuritized. Pyroxenes range from fresh unaltered crystals to ~90% altered within the same thin section. Clinopyroxene is variably altered to predominantly chlorite, which occurs as very pale green radiate arrays, occurs with rare biotite and muscovite, and as very fine-grained aggregates disseminated with secondary calcite. Orthopyroxene is variably altered to pleochroic, colourless to pale green-brown chlorite; most commonly along fractures and cleavage traces.

ANALYTICAL METHODS

EM Chemical Monazite Dating

EM chemical U-Th-total Pb dating was carried out on monazite in a polished thin section of one BD2 mafic dyke sample (JEF-00-30). The instrument employed was a

JEOL 8900 Electron Microprobe housed in the Department of Earth and Atmospheric Sciences (University of Alberta), equipped with five wavelength dispersive spectrometers (WDS). Analysis of monazite was conducted at 20kV accelerating voltage, 150nA beam current, and a 1 μ m beam diameter. The U M β , Th M α , and Pb M α X-ray lines were chosen during analysis of monazite, and an overlap correction was employed to account for interference of the Y Ly peak on Pb M α (Suzuki and Adachi, 1991), and count times were set at 120s (peak) and 60s (background) for U, 40s (peak) and 20s (background) for Th, and 180s (peak) and 90s (background) for Pb.

U-Pb LA-MC-ICP-MS monazite dating

The same monazite crystal dated by EM was subsequently targeted for an *in-situ* U-Pb dating study by LA-MC-ICP-MS. The instrument employed was a Nu Plasma MC-ICP-MS coupled to a Nd:YAG laser ablation system ($\lambda=213\text{nm}$), and the instrumental set-up was similar to that outlined in Simonetti et al. (2005). A beam diameter of $\sim 8\mu\text{m}$ was used during the analysis. Two natural monazite standards of known age were also analysed using the same instrumental set-up during that session including Late Archean monazite from Australia, and Cambrian monazite from Madagascar and both of these internal standards yielded accurate results.

U-Pb IDTIMS Geochronology

All mineral separation, IDTIMS, and LA-MC-ICP-MS analysis was carried out at the University of Alberta Radiogenic Isotope Facility. During mineral separation, stringent cleaning procedures were carried out to prevent cross-contamination between samples.

Mineral Separation

SAMPLE JEF-00-36: A ~15 kg sample of BD2 dyke JEF-00-36 was crushed using a Jaw Crusher followed by further comminution with a Bico Disk Mill equipped with hardened steel plates. The approximately <100 mesh rock powder was then slowly (~3 kg/hour) passed over a Wilfley shaking table to collect a heavy mineral concentrate, which was then dried and sized with a 70 mesh. After removal of the most magnetic material via freefall of the powder past a magnet, a Frantz Isodynamic Separator was then used to extract most of the paramagnetic minerals. The portion of material reporting to the relatively non-magnetic fraction (Frantz settings: 1.0A with a 15° side-tilt) was then processed to obtain a heavy mineral concentrate using the heavy liquid Methylene Iodide. A final series of magnetic separations was carried out using the Frantz, in efforts to isolate the most pristine zircon and baddeleyite blades based on slight differences in paramagnetism.

A large population (several hundred) of pale pink, heavily- to non-striated, stubby to elongate blade-like zircon fragments was recovered from the least magnetic mineral concentrates. These zircons range up to ~300 µm in length, occasionally exhibit minor orange staining on the exterior, and a small proportion have skeletal t-junctions. In addition, a modest population of perfectly euhedral, prismatic, colourless to very pale pink zircons were recovered, which have very thin (5-10 µm wide) clear cores, pyramidal terminations, and range in length up to ~120 µm. A large population (~300) of tan brown baddeleyite blades and fragments were also recovered, and ranged from elongate (up to 150 µm in length), striated, euhedral blades and fragments, to anhedral and sub-rounded fragments having significant clear colourless zircon overgrowth.

Zircon overgrowths were typically less than 5 μm thick, but up to 30-40 μm thick regions are present in some grains (Fig. 3-6a; Fig. A-4 in Appendix A). In general, the populations of pristine unaltered zircon and baddeleyite increased towards the least magnetic fractions, although the total number of grains in both cases was higher in the more magnetic fractions (Frantz settings: 0.6-1.0A and 15° side-tilt). Most of the grains selected for U-Pb analysis originated from the least magnetic fractions (1.8A, 2-5° side tilt), but some were chosen from magnetic splits. For instance, to target baddeleyite grains with the most abundant incipient zircon overgrowth, early magnetic splits (0.8A, 15° side-tilt) were processed with heavy liquids (Methylene Iodide) and the baddeleyite selected from these concentrates. For some of the baddeleyite fractions, an air abrasion technique was used (Krogh, 1982) to remove the potentially more discordant outer edges of grains and minor incipient zircon overgrowth.

SAMPLE JEF-00-30: A second BD2 dyke (JEF-00-30) was processed for baddeleyite. Based on petrographic and EM imaging, the baddeleyite crystals in this sample are miniscule (most less than 25 μm in the longest dimension) and standard crushing and mineral separation protocols do not often recover such crystals. In order to evaluate the effects of using contrasting rock crushing techniques in isolating such small baddeleyite crystals, two samples from this dyke were crushed using a jaw crusher and then pulverized using two different techniques. These two hand samples were collected from the same site and also represent different starting rock grain size, including dolerite and relatively coarse-grained dioritic gabbro. Approximately 1 kg of dolerite was pulverized via Disk Mill, and in order to produce a rock powder with a relatively smaller average grain size, a ~200 g sample of dioritic gabbro was pulverized via tungsten carbide puck

mill. Each powder was processed following the water-based Wilfley table separation technique developed by Söderlund and Johansson (2002). Baddeleyite yields from both the disk and puck mill powders were high and several hundred baddeleyite blades were successfully recovered from each. However, picking baddeleyite grains from the concentrate originating from the puck mill powder was significantly more labour intensive owing to the smaller average grain size. A comparison of representative samples of the largest baddeleyite grains recovered from each concentrate shows that contrary to what is expected, at this sample site the largest baddeleyite grains from the dioritic gabbro pocket are significantly smaller than the largest grains originating from the doleritic portion of the dyke. The baddeleyite grains isolated from the coarser grained dioritic gabbro pocket display an aspect ratio $\sim 1.5:1$ (atypical for baddeleyite) and were all $<30 \mu\text{m}$ long (Fig. 3-6d), while baddeleyite grains originating from the doleritic portion displayed aspect ratios up to $6:1$ and were up to $70 \mu\text{m}$ long (Fig. 3-6e). We conclude that the observed differences in baddeleyite grains from the two samples is a reflection of the contrast between crushing styles, and it demonstrates that as suggested by Söderlund and Johansson (2002) comminution by disk milling is superior to the puck mill method at conserving entire baddeleyite crystals during liberation of the grains. However, from our experience with samples where the average baddeleyite grain size is $<25 \mu\text{m}$, use of the puck mill seems to be more efficient at liberating such tiny grains, despite the fact that a high proportion may be broken. The baddeleyite blades recovered from the dolerite versus the dioritic pocket from JEF-00-30 are, except for the average size and aspect ratios of the respective grain populations, essentially identical and can be described as euhedral, light tan brown, commonly striated blades and fragments of

blades with no visible overgrowth of zircon, fractures or inclusions.

SAMPLE JEF-00-14: One sample from the HMD swarm was chosen for a U-Pb IDTIMS dating study. In an initial attempt to isolate relict baddeleyite grains that might have survived metamorphism, a ~2 kg sample was pulverized with a Bico Disk Mill, and then put through the method of water-based mineral separation outlined by Söderlund and Johansson (2002). The sample yield was many thousands of euhedral, orange to foxy-brown, equant to very elongate rutile blades, but unfortunately baddeleyite was not identified. Nevertheless, the occurrence of large quantities of rutile in the concentrate demonstrates that the simple water-based method of baddeleyite mineral separation also works exceptionally well for isolating rutile crystals from mafic dykes.

SAMPLE JEF-99-9: Mineral separation carried out on dolerite sample JEF-99-9 of the Pulivendla sill involved pulverizing the sample via jaw crusher and puck mill. An initial aliquot of puck mill powder (~500 g) was processed by the water-based method of Söderlund and Johansson (2002), and yielded a modest amount of baddeleyite grains (~50), which will be referred to as population 1. These comprise 25-70µm long, tan brown to dark brown, striated, euhedral baddeleyite grains and fragments, devoid of zircon overgrowth, fractures, inclusions, or turbidity. Another smaller (~200 gram) aliquot of the same puck mill powder was processed with the water-based baddeleyite separation technique in order to obtain more baddeleyite, and yielded a second population (population 2) of several hundred baddeleyite grains identical in nature to population 1.

U-Pb IDTIMS Analysis

The procedures for U-Pb IDTIMS analysis described in this section follow

closely those outlined in Heaman et al. (2002). After hand-picking the grains with a binocular microscope and custom built pipettes comprised of Tygon and Teflon, all grains were pre-cleaned with 2N HNO₃ for one hour at ~70°C, and then rinsed several times with millipore H₂O and distilled acetone. Most mineral fractions were weighed with a Mettler UTM-2 ultra-microbalance, and the uncertainty in the weights is generally ~0.5-1.0 µg. Some of the fractions of small (<25 µm) thin baddeleyite fragments were very difficult to weigh (denoted in Table 3-2), and the weights for these fractions were calculated based on the estimated dimensions of each crystal, and are only considered to be accurate to within one order of magnitude on account of the difficulty in estimating the baddeleyite thickness. All samples were spiked with a measured amount of a mixed ²⁰⁵Pb-²³⁵U tracer solution, and the samples were dissolved in TFE Teflon bombs in a mixture of distilled acids, comprising a 5:1 ratio of 48% HF and 7N HNO₃. Sample dissolution took place in an oven at 215°C over a 4-5 day period, in custom built metal carousels comprising Monel outer jackets which housed the Teflon bombs, and which were held together by tempered steel holding plates.

After digestion, the samples were visually inspected to ensure that complete dissolution of the grains had taken place, and then evaporated to dryness in a Class 10 cleanhood. These precipitates were then dissolved in 3.1N HCl over a 24h period at 215°C. For samples weighing >5µg, U and Pb were purified using ion exchange chromatography employing Dowex AG1 X8, 200-400 mesh, chloride form resin, similar to the HCl procedures outlined in Krogh (1973) and Heaman and Machado (1992). The purified U and Pb solutions were combined with 0.15N H₃PO₄ to facilitate locating the samples after evaporation to dryness.

Transfer of the samples from the ultra-clean hood to the loading station, was carried out in pre-cleaned Nalgene PMP beakers that were submerged in 6.1N HCl for two hours at $\sim 70^{\circ}\text{C}$, and then cleaned again in distilled 6.1N HCl for four hours at $\sim 70^{\circ}\text{C}$. Before loading onto outgassed Re-filaments, the samples were mixed with 2.9-4.0 μL of silica gel and 2.5-4.0 μL of 0.15N H_3PO_4 . All isotopic analyses were carried out on a VG 354 Mass Spectrometer operating in analogue Daly photomultiplier detector peak-hopping mode. Before each analysis, the ^{206}Pb beam was focussed to maximize signal and the peak shape was optimized by adjusting the Daly accelerating potential. Otherwise, operating conditions were similar to the set-up described in Heaman et al. (2002), except that the empirically determined Faraday-Daly conversion factors used in adjustment of all Daly measurements were slightly different (0.086%/amu Pb and 0.0052%/amu U). Calculation of the isotopic composition of Pb in excess of blank Pb was determined following the two-stage average crustal lead model of Stacey and Kramers (1975). The one-sigma errors listed in Table 3-2 were calculated using an in-house program, which numerically propagates all known sources of uncertainty (Heaman et al., 2002). The Isoplot/Ex3 (Ludwig, 2003) program was used for all age calculations, and the ages represent upper- or lower-intercept ages determined by two-error linear regression of the data, and concordia or weighted average $^{207}\text{Pb}/^{206}\text{Pb}$ ages where the data are concordant to near concordant. The decay constants for ^{238}U ($1.55125 \times 10^{-10}\text{a}^{-1}$) and ^{235}U ($9.8485 \times 10^{-10}\text{a}^{-1}$) and the present day $^{238}\text{U}/^{235}\text{U}$ ratio of 137.88 are those determined by Jaffey et al. (1971). Error ellipses shown in Figs. 3-7 and 3-8, and all age uncertainties on the concordia and weighted mean plots are reported at two-sigma.

RESULTS

U-Pb IDTIMS Data

BD2 mafic dyke swarm, Bastar craton

The U-Pb IDTIMS results for baddeleyite and zircon from two BD2 mafic dykes and the Pulivendla sill, and rutile separates from an HMD dyke are listed in Table 3-2, and all of the data are shown on concordia diagrams in Figs. 3-7 and 3-8. The U-Pb results for a total of 11 analyses of zircon and (or) baddeleyite fractions from sample JEF-00-36 are plotted in Figs. 3-7a and 3-7b. These grains yielded nearly concordant (0.5% discordant) to highly discordant (48.6%) analyses and all of the data overlap with or plot close to a discordia reference line that has concordia intercept ages of 1883 and 370 Ma. All zircon fractions are discordant, have moderate uranium contents (129-538 ppm) and Th/U (0.49-0.76), and have a range of $^{207}\text{Pb}/^{206}\text{Pb}$ ages between 1825 and 1871 Ma (except for fraction #9 which has a significantly younger $^{207}\text{Pb}/^{206}\text{Pb}$ age of ca. 1534 Ma). The amount of discordance tends to correlate with zircon grain type. For example, two fractions of elongate striated skeletal blades (#3,5) are 19.3% and 8.4% discordant, whereas a six-grain fraction (#4) of prismatic zircons are only 3.3% discordant. The separated zircon rim material (#9; estimated to be ~75% zircon) discussed below still contained a small amount of baddeleyite (Fig. 3-6b) but has the lowest uranium content (129 ppm) and is the most discordant (48.6%).

Three fractions of unabraded baddeleyite blades (#1,2,6) range from 7.9% to 10.8% discordant and some of the blades in two of these fractions (#1,2) had visible zircon overgrowth. For the baddeleyite fractions exhibiting the most zircon overgrowth, an attempt was made to analyse the zircon rims and baddeleyite cores separately by

mechanically separating zircon rim material from the unaltered baddeleyite cores (Figs. 3-6a, 3-6b, and 3-6c). The fragments were divided into one fraction of zircon rim material (#9) and two fractions of baddeleyite core fragments (#7,8). The mechanically separated baddeleyite cores were significantly less discordant (2.4% to 4.7%) than the aforementioned baddeleyite analyses and have some of the highest uranium contents (e.g. #8 has 2497 ppm). In order to more efficiently remove the zircon rims from baddeleyite cores, an air abrasion technique was used (Krogh, 1982), and the two most concordant analyses comprise two single grain fractions (#10,11) of abraded baddeleyite with no remaining zircon rim or evidence of internal fracturing. A regression line constructed using four baddeleyite analyses (Fig. 3-7b), including the two single grain abraded fractions and the two fractions of mechanically separated core fragments, define a discordia line with an upper intercept date of 1883.5 ± 4.4 Ma, and a lower intercept date of 769 ± 160 Ma (MSWD=1.6). We interpret this 1883.5 upper intercept date to be a reliable estimate for the age of baddeleyite crystallization and is in agreement with the preferred baddeleyite/zircon crystallization age of 1883.0 ± 1.4 Ma discussed below. The lower intercept age of 769 Ma may have no geological significance given the large uncertainty but could hint at an episode of Neoproterozoic Pb-loss that has affected the baddeleyite cores. The lower intercept date may be a reflection of Pan-African (ca. 500-600 Ma) isotopic resetting that is widespread across southern India (Miller et al., 1996) and reflected in the U-Pb zircon disturbance noted for granite from the SBC (Sarkar et al., 1993). Alternatively, and given the proximity of the Bastar field area to the Eastern Ghats Mobile Belt, this discordia line lower intercept age might represent the integrated effects of Grenvillian, Pan-African or younger Pb-loss. For instance, in the central

Eastern Ghats Belt adjacent to the Bastar craton, U-Pb titanite and $^{40}\text{Ar}/^{39}\text{Ar}$ hornblende ages indicate a ~520 Ma Pan-African thermal overprint superimposed on the ~960 Ma granulite-grade metamorphism (Mezger and Cosca, 1999).

A regression line calculated using five fractions (1, 2, 3, 9, and 11), including the most concordant baddeleyite fraction, two baddeleyite fractions with minor zircon overgrowth, one fraction of skeletal zircon blades, and the fraction of predominantly zircon rim material, form a well defined discordia line with an upper intercept date of 1883.0 ± 1.4 Ma, a lower intercept date of 370 ± 14 Ma, with an MSWD of 1.03 (Fig. 3-7a). We interpret this upper intercept date of 1883.0 ± 1.4 Ma to represent the most reliable estimate for the crystallization age of zircon and baddeleyite during emplacement of the dyke, and the lower intercept date of 370 ± 14 Ma to be a reliable estimate for the timing of hydrothermal alteration of the dyke, isotopic resetting of igneous zircon and the formation of zircon overgrowth on baddeleyite.

U-Pb isotopic data comprising four baddeleyite analyses for a second BD2 dyke sample (JEF-00-30) are presented in Table 3-2 and shown on a concordia diagram (Fig. 3-7c). Three analyses (#12, 14, and 15) have $^{207}\text{Pb}/^{206}\text{Pb}$ ages that overlap within analytical uncertainty, and yield a weighted mean $^{207}\text{Pb}/^{206}\text{Pb}$ age of 1891.1 ± 0.9 Ma (MSWD = 0.46), which we interpret to represent the most reliable estimate for the timing of baddeleyite crystallization and emplacement age of the dyke. We interpret the small amount of discordance for these three analyses (0.8% to 3.2%) to be associated with recent Pb-loss, because linear regression treatment of the data (excluding #13) yields a lower intercept date of 2 ± 280 Ma.

HMD metamorphosed mafic dyke, Bastar craton

The U-Pb isotopic data for two fractions of type 2 rutile grains (#16,17) from HMD sample JEF-00-14 are presented in Table 3-2 and shown on a concordia diagram in Fig. 3-7d. Both fractions contain low uranium (16-18 ppm) and Th/U (0.08-0.12) and have broadly similar $^{207}\text{Pb}/^{206}\text{Pb}$ ages of 2140.3 and 2103.8 Ma, respectively. One analysis (#16) shows slight reverse discordance (-2.0%), which may be attributed to either incomplete equilibration between the sample and spike, or an over-correction for common Pb on account of the very low Pb concentrations in the rutile (~7 ppm). The second analysis (#17) is concordant, and yields a concordia age of 2100 ± 11 Ma (2 sigma; MSWD of concordance = 0.25), which is considered to represent a good estimate for the timing of rutile formation. Rutile in this sample may have formed by exsolution from Ti-rich amphibole or clinopyroxene at a temperature above the closure temperature for Pb diffusion in rutile (380-420°C; Mezger et al., 1989), so the 2100 Ma age is best interpreted as a minimum crystallization age and likely represents the time at which rutile cooled below ~400°C.

Pulivendla sill, Dharwar craton

The U-Pb data for four baddeleyite fractions isolated from dolerite sample JEF-99-9 of the Pulivendla sill are presented in Table 3-2 and shown on a concordia diagram in Fig. 3-8. All four fractions contain low to moderate uranium contents (166 to 875 ppm) and slightly higher than typical Th/U (0.16-0.25) for baddeleyite. IDTIMS analysis of three baddeleyite fractions (#18, 19, and 20) that originated from baddeleyite population 1, and comprised relatively small fractions (3 to 6 grains each), yielded slightly different results. Two analyses (#18,20) yielded highly imprecise results that

plot on or slightly above concordia. A third analysis (#19) of four equant (30-50 μm) baddeleyite grains with relatively higher U concentrations gave a more precise result, which plots slightly below concordia. A fraction (#21) of 27 tiny (~10-25 μm) baddeleyite grains originating from baddeleyite population 2 yields a nearly identical result as analysis #19 from population 1. Fraction #21 contained many more baddeleyite blades than fraction #19, but because they were smaller and overall more elongate, the calculated weights of the two fractions are similar. The similarity in U-Pb results for fractions #19 and #21 attests to the reproducibility of the results, in that the baddeleyite originated from two separate sessions of water-based baddeleyite mineral separation. Although there is a slight overall spread of the data from reversely discordant (-3%) to normally discordant (1.8%), all analyses yield similar $^{207}\text{Pb}/^{206}\text{Pb}$ ages (1868 to 1887 Ma), and we interpret the weighted mean $^{207}\text{Pb}/^{206}\text{Pb}$ age of 1884.9 ± 7.2 Ma (MSWD=2.2) to represent a reliable estimate for the timing of baddeleyite crystallization and the age of emplacement of the Pulivendla sill. Three of these baddeleyite fractions (19-21) have an even more restricted range in $^{207}\text{Pb}/^{206}\text{Pb}$ ages between 1881.5 and 1887.3 Ma, and yield a similar weighted average (inset Fig. 3-8) age of 1885.4 ± 3.1 Ma (MSWD=1.6), which is considered as the best current estimate for the emplacement age of the Pulivendla sill.

Monazite dating

EM chemical U-Th-total Pb monazite dating

A euhedral monazite crystal hosted by late-crystallizing hornblende and measuring 12 x 15 μm was encountered in a thin section of sample JEF-00-30 for which a U-Pb baddeleyite age of 1891.1 ± 0.9 Ma is reported above. On the basis of its crystal

habit and its textural and spatial association with baddeleyite (Figs. 3-9a to 3-9c), we interpret the monazite to have crystallized directly from the mafic magma during emplacement of the dyke. Hydrothermal monazite can show a similar morphology as igneous monazite, but a hydrothermal origin for this monazite grain (Fig. 3-9) seems unlikely from a geochemical standpoint, because hydrothermal monazite characteristically contains only 0-1 wt% ThO₂ (Schandl and Gorton, 2004). In contrast, ThO₂ concentrations from individual WDS spot analyses in the JEF-00-30 monazite crystal ranged between 3.44 and 11.45 wt% (domain averages ranged between 4.7 and 11.2 wt%, Table 3-3), which is characteristic for igneous monazite (Schandl and Gorton, 2004). On a plot of Σ (La+Ce+Pr) versus La/Nd that is representative of the degree of LREE enrichment (Rapp and Watson, 1986), the data plot where the fields for carbonatite and alkalic rocks overlap (Fig. 3-10), and away from the field for hydrothermal monazite. Zoning is also evident in BSE images of the monazite (Fig. 3-9d), and WDS spot analyses of the brightest region ($n=3$) versus the remainder of the crystal ($n=21$) reveal two corresponding geochemically distinct domains (Table 3-3). EM chemical dating was carried out on the crystal (across both domains) and the data are shown on a ThO₂* versus PbO diagram in Fig. 3-11 and contextually in Fig. 3-9d. Age calculation was carried out following the method of Suzuki and Adachi (1991), except that the isochron was forced to pass through the origin with a fictive data-point containing no associated error. A linear regression of the 21 data points originating from the relatively Th-poor region of the monazite yields a well-defined chemical isochron age of 1881±20 Ma with an MSWD of 2.4 (Fig. 3-11); in agreement with the U-Pb baddeleyite age. Three data-points from the ThO₂-rich region of the monazite that

appears brightest in BSE images (Fig. 3-9d) yield slightly younger apparent ages and cluster along a 1756 Ma reference isochron (Fig. 3-11). The slightly younger apparent ages might reflect minor Pb-loss associated with regions of the crystal which have been damaged by relatively higher α -recoil doses associated with elevated U and Th concentrations, but this is doubtful because even at substantially high radiation doses, radiogenic Pb does not diffuse out of monazite at geologically measurable rates (Seydoux-Guillaume et al., 2004). Significant fractures exist throughout the crystal and this could have enabled localized alteration of the monazite, which might be reflected in the two distinct geochemical domains.

LA-MC-ICP-MS monazite dating

During LA-MC-ICP-MS analysis of the BD2 monazite grain, an ~ 3000 cps ^{206}Pb beam lasted for approximately 20 seconds, and the dataset acquired for that single spot yielded $\sim 1\%$ relative precision in the final age calculation. The U-Pb data corresponding to the laser ablation pit shown in Fig. 3-9e is listed in Table 3-2 and shown along with the IDTIMS data for sample JEF-00-30 on a concordia diagram in Fig. 3-7c. This single data point plots on concordia and yields a concordia age of 1887 ± 21 Ma (MSWD=2.4). Within analytical error, this LA-MC-ICP-MS age is identical to the 1881 ± 20 Ma chemical age determined for the same monazite crystal and the 1891.1 ± 0.9 Ma U-Pb baddeleyite IDTIMS age from the same sample. The occurrence of magmatic monazite in mafic magmas is not well documented but the chemical dating and *in situ* LA-MC-ICP-MS results presented here indicates that monazite is a viable U-Pb dating target in some mafic rocks.

DISCUSSION

The timing, duration, and extent of Southern Bastar-Cuddapah Magmatic Events

High precision U-Pb baddeleyite/zircon dates for two BD2 dykes of the SBC indicate that dyke emplacement occurred at 1891.1 ± 0.9 Ma (JEF-00-30) and 1883.0 ± 1.4 Ma (JEF-00-36), and that BD2 mafic magmatism spanned at least 8 m.y. in duration. In addition to baddeleyite, primary magmatic monazite was identified in BD2 dyke sample JEF-00-30 and identical but less precise monazite ages were obtained by *in situ* thin section EM (1881 ± 20 Ma) and LA-MC-ICP-MS (1887 ± 21 Ma) dating techniques. In a companion study (Appendix C), EM chemical baddeleyite dating was carried out on the full spectrum of petrographic subgroups of BD2 mafic dykes including fresh dolerite, altered dolerite, and hornblende dolerite, and indicate that all subgroups of BD2 dykes belong to a single mafic dyke swarm that was emplaced at ~ 1.9 Ga. The geochemical and geochronological database currently available (Srivastava et al., 1996; Srivastava and Singh, 2004; this study; Appendices C and D) indicates that BD2 dykes outcrop over a minimum area of ~ 1000 km², but there is evidence to suggest that this dyke swarm spans a much larger region of the Bastar craton (see above). Unmetamorphosed BK, NK and BS dykes of the central Bastar craton have the same orientation as BD2 (GT) dykes (Fig. 3-2) suggesting the possibility that all these dykes belong to a single, large dyke swarm. If this correlation is correct, the BD2 swarm spans a region of the Bastar craton in excess of 17,000 km² (Fig. 3-2).

The U-Pb IDTIMS baddeleyite age of 1885.4 ± 3.1 Ma determined for the Pulivendla dolerite sill (Fig. 3-8) provides an important constraint on the timing of mafic magmatism associated with early development of the Cuddapah basin. This more precise U-Pb age overlaps within experimental error the ⁴⁰Ar/³⁹Ar age phlogopite age of

1899±20 Ma reported for the same Pulivendla sill, and confirms the conclusion of Anand et al. (2003) that early basin development and coeval mafic magmatism took place at ~1.9 Ga. The U-Pb age of this sill also represents a minimum estimate for the timing of earliest deposition of the Tadpatri Formation and the underlying stratigraphy of the Cuddapah Supergroup. Importantly, the U-Pb IDTIMS and EM chemical age, and previously reported $^{40}\text{Ar}/^{39}\text{Ar}$ phlogopite ages for the Pulivendla sill, all overlap within experimental error the ages reported in this study for the BD2 dyke swarm in the SBC (see EM baddeleyite ages for this LIP that are also in agreement; Appendix C). The synchronism in ages confirms a record of widespread ~1.9 Ga mafic magmatic activity and extension across a large tract of the south-eastern margin of the Dharwar protocontinent. Currently this mafic magmatic province transects two cratons, spans a region approximately 600 x 150 km, and including speculative correlations with N-S to NNW-SSE dykes in the north-eastern Bastar craton, potentially comprises a LIP in excess of 900-km-long (Fig. 3-2).

The timing of emplacement of the BD1 and HMD dyke swarms of the SBC is currently unknown. The preliminary U-Pb IDTIMS rutile age of 2100±11 Ma for metamorphosed HMD dyke JEF-00-14 (Fig. 3-7c) provides a minimum emplacement age for the HMD swarm, and by inference the BD1 dyke swarm. If, as argued above, the rutile in the rock is metamorphic in origin, then this 2100 Ma date represents the age of regional greenschist-grade metamorphism that affected the HMD dyke swarm. The cause of this regional metamorphic event might be related to an episode of granite and pegmatite emplacement which occurred in the SBC at ~2.1 Ga (Sarkar et al, 1990; Ramesh Babu et al., 1993). Alternatively, the metamorphism of HMD mafic dykes in

the SBC might have been a far-field effect of the ultrahigh-temperature metamorphism that took place in the Bhanadara-Balaghat granulite belt at the north end of the craton. This metamorphic episode is associated with monazite growth in felsic granulites at 2089 ± 14 , 2086 ± 16 , 2048 ± 14 , and 2040 ± 17 Ma (EM chemical ages: Bhowmik et al., 2005) along the CITZ.

Implications for Paleoproterozoic crustal evolution of the Dharwar protocontinent

The BD2 swarm has been well characterized petrographically and geochemically (Srivastava et al., 1996; Srivastava and Singh, 2004) and can be readily distinguished from other mafic dykes in the region. For instance, some important geochemical features useful in discriminating BD1 and BD2 mafic dykes are the observed contrasts in whole-rock P_2O_5 , TiO_2 , and HFSE (including Nb, Zr, Y, and the REE) concentrations for samples with overlapping MgO concentrations (BD2 dykes show distinctly higher values in all cases: Srivastava and Singh, 2004). When combined with the precise U-Pb ages obtained in this study, the distinctive petrographic and geochemical features of the BD2 dyke swarm can be used as an important regional time marker for constraining the Paleoproterozoic crustal evolution in the SBC. The BD2 dyke swarm is the youngest suite of mafic dykes in the SBC, and appears to crosscut all geological formations and basement rocks in the area, except those of the Indravati Supergroup (Ramakrishnan, 1990). Therefore, the emplacement age of 1891-1883 Ma for two dykes in the BD2 swarm currently provides a reliable minimum age of formation for rocks that are intruded by the swarm, and indirectly places maximum age constraints on the timing of development of the Indravati basin and associated outliers.

A record of Late Paleoproterozoic to Neoproterozoic basin development is

widespread across southern peninsular India (Fig. 3-2) comprising a number of major intracratonic basins (classically known as the Purana basins), including the Cuddapah basin of the Dharwar craton, rift-related rocks of the Godavari Supergroup, and the Chattisgarh basin and associated smaller outliers which define a roughly N-S transect across the Bastar craton (Ramam and Murty, 1997; Chaudhuri et al., 2002). All of these basins are interpreted to have developed in a rift setting and to varying degrees contain evidence for episodic volcanic activity (Chatterjee and Bhattacharji, 2001; Deb, 2003; Anand et al., 2003). Chaudhuri (2003; and references therein) have proposed that all of these sub-basins may have emerged concomitantly along a single depository spanning a vast region of the Dharwar protocontinent. The presence of marine transgressions and repeated tidal and storm deposits within these basins suggests the development of an open seaway east of the Dharwar protocontinent by the Late Paleoproterozoic (Chaudhuri et al., 2002).

The similar U-Pb baddeleyite ages presented in this study for multiple dykes from the BD2 mafic dyke swarm and the Pulivendla sill located ~600 km to the southwest, hint that crustal extension and mafic magmatism may have occurred along a vast tract of the pre-Eastern Ghats paleocontinental margin of the Dharwar protocontinent at 1.9 Ga. The U-Pb IDTIMS baddeleyite age of 1885.4 ± 3.1 Ma determined for the Pulivendla sill in this study provides a temporal link between this Late Paleoproterozoic mafic magmatic activity in the Bastar craton and early tectonic development of the Cuddapah basin.

Based on stratigraphic correlation, there is some evidence that contemporaneous intracratonic basin development may have accompanied widespread mafic volcanic

activity in the SBC at this time. The $\sim 3000 \text{ km}^2$ Abujhmar basin contains a Proterozoic supracrustal succession with similar affinity to the “Purana” basins (Mishra et al., 1988; Saha and Chaudhuri, 2003). Abujhmar Group rocks of the $\sim 3000 \text{ km}^2$ Abujhmar basin (Fig. 3-2) form the uppermost stratigraphy of the Kotri Supergroup, and unconformably overly rocks of the Bengpal, Bailadila, and Nandgaon Groups (Mishra et al., 1988). The Abujhmar Group is thought to be older than the relatively undeformed sedimentary rocks of the Indravati basin (Mishra et al., 1988; Saha and Chaudhuri, 2003). Lithologically, the Abujhmar Group comprises a succession of polymictic conglomerate, arenitic sandstone, siltstone, and shale, and basaltic lava flows (Maspur Traps), which has been intruded by gabbro/dolerite dykes and sills (Mishra et al., 1987b; Mishra et al., 1988; Ramachandra et al., 1995). In particular, the succession comprising arenitic sandstones, shales, and mafic igneous rocks, has been correlated stratigraphically with similar rocks from the Cuddapah basin (Mishra et al., 1988; Saha and Chaudhuri, 2003). Interestingly, approximately 20 km to the northwest along strike of BD2 dolerite dyke JEF-00-36 (Fig. 3-3) dated in this study at $1883.0 \pm 1.4 \text{ Ma}$, a series of similarly oriented mafic dykes, predominantly unmetamorphosed gabbro sills and basaltic lava flows outcrop in the vicinity (and as a part of) of the southernmost reaches of the Abujhmar basin (Mishra et al., 1987b). At this locality, the basin tapers to a narrow arm only a few kilometres across with a strike that is parallel to the BD2 mafic dyke swarm. One interpretation of this outcrop pattern is that the southern Abujhmar basin dykes are contemporaneous with the BD2 dyke swarm and they represent feeder dykes for the Maspur Traps. By inference this provides a minimum age constraint for the timing of earliest sedimentation in the Abujhmar basin and would add support to the previous

stratigraphic correlations between the Abujhmar and lower Cuddapah stratigraphy (Mishra et al., 1987b; Mishra et al., 1988). It is notable however that the available radiometric ages of the Maspur Traps are inconsistent (Sarkar et al., 1990) ranging from 2490 ± 48 Ma (Rb-Sr), to ~ 2217 Ma and ~ 1456 Ma (K-Ar), and do not provide support for the present interpretation.

There is also a record of potentially widespread ~ 1.9 Ga mafic magmatism associated with rifting along the deformed northern margin of the Aravalli protocontinent, in the Lesser Himalaya. A gabbroic body within the Chail Group is interpreted as a remnant of a magma chamber, which fed a large Precambrian magmatic province south of the Main Central Thrust, has recently yielded an Rb-Sr whole rock age of 1907 ± 91 Ma (Ahmad et al., 1999). Ultimately, it may turn out that these potentially synchronous 1.9 Ga mafic magmatic events may have been the harbinger of intracontinental rifting and breakout of the Dharwar protocontinent (and potentially connected Aravalli protocontinent) from a larger parental supercontinent in the Late Paleoproterozoic.

On the basis of a single K-Ar date of 1330 ± 53 Ma on glauconitic minerals from Godavari Supergroup, and ~ 1.6 Ga EM chemical dates on zircon and monazite from the Bhopalpatnam granulite belt interpreted to imply a ~ 1.6 Ga suture between the Dharwar and Bastar cratons, it has been proposed that Godavari rifting took place in the interim period, perhaps at ~ 1.5 Ga (Rogers and Santosh, 2002; Santosh et al., 2004). The U-Pb ages for the BD2 dyke swarm and Pulivendla sill presented in this paper establish for the first time, the presence of a 1.9 Ga LIP that appears to bridge the Godavari Rift, occurring in both the Dharwar and Bastar cratons, and which is clearly associated with

concomitant intracontinental rifting and basin development (at least in the case of early development of the Cuddapah basin). This interpretation is at odds with the model of Santosh et al. (2004), which calls for collision between the Dharwar and Bastar cratons at ~1.6 Ga. Regardless of when Godavari rifting was actually initiated, the presence of a 1.9 Ga LIP that straddles the rift requires that a pre-rift collision could not have taken place later than 1.9 Ga. An alternative possibility is that the 1.9 Ga BD2 dyke swarm and Cuddapah igneous province, although of the same age, are genetically unrelated, and were brought together during collision of the Dharwar and Bastar cratons at 1.6 Ga. Our preferred interpretation of these geological features is that the cratonic join between the Bastar and Dharwar cratons originally dates to an older time (perhaps at 2.5-2.2 Ga during formation of the Karimnagar granulite belt: Santosh et al., 2004) and that the 1.6 Ga Bhopalpatnam belt represents an intracratonic compressional event which took place along this previously existing suture. This scenario allows for emplacement of a single 1.9 Ga Cuddapah-Southern Bastar large igneous province across the cratonic join between the Bastar and Dharwar cratons, and requires that Godavari rifting took place <1.6 Ga as suggested by Santosh et al. (2004).

Worldwide distribution of 1.9 Ga continental mafic igneous provinces

In addition to the newly recognized 1891-1883 Ma Cuddapah-Bastar LIP of peninsular India identified in this study, 1.9 Ga LIPs have been identified in at least two other Precambrian provinces worldwide, including the Superior (North America) and Kalahari (southern Africa) cratons. It is important to note that this intraplate mafic magmatism in North America, southern Africa, and India occurred during a period of global crustal amalgamation and contraction between 2.0 and 1.8 Ga. Also, the

paleotectonic regime during emplacement of each of these three 1.9 Ga LIPs was significantly different in each case, and so these geological provinces provide interesting examples for exploring LIP emplacement in contrasting geodynamic settings.

In North America, 1.9 Ga mafic magmatism is common along the margins of the Superior Province and occurs as margin parallel mafic dyke swarms, gabbro sills and tholeiitic basalts. Magmatism of this age occurs along the eastern margin of the Superior craton in the New Quebec orogen and includes the 1884.0 ± 1.6 Ma Montagnais gabbro sill (Findlay et al., 1995), 1874 ± 3 Ma upper Hellancourt Formation gabbro sill (Machado, 1990), ~ 1.9 Ga Hellancourt/Willbob Formation tholeiites (Rohon et al., 1993; Skulski et al., 1993), and a 1880 ± 2 Ma carbonatite dyke that is part of the Castignon Lake carbonatite complex (Chevé and Machado, 1988). At the northern margin in the Ungava Orogen a recent 1882.7 ± 1.3 Ma U-Pb zircon age has been reported for the mineralized Expo igneous suite in the Cape Smith Belt (Randall, 2005). On the north-western margin of the Superior craton, the NNE-SSW trending 1884-1877 Ma Molson dyke swarm (Heaman et al., 1986; Halls and Heaman, 2000; Heaman et al., 2006), 1883 Ma Thompson Nickel Belt gabbro and ultramafic sills (Hulbert et al., 2005; Heaman et al., 2006), and E-W trending $1882.9 \pm 1.5 / -1.4$ Ma Fox River sill (Heaman et al., 1986) comprise an important component of this Circum-Superior Paleoproterozoic mafic magmatism (Baragar and Scoates, 1981; Fahrig, 1987). A similar 1876 ± 8 Ma $^{40}\text{Ar}/^{39}\text{Ar}$ hornblende age was reported for the N-S trending Pickle Crow dolerite dyke some distance east of the main Molson dyke swarm and may also be part of this ~ 1.9 Ga magmatism (Buchan et al., 2003). In both the eastern and north-western Superior margins, the precise U-Pb IDTIMS zircon/baddeleyite ages indicate that most of this

mafic magmatism was relatively short-lived (<10 m.y.). In the New Quebec Orogen, this magmatism is linked to pre-collisional pull-apart basins (Skulski et al., 1993) whereas the evidence for rifting and development of pre-collisional pull-apart basins is generally lacking along the north-western margin; perhaps due to the strong 1.8 Ga deformational overprint along the Thompson Nickel Belt.

A major episode of 1.88-1.87 Ga mafic magmatism also occurred in the Kalahari craton (comprising the Kaapvaal and Zimbabwe cratons, and Limpopo belt which joins them) of southern Africa, and appears to have been associated with rifting and mafic volcanism in the ~400 km long Soutpansberg graben, (Jansen, 1975; Bumby et al., 2002; Hanson et al., 2004a). High precision U-Pb IDTIMS baddeleyite dating of three dolerite sills intrusive to the Waterberg Group along the northern margin of the Kaapvaal craton yielded ages of 1878.8 ± 0.5 , 1873.7 ± 0.8 , and 1871.9 ± 1.2 Ma for this mafic igneous province. Paleomagnetic data also indicate that the Sebang dykes of the Zimbabwe craton were also emplaced at this time (Hanson et al., 2004a). Slightly older U-Pb IDTIMS baddeleyite ages of 1927.7 ± 0.5 , 1927.1 ± 0.7 , and 1927.3 ± 0.5 Ma for three sills from the Moshaneng dolerite (Hanson et al., 2004a), a U-Pb zircon evaporation date of 1928 ± 4 Ma determined for the Hartley basalt formation (Cornell et al., 1998), and a U-Pb zircon age of 1915 ± 6 Ma determined by secondary ion mass spectrometry for a Trompsberg gabbro intrusion (Maier et al., 2003), collectively represent further evidence for a major regional intraplate mafic magmatic episode in the Kaapvaal craton at ~1.9 (Hanson et al., 2004a).

In order to understand the origin of this synchronous widely distributed ~1.88 Ga intracontinental mafic magmatism it is important to explore the geodynamic setting. A

number of collisional and accretionary orogenic belts, and magmatic arcs were forming at 2.0-1.8 Ga worldwide (Hoffman, 1988; Condie, 2002), and were possibly associated with the formation of a number of putative supercontinents including Columbia (Rogers and Santosh, 2002; Zhao et al., 2002), Ophthalmia and Capricornia (Krapez, 1999). The development of volcanic arcs in some of these orogens was coeval with mafic dyke and sill emplacement along the margins of adjacent cratons at 1880 Ma but it is unclear in all cases whether they correspond to major episodes of rifting and break-up of a supercontinent. For example, in the north-western Superior craton, mafic magmatism associated with extension and rifting began as early as ~2.1 Ga, leading to ocean opening for a period of approximately 150 m.y. and followed by convergence and building of the first island arcs at 1920 Ma (Heaman et al., 2006). Arc magmatism continued with significant construction between 1880 and 1860 Ma. The 1883 Ma Molson dyke swarm was emplaced as a continental margin parallel swarm at the time of major oceanic arc formation in the Trans Hudson Orogen during Laurentia assembly (Heaman et al., 1986; Hoffman, 1988; Heaman and Corkery, 1996). The Molson dykes could be related to back-arc spreading or pull-apart basin formation during a phase of arc building in the Manikewan Ocean (similar to the model proposed for the New Quebec Orogen; Skulski et al., 1993) or may simply represent the impact of a mantle plume at a convergent margin, similar to the setting of the Columbia River basalts (Hooper, 1997). The incompatible element composition and positive epsilon Nd isotopic composition for 1.88 Ga mafic volcanics, ultramafic/gabbro sills and Molson dykes in the NW Superior margin support a depleted mantle origin for this magmatism that is likely linked to up-welling asthenosphere (Heaman et al., 2006).

In contrast to the record preserved in Laurentia, coeval 1880 Ma mafic magmatism in the Kalahari craton and Dharwar protocontinent appears to have been directly related to major episodes of rifting and basin development. The Late Paleoproterozoic tectonic setting of these cratons also appears to have been somewhat similar, in that granulite facies tectonothermal events had taken place along the Limpopo belt (Kalahari craton) at 2020 Ma (Pb-Pb titanite ages: Schaller et al., 1999) and CITZ (at the northern margin of the Bastar craton) at 2040-2090 Ma (EM monazite ages: Bhowmik et al., 2004) during periods of reactivation along these cratonic joins. Emplacement of 1.9 Ga Kaapvaal (post-Waterberg) dolerites took place at the northern margin of the craton where the genetically associated Soutpansberg graben developed along the Palala shear zone of the Limpopo belt which had been recently active during a transpressive orogeny at 2.05-1.95 Ga and later at ca. 1.9 Ga (Schaller et al., 1999; Hanson et al., 2004a). In contrast however, early sedimentation and mafic magmatism in the intracratonic Cuddapah basin at 1.9 Ga was taking place far field from the CITZ in an environment of relative tectonic quiescence, and was not associated with any pre-existing suture or collisional belt within the underlying crystalline basement of the Dharwar craton. Emplacement of the 1.9 Ga BD2 mafic dyke swarm was also not spatially, structurally, or temporally associated with the CITZ. On the basis of these differences in tectonic setting, and without paleomagnetic data for the BD2 dyke swarm and Pulivendla sill, we consider any attempt at paleocontinental reconstructions based on correlation of 1.9 Ga mafic magmatism and rifting in the Kalahari craton and Dharwar protocontinent to be premature. However, it is important to note that both of these Precambrian provinces also comprise some of the major constituents of the

putative original continent Ur (Rogers, 1996). Ur was proposed as the oldest supercontinent on the basis that only five cratons worldwide are known to contain laterally extensive shallow water supracrustal deposits as old as ~3.0 Ga, and that these cratons were in close proximity in Gondwanaland and statistically unlikely to have only just amalgamated during Gondwanaland assembly (Rogers, 1993; 1996). A recent summary of paleomagnetic and geochronological data suggests that the principal crustal nuclei of Ur, which included the Kalahari craton, Dharwar protocontinent, and Pilbara craton, were in close proximity during the late Archean to Paleoproterozoic (Piper et al., 2003). As such, the identification of the aforementioned ~1.9 Ga mafic magmatic and rifting events in the Kalahari craton and Dharwar protocontinent could shed light on possible Late Paleoproterozoic Ur configurations, and this idea needs to be tested with paleomagnetic studies of the Cuddapah-Southern Bastar LIP.

Because dyke swarms can provide excellent piercing points for paleocontinental reconstructions (Heaman, 1997; Wingate et al, 1998; Harlan et al., 2003), and as outlined above at least three concentrations of ~1880 Ma mafic/ultramafic magmatism are now known to occur worldwide, it is tempting to consider the possibility that all of these swarms once comprised a single LIP, and that dyke swarm geometries could be used to attempt plate reconstructions at 1880 Ma. However, we caution that on the basis of contrasting paleotectonic settings for this mafic magmatism between host cratons at this time, attempts at paleocontinental reconstructions based on this 1880 Ma global mafic magmatism may be misleading. The 1880 Ma Molson dyke swarm and associated Circum-Superior mafic magmatism were clearly emplaced at a continental margin that had already been previously developed, and formed at a time when plate tectonic

convergence and ocean closure was taking place. This seemingly negates consideration of possible connections of the Molson dyke swarm to coeval swarms from other cratons across the north-western margin of the Superior craton. We therefore conclude that the recent identification of 1880 Ma mafic magmatism in the Kalahari (e.g.: Hanson et al., 2004a), Dharwar, and Bastar cratons (this study), provides compelling new evidence for a period of enhanced global mantle plume activity (superplume event) on Earth at 1.9 Ga (Isley and Abbott, 1999; Condie et al., 2001; Condie, 2002; Maier et al., 2003). In the geodynamic context of global orogenesis and continental assembly taking place at 2.0-1.8 Ga (Hoffman, 1988; Condie, 2002; Zhao et al., 2002), this newly recognized 1.9 Ga global mafic magmatism is analogous to 1.1 Ga global mafic magmatic events that took place during Rodinia assembly (Hanson et al., 2004b).

SUMMARY AND CONCLUSIONS

A multi-technique geochronological investigation employing isotopic (U-Pb: IDTIMS and LA-MC-ICP-MS) and chemical (EM U-Th-total Pb) dating methods, has been carried out on three mafic dykes from the southern Bastar craton, and the Pulivendla mafic sill, which intrudes the lower stratigraphy of the Cuddapah basin of the Dharwar craton. High precision U-Pb IDTIMS baddeleyite and zircon ages of 1891.1 ± 0.9 Ma and 1883.0 ± 1.4 Ma were obtained for two mafic dykes from the BD2 mafic dyke swarm of the southern Bastar craton and 1885.4 ± 3.1 Ma for the Pulivendla sill in the Cuddapah basin. U-Pb LA-MC-ICP-MS and EM chemical dating of a single *in situ* 12×15 μm monazite grain in a thin section of the BD2 dyke dated by IDTIMS baddeleyite at 1891.1 ± 0.9 Ma, yield similar results of 1887 ± 21 Ma and 1881 ± 20 Ma, respectively. From these data we conclude that late-crystallizing igneous monazite

shows excellent promise as a new geochronometer for mafic dykes, particularly in contextual isotopic and chemical dating studies. Preliminary U-Pb IDTIMS results for rutile originating from an HMD metamorphosed mafic dyke from the southern Bastar craton indicates that the timing of greenschist-grade metamorphism which affected the HMD swarm occurred at 2100 ± 11 Ma, providing a minimum age constraint for the timing of emplacement of this dyke swarm, and by inference the BD1 dyke swarm.

The similar ~ 1.88 - 1.89 Ga crystallization ages obtained in this study for widely separated mafic igneous rocks from the Bastar and Dharwar cratons are interpreted to indicate the presence of a previously unrecognized LIP spanning ~ 600 km of the south Indian shield. We conclude that there is abundant evidence for a major episode of 1.9 Ga, intraplate mafic magmatism and rifting that spanned a large tract of the Dharwar protocontinent. This 1.9 Ga southern Bastar-Cuddapah mafic magmatic province could have implications for Paleoproterozoic continental reconstructions involving the Dharwar and Bastar cratons, and may reflect a period of enhanced mantle plume activity taking place on Earth at this time.

REFERENCES

- Ahmad, T., Mukherjee, P.K., & Trivedi, J.R. (1999). Geochemistry of Precambrian mafic magmatic rocks of the Western Himalaya, India: petrogenetic and tectonic implications. *Chemical Geology* **160**, 103-119.
- Allègre, C.J., Birck, J.L., & Courtillot, V. (1999). Age of the Deccan traps using ^{187}Re - ^{187}Os systematics. *Earth and Planetary Science Letters* **170**, 197-204.
- Anand, M., Gibson, S.A., Subbarao, K.V., Kelly, S.P., & Dickin, A.P. (2003). Early Proterozoic melt generation processes beneath the intracratonic Cuddapah Basin, southern India. *Journal of Petrology* **44**, 2139-2171.
- Aswathanarayana, U. (1964). Isotopic ages from the Eastern Ghats and Cuddapahs of India. *Journal of Geophysical Research* **69**, 3479-3486.

Baragar, W.R.A. & Scoates, R.F.J. (1981). The Circum-Superior Belt: A Proterozoic plate margin. In: Kroner, A. (ed) Precambrian plate tectonics, Elsevier, Amsterdam: 297-330.

Bhaskar Rao, Y.J., Pantulu, G.V.C., Damodara Reddy, V., Gopalan, V. (1995). Time of early sedimentation and volcanism in the Proterozoic Cuddapah Basin, South India: Evidence from the Rb-Sr age of Pulivendla mafic sill. In: Devaraju, T.C., ed., *Mafic Dyke Swarms of Peninsular India, Geological Society of India Memoir* **33**, 329-338.

Bhowmik, S.K., Basu Sarbadhikari, A., Spiering, B., & Raith, M.M. (2005). Mesoproterozoic reworking of Paleoproterozoic ultrahigh-temperature granulites in the Central Indian Tectonic Zone and its implications. *Journal of Petrology* **46**, 1085-1119.

Biswal, T.K. & Sinha, S. (2003). Deformation history of the NW salient of the Eastern Ghats mobile belt, India. *Journal of Asian Earth Sciences* **22**, 157-169.

Biswas, S.K. (2003). Regional tectonic framework of the Pranhita-Godavari basin, India. *Journal of Asian Earth Sciences* **21**, 543-551.

Buchan, K.L., Harris, B.A., Ernst, R.E. and Hanes, J.A. (2003). Ar-Ar dating of the Pickle Crow diabase dyke in the western Superior craton of the Canadian Shield of Ontario and implications for a possible plume centre associated with ca. 1880 Ma Molson magmatism of Manitoba. *Geological Association of Canada / Mineralogical Association of Canada Abstracts. (no. 481 on CD-ROM, p. 17 in print volume)*.

Bumby, A.J., Eriksson, P.G., van der Merwe, R., Steyn, G.L. (2002). A half-graben setting for the Proterozoic Soutpansberg Group (South Africa): evidence from the Blouberg area. *Sedimentary Geology* **147**, 37-56.

Bumby, A.J., Eriksson, P.G., & Van Der Merwe, R. (2004). The early Proterozoic sedimentary record in the Blouberg area, Limpopo Province, South Africa; implications for the timing of the Limpopo orogenic event. *Journal of African Earth Sciences* **39**, 123-131.

Chalapathi Rao, N.V., Miller, J.A., Pyle, D.M., & Madhavan, V. (1996). New Proterozoic K-Ar ages for some kimberlites and lamproites from the Cuddapah Basin and Dharwar craton, South India: evidence for non-contemporaneous emplacement. *Precambrian Research* **79**, 363-369.

Chalapathi Rao, N.V., Miller, J.A., Gibson, S.A., Pyle, D.M., & Madhavan, V. (1999). Precise $^{40}\text{Ar}/^{39}\text{Ar}$ age determinations of the Kotakonda kimberlite and Chelima lamproite, India: Implication to the timing of mafic dyke swarm emplacement in the eastern Dharwar craton. *Journal of the Geological Society of India* **53**, 425-432.

Chatterjee, A. (1970). Structure, tectonics and metamorphism in a part of south Bastar

(M.P.). *Quarterly Journal of the Geological, Mining and Metallurgical Society of India* **42**, 75-95.

Chatterjee, N. & Bhattacharji, S. (2001). Petrology, geochemistry and tectonic settings of the mafic dikes and sills associated with the evolution of the Proterozoic Cuddapah Basin of South India. *Proc. Indian Acad. Sci. (Earth Planet. Sci.)* **110**, 433-453.

Chaudhuri, A.K., Saha, D., Deb, G.K., Deb, S.P., Mukherjee, M.K., Ghosh, G. (2002). The Purana basins of southern cratonic province of India – A case for Mesoproterozoic fossil rifts. *Gondwana Research* **5**, 22-33.

Chev , S.R. & Machado, N. (1988). Reinvestigation of the Castignon Lake carbonatite complex, Labrador Trough, New Qu bec: *Geological Association of Canada Program with Abstracts* **13**, A20.

Condie, K.C., Des Marais, D.J., & Abbott, D.H. (2001). Precambrian superplumes and supercontinents: a record in black shales, carbon isotopes, and paleoclimates. *Precambrian Research* **106**, 239-260.

Condie, K.C. (2002). Continental growth during a 1.9-Ga superplume event. *Journal of Geodynamics* **34**, 249-264.

Cornell, D.H., Armstrong, R.A., & Walraven, F. (1998). Geochronology of the Proterozoic Hartley Basalt Formation, South Africa: constraints on the Kheis tectogenesis and the Kaapvaal craton's earliest Wilson Cycle. *Journal of African Earth Sciences* **26**, 5-27.

Courtillot, V., Besse, J., Vandamme, D., Montigny, R., Jaeger, J.-J., & Capetta, H. (1986). Deccan flood basalts at the Cretaceous/Tertiary boundary? *Earth and Planetary Science Letters* **80**, 361-374.

Crawford, A.R. & Compston, W. (1973). The age of the Cuddapah and Kurnool systems, southern India. *Journal of the Geological Society of Australia* **19**, 453-464.

Crookshank, H. (1963). Geology of southern Bastar and Jeypore from the Bailadila range to the Eastern Ghats. *Memoirs of the Geological Survey of India* **87**, 149p.

Crowe, W.A., Nash, C.R., Harris, L.B., Leeming, P.M., & Rankin, L.R. (2003). The geology of the Rengali Province: implications for the tectonic development of north Orissa, India. *Journal of Asian Earth Sciences* **21**, 697-710.

Das, D.P., Chakraborty, D.K., & Sarkar, K. (2003). Significance of the regional lineament tectonics in the evolution of the Pranhita-Godavari sedimentary basin interpreted from the satellite data. *Journal of Asian Earth Sciences* **21**, 553-556.

Deb, S.P. (2003). Proterozoic felsic volcanism in the Pranhita-Godavari valley, India: its

implication on the origin of the basin. *Journal of Asian Earth Sciences* **21**, 632-631.

Deb, S.P. & Chaudhuri, A.K. (2002). Stratigraphic architecture of the Proterozoic succession in the eastern Chattisgarh basin, India: tectonic implications. *Sedimentary Geology* **147**, 105-125.

Drury, S.A. (1984). A Proterozoic intracratonic basin, dyke swarms and thermal evolution in south India. *Journal of the Geological Society of India* **25**, 437-444.

Ernst, R.E. & Buchan, K.L. (2001). The use of mafic dike swarms in identifying and locating mantle plumes. In: Ernst, R.E. & Buchan, K.L., eds., *Mantle Plumes: Their Identification Through Time – Geological Society of America Special Paper 352*, 247-265.

Fahrig, W.F. (1987). The tectonic settings of continental mafic dyke swarms: failed arm and early passive margin. In: Halls, H.C. and Fahrig, W.F., eds., *Mafic Dyke Swarms, Geological Association of Canada Special Paper 34*, 331-348.

Findlay, J.M., Parrish, R.R., Birkett, T.C., & Watanabe, D.H. (1995). U-Pb ages from the Nimish formation and Montagnais glomeroporphyritic gabbro of the central New Québec orogen, Canada. *Canadian Journal of Earth Sciences* **32**, 1208-1220.

Ghosh, J.G. (2004). 3.56 Ga tonalite in the central part of the Bastar craton, India: oldest Indian date. *Journal of Asian Earth Sciences* **23**, 359-364.

Ghosh, P.K., Prasad, U., & Banerjee, A.K. (1977). Geology and mineral occurrences of the part of the 'Abhuj Mar' area, Bastar District, Madhya Pradesh. *Geological Survey of India Records* **102**(2), 182-188.

GSI. (1998). Geological Map of India, 1:2,000,000 scale. Geological Survey of India, Hyderabad.

Halls, H.C. (1982). The importance and potential of mafic dyke swarms in studies of geodynamic processes. *Geoscience Canada* **9**, 145-154.

Halls, H.C. & Heaman, L.M. (2000). The paleomagnetic significance of new U-Pb age data from the Molson dyke swarm, Cauchon Lake area, Manitoba. *Canadian Journal of Earth Sciences* **37**, 957-966.

Hanson, R.E., Gose, W.A., Crowley, J.L., Ramezani, J., Bowring, S.A., Bullen, D.S., Hall, R.P., Pancake, J.A., & Mukwakwami, J. (2004a). Paleoproterozoic intraplate magmatism and basin development on the Kaapvaal craton: Age, paleomagnetism, and geochemistry of ~1.93 to ~1.87 Ga post-Waterberg dolerites. *South African Journal of Geology* **104**, 233-254.

Hanson, R.E., Crowley, J.L., Bowring, S.A., Ramezani, J., Gose, W.A., Dalziel, I.W.D.,

Pancake, J.A., Seidel, E.K., Blenkinsop, T.G., & Mukwakwami, J. (2004b). Coeval large-scale magmatism in the Kalahari and Laurentian cratons during Rodinia assembly. *Science* **304**, 1126-1129.

Harlan, S.S., Heaman, L., LeCheminant, A.N., & Premo, W.R. (2003). Gunbarrel mafic magmatic event: A key 780 Ma time marker for Rodinia plate reconstructions. *Geology* **31**, 1053-1056.

Heaman, L.M. & Machado, N. (1992). Timing and origin of midcontinent rift alkaline magmatism, North America: evidence from the Coldwell Complex. *Contributions to Mineralogy and Petrology* **110**, 289-303.

Heaman, L.M. (1997). Global mafic magmatism at 2.45 Ga: Remnants of an ancient large igneous province? *Geology* **25**, 299-302.

Heaman, L.M., Machado, N., Krogh, T.E., & Weber, W. (1986). Precise U-Pb zircon ages for the Molson dyke swarm and the Fox River sill: Constraints for Early Proterozoic crustal evolution in northeastern Manitoba, Canada. *Contributions to Mineralogy and Petrology* **94**, 82-89.

Heaman, L.M. & Corkery, T. (1996). U-Pb geochronology of the Split Lake block, Manitoba: preliminary results. In: Hajnal, Z. & Lewry, J., eds., *Trans-Hudson Orogen Transect. Lithoprobe Report* **55**, 60-67.

Heaman, L.M., Erdmer, P., & Owen, J.V. (2002). U-Pb geochronologic constraints on the crustal evolution of the Long Range Inlier, Newfoundland. *Canadian Journal of Earth Sciences* **39**, 845-865.

Heaman, L.M., Peck, D. & Toope, K. (2006). Tracing 1.88 Ga Molson Igneous Events Into The Thompson Nickel Belt, Manitoba. *Economic Geology* (submitted).

Hoffman, P.F. (1988). United plates of America, the birth of a craton; Early Proterozoic assembly and growth of Laurentia. *Annual Reviews of Earth and Planetary Sciences* **16**, 543-603.

Hooper, P.R. (1997). The Columbia River flood basalt province: Current status. In: Mahoney, J.J. & Coffin, M.F., eds., *Large igneous provinces: Continental, oceanic, and planetary flood volcanism: American Geophysical Union Geophysical Monograph* **100**, 1-27.

Hulbert, L.J., Hamilton, M.A., Horan, M.F., & Scoates, R.F.J. (2005). U-Pb zircon and Re-Os isotope geochronology of mineralized ultramafic intrusions and associated nickel ores from the Thompson Nickel Belt, Manitoba, Canada: *Economic Geology* **100**, 29-41.

Isley, A.E. & Abbott, D.H. (1999). Plume-related mafic volcanism and the deposition of banded iron formation. *Journal of Geophysical Research B* **104**, 15461-15477.

- Jaffey, A. H., Flynn, K. F., Glendenin, L. E., Bentley, W. C., & Essling, A. M. (1971). Precision measurement of half-lives and specific activities of ^{235}U and ^{238}U . *Physical Review C* **4**, 1889-1906.
- Jansen, H. (1975). The Soutpansberg trough (Northern Transvaal) – an aulacogen. *Transactions of the Geological Society of South Africa* **79**, 129-136.
- Jayananda, M., Moyen, J.-F., Martin, H., Peucat, J.-J., Auvray, B., & Mahabaleswar, B. (2000). Late Archean (2550-2520 Ma) juvenile magmatism in the eastern Dharwar craton, southern India: constraints from geochronology, Nd-Sr isotopes and whole rock geochemistry. *Precambrian Research* **99**, 225-254.
- Krapez, B. (1999). Stratigraphic record of an Atlantic-type global tectonic cycle in the Palaeoproterozoic Ashburton Province of Western Australia. *Australian Journal of Earth Sciences* **46**, 71-87.
- Krogh, T.E. (1982). Improved accuracy of U-Pb zircon ages by the creation of more concordant systems using an air abrasion technique. *Geochimica et Cosmochimica Acta* **46**, 387-393.
- LeCheminant, A.N. & Heaman, L.M. (1989). Mackenzie igneous events, Canada: Middle Proterozoic hotspot magmatism associated with ocean opening. *Earth and Planetary Science Letters* **96**, 38-48.
- Leelanandam, C. (1990). The Kandra volcanics in Andhra Pradesh: Possible ophiolite? *Current Science* **59**, 785-788.
- Ludwig, K. R. 2003. ISOPLOT a plotting and regression program for radiogenic isotope data, version Ex/3.00.
- Machado, N. (1990). Timing of collisional events in the Trans Hudson Orogen: Evidence from U-Pb geochronology for the New Québec Orogen, The Thompson belt, and the Reindeer Zone (Manitoba and Saskatchewan). In: Lewry, J.F. & Stauffer, M.R., eds., *The Early Proterozoic Trans-Hudson Orogen of North America*, Geological Survey of Canada Special Paper **37**, 433-441.
- Madhavan, V., Mallikharjuna Rao, J., & Srinivas, M. (1999). Mid-Proterozoic intraplate alkaline magmatism in the Eastern Dharwar craton of India: The Cuddapah Province. *Journal of the Geological Society of India* **53**, 143-162.
- Maier, W.D., Peltonen, P., Grantham, G., & Mänttari, I. (2003). A new 1.9 Ga age for the Trompsburg intrusion, South Africa. *Earth and Planetary Science Letters* **212**, 351-360.
- Mainkar, D., Lehmann, B., & Haggerty, S.E. (2004). The crater-facies kimberlite system

of Tokpal, Bastar District, Chhattisgarh, India. *Lithos* **76**, 201-217.

Mazumder, R., Bose, P.K., & Sarkar, S. (2000). A comment on the tectono-sedimentary record of the pre-2.0 Ga continental growth of India *vis-à-vis* a possible pre-Gondwana Afro-Indian supercontinent. *Journal of African Earth Sciences* **30**, 201-217.

Mazumder, R. (2005). Proterozoic sedimentation and volcanism in the Singhbhum crustal province, India and their implications. *Sedimentary Geology* **176**, 167-193.

Mertanen, S., Halls, H.C., Vuollo, J.I., Pesonen, L.J., & Stepanov, V.S. (1999). Paleomagnetism of 2.44 Ga mafic dykes in Russian Karelia, eastern Fennoscandian Shield – implications for continental reconstructions. *Precambrian Research* **98**, 197-221.

Mezger, K., Hanson, G.N., & Bohlen, S.R. (1989). High precision U-Pb ages of metamorphic rutile: application to the cooling history of high-grade terranes. *Earth and Planetary Science Letters* **96**, 106-118.

Mezger, K. & Cosca, M.A. (1999). The thermal history of the Eastern Ghats Belt (India) as revealed by U-Pb and $^{40}\text{Ar}/^{39}\text{Ar}$ dating of metamorphic and magmatic minerals: implications for the SWEAT correlation. *Precambrian Research* **94**, 251-271.

Miller, J.S., Santosh, M., Pressley, R.A., Clements, A.S., & Rogers, J.J.W. (1996). A Pan-African thermal event in south India. *Journal of Southeast Asian Earth Sciences* **14**, 127-136.

Mishra, D.C., Baburao, V., Laxman, G., Rao, M.B.S.V., & Rao, M.B.S.V. (1987a). Three-dimensional structural model of Cuddapah basin and adjacent eastern part from geophysical studies. In: *Radhakrishna, B.P., ed., Purana basins of peninsular India (Middle to Late Proterozoic), Geological Society of India Memoir* **6**, 311-329.

Mishra, D.C., Chandra Sekhar, D.V., Venkata Raju, D.Ch., & Vijaya Kumar, V. (1999). Crustal structure based on gravity-magnetic modelling constrained from seismic studies under Lambert rift, Antarctica and Godavari and Mahanadi rifts, India and their interrelationship. *Earth and Planetary Science Letters* **172**, 287-300.

Mishra, D.C., Singh, B., Tiwari, V.M., Gupta, S.B., & Rao, M.B.S.V. (2000). Two cases of continental collisions and related tectonics during the Proterozoic period in India – insights from gravity modelling constrained by seismic and magnetotelluric studies. *Precambrian Research* **99**, 149-169.

Mishra, V.P., Datta, N.K., Ramachandra, H.M., Bhattacharya, D.P., Das, K., Kumaran, K., Rama Murthy, S., Lakshmana, B.K. & Nageswara Rao, C. (1987b). Geological History of the Abujhmar Basin, Bastar District, Madhya Pradesh. In: *Radhakrishna, B.P., ed., Purana basins of peninsular India (Middle to Late Proterozoic), Geological Society of India Memoir* **6**, 311-329.

Mishra, V.P., Singh, P., & Dutta, N.K. (1988). Stratigraphy, structure and metamorphic history of Bastar craton. *Records of the Geological Survey of India* **117**, 1-26.

Murthy, N.G.K. (1987). Mafic dyke swarms of the Indian shield. In: *Halls, H.C. & Fahrig, W.F., eds., Mafic Dyke Swarms, Geological Association of Canada Special Paper* **34**, 393-400.

Murthy, N.G.K. (1995). Proterozoic mafic dykes in southern peninsular India: A review. In: *Devaraju, T.C., ed., Mafic Dyke Swarms of Peninsular India, Geological Society of India Memoir* **33**, 81-98.

Murthy, Y.G.K., Babu Rao, V., Guptasarma, D., Rao, J.M., Rao, M.N., & Bhattacharji, S. (1987). Tectonic, petrochemical and geophysical studies of mafic dyke swarms around the Proterozoic Cuddapah basin, South India. In: *Halls, H.C. & Fahrig, W.F., eds., Mafic Dyke Swarms, Geological Association of Canada Special Paper* **34**, p.303-316.

Nagaraja Rao, B.K., Rajurkar, S.T., Ramalingaswamy, G., & Ravindra Babu, B. (1987). Stratigraphy, Structure and Evolution of the Cuddapah Basin. In: *Purāna Basins of Peninsular India (Middle to Late Proterozoic), Geological Society of India Memoir* **6**, 33-86.

Naqvi, S.M., Divakara Rao, V., & Narain, H. (1974). The protocontinental growth of the Indian shield and the antiquity of its rift valleys. *Precambrian Research* **1**, 345-398.

Piper, J.D.A., Basu Mallik, S., Bandyopadhyay, G., Mondal, S., & Das, A.K. (2003). Paleomagnetic and rock magnetic study of a deeply exposed continental section in the Charnockite Belt of southern India: implications to crustal magnetisation and paleoproterozoic continental nuclei. *Precambrian Research* **121**, 185-219.

Rajurkar, S.T., Bhate, V.D., & Sharma, S.B. (1990). Lineament fabric of Madhya Pradesh and Maharashtra and its tectonic significance. *Geological Survey of India Special Publications* **28**, 241-259.

Ramachandra, H.M., Mishra, V.P., & Deshmukh, S.S. (1995). Mafic dykes in the Bastar Precambrian: study of the Bhanupratappur-Keskal mafic dyke swarm. In: *Devaraju, T.C., ed., Mafic Dyke Swarms of Peninsular, Geological Society of India Memoir* **33**, 183-207.

Ramachandra, H.M. & Roy, A. (2001). Evolution of the Bhandara-Balaghat granulite belt along the southern margin of the Sausar mobile belt of central India. *Proceedings of the Indian Academy of Sciences (Earth and Planetary Sciences)* **110**, 351-368.

Ramakrishnan, M. (1990). Crustal development in southern Bastar central Indian craton. *Geological Survey of India Special Publication* **28**, 44-66.

Ramam, P.K. & Murty, V.N. (1997). Geology of Andhra Pradesh. Geological Society of India, Bangalore, 245 p.

Ramanamurthy, B.V., & Parthasarathy, V.R. (1988). On the evolution of the Godavari Gondwana graben, based on LANDSAT imagery interpretation. *Journal of the Geological Society of India* **32**, 417-425.

Ramesh Babu, P.V., Pandey, B.K., & Dhana Raju, R. (1993). Rb-Sr ages on the granite and pegmatitic minerals from Bastar-Koraput pegmatite belt, Madhya Pradesh and Orissa, India. *Journal of the Geological Society of India* **42**, 33-38.

Randall, W. (2005). U-Pb geochronology of the Expo Igneous Suite, Cape Smith Belt, and the Kyak Bay intrusions, New Quebec Orogen: Implications for the tectonic evolution of the northeastern Trans-Hudson Orogen. *M.Sc. Thesis, University of Toronto, Toronto, Canada*.

Rao, V.V. & Reddy, P.R. (2002). A Mesoproterozoic supercontinent: evidence from the Indian shield. *Gondwana Research* **5**, 63-74.

Rapp, R.P. & Watson, B.E. (1986). Monazite solubility and dissolution kinetics: implications for the thorium and light rare earth chemistry of felsic magmas. *Contributions to Mineralogy and Petrology* **94**, 304-316.

Ray, J.S., Martin, M.W., Veizer, J., & Bowring, S.A. (2002). U-Pb zircon dating and Sr isotope systematics of the Vindhyan Supergroup, India. *Geology* **30**, 131-134.

Reddy, N.S. (1988). Pillowed spilitic basalts from the Tadpatri Formation of the Cuddapah basin. *Journal of the Geological Society of India* **32**, 65-67.

Rickers, K., Mezger, K., & Raith, M.M. (2001). Evolution of the continental crust in the Proterozoic Eastern Ghats Belt, India and new constraints for Rodinia reconstruction: implications from Sm-Nd, Rb-Sr, and Pb-Pb isotopes. *Precambrian Research* **112**, 183-210.

Rogers, J.J.W. (1986). The Dharwar craton and the assembly of peninsular India. *Journal of Geology* **94**, 129-143.

Rogers, J.J.W. (1993). India and Ur. *Journal of the Geological Society of India* **42**, 217-222.

Rogers, J.J.W. (1996). A history of continents in the past three billion years. *The Journal of Geology* **104**, 91-107.

Rogers, J.J.W & Santosh, M. (2002). Configuration of Columbia, a Mesoproterozoic supercontinent. *Gondwana Research* **5**, 5-22.

Rohon, M.-L., Vialette, Y., Clark, T., Roger, G., Ohnenstetter, D. & Vidal, P. (1993). Aphebian mafic-ultramafic magmatism in the Labrador Trough (New Quebec): Its age and the nature of its mantle source. *Canadian Journal of Earth Sciences* **30**, 1582-1593.

Roy, A. & Prasad, M.H. (2003). Tectonothermal events in Central Indian Tectonic Zone (CITZ) and its implications in Rodinian crustal assembly. *Journal of Asian Earth Sciences* **22**, 115-129.

Santosh, M., Yokoyama, K., & Acharyya, S.K. (2004). Geochronology and tectonic evolution of Karimnagar and Bhopalpatnam Granulite Belts, central India. *Gondwana Research* **7**, 501-518.

Sarkar, A., Sarkar, G., Paul, D.K., & Mitra, N.D. (1990). Precambrian geochronology of the central Indian shield – a review. *Geological Survey of India Special Publication* **28**, 453-482.

Sarkar, G., Corfu, F., Paul, D.K., McNaughton, N.J., Gupta, S.N., & Bishui, P.K. (1993). Early Archean crust in Bastar craton, central India – a geochemical and isotopic study. *Precambrian Research* **62**, 127-137.

Schandl, E.S. & Gorton, M.P. (2004). A textural and geochemical guide to the identification of hydrothermal monazite: criteria for selection of samples for dating epigenetic hydrothermal ore deposits. *Economic Geology and the Bulletin of the Society of Economic Geologists* **99**, 1027-1035.

Schaller, M., Steiner, O., Studer, I., Holzer, L., Herwegh, M., & Kramers, J.D. (1999). Exhumation of Limpopo central zone granulites and dextral continent-scale transcurrent movement at 2.0 Ga along the Palala shear zone, Northern Province, South Africa. *Precambrian Research* **96**, 263-288.

Sengupta, S. (2003). Gondwana sedimentation in the Pranhita-Godavari valley: A review. *Journal of Asian Earth Sciences* **21**, 633-642.

Seydoux-Guillaume, A.-M., Wirth, R., Deutsch, & Schärer, U. (2004). Microstructure of 24-1928 Ma concordant monazites; implications for geochronology and nuclear waste deposits. *Geochimica et Cosmochimica Acta* **68**, 2517-2527.

Simonetti, A., Heaman, L.M., Hartlaub, R.P., Creaser, R.A., MacHattie, T., & Böhm, C. (2005). Rapid and precise U-Pb zircon dating by laser ablation MC-ICP-MS using a new multiple ion counting-faraday collector array. *Journal of Analytical Atomic Spectroscopy* **20**, 677-686.

Singh, A.P. & Mishra, D.C. (2002). Tectonosedimentary evolution of the Cuddapah basin and Eastern Ghats mobile belt (India) as Proterozoic collision: gravity, seismic, and geodynamic constraints. *Journal of Geodynamics* **33**, 249-267.

- Skulski, T., Wares, R.P., & Smith, A.D. (1993). Early Proterozoic (1.88-1.87 Ga) tholeiitic magmatism in the new Québec orogen. *Canadian Journal of Earth Sciences* **30**, 1505-1520.
- Söderlund, U. & Johansson, L. (2002). A simple way to extract baddeleyite (ZrO₂). *Geochemistry Geophysics Geosystems* **3**(2), 1-7.
- Srikantia, S.V. (1984). Kuppalapalle volcanics – a distinct upper Papaghni volcanic activity in the Cuddapah basin. *Journal of the Geological Society of India* **25**, 775-779.
- Srivastava, R.K., Hall, R.P., Verma, R., & Singh, R.K. (1996). Contrasting Precambrian mafic dykes of the Bastar craton, central India: petrological and geochemical characteristics. *Journal of the Geological Society of India* **48**, 537-546.
- Srivastava, R.K., Heaman, L.M., French, J.E., & Singh, R.K. (2000). 1.8 Ga old dolerite dyke swarm from the southern Bastar craton, central India: implications on east Gondwanaland reconstruction. *Abstracts of Papers: The National Symposium on Milestones in Petrology & Annual Convention of Geological Society of India, Varanasi*. 50.
- Srivastava, R.K., & Singh, R.K. (2003). Geochemistry of high-Mg mafic dykes from the Bastar craton: evidence of late Archean boninite-like rocks in an intracratonic setting. *Current Science* **85**, 808-812.
- Srivastava, R.K. & Singh, R.K. (2004). Trace element geochemistry and genesis of Precambrian sub-alkaline mafic dikes from the central Indian craton: evidence for mantle metasomatism. *Journal of Asian Earth Sciences* **23**, 373-389.
- Stacey, J. S. & Kramers, J. D. (1975). Approximation of terrestrial lead isotope evolution by a two-stage model. *Earth and Planetary Science Letters* **26**, 207-221.
- Stein, H.J, Hannah, J.L., Zimmerman, A., Markey, R.J., Sarkar, S.C., & Pal, A.B. (2004). A 2.5 Ga porphyry Cu-Mo-Au deposit at Malanjhand, central India: implications for Late Archean continental assembly. *Precambrian Research* **134**, 189-226.
- Suzuki, K. & Adachi, M. (1991). Precambrian provenance and Silurian metamorphism of the Tsubonosawa paragneiss in the South Kitakami terrane, Northeast Japan, revealed by the chemical Th-U-total Pb isochron ages of monazite, zircon, and xenotime. *Geochemical Journal* **25**, 357-376.
- Tewari, H.C. & Rao, V.K. (1987). A high velocity intrusive body in the upper crust in the southwestern Cuddapah basin as delineated by deep seismic soundings and gravity modelling. In: *Radhakrishna, B.P., ed., Purana basins of peninsular India (Middle to Late Proterozoic), Geological Society of India Memoir* **6**, 349-356.

Wiedenbeck, M., Goswami, J.N., & Roy, A.B. (1996). Stabilization of the Aravalli craton of northwestern India at 2.5 Ga: An ion microprobe zircon study. *Chemical Geology* **129**, 325-340.

Wingate, M.T.D., Campbell, I.H., Compston, W., Gibson, & G.M. (1998). Ion microprobe U-Pb ages for Neoproterozoic basaltic magmatism in south-central Australia and implications for the breakup of Rodinia. *Precambrian Research* **87**, 135-159.

Wingate, M.T.D. & Giddings, J.W. (2000). Age and palaeomagnetism of the Mundine Well dyke swarm, Western Australia: implications for an Australia-Laurentia connection at 755 Ma. *Precambrian Research* **100**, 335-357.

Zacharia, J.K., Bhaskar Rao, Y.J., Srinivasan, R., & Gopalan, K. (1999). Pb, Sr, and Nd isotope systematics of uranium mineralised stromatolitic dolomites from the Proterozoic Cuddapah Supergroup, south India: constraints on age and provenance. *Chemical Geology* **162**, 49-64.

Zack, T., Moraes, R., & Kronz, A. (2004). Temperature dependence of Zr in rutile: empirical calibration of a rutile thermometer. *Contributions to Mineralogy and Petrology* **148**, 471-488.

Zhang, R.Y., Zhai, S.M., Fei, S.M., & Liou, J.G. (2003). Titanium solubility in coexisting garnet and clinopyroxene at very high pressure: the significance of exsolved rutile in garnet. *Earth and Planetary Science Letters* **216**, 591-601.

Zhao, G., Cawood, P.A., Wilde, S.A., & Sun, M. (2002). Review of global 2.1-1.8 Ga orogens: implications for a pre-Rodinia supercontinent. *Earth-Science Reviews* **59**, 125-162.

Zhao, G., Sun, M., & Wilde, S. (2003). Correlations between the eastern block of the North China craton and the South Indian block of the Indian shield: an Archean to Paleoproterozoic link. *Precambrian Research* **122**, 201-233.

Table 3-1. Summary of radiometric ages for rocks of the Cuddapah basin.

Material/Rock unit analysed	Host Formation	Method	Age (Ma)	Reference
mica, Chelima Lamproite dyke	Cumbum	K-Ar	1371±45	1
phlogopite, Chelima Lamproite dyke	Cumbum	K-Ar	1350±52	2
phlogopite, Chelima Lamproite dyke	Cumbum	⁴⁰ Ar/ ³⁹ Ar	1417.8±8.2	3
whole-rock, dolerite sill	Tadpatri	K-Ar	1080±40	4
whole-rock, dolerite	Tadpatri?	Rb-Sr	*961±110	5
whole-rock, mafic sill	Tadpatri	K-Ar	958±35	1
whole-rock, mafic sill	Tadpatri	K-Ar	809±29	1
whole-rock/mineral, mafic sill	Tadpatri	Rb-Sr	1817±24	6
U-mineralized stromatolitic dolomite	Tadpatri	Pb-Pb	**1756±29	7
phlogopite, mafic sill at Pulivendla	Tadpatri	⁴⁰ Ar/ ³⁹ Ar	1899±20	8
phlogopite, mafic sill at Tadpatri	Tadpatri	⁴⁰ Ar/ ³⁹ Ar	1899±20	8
baddeleyite, mafic sill	Tadpatri	U-Pb IDTIMS	1885.4±3.1	this study
baddeleyite, mafic sill	Tadpatri	EM U-Th-total Pb	1838±91	Appendix C
whole-rock, dolerite sill	Vempalle	K-Ar	570±25	4
whole-rock, dolerite sill	Vempalle	K-Ar	790±30	4
whole-rock, dolerite sill	Vempalle	K-Ar	860±35	4
whole-rock, dolerite sill	Vempalle	K-Ar	1160±50	4
whole-rock/plag/cpx, mafic lava flow	Vempalle	Rb-Sr	*1556±147	5
whole-rock, mafic lava flow	Vempalle	K-Ar	1841±71	1

References: 1) Murty et al., 1987; 2) Chalapathi Rao et al., 1996; 3) Chalapathi Rao et al., 1999; 4) Aswathanarayana, 1964; 5) Crawford and Compston, 1973; 6) Bhaskar Rao et al., 1995; 7) Zachariah et al., 1999; 8) Anand et al., 2003; *recalculated using 1.42×10^{-11} ; **implies a minimum age for carbonate formation and dolomitization.

Table 3-2. U-Pb IDTIMS and LA-MC-ICP-MS data for mafic dykes from the Bastar craton and the Pulivendla mafic sill, Dharwar craton.

Fraction #	Description of material analysed	Weight (µg)	Concentrations (ppm)			Model Th/U	TC Pb (pg)	Isotopic Ratios				Apparent Ages (Ma)			%Disc
			U	Model Th	Pb			²⁰⁶ Pb/ ²⁰⁴ Pb	²⁰⁶ Pb/ ²³⁸ U	²⁰⁷ Pb/ ²³⁵ U	²⁰⁷ Pb/ ²⁰⁶ Pb	²⁰⁶ Pb/ ²³⁸ U	²⁰⁷ Pb/ ²³⁵ U	²⁰⁷ Pb/ ²⁰⁶ Pb	
<i>JEF-00-36 dolerite Dyke near Gidam, BD2 dyke swarm, Bastar craton (18° 58.42' N, 81° 33.85' E)</i>															
1	B, euh/euh-fr, str, tan, min-zc, FF-1.4A/15°m [12]	11.6	856	84	260	0.098	27.7	6926	0.30859±39	4.84755±625	0.11393±3	1733.8±1.9	1793.2±1.1	1863.0±0.4	7.91
2	B, subh/euh-fr, tan, min-zc, FF-1.8A/5°m [9]	4.0	1162	118	346	0.102	24.7	3582	0.30269±38	4.74235±611	0.11363±3	1704.7±1.9	1774.8±1.1	1858.2±0.5	9.40
3	Z, pink, euh, cl, str, FF-1.8A/5°m [6]	7.3	538	261	154	0.485	20.3	3205	0.26394±36	4.05933±561	0.11154±5	1510.0±1.8	1646.2±1.2	1824.7±0.8	19.33
4	Z, vlp, cl, vc, prn, pyr, FF-1.8A/5°m [6]	8.0	325	223	120	0.686	16.4	3255	0.32567±44	5.13952±726	0.11446±6	1817.4±2.2	1842.7±1.2	1871.3±0.9	3.31
5	Z, pink, skel/euh-fr, str, Fe, FF-1.8A/5°m [10]	19.3	223	131	75	0.588	19.8	4148	0.30401±39	4.73516±626	0.11297±3	1711.1±1.9	1773.5±1.1	1847.7±0.5	8.41
6	B, euh-fr, str, tan, FF-1.8A/5°m [2]	3.0	329	31	97	0.094	15.7	1196	0.29952±41	4.71557±699	0.11419±8	1688.9±2.0	1770.0±1.3	1867.1±1.2	10.84
7	B, core, tan, IF-0.8A/15°m, MIH [1]	0.2*	1046	91	327	0.087	4.7	901	0.31899±71	5.00722±2024	0.11385±36	1784.8±3.5	1820.5±3.5	1861.7±5.7	4.73
8	B, core, tan, IF-0.8A/15°m, MIH [2]	0.15*	2497	180	798	0.072	6.4	1215	0.32745±45	5.14751±905	0.11401±13	1826.0±2.2	1844.0±1.5	1864.3±2.1	2.36
9	Z, rim, cl, cls, min-b, IF-0.8A/15°m, MIH [7]	1.0*	129	98	24	0.762	3.5	334	0.13796±51	1.81226±1772	0.09527±81	833.1±2.9	1049.9±6.5	1533.5±15.9	48.63
10	B, br, euh, abr, FF-1.4A/15°m [1]	1.0	603	46	194	0.077	8.4	1503	0.32933±39	5.18993±726	0.11429±10	1835.1±1.9	1851.0±1.2	1868.8±1.5	2.07
11	B, br, euh-fr, abr, FF-1.4A/15°m [1]	0.8	1439	73	471	0.051	4.7	5168	0.33697±40	5.34528±611	0.11505±7	1872.1±1.9	1876.1±1.0	1880.7±1.0	0.53
<i>JEF-00-30 dolerite dyke near Dantewara, BD2 dyke swarm, Bastar craton (18° 49.18' N, 81° 19.87' E)</i>															
12	B, lt-tan, euh-fr, str, S+J [22]	0.3*	1246	133	406	0.11	6.7	1164	0.32992±49	5.26460±906	0.11573±11	1837.9±2.3	1863.1±1.5	1891.3±1.7	3.24
13	B, lt-tan, euh-fr, str, S+J [10]	0.1*	2335	454	766	0.19	15.5	322	0.32533±72	5.11525±1816	0.11404±35	1815.7±3.5	1838.6±3.2	1864.7±5.5	3.01
14	B, lt-tan, euh, str, S+J [10]	0.4*	819	84	271	0.10	14.5	491	0.33613±52	5.35469±1112	0.11554±19	1868.1±2.5	1877.7±1.9	1888.4±2.9	1.24
15	B, lt-tan, euh, str, S+J [34]	1.5*	483	36	160	0.07	2.2	6920	0.33822±48	5.39660±781	0.11572±4	1878.1±2.3	1884.3±1.3	1891.2±0.5	0.80
LA-MC-ICP-MS data: single <i>in situ</i> analysis of the monazite grain shown in Fig. 3-9 (~8 µm beam width)								0.34855±268	5.49082±8242	0.11580±100	1927.7±12.8	1899.1±12.9	1892.3±15.5		
<i>JEF-00-14 metadolerite dyke near Gatam, HMD dyke swarm, Bastar craton (18° 49.37' N, 81° 34.71' E)</i>															
16	R, euh, tan, str, S+J [7]	3.7	16	1.9	6.5	0.12	7.3	222	0.40175±212	7.37748±5548	0.13318±67	2177.1±9.7	2158.2±7.1	2140.3±8.7	-2.02
17	R, euh, tan, str, S+J [13]	4.8	18	1.4	6.7	0.08	9.6	228	0.38465±156	6.91766±4236	0.13044±61	2097.9±7.3	2100.9±5.8	2103.8±8.2	0.33
<i>JEF-99-9 Dolerite sample of the Pulivendla sill, Dharwar craton (14° 25.83' N, 78° 12.85' E)</i>															
18	B, tan, str, euh-fr, S+J [6]	0.3*	327	52	122	0.158	5.0	613	0.34053±198	5.36434±4299	0.11425±58	1889.2±9.5	1879.2±7.0	1868.1±9.1	-1.30
19	B, br, str, euh-fr, S+J [4]	0.4*	467	73	159	0.157	2.6	2562	33392±66	5.31650±1196	0.11547±13	1857.4±3.2	1871.5±2.0	1887.3±1.9	1.82
20	B, br, euh-fr, str, S+J [3]	0.5*	166	41	100	0.249	24.2	99	35045±183	5.56718±4889	0.11521±104	1936.8±8.8	1911.0±8.3	1883.2±16.2	-3.29
21	B, tan, euh-fr, str, S+J [27]	0.4*	875	147	315	0.168	10.0	671	0.33267±66	5.27971±1248	0.11511±17	1851.3±3.2	1865.6±2.1	1881.5±2.7	1.85

Notes:

*estimated weights: along with corresponding concentrations of U, Th, and Pb, these values are estimated to be accurate only to within ~1 order of magnitude, and probably represent maximum estimates

The number of grains in each fraction is noted in parentheses [].

Th concentration estimated from abundance of ²⁰⁸Pb and corresponding ²⁰⁷Pb/²⁰⁶Pb ages

TC Pb refers to the total amount of common Pb in picograms measured in the analysis

The values used in this study for the decay constants for ²³⁸U (1.55125 × 10⁻¹⁰ a⁻¹) and ²³⁵U (9.8485 × 10⁻¹⁰ a⁻¹) and the present day ²³⁸U/²³⁵U ratio of 137.88, are those determined by Jaffey et al. (1971).

Atomic ratios are corrected for fractionation, blank, spike and common Pb (Stacey and Kramers, 1975), except ²⁰⁶Pb/²⁰⁴Pb ratios which are corrected for fractionation and spike only

All errors quoted in this table are 1 sigma uncertainties

All analyses determined using a VG354

Abbreviations: abr - grains treated with air abrasion by the method of Krogh (1982); B - baddeleyite; br - dark brown; cl - clear, transparent; cls - colourless; core - mechanically isolated anhedral core fragment; Disc. - discordancy; euh - euhedral bladed habit; euh-fr - fragments of euhedral blades; Fe - pronounced orange staining; IF or FF - Initial Frantz or Final Frantz, including conditions during operation of the Frantz isodynamic separator in A (amperes) and degree of side-tilt (°), where m denotes magnetic fraction and nm denotes non-magnetic fraction; lt-tan - light tan brown in colour; MIH - grains picked from Methyl Iodide heavy mineral concentrate; min-b - minor baddeleyite still attached; min-zc - minor zircon overgrowth; pink - pink in colour; prn - prismatic; pyr - some pyramidal terminations; R - rutile; rim - mechanically isolated anhedral fragments of zircon from overgrowth rims on baddeleyite; S+J - Isolation of grains by the water-based method of Söderlund and Johansson (2002); skel - skeletal; str - striated; subh - subhedral; tan - tan brown in colour; vc - thin clear colourless cores visible; vlp - very light pink in colour; Z - zircon.

Table 3-3. Chemical composition of monazite in BD2 dyke sample JEF-00-30.

	Monazite	
	bright BSE domain	dark BSE domain
P ₂ O ₅	22.1	25.3
Y ₂ O ₃	0.8	0.7
La ₂ O ₃	17.9	19.9
Ce ₂ O ₃	29.4	33.0
Pr ₂ O ₃	2.4	2.5
Nd ₂ O ₃	6.5	7.2
Sm ₂ O ₃	1.1	1.1
Gd ₂ O ₃	0.4	0.4
SiO ₂	4.4	2.4
CaO	0.6	0.3
ThO ₂	11.217	4.702
UO ₂	0.179	0.103
PbO	0.916	0.422
Total	97.9	98.0
<i>n</i>	3	21

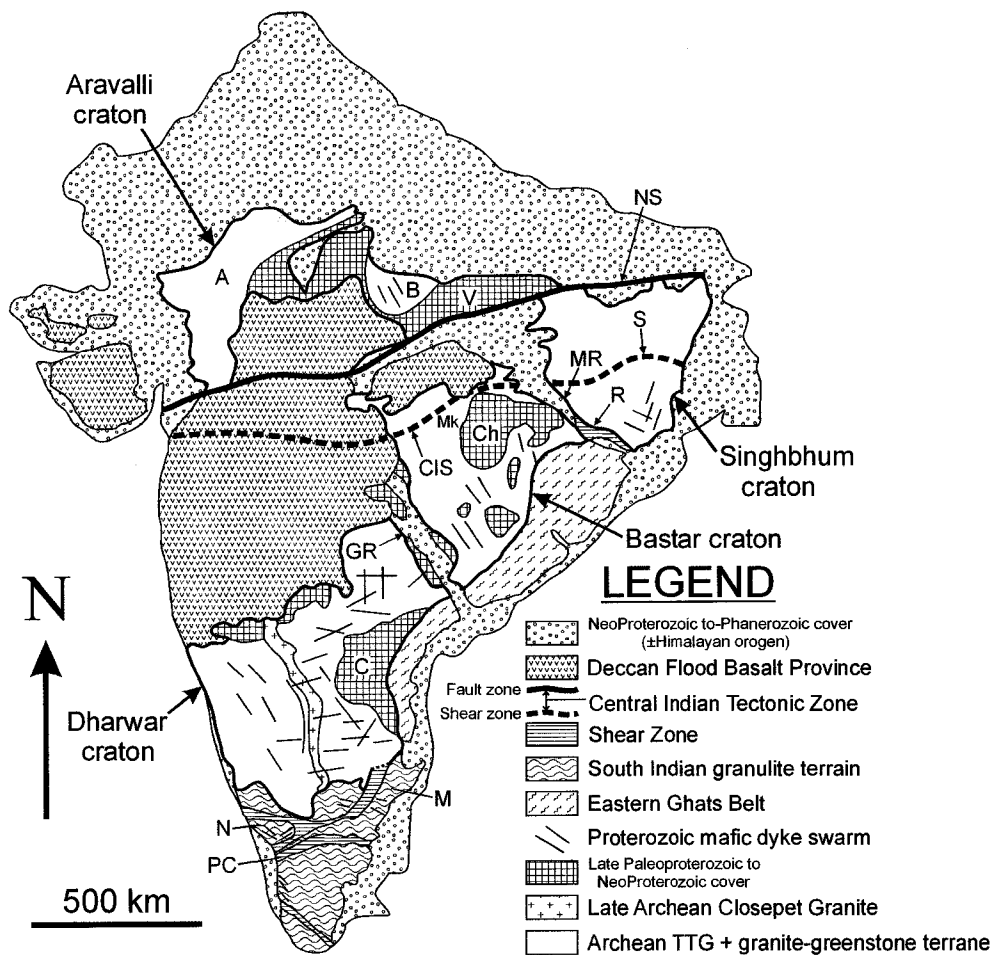


Fig. 3-1. Overview map of the principle geologic and tectonic elements of the Indian shield. Geology modified from: Crowe et al., 2003; GSI, 1998; Mishra et al., 2000; Murthy, 1995; Naqvi and Rogers, 1987. Abbreviations: A - Aravalli-Delhi Belt; B - Bundelkhand massif; C - Cuddapah basin; Ch - Chattisgarth basin; CIS - Central Indian shear zone; G - Godavari rift; M - Madras block; Mk - Malanjkhanda; MR - Mahanadi rift; N - Nilgiri block; NS - Narmada-Son lineament; PC - Palghat-Cauvery shear zone; R - Rengali Province and Kerajang shear zone; S - Singhbhum shear zone; V - Vindhyan basin.

Fig. 3-2. Geological map of east-central peninsular India, highlighting the locations of U-Pb geochronology samples of mafic igneous rocks. Geology modified from: Halls, 1982; Murty et al., 1987; Naqvi and Rogers, 1987; Leelanandam, 1990; Ramachandra et al., 1995; Ramam and Murty, 1997; GSI, 1998; Madhavan et al., 1999; Mishra et al., 2000; Ramachandra and Roy, 2001; Biswal and Sinha, 2003; Deb, 2003; Das et al., 2003; Mainkar et al., 2004.

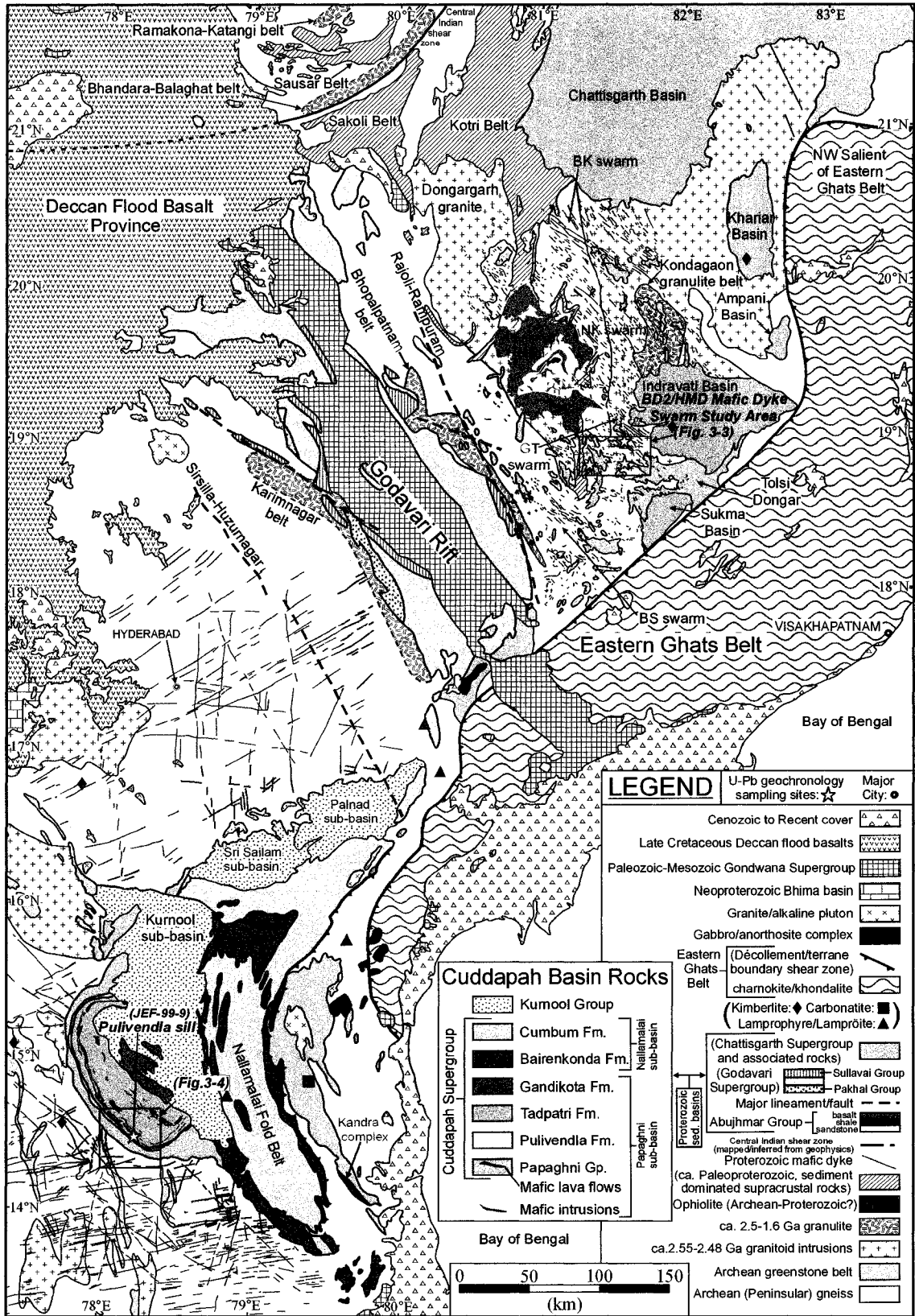


Figure 3-2

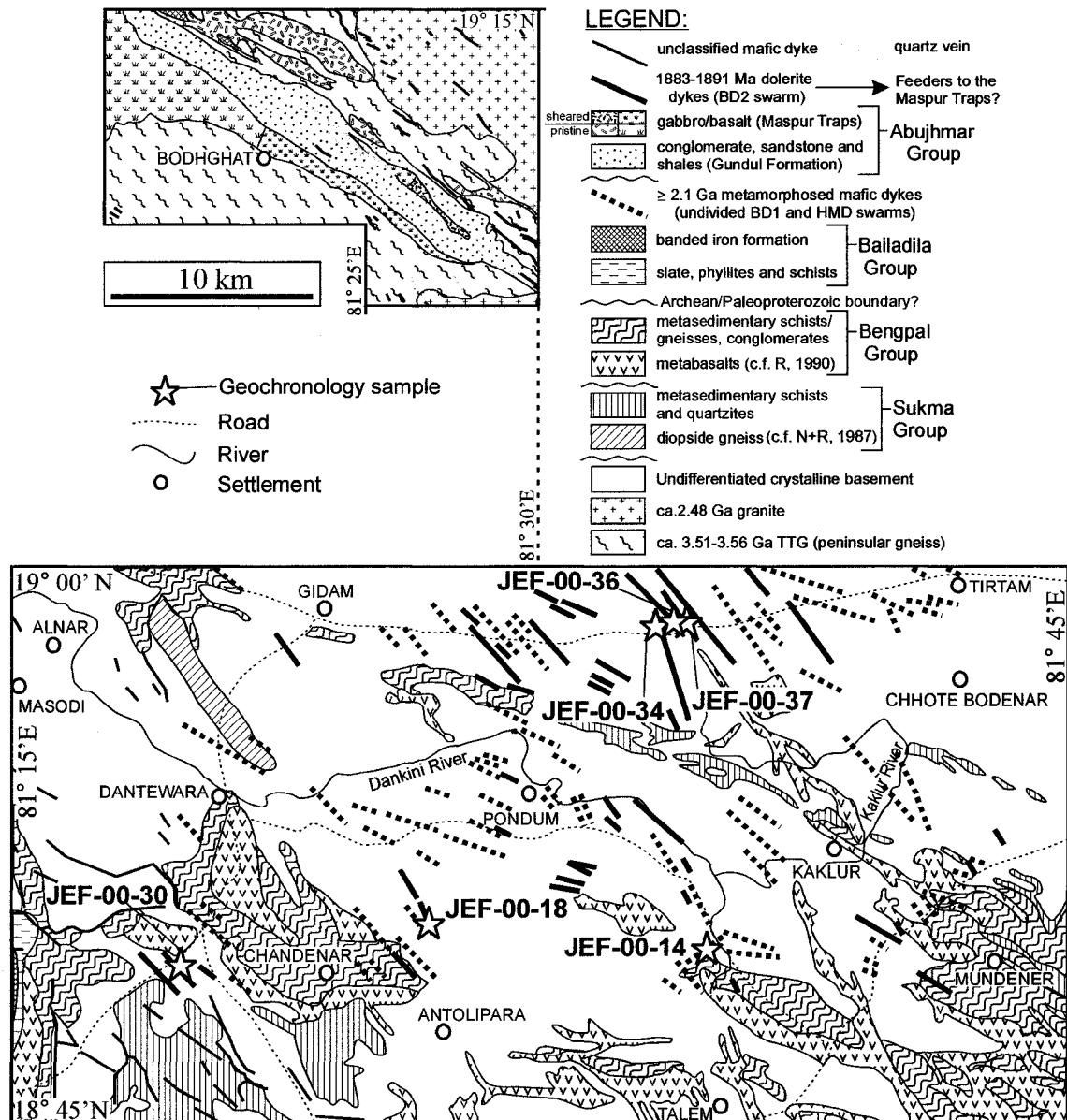


Fig. 3-3. Geological maps of the southern Bastar craton shown to proper scale, relative position and orientation, and depicting the locations of mafic dykes sampled for isotopic and chemical dating. Geological maps modified from: Crookshank, 1963; Mishra et al., 1987b; Naqvi and Rogers, 1987; Ramakrishnan, 1990; Srivastava and Singh, 2003.

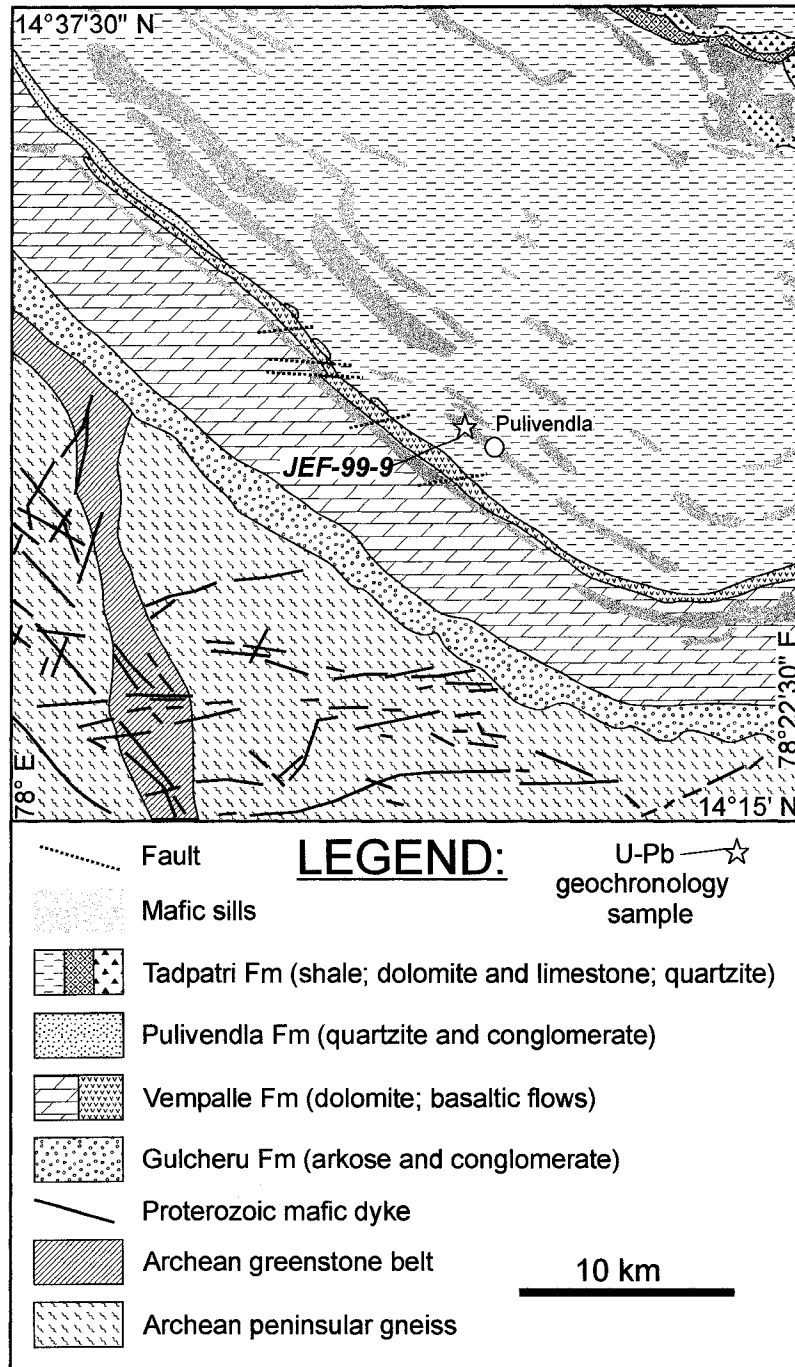


Fig. 3-4. Geological map of the southwest Cuddapah basin showing the location of the Pulivendla dolerite sill sampled for U-Pb dating. Geology and stratigraphy modified from: Murty et al., 1987; Nagaraja Rao et al., 1987; Ramam and Murty, 1997.

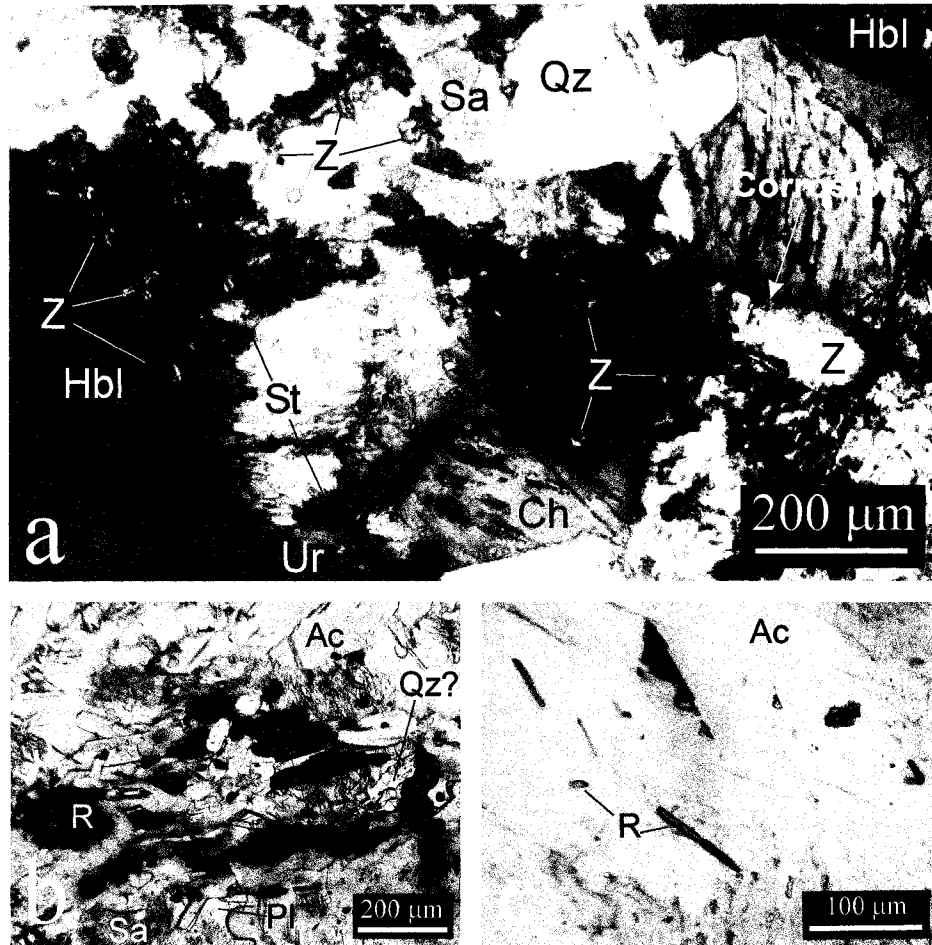


Fig. 3-5. Thin section photomicrographs (plain light) showing petrographic textures of mafic dykes from the southern Bastar craton: a) photomicrograph of sample JEF-00-36, showing hydrothermal alteration of hornblende to fibrous blue-green amphibole (uralite), and pleochroic halos surrounding zircon. b) photomicrograph of sample JEF-00-14 showing Type 1 prograde rutile. c) photomicrograph of sample JEF-00-14 showing Type 2 retrograde rutile. Abbreviations: Ac - actinolite; Bi - biotite; Ch - chlorite; Hbl - hornblende; Pl - plagioclase; Qz - quartz; R - rutile; Sa - saussurite; St - stilpnomelane; Ur - uralite; Z - zircon.

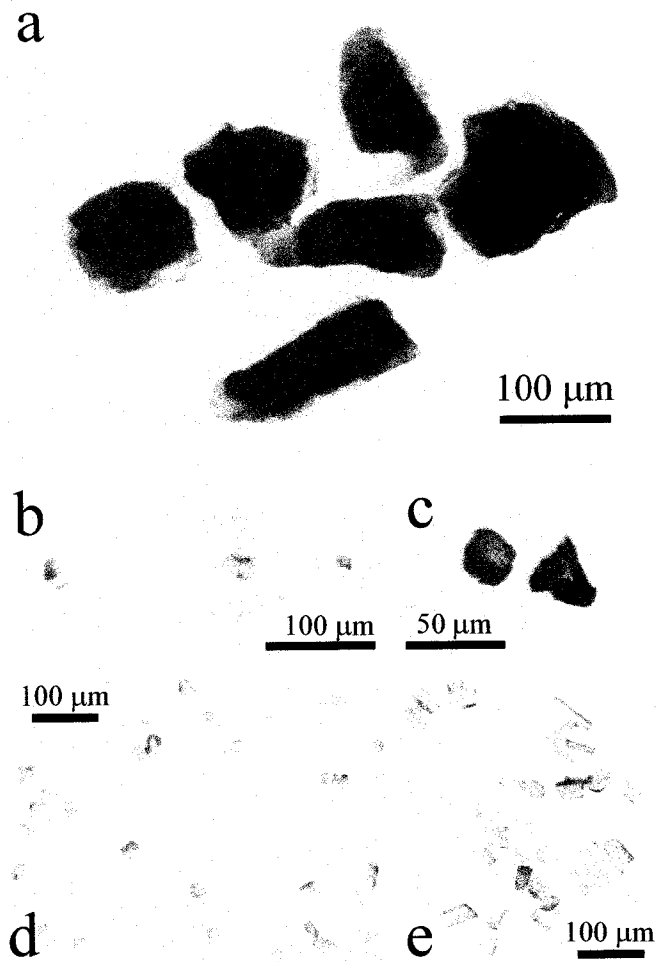


Fig. 3-6. Photomicrographs of baddeleyite and zircon isolated from samples of the BD2 mafic dyke swarm, Bastar craton. a) Baddeleyite crystals displaying zircon overgrowth isolated from sample JEF-00-36 by conventional mineral separation. b) Fragments of zircon rim (with minor baddeleyite still attached to some fragments) mechanically isolated from the grains shown in (a), comprising the material incorporated in fraction #9. c) Fragments of baddeleyite mechanically isolated from the grains shown in (a), comprising the material incorporated into fraction #8. d) Baddeleyite grains (including the largest grain size) isolated from a coarse grained dioritic portion of sample JEF-00-30, employing a puck mill for sample comminution followed by the water-based method of baddeleyite separation. The baddeleyite grains incorporated into fraction #12 were picked from the grains shown in this photomicrograph. e) Baddeleyite grains (including the largest grain size) isolated from a doleritic portion of sample JEF-00-30, employing a Bico Disk Mill for sample comminution followed by the water-based method of baddeleyite separation. The baddeleyite grains in this photomicrograph comprise most of the grains included in fraction #15. Fraction numbers correspond to Table 3-2.

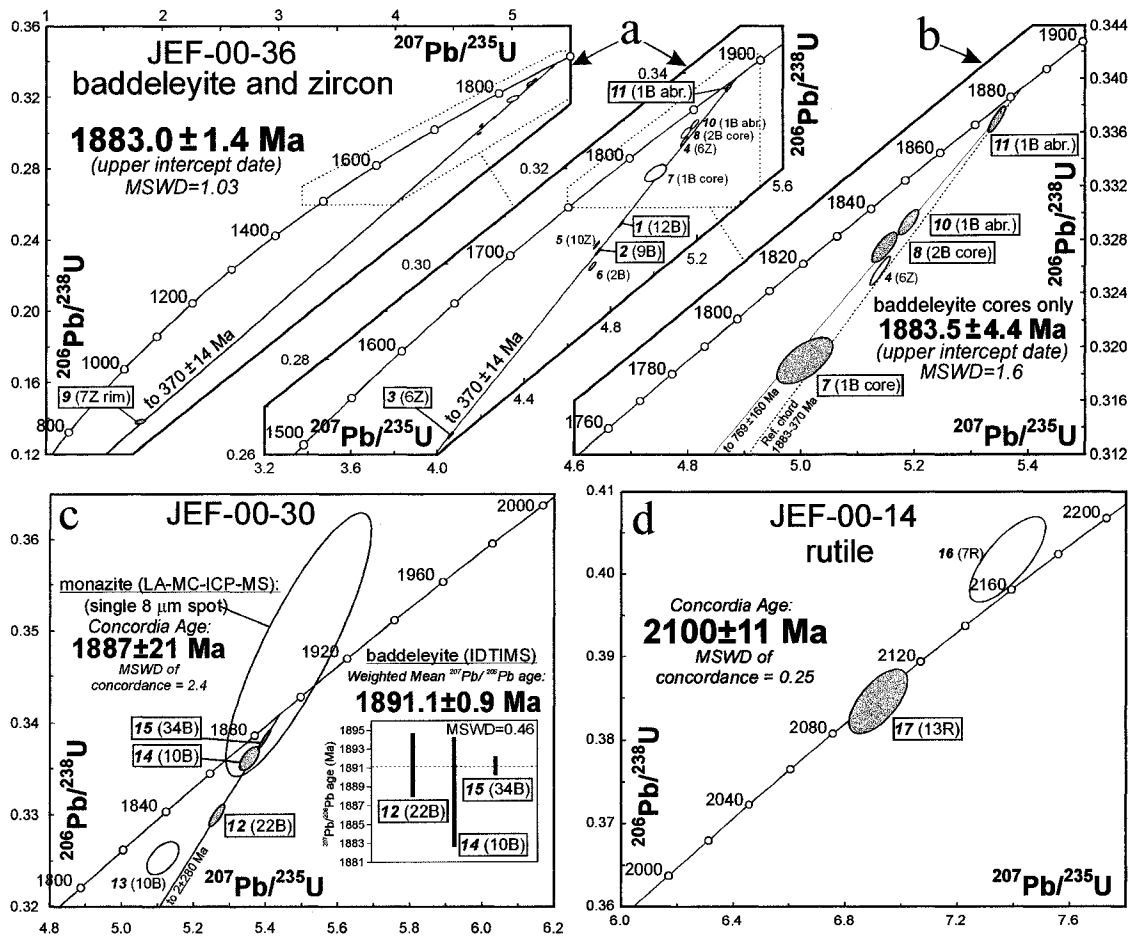


Fig. 3-7. Concordia diagrams showing U-Pb isotopic data for baddeleyite, zircon, and rutile from mafic dykes of the southern Bastar craton. Error ellipses, error bars, and errors on the final ages are shown at the 2σ level and the data point labels are keyed to Table 3-2. For the IDTIMS data, shaded ellipses, labelled with larger lettering in boxes represent the data points used in the final age calculation for a given plot. a) U-Pb IDTIMS data for baddeleyite and zircon from BD2 dolerite dyke sample JEF-00-36, showing a composite baddeleyite/zircon linear regression. b) Close-up view of nearly concordant data from (a) showing a linear regression of exclusively the abraded and mechanically isolated baddeleyite cores. c) U-Pb IDTIMS data for baddeleyite, and LA-MC-ICP-MS data for igneous monazite from BD2 dolerite dyke sample JEF-00-30. The inset Figure shows a weighted mean plot of IDTIMS baddeleyite $^{207}\text{Pb}/^{206}\text{Pb}$ ages. d) U-Pb IDTIMS data for rutile from metamorphosed HMD mafic dyke sample JEF-00-14. Abbreviations: B- baddeleyite; abr. - grain treated with air abrasion; core - mechanically isolated core fragment(s); rim - mechanically isolated fragments of zircon overgrowth rims (on baddeleyite); R- rutile; Z- zircon.

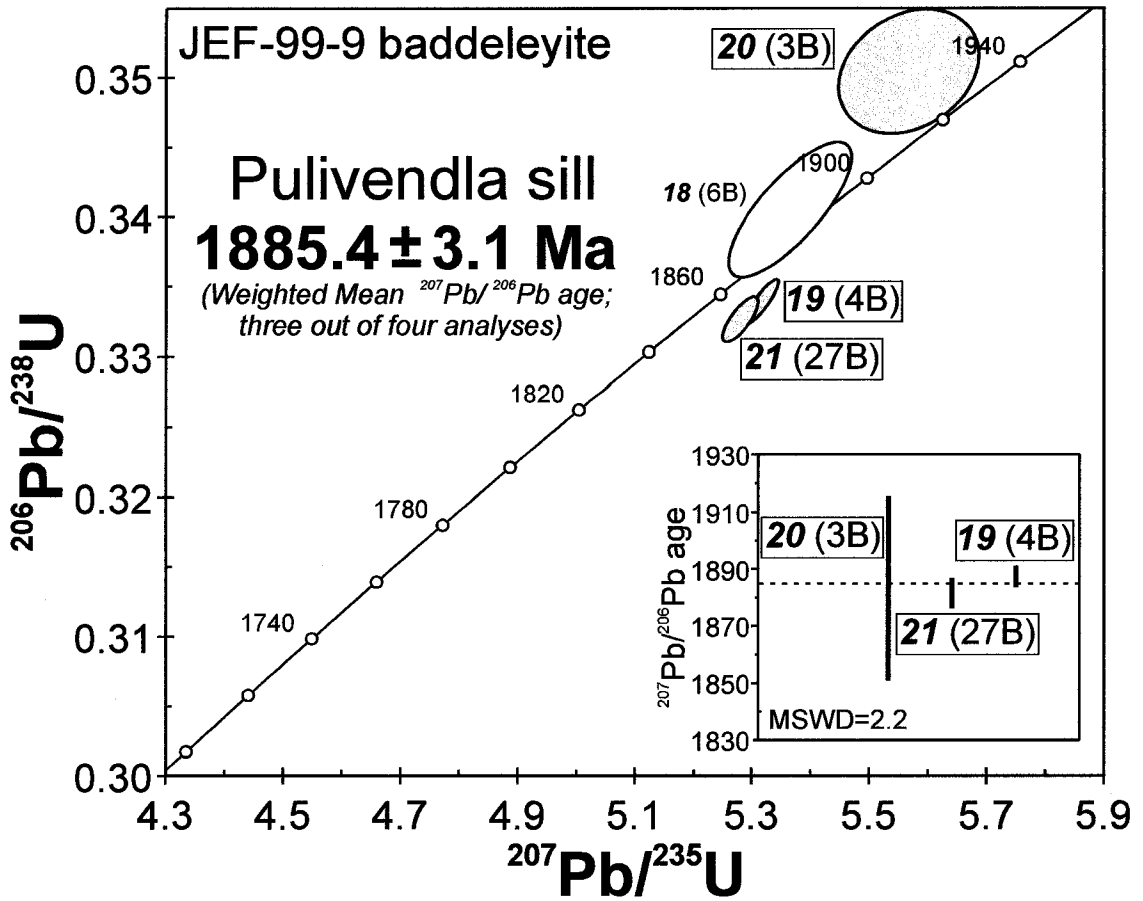


Fig. 3-8. Concordia diagram, showing U-Pb IDTIMS isotopic data for baddeleyite from Pulivendla dolerite sill sample JEF-99-9. The shaded ellipses, labelled with larger lettering in boxes represent the data points used in the final age calculation. Error ellipses, error bars, and error on the final age are shown at the 2σ level and the data point labels are keyed to Table 3-2. The inset Figure shows a weighted mean plot of baddeleyite $^{207}\text{Pb}/^{206}\text{Pb}$ ages. Abbreviations: B - baddeleyite.

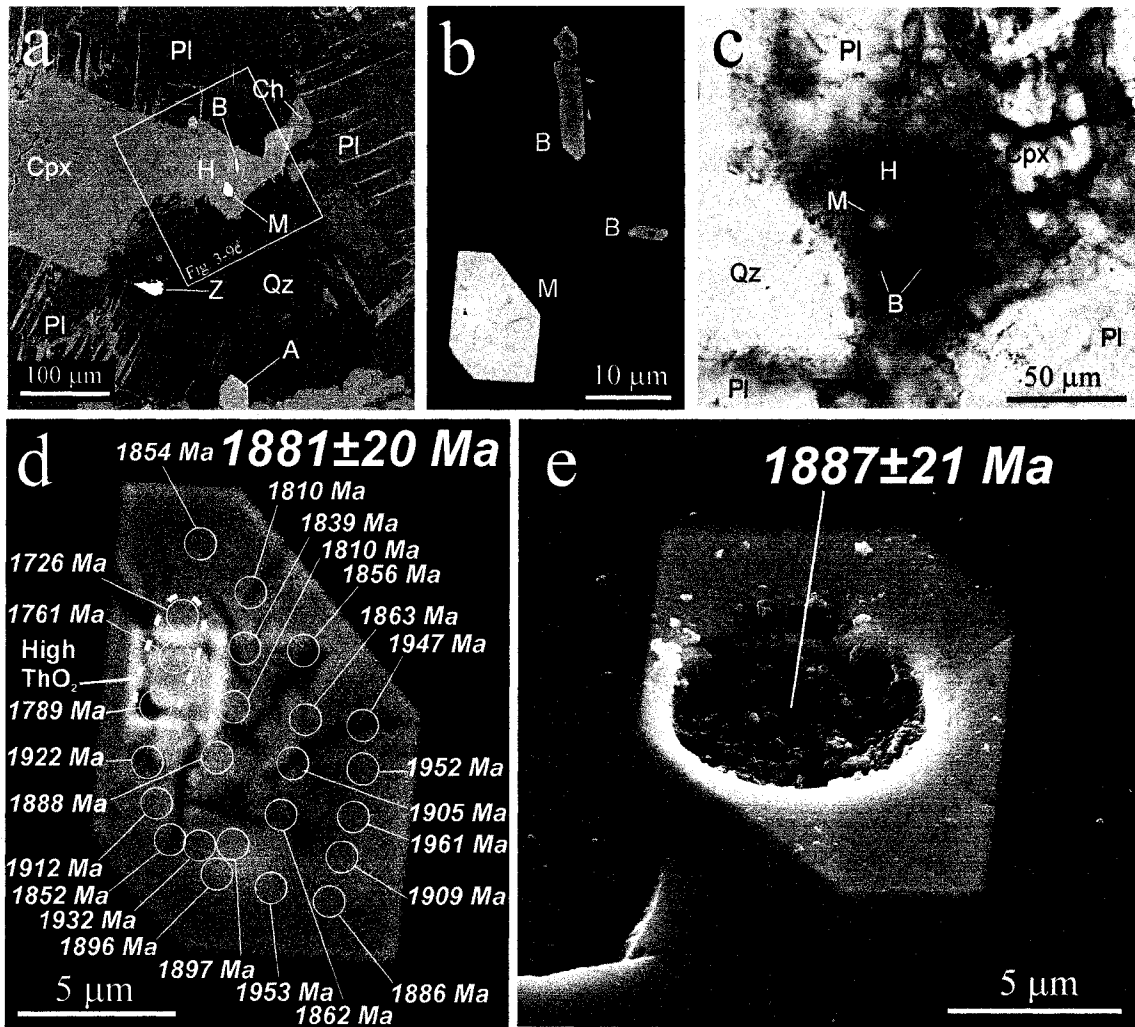


Fig. 3-9. a) Electron microprobe (EM) back-scattered electron (BSE) image of a polished thin section of BD2 dolerite dyke sample JEF-00-30, showing the petrographic context of the monazite crystal dated in this study by EM chemical U-Th-total Pb dating and U-Pb (LA-MC-ICP-MS). b) A close-up BSE image of (a) at higher contrast showing the spatial association of baddeleyite and monazite, and the euhedral form of the monazite crystal. c) Thin section photomicrograph (plain light) of a close-up region of (a) showing the petrographic context of the monazite crystal within late retrograde hornblende rimming clinopyroxene. d) Close-up BSE image at very high contrast showing oscillatory zoning and internal fracturing within the monazite crystal. The circles indicate the approximate locations of individual EM wavelength dispersive quantitative analyses, and the labels represent the corresponding apparent age t calculated for each spot. The dashed line encircles a high ThO_2 domain (Table 3-3) within the monazite. e) Scanning electron microscope (SEM), secondary electron image of the monazite, taken at an oblique angle and showing the location of the laser ablation pit generated during U-Pb dating by LA-MC-ICP-MS. The thin section was polished with aluminum oxide powder before SEM imaging, and some residual powder is visible within and around the laser ablation pit. The edges of this $\sim 8 \mu\text{m}$ pit occur entirely within the monazite grain. Note the typical $60^\circ/120^\circ$ amphibole cleavage in the hornblende adjacent to the monazite. Abbreviations: A - apatite; B - baddeleyite; Cpx - clinopyroxene; H - hornblende; M - monazite; Pl - plagioclase; Qz - quartz.

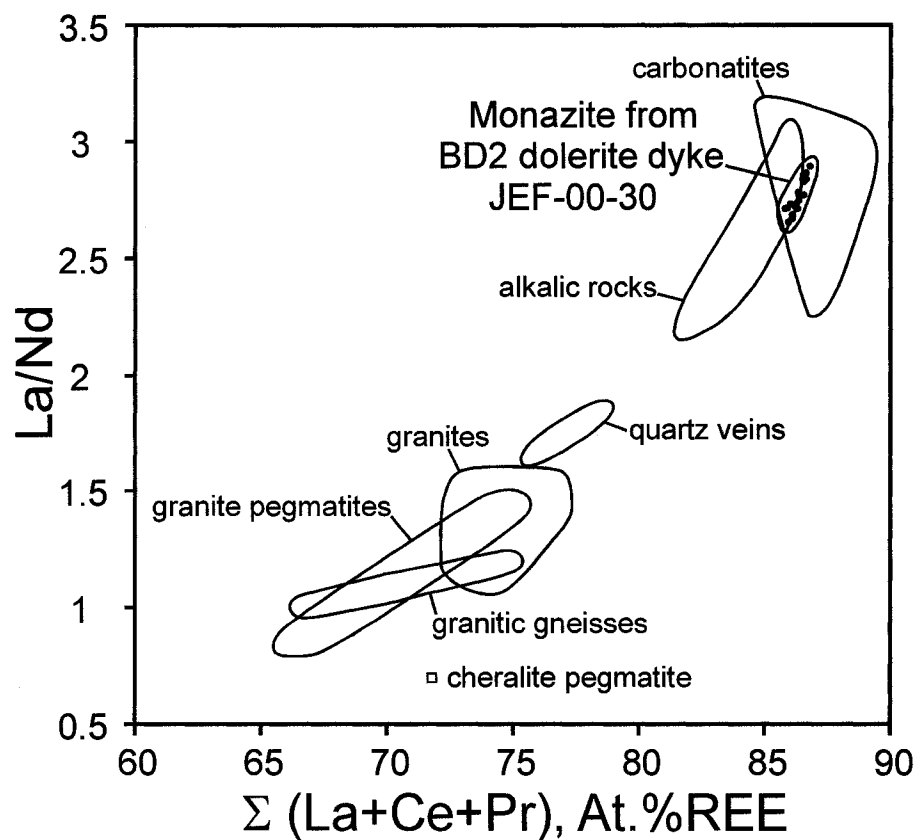


Fig. 3-10. Plot of $\Sigma(\text{La}+\text{Ce}+\text{Pr})$ in atomic% REE versus La/Nd for igneous monazite from BD2 dyke JEF-00-30. Monazite paragenetic fields are from Rapp and Watson (1986).

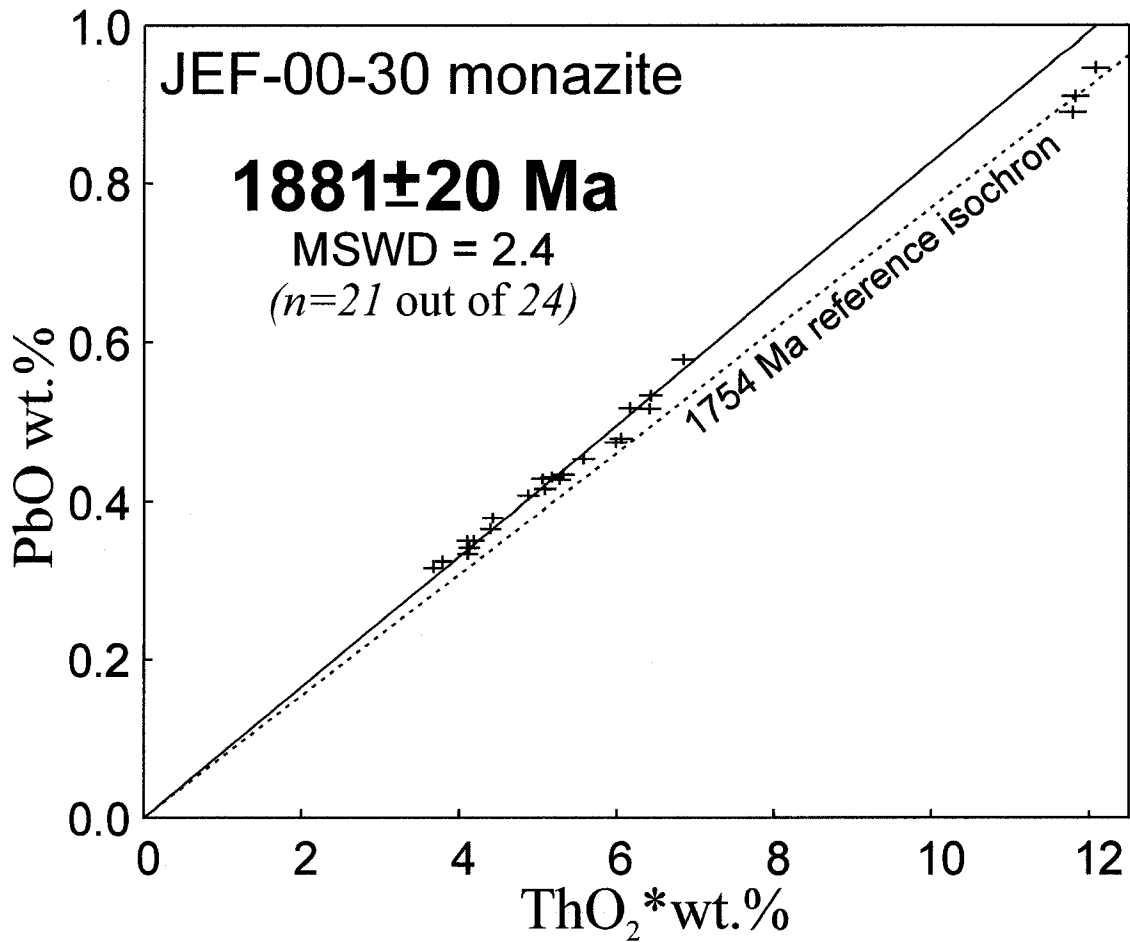


Fig. 3-11. ThO₂* versus PbO diagram for the monazite crystal analysed by EM *in situ* from a polished thin section of BD2 dolerite dyke sample JEF-00-30 (see images of the grain in Fig. 3-9). Error bars represent 2 σ analytical uncertainty and error on the final age is reported at 2 σ .

CHAPTER 4

U-Pb IDTIMS ages for Paleoproterozoic mafic dyke swarms of the Dharwar craton, south India: implications for an Ur-Kenorland connection

Jason E. French and Larry M. Heaman

Department of Earth and Atmospheric Sciences, University of Alberta, 1-26 Earth Sciences Building, Edmonton, AB, Canada, T6G 2E3

INTRODUCTION

Determining accurate and precise emplacement ages of mafic dyke swarms preserved in Precambrian shield areas is pivotal in studies of crustal evolution, because they can provide excellent regional time markers and may be genetically linked with major geodynamic processes on Earth, such as mantle plume activity, intracontinental rifting, and supercontinent break-up (Fahrig, 1987; LeCheminant and Heaman, 1989). Moreover, high precision U-Pb ages for mafic dyke swarms combined with primary paleomagnetic constraints on paleolatitude for the same sample are critical in establishing apparent polar wander paths for cratonic blocks (Halls and Heaman, 2000; Wingate and Giddings, 2000), and may provide robust piercing points for paleocontinental reconstructions (Heaman, 1997; Harlan et al., 2003). Advancements in high precision U-Pb IDTIMS geochronological studies of baddeleyite and zircon from mafic dykes (Heaman et al., 1986; Krogh et al., 1987) have facilitated the development of a considerable database of high precision emplacement ages for mafic dyke swarms in many Archean cratons in North America and to a lesser extent worldwide (Ernst and Buchan, 2001a). Recent improvements in baddeleyite mineral separation have

facilitated rapid and efficient isolation of minuscule (<25 μm) baddeleyite blades (Söderlund and Johansson, 2002; Söderlund et al, 2004), increasing substantially the number of mafic dyke samples that can be dated using the U-Pb IDTIMS (Isotope Dilution Thermal Ionization Mass Spectrometry) technique. In addition, more recent applications of other geochronological techniques to U-Pb dating of mafic dykes including Sensitive High Resolution Ion Microprobe (SHRIMP) analysis of baddeleyite, zircon and zirconolite (Wingate et al., 1998; Wingate and Compston, 2000; Rasmussen and Fletcher, 2004), and Electron Microprobe (EM) U-Th-total Pb chemical dating of baddeleyite (French et al., 2002; Chapter 3 this thesis) have also expanded the age database. Nevertheless, there still remains a paucity of U-Pb geochronological constraints on mafic dykes from a number of Archean cratons worldwide, including several large cratons located in peninsular India.

Major Precambrian mafic dyke swarms transect all Archean cratons of the Indian shield, and the densest concentration of dykes occurs in the Dharwar craton (Halls, 1982; Drury, 1984; Murthy, 1987; Murthy, 1995). On the basis of crosscutting relationships and available radiometric ages, most dyke swarms in the Dharwar craton appear to have been emplaced in the Proterozoic. Nevertheless, there is currently a complete lack of published, high precision age constraints for any mafic dyke swarm in the Dharwar craton. Determining precise emplacement ages for these dyke swarms is particularly important because the Dharwar craton is central to many proposed ancient supercontinent reconstructions including ~ 3.0 Ga Ur (Rogers 1996), ~ 1.7 Ga Capricornia (Krapez, 1999), and ~ 1.5 Ga Columbia (Rogers and Santosh, 2002). In this study, we report U-Pb IDTIMS baddeleyite and zircon ages for seven mafic dykes

spanning a vast tract of the Dharwar craton. Particular emphasis is placed on dykes from the eastern block of the craton, because these prominent dyke swarms appear to extend over distances of hundreds of kilometres and potentially record major continental break-up events. Several dykes from one giant E-W trending swarm (the Bangalore dyke swarm) have been the subject of previous paleomagnetic investigations (Kumar and Bhall, 1983; Dawson and Hargraves, 1994; Prasad et al., 1999; Radhakrishna et al., 2003). The results of this study define a protracted history of extension and mafic magmatism across much of the Dharwar craton during the Paleoproterozoic, providing key geochronological constraints for Precambrian plate reconstructions.

GEOLOGICAL SETTING

The Archean Dharwar craton of the Indian shield (Fig. 4-1) is exposed as a ~500 km N-S by ~700 km E-W crustal domain that is bordered by the ~66 Ma Deccan Flood Basalt Province to the north, the Arabian sea to the west, the Godavari rift and Eastern Ghats Belt to the east, and the transition to a granulite terrane in the south (Rogers, 1986; Naqvi and Rogers, 1987). It is one of three Archean nuclei (in addition to the Bastar and Singhbhum cratons) that form the composite Dharwar protocontinent (South Indian Block of the Indian shield), which is separated from the Aravalli protocontinent (North Indian Block) by the Central Indian Tectonic Zone (Fig. 4-1).

Archean geology of the Dharwar craton

Bisecting the entire Dharwar craton is a prominent N-S trending array of Late Archean granitoid plutons known as the Closepet batholith, the main body of which measures ~25-30 km in width and >400 km long (Fig. 4-2). The batholith parallels the regional structural grain of crust on either side of it which trends NNW-SSE in the

northern part of the craton but swings N-S towards the south. The Dharwar craton is classically divided into two contrasting blocks, the Eastern Dharwar craton (EDC) and the Western Dharwar craton (WDC), which are separated by a crustal-scale thrust fault that parallels the Closepet batholith approximately 20-40 km to the west of it (Naqvi and Rogers, 1987; Bhaskar Rao et al., 1992). This craton-transecting geological structure acts as the eastern boundary of the Archean Dharwar Supergroup (except the Sandur Greenstone Belt: Radhakrishna and Vaidyanadhan, 1997) and has more recently been interpreted as a steep, sinistral shear zone (Chadwick et al., 2000).

Western Dharwar craton

Two contrasting Archean supracrustal sequences known as the Sargur Group and Dharwar Supergroup are preserved as greenstone belts in the WDC, and are exposed within a large tract of tonalite-trondjemite-granodiorite (TTG) gneisses known as the Peninsular gneiss (Fig. 4-2). The oldest known mineral ages in the WDC come from Sargur Group pelitic schists of the Holenarsipur greenstone belt (Fig. 4-2), which contain detrital zircons as old as 3581 ± 10 and 3586 ± 4 Ma (SHRIMP $^{207}\text{Pb}/^{206}\text{Pb}$ ages: Nutman et al., 1992). A SHRIMP $^{207}\text{Pb}/^{206}\text{Pb}$ age of 3298 ± 7 Ma determined on zircon from a rhyolite flow within this belt indicates that the Sargur Group comprises the oldest documented supracrustal sequence within the Dharwar craton (Peucat et al., 1995). Peninsular gneiss of the WDC was extracted from the mantle in a complex multi-stage process between >3.4 to ~ 3.0 Ga, and basement stabilization was essentially complete by ~ 3.0 Ga (Beckinsale et al., 1980; Rogers et al., 1986; Meen et al., 1992). Some of the younger (3.1-3.0 Ga) gneisses and trondhjemitic plutons intrude Sargur Group supracrustals (Rogers et al., 1986; Meen et al., 1992; Peucat et al., 1995). U-Pb zircon

(IDTIMS) concordia upper intercept ages of $3509 \pm 14/-7$ Ma (Sarkar et al., 1993) and 3561 ± 11 Ma (Ghosh, 2004) for Peninsular gneiss from the Bastar craton (Ghosh, 2004), and $^{207}\text{Pb}/^{206}\text{Pb}$ (SHRIMP) ages of 3.5-3.6 Ga determined on detrital zircons from the oldest metasedimentary rocks of the Singhbhum craton confirm that a major episode of crust formation began by 3.6 Ga in all three cratonic nuclei of the Dharwar protocontinent (Mishra et al., 1999). Similar protolith crystallization ages of 3307 ± 33 Ma (whole-rock Sm-Nd isochron age, 1σ error: Gopalan et al., 1990) and 3281 ± 3 Ma (mean $^{207}\text{Pb}/^{206}\text{Pb}$ age of zircon determined by SIMS: Wiedenbeck and Goswami, 1994) for the same orthogneiss samples from the Aravalli craton, and 3270 ± 3 to 3297 ± 8 Ma (mean $^{207}\text{Pb}/^{206}\text{Pb}$ ages of zircon also determined by SIMS: Mondal et al., 2002) for TTG gneiss from the Bundelkhand craton indicate a joint early evolution for those two cratons (Mondal et al., 2002). However, basement stabilization of the Aravalli protocontinent appears to have occurred later than in the Bastar, Singhbhum, and Western Dharwar cratons (i.e. later than ~ 3.0 Ga), at ~ 2.5 Ga (Mishra et al., 1999; Mondal et al., 2002). The older ortho-amphibolite dominated, Sargur Group supracrustal belts of the WDC, which range in size from small enclaves only metres across to elongate or amoeboid belts up to a few ten's of kilometres long by several kilometres across, are unconformably overlain by the younger and much more aerially extensive supracrustal belts of the Dharwar Supergroup (Naqvi, 1981; Viswanatha et al., 1982; Radhakrishna and Vaidyanadhan, 1997; Chardon et al., 1998). The stratigraphy of the Dharwar Supergroup is subdivided into older mafic volcanic dominated Bababudan Group rocks, and younger, more voluminous, sediment-dominated rocks of the Chitradurga Group (Naqvi, 1981; Naqvi and Rogers, 1987). The Bababudan Group

is dominated by metabasalts with back-arc affinity, and has subordinate quartz-pebble conglomerates (basal), cross-bedded quartzites, argillites and banded iron formations, with the overall succession locally approaching ~5 km in maximum thickness (Chadwick et al., 1985; Chadwick et al., 2000) and is well-exposed in the Bababudan basin (Fig. 4-2). Zircon from two tuffaceous samples from the middle stratigraphy (Mulaingiri Formation) of the Bababudan Group, yielded ages of 2720 ± 7 Ma and 2718 ± 6 Ma determined by U-Pb SHRIMP, and preliminary ages of 2819 ± 10 Ma and 2816 ± 16 Ma were also determined for detrital zircons from the basal quartzite of this Group (Trendall et al., 1997a and reference therein). The Chitradurga Group is well exposed in two major supracrustal belts known as the Shimoga and Chitradurga belts (Fig. 4-2), and fluvial and marine sedimentation during this late stage of basin development was accompanied by bimodal volcanism, producing a stratigraphic sequence at least 7 km thick (Chadwick et al., 2000). From stratigraphically oldest to youngest, the Chitradurga Group comprises a basal polymictic conglomerate, a succession of phyllite and argillite with intercalated stromatolitic limestone/dolomite, iron and manganese formations, a bimodal volcanic succession with intercalated minor chert and phyllite, and a thick succession of greywacke and argillite with minor volcanics, chert, and polymictic conglomerate (Bhaskar Rao et al., 1992; Chadwick et al., 2000). SHRIMP U-Pb zircon ages of 2614 ± 8 Ma (Nutman et al., 1996) and 2606 ± 6 Ma (Trendall et al., 1997b) constrain the age of extrusion of volcanic rocks within the upper part of the Chitradurga Group (Daginkatte Formation) of the Shimoga supracrustal belt. Late granite plutons are relatively scarce in the WDC but include the Chitradurga granite dated at 2605 ± 18 Ma (Pb-Pb whole-rock isochron: Taylor et al., 1984) and

2603±28 Ma (Rb-Sr whole-rock: Bhaskar Rao et al., 1992), and the Arsikere granite dated at ~2.56 Ga (Rb-Sr whole-rock: Rogers, 1988 and reference therein), ~2540 Ma (whole-rock Pb-Pb: Meen et al., 1992), and 2618±38 Ma (U-Pb zircon and titanite: Miller et al., 1996).

Eastern Dharwar craton

In contrast to the WDC, TTG (Peninsular) gneiss protolith ages for the EDC are relatively young (3.1-2.5 Ga), Late Archean juvenile granitoid plutons are abundant, and greenstone belts are relatively limited in aerial extent (Fig. 4-2). A single zircon evaporation age of 3127±8 Ma (Jayananda et al., 2000) defines a minimum age for TTG basement gneiss in the Bangalore area. Orthogneisses from the Kolar area yielded U-Pb zircon ages ranging from 2631+6.5/-6.0 Ma to 2532+3.5/-3.0 Ma; interpreted to represent the timing of emplacement of the tonalitic to granodioritic protolith magmas, with evidence for older (>2800 and ~2850 Ma) basement from U-Pb dating of inherited zircons (Krogstad et al., 1991; Jayananda et al., 2000). Peucat et al. (1993) analysed tonalite-trondhjemite, granite and charnockite gneisses from the granulite transition zone at the southern margin of the EDC (Krishnagiri area), and determined emplacement ages for the protoliths of 2550-2530 Ma (U-Pb zircon: TIMS and single grain evaporation methods) for the gneisses. On the basis of Sr-Nd isotope studies, these 2.55-2.53 Ga gneisses appear to be juvenile, and $^{207}\text{Pb}/^{206}\text{Pb}$ ages of 2506±10 and 2517±10 Ma for monazite (two slightly discordant analyses determined by TIMS) from the granite and charnockite gneisses, respectively, are interpreted to represent the timing of granulite grade metamorphism in the area (Peucat et al., 1993). Northward tilting and differential erosion of the Dharwar craton have apparently resulted in the observed decrease in

metamorphic conditions from about 750°C and 6-7 kbar at the southern transition zone, to about 450°C and ~3 kbar at the northern reaches of the Dharwar Supergroup (Rogers, 1986; Moyen et al., 2001). Immediately east of the shear zone that separates the EDC from the WDC, a narrow (~25-km-wide) belt of TTG gneiss occurs that has been correlated with pre-2.9 Ga Peninsular gneiss of the WDC (Chadwick et al., 2000). In contrast with the gneiss immediately west of the shear zone, this belt of Peninsular gneiss shows variable degrees of partial melting and transitions to pink granite with remnant precursor gneissic enclaves (Chadwick et al., 2000). These anatectic granites have been grouped, along with the Closepet batholith and a large calc-alkaline complex composed of anatectic granite, granodiorite, monzonite, and diorite plutons that spans much of the EDC, as a part of the composite Late Archean Dharwar batholith (Chadwick et al., 2000). These linear plutonic belts are interspersed with and roughly parallel to numerous elongate Late Archean (ca. 2.8-2.55 Ga) greenstone belts, and this composite crustal domain (comprising most of the EDC) is transected by numerous crustal-scale, sinistral shear zones that are associated with gold mineralization of economic importance where they cross the greenstone belts (Chadwick et al., 2000; Manikyamba et al., 2004). Similar emplacement ages of 2513 ± 5 Ma (SHRIMP U-Pb zircon: Friend and Nutman, 1991) and 2518 ± 5 Ma (single zircon evaporation: Jayananda et al., 1995) were determined for two different phases of the Closepet batholith southwest of Bangalore, with evidence for a slightly earlier associated migmatization event at 2528 ± 5 Ma (SHRIMP U-Pb zircon: Friend and Nutman, 1991). A Rb-Sr whole-rock age of 2452 ± 50 Ma for the Torangallu granite which intrudes the northern part of the Sandur greenstone belt (Bhaskar Rao et al., 1992) and a U-Pb zircon age of 2433 ± 54 Ma for a

granite south of this belt (see reference in Russell et al., 1996), provide some evidence to suggest that emplacement of the polyphase Closepet batholith continued into the Paleoproterozoic. In addition, Pandey et al. (1997, and references therein) provide a summary of several Rb-Sr ages for granites of the EDC ranging from ~2.5 to ~2.1 Ga. Emplacement of the Closepet batholith post-dates a number of other 2.55-2.53 Ga granitoids dated by U-Pb zircon (TIMS or thermal evaporation methods: Krogstad et al., 1989; Krogstad et al., 1991; Peucat et al., 1993; see summaries in Jayananda et al., 2000 and Balakrishnan et al., 1999) extending across a region >100 km eastward to the Kolar area. Numerous U-Pb TIMS ages have also been determined for granitoid rocks intrusive to the Ramagiri greenstone belt including 2613±6 Ma (zircon) and 2614±4 Ma (titanite) for a granodiorite, 2528±1 Ma (zircon) and 2516±3 Ma (titanite) for another granodiorite, 2595±1 Ma (titanite) for a quartz diorite, 2510±2 Ma (titanite) for a monzodiorite, and 2468±4 Ma (titanite) for a granitic vein (Balakrishnan et al., 1999). Geochronological investigations of the northernmost reaches of the Closepet batholith and extending ~100 km east, have also revealed a similar history of granitoid plutonism from ~2.58 to 2.53 Ga, in addition to one older ~2.72 Ga date (SHRIMP U-Pb zircon ages of 2719±40 Ma for a gneissose granite intruding the Sandur greenstone belt, 2580±31 Ma for a granodiorite body west of Gooty, 2570±62 Ma for the Joga granite, 2526±8 Ma for the Koppal syenite: Nutman et al., 1996; Chadwick et al., 2000 and references therein). Age constraints for greenstone belts of the EDC are less abundant, but include a U-Pb TIMS zircon age of 2707±18 Ma (Balakrishnan et al., 1999) for felsic pyroclastic rocks from the Ramagiri greenstone belt, a Pb-Pb isochron age of 2746±64 Ma for associated amphibolites (Zachariah et al., 1995), a U-Pb zircon

(SHRIMP) age of 2658 ± 14 Ma for a rhyolite from the Sandur greenstone belt (Nutman et al., 1996), and a U-Pb zircon (SHRIMP) age of 2576 ± 12 Ma for a granodiorite clast within a conglomerate from the Hutti greenstone belt (Vasudev et al., 2000). Less robust age constraints for amphibolites from the Kolar greenstone belt include a Rb-Sr isochron age of 2710 ± 48 Ma (Walker et al., 1989) and a Pb-Pb isochron age of 2732 ± 155 Ma (Balakrishnan et al., 1991). Some lithological and age similarities exist between greenstone belts of the EDC and those of the WDC, but it is not entirely clear whether the belts may be correlated across the two blocks (Chadwick et al., 2000), although some have grouped the Sandur greenstone belt with the Dharwar Supergroup (Radhakrishna and Vaidyanadhan, 1997). Balakrishnan et al. (1999) suggest that overall, the greenstone belts and granitoid rocks of the EDC and WDC could have formed through fundamentally different processes. The “Kolar type” greenstone belts which predominate in the EDC, differ from greenstone belts in the WDC in that they show no clear indication of a basement, comprise predominantly komatiitic to tholeiitic metabasalts and felsic volcanics, with subordinate clastic or chemical sediments, and most of the belts are gold-bearing (Radhakrishna and Vaidyanadhan, 1997; Ramam and Murty, 1997; Balakrishnan et al., 1999). Some of the greenstone belts of the EDC may represent important sutures or terrain boundaries in the Dharwar craton (Krogstad et al., 1995; Balakrishnan et al. 1999). They may have formed as intra-arc basins on the Dharwar batholith in a Late Archean oblique convergent tectonic setting, with coeval greenstone belts of the WDC representing the foreland to this accretionary arc (Chadwick et al., 2000). The effects of high temperature/low pressure metamorphism, NE-SW shortening, and transcurrent sinistral displacements along steep anastomosing

shear zones, appear to have accompanied development of the Dharwar batholith in the Late Archean (Chadwick et al., 2000), but some terrains in the EDC may not have been juxtaposed until as late as 2468 Ma (Balakrishnan et al., 1999).

Proterozoic mafic dyke swarms of the Dharwar craton

Tholeiitic basaltic dykes (and subordinate alkali basaltic dykes) of numerous orientations and relative ages, transect Archean greenstone belts, gneisses, and granites of the Dharwar craton (Fig. 4-2). These Proterozoic mafic dykes are exposed particularly well in the EDC craton as linear topographic ridges, and trains of spheroidally weathering boulders that are readily visible in Landsat imagery (Drury and Holt, 1980; Halls, 1982; Drury, 1984; this study), and many are being quarried as ornamental stone under the trade name of “Black Granite” (Murthy, 1995). On the basis of crosscutting relationships and some of the available geochronological information, a prolific period of mafic dyke swarm emplacement took place in the Dharwar craton during post-Archean, pre-Cuddapah times (Ikramuddin and Stueber, 1976, Drury and Holt, 1980; Drury, 1984; Murty et al., 1987). Mafic dykes transecting the crystalline basement of the EDC truncate along the basal unconformity of the Cuddapah basin, with the exception of at least one mafic dyke (Vijayam, 1968; Murthy, 1987; Murty et al., 1987). Mafic igneous rocks are abundant within the lower stratigraphy of the Cuddapah Supergroup however, comprising an arc-concentric array of mafic to ultramafic sills and basaltic lava flows (Chatterjee and Bhattacharji, 2001; Anand et al., 2003). Geophysical studies indicate that this mafic igneous province appears to be associated with a large (up to 4-5 km thick) lopolithic intrusion in the crust below the basin (Tewari and Rao, 1987; Mishra et al., 1987). The Pulivendla mafic sill, which intrudes the Tadpatri

Formation of the Cuddapah Supergroup, has been dated at 1817 ± 24 Ma (Rb-Sr whole-rock: Bhaskar Rao et al., 1995), 1899 ± 20 Ma ($^{40}\text{Ar}/^{39}\text{Ar}$ phlogopite: Anand et al., 2003), and 1885.4 ± 3.1 Ma (U-Pb baddeleyite: Chapter 3, this thesis), and so the mafic dyke swarms in the EDC which truncate against the Papaghni sub-basin (Fig. 4-2) are older than ~ 1.9 Ga. It was recognized early on, through geological mapping (Smeeth, 1915; GSI, 1981) and remote sensing studies (Drury and Holt, 1980; Halls, 1982; Drury, 1984), that the most prominent mafic dyke swarm in the Dharwar craton is a predominantly E-W trending swarm that extends across a large tract of the craton (the Bangalore dyke swarm). Dykes from this swarm outcrop in the highest density southwest of the Cuddapah basin, and can be traced along strike in a westerly direction from the southern tip of the basin (near Tirupati), some 450 km across the Dharwar craton to the Western Ghats (Smeeth, 1915; Drury, 1984; Murty et al., 1987). This swarm extends at least as far south as the southern margin of the Dharwar craton, near the transition from granite-greenstone to granulite terrane (Ikramuddin and Stueber, 1976; this study). Murthy (1995) indicated that this swarm appears to extend southward from Chittoor into the south Indian granulite terrane, where towards the Cauvery valley it assumes a WNW-ESE strike. Towards the north, the E-W trending Bangalore swarm appears to swing in sympathy with the structural grain of the craton into a NE-SW orientation and may extend as far north as Hyderabad (Halls, 1982) for a maximum estimated across strike width of ~ 500 km. A number of other prominent mafic dyke swarms also occur in the EDC and the dominant orientations of dyke swarms changes from the southern to northern regions of the craton (Halls, 1982; Murty et al., 1987; Murthy, 1995). In the southern half of the EDC, relatively widely spaced mafic dykes of

NW-SE, N-S, and NNE-SSW orientations also occur in addition to the E-W trending Bangalore dyke swarm. In the northern half of the EDC, where the Bangalore swarm appears to assume a NE-SW orientation, prominent N-S, and E-W to ESE-WNW mafic dyke swarms also occur. One great mafic dyke that appears to approach 300m in width in Landsat 7 imagery, outcrops a few kilometres west of the Closepet batholith and runs sub-parallel to it for ~300 km (Fig. 4-2), and this dyke has a K-Ar age of ~1.9 Ga (see reference in Murthy, 1995). Mafic dykes of many orientations outcrop across much of the WDC as well, but the most prominent mafic dyke swarm appears to be a NNW-SSE to NW-SE trending swarm that roughly parallels the structural grain of the WDC and might be correlated with parallel dykes that extend into the southern granulite terrain (GSI, 1981; Murthy, 1987; Gokhale and Waghmare, 1989). Most of the mafic dykes exposed in the Dharwar craton appear to be Proterozoic in age, but one dyke from the Chitradurga greenstone belt yielded a K-Ar age of 76 Ma and might be linked with eruption of the Deccan Flood Basalt Province (Murthy, 1995).

Previous geochronology of Proterozoic mafic dykes of the Dharwar craton

A number of previous radiometric dating studies have been carried out on Proterozoic mafic dykes from the Dharwar craton and have employed a diversity of isotopic systems including K-Ar (Balasubrahmanyam, 1975; Paul et al., 1975; Balakrishna et al., 1979; Dayal and Padmakumari, 1985; Murthy et al., 1987; Padmakumari and Dayal, 1987; Gokhale and Waghmore, 1989; Mallik and Bishul, 1990; Dayal and Padmakumari, 1995; Mallikarjuna Rao et al., 1995; Sarkar and Mallik, 1995; Chatterjee and Bhattacharji, 2001; see additional references in Murthy, 1995), Rb-Sr (Ikramuddin and Stueber, 1976; Sarkar and Mallik, 1995; Pandey et al., 1997; see

additional references in Murthy, 1995), $^{40}\text{Ar}/^{39}\text{Ar}$ (Chatterjee and Bhattacharji, 2001), Pb-Pb (Pandey et al., 1997), and Sm-Nd (Drury, 1984; Zachariah et al., 1995; Pandey et al., 1997), and a summary of these ages is presented in Fig. 4-3. On the basis of this compilation it appears that the most prolific period of mafic dyke swarm emplacement in the Dharwar craton took place in the Mesoproterozoic, between ~ 1.7 and ~ 1.0 Ga (Fig. 4-3).

In the region of the EDC surrounding the western margin of the Cuddapah basin, there is evidence to suggest that the history of mafic dyke swarm emplacement is very complex. On the basis of relative radiometric ages (K-Ar), dyke trends, and crosscutting relationships interpreted from aerial photographs and field observations, these dykes have been subdivided into as many as 18 separate mafic dyke swarms spanning 2068 ± 79 Ma to 656 ± 29 Ma (Murty et al., 1987). A more recent summary of the available geochronological and geochemical data for mafic dykes (30 K-Ar and $^{40}\text{Ar}/^{39}\text{Ar}$ ages) surrounding the Cuddapah basin indicates three major age groupings of 1.9-1.7 Ga, 1.4-1.3 Ga, 1.2-1.0 Ga, with a minor event at 650 Ma (Mallikarjuna Rao et al., 1995). As noted in both of these studies, however, some of the dyke emplacement ages could be older on account of Ar-loss, and so the age complexity may in part be attributed to limitations of the K-Ar system, especially when applied to Precambrian samples. This may also explain why K-Ar and $^{40}\text{Ar}/^{39}\text{Ar}$ dating of multiple parallel mafic dykes from each of the major swarms surrounding the Cuddapah basin (E-W, NW-SE, NE-SE, and N-S) has yielded a range of ages in each case (Mallikarjuna Rao et al., 1995). The accuracy of many of the age determinations for these dyke swarms is also in question because the ages appear to be at odds with the observation that all of the swarms appear

to terminate at the basal unconformity of the Cuddapah basin (i.e. must be older than 1.9 Ga). This discrepancy arises because virtually all of the available geochronological information indicates that these dyke swarms are younger than recent estimates for the timing of early development of the Cuddapah basin of ~1.9 Ga (Anand et al., 2003; Chapter 3, this thesis). Ikramuddin and Stueber (1976) reported an Rb-Sr age of 2420 ± 246 Ma (recalculated at 2370 Ma using a ^{87}Rb decay constant of 1.42×10^{-11} by Dawson and Hargraves, 1994) for seven samples from six mafic dykes from the Harohalli area, three of which are E-W trending Bangalore dykes in addition to N-S, NW-SE, and ENE-WSW trending dykes. The three E-W trending dyke samples from the 2.42 Ga Rb-Sr isochron reported by Ikramuddin and Stueber (1976), when considered exclusively, yield a regression line with a slope that is equivalent to an age of ~2100 Ma (noted by Radhakrishna et al., 1999), and including the original data for a fourth small ENE-WSW trending dyke (BH279) on the isochron yields an age of 2244 ± 432 Ma (Dayal and Padmakumari, 1995). A 20-m-wide E-W trending mafic dyke that transects the Ramagiri greenstone belt of the EDC yielded a composite whole-rock and mineral Sm-Nd isochron age of 2454 ± 100 Ma (Zachariah et al., 1995). Taken together, the available radiometric ages for the timing of emplacement of the Bangalore dyke swarm in the southern EDC range from ~2.5 to ~1.1 Ga (Ikramuddin and Stueber, 1976; Balakrishna et al., 1979; Padmakumari and Dayal, 1987; Murty et al., 1987; Sarkar and Mallik, 1995; Dayal and Padmakumari, 1995; Mallikarjuna Rao et al., 1995; Zachariah et al., 1995), possibly suggesting a long (>1 b.y.) protracted history of emplacement for the swarm. Dolerite dykes trending mainly E-W to NE-SW, which intrude the Closepet batholith north of Tumkur, yielded K-Ar whole-rock ages ranging

from ~2.5 Ga to ~1.3 Ga, and two ages of 2575 ± 226 Ma and 2504 ± 118 Ma suggest that some NE-SW trending dykes could have been emplaced during the final stages of cratonization (Dayal and Padmakumari, 1995).

In a geochronological investigation of tholeiite dykes from the Mahbubnagar area of the EDC, whole-rock and mineral data from four gabbro samples (comprising two samples of a NW-SE trending dyke and two samples of a NE-SW trending dyke) and one dolerite (trending ENE-WSW) including 15 mineral fractions from these samples, yielded a composite Sm-Nd isochron age of 2173 ± 64 Ma, and Sm-Nd mineral and whole-rock data for an E-W trending metapyroxenite yielded a similar isochron age of 2189 ± 123 Ma (Pandey et al., 1997). Murthy (1995) also reports a series of unpublished Rb-Sr and Sm-Nd ages for numerous gabbro, dolerite, and pyroxenite dykes from the Mahbubnagar area ranging from ~2.3 to ~1.5 Ga.

In contrast with the EDC, published radiometric ages for Proterozoic mafic dykes of the WDC are comparatively scarce, and the available K-Ar ages suggest a protracted history of dyke emplacement between ~2.2 to ~1.0 Ga (Murthy, 1995). An ENE-WSW trending dolerite dyke that intrudes granite from a coastal area of the southern WDC has been dated at 2193 ± 45 Ma (K-Ar whole-rock: Balasubrahmanyam, 1975). Three intersecting dolerite dykes from the Gadag greenstone belt yielded K-Ar ages of 1535 ± 61 Ma (335° trend), 1082 ± 54 Ma (E-W trend), and 1018 ± 50 Ma (352° trend) that are consistent with the crosscutting relationships observed in the field (Gokhale and Waghamare, 1989). Additional unpublished ages for mafic dykes of the WDC include a Sm-Nd model age of ~1700 Ma for a dyke in central Karnataka, and 1400-1600 Ma K-Ar ages in addition to whole-rock and mineral Rb-Sr isochron ages of

1986±53 Ma and 1960±50 Ma, for dykes near the Kunigal greenstone belt (Murthy, 1995; Drury, 1984).

DYKE SWARM SAMPLING AND PETROGRAPHY

The Bangalore Dyke Swarm

Harohalli dyke (JEF-99-1): 12° 38.92' N; 77° 29.80' E

An E-W trending gabbro dyke located ~5 km SSE of Harohalli was sampled for U-Pb dating, and is one of the suite of dykes dated by Ikramuddin and Stueber (1976). This dyke has also been the subject of a number of subsequent paleomagnetic studies (Prasad et al., 1999; Dawson and Hargraves, 1994; Radhakrishna et al., 2003). At the sampling site (Fig. 4-4), the dyke is exposed as a modest (~10-m-high) ridge of solid bedrock and the dyke has an estimated width of ~95 m. In hand specimen the sample has distinctive poikilitic plagioclase crystals ranging up to 4 cm in length that locally show feldspar clouding (c.f. Halls and Zhang, 1995). These crystals comprise ~60% of the rock, show slight sericitization, and envelop individual grains and aggregates of subhedral to euhedral clinopyroxene (comprising ~35% of the mode), subordinate orthopyroxene and opaques (3%). Clinopyroxene shows minor alteration to hornblende, chlorite and sericite. Late-stage interstitial minerals include biotite, alkali feldspar granophyre, and up ~120 µm long, skeletal to euhedral baddeleyite blades.

Penukonda dyke (JEF-99-6): 14° 08.06' N; 77° 36.03' E

At the sampling site ~5 km north of Penukonda, this dyke trends E-W and forms a prominent ~130-m-high ridge that was observed in the field to extend along strike for several kilometres in both directions (Figs. 4-5b and 4-5c). The dyke is traceable in Landsat 7 imagery (Figs. 4-6 and 4-7) and previously published maps (Fig. 4-2) semi-

continuously in an easterly direction along strike for ~80 km where it abuts the Cuddapah basin (e.g. Balakrishna et al., 1979; Murty et al., 1987; Padmakumari and Dayal, 1987). The dyke is at least 50 m wide and comprises a medium grained dolerite with up to ~0.5 cm long plagioclase laths. Overall, the sample is a relatively fresh dolerite showing an intergranular texture, and the modal mineralogy comprises ~50% plagioclase, ~20% clinopyroxene, ~20% orthopyroxene, and interstitial quartz/K-feldspar granophyre associated with trace biotite, opaques (including ilmenite), apatite, baddeleyite, and zirconolite. Orthopyroxene forms rare large phenocrysts (up to 6mm long) and shows distinctive pink to pale green pleochroism. Plagioclase shows oscillatory zoning and polysynthetic twinning, and in addition to the mafic minerals is variably saussuritized (~20% overall). Where juxtaposed with late stage assemblages, the mafic minerals are locally altered to an assemblage of hornblende ± chlorite ± disseminated opaques ± prehnite (which shows a radial “hourglass” pattern and is associated with biotite). This alteration assemblage is interpreted to be the result of alteration by magmatic fluids in the last stages of crystallization of the dyke.

Chennekottapalle dyke (JEF-99-7): 14° 15.06' N; 77° 37.33' E

Approximately 12 km north of the Penukonda dyke and ~2 km south of the settlement of Chennekottapalle, an E-W trending gabbro dyke forms a prominent ~150-m-high ridge (Fig. 4-5a) and was sampled for U-Pb dating. This ~50-m-wide dyke is part of a ~4.5 km wide, highly dense array of up to 6 E-W trending dykes, all of which form prominent, semi-continuous, anastomosing ridges that are clearly visible in Landsat 7 imagery (Figs. 4-6 and 4-7) and 1:50 000 scale topographic maps. Assuming a width of 50 m per dyke, this indicates that, at least locally, crustal extension associated with

emplacement of the E-W trending Bangalore dyke swarm approached 7%. Many mafic dykes from this dense array extend westward from the sampling site and crosscut the Ramagiri greenstone belt (Fig. 4-7), and towards the east outcrop substantially more discontinuously, but can be traced as far as the Cuddapah basin which truncates the dykes (Kumar and Bhall, 1983; Balakrishna et al., 1979; Murty et al., 1987). Sample JEF-99-7 has a somewhat similar appearance in hand specimen to the Harohalli dyke (JEF-99-1), with distinctive poikilitic plagioclase crystals ranging up to 2 cm long. These crystals comprise ~40 modal %, are almost entirely saussuritized and enclose individual grains and aggregates of subhedral to euhedral clinopyroxenes (which range up to 6mm long euhedral crystals and comprise ~50 modal %), with subordinate orthopyroxene and trace opaques. Clinopyroxene shows weak oscillatory zoning, and overall the mafic minerals have been ~30% altered to chlorite ± fine grained disseminated opaques. Interstitial minerals include plagioclase, and late biotite, quartz/alkali feldspar granophyre, highly elongate apatite needles, baddeleyite, and monazite (in quartz and spatially associated with apatite). In association with late-crystallizing interstitial pockets, clinopyroxene is mantled by retrograde hornblende.

NW-SE trending dyke swarm, south-eastern Dharwar craton

Somala dyke (JEF-99-11): 13° 29.29' N; 78° 49.86' E

A ~30-m-wide dolerite dyke trending ~150° was sampled for U-Pb dating approximately 2 km northeast of Somala (Fig. 4-2). At the sampling site, this dyke can be seen to outcrop for a few kilometres along strike in both directions. The Somala dyke appears to be part of a prominent NW-SE trending dyke swarm which extends from the southern tip of the Cuddapah basin and spans a large region west and southwest of the

basin (Fig. 4-2). The rock shows a variety of igneous textures in thin section including ophitic texture whereby large (up to ~5mm) euhedral to subhedral orthopyroxene grains are surrounded by relatively smaller plagioclase laths showing intersertal texture and which are poikilitic, containing small (<2mm) clinopyroxene and orthopyroxene grains. Clinopyroxene commonly occurs as clusters of small (<2 mm) intergrown subhedral grains. The modal mineralogy is dominated by plagioclase (~35% modal), orthopyroxene (~35% modal), and clinopyroxene (~25% modal). Accessory minerals include opaques (~2% modal), and trace biotite, quartz, and baddeleyite. Orthopyroxene and clinopyroxene are rarely mantled by biotite in association with late quartz. Plagioclase is mostly fresh, with ~5% alteration to chlorite or saussurite. Overall, the mafic minerals are ~10% altered to chlorite, saussurite, disseminated opaques, muscovite, and rarely biotite, and commonly along grain boundaries, cleavage traces and fractures. Some of the smaller mafic minerals have been completely altered, with a core comprising disseminated opaques, sausserite ± muscovite, that is rimmed by a halo of fine-grained chlorite.

N-S trending dyke swarm, south-eastern Dharwar craton

Kandlamadugu dyke (JEF-00-55): 13° 40.20' N; 78° 25.78' E

A ~20-m-wide medium grained (up to ~5mm long plagioclase laths) dolerite dyke striking ~165° (at the sampling site), was sampled at Kandlamadugu, about 15 km northwest of Madanapalle, and was observed in the field to outcrop along strike for a minimum of several hundred meters. The rock contains predominantly plagioclase (~55% modal %) and clinopyroxene (~40 modal %) and exhibits a sub-ophitic texture. Overall these two minerals are ~15% altered/saussuritized. Fresh plagioclase commonly

contains fractures that have abundant, randomly oriented, blue-green to pale brown pleochroic needles of amphibole, which penetrate into the fresh plagioclase. Clinopyroxene crystals are commonly twinned, and tend to be rimmed and/or altered along cleavage traces and fractures by hornblende \pm disseminated opaques \pm chlorite \pm prehnite \pm saussurite. Accessory minerals include opaques (~3 modal%), in addition to late crystallizing apatite, quartz, and up to 60 μ m long baddeleyite blades.

E-W trending dyke swarm, north-eastern Dharwar craton

Bandepalem dyke (JEF-00-43): 17° 08.63' N; 79° 27.50' E

Sample JEF-00-43 was collected from the Bandepalem quarry near Inpamla in the district of Nalgonda, Andhra Pradesh (Fig. 4-8). This E-W trending dyke is a ~40-m-wide gabbro which outcrops for approximately 500 meters at the sampling site, but may be traced discontinuously along strike for approximately 180 km in satellite imagery, 1:50000 topographic map sheets, and geological maps (Figs. 4-2 and 4-8). The sample shows ophitic texture in thin section, and the primary igneous minerals consist of plagioclase (~65 modal %), clinopyroxene (~35 modal %), and minor opaques (~5 modal %). In hand sample there is some evidence for a weak porphyritic texture with occasional plagioclase phenocrysts up to 1 cm long. Plagioclase is ~25% saussuritized and clinopyroxene has been ~75% replaced by an assemblage of hornblende \pm chlorite \pm sericite \pm disseminated opaques. Late crystallizing accessory minerals include biotite, quartz, apatite, skeletal zircon, and rare baddeleyite. Grain boundaries and fractures in fresh plagioclase crystals are lined with randomly oriented needles of hornblende showing deccusate texture, which penetrate the fresh plagioclase, and are associated with subordinate prehnite.

NW-SE trending swarm, Western Dharwar craton

Dandeli dyke (JEF-00-1): 15° 19.49' N; 74° 36.06' E

The Dandeli dyke is situated within the northwestern reaches of the Shimoga supracrustal belt in the WDC, and was collected approximately 7 km N of Dandeli (Fig. 4-9) at a river-side exposure along the Barchi N subsidiary arm of the Kali-Nadi river. This mafic dyke has a minimum thickness of ~12 m and outcrops along a ~120° bearing for more than 100 m, and comprises a gabbro with plagioclase laths up to ~8 mm long. Petrographically the rock shows sub-ophitic texture, and is comprised predominantly of plagioclase (~55 modal %) and hornblende (~30 modal %), with minor quartz and opaques. Plagioclase is >95% saussuritized, and only minor relict clinopyroxene (~10 modal %) is present and is mantled by hornblende ± chlorite ± disseminated opaques. Late crystallizing accessory minerals include quartz, biotite, apatite, zircon, and baddeleyite. Very rare, minor (<5 µm across), isolated regions of zircon overgrowth were observed along grain boundaries of one baddeleyite blade in thin section.

GEOCHEMICAL CLASSIFICATION OF DHARWAR MAFIC DYKES

A representative portion of each sample dated by U-Pb in this study was also selected for whole-rock geochemical analysis, and only fresh rock fragments devoid of any visible signs of weathering were included in these aliquots. Samples were crushed using a jaw crusher equipped with hardened steel plates and pulverized with a tungsten carbide puck mill at the University of Alberta Radiogenic Isotope Facility. These rock powders were sent to Activation Laboratories Ltd. (Ancaster, ON, Canada) and analysed by ICP-MS methods in accordance with their code 4LithoResearch package for major, trace and Rare Earth Element (REE) compositions. These data are presented in Table 4-

1. Geochronology sampling involved collecting 15-25 kg of material from multiple sites across the central portion of the dykes, and so the whole-rock geochemical data presented here are interpreted to approximate the composition of the evolved centres of the dykes and not necessarily that of the originally injected magma.

Major-element data for the seven Dharwar mafic dykes are plotted in Fig. 4-10, on a total-alkalis versus silica (TAS) diagram (Le Maitre, 2002), a ternary (Na₂O+K₂O)-(FeO+0.8998Fe₂O₃)-MgO (AFM) diagram (Irvine and Baragar, 1971), and the CIPW normative mineralogy of the dykes is plotted on the basalt tetrahedron (Yoder and Tilley, 1962). Also shown for reference is a suite of data for numerous Paleoproterozoic mafic dykes from the EDC around the Cuddapah basin (Mallikarjuna Rao et al., 1995), and the TAS fields for the major Paleoproterozoic mafic dyke swarms of the Slave craton (Wilkinson et al., 2001). The data for six dykes in this study plot within the subalkali series of igneous rocks on the TAS diagram, and suitably none of these samples are nepheline normative (Figs. 4-10a and 4-10c). The Somala dyke (JEF-99-11) has a very high MgO content (15.51 wt%) and is classified as a picrite based on the criteria outlined in Le Maitre (2002), and so the data for this sample are not shown on the TAS diagram. Samples from the Bangalore dyke swarm (JEF-99-1; JEF-99-6 and JEF-99-7) plot within the basaltic andesite field, whereas the remaining three samples plot as subalkali basalts. The three Bangalore dykes nearly classify as boninites because of their relatively high MgO (>8 wt%) and SiO₂ (>52 wt%) contents, but they do not meet the criterion that TiO₂ is less than 0.5 wt% (Le Maitre, 2002). The data for all seven dykes (Fig. 4-10b) plots along the tholeiitic differentiation trend (Irvine and Baragar, 1971), and all samples are quartz normative with the exception of sample JEF-

99-11, which is olivine normative (Fig. 4-10c).

Trace-element data for the seven Dharwar dykes in this study are shown in Fig. 4-11 on a Mid Ocean Ridge Basalt (MORB)-normalized (Pearce, 1982) trace element spider diagram, and a chondrite-normalized REE diagram (Nakamura, 1974). Also shown for reference are the average compositions of a number of major Paleoproterozoic mafic dyke swarms of the Slave craton (Wilkinson et al., 2001). All Dharwar samples show a distinctive negative Nb anomaly, which is interpreted to be an indication of crustal contamination (Saunders et al., 1992). Five of these samples show a very small negative Eu anomaly, which may be indicative of plagioclase fractionation before dyke emplacement. Two mafic dykes (JEF-00-1 and JEF-00-43) can clearly be distinguished from the others by their trace element geochemistry in that relative to the other samples they show the flattest REE patterns ($La/Yb=1.9-2.3$), the highest total REE concentrations, and some of the other trace elements are also relatively high. Cr concentrations are distinctively low for these two samples (22-64 ppm), but this is also the case for sample JEF-00-55 (48 ppm). In contrast, Cr is exceptionally high for sample JEF-99-11 (1220 ppm), and the range in Cr concentrations for the three dykes from the Bangalore dyke swarm is also distinctive from the other samples (469-599 ppm). Ni concentrations show similar sample-to-sample characteristics as Cr, in that samples JEF-00-1, JEF-00-43, and JEF-00-55 show the lowest range (38-47 ppm), JEF-99-11 yielded the highest value (298 ppm), and the three Bangalore dykes yield a distinctive cluster (120-137 ppm). The two poikilitic gabbro samples from the Bangalore dyke swarm (JEF-99-1 and JEF-99-7) have very similar trace-element signatures, which are also distinct from all other samples in that they show by far the

highest enrichment in LREE (La/Yb=10.1-10.3). In comparison, the dolerite sample from this swarm (JEF-99-6) has slightly lower trace element abundances and a flatter REE pattern (La/Yb=4.0).

MINERAL SEPARATION AND ANALYTICAL TECHNIQUES

Mineral separation and isotopic analysis of all samples was carried out in the Radiogenic Isotope Facility, in the Department of Earth and Atmospheric Sciences at the University of Alberta. Isolating baddeleyite and zircon crystals for U-Pb dating involved conventional mineral separation techniques, in addition to the recently developed water-based baddeleyite separation technique (Söderlund and Johansson, 2002). During mineral separation, the most stringent cleaning procedures were employed during each step to prevent cross-contamination between samples. All baddeleyite and zircon fractions to be analysed by IDTIMS were hand picked from filtered ethanol using a binocular microscope, and custom-built pipettes made of Tygon and Teflon.

Conventional mineral separation

All samples that underwent conventional baddeleyite/zircon mineral separation techniques (i.e. JEF-99-1, JEF-99-7, JEF-99-11, JEF-00-1, JEF-00-43, and JEF-00-55) were pulverized with a jaw crusher and disk mill equipped with hardened steel plates, and comprised between 10 and 15kg of rock. These powders were then passed over a Wilfley Table at a rate of ~3 kg/hour and reduced to a relatively small amount (typically 100-200 g) of heavy mineral concentrate, which was sized with a 70 mesh disposable nylon sieve. Material reporting to the lower specific gravity (light) sample-split at the end of the Wilfley Table, and the predominantly clay and silt fraction that exited along

the long edge of the table were also collected, rinsed with ethanol, and dried down separately for later processing if necessary. The heavy concentrate was passed in front of a large magnet, in order to remove the most magnetic minerals, in addition to fragments of steel originating from the disk mill. A series of magnetic separations was then carried out with a Frantz Isodynamic Separator using a 15° side-tilt and a current ranging up to ~0.8A. This initial series of magnetic separations typically involved a ~25% reduction in sample size at each step, and involved approximately 10-12 passes. Density separation with heavy liquid (Methylene Iodide) was used to remove minerals with a specific gravity of $\leq 3.3 \text{ g/cm}^3$ from the least magnetic fraction, and this involved a minimum of five agitation periods. At this point the heavy mineral concentrate which typically consisted of a few grams of material, then underwent a second sequence of magnetic separations with the Frantz Isodynamic Separator employing a 15° side-tilt and a current ranging from 1.0A up to 1.8A, followed by progressive reductions in side-tilt down to 5°. The least magnetic fractions typically contained the most pristine baddeleyite and zircon blades, but both minerals occur in more magnetic side cuts as far back as 0.8A.

Water-based baddeleyite mineral separation

The water-based mineral separation technique can be used to isolate miniscule baddeleyite grains efficiently (Söderlund and Johansson, 2002; Söderlund et al., 2004), and some of the samples in the current study were processed using this water-based technique. In three cases (samples JEF-99-7, JEF-99-11, and JEF-00-55), conventional mineral separation yielded no baddeleyite or zircon (except for a few ostensibly xenocrystic zircons), and so for these samples the water-based technique was

subsequently used in further attempts to recover baddeleyite. During these second attempts at baddeleyite recovery, the material re-processed comprised the clay and silt fractions that were saved from the original Wilfley table side-cuts, and the amount of material reprocessed in each case was ~0.5 kg. One additional sample was also processed with the water-based technique (JEF-99-6), but the crushing strategy was slightly different in this case. The baddeleyite crystals examined in thin section were all less than 25 μ m in the longest dimension, so after crushing with a jaw crusher, the sample was pulverized in a shatter-box (puck mill) to achieve a smaller average grain size and to ensure liberation of as many baddeleyite grains as possible. To further push the limits of the water-based baddeleyite separation technique, only a very small quantity (42 grams) of sample JEF-99-6 was processed. To minimize the effects of overloading the water medium with sediment and consequently allow the grains to separate more efficiently, only ~5-10 g of material was loaded onto the Wilfley Table for any given run, and this was further minimized for sample JEF-99-6 at ~2-3g per run. Employment of the water-based technique in this study has yielded excellent results, and essentially more than doubled the number of mafic dyke samples that are amenable to U-Pb isotopic dating by U-Pb IDTIMS. As suggested by Söderlund and Johansson (2002), the technique has proven to be well suited for isolating exceptionally tiny (<25 μ m) baddeleyite from mafic dykes. In three cases where conventional baddeleyite mineral separation failed to yield baddeleyite (samples JEF-99-7, JEF-99-11, and JEF-00-55), the water-based method was successful. The baddeleyite grains recovered by the water-based technique are generally much smaller than those recovered by conventional mineral separation (Fig. 4-12), and baddeleyite grains down to the ~15 μ m

grain size were recovered (Fig. 4-12 j and k).

U-Pb IDTIMS Analysis

Analytical procedures for U-Pb IDTIMS analysis followed closely those outlined in Chapter 3. Isotopic ratios were measured using a VG354 mass spectrometer, data processing (Table 4-2) was done using an in-house program, and the final age calculations were carried out using the Isoplot/Ex3 program (Ludwig, 2003).

RESULTS

The U-Pb IDTIMS data for baddeleyite and zircon for seven mafic dyke samples from the Dharwar craton is summarized in Table 4-2, and shown on concordia diagrams in Figs. 4-13, 4-14, 4-16, 4-17, 4-18, and 4-20.

Harohalli dyke (JEF-99-1)

For sample JEF-99-1, conventional mineral separation yielded a substantial population (~150 grains) of brown, commonly striated, euhedral blades and fragments of baddeleyite ranging up to ~150 μm in length (Fig. 4-12b) and devoid of zircon overgrowth. These baddeleyite crystals have exceptionally high U concentrations for baddeleyite, ranging up to 5000 ppm (Table 4-2), but typical model Th/U ratios ranging from 0.014 to 0.028. The U-Pb data for six fractions of JEF-99-1 baddeleyite are shown in Table 4-2 and on a concordia diagram in Fig. 4-13. In attempts to isolate the most concordant systems for U-Pb analysis, an air abrasion technique (Krogh, 1982) was carried out on two of the baddeleyite fractions (#5 and #6). Most of the analyses plot on or close to concordia, but one fraction (#2) is ~20% discordant. The two abraded fractions plot slightly above concordia and are -0.35% and -1.12% discordant. Reversely discordant baddeleyite analyses from mafic dykes are rare and may arise if the

sample has not achieved equilibration with the spike, or if the sample was susceptible to open system behaviour involving preferential loss of U (Halls and Davis, 2004). In the present study (analyses #5 and #6), non-equilibration between spike and sample arising from incomplete dissolution of the baddeleyite crystals seems unlikely, because the samples were dissolved under the same conditions (in the same carousel at the same time) as fractions #18 and #19 from sample JEF-00-1 which comprised substantially larger abraded baddeleyite crystals that plot on or slightly below concordia (Fig. 4-16a). From the present dataset (Fig. 4-13) the most logical time for U-loss seems to be during recent times. The analyses are not all co-linear, and the $^{207}\text{Pb}/^{206}\text{Pb}$ ages for the four least discordant analyses (i.e. 1.18% to -1.12%) span approximately 10 m.y. from 2372.2±0.8 Ma (#6; 2 σ error) down to 2361.6±2.2 Ma (#1; 2 σ error). Four out of six baddeleyite analyses have $^{207}\text{Pb}/^{206}\text{Pb}$ ages (analyses #2-5) that overlap within 2 σ experimental error and yield a weighted mean $^{207}\text{Pb}/^{206}\text{Pb}$ age of 2365.0±1.7 Ma (MSWD=1.5). Linear regression treatment of these four analyses (#2-5) yields a similar upper intercept age of 2365.4±1.0 Ma (MSWD=0.38; 69% probability of fit), and we interpret this to represent the most accurate estimate for the crystallization age of baddeleyite and the age of emplacement of the Harohalli dyke. The lower intercept age from this regression of 20±21 Ma, suggests that some of the analysed baddeleyite grains were variably affected by Pb-loss during recent weathering, and this could have accompanied U loss for analyses #5 and #6. An alternative linear regression was also considered (shown as a dashed line on Fig. 4-13), and was constructed to pass through analyses #3, #4 and #6, and this yields a significantly older upper intercept age of 2369.3±1.5 Ma (MSWD=1.5; probability of fit = 23%), and a lower intercept date of

1007±210 Ma. Although the error ellipse for analysis #4 plots on concordia and was included in the first regression (through #2-5), it also overlaps significantly with the second regression line, and so even the most concordant analysis seems to support both interpretations. This means, however, that for the second regression the upper-intercept age is significantly older mostly because of a single data-point (#6), which happens to be the most precise analysis. The negative discordance of that analysis is problematic because increasing negative discordance will bias towards younger upper-intercept ages in such a regression. The agreement between 4 out of 6 $^{207}\text{Pb}/^{206}\text{Pb}$ ages within 2σ experimental error (including one concordant analysis), coupled with the relatively low MSWD of 0.38 and high probability of fit 69% for linear regression of these analyses (#2-5), is the basis for our interpretation that the upper intercept age of 2365.4±1.0 Ma is accurate and that the $^{207}\text{Pb}/^{206}\text{Pb}$ age of 2372.2±0.8 Ma for analysis #6 is anomalously old. Development of a ^{206}Pb deficiency owing to ^{222}Rn diffusion out of baddeleyite can lead to anomalously old $^{207}\text{Pb}/^{206}\text{Pb}$ ages and this may be enhanced by alpha-recoil and leaching effects (Davis and Sutcliffe, 1985; Heaman and LeCheminant, 2000; Halls and Davis, 2004). For analysis #6, alpha-recoil and leaching effects can be effectively ruled out because the baddeleyite crystals were abraded, but unequivocally constraining a potential role of ^{222}Rn diffusion (escape) in the history of the baddeleyite is difficult. Another plausible explanation is that incorporation of ^{231}Pa into baddeleyite during crystallization could have lead to an excess of ^{207}Pb in the crystal resulting in an anomalously old $^{207}\text{Pb}/^{206}\text{Pb}$ age for analysis #6 (Heaman and LeCheminant, 2000; Halls and Davis, 2004). Alternatively, fraction #6 might have contained baddeleyite of xenocrystic origin that was incorporated into the magma during ascent of the dyke

through previously crystallized (under-plated) mafic rocks encountered at depth (Halls and Davis, 2004).

Chennekottapalle dyke (JEF-99-7)

Conventional mineral separation carried out on a ~10 kg sample of JEF-99-7 yielded no baddeleyite or zircon crystals, except for a few ostensibly xenocrystic zircons. In a second attempt that was targeted at baddeleyite mineral separation, a ~0.5 kg sample of the clay/silt fraction recovered from the original Wilfley Table runs was reprocessed using the water-based method of baddeleyite mineral separation. This second attempt yielded a large population of baddeleyite crystals (>300), comprising euhedral blades or fragments of blades ranging from ~15 μ m to ~70 μ m in their longest dimension and averaging ~5 μ m thick (Figs. 4-12d and 4-12h to 4-12j). Recovery of a substantially large number of baddeleyite crystals originating from the clay/silt fraction of the conventional Wilfley Table split provides unequivocal evidence that many small grains of baddeleyite are lost during conventional use of the Wilfley Table. The loss of tiny baddeleyite crystals is likely a result of their lower settling velocity compared to large grains, and this is coupled with the fact that during conventional use of the Wilfley Table the water medium is continually being overloaded with sediment. The baddeleyite crystals are tan brown to light tan brown in colour, striated, and have no visible signs of zircon alteration by binocular microscope.

The U-Pb IDTIMS analyses for three fractions of baddeleyite from sample JEF-99-7 are shown on a concordia diagram in Fig. 4-14a. Two of the analyses plot close to concordia (1.12-1.17% discordant) and a third fraction is significantly more discordant (5.73%). Linear regression treatment of the data yields a well-defined upper intercept

date of 2368.6 ± 1.3 Ma (MSWD=1.8; probability of fit = 18%), which is interpreted as a reliable estimate for the timing of crystallization of the Chennekottapalle dyke. The lower intercept date of 129 ± 180 Ma from this regression line suggests that Pb-loss was apparently from recent weathering.

Penukonda dyke (JEF-99-6)

Water-based mineral separation carried out on the 42 g shatter-box powder from sample JEF-99-6 yielded a substantial population of tiny baddeleyite crystals (>100). Owing to the small sample size and efficiency of the water-based method, the total amount of processing time from crushing the rock to picking the baddeleyite crystals for U-Pb analysis was less than 10 hours. Despite the substantial number of isolated grains the baddeleyite crystals are exceptionally tiny, with an average grain size of ~25 μm and ranging between ~10 μm to ~40 μm long (Figs. 4-12f and 4-12k). These crystals are light tan brown to tan brown in colour, weakly striated, and show no evidence of fracturing or alteration to zircon that is visible with a binocular microscope. The U-Pb results for three baddeleyite fractions are shown in Table 4-2 and on a concordia diagram in Fig. 4-14b. All three fractions plot on or close to the concordia curve, ranging between -0.24 to 0.67% discordant. Similar to the results for sample JEF-99-7, the relative sizes of error ellipses correlate well with the total number of grains included in each fraction. Two out of three analyses yield nearly identical $^{207}\text{Pb}/^{206}\text{Pb}$ ages of 2366.3 ± 1.8 Ma (#7; 2σ error) and 2364.8 ± 2.8 Ma (#9; 2σ error), and one of these analyses (#9) plots on concordia. Analysis #8 however, yields a significantly older $^{207}\text{Pb}/^{206}\text{Pb}$ age of 2380.3 ± 3.6 Ma (2σ). On the basis that analysis #9 is concordant and yields a similar $^{207}\text{Pb}/^{206}\text{Pb}$ age as analysis #7, we interpret the weighted mean $^{207}\text{Pb}/^{206}\text{Pb}$ age of those

two analyses of 2365.9 ± 1.5 Ma (MSWD=0.81; probability of fit = 37%) to represent the most accurate estimate for the crystallization age of baddeleyite and the timing of emplacement of the Penukonda dyke. The range of possible explanations for the apparently anomalously old $^{207}\text{Pb}/^{206}\text{Pb}$ age for analysis #8 are similar to that discussed for analysis #6 from sample JEF-99-1.

Dandeli dyke (JEF-00-1)

Conventional mineral separation carried out on sample JEF-00-1 yielded a substantial population of baddeleyite grains (~150) and a modest population of zircon grains (~50). The baddeleyite grains from that sample are relatively large, ranging up to ~300 μm long. These baddeleyite crystals are brown to tan brown in colour, commonly striated, and show a slightly thicker profile along the central portion of the grain resulting in a darker colour along the central axis (Fig. 4-12a). Very minor zircon overgrowth was visible on some of the baddeleyite grains by binocular microscope, and this was confirmed in an electron microprobe study. Zircons recovered from sample JEF-00-1 are typically elongate subhedral to euhedral fragments up to ~250 μm in length, and range from colourless to slight pink or yellow-pink in colour (Fig. 4-15d). These crystals are inclusion free and show no turbidity, and minimal signs of internal fracturing. Zircon was most abundant in the 1.4A magnetic fraction, and the zircons analysed from fractions #13 and #17 were picked from this population. Such high magnetic susceptibility may be a reflection of the high trace-element content typical for late-crystallizing zircon in mafic rocks (Heaman et al., 1990), and is consistent with the high U and model Th concentrations reported for JEF-00-1 zircon (Table 4-2). Some zircons show striations and the coloured variety has a slightly bladed habit. Colourless

zircon show pyramidal terminations and a prismatic habit in some cases. The model Th/U ratios for JEF-00-1 zircon are similar (0.775 and 0.821) and comparable with values reported for igneous zircon crystallizing from a mafic magma (Heaman et al., 1990). The U-Pb results for five baddeleyite fractions and two zircon fractions from JEF-00-1 are shown in Table 4-2 and on concordia diagrams in Fig. 4-16. Two baddeleyite fractions (#18 and #19) were given an air abrasion treatment (Krogh, 1982) in order to remove zircon alteration and the outer rims of the grains, and these plotted on or slightly below concordia. In general the two abraded fractions yield more concordant results than the other fractions, but one analysis (#15), which comprised three of the most pristine looking blades of unabraded baddeleyite, also yields a concordant result. A regression of all five baddeleyite analyses yields an upper concordia intercept age of 2180.3 ± 2.3 Ma (MSWD=3.1; probability of fit = 3%). Although analysis #15 also gave a concordant result, the $^{207}\text{Pb}/^{206}\text{Pb}$ age of 2177.8 ± 2.0 Ma (2σ) for that analysis is slightly younger than the $^{207}\text{Pb}/^{206}\text{Pb}$ age for fraction #19 of 2180.8 ± 1.2 Ma (2σ). The latter is interpreted to be more accurate because the baddeleyite from that fraction was abraded. The linear regression shown in Fig. 4-16a is therefore constructed to pass through four fractions (#'s 14, 15, 16, and 19) and yields a more precise upper intercept age of 2180.8 ± 0.9 Ma (MSWD=0.55; probability of fit = 58%), which we interpret to represent the baddeleyite crystallization age and timing of emplacement of the Dandeli dyke. The lower intercept age from that regression of 291 ± 51 Ma may or may not be geologically meaningless. The zircon fractions from sample JEF-00-1 are highly discordant (36-44%), and together with baddeleyite fraction #19 plot along a discordia line, and linear regression of these three analyses (Fig. 4-16b) defines a lower intercept

age of 535.6 ± 4.1 Ma (MSWD=0.69). This lower intercept age is consistent with variable U-Pb isotopic resetting of zircon associated with a Pan-African thermal event that is widespread in south India (Miller et al, 1996).

Bandepalem dyke (JEF-00-43)

A relatively modest amount of zircon (~50 grains) and baddeleyite (7 grains) was recovered from sample JEF-00-43 by conventional mineral separation, and owing to the small amount of recovered material, all of these grains were picked from the Methyl Iodide heavy concentrate and did not undergo a final magnetic separation with a Frantz Isodynamic Separator. In all, three distinctive populations of zircon were identified including: 1) elongate (up to ~200 μm long), anhedral to subhedral, colourless to very light pink, striated, skeletal, commonly blade-like fragments that are devoid of inclusions and turbidity, but contain visible internal fracturing and minor evidence for Fe-staining (Fig. 4-15a); 2) pristine, very prismatic and elongate (dimensions of 1:1:4 and up to ~230 μm long), colourless, non-striated crystals devoid of inclusions, fractures or turbidity, showing flat to curvilinear non-pyramidal terminations (Fig. 4-15b); 3) very anhedral, colourless fragments showing turbidity, ranging up to ~150 μm long (Fig. 4-15c). U concentrations in the zircons ranged from 160 to 402 ppm, and the model Th/U ratios were generally >1 (Table 4-2), which is typical for zircon crystallizing from a mafic magma (Heaman et al, 1990). Baddeleyite grains from JEF-00-43 are tan brown in colour, weakly striated subhedral to euhedral blades, and some grains showed evidence of internal fracturing and minor zircon alteration (Fig. 4-12c). These crystals had relatively low U contents (78-123 ppm) and somewhat high model Th/U (0.216-0.249) for typical baddeleyite (i.e. <0.1). U-Pb data for four zircon fractions and two

baddeleyite fractions is shown in Table 4-2 and on a concordia diagram in Fig. 4-17. The data for all four zircon fractions are discordant (5.9 to 35.6%) and the data are not colinear. The most concordant zircon fraction (#23) yields a $^{207}\text{Pb}/^{206}\text{Pb}$ age of 2177.3 ± 1.6 Ma (2σ). On account of the low U concentrations and the limited amount of total grains the two baddeleyite fractions yielded relatively imprecise data. One baddeleyite analysis (#21) overlaps within error of concordia and yields a $^{207}\text{Pb}/^{206}\text{Pb}$ age of 2170.5 ± 13 Ma (2σ), which is similar to the $^{207}\text{Pb}/^{206}\text{Pb}$ age of zircon analysis #23 of 2177.3 ± 1.6 Ma (2σ). Linear regression treatment of the data does not yield a unique solution, and two four-point linear regressions are presented. The first regression is constructed to pass through the baddeleyite data in addition to the data for two zircon fractions (#20 and #25), and yields an upper intercept age of 2169.4 ± 3.0 (MSWD=0.72; probability of fit = 49%), which could be taken to represent the emplacement age of the dyke. This regression is shown as a dashed line on Fig. 4-17 and yields a lower intercept age of 426 ± 11 Ma. A second regression is constructed to pass through the baddeleyite data in addition to the data for two zircon fractions (#20 and #22), and yields an upper intercept age of 2176.5 ± 3.7 Ma (MSWD=0.86; probability of fit = 42%), which we interpret to represent the most accurate estimate for the emplacement age of the dyke. This regression is shown as a solid line on Fig. 4-17 and yields a lower intercept age of 485 ± 14 Ma. It is clear from the data that a complex record of Pb-loss is present in these zircons. The error ellipse for zircon fraction #23 overlaps with a reference chord passing through 2176.5 Ma and the origin, which is consistent with crystallization at ca. 2176.5 Ma followed by partial Pb-loss during recent weathering. The lower intercept ages from both linear regressions are an indication that some older Pb-loss event also affected

some of these grains, and the oldest lower intercept age of 485 ± 14 Ma suggests that this may have occurred at least as early as latest Pan-African times. The first regression (dashed line) yields a significantly younger lower intercept date, which is probably geologically meaningless and a reflection of multiple Pb-loss events. This apparently complex Pb-loss history is the main basis for the interpretation that the first regression may be slightly inaccurate, because some grains (i.e. fraction #25) may have been more prone to younger Pb-loss and bias the upper intercept towards a younger age.

Somala dyke (JEF-99-11)

Conventional mineral separation carried out on sample JEF-99-11 yielded no primary baddeleyite or zircon crystals, but a modest population of small baddeleyite blades (55) was recovered by water-based mineral separation of the saved Wilfley Table clay/silt split. These baddeleyite crystals are tan brown, striated, euhedral blades and fragments showing no signs of zircon alteration observable under binocular microscope (Fig. 4-12g). The U-Pb data for three baddeleyite fractions from JEF-99-11 is shown in Table 4-2 and presented on a concordia diagram in Fig. 4-18a. Th/U ratios of the analysed grains range between 0.140 and 0.233 and are slightly higher than typical values reported for baddeleyite (<0.1 ; Heaman and LeCheminant, 1993). Two analyses plot on or close to concordia (#27 and #28) but a third analysis (#26) is 15.68% discordant, and the three analyses are not colinear. The concordant analysis yields a concordia age of 2209.3 ± 2.8 Ma (2σ ; MSWD=1.4), which we interpret to represent the most reasonable estimate for the crystallization age of baddeleyite and the age of emplacement of the Somala dyke.

Kandlamadugu dyke (JEF-00-55)

Similar to many other samples in this study, conventional mineral separation yielded no baddeleyite or zircon from sample JEF-00-55, but water-based baddeleyite mineral separation yielded a significant number of baddeleyite grains (~50). These baddeleyite crystals are elongate, tan brown euhedral blades and fragments that are commonly striated and show no discernable zircon alteration under binocular microscope (Fig. 4-12e). U-Pb data for three baddeleyite fractions is shown in Table 4-2, and on a concordia diagram in Fig. 4-18b. All three analyses plot close to concordia, and range from 1.13% to 2.31% discordant; the data are not colinear. The three possible unanchored linear regressions of the data yield poorly constrained upper intercept ages between 2222 Ma and 2267 Ma, and so the crystallization age of baddeleyite could be older than the oldest $^{207}\text{Pb}/^{206}\text{Pb}$ age of 2216.7 ± 6.0 Ma (2σ). A linear regression of analyses #29 and #30 that is anchored to the origin (Fig. 4-18b) yields an upper intercept age of 2213.6 ± 3.9 Ma (MSWD=1.8; probability of fit = 18%), which is interpreted to represent the current best age estimate for the emplacement of the Kandlamadugu dyke.

DISCUSSION

The U-Pb ages determined in this study provide, for the first time, robust timing constraints for the emplacement ages of numerous mafic dyke swarms surrounding the Cuddapah basin (Fig. 4-19). Emplacement ages of 2.37, 2.21, and 2.18 Ga are consistent with the observation that all of these dyke swarms appear to terminate at the basal unconformity of the Cuddapah basin (Padmakumari and Dayal, 1987; Murty et al., 1987), which formed at least as early as ~1.88 Ga (Anand et al., 2003; Chapter 3, this thesis). This resolves a major geochronological paradox in the Paleoproterozoic crustal evolution of the EDC, in that summaries of previously determined $^{40}\text{Ar}/^{39}\text{Ar}$ and K-Ar

ages for mafic dykes in this region (Murty et al., 1987; Mallikarjuna Rao et al., 1995) indicated that these swarms are predominantly younger (peak emplacement events at 1.9-1.7 Ga, 1.4-1.3 Ga, and 1.2-1.1 Ga) than the basal unconformity of the Cuddapah Basin. On the basis of these new U-Pb ages for mafic dykes of the Dharwar craton, it now also appears that the most prolific period of mafic dyke swarm emplacement took place during the Paleoproterozoic, rather than in the Mesoproterozoic (Fig. 4-3).

Regional extent and timing of emplacement of the Bangalore dyke swarm

U-Pb baddeleyite ages are reported here for three E-W trending mafic dykes from the eastern Dharwar craton including 2365.4 ± 1.0 Ma for the Harohalli dyke, 2365.9 ± 1.5 Ma for the Penukonda dyke, and 2368.6 ± 1.3 Ma for the Chennekottapalle dyke. These similar emplacement ages for parallel mafic dykes collected along a ~175 km across strike transect near Bangalore (Fig. 4-2), suggest that a vast tract of this dyke swarm was emplaced in a geologically short time span of only 2 or 3 million years. These mafic dykes are a part of the most prominent dyke swarm in the Dharwar craton (the Bangalore dyke swarm), and this major E-W trending swarm outcrops as a highly dense array of mafic dykes to the south and southwest of the Cuddapah basin (Fig. 4-2). Although we consider these U-Pb ages to represent the most accurate independent estimates for the timing of emplacement of each individual dyke as discussed above, we have also considered the composite dataset of all Bangalore dyke swarm samples (c.f. Gunbarrel Igneous Events, Harlan et al., 2003). The majority of U-Pb baddeleyite data for the Bangalore dyke swarm including multiple data points from all three mafic dykes (8 out of 12 analyses, comprising the statistically most similar 2/3 of the dataset for every sample), plot along a single common discordia line (Fig. 4-20) yielding a

composite upper intercept age of 2365.9 ± 0.7 Ma (95% confidence; MSWD = 0.70; probability of fit = 65%). We interpret this composite upper intercept age (Fig. 4-20) to represent the best estimate for the timing of emplacement of the Bangalore dyke swarm. At least two petrographically distinct varieties of Bangalore dykes including poikilitic gabbros (Harohalli and Chennekottapalle dykes) and medium-grained dolerites (Penukonda dyke) were emplaced contemporaneously at 2366 Ma. As noted by Halls (1982), towards the north this dyke swarm seems to swing in line with the structural grain of the craton and may extend as far north as Hyderabad where it assumes a NE-SW orientation. This hypothesis needs to be explored with further U-Pb dating studies in that region. In this scenario the Bangalore dyke swarm appears to radiate across a $\sim 25^\circ$ arc with a focal point outboard of the present-day western edge of the Dharwar craton (Fig. 4-19). Thus, this radial dyke pattern can be taken as evidence of a mantle plume centre (c.f. Ernst and Buchan 2001b). However, the densest array of dykes seems to occur towards the southeast part of the craton, away from this focal point. An alternative explanation for the radial dyke pattern is that it may be a consequence of long-lived Late Archean plate boundary forces that persisted into the Paleoproterozoic. In this interpretation, the orthogonality of the Bangalore dyke swarm to the granite-greenstone structural grain in the Dharwar craton may be an indication that the direction of maximum horizontal stress at the time of the final stages of cratonization in the Late Archean carried through until the time of dyke emplacement at 2366 Ma (Halls, 1978; Halls, 1982). It is important to note, however, that some dykes from the NE-SW trending Karimnagar mafic dyke swarm (Fig. 4-1), which appears to link up geographically with the Bangalore swarm in the north-eastern part of the craton, are

known to intrude the banded magnetite quartzites of the Pakhal Group of the approximately Middle Proterozoic Godavari graben (Rao et al., 1990). This suggests that at least some NE-SW trending mafic dykes in the north-eastern part of the craton are part of a dyke swarm that is significantly younger in age than the Bangalore swarm. Paleomagnetic studies of several NE-SW trending dykes from the Karimnagar area (Rao et al., 1990) yielded remanent magnetic vectors with inclinations that are for the most part quite shallow (-25°), in contrast to those reported for E-W dykes of the Bangalore swarm (Fig. 4-4) which have very steep inclinations (-69 to -88°), and this also suggests that dykes in the Karimnagar area are not part of the Bangalore swarm. Padmakumari and Dayal (1987) reported that in the region to the southwest of the Cuddapah basin, at least one NE-SW trending mafic dyke was observed in the field to be crosscut by a major E-W trending dyke. Based on their geological map, this E-W trending dyke appears to be the Penukonda dyke (sample JEF-99-6) dated by U-Pb baddeleyite in the present study. Their observation suggests that at least one older episode of NE-SW mafic dyke emplacement also occurred in the southern EDC prior to emplacement of the Bangalore dyke swarm at 2365.9 ± 0.7 Ma. This same cross-cutting relationship between an older NE-SW trending mafic dyke and the younger Penukonda dyke was also observed by Kumar and Bhall (1983), who noted that contrasting paleomagnetic data for the two crosscutting dykes also suggests different periods of emplacement. The U-Pb baddeleyite age of 2365.9 ± 1.5 Ma for the Penukonda dyke (Fig. 4-14b) is significantly older than two previously determined and contrasting K-Ar age determinations of 1100 ± 25 Ma (Balakrishna et al., 1979) and 1518 ± 37 Ma (Padmakumari and Dayal, 1987) for this same dyke. The database of previously determined isotopic ages for the

Bangalore dyke swarm indicates a protracted >1 b.y. history of emplacement from ~2.5 to ~1.1 Ga (Ikramuddin and Stueber, 1976; Balakrishna et al., 1979; Padmakumari and Dayal, 1987; Murty et al., 1987; Sarkar and Mallik, 1995; Dayal and Padmakumari, 1995; Mallikarjuna Rao et al., 1995; Zachariah et al., 1995). In contrast, U-Pb baddeleyite ages for three Bangalore dykes presented in this study suggest that emplacement of this swarm appears to have occurred early at 2365.9 ± 0.7 Ma, and in a rapid (<1-2 m.y.) catastrophic fashion. An E-W trending dolerite dyke that crosscuts the Ramagiri greenstone belt, and outcrops along strike of a dense clustering of dykes that occurs ~2 km south of the Chennekottapalle dyke (Fig. 4-7), was dated at 2454 ± 100 Ma (Sm-Nd isochron age: Zachariah et al., 1995), which is consistent with inclusion of this dyke cluster with the Bangalore swarm. The available geochronological information indicates that Bangalore dyke swarm does not appear to extend a significant distance into the south Indian granulite terrane. Recent $^{40}\text{Ar}/^{39}\text{Ar}$ and K-Ar dating of the predominantly NW-SE trending Tiruvannamalai and Dharmapuri dolerite dyke swarms from the northern part of the south Indian granulite terrain (Fig. 4-2) indicate emplacement ages of 2000-1650 Ma (Radhakrishna et al., 1999), which are significantly younger than the U-Pb ages reported in the present study for the Bangalore dyke swarm. In contrast, paleomagnetic data for the Tiruvannamalai dykes are similar to results for mafic dykes across much of the southern Dharwar craton (including the E-W trending Harohalli dolerite dykes), which may indicate the presence of a single large consanguineous igneous suite (Radhakrishna et al., 2003).

U-Pb evidence for ~2.2 Ga pan-Dharwar mafic magmatism

The U-Pb baddeleyite age of 2180.8 ± 0.9 Ma reported here (Fig. 4-16a) for the

timing of emplacement of the NW-SE trending Dandeli dyke of the western Dharwar craton provides a critical new time marker that is useful in unravelling the Paleoproterozoic geological history of the region. The Dandeli dyke appears to be part of a prominent NW-SE trending dyke swarm that transects a large tract of the Shimoga greenstone belt and granites in the region (Fig. 4-9). The swarm is broadly parallel to the regional trend and fold axial traces of the Shimoga belt (Figs. 4-2 and 4-9), indicating NE-SW extension during dyke emplacement in this part of the craton. As the dominant trend of mafic dykes in the western Dharwar craton is NW-SE, there is potential for this 2.18 Ga swarm to extend southward into the Chitradurga greenstone belt, and potentially as far as the southwest corner of the Dharwar craton (Fig. 4-2). Some evidence to support such a southerly extent for the swarm includes a K-Ar whole rock age of 2193 ± 45 Ma for an ENE-WSW trending dolerite dyke north of Mangalore (Balasubrahmanyan, 1975). U-Pb dating of zircon and baddeleyite from the Bandepalem dyke (north of the Cuddapah basin) yields an emplacement age of 2176.5 ± 3.7 Ma (Fig. 4-17), which within analytical uncertainty overlaps the U-Pb baddeleyite age of 2180.8 ± 0.9 Ma for the Dandeli dyke. The similar emplacement ages for these dykes provides unequivocal evidence that mafic magmatism at 2.18 Ga spanned a region of the northern Dharwar craton at least 550 km across (Fig. 4-19). The Bandepalem dyke, which appears to extend E-W along strike for about 180 km, appears to be part of a prominent but somewhat widely spaced dyke swarm in the north-eastern Dharwar craton, indicating N-S crustal extension of this region during dyke emplacement at 2.18 Ga. This dyke swarm, together with the 2.18 Ga NW-SE trending mafic dyke swarm at Dandeli, can be interpreted to form a radiating pattern across the

northern Dharwar craton with a focal point west of the present day Deccan Flood Basalt Province (Fig. 4-19). Additional U-Pb dating studies are required to associate more clearly emplacement ages with regional dyke patterns, but at present, the available data suggest the presence of a 2.18 Ga giant radiating Northern Dharwar mafic dyke swarm (Fig. 4-19). Additional support for this regional correlation comes from Sm-Nd isochron ages of 2173 ± 64 Ma and 2189 ± 123 Ma for mafic dykes in the intervening region (Fig. 4-2) at Mahbubnagar (Pandey et al., 1997). Moreover, the Dandeli and Bandepalem dykes plot in similar fields on major-element geochemical classification diagrams (Fig. 4-9), and trace element and REE patterns are very similar, except that the Dandeli dyke is relatively enriched in Sr, K, and Rb (Fig. 4-11).

U-Pb baddeleyite dating of two mafic dykes that occur south of the Cuddapah basin in this study including the 2209.3 ± 2.8 Ma Somala dyke and the 2213.6 ± 3.9 Ma Kandlamadugu dyke, indicates that ~ 2.2 Ga mafic magmatism also affected the southern Dharwar craton. The Somala dyke appears to belong to a prominent NW-SE trending dyke swarm that occurs west and southwest of the Cuddapah basin, and consequently the U-Pb baddeleyite age of 2209.3 ± 2.8 Ma for this dyke records the timing of a mafic magmatic event that may have spanned this geographic region and accompanied significant NE-SW crustal extension at that time. It is interesting to note that the orientation of this dyke swarm broadly fits within the radiating pattern of the aforementioned 2.18 Ga Northern Dharwar dyke swarm (Fig. 4-19), possibly linking all of these dyke swarms to a single longer-lived ~ 30 m.y. mantle plume event similar in size and timescale to Matachewan igneous events in the Superior craton, North America (Halls, 1991; Ernst et al., 1995; Heaman, 1997).

In contrast to the Somala dyke, the N-S orientation of the Kandlamadugu dyke is clearly oblique to the trend of the prominent NW-SE trending dyke swarm in the region, and this dyke is petrographically and geochemically quite distinct from the Somala dyke. The Kandlamadugu dyke is a quartz normative sub-alkali basaltic dyke and shows no feldspar clouding, whereas the Somala dyke is an olivine normative picrite and shows pronounced feldspar clouding. The trace-element patterns for the two dykes are different and although the REE profiles are similar, the Kandlamadugu dyke is enriched in the REEs by a factor of two to three relative to the Somala dyke (Fig. 4-11). Our interpretation is that the U-Pb baddeleyite age of 2213.6 ± 3.9 Ma for the Kandlamadugu dyke is a robust estimate for the timing of emplacement of this dyke. It is important to note that this age overlaps within error of the U-Pb baddeleyite concordia age of 2209.3 ± 2.8 Ma for the Somala dyke. The similar U-Pb ages for these geochemically and petrographically distinct mafic dykes may indicate contemporaneous emplacement, but further U-Pb baddeleyite dating of these samples will be required to try and rule out a possible time gap of <5 m.y. between dyke emplacement events. Given the contrasting petrological and geochemical features, the distinctly different orientations of these dykes, and the available geochronological information, it remains unclear whether these features reflect chemical variability within a single magmatic event or two distinct events. A common feature in the development of many continental flood basalt provinces is the eruption of a small volume of picrite lavas during the earliest stages of volcanism (Gill et al., 1992). This normal sequence of magma evolution is, however, at odds with the age data of this study, which indicates that the picritic Somala dyke is younger than the quartz-normative Kandlamadugu dyke.

In contrast to the N-W trending Somala and parallel dykes, the Kandlamadugu dyke appears to be part of a more widely spaced N-S trending mafic dyke swarm, which comprises a relatively small number dykes that occurs south of the Cuddapah basin (Fig. 4-19). This may also be an indication that the two swarms were emplaced at slightly different times. Testing either scenario will require further U-Pb dating, but at present we speculate that these two dykes belong to dyke swarms emplaced at slightly different times (<5 m.y. apart) under different crustal stress regimes (Fig. 4-19).

Tectonic Implications

Mafic dyke swarms can be emplaced over vast expanses of continental crust in relatively short geological time-spans (~5 m.y. or less), and may therefore prove useful in paleocontinental reconstructions (e.g. Heaman, 1997; Mertanen et al., 1999). Well studied examples of catastrophic mafic magmatic activity associated with continental break-up, ocean opening and mantle plume activity include the Mesoproterozoic (1267 Ma) Mackenzie Igneous Events associated with opening of the Poseidon Ocean (LeCheminant and Heaman, 1989) and break-up of the supercontinent Columbia (Rogers and Santosh, 2002), the Neoproterozoic (780 Ma) Gunbarrel Igneous Events associated with opening of the proto-Pacific ocean and the break-up of Rodinia (Harlan et al., 2003), and the Phanerozoic (~130 Ma) Paraná-Etendeka and (~200 Ma) Central Atlantic Magmatic Provinces associated with opening of the Atlantic Ocean and the break-up of Pangea (Hawkesworth et al., 2000; Deckart et al., 2005). Paleoproterozoic and older examples of such events are more difficult to identify because mafic dyke swarms, which may be the only surviving erosional remnants of the associated large igneous provinces (LIPs), may have been fragmented, globally dispersed, and partially

destroyed by numerous Wilson cycles. The record of ~2.45 Ga, and ~1.9 Ga mafic magmatism preserved in many Archean cratons worldwide may represent remnants of two such ancient LIPs that were associated with ocean opening and supercontinent break-up (Heaman, 1997; Chapter 3, this thesis). An alternative interpretation of the global synchronicity of Paleoproterozoic mafic magmatism in multiple Archean cratons is that it represents a record of magmatic activity that affected different geographic regions on Earth at the same time rather than formerly contiguous LIPs that were separated by rifting and ocean opening. LIPs associated with mantle plume activity may also form during supercontinent assembly, and this appears to be the case for coeval mafic magmatism in Laurentia and the Kalahari craton at 1.1 Ga during the assembly of Rodinia (Hanson et al., 2004a).

U-Pb dating of Southern Bastar-Cuddapah igneous events (Chapter 3, this thesis) indicates the presence of a 1891-1883 Ma LIP that bridges the Godavari rift, occurring in both the Dharwar and Bastar cratons. This ~1.9 Ga LIP appears to have been genetically associated with coeval basin development and rifting in south India that may have been linked with breakout of the Dharwar protocontinent from a larger parental paleocontinent. In contrast to ~1.9 Ga Bastar-Cuddapah igneous events, widespread mafic magmatism at 2.37 and ~2.2 Ga in the Dharwar craton identified in the present study (Fig. 4-19) cannot be clearly linked with basin development or rifting events because there have been no Paleoproterozoic supracrustal rocks older than ~1.9 Ga identified in the Dharwar craton. Nevertheless, these 2.37 and ~2.2 Ga craton-transsecting mafic dyke swarms are interpreted to record major break-up events that affected the Dharwar craton at this time, which may have been related to development of

local or possibly far-field rifted margins within a disintegrating Paleoproterozoic supercontinent.

The U-Pb baddeleyite and zircon ages presented for Bastar-Cuddapah igneous events (Chapter 3, this thesis) and seven mafic dykes from the Dharwar craton in this study, provide a new database with which to compare the record of Paleoproterozoic mafic magmatism preserved in the Dharwar and Bastar cratons to the record preserved in other cratons worldwide (Table 4-3 and Fig. 4-21). In this way, Archean cratons with similar Paleoproterozoic break-up histories can be identified as targets for attempting Paleoproterozoic plate reconstructions. Global correlation of high precision U-Pb baddeleyite and zircon ages for Paleoproterozoic mafic igneous provinces demonstrates that all of the mafic magmatic events presently identified in the Dharwar and Bastar craton in this thesis including 2.37, 2.21, 2.18, and 1.89-1.88 Ga, have one or more counterparts in other Archean cratons worldwide (Fig. 4-21). Construction of this correlation chart (Fig. 4-21) was greatly facilitated by examining earlier and more comprehensive data compilations (Ernst et al., 1996; Ernst and Buchan, 2001a; Ernst and Buchan, 2004).

At present there are no published U-Pb zircon or baddeleyite ages for mafic dykes outside the Dharwar craton that can be correlated with the 2366 Ma Bangalore dyke swarm, but a recent U-Pb dating study of a Scourie dyke from the Lewisian craton, Scotland (Heaman, 2004), yields one mafic dyke emplacement age of ca. 2.37 Ga. Although these ages hint at a similar, or more remotely, a joint evolution of the Dharwar and Lewisian cratons in the Paleoproterozoic, it is important to note that 2418^{+7/-4} Ma and 1992^{+3/-2} Ma Scourie events (U-Pb baddeleyite ages: Heaman and Tarney, 1989)

have as of yet, no counterpart in the Dharwar craton (with the exception of a preliminary electron microprobe chemical baddeleyite age of $2413 \pm 22/-23$ Ma for one dyke, Appendix C). Similarly, 2.21 Ga, 2.18 Ga, and 1.88 Ga Dharwar mafic magmatism has not been identified in the Lewisian craton. The potential global extent of ~ 2.37 Ga mafic magmatism has yet to be defined, but in addition to the Bangalore dyke swarm and coeval ~ 2.37 Ga Scourie event, a Rb-Sr age of 2350 ± 48 Ma for high-Mg tholeiites from East Antarctica (Sheraton and Black, 1981) and a Sm-Nd age of 2349 ± 30 Ma for a Fe-tholeiite dyke from the eastern Fennoscandian shield (reference in Mertanen et al., 1999), provide additional evidence to suggest a more widespread occurrence of this mafic magmatic event. However, due to the limitations of the Sm-Nd and Rb-Sr isotopic systems used in determining these ~ 2.35 Ga emplacement ages for Antarctic and Fennoscandian mafic dykes, robust correlation with the Bangalore dyke swarm awaits U-Pb dating of these dykes. U-Pb ages for the 2366 Ma Bangalore mafic dyke swarm presented in this study, comprise the first concrete evidence for a previously unidentified period of mafic magmatism in the Paleoproterozoic that otherwise occurs within a ~ 150 m.y. time-gap between emplacement of the 2262 ± 2 Ma Chimbadzi Hill intrusion of Zimbabwe (Manyeruke et al., 2004) and the 2410-2418 Ma Widgiemooltha dykes of the Yilgarn craton, Australia (Doehler and Heaman, 1998; Nemchin and Pidgeon, 1998).

U-Pb dating of baddeleyite and zircon from numerous mafic dyke swarms or associated sill complexes in North America indicates that multiple Archean cratons from the Canadian shield contain a prolific record of mafic magmatic activity between 2.23 and 2.21 Ga (Corfu and Andrews, 1986; Noble and Lightfoot, 1992; Buchan et al., 1993;

LeCheminant and van Breemen, 1994; Cadman et al., 1993; LeCheminant et al., 1996; Buchan et al., 1998), coeval with emplacement of the Kandlamadugu and Somala dykes of the Dharwar craton. Emplacement of the NE-SW trending Malley dykes and E-W trending Mackay dykes in the Slave craton at 2.23 Ga and 2.21 Ga (Fig. 4-22), respectively, may have been linked to rifting and break-up events along the eastern and southern margins of the craton (LeCheminant and van Breemen, 1994; LeCheminant et al., 1996). In the Superior craton, the 2229^{+35/-29} Ma Maguire, 2216^{+8/-4} Ma Senneterre, and 2209.7 \pm 0.8 Ma Klotz mafic dykes, together form the giant Ungava radiating swarm (Fig. 4-22), which may have fed the 2.22-2.21 Ga Nipissing sills further to the south (Buchan et al., 1998). The focal point of the Ungava radiating swarm may indicate the location of a mantle plume that could have been responsible for 2.23-2.21 Ga break-up along the eastern margin of the Superior craton (Buchan et al., 1998). Similar aged mafic dyke swarms have also been identified in the Nain province including the 2235 \pm 2 Ma Kikkertavak dykes of the Hopedale block, Labrador (Cadman et al., 1993), and 2214 \pm 10 Ma noritic dykes at Isukasia, West Greenland (Nutman et al., 1995). U-Pb dating of Karjalitic dolerite sills from the eastern Fennoscandian Shield has also yielded similar emplacement ages of 2220 \pm 11 Ma (Tyrväinen, 1983) and 2206 \pm 9 Ma (Silvennoinen, 1991; additional U-Pb data for Fennoscandian dykes in Vuollo et al., 1995). Correlative mafic igneous provinces from the southern hemisphere include 2.24 Ga mafic dykes of the Vestfold Hills cratonic block, East Antarctic Shield (Lanyon et al., 1993), and 2.21 Ga mafic sills (U-Pb baddeleyite: Mueller et al., 2004) and 2209 \pm 15 Ma volcanics (U-Pb zircon: Martin et al., 1998) within the Hammersley basin of the Pilbara craton, Australia. In this preliminary global survey, at least six Archean

provinces contain evidence for mafic dyke swarm emplacement (or dolerite sill provinces) between 2.24-2.21 Ga including the Superior, Slave, and Nain provinces of North America, and the Vestfold Hills, Pilbara, and Dharwar cratonic blocks of the southern hemisphere.

Emplacement of the 2.18 Ga Northern Dharwar mafic dyke swarm was also coeval with mafic magmatism in a large number of other Archean cratons worldwide (Fig. 4-21). Most notably, the U-Pb baddeleyite age of 2180.8 ± 0.9 Ma reported in this study for the Dandeli dyke is nearly identical to a U-Pb age of 2181 ± 2 Ma determined on baddeleyite and zircon from the Duck Lake sill, Slave craton (Bleeker and Kamo, 2003). Both of these 2.18 Ga mafic intrusions appear to be part of much larger igneous provinces that intrude major greywacke/mudstone-dominated supracrustal packages of similar age and transect large portions of their respective cratons. The Duck Lake sill intrudes Burwash Formation turbidites and may be genetically linked with the major E-W trending Dogrib mafic dyke swarm that has been dated at 2188 Ma (Bleeker and Kamo 2003; LeCheminant et al., 1997). The Burwash Formation is part of a major 2725-2610 Ma greenstone belt/turbiditic flysch association (Yellowknife Supergroup and correlatives) which spans much of the Slave Province, and which is underlain by a siliciclastic-dominated craton cover succession (Bell Lake Group) that has been correlated stratigraphically with the Bababudan Group of the Dharwar craton (Mueller et al., 2005). It is interesting to note here that the age of formation of the upper Bababudan Group and the majority of the greywacke/turbidite dominated Chitradurga Group, of the Dharwar craton, is bracketed between 2720-2610 Ma (details above) by U-Pb zircon dates of volcanic rocks (Trendall et al., 1997a; Trendall et al., 1997b). As a comparison

from the Slave craton, zircon from a tuff layer in the mafic volcanic dominated Kam Group yields a precise U-Pb age of 2722 ± 2 Ma (Isachsen and Bowring, 1994), and U-Pb zircon dating of interbedded volcanic rocks within widespread Late Archean turbidites yield ages of 2661 ± 2 Ma (Burwash Formation: van Breemen et al., 1992) down to 2612 ± 1 Ma (Isachsen and Bowring, 1994), which suggests that supracrustal rocks which dominate the WDC are of similar age and affinity to those which dominate the Slave craton (Bleeker, 2002). This observation, coupled with the presence of old (>3.4 Ga) TTG gneiss in the Slave and Dharwar cratons may indicate that they were nearest neighbours and possibly connected in a ~ 2.6 - 2.2 Ga Sclavia supercraton (Bleeker, 2002). Identical 2.18 Ga U-Pb dates for mafic igneous rocks within the Chitradurga Group of the WDC (Dandeli dyke, this study), and within correlative rocks of the Yellowknife Supergroup of the Slave craton (Duck Lake sill: Bleeker and Kamo, 2003) provide new support for a joint evolution of the Slave and Dharwar cratons from the Late Archean into the Paleoproterozoic. One problem with this correlation however is that the major ~ 2.55 - 2.51 Ga granitoid bloom associated with emplacement of the Dharwar batholith (including the Closepet granite) in the EDC has no counterpart in the Slave craton. A similar U-Pb baddeleyite age of 2.19 Ga was also determined for the E-W striking Tulemalu dykes of the Hearne craton (LeCheminant et al., 1997). A comparison of paleomagnetic data for these dykes with data for the coeval 2.19 Ga Dogrib dyke swarm indicates that the Slave and Rae cratons were not juxtaposed in their present day relative orientations during dyke emplacement at 2.19 Ga (LeCheminant et al., 1997), but questions remain as to whether or not the Dogrib and Tulemalu dyke swarms constitute parts of the same LIP. U-Pb ages of 2192 Ma and 2176 Ma

determined on igneous zircon from metadiabases of the Kainuu schist belt (Laajoki, 1991) indicate that a record of similar-aged mafic magmatism is also preserved in the Fennoscandian Shield. The Biscotasing dyke swarm which spans $\sim 300\,000\text{ km}^2$ of the southern Superior craton has yielded slightly younger U-Pb dates ranging from $2166.7 \pm 1.4\text{ Ma}$ to $2171.6 \pm 1.2\text{ Ma}$, which indicate that this swarm was emplaced within a short geological time-span of $\sim 5\text{ Ma}$ (Buchan et al., 1993; Halls and Davis, 2004). In summary, there are at least five Archean provinces worldwide which contain a record of 2.19-2.17 Ga mafic magmatism including the Slave, Rae, and Superior cratons of North America, the Fennoscandian Shield, and the Dharwar craton. Three out of five of these Archean provinces including the Slave, Superior, and Dharwar cratons (Fig. 4-22), also contain records of mafic magmatism at 2.23-2.21 Ga (outlined above) and 1.88 Ga (outlined in Chapter 3). Some of these mafic magmatic events appear to have been related to rifting and break-up events that resulted in the formation of specific paleocontinental margins including break-up along the eastern and southern margins of the Slave craton at 2.23-2.21 Ga (LeCheminant et al., 1996), and break-up along the eastern margin of the Superior craton at 2.23-2.21 Ga (Buchan et al., 1998).

An overview of these three Archean provinces showing the distribution of the aforementioned 2.23-2.21 Ga, 2.19-2.17 Ga, and 1.88 Ga mafic igneous provinces is presented in Fig. 4-22 and, where possible, representations of possible mantle plume centres inferred from dyke swarm orientations are also shown. Break-up of the Superior craton commenced at 2.5-2.45 Ga in association with emplacement of the 2.47-2.45 Ga Hearst-Matachewan dyke swarm (Heaman, 1997), the 2.47 Ga Mistassini dyke swarm (Heaman, 1994), and the 2505 Ma Ptarmigan dykes (Buchan et al., 1998), and break-up

of the Dharwar craton commenced by at least 2366 Ma with emplacement of the Bangalore dyke swarm (but probably earlier, perhaps between 2.5-2.4 Ga during emplacement of the aforementioned pre-2366 Ma NE-SW trending dykes). In contrast, there are no dyke swarms older than 2.23 Ga yet identified in the Slave craton (Ernst et al., 2004). On the basis of this contrast, Bleeker (2002) suggests that the Superior and Slave cratons do not share a similar break-up history in the Paleoproterozoic and that in addition to consideration of other fundamental differences between these cratons, they likely originated from different parent supercratons, Superia and Sclavia. Here we highlight that the break-up histories of the Superior and Slave craton in the Paleoproterozoic are remarkably similar, considering that intracratonic dyke swarm emplacement took place in both cratons between 2.23-2.21 Ga, 2.19-2.17 Ga, and at 1.88 Ga (Fig. 4-22). Although break-up along the southern margin of the Superior craton took place early at 2.47-2.45 Ga (Heaman, 1994; Heaman, 1997), break-up along the eastern margin took place at 2.23-2.21 Ga (Buchan et al., 1998), coeval with break-up along the eastern and southern margins of the Slave craton (LeCheminant et al., 1996).

It is now evident from the U-Pb geochronological database for the Superior, Slave, and Dharwar cratons that prolific periods of continental mafic dyke swarm emplacement took place between 2.23-2.21 Ga and 2.19-2.17 Ga, possibly suggesting a major ~2.2 Ga episode of continental break-up and/or a major outbreak of mantle plume activity at that time. One possible interpretation is that these coeval mafic dyke swarms are genetically linked with common mantle plume centres, and that these three cratons were part of a larger paleocontinent which broke up at ~2.2 Ga. In this scenario, the

hypothetical paleocontinent could have been impacted by 2.23-2.17 Ga mantle plume activity comprising: a) a sequence of upwards of three geographically isolated mantle plumes affecting different parts of this paleocontinent and defining break-up margins, b) movement of this paleocontinent over a long-lasting (~60 m.y.) stationary mantle plume centre during break-up, and/or migration of a long-lasting (~60 m.y.) mantle plume centre during break-up. The relative ages and orientations of 2.23-2.17 Ga mafic dyke swarms in the Superior, Slave, and Dharwar cratons are used to constrain one hypothetical paleocontinental reconstruction (Fig. 4-23) which can be interpreted in terms of either of the aforementioned common plume source break-up scenarios a) and b). This reconstruction is, however, limited by the assumption that seafloor spreading does not ensue until the end of the last stage of break-up at 2.17 Ga (i.e. no relative motion between cratons from 2.23-2.17 Ga). Assuming plate movement over a long-lived stationary mantle plume or strictly plume migration beneath a slow-moving plate in Fig. 4-22, absolute plate/plume velocities range from ~1 to 5 cm/y during the ~60 m.y. episode, well within accepted values for modern day motions (Keary and Vine, 1996). If these 2.23-2.17 Ga coeval mafic dyke swarms can be linked to common plume sources, it seems more likely that break-up and ocean opening would occur progressively in sequence, with ocean opening possibly developing in an ever widening zipper-like fashion similar to emplacement of the ~130 Ma Paraná-Etendeka and ~200 Ma Central Atlantic Magmatic Provinces during opening of the Atlantic Ocean. This type of break-up would lead to significant relative motions between cratons from 2.23 Ga onwards. An alternative possibility is that 2.23-2.17 Ga mafic magmatism was happening at multiple, very distal geographic locations on Earth at that time (c.f. Mid-

Cretaceous superplume event: Larson, 1991), and that this magmatism was not necessarily associated with supercontinent break-up (c.f. 1.1 Ga mafic magmatism during Rodinia assembly: Hanson et al., 2004a). Testing of any of these scenarios, and constraining more robust plate reconstructions at ~2.2 Ga will require paleomagnetic investigations of dated mafic dykes, potentially linking other aspects of the regional geology of these cratons, and further defining the global extent of ~2.2 Ga mafic magmatism. Nevertheless, the reconstruction in Fig. 4-23 demonstrates how knowledge of the relative ages and orientations of multiple mafic dyke swarms from multiple disparate Archean cratons has great potential for providing some geometrical constraints in plate reconstructions where a Central Atlantic Magmatic Province-type radiating geometry (Ernst and Buchan, 2001b) is assumed for multiple swarms impacting a large coherent paleocontinent.

There have been a number of paleomagnetic studies of Proterozoic mafic dykes of southern India including the Karimnagar mafic dykes of the northern Dharwar craton (Rao et al., 1990), dolerite dykes and Neoproterozoic alkaline dykes at Harohalli (Dawson and Hargraves, 1994; Radhakrishna and Mathew, 1996; Prasad et al., 1999; Radhakrishna et al., 2003), mafic dykes from the south Indian granulite terrain (Radhakrishna et al., 1994; Radhakrishna and Joseph, 1996), mafic dykes west of the Cuddapah basin (Kumar and Bhall, 1983), and a regional study of mafic dykes from the southern Dharwar craton (Radhakrishna et al., 2003). A summary of paleomagnetic data for mafic dykes from the Dharwar craton that is relevant to the present study is summarized in Table 4-4. The paleolatitudes presented (Table 4-4) are the reciprocals of the colatitude (θ) for each set of paleomagnetic data, where $\tan I = 2 \cot \theta$, and (I) is the

inclination of the characteristic remanent magnetization direction (Piper, 1987).

The Harohalli dyke dated at 2365.4 ± 1.0 Ma in the present study appears to be the same dyke that was sampled in two previous paleomagnetic investigations (dyke #12 in Dawson and Hargraves, 1994; dyke #3 in Prasad et al., 1999). In these studies, E-W trending dolerite dykes of the Harohalli area yielded similar paleomagnetic poles of 9.5°S , 242.4°E (Dawson and Hargraves, 1994) and 15°S , 254°E (Prasad et al., 1999), and an updated Harohalli pole of 19.4°N , 73.2°E is presented by Radhakrishna et al. (2003) that also includes this dyke. If these stable remnant magnetizations indeed date from the timing of intrusion of these dykes (e.g. Dawson and Hargraves, 1994), then the U-Pb baddeleyite age of 2365.4 ± 1.0 Ma for the Harohalli dyke provides a rigid time constraint with which to compare this paleomagnetic data to that from other Precambrian provinces. On the basis of U-Pb dating and paleomagnetic data for the Hearst-Matachewan dyke swarm, the Superior craton appears to have been near the equator ($\sim 10^\circ$ latitude either N or S) at 2.45 Ga (Heaman, 1997; Buchan et al., 1998; Mertanen et al., 1999). In contrast, on the basis of paleomagnetic data for E-W trending Harohalli dykes (Dawson and Hargraves, 1994; Prasad et al., 1999; Radhakrishna et al., 2003) and the U-Pb age of 2365.4 ± 1.0 Ma for the Harohalli dyke (this study), the Dharwar craton appears to have been at very high latitudes (74.9° , 86.0° , or 82.0° , either N or S) in the early Paleoproterozoic. Paleomagnetic studies (Kumar and Bhall, 1983) of two E-W trending dykes west of the Cuddapah basin yield consistent characteristic remanent magnetization directions that are slightly different than results reported for E-W trending Harohalli dykes (Table 4-4). One of these dykes (dyke ii of Kumar and Bhall, 1983) appears to be the Penukonda dyke (Fig. 4-7) dated at 2365.9 ± 1.5 Ma by U-Pb

baddeleyite in this study, and the other (dyke i of Kumar and Bhall, 1983) is part of a dense array of dykes that outcrop ~2km south of, and which are parallel to, the Chennekottapalle dyke dated at 2368.6 ± 1.3 Ma by U-Pb baddeleyite in this study. If the characteristic remanent magnetization in these dykes dates to the timing of intrusion at 2366-2368 Ma, the data indicate that the Dharwar craton was located at moderately high latitudes of 52.5 - 57° (either N or S) at this time, significantly different than what paleomagnetic data for the 2366 Ma Harohalli dykes indicates. Nevertheless, the speculation that the Superior craton was at very low latitudes at ~2.45 Ga and the Dharwar craton at moderately high to very high latitudes at ~2.37 Ga, does not support the tentative reconstruction shown in Fig. 4-23, because these two cratons should presumably have been together for a few hundred million years prior to break-up at ~2.2 Ga. This comparison of paleomagnetic poles from the Matachewan and Bangalore dyke swarms is quite tenuous, however, because of the ~80 m.y. difference in age between swarms, and also because baked contact tests were not carried out during acquisition of most of the paleomagnetic data for the Bangalore dyke swarm.

There is some paleomagnetic data that supports juxtaposition of the Dharwar and Superior cratons during possible break-up at ~2.2 Ga. A paleomagnetic study of a NW-SE trending dyke in the Bukkapatnam area (dyke v of Kumar and Bhall, 1983) indicates a paleolatitude of 18.6° (N or S) for that part of the Dharwar craton at the time of dyke emplacement. This dyke is parallel to, and ~125 km along strike of, the NW-SE trending Somala dyke dated at 2209.3 ± 2.8 Ma by U-Pb baddeleyite in this study. By inference, if the NW-SE trending Somala swarm extends as far NW as the Bukkapatnam area (as is shown in Fig. 4-19), then the paleomagnetic pole determined for dyke v

(Kumar and Bhall, 1983) may relate to its paleolatitude at 2.21 Ga. If this is the case, then at 2.21 Ga, the Senneterre region of the Superior craton (paleomagnetic and geochronological data used are from Buchan et al., 1993: U-Pb baddeleyite age of 2214.3 ± 12.4 Ma; paleomagnetic results: declination 357.2° ; inclination -44.2° ; mean site co-ordinates 48°N , 79°W) and the Bukkapatnam region of the Dharwar craton appear to have been at similar paleolatitudes of 25.9° and 18.6° (either N or S), respectively.

Another possible plate reconstruction at ~ 2.21 Ga involving the Dharwar and Superior cratons is shown in Fig. 4-24, and the latitudes and orientations of the two cratons is constrained by the available paleomagnetic data for the ~ 2.21 Ga Somala and Senneterre dyke swarms (assuming they were both in the northern hemisphere). Relative longitudinal positions for the two cratons in this reconstruction are constrained by assuming that ~ 2.21 Ga mafic magmatism included emplacement of a giant radiating dyke swarm similar in radius (~ 2500 km) to the Mackenzie dyke swarm, and fitting the two cratons into this pattern using the inferred plume centre for the Ungava radiating swarm (Buchan et al., 1998). Also shown are reconstructed radiating dyke swarms and inferred mantle plume centres for ~ 2.23 Ga and 2.19-2.17 Ga mafic magmatic events, assuming (as in Fig. 4-23) that relative motions between cratons does not occur from 2.23-2.17 Ga. By 2.17 Ga, the Superior craton had rotated $\sim 90^\circ$ counter clockwise and drifted to intermediate latitudes of $30-40^\circ$, and the 2.23 Ga Maguire dykes yield a slightly different paleomagnetic pole than the 2.21 Ga Senneterre dykes (Buchan et al., 1998), and so the paleolatitude for the Superior and Dharwar cratons in Fig. 4-24 pertains only to ~ 2.21 Ga. The position and orientation of the Slave craton in Fig. 4-24 is constrained only by the relative ages and orientations of the Malley, Mackay, and

Dogrib dyke swarms, and three possible positions and orientations are constrained by building on the Superior-Dharwar configuration, assuming emplacement of three giant radiating dyke swarms in a coherent paleocontinent at ~2.23 Ga, ~2.21 Ga, and 2.19-2.17 Ga (i.e. the method of paleocontinental reconstruction outlined in Fig. 4-23). For reference the dominant trends of first-order structures (including greenstone belts and Late Archean terrane boundaries) is shown for each craton, along with estimates for Late Archean subduction polarities (Superior and Slave cratons: Hoffman, 1989, and Calvert et al., 1995; Dharwar craton: Chadwick et al., 2000). This provides additional support for the reconstruction of the Dharwar and Superior cratons shown in Fig. 4-24, because both the dominant structural grain and Late Archean subduction polarities for the two cratons are aligned quite well. In addition, the locations of old (>3.4 Ga) TTG gneiss terrains including the Minnesota Foreland (Hoffman, 1989) and Peninsular gneiss of the western Dharwar craton (Meen et al., 1992) are in relative proximity (Fig. 4-24).

One major problem with this paleocontinental reconstruction (Fig. 4-24) is that it does not allow for the plausible break-up of the Superior and Karelian cratons at ~2.45 Ga (Heaman, 1997; Mertanen et al., 1999). This may be because the paleomagnetic data used for the Somala dyke swarm in Fig. 4-24 does not truly apply to ~2.21 Ga but to a different age of mafic dyke emplacement parallel to the Somala swarm, but also because the data are very limited in that they originate from only two sites from one dyke. Moreover, no baked contact tests were carried out, and α_{95} for the paleomagnetic pole is quite large for the data acquired for this dyke (14°). For that reason, we have considered a third possible paleocontinental reconstruction that allows for break-out of the Wyoming and Karelian cratons from 2.5-2.45 Ga (Heaman, 1997), and also allows for

possible break-out of additional continental crust at 2.37 Ga in association with emplacement of the Bangalore dyke swarm (Fig. 4-25a).

Given the emplacement of Scourie dykes at 2.42 Ga (Heaman and Tarney, 1989) and at 2.37 Ga (Heaman, 2004) in the Lewisian craton, it is possible that the NE-SW pre-Bangalore dykes (yellow bars in Fig. 4-25a) may have been emplaced at 2.42 Ga. On this basis, in addition to correlations between the 2.42 Ga Scourie and 2.42-2.41 Ga Widgiemooltha dykes (Doehler and Heaman, 1998; Nemchin and Pidgeon, 1998), a range of localities where break-out of the Yilgarn and Lewisian cratons may have occurred from 2.42-2.37 Ga is also shown. This range should extend as far as the location of the Pilbara craton in Fig. 4-25a (inset), if the Yilgarn craton is placed in the position shown in a recent reconstruction of 2.45 Ga Kenorland (Pesonen et al., 2003). To enable a tighter fit for the Dharwar, Superior, and Slave cratons, it is assumed in this reconstruction (Fig. 4-25a) that the 2229^{+35/-20} Ma Maguire dykes are coeval with 2.21 Ga mafic magmatism (i.e. that the entire Ungava radiating swarm was emplaced within <10 m.y. at 2.21 Ga). The relative positions and orientations of the Superior, Slave, and Dharwar cratons in Fig. 4-25a is constrained by the method outlined in Fig. 4-23, and the Wyoming and Karelian cratons are positioned based on previous correlations (Heaman, 1997; Mertanen et al., 1999; Pesonen et al., 2003).

In addition to the Dharwar craton, a number of other continental fragments including the Pilbara, Bastar, Singhbhum, and Kaapvaal cratons and eastern Madagascar were also very likely constituents in the Late Archean to Paleoproterozoic Ur continent (Rogers, 1996; Rogers and Santosh, 2002; Piper et al., 2003). Two possible configurations for this 'original' continent have been proposed (Rogers, 1996; Piper et

al., 2003). For reference (inset: Fig. 4-25a) these additional constituents are also shown in the classic Ur configuration of Rogers (1996), and built off of the Dharwar craton as it appears in Fig. 4-25a by placing the additional cratons as shown in a recent Gondwanaland reconstruction (Collins and Pisarevsky, 2005). There is accumulating evidence to suggest that some cratons from the southern hemisphere (e.g.: the Kaapvaal craton: Pesonen et al., 2003) should also be included in the original Kenorland of Williams et al. (1991). Here we suggest that the Dharwar craton and by inference additional continental blocks from Ur (Rogers, 1996), may have been connected to Kenorland in the early Paleoproterozoic as a single large continent called Kurnorland (inset: Fig. 4-25a). The relative positions of the Kaapvaal and Superior cratons shown in this Kurnorland reconstruction (inset: Fig. 4-25a) are consistent with a recent reconstruction of 2.45 Ga Kenorland (Pesonen et al., 2003).

The reconstruction shown in Fig. 4-25a is based on the interpretation that the break-up of Kurnorland occurred in two protracted, episodic stages at 2.5-2.37 Ga and 2.23-2.17 Ga, possibly in association with changes in plate boundary forces, mantle plume activity, and emplacement of several giant radiating mafic dyke swarms. The first episode commences with an initial period of break-up (Fig. 4-25b) during mafic magmatism and rifting in the Superior, Karelian and Wyoming cratons between 2.5 Ga-2.47 Ga (orange events) and 2.47-2.45 Ga (lavender events), followed by emplacement of 2.42 (yellow events) to 2.37 Ga (green events) mafic dykes in the Lewisian, Yilgarn and Dharwar cratons. Break-up and ocean opening along this linear track of mantle plume activity (Fig. 4-25c), could have separated the Karelian, Wyoming, and potentially the Yilgarn and Lewisian cratons from the Dharwar, Slave, and Superior

cratons (and the other cratons of Ur) into two separate paleocontinents. After ~150 m.y., a switch from passive to active margins could have triggered the commencement of ocean closure, and a combination of ~2.2 Ga mantle plume activity with intra-continental tension developing in association with newly forming (peripheral?) subduction zones, initiates a second punctuated sequence of mafic magmatism, rifting and continental break-up (Fig. 4-25d). In this interpretation, the disintegration of Kurnorland in the Paleoproterozoic appears to have culminated at ~2.2 Ga, and the occurrence of a large number of newly dispersed continental fragments could have set the stage (Fig. 4-25e) for a widespread episode of global orogenesis at 2.1-1.8 Ga during the growth of Columbia (Zhao et al., 2002), during the culmination of a Paleoproterozoic Wilson cycle.

The distribution of 2.37 Ga, 2.21 Ga, and 2.18 Ga mafic dyke swarms in the Dharwar craton shown in Fig. 4-19 is a preliminary interpretation which needs to be tested with integration of further U-Pb dating, geochemical, and paleomagnetic studies of these swarms, and the most rigid paleocontinental reconstruction attempted in this study (Fig. 4-25) is also considered to be a very preliminary effort. There is also evidence to suggest the presence of a number of mafic dyke swarms of other ages including post-Pakhal Group Karimnagar dykes (Rao et al., 1990), an old (2.5-2.42 Ga?) NE-SW swarm that appears to be crosscut (Padmakumari and Dayal, 1987; Kumar and Bhall, 1983) by the Penukonda dyke dated at 2365.9 ± 1.5 Ma in this study, and a prominent N-S swarm of unknown age at Hyderabad (Fig. 4-2). Electron microprobe chemical U-Th-total Pb baddeleyite dating studies of one dyke from the N-S Hyderabad swarm (JEF-00-51), and one NE-SW dyke (JEF-99-12) possibly correlative with the

aforementioned pre-Bangalore dykes, yield ages of 2248 ± 43 Ma and $2413 \pm 22/-23$ Ma, respectively (Appendix C). An emplacement age of 2.37 Ga for the NE-SW trending, northern extension of the Bangalore dyke swarm (Fig. 4-19) needs to be confirmed, and there may yet prove to be other age components to this swarm. U-Pb dating and paleomagnetic studies of the large dyke west of the Closepet batholith (Fig. 4-2) would also be of great value, because the along strike continuity of this dyke indicates that it may provide an excellent N-S regional time marker and valuable piercing point for plate reconstructions.

SUMMARY AND CONCLUSIONS

High precision U-Pb IDTIMS dating of baddeleyite and zircon from seven mafic dykes spanning a large tract of the Dharwar craton, define at least three distinct episodes of mafic dyke swarm emplacement during the Paleoproterozoic. Three E-W trending mafic dykes from the Bangalore dyke swarm including two poikilitic gabbros and one dolerite collected along a ~175 km across strike transect, yield similar U-Pb baddeleyite ages of 2365.4 ± 1.0 Ma (Harohalli gabbro dyke), 2365.9 ± 1.5 Ma (Penukonda dolerite dyke), and 2368.6 ± 1.3 Ma (Chennekottapalle gabbro dyke). The Bangalore dyke swarm is the most prominent dyke swarm in the Dharwar craton, and a pooled U-Pb baddeleyite age of 2365.9 ± 0.7 Ma for three dykes indicates that the entire swarm may have been emplaced within a geologically short time-span of two million years or less, and that break-up of the Dharwar craton may have begun as early as 2366 Ma. The Dandeli dyke, part of a prominent NW-SE trending mafic dyke swarm that intrudes the Shimoga basin, in the north-western part of the craton yields a U-Pb baddeleyite age of 2180.8 ± 0.9 Ma. A similar U-Pb age of 2176.5 ± 3.7 Ma was determined on baddeleyite

and zircon from a mafic dyke located ~550 km away at Bandepalem, and which is part of a prominent E-W trending dyke swarm in the north-eastern part of the craton. Together these data suggest the presence of a ~2.18 Ga LIP spanning the northern Dharwar craton (Northern Dharwar dyke swarm). U-Pb dating of two mafic dykes from the south-eastern part of the craton and south of the Cuddapah basin, including the Kandlamadugu dyke (part of small N-S trending swarm) and the Somala dyke (part of a prominent NW-SE trending swarm) yield baddeleyite ages of 2213.6 ± 3.9 Ma, and 2209.3 ± 2.8 Ma, respectively. Collectively these U-Pb ages may be linked with specific break-up events at 2.37, 2.21, and 2.18 Ga, and provide a critical new database with which to compare the Paleoproterozoic mafic magmatic history of the Dharwar craton to other cratons worldwide. Global correlation of U-Pb ages for mafic dyke swarms suggests that the Superior, Slave, and Dharwar cratons shared the most similar mafic magmatic histories in the Paleoproterozoic, with coeval mafic magmatism in all cratons between 2.23-2.21 Ga and 2.19-2.17 Ga, and at 1.88 Ga. These correlations suggest that the Superior, Slave, and Dharwar cratons could have been part of a large continent that contained both Ur and Kenorland, and underwent episodic break-up in two stages at 2.5-2.37 Ga and ~2.23-2.17 Ga.

REFERENCES

- Amelin, Y.V., Heaman, L.M., & Semenov, V.S. (1995). U-Pb geochronology of layered mafic intrusions in the eastern Baltic Shield: implications for the timing and duration of Paleoproterozoic continental rifting. *Precambrian Research* **75**, 31-46.
- Anand, M., Gibson, S.A., Subbarao, K.V., Kelly, S.P., & Dickin, A.P. (2003). Early Proterozoic melt generation processes beneath the intracratonic Cuddapah Basin, southern India. *Journal of Petrology* **44**, 2139-2171.
- Atkinson, B. (2004). Petrogenesis of Diabase Dykes in the Germaine Lake Area, NWT. *B.Sc. thesis, Department of Earth and Atmospheric Sciences, University of Alberta.*

Balakrishna, S., Rao, M.N., & Venkatarayana, B. (1979). Some geological studies on a dyke swarm near Bukkapatnam, Anantapur District, Andhra Pradesh. *Proceedings of 3rd Workshop on status, problems and programmes in Cuddapah basin, Hyderabad, A.P., India (Inst. Indian Penn. Geol Publ.)*, 68-71.

Balakrishnan, S., Hanson, G.N., & Rajamani, V. (1991). Pb and Nd isotope constraints on the origin of high-Mg amphibolites (komatiitic and picritic) and tholeiitic amphibolites, Kolar Schist Belt, south India. *Contributions to Mineralogy and Petrology* **107**, 279-292.

Balakrishnan, S., Rajamani, V., & Hanson, G.N. (1999). U-Pb Ages for Zircon and Titanite from the Ramagiri Area, Southern India: Evidence for Accretionary Origin of the Eastern Dharwar Craton during the Late Archean. *The Journal of Geology* **107**, 69-86.

Balasubrahmanyam, M.N. (1975). The age of the dykes of South Kanara, Mysore State. *Geological Survey of India Miscellaneous Publication* **23**, 236-239.

Barley, M.E., Pickard, A.L., & Sylvester, P.J. (1997). Emplacement of a large igneous province as a possible cause of banded iron formation 2.45 billion years ago. *Nature* **385**, 55-58.

Beckinsale, R.D., Drury, S.A., & Holt, R.W. (1980). 3,360-Myr old gneisses from the South Indian Craton. *Nature* **283**, 469-470.

Bhaskar Rao, Y.J., Sivaraman, T.V., Pantulu, G.V.C., Gopalan, K., & Naqvi, S.M. (1992). Rb-Sr ages of Late Archean metavolcanics and granites, Dharwar craton, South India and evidence for Early Proterozoic thermotectonic event(s). *Precambrian Research* **59**, 145-170.

Bhaskar Rao, Y.J., Pantulu, G.V.C., Damodara Reddy, V., & Gopalan, V. (1995). Time of early sedimentation and volcanism in the Proterozoic Cuddapah Basin, South India: Evidence from the Rb-Sr age of Pulivendla mafic sill. In: *Devaraju, T.C., ed., Mafic Dyke Swarms of Peninsular India, Geological Society of India Memoir* **33**, 329-338.

Bleeker, W. (2002). The late Archean record: a puzzle in ca. 35 pieces. *Lithos* **71**, 99-134.

Bleeker, W. & Kamo, S. (2003). A precise age for the Duck Lake sill and its relevance for fitting the Slave in a global Archean context. *Program and Abstracts of Talks and Posters, 31st Yellowknife Geoscience Forum*, 7-8.

Bostock, H.H. & van Breemen, O. (1992). The timing of emplacement and distribution of the Sparrow diabase dyke swarm, District of Mackenzie, Northwest Territories. In: *Radiogenic Age and Isotopic Studies, Report 6: Geological Survey of Canada Paper* **92-**

2, 49-55.

Buchan, K.L., Mortensen, J.K., & Card, K.D. (1993). Northeast-trending Early Proterozoic dykes of southern Superior Province: multiple episodes of emplacement recognized from integrated paleomagnetism and U-Pb geochronology. *Canadian Journal of Earth Sciences* **30**, 1286-1296.

Buchan, K.L., Mortensen, J.K., & Card, K.D. (1994). Integrated paleomagnetic and U-Pb geochronologic studies of mafic intrusions in the southern Canadian Shield: implications for the Early Proterozoic polar wander path. *Precambrian Research* **69**, 1-10.

Buchan, K.L., Halls, H.C., & Mortensen, J.K. (1996). Paleomagnetism, U-Pb geochronology, and geochemistry of Marathon dykes, Superior Province, and comparison with the Fort Frances swarm. *Canadian Journal of Earth Sciences* **33**, 1583-1595.

Buchan, K.L., Mortensen, J.K., Card, K.D., & Percival, J.A. (1998). Paleomagnetism and U-Pb geochronology of diabase dyke swarms of Minto block, Superior Province, Quebec, Canada. *Canadian Journal of Earth Sciences* **35**, 1054-1069.

Buchan, K.L., Harris, B.A., Ernst, R.E. and Hanes, J.A. (2003). Ar-Ar dating of the Pickle Crow diabase dyke in the western Superior craton of the Canadian Shield of Ontario and implications for a possible plume centre associated with ca. 1880 Ma Molson magmatism of Manitoba. *Geological Association of Canada / Mineralogical Association of Canada Abstracts* **28** (no. 481 on CD-ROM, p. 17 in print volume).

Buick, I.S., Maas, R., & Gibson, R. (2001). Precise U-Pb titanite age constraints on the emplacement of the Bushveld Complex, South Africa. *Journal of the Geological Society of London* **158**, 3-6.

Cadman, A.C., Heaman, L., Tarney, J., Wardle, R., & Krogh, T.E. (1993). U-Pb geochronology and geochemical variation within two Proterozoic mafic dyke swarms, Labrador. *Canadian Journal of Earth Sciences* **30**, 1490-1504.

Calvert, A.J., Sawyer, E.W., Davis, W.J., & Ludden, J.N. (1995). Archean subduction inferred from seismic images of a mantle suture in the Superior Province. *Nature* **375**, 670-674.

Chadwick, B., Ramakrishnan, M., & Viswanatha, M.N. (1985). Bababudan – A Late Archean intracratonic volcanosedimentary basin, Karnataka, southern India. *Journal of the Geological Society of India* **26**, 769-801.

Chadwick, B., Vasudev, V.N., & Hedge, G.V. (2000). The Dharwar craton, southern India, interpreted as the result of Late Archean oblique convergence. *Precambrian Research* **99**, 91-111.

- Chardon, D., Choukroune, P., & Jayananda, M. (1998). Sinking of the Dharwar Basin (South India): Implications for Archaean tectonics. *Precambrian Research* **91**, 15-39.
- Chatterjee, N. & Bhattacharji, S. (2001). Petrology, geochemistry and tectonic settings of the mafic dikes and sills associated with the evolution of the Proterozoic Cuddapah Basin of South India. *Proc. Indian Acad. Sci. (Earth Planet. Sci.)* **110**, 433-453.
- Collins, A.S. & Pisarevsky, S.A. (2005). Amalgamating eastern Gondwana: the evolution of Circum-Indian orogens. *Earth Science Reviews* **71**, 229-270.
- Corfu, F. & Andrews, A.J. (1986). A U-Pb age for mineralized Nipissing diabase, Gowganda, Ontario. *Canadian Journal of Earth Sciences* **23**, 107-109.
- Cornell, D.H., Armstrong, R.A., & Walraven, F. (1998). Geochronology of the Proterozoic Hartley Basalt Formation, South Africa: constraints on the Kheis tectogenesis and the Kaapvaal Craton's earliest Wilson Cycle. *Journal of African Earth Sciences* **26**, 5-27.
- Cox, D.M., Frost, C.D., & Chamberlain, K.R. (2000). 2.01-Ga Kennedy dike swarm, southeastern Wyoming: Record of a rifted margin along the southern Wyoming province. *Rocky Mountain Geology* **35**, 7-30.
- Davis, D.W. & Sutcliffe. (1985). U-Pb ages from the Nipigon plate and northern Lake Superior. *Geological Society of America Bulletin* **96**, 1572-1579.
- Dawson, E.M. & Hargraves, R.B. (1994). Paleomagnetism of Precambrian dike swarms in the Harohalli area, south of Bangalore, India. *Precambrian Research* **69**, 157-167.
- Dayal, A.M. & Padmakumari, V.M. (1985). K-Ar Ages of Dolerite Dykes from Southwestern Margin of Cuddapah Basin. *Presented at the 3rd National Symposium on Mass Spectrometry, Hyderabad, India.*
- Dayal, A.M. & Padmakumari, V.M. (1995). Potassium-Argon Ages of Dolerite Dykes in Late Archean/Early Proterozoic Closepet Granite. *Journal of the Geological Society of India* **46**, 47-51.
- Deckart, K., Bertrand, H., & Liégeois, J.-P. (2005). Geochemistry and Sr, Nd, Pb isotopic composition of the Central Atlantic Magmatic Province (CAMP) in Guyana and Guinea. *Lithos* **82**, 289-314.
- Doehler, J.S., and Heaman, L.M. (1998). 2.41 Ga U-Pb baddeleyite ages for two gabbroic dykes from the Widgiemooltha swarm, western Australia: A Yilgarn-Lewisian connection? *Geological Society of America Abstracts with Programs* **30**, A291-292.
- Drury, S.A. & Holt, R.W. (1980). The tectonic framework of the South Indian craton: a

reconnaissance involving Landsat imagery. *Tectonophysics* **65**, T1-T15.

Drury, S.A. (1984). A Proterozoic intracratonic basin, dyke swarms and thermal evolution in south India. *Journal of the Geological Society of India* **25**, 437-444.

Ernst, R.E. (2004). Ca. 1880 Ma Circum-Superior LIP. *LIP of the month, May 2004*: Located online at: www.largeigneousprovinces.org.

Ernst, R.E., Head, J.W., Parfitt, E., Grosfils, E., & Wilson, L. (1995). Giant radiating dyke swarms on Earth and Venus. *Earth-Science Reviews* **39**, 1-58.

Ernst, R.E., Buchan, K.L., West, T.D., & Palmer, H.C. (1996). *Diabase (dolerite) dyke swarms of the world: first edition*. Geological Survey of Canada, Open File **3241**.

Ernst, R.E. & Buchan, K.L. (2001a). Large mafic magmatic events through time and links to mantle-plume heads. In: Ernst, R.E. & Buchan, K.L., eds., *Mantle Plumes: Their Identification Through Time – Geological Society of America Special Paper 352*, 483-566.

Ernst, R.E. & Buchan, K.L. (2001b). The use of mafic dike swarms in identifying and locating mantle plumes. In: Ernst, R.E. & Buchan, K.L., eds., *Mantle Plumes: Their Identification Through Time – Geological Society of America Special Paper 352*, 247-265.

Ernst, R.E. & Buchan, K.L. (2004). Igneous Rock Associations in Canada 3. Large Igneous Provinces (LIPs) in Canada and Adjacent Regions: 3 Ga to Present. *Geoscience Canada* **31**, 103-126.

Fahrig, W.F. (1987). The tectonic settings of continental mafic dyke swarms: failed arm and early passive margin, In: Halls, H.C. and Fahrig, W.F., eds., *Mafic Dyke Swarms, Geological Association of Canada Special Paper 34*, 331-348.

Findlay, J.M., Parrish, R.R., Birkett, T.C., & Watanabe, D.H. (1995). U-Pb ages from the Nimish formation and Montagnais glomeroporphyritic gabbro of the central New Québec orogen, Canada. *Canadian Journal of Earth Sciences* **32**, 1208-1220.

French, J.E., Heaman, L.M., & Chacko, T. (2002). Feasibility of chemical U-Th-total Pb baddeleyite dating by electron microprobe. *Chemical Geology* **188**, 85-104.

Friend, C.R.L. & Nutman, P. (1991). SHRIMP U-Pb Geochronology of the Closepet Granite and Peninsular Gneiss, Karnataka, South India. *Journal of the Geological Society of India* **38**, 357-368.

Ghosh, J.G. (2004). 3.56 Ga tonalite in the central part of the Bastar craton, India: oldest Indian date. *Journal of Asian Earth Sciences* **23**, 359-364.

- Gill, R.C.O., Pederson, A.K., & Larsen, J.G. (1992). Tertiary picrites in West Greenland: melting at the periphery of a plume? In: Storey, B.C., Alabaster, T., & Pankhurst, R.J. (eds.), *Magmatism and the Causes of Continental Break-up*, Geological Society Special Publication **68**, 335-348.
- Gokhale, N.W. & Waghmare, B.P. (1989). K-Ar Ages on Three Basic Intersecting Dykes from Gadag Schist Belt, Karnataka. *Journal of the Geological Society of India* **34**, 663-664.
- Gopalan, K., Macdougall, J.D., Roy, A.B., & Murali, A.V. (1990). Sm-Nd evidence for 3.3 Ga old rocks in Rajasthan, northwestern India. *Precambrian Research* **48**, 287-297.
- GSI. (1981). Geological and Mineral Map of Karnataka and Goa, 1:500,000 scale. Geological Survey of India, Hyderabad.
- GSI. (1998). Geological Map of India, 1:2,000,000 scale. Geological Survey of India, Hyderabad.
- Halls, H.C. (1978). The structural relationship between Archean granite-greenstone terrains and late Archean mafic dikes. *Canadian Journal of Earth Sciences* **15**, 1665-1668.
- Halls, H.C. (1982). The importance and potential of mafic dyke swarms in studies of geodynamic processes. *Geoscience Canada* **9**, 145-153.
- Halls, H.C. (1991). The Matachewan dyke swarm, Canada: An early Proterozoic magnetic field reversal. *Earth and Planetary Science Letters* **105**, 279-292.
- Halls, H.C. & Zhang, B. (1995). Tectonic Implications of Clouded Feldspar in Proterozoic Mafic Dyke Swarms. In: Devaraju, T.C., ed., *Mafic Dyke Swarms of Peninsular India*, Geological Society of India Memoir **33**, 65-80.
- Halls, H.C. & Davis, D.W. (2004). Paleomagnetism and U-Pb geochronology of the 2.17 Ga Biscotasing dyke swarm, Ontario, Canada: evidence for vertical axis crustal rotation across the Kapuskasing Zone. *Canadian Journal of Earth Science* **41**, 255-269.
- Halls, H.C. & Heaman, L.M. (2000). The paleomagnetic significance of new U-Pb age data from the Molson dyke swarm, Cauchon Lake area, Manitoba. *Canadian Journal of Earth Sciences* **37**, 957-966.
- Halls, H.C., Li, J., Davis, D., Hou, G., Zhang, B., & Qian, X. (2000). A precisely dated Proterozoic paleomagnetic pole from the North China craton, and its relevance to paleocontinental reconstruction. *Geophysical Journal International* **143**, 185-203.
- Halls, H.C., Campal, N., Davis, D.W., & Bossi, J. (2001). Magnetic studies and U-Pb geochronology of the Uruguayan dyke swarm, Rio de la Plata craton, Uruguay:

paleomagnetic and economic implications. *Journal of South American Earth Sciences* **14**, 349-361.

Hamilton, M.A., Goutier, J., & Matthews, W. (2001). U-Pb baddeleyite age for the Paleoproterozoic Lac Esprit dyke swarm, James Bay region, Quebec. *Geological Survey of Canada, Current Research* **2001-F5**, 15p.

Hamilton, M.A., Davis, D.W., Buchan, K.L., & Halls, H.C. (2002). Precise U-Pb dating of reversely magnetized Marathon diabase dykes and implications for emplacement of giant dyke swarms along the southern margin of the Superior Province, Ontario. *Geological Survey of Canada, Current Research* **2002-F6**, 8p.

Hanson, R.E., Crowley, J.L., Bowring, S.A., Ramezani, J., Gose, W.A., Dalziel, I.W.D., Pancake, J.A., Seidel, E.K., Blenkinsop, T.G., & Mukwakwami, J. (2004a). Coeval large-scale magmatism in the Kalahari and Laurentian cratons during Rodinia assembly. *Science* **304**, 1126-1129.

Hanson, R.E., Gose, W.A., Crowley, J.L., Ramezani, J., Bowring, S.A., Bullen, D.S., Hall, R.P., & Pancake, J.A. (2004b). Paleoproterozoic intraplate magmatism and basin development on the Kaapvaal Craton: Age, paleomagnetism and geochemistry of ~1.93 to ~1.87 Ga post-Waterberg dolerites. *South African Journal of Geology* **107**, 233-254.

Harlan, S.S., Heaman, L., LeCheminant, A.N., & Premo, W.R. (2003). Gunbarrel mafic magmatic event: A key 780 Ma time marker for Rodinia plate reconstructions. *Geology* **31**, 1053-1056.

Hawkesworth, C.J., Gallagher, K., Kirstein, L., Mantovani, M.S.M., Peate, D.W., & Turner, S.P. (2000). Tectonic controls on magmatism associated with continental break-up: an example from the Paraná-Etendeka Province. *Earth and Planetary Science Letters* **179**, 335-349.

Heaman, L.M. (1994). 2.45 Ga global mafic magmatism: Earth's oldest superplume?, *In: Lanphere, M.A., et al., eds., Eight International Conference on Geochronology, Cosmochronology and Isotope Geology, Program with Abstracts (Berkeley, California): U.S. Geological Survey Circular* **1107**, p.132.

Heaman, L.M. (1997). Global mafic magmatism at 2.45 Ga: Remnants of an ancient large igneous province? *Geology* **25**, 299-302.

Heaman, L.M. (2004). 2.5-2.4 Ga Global magmatism: remnants of supercontinents or products of superplumes? *Geological Society of America Abstracts with Programs* **36**, 255.

Heaman, L.M., Machado, N., Krogh, T.E., & Weber, W. (1986). Precise U-Pb zircon ages for the Molson dyke swarm and the Fox River sill: Constraints for Early Proterozoic crustal evolution in northeastern Manitoba, Canada. *Contributions to*

Mineralogy and Petrology **94**, 82-89.

Heaman, L.M. & Tarney, J. (1989). U-Pb baddeleyite ages for the Scourie dyke swarm, Scotland: evidence for two distinct intrusion events. *Nature* **340**, 705-708.

Heaman, L.M., Bowins, R., & Crocket, J. (1990). The chemical composition of igneous zircon suites: Implications for geochemical tracer studies. *Geochimica et Cosmochimica Acta* **54**, 1597-1607.

Heaman, L.M., LeCheminant, A.N., & Rainbird, R.H. (1992). Nature and timing of Franklin igneous events, Canada: Implications for a Late Proterozoic mantle plume and the break-up of Laurentia. *Earth and Planetary Science Letters* **109**, 117-131.

Heaman, L.M. & LeCheminant, A.N. (1993). Paragenesis and U-Pb systematics of baddeleyite (ZrO₂). *Chemical Geology* **110**, 95-126.

Heaman, L.M. & Corkery, T. (1996). U-Pb geochronology of the Split Lake Block, Manitoba: Preliminary results. In: Hajnal, Z. & Lewry, J., eds., *Lithoprobe, Trans-Hudson Orogen Transect: Report of Sixth Transect Meeting*, no. **55**, 60-68.

Heaman, L.M. & LeCheminant, A.N. (2000). Anomalous U-Pb systematics in mantle-derived baddeleyite xenocrysts from Île Bizard: evidence for high temperature radon diffusion? *Chemical Geology* **172**, 77-93.

Hoffman, P.F. (1989). Precambrian geology and tectonic history of North America. In: Balley, A.W. & Palmer, A.R. (eds.), *The Geology of North America – An overview: Boulder, Colorado, Geological Society of America, The Geology of North America*, v. **A**, 447-512.

Ikramuddin, M. & Stueber, A.M. (1976). Rb-Sr ages of Precambrian dolerite and alkaline dikes, southeast Mysore State, India. *Lithos* **9**, 235-241.

Irvine, T.N. & Baragar, W.R.A. (1971). A guide to the Chemical Classification of the Common Volcanic Rocks. *Canadian Journal of Earth Sciences* **8**, 523-548.

Isachsen, C.E. & Bowring, S.A. (1994). Evolution of the Slave craton. *Geology* **22**, 917-920.

Jaffey, A. H., Flynn, K. F., Glendenin, L. E., Bentley, W. C., & Essling, A. M. (1971). Precision measurement of half-lives and specific activities of ²³⁵U and ²³⁸U. *Physical Review C* **4**, 1889-1906.

Jayananda, M., Martin, H., Peucat, J.J., & Mahabaleswar, B. (1995). Late Archean crust-mantle interactions: geochemistry of LREE-enriched mantle derived magmas. Example of the Closepet Batholith, southern India. *Contributions to Mineralogy and Petrology* **119**, 314-329.

Jayananda, M., Moyen, J.-F., Martin, H., Peucat, J.-J., Auvray, B., & Mahabaleswar, B. (2000). Late Archean (2550-2520 Ma) juvenile magmatism in the eastern Dharwar craton, southern India: constraints from geochronology, Nd-Sr isotopes and whole rock geochemistry. *Precambrian Research* **99**, 225-254.

Keary, P. & Vine, F.J., eds. (1996). *Global Tectonics* (Blackwell Science, Cambridge University Press), 333p.

Krapez, B. (1999). Stratigraphic record of an Atlantic-type global tectonic cycle in the Palaeoproterozoic Ashburton Province of Western Australia. *Australian Journal of Earth Sciences* **46**, 71-87.

Krogh, T.E. (1982). Improved accuracy of U-Pb zircon ages by the creation of more concordant systems using an air abrasion technique. *Geochimica et Cosmochimica Acta* **46**, 387-393.

Krogh, T.E. (1994). Precise U-Pb ages for Grenvillian and pre-Grenvillian thrusting of Proterozoic and Archean metamorphic assemblages in the Grenville Front tectonic zone, Canada. *Tectonics* **13**, 963-982.

Krogh, T.E., McNutt, R.H., & Davis, G.L. (1982). Two high precision U-Pb zircon ages for the Sudbury Nickel Irruptive. *Canadian Journal of Earth Sciences* **19**, 723-728.

Krogh, T.E., Corfu, F., Davis, D.W., Dunning, G.R., Heaman, L.M., Kamo, S.L., Machado, N., Greenough, J.D., & Nakamura, E. (1987). Precise U-Pb isotopic ages of diabase dykes and mafic to ultramafic rocks using trace amounts of baddeleyite and zircon. In: Halls, H.C. and Fahrig, W.F., eds., *Mafic Dyke Swarms, Geological Association of Canada Special Paper* **34**, 147-152.

Krogstad, E.J., Balakrishnan, S., Mukhopadhyay, D.K., Rajamani, V., & Hanson, G.N. (1989). Plate tectonics 2.5 billion years ago: evidence at Kolar, South India. *Science* **243**, 1337-1340.

Krogstad, E.J., Hanson, G.N., & Rajamani, V. (1991). U-Pb ages of zircon and sphene for two gneiss terranes adjacent to the Kolar schist belt, south India: evidence for separate crustal evolution histories. *Journal of Geology* **99**, 801-816.

Krogstad, E.J., Hanson, G.N., & Rajamani, V. (1995). Sources of continental magmatism adjacent to the late Archean Kolar Suture Zone, south India: distinct isotopic and elemental signatures of two late Archean magmatic series. *Contributions to Mineralogy and Petrology* **122**, 159-173.

Kumar, A. & Bhall, M.S. (1983). Palaeomagnetism and igneous activity of the area adjoining the south-western margin of the Cuddapah basin, India. *Geophysical Journal of the Royal Astronomical Society* **73**, 27-37.

Laajoki, K. (1991). Stratigraphy of the northern end of the early Proterozoic (Karelian) Kainuu Schist Belt and associated gneiss complexes, Finland. *Geological Survey of Finland Bulletin* **358**.

Lanyon, R., Black, L.P., & Seitz, H.-M. (1993). U-Pb zircon dating of mafic dykes and its application to the Proterozoic geological history of the Vestfold Hills, East Antarctica. *Contributions to Mineralogy and Petrology* **115**, 184-203.

Larson, R.L. (1991). Latest pulse of Earth: Evidence for a mid-Cretaceous superplume. *Geology* **19**, 547-550.

Le Maitre, R.W. & International Union of Geological Sciences. (2002). *Igneous Rocks: A Classification and Glossary of Terms* (ed: Le Maitre, R.W.), 252p.

LeCheminant, A.N. & Heaman, L.M. (1989). Mackenzie igneous events, Canada: Middle Proterozoic hotspot magmatism associated with ocean opening. *Earth and Planetary Science Letters* **96**, 38-48.

LeCheminant, A.N. & van Breemen, O. (1994). U-Pb ages of Proterozoic dyke swarms, Lac de Gras area, N.W.T.: Evidence for progressive break-up of an Archean supercontinent: Geological Association of Canada/Mineralogical Association of Canada, Program with Abstracts, v. 19, p. A62.

LeCheminant, A.N., Heaman, L.M., van Breemen, O., Ernst, R.E., Baragar, W.R.A., & Buchan, K.L. (1996). Mafic magmatism, mantle roots, and kimberlites in the Slave craton. In: A.N. LeCheminant, Richardson, D.G., DiLabio, R.N.W., & Richardson, K.A. eds., *Searching for Diamonds in Canada*, Geological Survey of Canada, Open File **3228**, 161-169.

LeCheminant, A.N., Buchan, K.L., van Breemen, O., & Heaman, L.M. (1997). Paleoproterozoic continental break-up and reassembly: Evidence from 2.19 Ga diabase dyke swarms in the Slave and Western Churchill Provinces, Canada. *Geological Association of Canada/Mineralogical Association of Canada, Abstract Volume* **22**, p.A86.

Ludwig, K. R. (2003). ISOPLOT a plotting and regression program for radiogenic isotope data, version Ex/3.00.

Machado, N. (1990). Timing of collisional events in the Trans Hudson Orogen: Evidence from U-Pb geochronology for the New Québec Orogen, The Thompson belt, and the Reindeer Zone (Manitoba and Saskatchewan). In: Lewry, J.F. & Stauffer, M.R., eds., *The Early Proterozoic Trans-Hudson Orogen of North America*, Geological Survey of Canada Special Paper **37**, 433-441.

Machado, N., David, J., Scott, D.J., Lamothe, D., Philippe, S. & Gariépy, C. (1993). U-

Pb geochronology of the western Cape Smith Belt: New insights on the age of initial rifting and arc-magmatism. *Precambrian Research* **63**, 211-223.

Maier, W.D., Peltonen, P., Grantham, G., & Mänttari, I. (2003). A new 1.9 Ga age for the Trompsburg intrusion, South Africa. *Earth and Planetary Science Letters* **212**, 351-360.

Mallik, A.K. & Bishul, P.K. (1990). Isotopic ages, chemical characteristics and emplacement history of mafic dyke swarms in Kolar Gold Field, Karnataka. *Geological Survey of India Records* **123** (2), 21-22.

Mallikarjuna Rao, J., Bhattacharji, S., Rao, M.N., & Hermes, O.D. (1995). ^{40}Ar - ^{39}Ar Ages and Geochemical Characteristics of Dolerite Dykes Around the Proterozoic Cuddapah Basin, South India. In: Devaraju, T.C., ed., *Mafic Dyke Swarms of Peninsular India*, Geological Society of India Memoir **33**, 307-328.

Manikyamba, C., Naqvi, S.M., Ram Mohan, M., & Gnaneshwar Rao, T. (2004). Gold mineralisation and alteration of Penakacherla schist belt, India, constraints on Archaean subduction and fluid processes. *Ore Geology Reviews* **24**, 199-227.

Manyeruke, T.D., Blenkinsop, T.G., Buchholz, P., Love, D., Oberthür, T., Vetter, U.K., & Davis, D.W. (2004). The age and petrology of the Chimbadzi Hill Intrusion, NW Zimbabwe: first evidence for early Paleoproterozoic magmatism in Zimbabwe. *Journal of African Earth Sciences* **40**, 281-292.

Martin, D.M., Li, Z.X., Nemchin, A.A., & Powell, C.M. (1998). A pre-2.2 Ga age for giant hematite ores of the Hamersley province, Australia. *Economic Geology* **93**, 1084-1090.

Meen, J.K., Rogers, J.J.W., & Fullagar, P.D. (1992). Lead isotopic compositions of the Western Dharwar Craton, southern India: Evidence for distinct Middle Archean terranes in a Late Archean craton. *Geochimica et Cosmochimica Acta* **56**, 2455-2470.

Mertanen, S., Halls, H.C., Vuollo, J.I., Pesonen, L.J., & Stepanov, V.S. (1999). Paleomagnetism of 2.44 Ga mafic dykes in Russian Karelia, eastern Fennoscandian Shield – implications for continental reconstructions. *Precambrian Research* **98**, 197-221.

Miller, J.S., Santosh, M., Pressley, R.A., Clements, A.S., & Rogers, J.J.W. (1996). A Pan-African thermal event in south India. *Journal of Southeast Asian Earth Sciences* **14**, 127-136.

Mishra, D.C., Baburao, V., Laxman, G., Rao, M.B.S.V., & Rao, M.B.S.V. (1987). Three-dimensional structural model of Cuddapah basin and adjacent eastern part from geophysical studies. In: Radhakrishna, B.P., ed., *Purana basins of peninsular India (Middle to Late Proterozoic)*, Geological Society of India Memoir **6**, 311-329.

Mishra, D.C., Singh, B., Tiwari, V.M., Gupta, S.B., & Rao, M.B.S.V. (2000). Two cases of continental collisions and related tectonics during the Proterozoic period in India – insights from gravity modelling constrained by seismic and magnetotelluric studies. *Precambrian Research* **99**, 149-169.

Mishra, S., Deomurari, M.P., Wiedenbeck, M., Goswami, J.N., Ray, S., & Saha, A.K. (1999). $^{207}\text{Pb}/^{206}\text{Pb}$ zircon ages and the evolution of the Singhbhum Craton, eastern India: an ion microprobe study. *Precambrian Research* **93**, 139-151.

Mondal, M.E.A., Goswami, J.N., Deomurari, M.P., & Sharma, K.K. (2002). Ion microprobe $^{207}\text{Pb}/^{206}\text{Pb}$ ages of zircons from the Bundelkhand massif, northern India: implications for crustal evolution of the Bundelkhand-Aravalli protocontinent. *Precambrian Research* **117**, 85-100.

Moyen, J.-F., Martin, H., & Jayananda, M. (2001). Multi-element geochemical modelling of crust-mantle interactions during late-Archean crustal growth: the Closepet granite (South India). *Precambrian Research* **112**, 87-105.

Moyen, J.-F., Nédélec, A., Martin, H., & Jayananda, M. (2003). Syntectonic granite emplacement at different structural levels: the Closepet granite, South India. *Journal of Structural Geology* **25**, 611-631.

Mueller, S.G., Krapez, B., Fletcher, I.R., & Barley, M.E. (2004). New geochronological constraints on the tectonic evolution of the Hamersley and Ashburton provinces in Western Australia between 2.4 and 2.0 Ga and the tectonic setting of iron-ore formation. *Geological Society of America, Abstracts with Programs* **36**, 340.

Mueller, W.U., Corcoran, P.L., & Pickett, C. (2005). Mesoarchean Continental Break-up: Evolution and Inferences from the >2.8 Ga Slave Craton-Cover Succession, Canada. *The Journal of Geology* **113**, 23-45.

Murthy, N.G.K. (1987). Mafic dyke swarms of the Indian shield. In: Halls, H.C. & Fahrig, W.F., eds., *Mafic Dyke Swarms, Geological Association of Canada Special Paper* **34**, 393-400.

Murthy, N.G.K. (1995). Proterozoic mafic dykes in southern peninsular India: A review. In: Devaraju, T.C., ed., *Mafic Dyke Swarms of Peninsular India, Geological Society of India Memoir* **33**, 81-98.

Murty, Y.G.K., Babu Rao, V., Guptasarma, D., Rao, J.M., Rao, M.N., & Bhattacharji, S. (1987). Tectonic, petrochemical and geophysical studies of mafic dyke swarms around the Proterozoic Cuddapah basin, South India. In: Halls, H.C. & Fahrig, W.F., eds., *Mafic Dyke Swarms, Geological Association of Canada Special Paper* **34**, p.303-316.

Nagaraja Rao, B.K., Rajurkar, S.T., Ramalingaswamy, G., & Ravindra Babu, B. (1987).

Stratigraphy, Structure and Evolution of the Cuddapah Basin. In: *Purāna Basins of Peninsular India (Middle to Late Proterozoic)*, Geological Society of India Memoir **6**, 33-86.

Nakamura, N. (1974). Determination of REE, Ba, Fe, Mg, Na and K in carbonaceous and ordinary chondrites. *Geochimica et Cosmochimica Acta* **38**, 757-775.

Naqvi, S.M. (1981). The oldest supracrustals of the Dharwar craton, India. *Journal of the Geological Society of India* **22**, 458-469.

Naqvi, S.M. & Rogers, J.J.W. (1987). Precambrian Geology of India, *Oxford monographs on geology and geophysics* **6**, 233p.

Nemchin, A.A. & Pidgeon, R.T. (1998). Precise conventional and SHRIMP baddeleyite U-Pb age for the Binneringie Dyke, near Narrogin, Western Australia. *Australian Journal of Earth Sciences* **45**, 673-675.

Noble, S.R. & Lightfoot, P.C. (1992). U-Pb baddeleyite ages of the Kerns and Triangle Mountain intrusions, Nipissing Diabase, Ontario. *Canadian Journal of Earth Sciences* **29**, 1424-1429.

Norcross, C., Davis, D.W., Spooner, E.T.C., & Rust, A. (2000). U-Pb and Pb-Pb age constraints on Paleoproterozoic magmatism, deformation and gold mineralization in the Omai area, Guyana Shield. *Precambrian Research* **102**, 69-86.

Nutman, A.P., Chadwick, B., Ramakrishnan, M., & Viswanatha, M.N. (1992). SHRIMP U-Pb ages of Detrital Zircon in Sargur Supracrustal Rocks in Western Karnataka, Southern India. *Journal of the Geological Society of India* **39**, 367-374.

Nutman, A.P., Hagiya, H. & Maruyama, S. (1995). SHRIMP U-Pb single zircon geochronology of a Proterozoic mafic dyke, Isukasia, southern West Greenland. *Bulletin of the Geological Society of Denmark* **42**, 17-22.

Nutman, A.P., Chadwick, B., Krishna Rao, B., & Vasudev, V.N. (1996). SHRIMP U/Pb Zircon Ages of Acid Volcanic Rocks in the Chitradurga and Sandur Groups, and Granites Adjacent to the Sandur Schist Belt, Karnataka. *Journal of the Geological Society of India* **47**, 153-164.

Nutman, A.P., Kalsbeek, F., Marker, M., van Gool, J.A.M., & Bridgwater, D. (1999). U-Pb zircon ages of Kangâmiut dykes and detrital zircons in metasediments in the Paleoproterozoic Nagssugtoqidian Orogen (West Greenland) Clues to the pre-collisional history of the orogen. *Precambrian Research* **93**, 87-104.

Oberthür, T., Davis, D.W., Blenkinsop, T.G., & Höhndorf, A. (2002). Precise U-Pb mineral ages, Rb-Sr and Sm-Nd systematics for the Great Dyke, Zimbabwe-constraints on late Archean events in the Zimbabwe craton and Limpopo belt. *Precambrian*

Research **113**, 293-305.

Padmukari, V.M. & Dayal, A.M. (1987). Geochronological studies of some mafic dykes around the Cuddapah basin, south India. In: *Radhakrishna, B.P., ed., Purana basins of peninsular India (Middle to Late Proterozoic), Geological Society of India Memoir* **6**, 369-373.

Pandey, B.K., Gupta, J.N., Sarma, K.J., & Sastry, C.A. (1997). Sm-Nd, Pb-Pb and Rb-Sr geochronology and petrogenesis of the mafic dyke swarm of Mahbubnagar, South India: implications for Paleoproterozoic crustal evolution of the Eastern Dharwar Craton. *Precambrian Research* **84**, 181-196.

Parrish, R.R. (1989). U-Pb geochronology of the Cape Smith Belt and Sugluk block, northern Québec. *Geoscience Canada* **16**, 126-130.

Paul, D.K., Rex, D.C., & Harris, P.G. (1975). Chemical Characteristics and K-Ar Ages of Indian Kimberlite. *Geological Society of America Bulletin* **86**, 364-366.

Pearce, J.A. (1982). Trace element characteristics of lavas from destructive plate boundaries. In: *Thorpe, R.S. (ed.), Andesites; orogenic andesites and related rocks*. John Wiley & Sons, Chichester, United Kingdom. 525-548.

Pehrsson, S.J., van Breemen, O., & Hanmer, S. (1993). Ages of diabase dyke intrusions, Great Slave Lake shear zone, Northwest Territories. In: *Radiogenic Age and Isotopic Studies: Report 7; Geological Survey of Canada, Paper* **93-2**, 23-28.

Pekkarinen, L.J. & Lukkarinen, H. (1991). Paleoproterozoic volcanism in the Kiihtelysvaara-Tohmajärvi district, eastern Finland. *Geological Survey of Finland Bulletin* **357**, 30p.

Perttunen, V. (1987). Mafic dykes in the northwestern part of the Pudasjärvi granite gneiss complex (in Finnish). In: *Aro, K. & Laitakari, I., eds., Diabases and other mafic dyke rocks in Finland: Geological Survey of Finland, Report of Investigation* **76**, 29-34.

Pesonen, L.J., Elming, S.-Å., Mertanen, S., Pisarevsky, S., D'Agrella-Filho, M.S., Meert, J.G., Schmidt, P.W., Abrahamsen, N. & Bylund, G. (2003). Paleomagnetic configuration of continents during the Proterozoic. *Tectonophysics* **375**, 289-324.

Peucat, J.J., Mahabaleswar, B., & Jayananda, M. (1991). Age of younger tonalitic magmatism and granulitic metamorphism in the South Indian transition zone (Krishnagiri area); comparison with older Peninsular gneisses from the Gorur-Hassan area. *Journal of Metamorphic Geology* **11**, 879-888.

Peucat, J.J., Mahabaleswar, B., & Jayananda, M. (1993). Age of younger tonalitic magmatism and granulitic metamorphism in the South Indian transition zone (Krishnagiri area); comparison with older Peninsular gneisses from the Gorur-Hassan

area. *Journal of Metamorphic Geology* **11**, 879-888.

Peucat, J.J., Bouhallier, H., Fanning, C.M., & Jayananda, M. (1995). Age of the Holenarsipur Greenstone Belt, Relationships with the Surrounding Gneisses (Karnataka, South India). *The Journal of Geology* **103**, 701-710.

Piper, J.D.A. (1987). *Palaeomagnetism and the Continental Crust*. Open University Press, England. 434p.

Piper, J.D.A., Basu Mallik, S., Bandyopadhyay, G., Mondal, S., & Das, A.K. (2003). Paleomagnetic and rock magnetic study of a deeply exposed continental section in the Charnockite Belt of southern India: implications to crustal magnetisation and paleoproterozoic continental nuclei. *Precambrian Research* **121**, 185-219.

Prasad, J.N., Satyanarayana, K.V.V., & Gawali, P.B. (1999). Paleomagnetic and Low-Field AMS Studies of Proterozoic Dykes and their Basement Rocks Around Harohalli, South India. *Journal of the Geological Society of India* **54**, 57-67.

Premo, W.R. & van Schmus, W.R. (1989). Zircon geochronology of Precambrian rocks in southeastern Wyoming and northern Colorado. In: Grambling, J.A. & Tewksbury, B.J., eds., *Proterozoic geology of the southern Rocky Mountains: Geological Society of America Special Paper* **235**, 13-32.

Puchtel, I.S., Arndt, N.T., Hofmann, A.W., Haase, K.M., Kröner, A., Kulikov, V.S., Kulikova, V.V., Garbe-Schönberg, C.-D., & Nemchin, A.A. (1998). Petrology of mafic lavas within the Onega plateau, central Karelia: Evidence for 2.0 Ga plume-related continental crustal growth in the Baltic Shield. *Contributions to Mineralogy and Petrology* **130**, 134-153.

Radhakrishna, B.P. & Vaidyanadhan, R. (1997). *Geology of Karnataka*. Geological Society of India, Bangalore, 353p.

Radhakrishna, T., Dallmeyer, R.D., & Joseph, M. (1994). Paleomagnetism and $^{36}\text{Ar}/^{40}\text{Ar}$ vs $^{39}\text{Ar}/^{40}\text{Ar}$ isotope correlation ages of dyke swarms in central Kerala, India: tectonic implications. *Earth and Planetary Science Letters* **121**, 213-226.

Radhakrishna, T. & Joseph, M. (1996). Proterozoic palaeomagnetism of the mafic dyke swarms in the high-grade region of southern India. *Precambrian Research* **76**, 31-46.

Radhakrishna, T. & Mathew, J. (1996). Late Precambrian (850-800 Ma) paleomagnetic pole for the south Indian shield from the Harohalli alkaline dykes: geotectonic implications for Gondwana reconstructions. *Precambrian Research* **80**, 77-87.

Radhakrishna, T. & Joseph, M. (1998). Geochemistry and petrogenesis of the Proterozoic dykes in Tamil Nadu, southern India: another example of the Archaean lithospheric mantle source. *International Journal of Earth Sciences* **87**, 268-282.

- Radhakrishna, T., Maluski, H., Mitchell, J.G., & Joseph, M. (1999). $^{40}\text{Ar}/^{39}\text{Ar}$ and K/Ar geochronology of the dykes from the south Indian granulite terrain. *Tectonophysics* **304**, 109-129.
- Radhakrishna, T., Joseph, M., Krishnendu, N.R., & Balasubramonian, G. (2003). Paleomagnetism of Mafic Dykes in Dharwar Craton: Possible Geodynamic Implications. In: Ramakrishnan, M., ed., *Tectonics of Southern Granulite Terrain, Geological Society of India Memoir* **50**, 193-224.
- Ramam, P.K. & Murty, V.N. (1997). *Geology of Andhra Pradesh. Geological Society of India, Bangalore*, 245 p.
- Rao, J.M., Rao, G.V.S.P., & Patil, S.K. (1990). Geochemical and paleomagnetic studies on the Middle Proterozoic Karimnagar mafic dyke swarm, India. In: Parker, Rickwood & Tucker, eds., *Mafic Dykes and Emplacement Mechanisms*, 373-382.
- Rasmussen, B. & Fletcher, I.R. (2004). Zirconolite: A new U-Pb geochronometer for mafic igneous rocks. *Geology* **32**(9), 785-788.
- Rogers, J.J.W. (1986). The Dharwar craton and the assembly of peninsular India. *Journal of Geology* **94**, 129-143.
- Rogers, J.J.W. (1988). The Arsikere granite of southern India: magmatism and metamorphism in a previously depleted crust. *Chemical Geology* **67**, 155-163.
- Rogers, J.J.W. (1996). A history of continents in the past three billion years. *The Journal of Geology* **104**, 91-107.
- Rogers, J.J.W., Callahan, E.J., Dennen, K.O., Fullagar, P.D., Stroh, P.T., & Wood, L.F. (1986). Chemical evolution of Peninsular gneiss in the western Dharwar craton, southern India. *Journal of Geology* **94**, 233-246.
- Rogers, J.J.W & Santosh, M. (2002). Configuration of Columbia, a Mesoproterozoic supercontinent. *Gondwana Research* **5**, 5-22.
- Russell, J., Chadwick, B., Krishna Rao, B., & Vasudev, V.N. (1996). Whole-rock Pb/Pb isotopic ages of Late Archean limestones, Karnataka, India. *Precambrian Research* **78**, 261-272.
- Santos, J.O.S., Hartmann, L.A., McNaughton, N.J., & Fletcher, I.R. (2002). Timing of mafic magmatism in the Tapajós Province (Brazil) and implications for the evolution of the Amazon Craton: evidence from baddeleyite and zircon U-Pb SHRIMP geochronology. *Journal of South American Earth Sciences* **15**, 409-429.
- Sarkar, A. & Mallik, A.K. (1995). Geochronology and Geochemistry of Precambrian

Mafic Dykes from Kolar Gold Field, Karnataka. In: Devaraju, T.C., ed., *Mafic Dyke Swarms of Peninsular India, Geological Society of India Memoir* **33**, 307-328.

Sarkar, G., Corfu, F., Paul, D.K., McNaughton, N.J., Gupta, S.N., & Bishui, P.K. (1993). Early Archean crust in Bastar craton, central India – a geochemical and isotopic study. *Precambrian Research* **62**, 127-137.

Saunders, A.D., Storey, M., Kent, R., & Norry, M.J. (1992). Consequences of plum–lithosphere interactions. In: Storey, B.C., Alabaster, T., Pankhurst, R.J., eds., *Magmatism and the Causes of Continental Break-up, Geological Society of London Special Publication* **68**, 41–60.

Scott, D.J. (1995). U-Pb geochronology of the Nain craton on the eastern margin of the Torngat Orogen, Labrador. *Canadian Journal of Earth Sciences* **32**, 1859-1869.

Sheraton, J.W. & Black, L.P. (1981). Geochemistry and Geochronology of Proterozoic Tholeiite Dykes of East Antarctica: Evidence for Mantle Metasomatism. *Contributions to Mineralogy and Petrology* **78**, 305-317.

Silvennoinen, A. 1991. Kuusamon ja Rukatunturin kartta-alueiden kallioperä. Kallioperäkarttojen selitykset, lehdet 4524+4542 ja 4613: Suomen geologinen kartta 1:100000. Pre-Quaternary rocks of the Kuusamo and Rukatunturi map-sheet areas. *Geological Survey of Finland*, 63p.

Smeeth, W.F. (1915). Geological map of Mysore (1 inch = 8 miles). Mysore Geological Department, Bangalore.

Söderlund, U. & Johansson, L. (2002). A simple way to extract baddeleyite (ZrO₂). *Geochemistry Geophysics Geosystems* **3**(2), 1-7.

Söderlund, U., Patchett, P.J., Vervoort, J.D., & Isachsen, C.E. (2004). The ¹⁷⁶Lu decay constant determined by Lu-Hf and U-Pb isotope systematics of Precambrian mafic intrusions. *Earth and Planetary Science Letters* **219**, 311-324.

Stacey, J. S., & Kramers, J. D. (1975). Approximation of terrestrial lead isotope evolution by a two-stage model. *Earth and Planetary Science Letters* **29**, 207-221.

St-Onge, M.R., Lucas, S.B., & Scott, D.J. (1997). The Ungava orogen and the Cape Smith thrust belt. In: De Wit, M. & Ashwal, L.D., eds., *Greenstone Belts*. Oxford, Clarendon Press. 772-780.

Taylor, P.N., Chadwick, B., Moor bath, S., Ramakrishnan, M., & Viswanatha, M.N. (1984). Petrography, chemistry and isotopic ages of Peninsular gneiss, Dharwar acid volcanic rocks and the Chitradurga granite with special reference to the Late Archean evolution of the Karnataka craton, southern India. *Precambrian Research* **23**, 349-375.

- Tewari, H.C. & Rao, V.K. (1987). A high velocity intrusive body in the upper crust in the southwestern Cuddapah basin as delineated by deep seismic soundings and gravity modelling. In: Radhakrishna, B.P., ed., *Purana basins of peninsular India (Middle to Late Proterozoic)*, Geological Society of India Memoir 6, 349-356.
- Trendall, A.F., de Laeter, J.R., Nelson, D.R., & Mukhopadhyay, D. (1997a). A Precise Zircon U-Pb Age for the Base of the BIF of the Mulaingiri Formation, (Bababudan Group, Dharwar Supergroup) of the Karnataka Craton. *Journal of the Geological Society of India* 50, 161-170.
- Trendall, A.F., de Laeter, J.R., Nelson, D.R., & Bhaskar Rao, Y.J. (1997b). Further zircon U-Pb age for the Daginkatte Formation, Dharwar Supergroup, Karnataka Craton. *Journal of the Geological Society of India* 50, 25-30.
- Tyrväinen, A. (1983). Sodankylän ja Sattasen kartta-alueiden kallioperä. Kallioperäkarttojen selitykset, lehdet 3713 ja 3714: Suomen geologinen kartta 1:100000. Pre-Quaternary rocks of the Sodankylä and Sattanen map-sheet areas. *Geological Survey of Finland*, 59p.
- van Breemen, O., Davis, W.J., & King, J.E. (1992). Temporal distribution of granitoid plutonic rocks in the Archean Slave Province, northwest Canadian Shield. *Canadian Journal of Earth Sciences* 29, 2186-2199.
- Vasudev, V.N., Chadwick, B., Nutman, A.P., & Hegde, G.V. (2000). Rapid Development of the Late Archaean Hutti Schist Belt, Northern Karnataka: Implications of New Field Data and SHRIMP U/Pb Zircon Ages. *Journal of the Geological Society of India* 55, 529-540.
- Vijayam, E. (1968). An interesting dyke near Archean-Cuddapah boundary Veldurthi, Kurnool District, Andhra Pradesh. *Current Science* 37, 15.
- Viswanatha, M.N., Ramakrishnan, M., & Swami Nath, J. (1982). Angular unconformity between Sargur and Dharwar supracrustals in Sigegudda, Karnataka craton, south India. *Journal of the Geological Society of India* 23, 85-89.
- Vuollo, J., Piirainen, T., & Huhma, H. (1992). Two Early Proterozoic tholeiitic diabase dyke swarms in the Koli-Kaltimo area, Eastern Finland – their geological significance. *Geological Survey of Finland Bulletin* 363, 32p.
- Vuollo, J.I., V.M. Nykänen, Liipo, J.P., & Piirainen. (1995). Paleoproterozoic mafic dyke swarms in the Eastern Fennoscandian Shield, Finland: A review. In: Baer & Heimann, eds., *Physics and Chemistry of Dykes*, 179-192.
- Walker, R.J., Shirey, S.B., Hanson, G.N., Rajamani, V., & Horan, M.F. (1989). Re-Os, Rb-Sr, and O isotopic systematics of the Archean Kolar schist belt, Karnataka, India. *Geochimica et Cosmochimica Acta* 53, 3005-3013.

- Wiedenbeck, M. & Goswami, J.N. (1994). High precision $^{207}\text{Pb}/^{206}\text{Pb}$ zircon geochronology using a small ion microprobe. *Geochimica et Cosmochimica Acta* **58**, 2135-2141.
- Wilkinson, L., Kjarsgaard, B.A., LeCheminant, A.N., & Harris, J. (2001). Diabase dyke swarms in the Lac de Gras area, Northwest Territories, and their significance to kimberlite exploration: initial results. *Current Research, Geological Survey of Canada* **2001-C8**, 24p.
- Williams, H., Hoffman, P.F., Lewry, J.F., Monger, J.W.H., & Rivers, T. (1991). Anatomy of North America: Thematic geologic portrayals of the continent. In: Hilde, T.W.G. and Carlson, R.L., eds., *Silver anniversary of plate tectonics: Tectonophysics* **187**, 117-134.
- Wingate, M.T.D., Campbell, I.H., Compston, W., Gibson, & G.M. (1998). Ion microprobe U-Pb ages for Neoproterozoic basaltic magmatism in south-central Australia and implications for the breakup of Rodinia. *Precambrian Research* **87**, 135-159.
- Wingate, M.T.D. & Compston, W. (2000). Crystal orientation effects during ion microprobe U-Pb analysis of baddeleyite. *Chemical Geology*, **168**, p. 75-97.
- Wingate, M.T.D., Giddings, J.W. (2000). Age and palaeomagnetism of the Mundine Well dyke swarm, Western Australia: implications for an Australia-Laurentia connection at 755 Ma. *Precambrian Research* **100**, 335-357.
- Yoder, H.S. & Tilley, C.E. (1962). Origin of Basalt Magmas: An Experimental Study of Natural and Synthetic Rock Systems. *Journal of Petrology* **3**, 342-532.
- Zachariah, J.K., Hanson, G.N., & Rajamani, V. (1995). Postcrystallization disturbance in the Neodymium and lead isotope systems of metabasalts from the Ramagiri schist belt, southern India. *Geochimica et Cosmochimica Acta* **59**, 3189-3203.
- Zhao, G., Cawood, P.A., Wilde, S., & Sun, M. (2002). Review of global 2.1-1.8 Ga orogens: implications for a pre-Rodinia supercontinent. *Earth Science Reviews* **59**, 125-162.
- Zhao, G., Sun, M., & Wilde, S. (2003). Correlations between the eastern block of the North China craton and the South Indian block of the Indian shield: an Archean to Paleoproterozoic link. *Precambrian Research* **122**, 201-233.

Table 4-1. Major and trace element geochemistry for mafic dykes of the Dharwar craton dated by U-Pb in this study.

Sample ID:	JEF-99-1	JEF-99-6	JEF-99-7	JEF-99-11	JEF-00-55	JEF-00-43	JEF-00-1
Dyke trend:	E-W	E-W	E-W	NW-SE	N-S	E-W	NW-SE
Latitude:	12°38.92' N	14°08.06' N	14°15.06' N	13°29.29' N	13°40.20' N	17°08.63' N	15°19.49' N
Longitude:	77°29.80' E	77°36.03' E	77°37.33' E	78°49.86' E	78°25.78' E	79°27.50' E	74°36.06' E
wt%							
SiO ₂	53.28	52.45	53.06	49.42	49.01	49.19	49.09
TiO ₂	0.926	0.549	0.754	0.507	1.603	1.898	1.637
Al ₂ O ₃	10.55	11.84	8.08	9.79	13.82	17.33	11.98
Fe ₂ O ₃ *	12.73	10.53	11.30	11.44	14.93	14.10	16.84
MnO	0.165	0.166	0.167	0.180	0.206	0.174	0.282
MgO	9.13	10.72	11.07	15.51	5.33	2.77	5.45
CaO	9.10	9.98	10.64	9.43	9.32	10.36	8.67
Na ₂ O	2.92	1.64	1.97	1.08	2.39	2.62	2.56
K ₂ O	1.05	0.49	1.09	0.45	0.90	0.30	1.16
P ₂ O ₅	0.14	0.08	0.13	0.06	0.23	0.24	0.15
LOI	-0.07	0.39	0.52	1.23	0.86	0.12	1.38
TOTAL	99.94	98.84	98.79	99.08	98.62	99.11	99.19
ppm							
V	225	222	170	187	337	229	289
Cr	469	599	591	1,220	48	22	64
Co	76	75	61	67	55	60	53
Ni	137	131	120	298	47	41	38
Cu	119	79	72	67	67	354	107
Zn	92	78	68	77	102	110	193
Ga	11	10	8	8	14	20	14
Ge	1.3	1.4	1.2	1.0	1.0	1.2	1.2
Rb	30	18	30	25	20	8	54
Sr	462	144	232	88	229	138	340
Y	12.6	14.1	11.5	11.4	24.0	43.2	33.7
Zr	72	48	63	40	96	158	99
Nb	4.9	2.7	3.3	1.9	4.9	6.2	4.4
Sn	4	3	3	3	3	4	3
Cs	1.1	1.1	1.6	2.0	0.9	0.3	0.6
Ba	400	164	327	66	342	97	102
La	9.59	5.06	9.31	4.42	11.8	8.42	5.81
Ce	19.9	10.7	19.0	9.02	25.0	20.4	14.3
Pr	2.45	1.32	2.26	1.09	3.12	2.94	2.04
Nd	10.4	5.79	9.46	4.79	14.0	14.8	10.9
Sm	2.44	1.51	2.20	1.27	3.55	4.57	3.41
Eu	0.814	0.516	0.666	0.408	1.19	1.50	1.14
Gd	2.41	1.83	2.19	1.49	3.79	6.00	4.40
Tb	0.39	0.34	0.35	0.27	0.65	1.09	0.84
Dy	2.11	2.14	1.98	1.67	3.90	6.60	5.08
Ho	0.41	0.45	0.38	0.35	0.78	1.35	1.05
Er	1.14	1.37	1.05	1.07	2.26	4.04	3.30
Tm	0.155	0.203	0.149	0.157	0.333	0.597	0.494
Yb	0.95	1.27	0.90	0.99	2.02	3.64	3.05
Lu	0.145	0.201	0.135	0.148	0.310	0.551	0.475
Hf	1.8	1.2	1.5	1.0	2.4	3.9	2.6
Ta	0.78	0.74	0.66	0.38	0.61	0.88	0.53
W	260	323	239	170	191	267	141
Tl	0.20	0.11	0.23	0.24	0.13	0.06	0.29
Th	2.38	1.42	2.89	1.30	1.69	1.16	1.01
U	0.73	0.43	0.85	0.38	0.39	0.30	0.26

(* the Fe₂O₃ represents total Fe-oxide and has not been adjusted for FeO)

Table 4-2. U-Pb IDTIMS baddeleyite/zircon results for mafic dykes of the Dharwar craton.

Fraction #	Description of material analysed	Weight (µg)	Concentrations (ppm)				TCPb (pg)	Isotopic Ratios				Apparent Ages (Ma)			%Disc.
			U	Model Th	Pb	Model Th/U		²⁰⁶ Pb/ ²⁰⁴ Pb	²⁰⁶ Pb/ ²³⁸ U	²⁰⁷ Pb/ ²³⁵ U	²⁰⁷ Pb/ ²⁰⁶ Pb	²⁰⁶ Pb/ ²³⁸ U	²⁰⁷ Pb/ ²³⁵ U	²⁰⁷ Pb/ ²⁰⁶ Pb	
<i>JEF-99-1 Harohalli dyke (12° 38.92' N, 77° 29.80' E)</i>															
1	B, euh/euh-fr, tan, IF-1.00A/15°nm, MIH [20]	4.6	2278	63	997	0.028	23.5	12230	0.43721±82	9.12570±1850	0.15138±10	2338.1±3.7	2350.7±1.9	2361.6±1.1	1.18
2	B, euh-fr, tan, FF-1.79A/15°m [8]	2.7	1833	27	648	0.015	10.8	10217	0.35430±68	7.40226±1549	0.15153±9	1955.1±3.2	2161.2±1.9	2363.2±1.0	19.99
3	B, euh-fr, tan, str, FF-1.79A/15°m [5]	1.3	1084	24	474	0.022	9.3	4145	0.43418±76	9.08619±1781	0.15178±9	2324.5±3.4	2346.7±1.8	2366.1±1.0	2.09
4	B, euh-fr, tan, str, FF-1.79A/15°m [7]	1.0	4999	95	2197	0.019	5.7	24446	0.44183±82	9.24153±1730	0.15170±6	2358.8±3.7	2362.2±1.7	2365.2±0.6	0.32
5	B, euh, tan, str, FF-1.79A/15°nm, abr [1]	0.2	3369	66	1587	0.020	20.0	959	0.44826±55	9.37683±1258	0.15171±10	2387.5±2.4	2375.6±1.3	2365.3±1.2	-1.12
6	B, euh, tan, str, FF-1.79A/15°m, abr [6]	1.4	2553	37	1140	0.014	11.8	8475	0.44640±50	9.37550±1057	0.15233±3	2379.2±2.2	2375.4±1.1	2372.2±0.4	-0.35
<i>JEF-99-6 Penikonda dyke (14° 08.06' N, 77° 36.03' E)</i>															
7	B, euh-fr, lt-tan, str, S+J [33]	1.1*	1471	121	661	0.082	4.2	4900	0.44053±62	9.22040±1266	0.15180±8	2353.0±2.8	2360.1±1.3	2366.3±0.9	0.67
8	B, euh-fr, lt-tan, str, S+J [22]	0.7*	909	64	414	0.070	3.4	2259	0.44386±80	9.36643±1906	0.15305±16	2367.9±3.6	2374.5±1.9	2380.3±1.8	0.62
9	B, euh-fr, lt-tan, S+J [12]	0.4*	1408	102	646	0.073	2.8	1420	0.44422±105	9.28938±2347	0.15167±12	2369.5±4.7	2367.0±2.4	2364.8±1.4	-0.24
<i>JEF-99-7 Chennekottapalle dyke (14° 15.06' N, 77° 37.33' E)</i>															
10	B, euh-fr, lt-tan, str, S+J [7]	0.2*	422	34	178	0.081	22.1	514	0.41791±62	8.74235±1515	0.15172±18	2251.0±2.8	2311.5±1.8	2365.4±2.1	5.73
11	B, euh/euh-fr, lt-tan, str, S+J [38]	1.3*	3524	117	1550	0.033	4.4	8913	0.43843±116	9.17932±2404	0.15185±7	2343.6±5.2	2356.1±2.4	2366.8±0.8	1.17
12	B, euh/euh-fr, lt-tan, str, S+J [122]	4.1*	7922	365	3492	0.046	10.5	20759	0.43892±63	9.19655±1319	0.15196±3	2345.8±2.8	2357.8±1.3	2368.1±0.4	1.12
<i>JEF-00-1 Dandeli dyke (15° 19.49' N, 74° 36.06' E)</i>															
13	Z, cl, euh, elon, str, yp, FF-1.4A/15°m [5]	8.2	1030	798	271	0.775	269.5	366	0.17909±29	2.69957±680	0.10932±24	1062.0±1.6	1328.3±2.2	1788.2±4.0	43.98
14	B, tan, min-zc, FF-1.4A/15°m [8]	8.2	445	75	173	0.168	18.3	4728	0.37743±51	7.05571±931	0.13558±6	2064.3±2.4	2118.5±1.2	2171.5±0.7	5.77
15	B, euh, tan, str, FF-1.8A/15°m [3]	1.5	301	8	121	0.027	3.9	2927	0.40344±110	7.56931±2108	0.13607±8	2184.9±5.0	2181.2±2.5	2177.8±1.0	-0.38
16	B, euh, tan, str, FF-1.4A/15°m [15]	10.1	406	37	159	0.091	18.1	5857	0.38879±44	7.28517±827	0.13590±4	2117.2±2.0	2147.0±1.0	2175.6±0.5	3.15
17	Z, cls/vlp, subh/euh, elon, cl, FF-1.4A/15°m [13]	13.4	719	590	197	0.821	23.8	5979	0.22573±26	3.71905±417	0.11950±4	1312.1±1.3	1575.5±0.9	1948.7±0.6	36.05
18	B, euh, str, tan, FF-1.4A/15°m, abr [11]	4.2	408	18	161	0.045	4.8	8964	0.39741±78	7.46263±1465	0.13619±3	2157.1±3.6	2168.5±1.8	2179.3±0.4	1.20
19	B, euh, str, tan, FF-1.8A/10°m, abr [7]	2.5	533	14	213	0.027	3.9	8706	0.40387±54	7.59043±1007	0.13631±5	2186.9±2.5	2183.7±1.2	2180.8±0.6	-0.33
<i>JEF-00-43 Bandepalem dyke (17° 08.63' N, 79° 27.50' E)</i>															
20	Z, cl, cls, skel, str, IF-0.75A/15°nm, MIH [6]	3.8	227	297	102	1.307	11.6	1582	0.33491±43	6.10390±848	0.13218±7	1862.1±2.1	1990.8±1.3	2127.2±0.9	14.33
21	B, subh, lt-tan, IF-0.75A/15°nm, MIH [4]	1.2	78	20	33	0.249	7.3	341	0.40542±165	7.57471±4231	0.13551±50	2194.0±7.5	2181.9±5.2	2170.5±6.5	-1.27
22	Z, anh, cls, skel, turb, IF-0.75A/15°nm, MIH [11]	7.1	402.52	454.67	144.77	1.13	15.81	3153	0.27752±36	4.87520±664	0.12741±4	1578.9±1.8	1798.0±1.2	2062.5±0.6	26.40
23	Z, skel, cls, cl, str, IF-0.75A/15°nm, MIH [12]	7.9	266.65	292.37	127.24	1.096	6.53	9026	0.37811±45	7.09129±814	0.13603±6	2067.4±2.1	2123.0±1.0	2177.3±0.8	5.90
24	B, subh, lt-tan, str, IF-0.75A/15°nm, MIH [3]	1.2	123.01	26.52	53.32	0.216	8.77	460	0.37465±101	6.95392±2277	0.13462±28	2051.3±4.7	2105.6±3.1	2159.1±3.6	5.83
25	Z, prn, cls, cl, IF-0.75A/15°nm, MIH [2]	3.2	160.15	138.53	47.08	0.865	4.24	2280	0.23615±34	4.03664±628	0.12397±10	1366.7±1.8	1641.6±1.3	2014.2±1.4	35.61
<i>JEF-99-11 Somala dyke (13° 29.29' N, 78° 49.86' E)</i>															
26	B, euh-fr, lt-tan, str, S+J [3]	0.1*	604	141	252	0.233	15.3	281	0.33612±83	6.25154±2458	0.13489±43	1868.0±4.0	2011.7±3.9	2162.6±5.5	15.68
27	B, euh-fr, lt-tan, S+J [6]	0.2*	507	72	220	0.142	6.1	1300	0.40958±74	7.82170±1572	0.13850±12	2213.0±3.4	2210.7±1.9	2208.6±1.5	-0.23
28	B, euh/euh-fr, str, lt-tan, S+J [6]	0.2*	680	95	277	0.140	7.7	1301	0.40225±58	7.62677±1162	0.13751±10	2179.4±2.7	2188.0±1.4	2196.1±1.2	0.90
<i>JEF-00-55 Kandlamadugu dyke (13° 40.20' N, 78° 25.78' E)</i>															
29	B, euh/euh-fr, lt-tan, str, S+J [8]	0.3*	124	22	52	0.180	2.1	2777	0.39977±110	7.64657±2431	0.13873±21	2168.0±5.1	2190.3±2.9	2211.4±2.6	2.31
30	B, euh/euh-fr, lt-tan, str, min-zc, S+J [7]	0.2*	392	73	185	0.185	13.4	415	0.40574±90	7.78483±2005	0.13915±24	2195.4±4.1	2206.5±2.5	2216.7±3.0	1.13
31	B, euh/euh-fr, str, lt-tan, S+J [21]	0.7*	791	106	327	0.134	3.7	2724	0.40260±54	7.67692±1078	0.13830±6	2181.0±1.5	2193.9±1.3	2206.0±0.8	1.34

Note: concentrations in green still need to be recalculated (i.e. may be misleading) because I've updated the estimates for the weights of these fractions with more accurate values.

Notes:

*estimated weights: along with corresponding concentrations of U, Th, and Pb, these weights are estimated to be accurate only to within -1 order of magnitude, and probably represent maximum estimates
The number of grains in each fraction is noted in parentheses [].

Th concentration estimated from abundance of ²⁰⁸Pb and corresponding ²⁰⁷Pb/²⁰⁶Pb ages

TCPb refers to the total amount of common Pb in picograms measured in the analysis

The values used in this study for the decay constants for ²³⁸U (1.55125 × 10⁻¹⁰a⁻¹) and ²³⁵U (9.8485 × 10⁻¹⁰a⁻¹) and the present day ²³⁸U/²³⁵U ratio of 137.88, are those determined by Jaffey et al. (1971).

Atomic ratios are corrected for fractionation, blank, spike and common Pb (Stacey and Kramers, 1975), except ²⁰⁶Pb/²⁰⁴Pb ratios which are corrected for fractionation and spike only

All errors quoted in this table are 1 sigma uncertainties

All analyses determined using a VG354

Abbreviations: abr - grains treated with air abrasion technique (Krogh, 1982); B - baddeleyite; cl - clear, transparent; cls - colourless; Disc. - discordancy; euh - euhedral blades; euh-fr - fragments of euhedral blades; IF or FF - Initial Frantz or Final Frantz, including conditions during operation of the Frantz isodynamic separator in A (amperes) and degree of side-tilt (°), where m denotes magnetic fraction and nm denotes non-magnetic fraction; lt-tan - light tan brown in colour; MIH - grains picked from Methyl Iodide heavy mineral concentrate; min-zc - minor zircon overgrowth; prn - prismatic; S+J - Isolation of baddeleyite by the water-based method of Söderlund and Johansson (2002); skel - skeletal; str - striated; subh - subhedral; tan - tan brown in colour; turb - turbidity observed; vlp - very light pink in colour; yp - faint yellow-pink in colour; Z - zircon

Table 4-3. Summary chart of available high precision U-Pb baddeleyite/zircon ages for Paleoproterozoic mafic magmatic events on Earth. Abbreviations: B-baddeleyite; Z-zircon; R-rutile; T-titanite.

Precambrian province	U-Pb Age	Error	Mineral	Name	Reference
Superior craton (North America)	2505.3	+2/1.3	B+Z	Ptarmigan	Buchan et al., 1998
	2488	12	B?	Mirond Lake - in Sask or Superior craton?	L.M.H. (unpublished data - presented at GSA 2004)
	2473	+16/-9	B	Matachewan	Heaman, 1997
	2470	?	?	Mistassini	Heaman, 1994
	2445.8	+2.9/-2.6	B+Z	Hearst	Heaman, 1997
	2408	3	Z	Du Chef	Krogh, 1994
	2229	+35/-20	B	Maguire	Buchan et al., 1998
	2219.4	+3.6/-3.5	B+R	Nipissing	Corfu and Andrews, 1986
	2217.8	+6/-3	B	Nipissing	J.K. Mortensen unpublished data referred to in Buchan et al. (1994)
	2217.2	4	B	Nipissing	Noble and Lightfoot, 1992
	2216	+8/-4	Z/B?	Senneterre	J.K. Mortensen unpublished data referred to in Buchan et al. (1996)
	2214.3	12.4	B	Senneterre	Buchan et al., 1993
	2209.7	0.8	B+Z	Klotz	Buchan et al., 1998
	2209.6	3.5	B	Nipissing	Noble and Lightfoot, 1992
	2171.6	1.2	B	Biscotasing	Halls and Davis, 2004
	2167.8	2.2	B	Biscotasing	Halls and Davis, 2004
	2166.7	1.4	B+Z	Biscotasing	Buchan et al., 1993
	2121	+14/-7	B	Marathon	Buchan et al., 1996
	2113.6	+17.2/-6.5	B	Marathon	Buchan et al., 1994, and reference therein
	2101.8	1.9	B	Marathon	Hamilton et al., 2002
	2101	1.6	B	Marathon	Hamilton et al., 2002
	2091	2	B+Z	Cauchon	Halls and Heaman, 2000
	2076.3	+5/-4	B+Z	Fort Frances	Buchan et al., 1996
	2072	3	Z	Birthday Rapids	Heaman and Corkery, 1996
	2069	1	B	Lac Esprit	Hamilton et al., 2001
	2038	+4/-2	Z	Korak	Machado et al., 1993
	1998.4	1.3	B+Z	Minto	Buchan et al., 1998
	1918	+9/-7	B+Z	Katimiq sill	Parrish, 1989
	1884	2	Z	Montagnais sill	Findlay et al., 1995
	1883.7	+1.7/-1.5	Z	Molson	Heaman et al., 1986
	1883	2	Z	Molson	Heaman et al., 1986
	1882.9	+1.5/-1.4	Z	Fox River	Heaman et al., 1986
	1877	+7/-4	Z	Molson	Halls and Heaman, 2000
	1874	3	?	Montagnais sill	Machado, 1990
	1870	4	Z	upper Chukotat Group volcanic	St.Onge et al., 1997
	1849.6	+3.4/-3.0	Z	Sudbury norite	Krogh et al., 1982
1849.4	+1.9/-1.8	Z	Sudbury norite	Krogh et al., 1982	

Table 4-3 cont'd. Summary chart of available high precision U-Pb baddeleyite/zircon ages for Paleoproterozoic mafic magmatic events on Earth. Abbreviations: B-baddeleyite; Z-zircon; R-rutile; T-titanite.

Precambrian province	U-Pb Age	Error	Mineral	Name	Reference
Slave craton (North America)	2230	??	B	Malley	LeCheminant and van Breemen, 1994
	2227.6	0.9	B	Malley	J.E.F. (unpublished data)
	2210	??	B	Mackay	LeCheminant and van Breemen, 1994
	2190	??	B	Dogrib	LeCheminant et al., 1997
	2181	2	B+Z	Duck Lake sill	Bleeker and Kamo, 2003
	2038	3	B	Hearne	Pehrsson et al., 1993
	2020-2030	??	B	Lac de Gras	LeCheminant and van Breemen, 1994
	1884	5.5	B	Germaine Lake dyke	Atkinson, 2004 (undergraduate thesis)
Rae/Hearne cratons (North America)	2497	2	B?	Kaminak	L.M.H (unpublished data)
	2190	??	B	Tulemalu	LeCheminant et al., 1997
	2111.2	0.6	B	Hurwitz	Heaman and LeCheminant, 1993
	1827	4	B	Sparrow	Bostock and van Breemen, 1992
Nain craton (North America/Greenland)	2235	2	B	Kikkertavak	Cadman et al., 1993
	2214	10	Z	Isukasia	Nutman et al., 1995
	2048	17	-	possible Kangamiut extension to east coast of greenland	Nutman and Bridgewater unpublished data referred to in Nutman et al., 1999
	2046	8	Z	Kangamiut	Nutman et al., 1999
	2036	5	Z	Kangamiut	Nutman et al., 1999
	1834	+7/-3	Z	Avayalik	Scott, 1995
Wyoming craton (North America)	2092	9	Z	gabbro intruding Snowy Pass Supergroup	Premo and van Schmus, 1989
	2011	1.2	Z	Kennedy diabase	Cox et al., 2000
	2005	7	Z	Kennedy peridotite	Cox et al., 2000
Kaapvaal craton (Southern Africa)	2058.9	0.8	T	Bushveld layered suite	Buick et al., 2001
	1927.7	0.5	B	Waterburg intrusive dolerite sill	Hanson et al., 2004b
	1927.3	0.7	B	Waterburg intrusive dolerite sill	Hanson et al., 2004b
	1927.1	0.7	B	Waterburg intrusive dolerite sill	Hanson et al., 2004b
	1928	4	Z	Hartley basalt	Cornell et al., 1998
	1915	6	Z	Trompsberg gabbro	Maier et al., 2003
	1878.8	0.5	B	Waterburg intrusive dolerite sill	Hanson et al., 2004b
	1873.7	0.8	B	Waterburg intrusive dolerite sill	Hanson et al., 2004b
1871.9	1.2	B	Waterburg intrusive dolerite sill	Hanson et al., 2004b	
Zimbabwe craton	2575.4	0.7	Z+R	Great Dyke	Oberthür et al., 2002
	2262	2	B	Chimbadzi Hill intrusion	Manyeruke et al., 2004
Amazon craton (South America)	1794	4	Z+B	Avanavero gabbro	Norcross et al., 2000
	1780	7	B	Crepori dolerite	Santos et al., 2002
Rio de la Plata craton (S.Am.)	1790	5	B	Uruguayan dyke swarm	Halls et al., 2001
Lewisian craton (Scotland)	2418	+7/-4	B	Scourie dyke	Heaman and Tarney, 1989
	~2.37	?	?	Scourie dyke	L.M.H. (unpublished data - presented at GSA 2004)
	1992	+3/-2	B	Scourie dyke	Heaman and Tarney, 1989

Table 4-3 cont'd. Summary chart of available high precision U-Pb baddeleyite/zircon ages for Paleoproterozoic mafic magmatic events on Earth. Abbreviations: B-baddeleyite; Z-zircon; R-rutile; T-titanite.

Precambrian province	U-Pb Age	Error	Mineral	Name	Reference
Fennoscandian craton (Finland/Russia)	2505.1	1.6	Z	Pechenga-Imandra-Varzuga belt	Amelin et al., 1995
	2504.4	1.5	Z	Pechenga-Imandra-Varzuga belt	Amelin et al., 1995
	2501.5	1.7	Z	Pechenga-Imandra-Varzuga belt	Amelin et al., 1995
	2449	1.1	Z	Sumi-Sariola belt	Amelin et al., 1995
	2446	5	B	Suoperä	unpublished data referred to in Mertanen et al., 1999
	2442.2	1.7	B	Pechenga-Imandra-Varzuga belt	Amelin et al., 1995
	2442.1	1.4	Z	Sumi-Sariola belt	Amelin et al., 1995
	2441.3	1.2	Z	Sumi-Sariola belt	Amelin et al., 1995
	2441	1.6	Z	Pechenga-Imandra-Varzuga belt	Amelin et al., 1995
	2220	11	-	Lapland karjalite sill	Tyrväinen, 1983
	2206	9	-	Kuusamo karjalite sill	Silvennoinen, 1991
	2192	-	Z	Kainuu schist belt intrusive metadiabase	Laajoki, 1991
	2176	-	Z	Kainuu schist belt intrusive metadiabase	Laajoki, 1991
	2150	-	Z	Kainuu schist belt intrusive metadiabase	Laajoki, 1991
	2138	-	Z	Kainuu schist belt intrusive metadiabase	Laajoki, 1991
	2114	14	-	Fe-tholeiitic dyke, Perä-Pohja	Perttunen, 1987
	2113	4	-	Fe-tholeiitic dyke, North Karelia	Pekkarinen and Lukkarinen, 1991
	2078	8	-	Fe-tholeiitic dyke, Kuusamo	Silvennoinen, 1991
	2070	-	Z	Kainuu schist belt intrusive metadiabase	Laajoki, 1991
	1976	9	Z	Onega lava	Puchtel et al., 1998
1970	5	Z	Pechenga lava	Puchtel et al., 1998	
1965	10	Z	Koli-Kaltimo	Vuollo et al., 1992	
Yilgarn craton (Australia)	2418	3	B	Binneringie dyke (Widgiemooltha swarm)	Nemchin and Pidgeon, 1998
	2410.3	2.1	B	Binneringie dyke (Widgiemooltha swarm)	Doehler and Heaman, 1998; French et al., 2002
	2410.6	+2.1/-1.6	B	Celebration dyke (Widgiemooltha swarm)	Doehler and Heaman, 1998
East Antarctic Shield	2241	4	Z	Vestfold Hills	Lanyon et al., 1993
	2238	7	Z	Vestfold Hills	Lanyon et al., 1993
	1754	16	Z	Vestfold Hills	Lanyon et al., 1993
North China craton	1769.1	2.5	B	Taihing dyke swarm	Halls et al., 2000
Pilbara craton (Australia)	2449	3	Z	Tuff in Weeli Wolli dolerites and basalts	Barley et al., 1997
	2210	-	B	Hammersley Intrusive sill	Mueller et al., 2004
	2209	15	Z	Cheela Springs volcanics	Martin et al., 1998
	2010	-	B	Hammersley Intrusive dyke	Mueller et al., 2004
Bastar craton (India)	1891.1	0.9	B	BD2 dyke swarm, Southern Bastar craton	Chapter 3, this thesis
	1883	1.4	B+Z	BD2 dyke swarm, Southern Bastar craton	Chapter 3, this thesis
Dharwar craton (India)	2368.6	1.3	B	Bangalore dyke swarm	This study
	2365.9	1.5	B	Bangalore dyke swarm	This study
	2365.4	1	B	Bangalore dyke swarm	This study
	2213.6	3.9	B	Kandlamadugu dyke swarm	This study
	2209.3	2.8	B	Somala dyke swarm	This study
	2180.8	0.9	B	Northern Dharwar dyke swarm	This study
	2176.5	3.7	B	Northern Dharwar dyke swarm	This study
1885.4	3.1	B	Cuddapah sill	Chapter 3, this thesis	

Table 4-4. Summary of previously determined paleomagnetic data for Dharwar mafic dyke swarms dated by U-Pb baddeleyite in this study.

Mafic dykes studied	α_{95}	Characteristic remanent magnetization direction		Approximate site mean co-ordinates		Paleomagnetic pole		Baked contact test carried out?	Reference	U-Pb baddeleyite age constraints (present study)		
		<i>D</i>	<i>I</i>	Lat (N)	Long (E)	colatitude	paleolatitude				Latitude	Longitude
Bangalore dyke swarm												
Three E-W dykes, Harohalli	9°	79.6°	-82.3°	12.5°	77.5°	-15.1°	74.9°	9.5°S	242.4°E	no	Dawson and Hargraves, 1994	2365.4±1.0 Ma: dyke 12 (D+H, 1994)
Two E-W dykes, Harohalli	33°	130°	-88°	12.5°	77.5°	-4°	86°	15°S	254°E	no	Prasad et al., 1999	2365.4±1.0 Ma: dyke 3 (P et al., 1999)
3 E-W + 4 NW-SE dykes, Harohalli	9.8°	329°	86°	12.5°	77.5°	8°	82°	19.4°N	73.2°E	no	Radhakrishna et al., 2003	2365.4±1.0 Ma: D124 listed in R et al. (2003)
One E-W dyke, Penukonda area	7°	57°	-69°	14.2°	77.75°	-37.5°	52.5°	7°S	47°E	no	Kumar and Bhall, 1983	2368.6±1.3 Ma: parallel dyke 2km N of dyke i (K+B, 1983)
One E-W dyke, Penukonda area	6°	71°	-72°	14.2°	77.75°	-33°	57°	3°N	47°E	yes	Kumar and Bhall, 1983	2365.9±1.5 Ma (dyke ii of K+B, 1983)
Somala dyke swarm?												
One NW-SE dyke, Bukkapatnam	14°	320°	-34°	14.2°	77.75°	-71.4°	18.6°	38°N	68°W	no	Kumar and Bhall, 1983	2209.3±2.8 Ma: parallel dyke ~125 km SE (along strike) of dyke v (K+B, 1983)

Abbreviations: α_{95} - radius of the circle of 95% confidence about the magnetic direction; *D* - declination; *I* - inclination

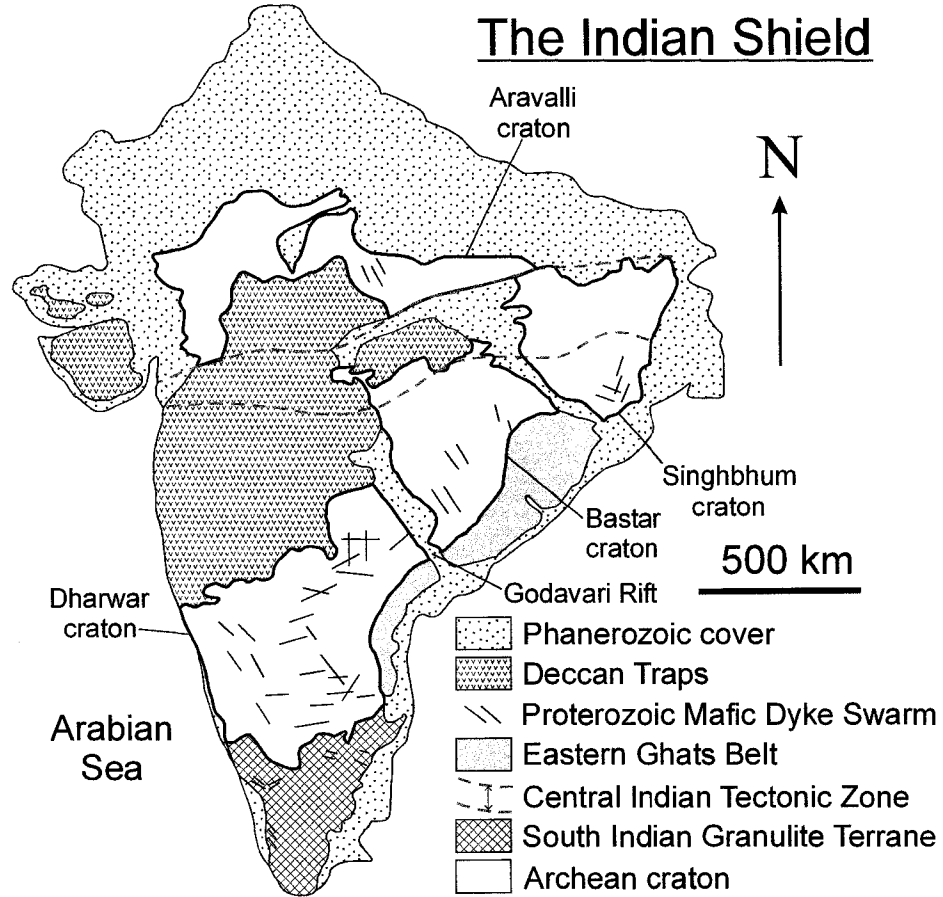


Fig. 4-1. The principal tectonic elements of the Indian shield including Archean cratons and major Proterozoic mafic dyke swarms. Geology modified from: Naqvi and Rogers, 1987; Murthy, 1995; GSI, 1998; Mishra et al., 2000; Zhao et al., 2003.

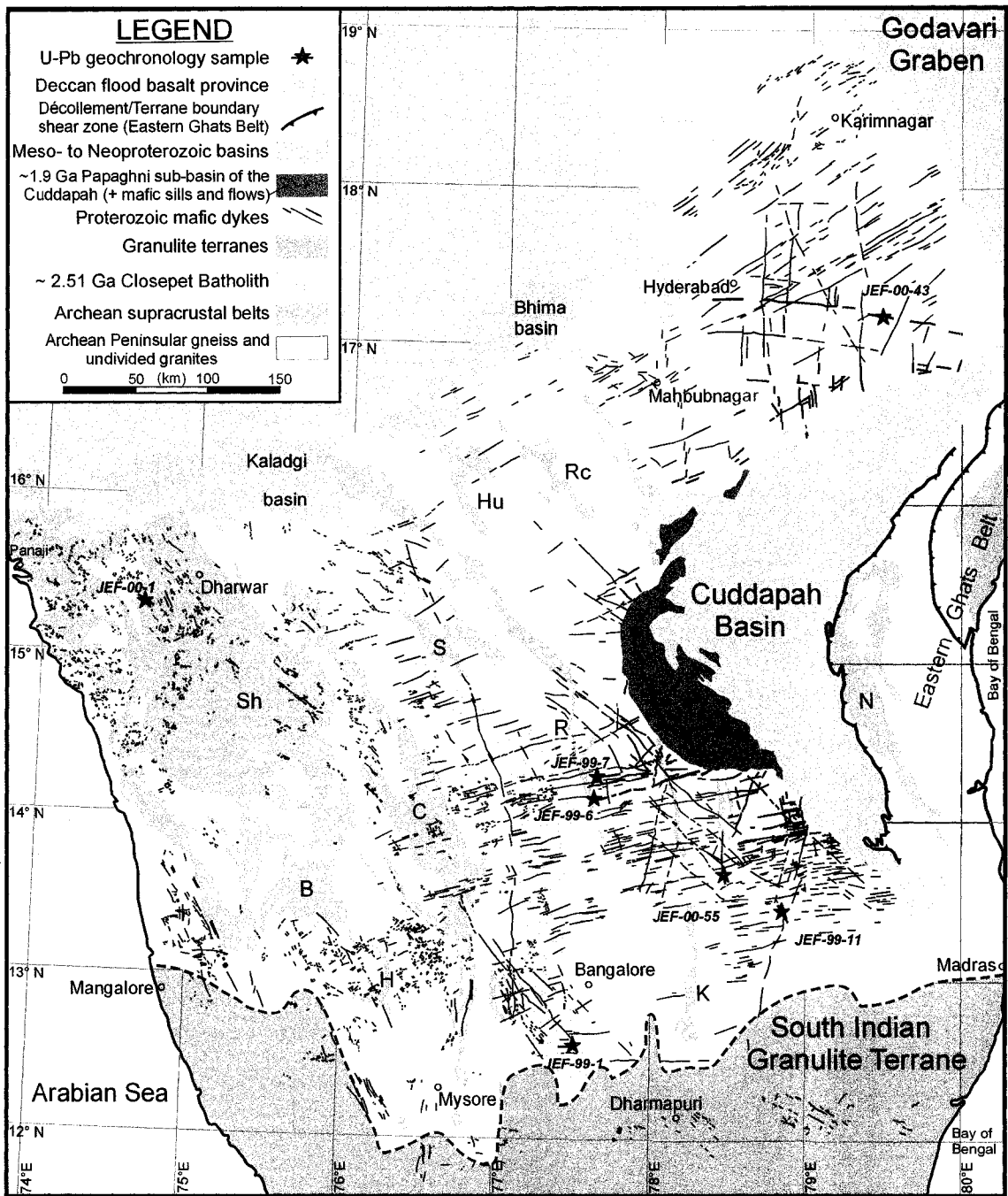


Fig. 4-2. Geological map of the Dharwar craton showing the distribution of Proterozoic mafic dykes and the locations of mafic dykes sampled for U-Pb dating in this study. Greenstone belts: B - Bababudan; C - Chitradurga; H - Holenarsipur; Hu - Hutti; K - Kolar; N - Nellore; R - Ramagiri; Rc - Raichur; S - Sandur; Sh - Shimoga. Geology modified from: GSI, 1981; Halls, 1982; Nagaraja Rao et al., 1987; Murty et al., 1987; Rao et al., 1990; Pandey et al., 1997; GSI, 1998; Radhakrishna and Joseph, 1998; Moyen et al., 2003.

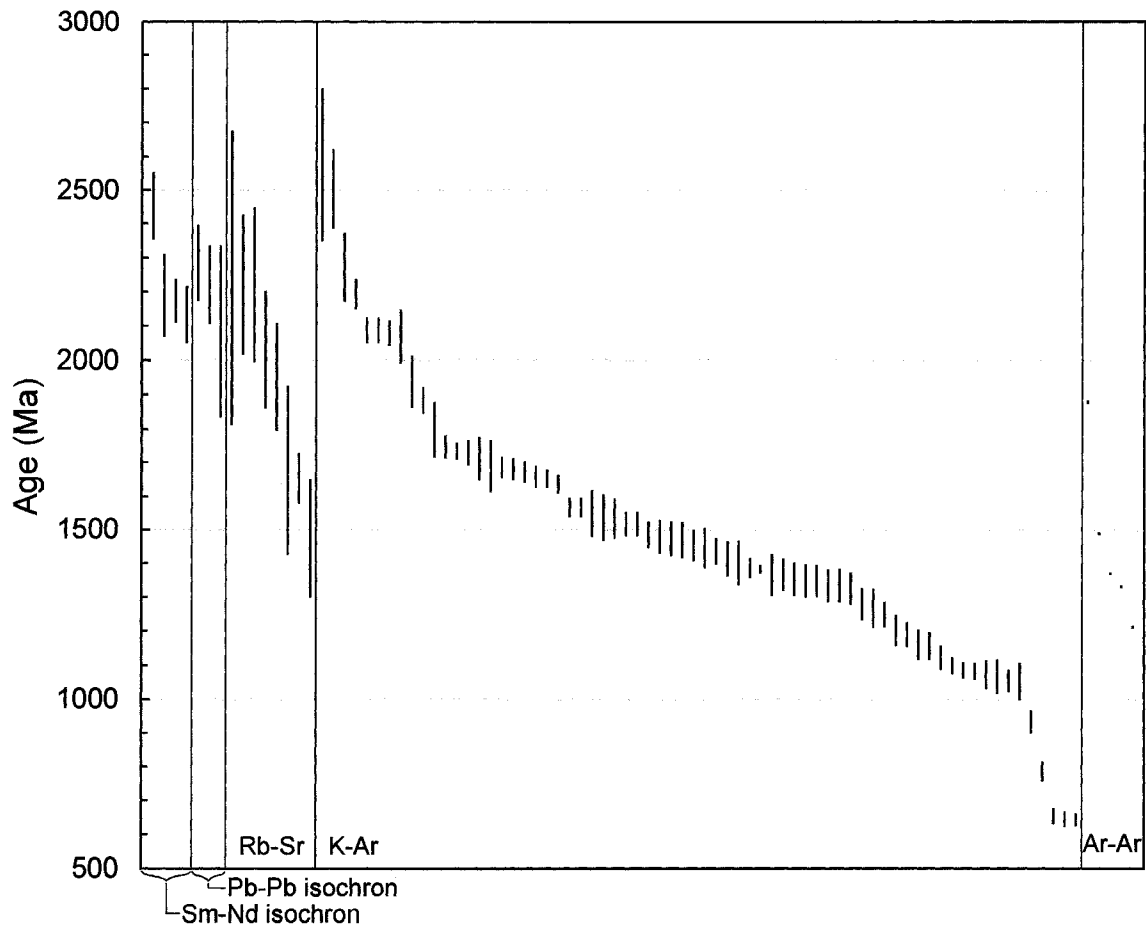


Fig. 4-3. Summary chart of previously determined isotopic ages for mafic dykes intruding Archean basement rocks of the Dharwar craton. Sm-Nd isochron ages: Zacharia et al., 1995; Pandey et al., 1997; Pb-Pb isochron ages: Pandey et al., 1997; Rb-Sr ages: Ikramuddin and Stueber, 1976 recalculated age of Dayal and Padmukari, 1995; Sarkar and Mallik, 1995; Pandey et al., 1997; K-Ar ages: Balasubrahmanyam, 1975; Paul et al., 1975; Balakrishna et al., 1979; Dayal and Padmakumari, 1985; Murty et al., 1987; Padmakumari and Dayal, 1987; Gokhale and Waghmore, 1989; Mallik and Bishul, 1990; Dayal and Padmakumari, 1995; Mallikarjuna Rao et al., 1995; Sarkar and Mallik, 1995; Chatterjee and Bhattacharji, 2001; $^{40}\text{Ar}/^{39}\text{Ar}$ ages: Chatterjee and Bhattacharji, 2001.

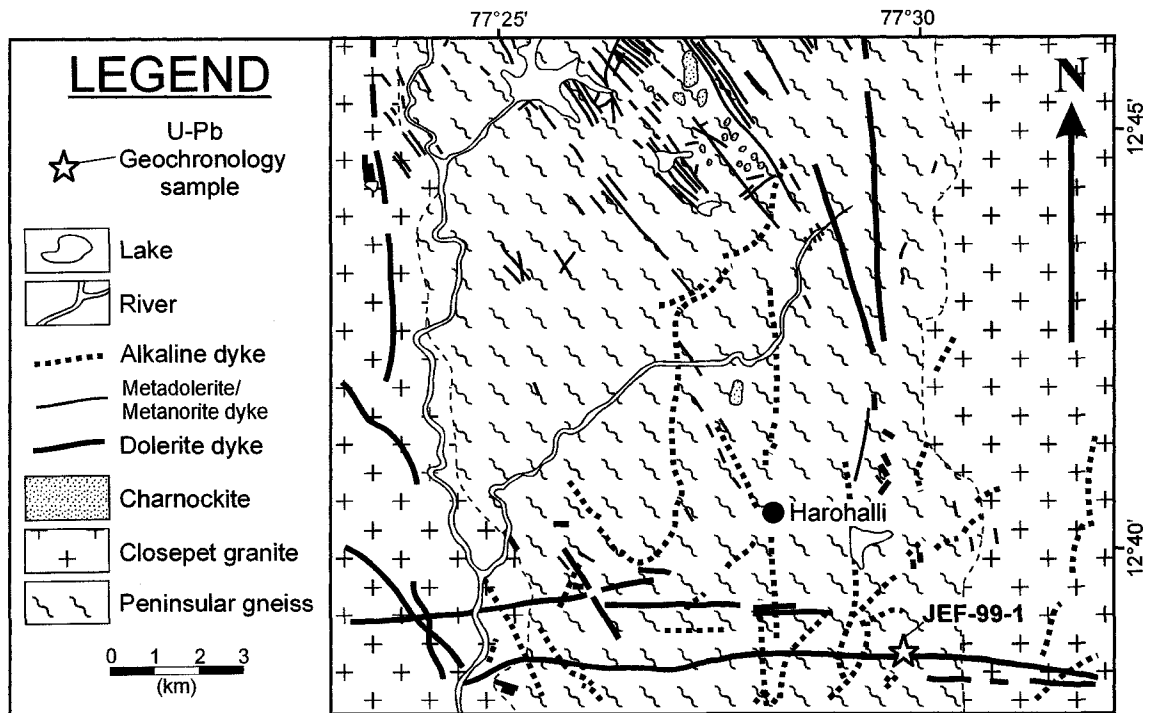


Fig. 4-4. Geological map of the Harohalli area showing the location of gabbro sample JEF-99-1. Geology modified from Ikramuddin and Stueber (1976).

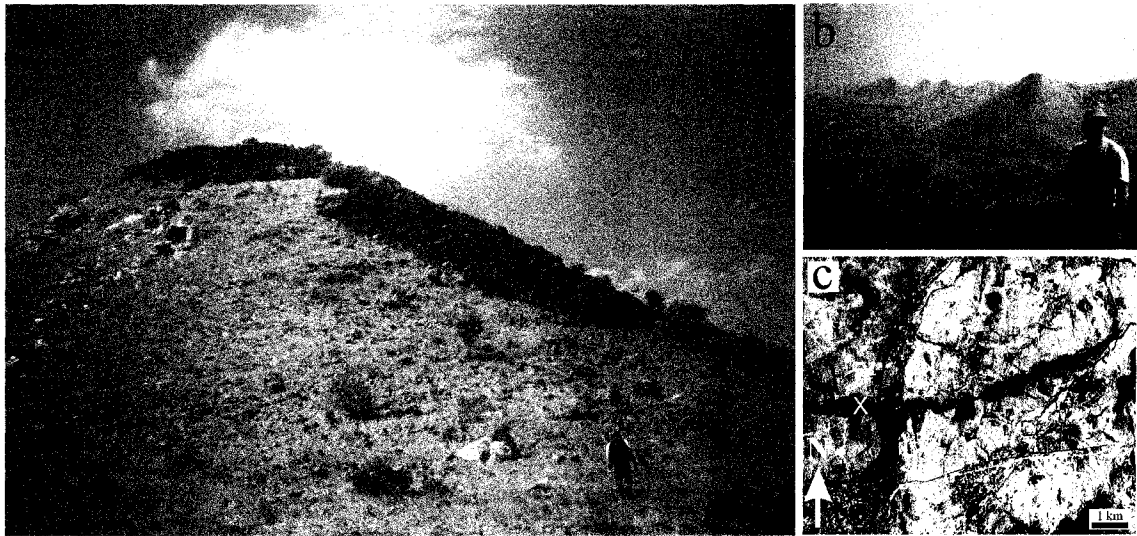


Fig. 4-5. Photographic and Landsat7 imagery of mafic dykes from the Bangalore dyke swarm of South India. a) Photograph of the Chennekottapalle dyke. b) Photograph of the Penukonda dyke looking towards the east. This dyke is seen to progressively outcrop towards the north (left) into the distance, as a receding series of ~130 m high ridges. c) Panchromatic Landsat7 imagery showing the sampling site (X: where the photo in b) was taken) of the Penukonda dyke, and a peculiar bend in strike of this dyke from E-W at the sampling progressively to a N-S orientation a few kilometers east. Immediately to the east of this image, the dyke is seen to continue along an ENE-SWS strike again, which is visible in a more regional Landsat7 image (Figs. 4-6 and 4-7).

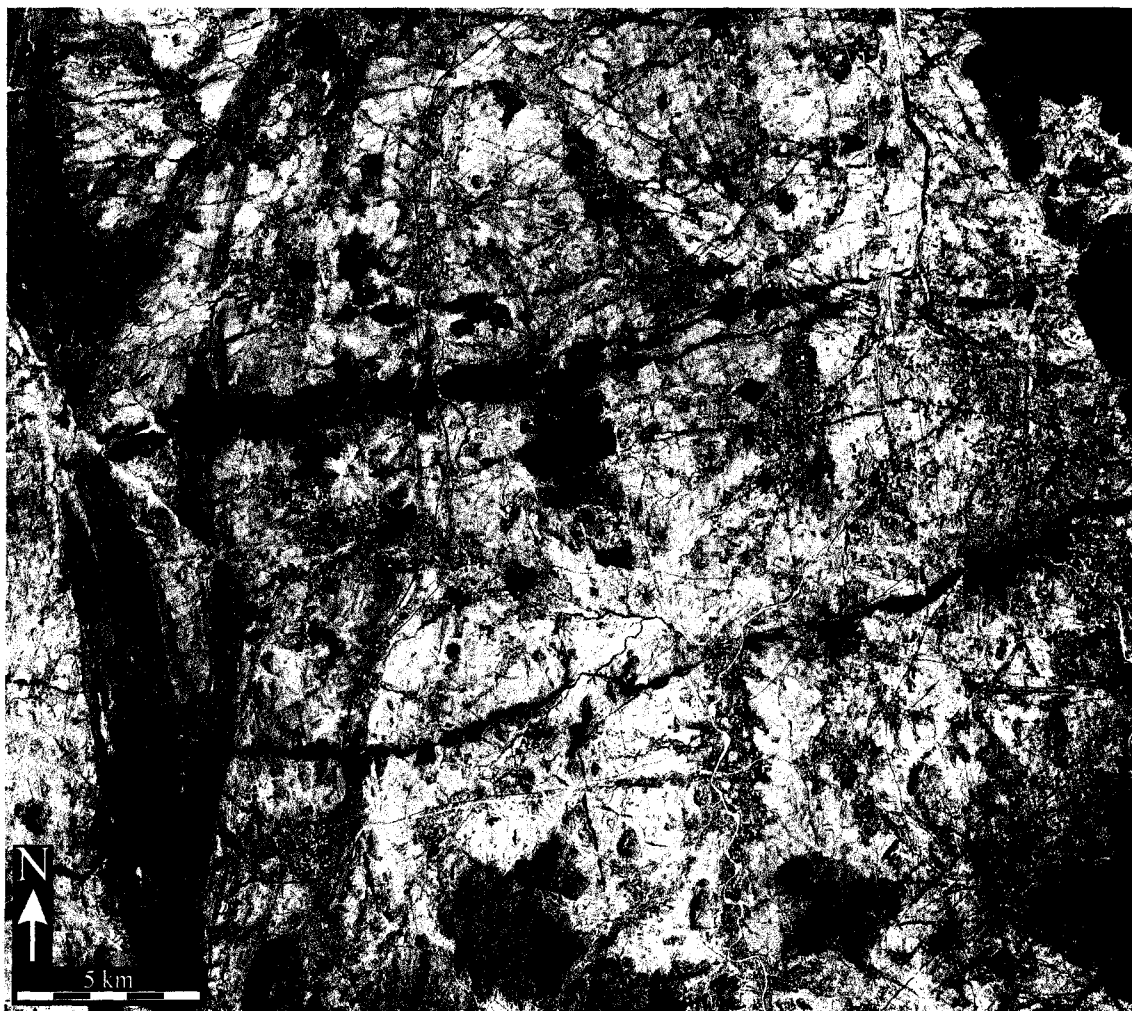


Fig. 4-6. Panchromatic Landsat7 image highlighting a prominent outcropping of the Bangalore dyke swarm (prominent E-W to ENE-WSW trending dark lineaments). A geological interpretation of the image is shown in Fig. 4-7.

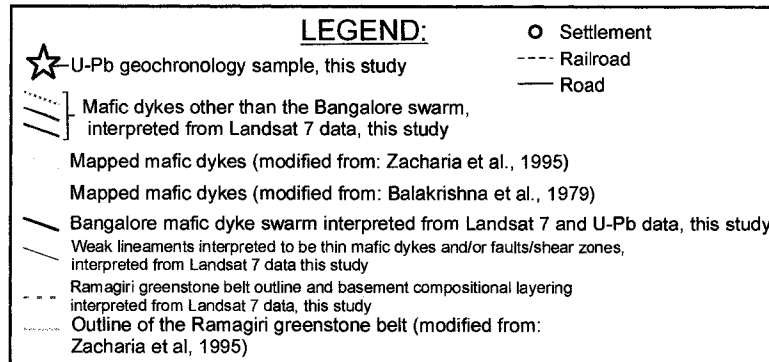
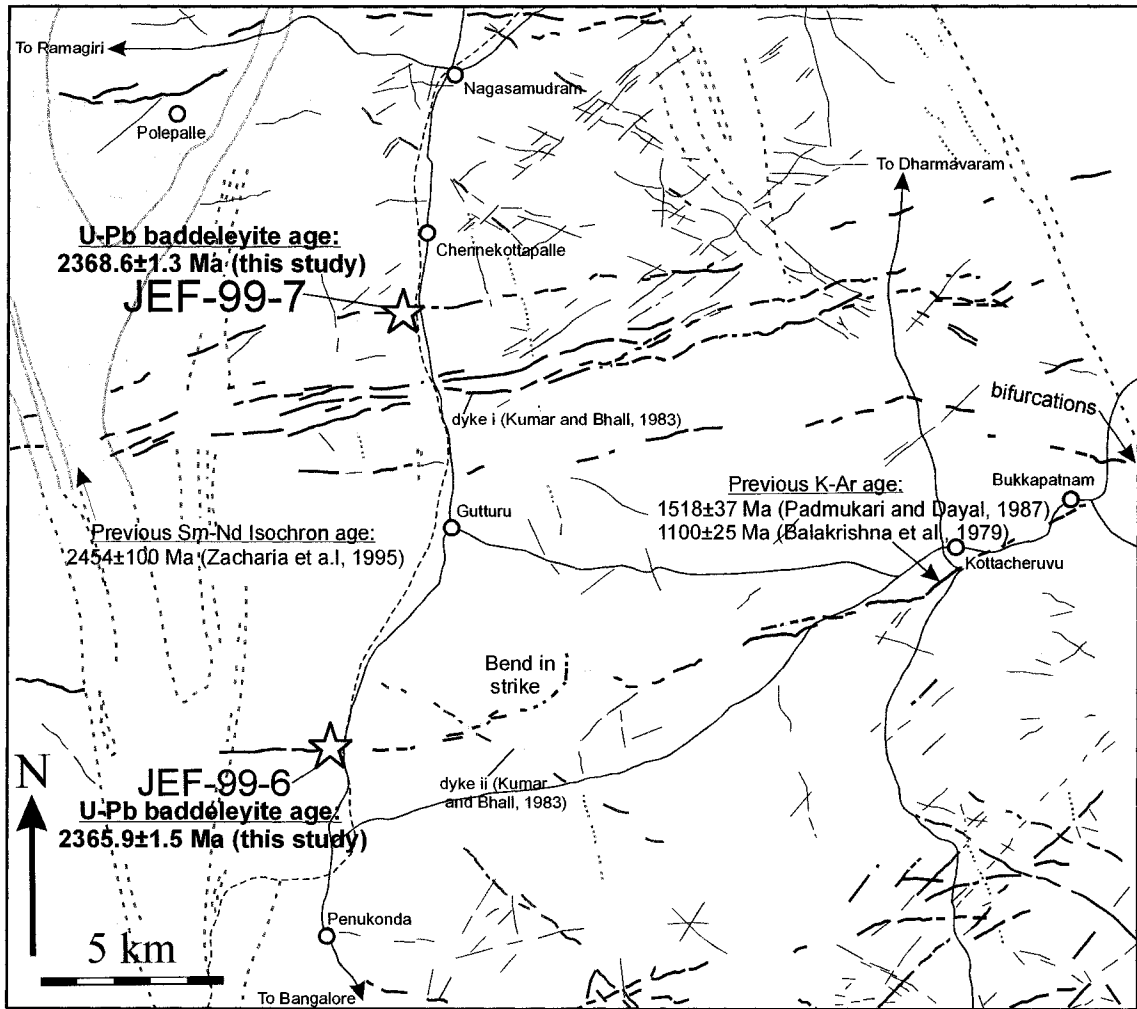


Fig. 4-7. Lineament map interpreted from the Landsat7 image shown in Fig. 4-6. The interpretation of many of these lineaments including mafic dykes, greenstone belts, roads, and railways matches closely the maps of Balakrishna et al. (1979) and Zacharia et al. (1995).

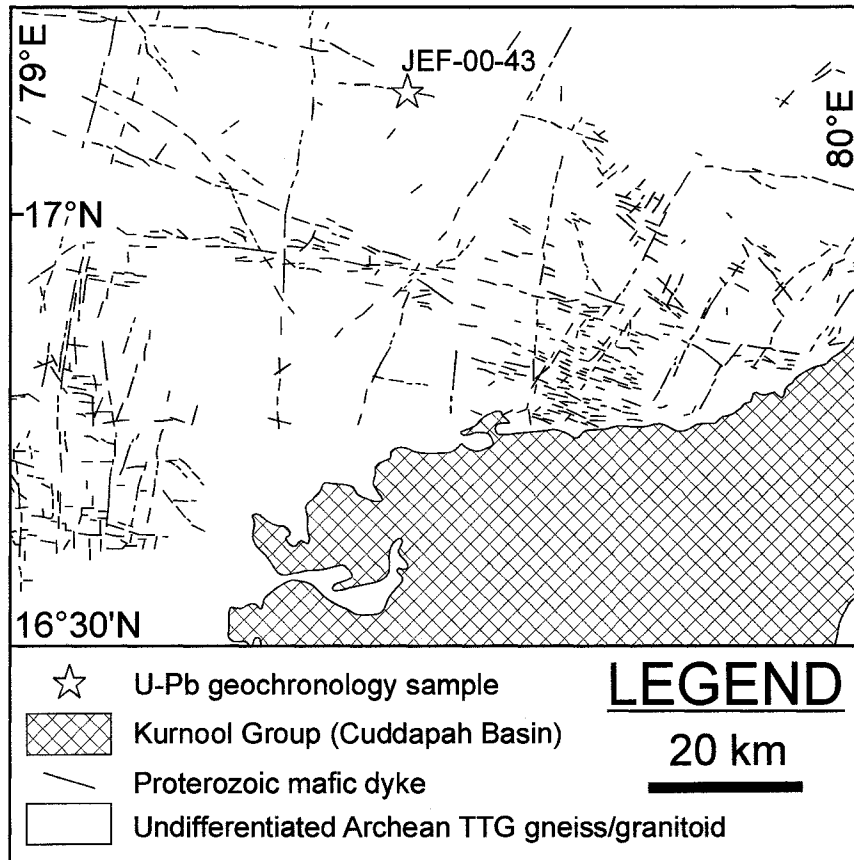


Fig. 4-8. Geological map of the region north of the Cuddapah basin where gabbro sample JEF-00-43 of the Bandepalem dyke was collected. Geology modified from Murty et al. (1987).

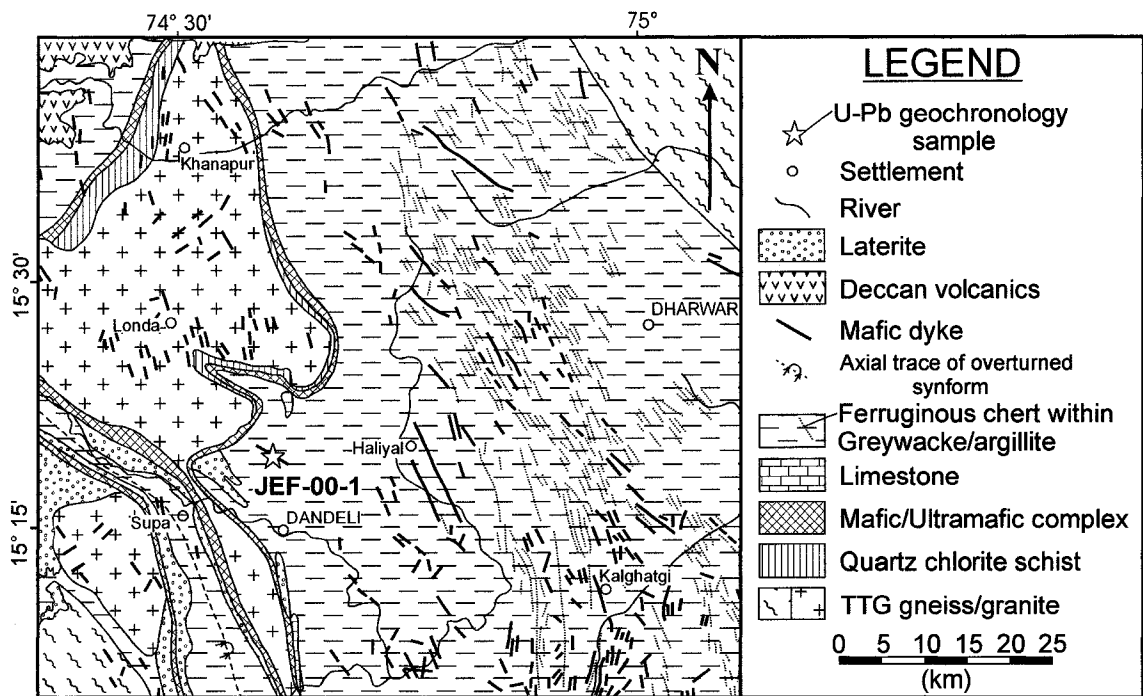


Fig. 4-9. Geological map of the northern Shimoga supracrustal belt where sample JEF-00-1 of the Dandeli gabbro dyke was collected. Geology modified from GSI (1981).

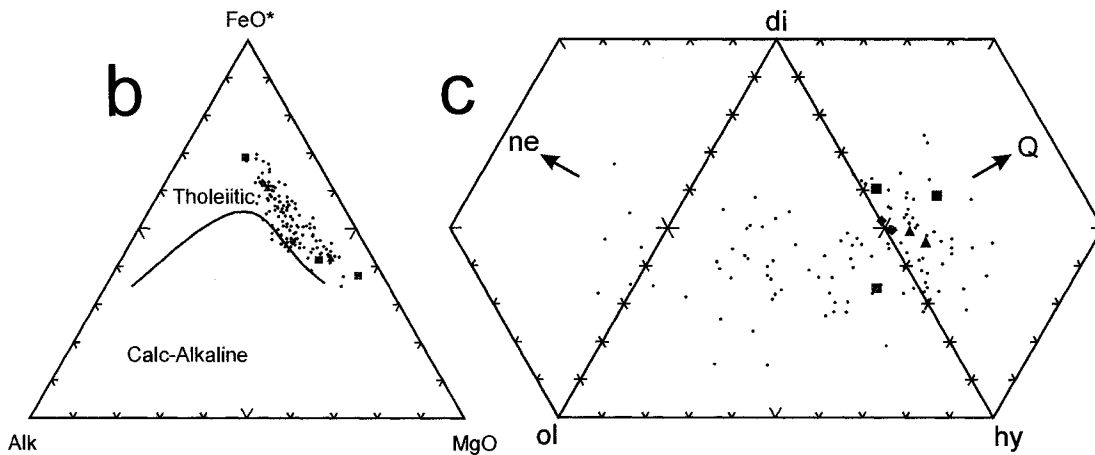
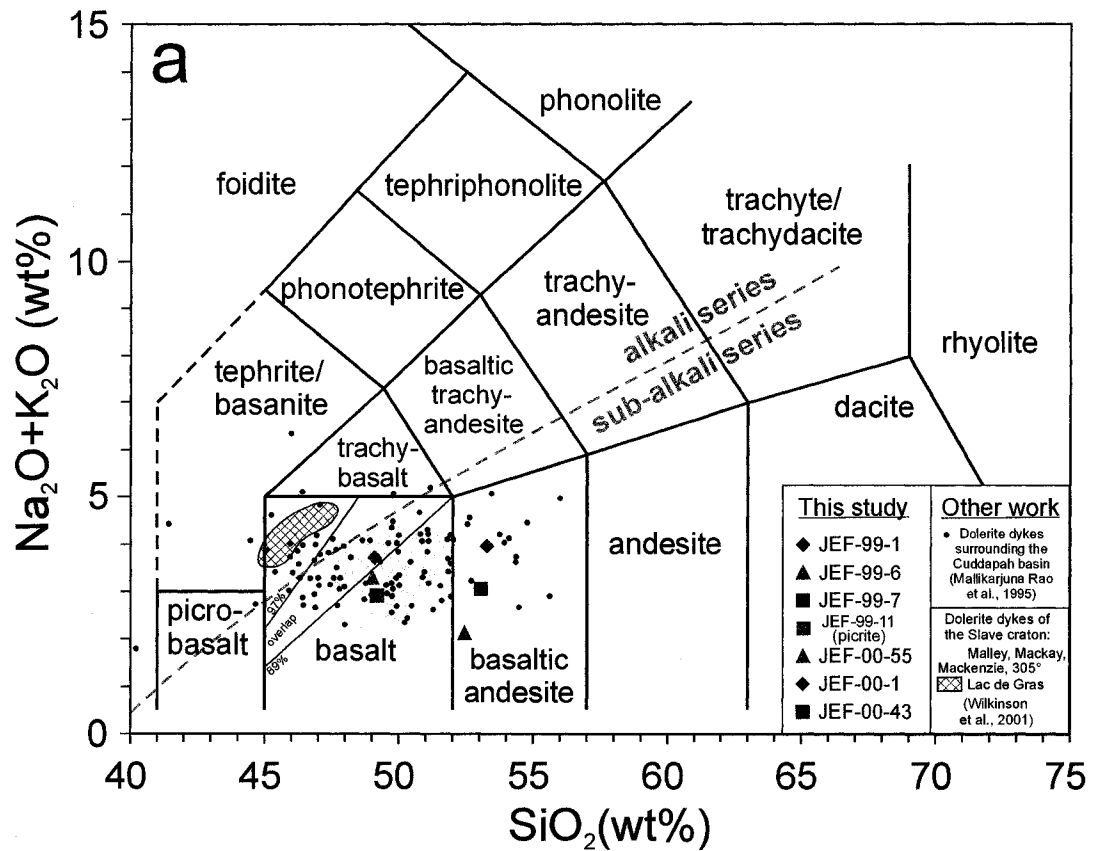


Fig. 4-10. a) Total alkalis versus silica diagram (Le Maitre, 2002) showing geochemical data for mafic dykes from the Dharwar (this study; Mallikarjuna Rao et al., 1995) and Slave cratons (Wilkinson et al., 2001). b) A ternary $(\text{Na}_2\text{O}+\text{K}_2\text{O})-(\text{FeO}+0.8998\text{Fe}_2\text{O}_3)-\text{MgO}$ (AFM) diagram (Irvine and Baragar, 1971) showing geochemical data for Dharwar mafic dykes (this study; Mallikarjuna Rao et al., 1995). c) CIPW normative mineralogy for Dharwar mafic dykes (this study; Mallikarjuna Rao et al., 1995), plotted on the basalt tetrahedron of Yoder and Tilley (1962). Legend in (a) also corresponds to (b) and (c), and colours relate to U-Pb ages for Dharwar samples (red=2.37 Ga; blue=2.21 Ga; green=2.18 Ga).

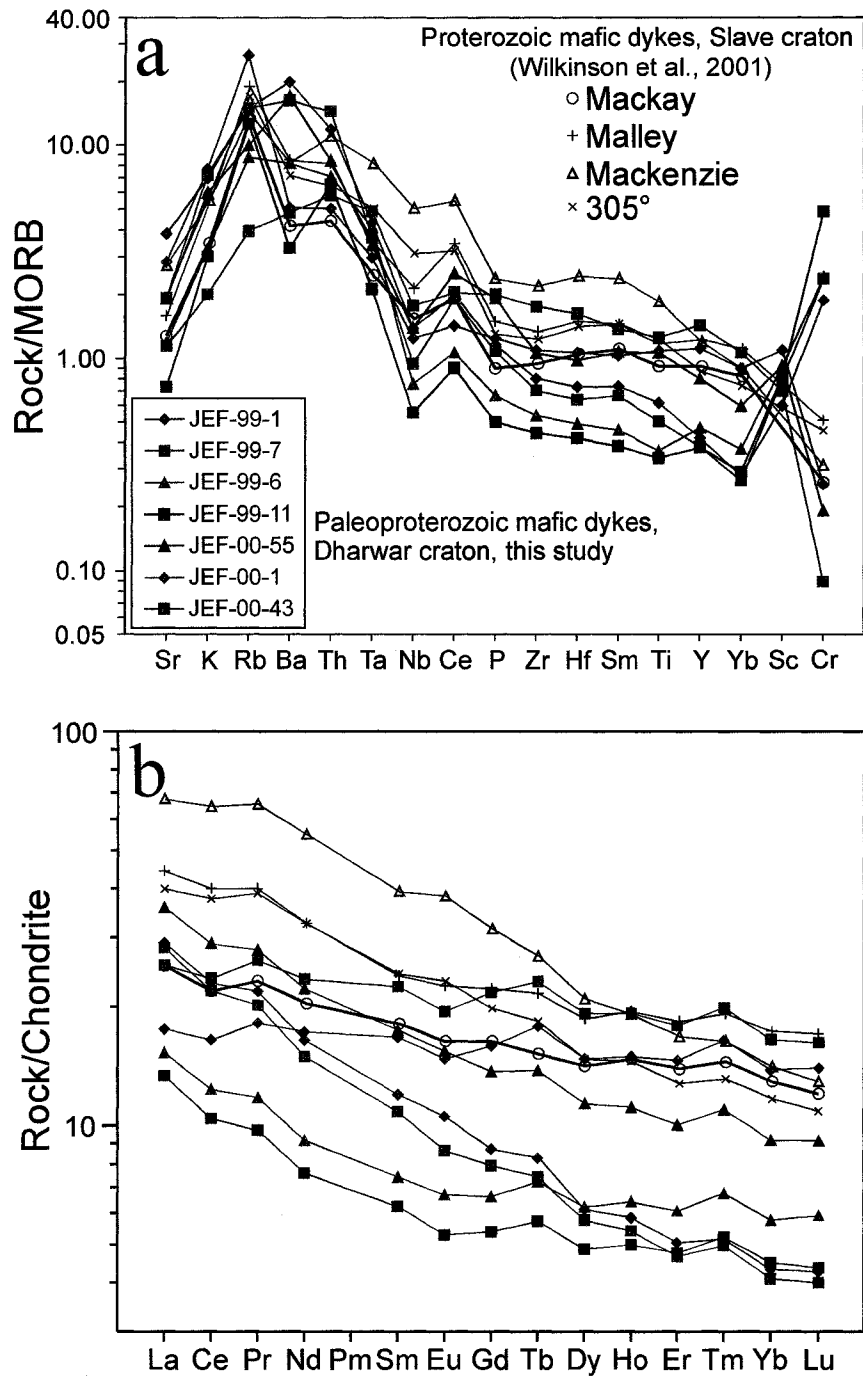


Fig. 4-11. a) Mid Ocean Ridge Basalt (MORB)-normalized Pearce (1982) plot showing data for Dharwar mafic dyke samples (this study) and mean values for Proterozoic mafic dyke swarms of the Slave craton (Wilkinson et al., 2001). b) REE spider diagram normalized to average chondrite (Nakamura, 1974) for Dharwar mafic dyke samples (this study) and mean values for Proterozoic mafic dyke swarms of the Slave craton (Wilkinson et al., 2001). Data point labels as in (a). Colours in (a) and (b) relate to U-Pb ages for Dharwar samples (red=2.37 Ga; blue=2.21 Ga; green=2.18 Ga).

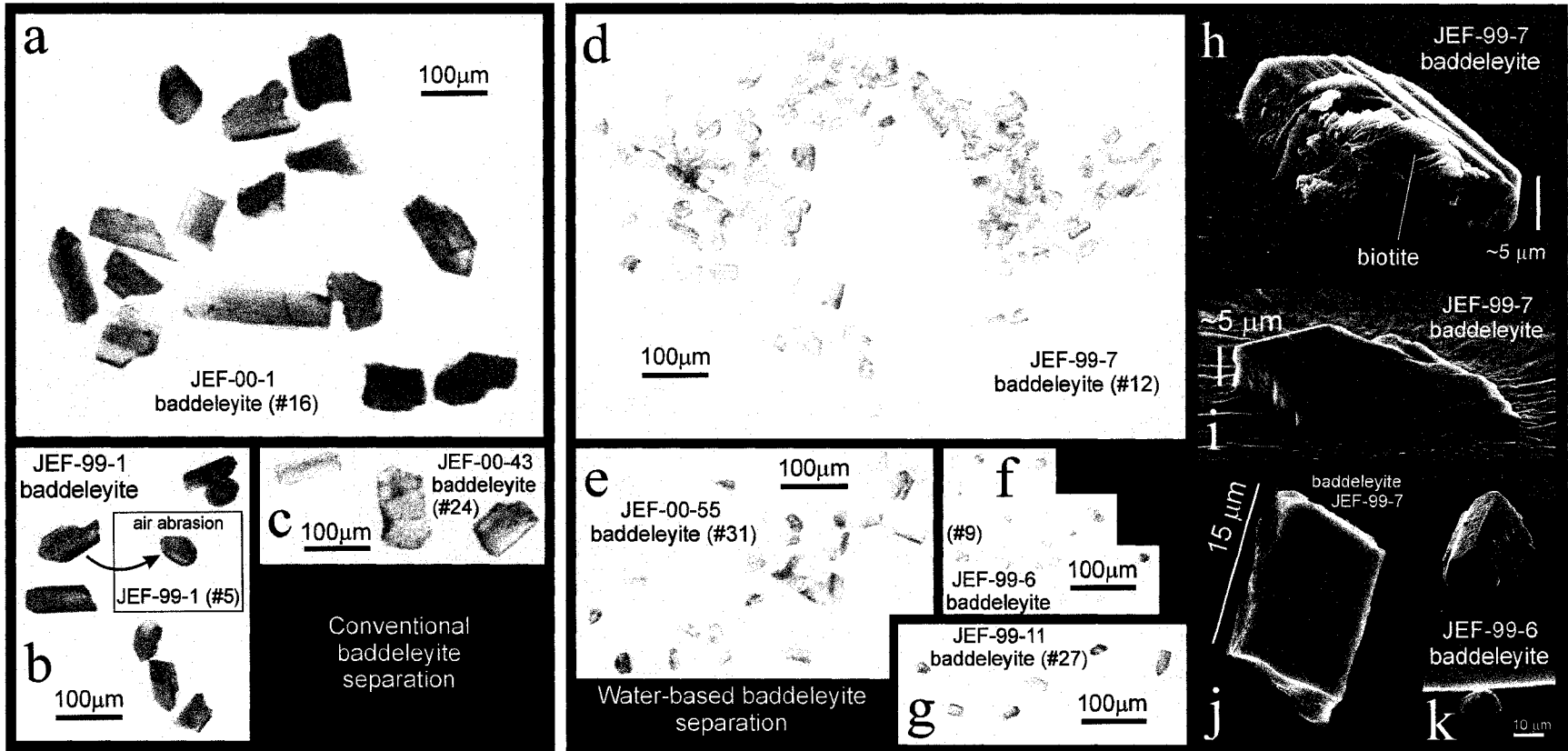


Fig. 4-12. a-c) Photomicrographs of baddeleyite crystals isolated from Dharwar mafic dyke samples by conventional mineral separation. Sample names and fraction #'s are keyed to Table 4-2. d-g) Photomicrographs of baddeleyite crystals isolated from Dharwar mafic dyke samples by the water-based method of Söderlund and Johansson (2002). Sample names and fraction #, correspond to the data in Table 4-2. On account of the difficulty in manipulating minuscule baddeleyite grains, some grains were left behind during the grain-cleaning procedures, and so the number of grains in each photograph does not necessarily match the number of grains analysed for each fraction. h-k) Secondary electron images acquired by scanning electron microscope of representative baddeleyite crystals from Dharwar mafic dykes isolated by the water-based method of Söderlund and Johansson (2002).

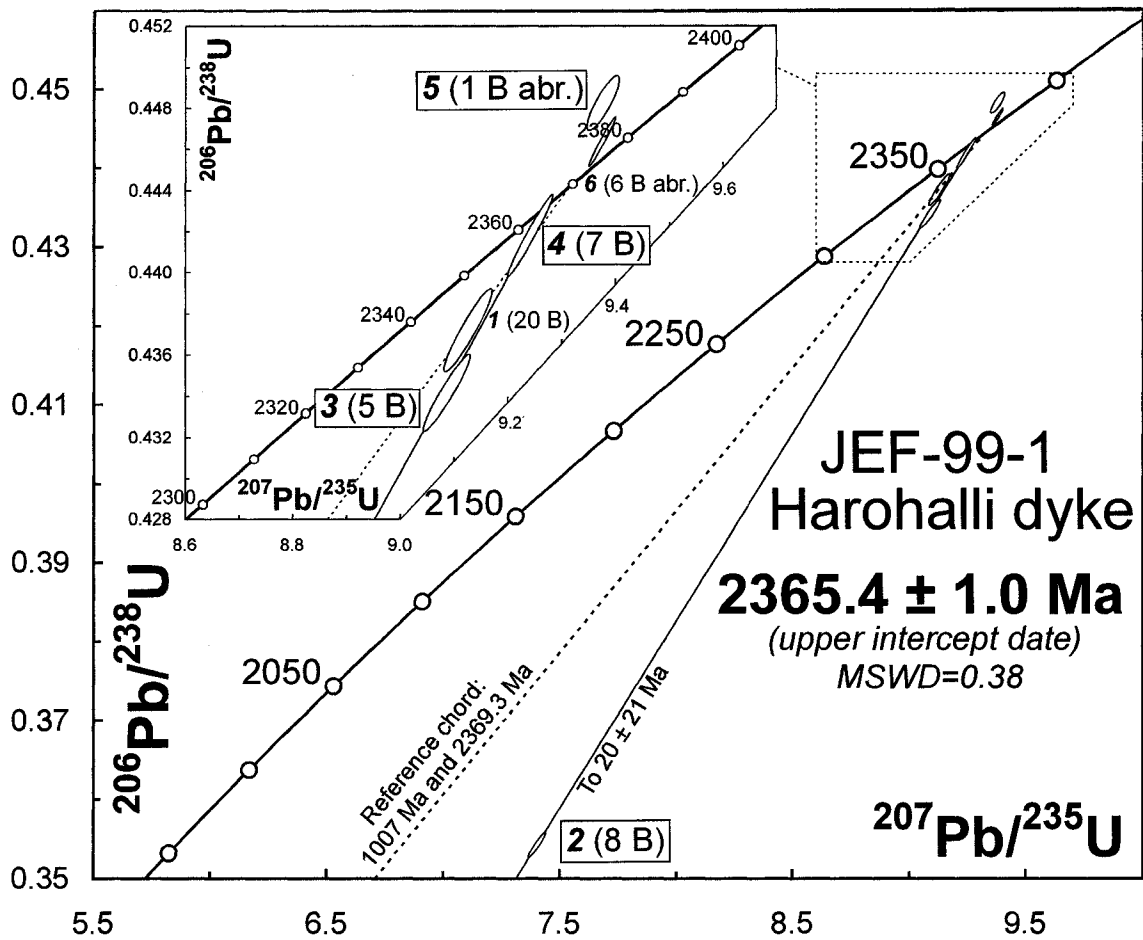


Fig. 4-13. Concordia diagram showing U-Pb IDTIMS data for baddeleyite isolated from the Harohalli dyke. Data point labels with larger lettering and enclosed within boxes are those used in the final age calculation, and the fraction numbers (italicized and in bold) are keyed to Table 4-2. Error ellipses and age calculations are shown at 2σ , and decay constant errors are ignored. Abbreviations: abr. - abraded; B - baddeleyite.

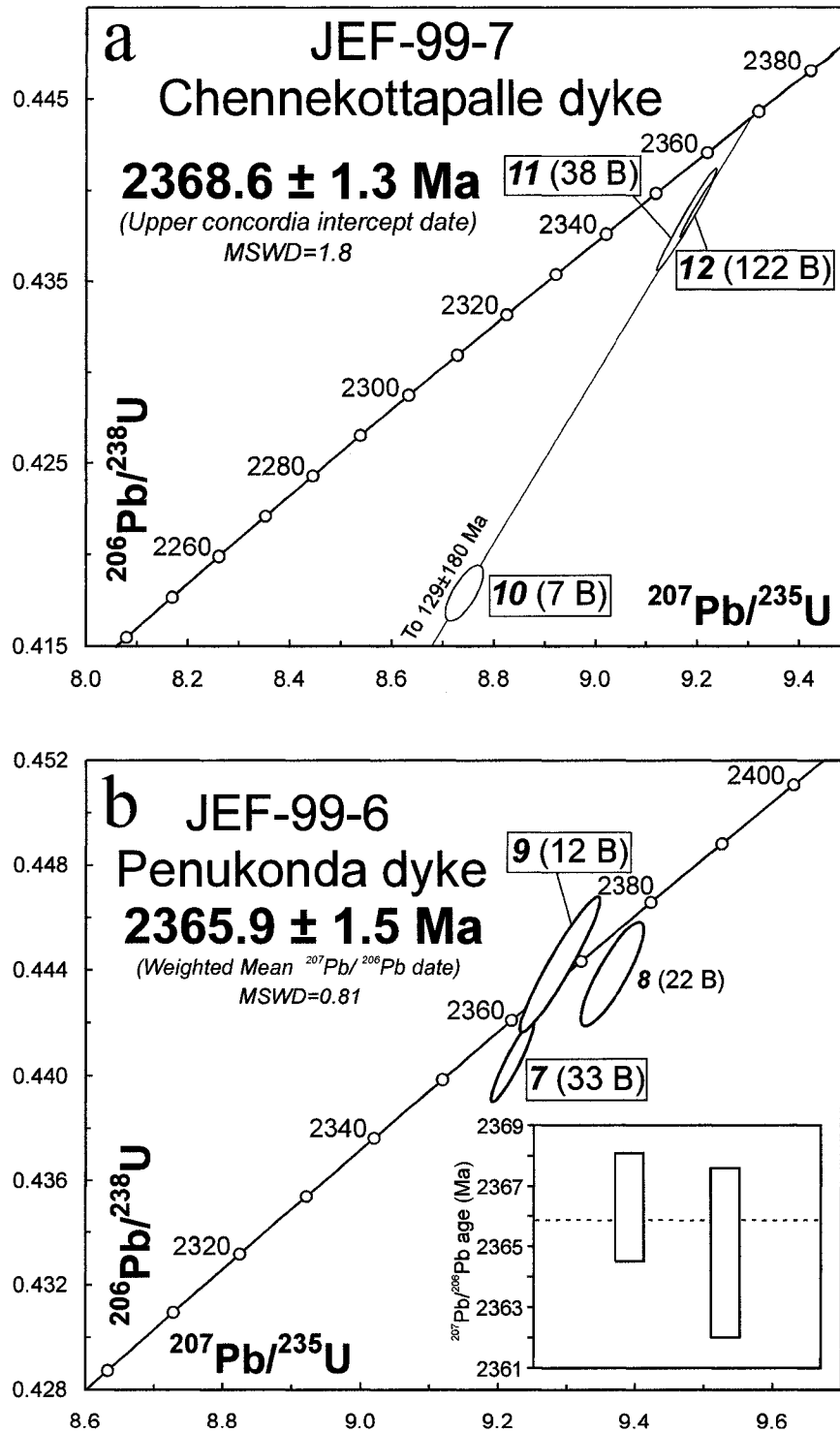


Fig. 4-14. Concordia diagrams showing U-Pb IDTIMS data for baddeleyite isolated from the Chennekottapalle (a) and Penukonda (b) dykes. Data point labels with larger lettering and enclosed within boxes are those used in the final age calculation, and the fraction numbers (italicized and in bold) are keyed to Table 4-2. Error ellipses, error bars (inset weighted mean plot in b), and age calculations are shown at 2σ , and decay constant errors are ignored. Abbreviations: B baddeleyite.

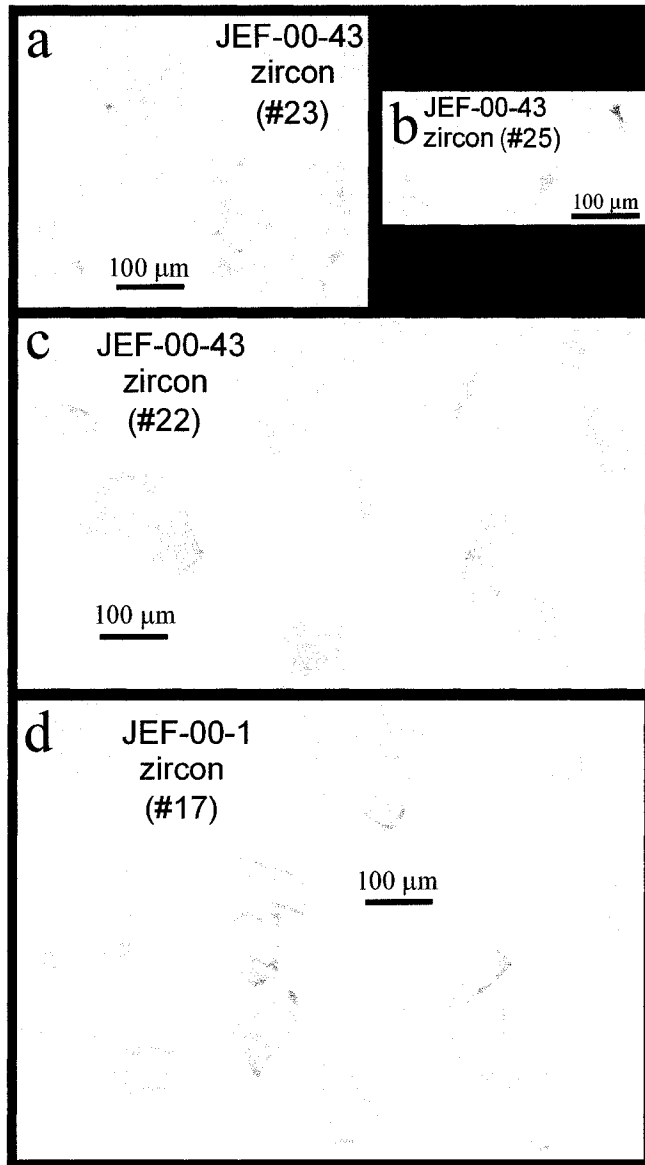


Fig. 4-15. Photomicrographs of representative zircon crystals isolated from the Bandepalem (a-c) and Dandeli (d) dykes. Sample names and fraction #'s are keyed to Table 4-2.

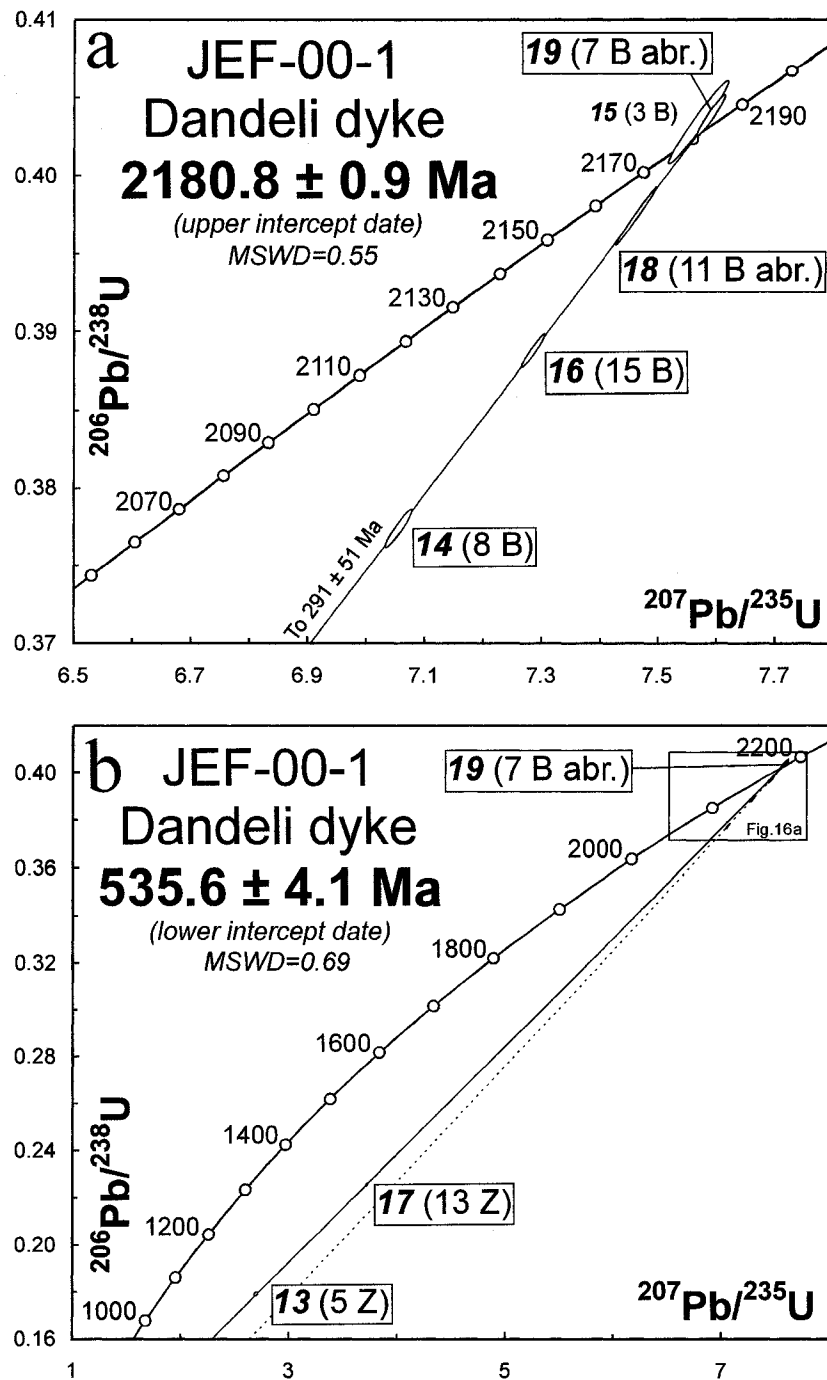


Fig. 4-16. Concordia diagrams showing U-Pb IDTIMS data for baddeleyite and zircon isolated from the Dandeli dyke. Data point labels with larger lettering and enclosed within boxes are those used in the final age calculations, and the fraction numbers (italicized and in bold) are keyed to Table 4-2. Dashed line in (b) is the regression from (a). Error ellipses and age calculations are shown at 2σ , and decay constant errors are ignored. Abbreviations: abr. abraded; B baddeleyite; Z zircon.

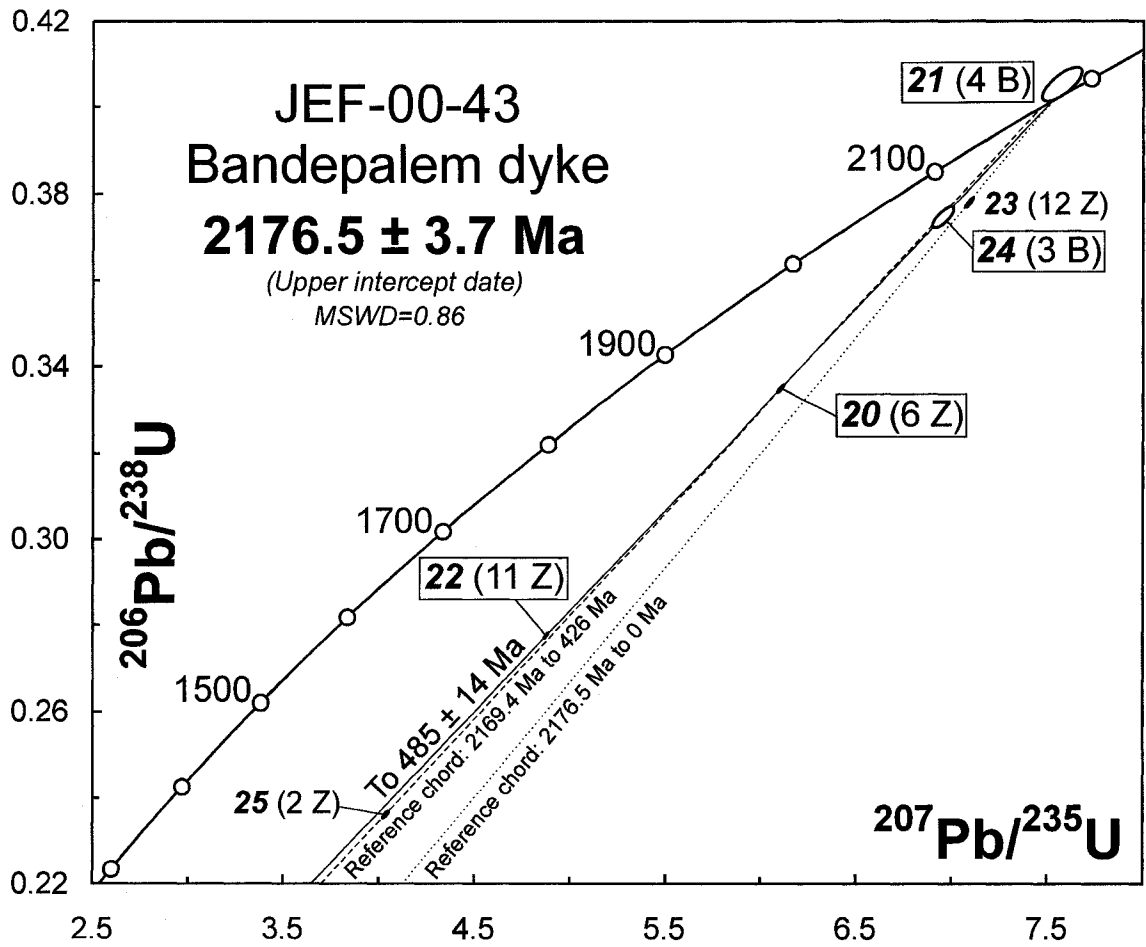


Fig. 4-17. Concordia diagram showing U-Pb IDTIMS data for baddeleyite and zircon isolated from the Bandepalem dyke. Data point labels with larger lettering and enclosed within boxes are those used in the final age calculation, and the fraction numbers (italicized and in bold) are keyed to Table 4-2. Error ellipses and age calculations are shown at 2σ , and decay constant errors are ignored. Abbreviations: B baddeleyite; Z zircon.

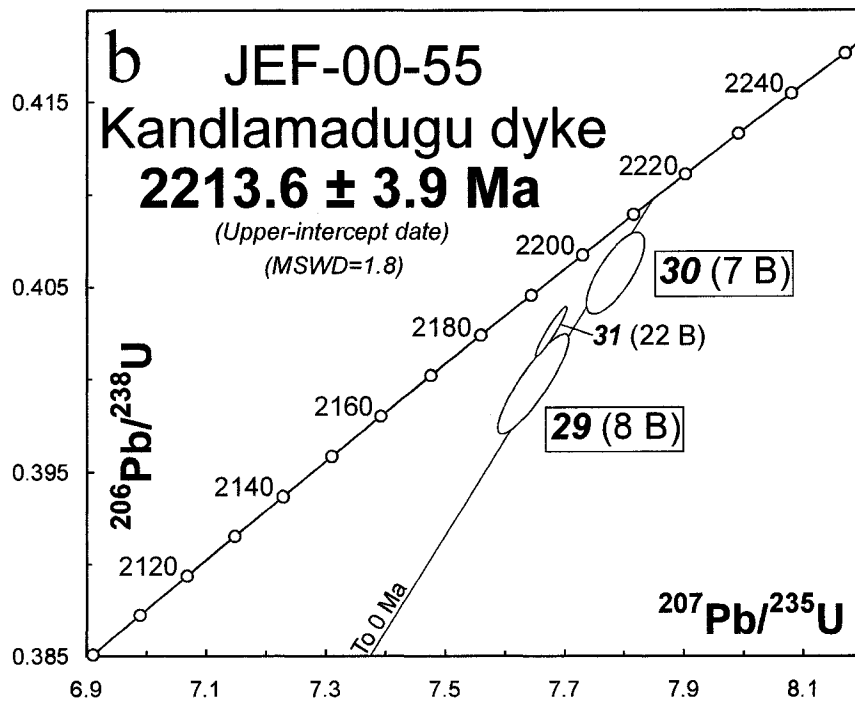
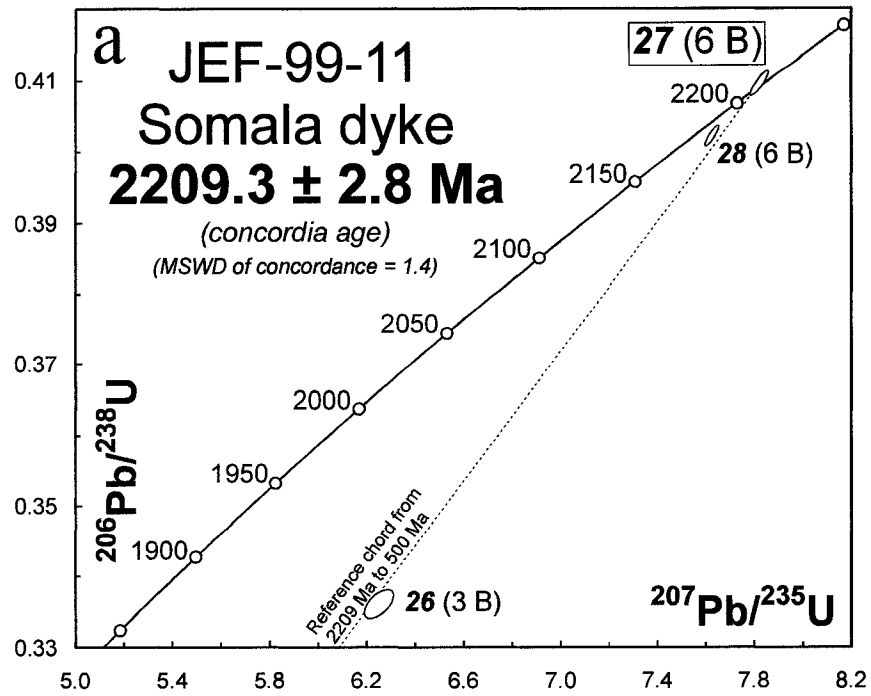


Fig. 4-18. Concordia diagrams showing U-Pb IDTIMS data for baddeleyite isolated from the Somala (a) and Kandlamadugu (b) dykes. Data point labels with larger lettering and enclosed within boxes are those used in the final age calculation, and the fraction numbers (italicized and in bold) are keyed to Table 4-2. Error ellipses and age calculations are shown at 2σ , and decay constant errors are ignored. Abbreviations: B baddeleyite.

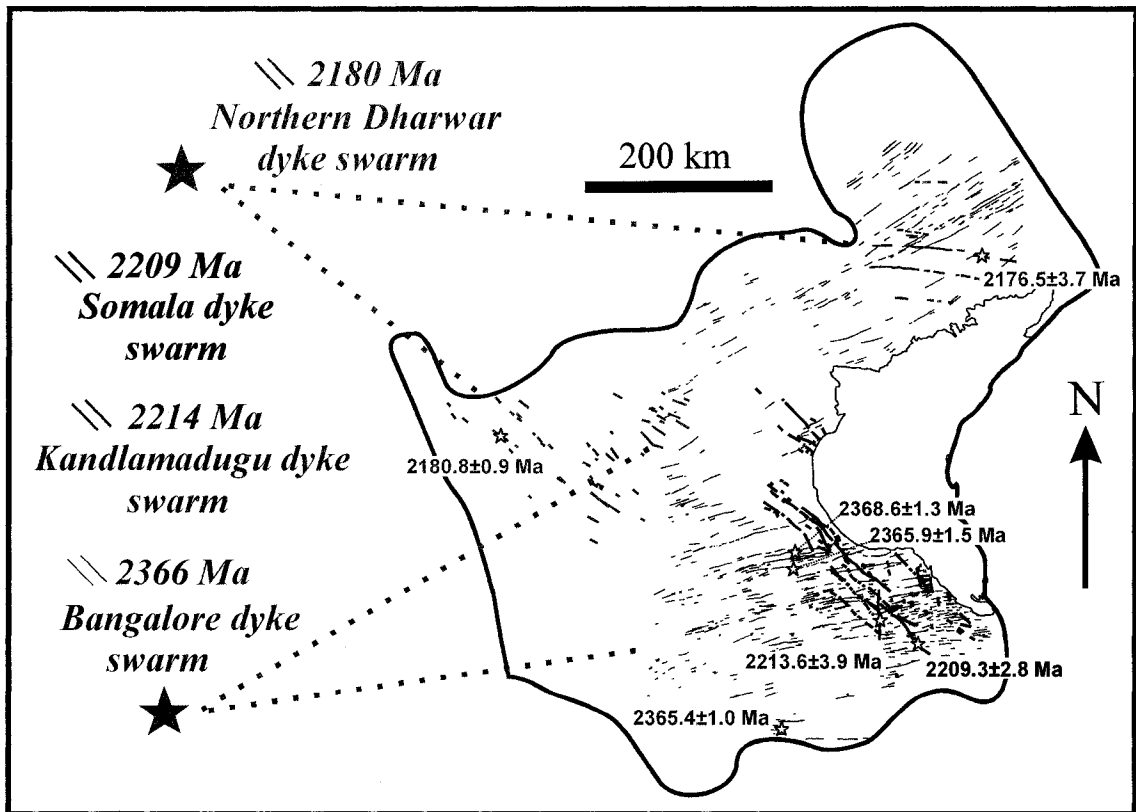


Fig. 4-19. Overview of the Dharwar craton showing an interpretation of the plausible regional extent of mafic dyke swarms dated by U-Pb in this study. Stars indicate the focal points of radiating swarms and may indicate the location of magma source regions associated with mantle plumes. Dyke swarm distributions are modified from Fig. 4-2.

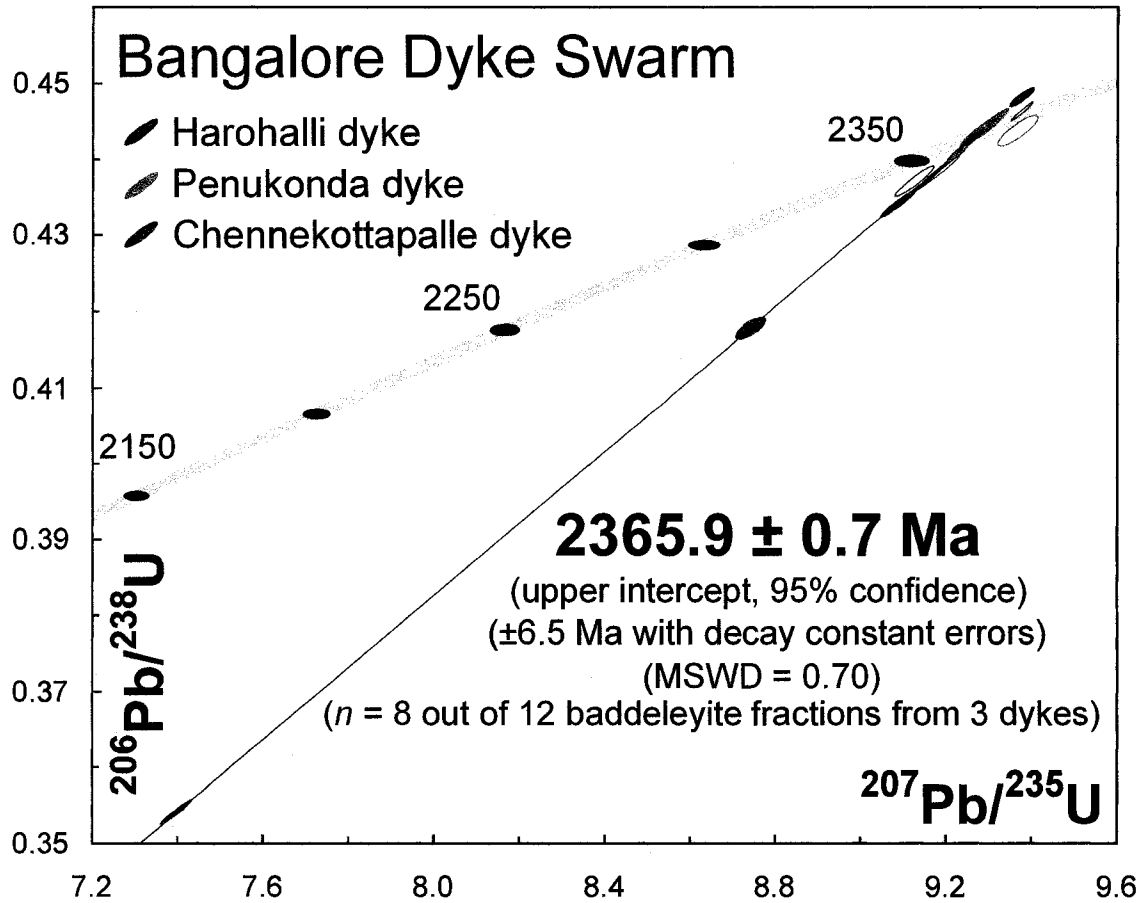
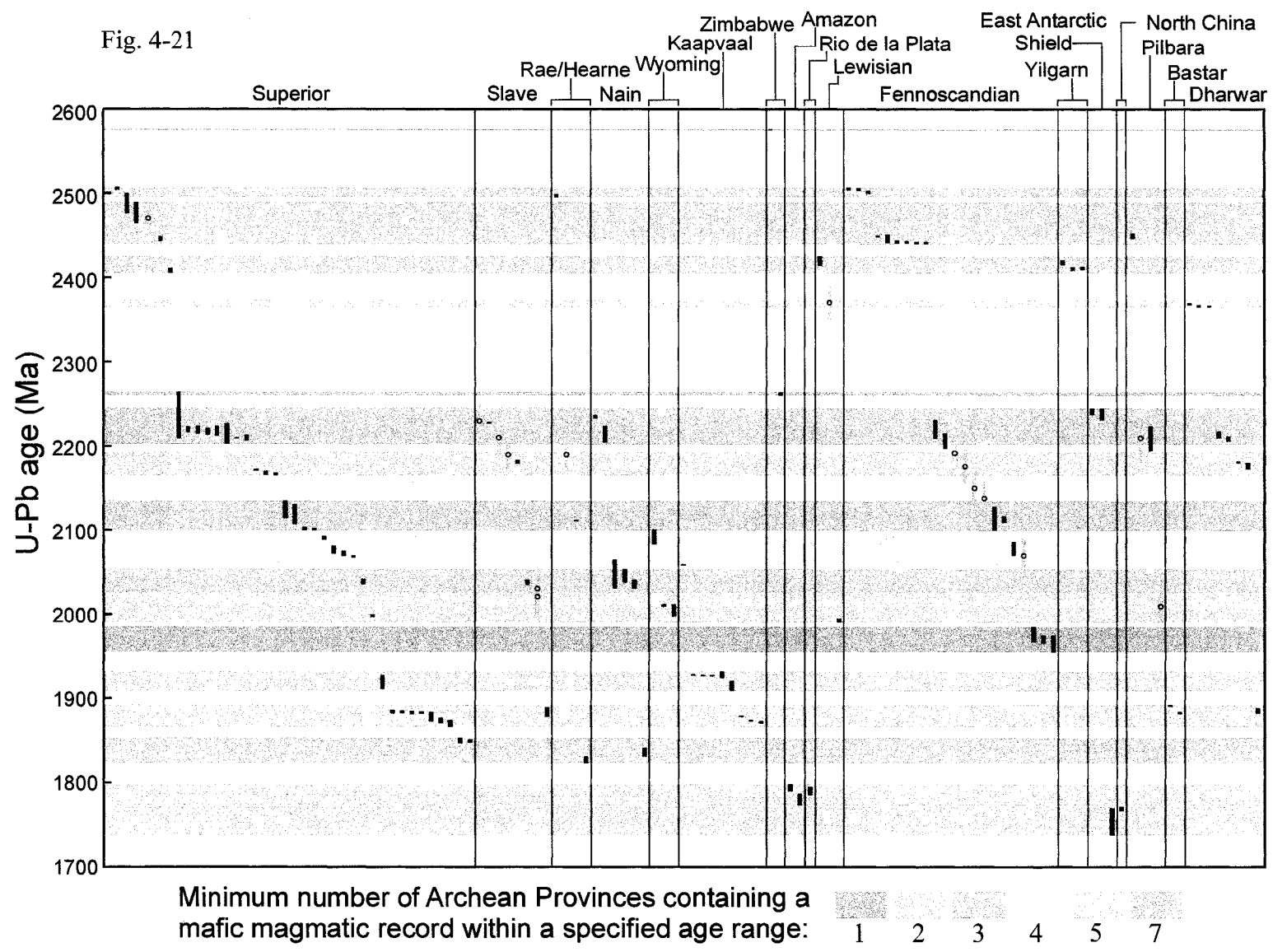


Fig. 4-20. Concordia diagram showing a composite regression based on U-Pb IDTIMS baddeleyite data for three dykes from the Bangalore mafic dyke swarm. Data points correspond to those shown in Figs. 4-13 and 4-14, and error ellipses are shown at the 2σ level. The composite regression line is constructed to pass through the statistically most similar two thirds of the data-points for each dyke (ellipses with white fill are excluded from the regression).

Fig. 4-21. Summary chart of U-Pb ages for Paleoproterozoic mafic igneous provinces from Archean provinces worldwide. Data points correspond to the summary presented in Table 4-3. Data points plotted as circles have arbitrary ± 20 Ma error bars (in grey) assigned to them because the errors are not published or were not located in the literature search. The time intervals for the age correlations, where possible, are chosen based on known genetic associations (e.g. inclusion of both 2.47 Ga and 2.45 Ga Hearst-Matachewan dykes in a single interval), but many of the time intervals are subjectively assigned.



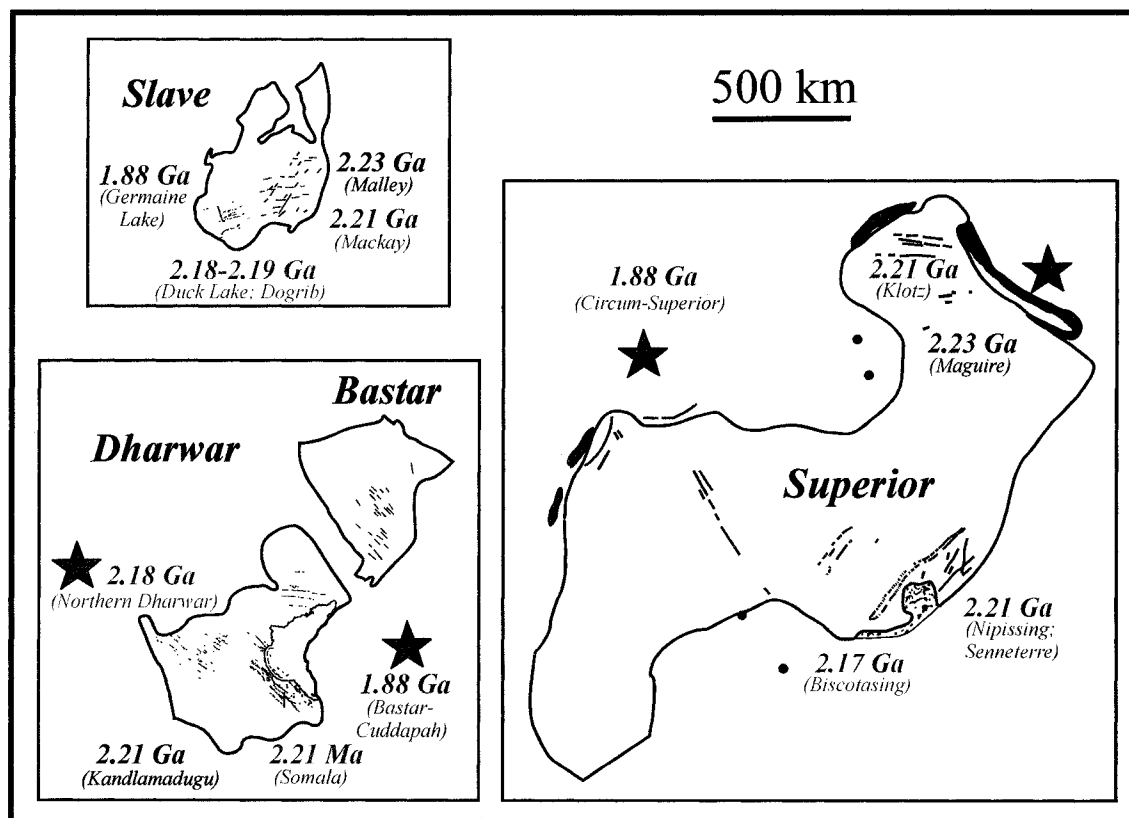


Fig. 4-22. Overview of the three Archean cratons which share the most similar records of Paleoproterozoic mafic magmatism, on the basis of global correlation of U-Pb ages (Fig. 4-21). These three cratons may represent fragments of an Early Paleoproterozoic continent or supercontinent that broke apart at ~ 2.2 Ga. Distribution of Slave dyke swarms is modified from LeCheminant et al. (1996) and Atkinson (2004), the 1.88 Ga circum-Superior event is modified from (Ernst, 2004) and the location of the plume centre is estimated based on the comments in (Buchan et al., 2003), the 1.88 Ga Bastar-Cuddapah event is modified from Chapter 3 (this thesis), the Ungava radiating swarm (and plume centre) comprising the Klotz, Maguire, Nipissing, and Senneterre events is modified from Buchan et al., (1998), and the Biscotasing event is modified from Halls and Davis (2004).

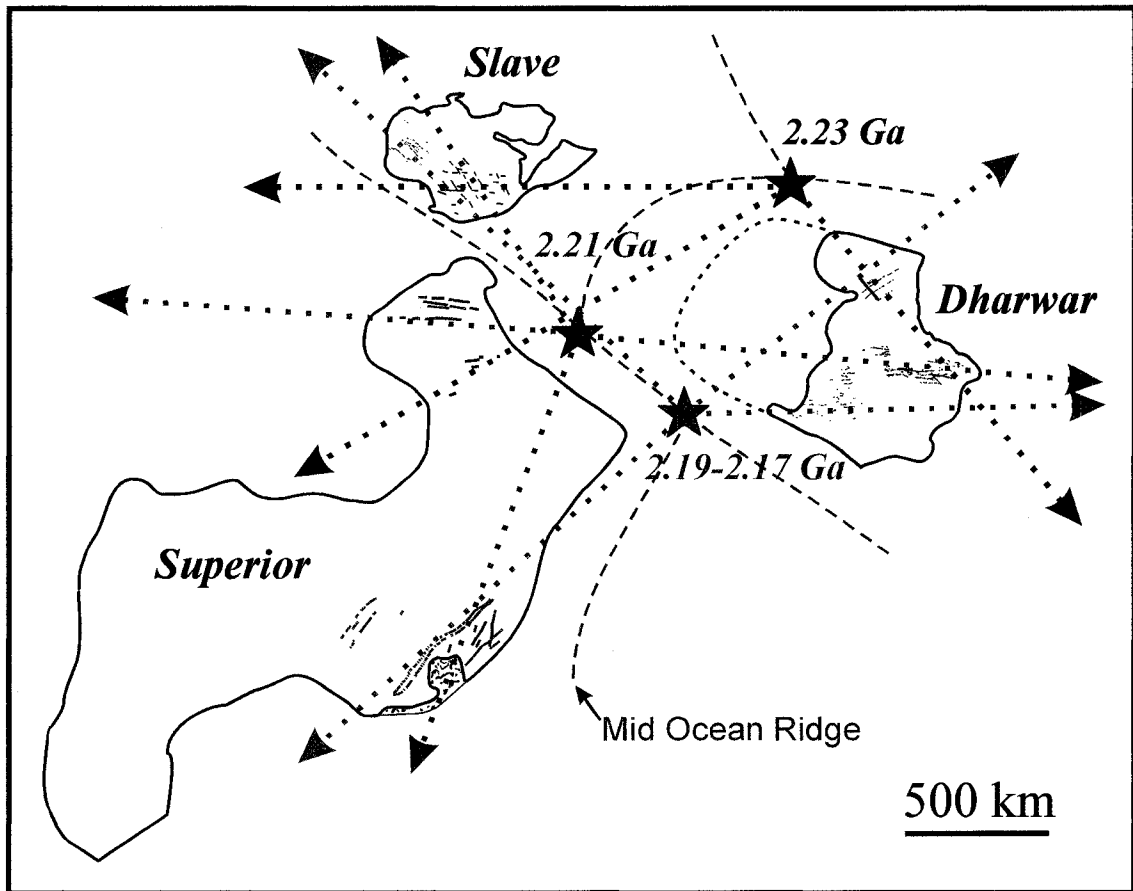


Fig. 4-23. Paleocontinental reconstruction involving the Dharwar, Superior, and Slave cratons at ~ 2.2 Ga. This configuration is constrained only by the relative ages and orientations of 2.23-2.17 Ga mafic dyke swarms in each craton (Superior and Slave events referenced in Fig. 4-22), assuming that sub-swarms of a similar age may be linked to a common mantle plume centre (shown as stars - radiating dotted lines with arrows show inferred magma flow away from the plume centres), and that relative motions between cratons does not ensue until final break-up at 2.18-2.17 Ga. A dyke from the N-S trending Hyderabad swarm of the Dharwar craton is shown (black line) as possibly correlative with a 2.23 Ga radiating swarm, on the basis of a preliminary electron microprobe baddeleyite date of 2248 ± 43 Ma (sample JEF-00-51; Appendix C).

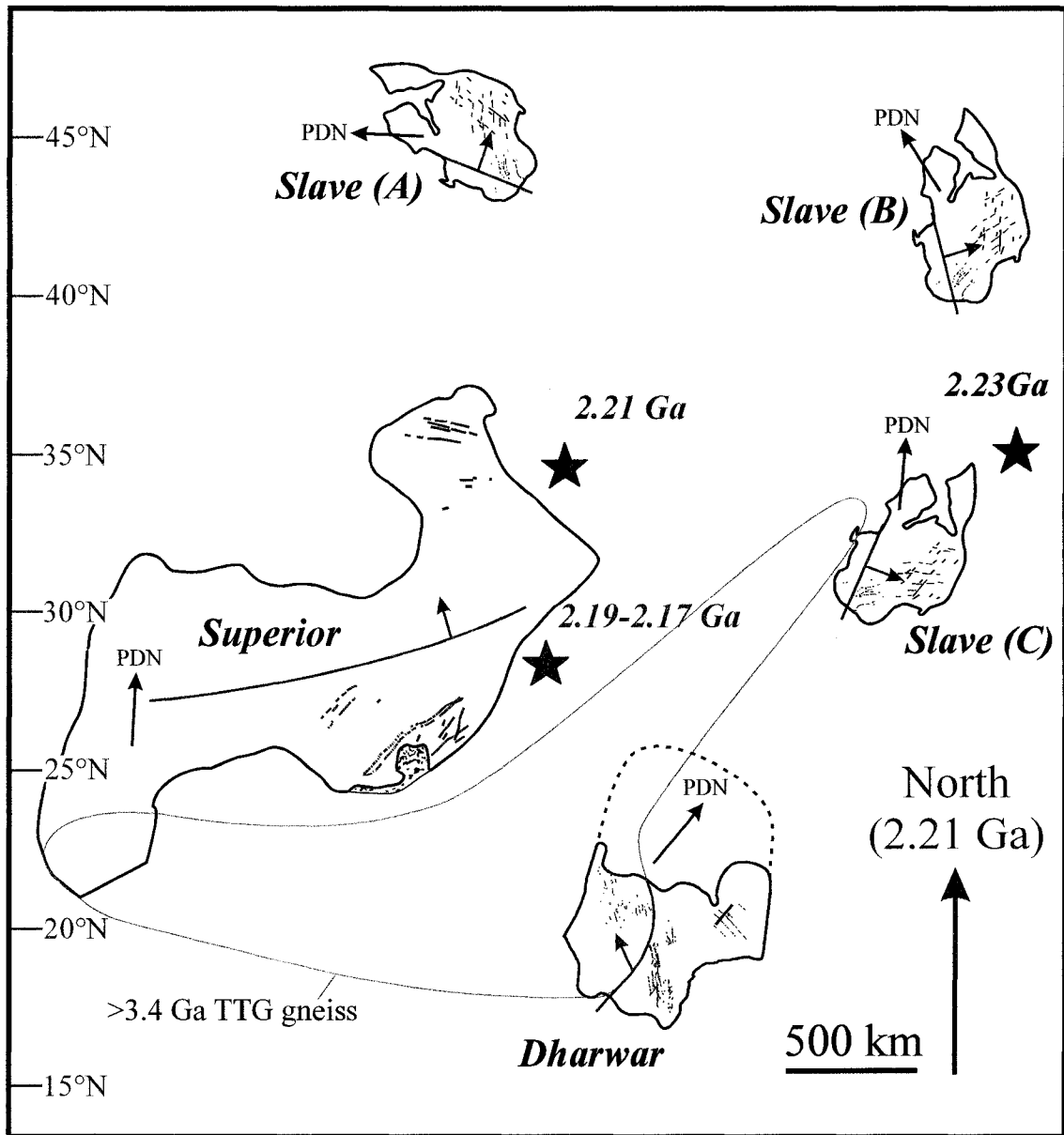


Fig. 4-24. Paleocontinental reconstruction involving the Dharwar, Superior, and Slave cratons at ~ 2.2 Ga. Paleolatitude and orientation of the Superior craton at 2.21 Ga is constrained from paleomagnetic and geochronological data for the Senneterre dyke swarm (Buchan et al., 1993), and similar constraints for the Dharwar craton are from the Somala dyke swarm (this study; Kumar and Bhall, 1983). Otherwise, the reconstruction has been attempted in a similar fashion and with the same assumptions as that shown in Fig. 4-23 (~ 2.2 Ga Superior and Slave events referenced in Fig. 4-22), and includes three possibilities for the location and orientation of the Slave craton (A, B, and C). Also shown is a correlation of old (>3.4 Ga) gneiss terrains, the trends of first-order structures (green lines) and subduction polarities (green arrows) for the Late Archean (Superior and Slave: Hoffman, 1989; and Calvert et al., 1995; Dharwar: Chadwick et al., 2000), and the orientation of present-day north (black arrows labelled PDN) for each craton.

Fig. 4-25. a) Paleocontinental reconstruction of Kurnorland including the Dharwar, Slave, Superior, Karelian, and Wyoming cratons, showing break-up in two stages at 2.5-2.37 and 2.23-2.17 Ga. The distribution of ~2.45 Ga mafic dyke swarms and supracrustal rocks and the pre-break-up juxtaposition of the Superior, Wyoming, and Karelian cratons at ~2.45 Ga is modified from Heaman (1997). The positions and orientations of the Slave and Dharwar cratons in relation to the Superior craton are constrained using the method outlined in Fig. 4-23, but with the additional assumption that the entire Ungava radiating swarm was emplaced in a geologically short time span of <10 Ma at ~2.21 Ga. Geological features including mafic dykes (lines), supracrustal rocks (solid colour), and inferred mantle plume centres (stars) are colour-coded to specific ages as indicated. The location of the 2.5-2.47 Ga mantle plume centre and associated 2.5 Ga Ptarmigan (P) and 2.47 Ga Mistassini (M) mafic dyke swarms are modified from: Heaman, 1994; Buchan et al., 1998; Ernst and Buchan, 2001b. The locations of ~2.5 Ga (orange dots) and ~2.2 Ga mafic sills (red squares) in Karelia are modified from Amelin et al. (1995) and Vuollo et al. (1995), respectively. The distribution of ~2.21 Ga mafic magmatism in the Superior and the inferred mantle plume centre are from Buchan et al. (1998). The 2.17 Ga Biscotasing swarm of the Superior is modified from Halls and Davis (2004), and 2.23-2.18 Ga mafic dyke swarms in the Slave are modified from LeCheminant et al. (1996). The main trends of first-order geological structures (thick green lines) and subduction polarities (green arrows) for the Late Archean are modified from: Hoffman, 1989, and Calvert et al., 1995 (Superior and Slave); Chadwick et al., 2000 (Dharwar). Distribution of mafic dyke swarms in the Dharwar craton is modified from Fig. 4-19, and the orientation and location of two (2.42 Ga?) pre-Bangalore mafic dykes are shown as a yellow bars, on the basis of crosscutting relationships (Kumar and Bhall, 1983; Padmakumari and Dayal, 1987) reported for old NE-SW dykes crosscut by the 2366 Ma Penukonda dyke (dated in this study), and an electron microprobe chemical baddeleyite date of 2413±22/-23 Ma (Appendix C) for a NE-SW trending dyke (labelled JEF-99-12). Inset figure includes the remaining constituents of Ur (Rogers, 1996), built off of the Dharwar craton and as shown in their relative positions and orientations in a recent Gondwanaland reconstruction (Collins and Pisarevsky, 2005). (Abbreviations: D Dharwar protocontinent; K Karelia; Ka Kaapvaal craton; P Pilbara craton; S Slave craton; Su Superior craton; W Wyoming craton). b-e) Simplified schematics showing a geodynamic interpretation of dyke swarm patterns in (a) as evidence for two stages (2.5-2.37 Ga and 2.23-2.17 Ga) of episodic break-up of a Late Archean paleocontinent (Kurnorland) preceding 2.1-1.8 Ga global orogenesis. b) An initial protracted phase of mantle plume activity, rifting and continental break-up from 2.5-2.37 Ga. c) Ocean opening from 2.37-2.23 Ga. d) A switch from passive to active margins with development of old (150 Ma) oceanic crust, leads to peripheral subduction and generation of intracontinental extension leading to a second stage of mafic magmatism and break-up from 2.23-2.17 Ga. e) A now highly fragmentary distribution of continents sets the scene for global orogenesis and the formation of Columbia between 2.1-1.8 Ga (Zhao et al., 2002).

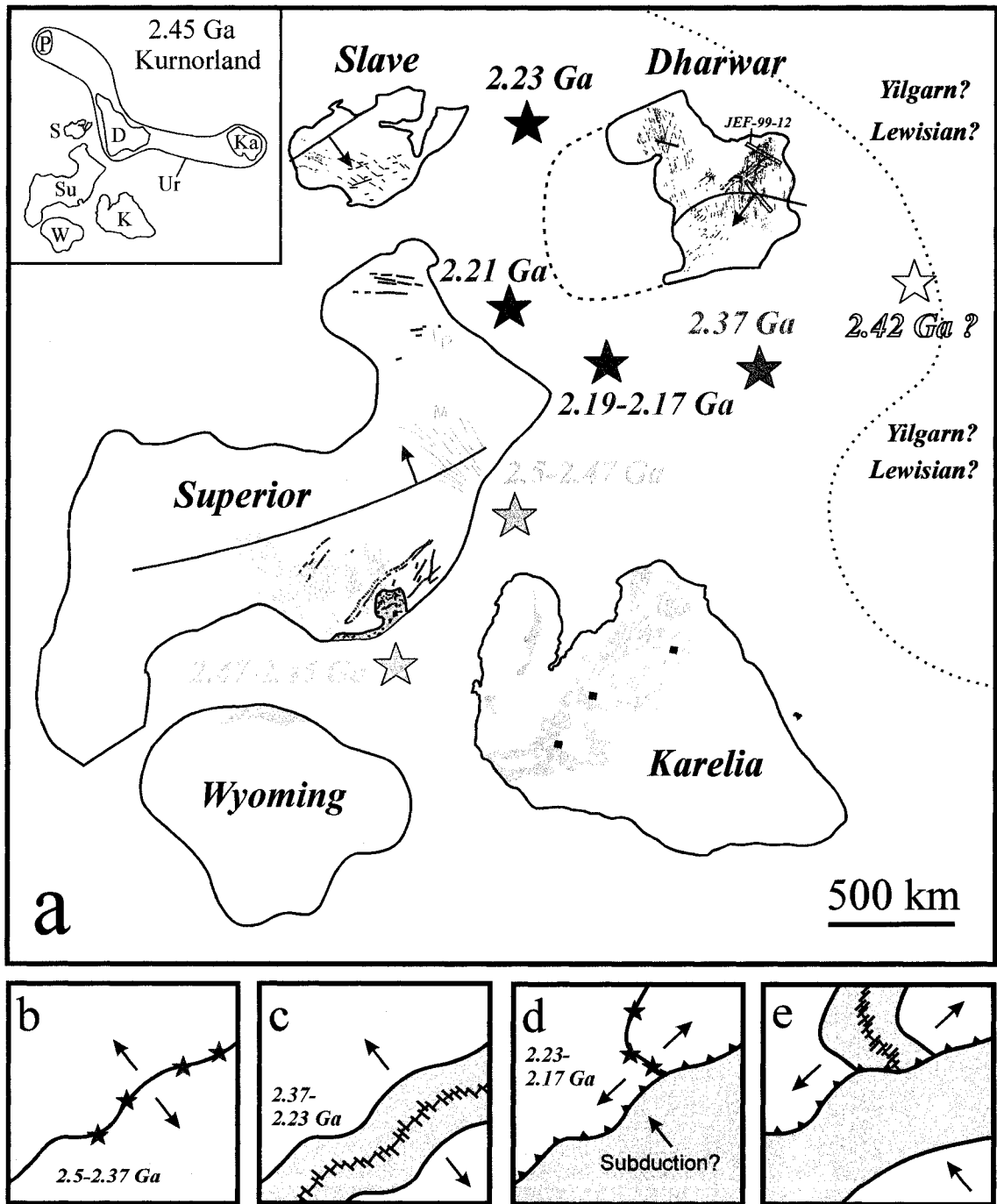


Fig. 4-25

CHAPTER 5

Conclusions

Summary

This study focused on geochronological studies of mafic rocks from India using multiple radiometric dating techniques including U-Pb isotope dilution thermal ionization mass spectrometry (IDTIMS), electron microprobe (EM) chemical U-Th-total Pb dating, and U-Pb laser ablation multi-collector inductively coupled plasma mass spectrometry (LA-MC-ICP-MS). The principal aim was to use these techniques to determine the crystallization ages of U-(±Th)-bearing accessory minerals from mafic dykes including baddeleyite (ZrO_2), zircon ($ZrSiO_4$), zirconolite ($CaTiZr_2O_7$), monazite (Ce,La,Nd,Th) PO_4 , and rutile (TiO_2). This required extensive training and familiarization with established conventional methods and theory of isotopic and chemical dating of these minerals (Krogh et al., 1987; Suzuki and Adachi, 1991; Heaman and Parrish, 1991; Heaman and Machado, 1992). However, to some degree all of these radiometric dating techniques were also used in novel ways in this project, and required the use of cutting edge technology and methods (Söderlund and Johansson, 2002; Simonetti et al., 2005; Simonetti et al., 2006). Particularly novel applications included the first ever EM dating studies of baddeleyite (French et al., 2002a; Chapter 2; Appendix C) and zirconolite (French et al. 2002b; Appendix E), and the first successful attempt to date the timing of mafic dyke emplacement by *in situ* chemical and isotopic dating of monazite (Chapter 3).

U-Pb dating was focussed on Proterozoic mafic dyke swarms of the south Indian shield (Fig. 5-1). High precision U-Pb IDTIMS ages presented for mafic dyke swarms

from south India in this study, build upon the existing geochronological database and resolve many outstanding problems in Proterozoic crustal evolution of the Indian shield. The data demonstrate unequivocally, that Paleoproterozoic mafic dyke swarm emplacement across the Dharwar and Bastar cratons comprised several craton-transsecting magmatic events that took place over short geological time spans (a few million years or less) at specific time periods including 2.37, 2.21, 2.18, and 1.88-1.89 Ga. These results raise the level of knowledge about the timing of dyke emplacement events in the south Indian shield to that of other well-studied Precambrian provinces such as the Slave craton, Canada. As a result, rigid time correlations are now possible between major Paleoproterozoic mafic dyke swarms of south India and similar records preserved in a number of other Archean provinces worldwide, ultimately facilitating reconstruction of ancient (pre-Rodinia) supercontinents and increasing our understanding of a pivotal time period in Earth evolution.

EM Dating of Mafic Dykes: Exploration of New Applications and Geochronometers

Mafic dykes that have a small baddeleyite grain size (<30 μm) are not normally amenable to conventional baddeleyite mineral separation and U-Pb dating, and so one of the first goals of this thesis project was to evaluate the feasibility of EM dating of baddeleyite. The high spatial resolution of this technique (1 μm) allows for accurate chemical U-Th-total Pb dating of very tiny crystal domains (~5 μm across and larger) in polished thin section, as long as the mineral being analysed contains sufficient U and/or Th and radiogenic Pb for EM analysis (generally a few hundred ppm and higher for each element), contains negligible common Pb, and has remained closed to the migration of

U, Th, Pb and all intermediate daughter products throughout its history. As baddeleyite in mafic dykes generally meets all of these criteria (Heaman and LeCheminant, 1993) and because many mafic dykes have a small baddeleyite grain size, the EM dating technique (Suzuki and Adachi, 1991) therefore shows great promise for increasing the number of mafic dyke samples suitable for baddeleyite dating.

For this EM baddeleyite dating feasibility study (Chapter 2, French et al., 2002a), five baddeleyite reference samples were selected for which IDTIMS age information was available or determined as a part of the study, and suitably spanned a large Proterozoic age range (2.4-0.8 Ga). The study was an overall success and demonstrated that typical baddeleyite in Proterozoic mafic dykes yields EM ages that are accurate to within ~140 m.y. (but usually better) and with a routine precision of about 50-100 m.y.. The principal conclusion of this study is that EM dating is an excellent tool for determining rapid, cost effective, first-order age information from baddeleyite in mafic dyke samples, especially those which are otherwise unsuitable for conventional U-Pb dating because of the small baddeleyite grain size. Used in combination with conventional U-Pb dating studies of mafic dyke swarms, EM baddeleyite dating can provide a very useful reconnaissance tool in determining the ages of a large number of mafic dyke samples, particularly in Precambrian provinces where multiple mafic dyke swarms were emplaced a few hundred million years apart.

A summary of the results of this study is shown in Fig. 5-2, along with an updated suite of baddeleyite data from eight additional mafic rocks for which conventional U-Pb ages are available, and for which EM ages have recently been determined in peripheral side projects during this study. Most of the updated

baddeleyite data plot on or close to a reference line showing 1:1 correlation between the two techniques, providing additional support for the conclusions of the original paper (French et al., 2002a). One sample however, plots significantly further away from the trend line than all other samples; the EM baddeleyite age for sample JEF-02-6 (a Malley dyke, Slave craton: French et al., 2004) is ~400 m.y. too young. These new data indicate that for some baddeleyite samples there may be X-ray line interference problems relating to anomalously high trace-element concentrations (such as Nb – which was the case for JEF-02-6, data not presented) in baddeleyite (see further discussion on this in Appendix C). An important future direction of research in EM baddeleyite dating would be to explore these complexities in detail, in an effort to try to improve the accuracy of the technique. EM baddeleyite dating of 13 mafic igneous rocks from the South Indian Shield (Appendix C), many of which now have known U-Pb IDTIMS ages, further demonstrates the value of this technique as a rapid, cost-effective, dating tool in reconnaissance geochronological studies of Precambrian mafic dyke swarms.

A number of other late-crystallizing U- and Th-bearing accessory minerals were also the subject of EM chemical dating studies in this thesis project including zircon (Appendices A and C), monazite (Chapter 3), and zirconolite (Appendix E). EM dating of igneous zircon from the BD2 mafic dyke swarm, Bastar craton (Appendix A), yielded a highly complex geochronological dataset as has been observed in EM dating studies of zircon from granitic rocks (e.g. Geisler and Schleicher, 2000). It was concluded in that study (Appendix A) that EM dating of zircon is currently not a very reliable method for dating the timing of emplacement of mafic dykes (especially hydrothermally altered dykes), but that certain types of zircon apparently yield highly precise apparent

hydrothermal alteration ages in agreement with U-Pb IDTIMS (lower intercept) age constraints. Determination of mafic dyke emplacement ages by EM zircon dating may currently be possible in exceptionally fresh samples containing zircon with moderate U and Th concentrations (ca. 200-300 ppm - with detectable radiogenic Pb) that have not been affected by extensive radiation damage and subsequent Pb-loss. Because zircon domains with the lowest U and Th contents tend to yield the most accurate but least precise EM ages (Geisler and Schleicher, 2000; Appendix A), such studies will be more feasible when employing higher sensitivity (i.e. ppm level of detection) next-generation electron microprobes.

In searching for baddeleyite and zircon crystals in polished thin section during reconnaissance dating studies by EM, the presence of other U- and Th-bearing accessory minerals including monazite and zirconolite was also documented for a number of mafic dyke samples. Monazite was discovered in 3 mafic dykes from south India (JEF-99-2; JEF-99-7; JEF-00-30), and in one case (JEF-00-30) was the subject of a multi-technique (EM and LA-MC-ICP-MS) radiometric dating study (Chapter 3). The discovery of monazite in several mafic dyke samples in this project, coupled with the accuracy and good precision of the chemical and isotopic ages determined for one unequivocally igneous grain (Chapter 3), indicates that monazite has been overlooked in the past as a geochronometer for determining emplacement ages of mafic dykes. Preliminary EM dating results for zirconolite crystals from the Duck Lake sill (Slave craton) and the Phalaborwa carbonatite (South Africa) indicate that zirconolite shows promise as a geochronometer for dating the timing of crystallization of mafic rocks (as recently demonstrated by sensitive high resolution ion microprobe analysis: Rasmussen and

Fletcher, 2004; and NanoSIMS: Stern et al., 2005). It should be noted, however, that there are previously undocumented complexities in EM zirconolite dating which still need to be understood (French et al., 2002b; Appendix E).

The Paleoproterozoic record of mafic dyke swarm emplacement in the south Indian shield: New high precision age constraints from U-Pb IDTIMS dating of baddeleyite and zircon

High precision U-Pb IDTIMS ages were determined for a total of ten mafic dykes and one mafic sill in this study (Chapters 3 and 4), establishing for the first time robust constraints on the timing and extent of several major Paleoproterozoic mafic magmatic events across a vast tract of the southern block of the Indian shield (Fig. 5-1). Similar U-Pb baddeleyite ages of 2365.4 ± 1.0 Ma, 2365.9 ± 1.5 Ma and 2368.6 ± 1.3 Ma were determined for three parallel mafic (basaltic andesite) dykes from the prominent E-W trending Bangalore dyke swarm of the eastern Dharwar craton, sampled along a ~175 km across strike transect. A composite regression of U-Pb baddeleyite data from all three dyke samples yields an upper concordia intercept date of 2365.9 ± 0.7 Ma (MSWD=0.7; $n=8$, comprising the statistically most similar 2/3 of the dataset for each dyke), suggesting that emplacement of the Bangalore dyke swarm took place over a large region (~60,000 km²), in a short geological time span of less than two million years at 2366 Ma. A second major outbreak of mafic magmatic activity took place across much of the Dharwar craton at ~2.2 Ga commencing with emplacement of N-S trending sub-alkalic basaltic and NW-SE trending picritic dykes at 2213.6 ± 3.9 Ma (U-Pb baddeleyite age) and 2209.3 ± 2.8 Ma (U-Pb baddeleyite age), respectively, in the region south of the Cuddapah basin. This magmatism was followed shortly by another

widespread magmatic pulse at ~ 2.18 Ga, recorded by a U-Pb baddeleyite age of 2180.8 ± 0.9 Ma for a NW-SE trending sub-alkalic basaltic dyke from the north-western reaches of the Shimoga supracrustal belt of the Western Dharwar craton, and a U-Pb baddeleyite/zircon age of 2176.5 ± 3.7 Ma for a geochemically similar E-W trending gabbro dyke located north of the Cuddapah basin in the Eastern Dharwar craton, ~ 550 km away. A U-Pb age of 2100 ± 11 Ma determined on rutile from a NE-SW trending metamorphosed HMD mafic dyke from the southern Bastar craton is interpreted to provide a minimum emplacement age for this predominantly NW-SE trending swarm, and may coincide with the timing of regional greenschist-grade metamorphism. U-Pb ages of 1891.1 ± 0.9 Ma (baddeleyite) and 1883.0 ± 1.4 Ma (baddeleyite and zircon) for two NW-SE trending dykes from the BD2 mafic dyke swarm, southern Bastar craton, and 1885.4 ± 3.1 Ma (baddeleyite) for a mafic sill from the Cuddapah basin, indicate the existence of a ~ 600 km long, 1891-1883 Ma large igneous province (LIP) that spans $\sim 90,000$ km² within the south Indian shield.

Implications for Paleoproterozoic crustal evolution of the south Indian shield

Tectonic Significance of the 1.9 Ga Southern Bastar-Cuddapah LIP

Mafic magmatism in the south Indian shield at 1.9 Ga during emplacement of the Southern Bastar-Cuddapah LIP was clearly associated with early stages of extension and sedimentation in the Proterozoic Cuddapah basin (Anand et al., 2003; Chapter 3), although it is not clear whether this event was linked with continental break-up. Lithospheric stretching, and mantle melting beneath the Cuddapah basin could have been caused by passive rather than active rifting (Anand et al., 2003), but a mantle plume origin for the Southern Bastar-Cuddapah LIP has not currently been ruled out.

Although there is no clear-cut radiating pattern observed for the NW-SE trending BD2 dyke swarm, towards the northeast corner of the craton where dolerite dykes truncate against the Terrane Boundary Shear Zone of the Eastern Ghats Belt (Fig. 3-2, Chapter 3), the main orientation of dolerite dykes is NNW-SSE (Biswal and Sinha, 2003). If some of these dykes also belong to the BD2 dyke swarm it would approximately double again, the maximum estimated aerial extent of the swarm within the Bastar craton. In this scenario, the geometry of the swarm would be consistent with emplacement of BD2 dykes as a giant radiating mafic dyke swarm with a focal point some distance outboard of the current south-eastern margin of the Bastar craton (and east of the Cuddapah basin). This proposal needs to be tested with further U-Pb dating studies. The widespread occurrence of WNW-ESE and NNE-SSW trending, Proterozoic Newer dolerite dykes within the Singhbhum nucleus (Naqvi and Rogers, 1987; Nash et al., 1996) provides additional speculative evidence to suggest that 1.88 Ga mafic magmatism could have spanned the entirety of the eastern margin of the Dharwar protocontinent. This is consistent with the structural geology of the Rengali Province (between the Bastar and Singhbhum cratons), which indicates that the Singhbhum nucleus may have been the northern extension of the Bastar craton, prior to ~200 km of dextral displacement along the Kerajang Fault Zone in the Paleo/Mesoproterozoic (Nash et al., 1996; Crowe et al., 2003). In this scenario, the NNE-SSW trending Newer dolerite dykes of the Singhbhum nucleus might represent a further continuation of the putative radiating pattern of BD2 dykes.

In the present interpretation, the 1891-1883 Ma BD2 mafic dyke swarm and 1885 Ma Cuddapah mafic magmatism, are considered to represent segments of a single

LIP (the Southern Bastar-Cuddapah LIP) that bridges the Godavari rift occurring in both the Bastar and Dharwar cratons. This interpretation contradicts a recently proposed model for the origin of the 1.6 Ga Bhopalpatnam granulite belt (which occurs along the southwest margin of the Bastar craton and is adjacent and parallel to the Godavari rift: Fig. 3-2, Chapter 3), as a collisional join between the Dharwar and Bastar cratons (Santosh et al., 2004). If the present interpretation of the 1.9 Ga Southern Bastar-Cuddapah LIP is correct, then the join between the Bastar and Dharwar cratons may originally date to an older time (perhaps at 2.5-2.2 Ga during formation of the Karimnagar granulite belt: Santosh et al., 2004). An alternative interpretation of the 1.6 Ga Bhopalpatnam belt is that it represents an intracratonic collision zone that occurs along a previously existing suture.

New Regional Time-Markers and Paleo-Stress Indicators for the South Indian Shield

Several of the mafic igneous provinces identified in this project by U-Pb dating appear to be substantial in size (Fig. 5-1). Strictly on the basis of correlation of mafic igneous rocks with overlapping U-Pb IDTIMS baddeleyite and zircon ages, two provinces including the 2.18 Ga Northern Dharwar dyke swarm and the 1891-1883 Ma Southern Bastar-Cuddapah province exceed 500 km in length, and including plausible regional correlations with other dykes as shown (Fig. 5-1) each comprise LIPs that span $\sim 90,000 \text{ km}^2$ of the south Indian shield. The 2366 Ma Bangalore dyke swarm outcrops as a dense array of E-W trending dykes in the region south and southwest of the Cuddapah basin, where it outcrops over a minimum area of $\sim 60,000 \text{ km}^2$, but including the plausible northern extension (Halls, 1982), this swarm spans $>150,000 \text{ km}^2$ of the Dharwar craton (Fig. 5-1). These three LIPs are interpreted to represent the erosional

remnants of volumetrically much larger provinces that may also have included ancient flood basalt provinces, and possibly rifted fragments now in other cratons. On the basis of U-Pb IDTIMS ages determined in this project, regional dyke patterns, distinctive petrographic and geochemical features (e.g. Srivastava et al., 2004), and cross-cutting relationships with country rocks, these newly identified LIPs represent excellent regional time markers that provide useful tools for deciphering the Paleoproterozoic crustal evolution of the Dharwar and Bastar cratons. The geographic extent of 2.21 Ga mafic magmatism in the Dharwar craton is less clear, but based on inclusion of regional dykes that are parallel to the ones dated by U-Pb, it may also span a substantial area of the eastern Dharwar craton (Fig. 5-1).

Prior to this U-Pb dating study, a major unresolved paradox existed in the Proterozoic record of mafic magmatism in the eastern Dharwar craton. Accumulating geochronological evidence for mafic igneous rocks intruding the Tadpatri Formation of the Cuddapah Basin, has suggested that early basin development took place in the Late Paleoproterozoic (Rb-Sr age of 1817 ± 24 Ma: Bhaskar Rao et al., 1995; $^{40}\text{Ar}/^{39}\text{Ar}$ laser fusion age on phlogopite separates: 1899 ± 20 Ma: Anand et al., 2003; U-Pb baddeleyite age of 1885.4 ± 3.1 Ma: Chapter 3). Numerous crosscutting Proterozoic mafic dyke swarms of various orientations are seen to outcrop around the western margin of the Cuddapah basin (Fig. 5-1), where they are truncated at the basal unconformity (Padmakumari and Dayal, 1987; Murty et al., 1987). Despite this crosscutting relationship, the geochronological database (predominantly $^{40}\text{Ar}/^{39}\text{Ar}$ and K-Ar ages) indicated peak episodes of mafic dyke emplacement around the basin at 1900-1700 Ma, 1400-1300 Ma, and 1200-1000 Ma (Mallikarjuna Rao et al., 1995), and potentially

comprising as many as 18 separate mafic dyke swarms spanning 2070 to 660 Ma (Murty et al., 1987). In contrast, the U-Pb ages presented in this study for mafic dykes surrounding the Cuddapah basin (Fig. 5-1) indicate that these major dyke swarms indeed predate early development of the Cuddapah basin. Collectively these U-Pb ages also indicate that mafic dyke emplacement appears to have occurred in a punctuated fashion during very specific time periods at 2366 Ma, 2.22-2.21 Ga, and 2.18 Ga, with peak mafic dyke swarm emplacement in the Paleoproterozoic.

Two large mafic dyke swarms dated by U-Pb in this study, the 2366 Ma Bangalore and 2.18 Ga Northern Dharwar swarms, appear to radiate through $\sim 25^\circ$ of arc (Fig. 5-1). The focal points of these radiating dyke patterns might be used to infer ancient mantle plume centres (Ernst and Buchan, 2001a), but such interpretations are considered to be highly speculative at this stage. This is because only two or three dykes have been dated from each swarm, and the radiating pattern shown by the Bangalore swarm swings in sympathy with the structural grain of the granite-greenstone terrain it intrudes, possibly suggesting the persistence of Late Archean plate boundary forces into the Paleoproterozoic (Halls, 1978; Halls, 1982). The geometry of mafic dyke swarms may provide valuable glimpses of regional plate stresses at the time of their intrusion (Halls, 1982; Féraud et al., 1987; Ernst et al., 1995), and so the crustal-scale patterns exhibited by the dyke swarms dated by U-Pb in this study provide useful paleo-stress indicators for very specific time periods during the Paleoproterozoic crustal evolution of the south Indian shield. Although it is not entirely clear in each case as of yet, emplacement of continental mafic dyke swarms in the south Indian shield at 2.37 Ga, 2.21 Ga, 2.18 Ga, and 1.89-1.88 Ma, may have been linked with specific continental

break-up events at these times, possibly associated with break out of the Dharwar and Bastar cratons from a larger parental supercontinent in the Paleoproterozoic.

Global correlation of Paleoproterozoic mafic magmatic events: Implications for paleocontinental reconstructions involving the Dharwar and Bastar cratons and identifying ancient superplume events

Emplacement of large continental mafic dyke swarms may be linked with a number of other major geodynamic processes including eruption of continental flood basalt provinces, intracontinental rifting, ocean opening, and mantle plume activity (Fahrig, 1987; LeCheminant and Heaman, 1989; Ernst et al., 1995). As such, global correlation of Precambrian mafic dyke swarms is pivotal in constraining ancient plate reconstructions (Heaman 1997; Wingate et al., 1998; Mertanen et al., 1999; Harlan et al., 2003; Hanson et al., 2004) and unravelling the history of mantle plume activity on Earth (Ernst and Buchan, 2001a; Ernst and Buchan, 2001b). The U-Pb IDTIMS ages presented in this study enable for the first time, robust age correlations of Paleoproterozoic mafic magmatism in the Dharwar and Bastar cratons to well-dated events in other Archean cratons worldwide (Fig. 5-3).

A comparison of Paleoproterozoic Dharwar mafic magmatism dated by U-Pb in this study to the global database shows that the Dharwar craton has a unique record, in terms of the distribution of Paleoproterozoic mafic magmatic events through time (Fig. 5-3). U-Pb ages for the 2366 Ma Bangalore mafic dyke swarm presented in this study comprise the first concrete evidence for a large-scale (>150 km) mafic magmatic event of this age anywhere on Earth. With the exception of Scourie II mafic magmatism in the Lewisian craton (Heaman, 2004), this event occurs within a ~150 m.y. time gap in the

Paleoproterozoic mafic magmatic record between emplacement of the 2262±2 Ma Chimbadzi Hill intrusion of Zimbabwe (Manyeruke et al., 2004) and the 2410-2418 Ma Widgiemooltha dykes of the Yilgarn craton, Australia (Doehler and Heaman, 1998; Nemchin and Pidgeon, 1998). Although on the basis of global correlations of Paleoproterozoic mafic magmatism (Fig. 5-3) the Dharwar does not match-up exactly with any other Archean craton on Earth, this craton does share many notable similarities with the Superior and Slave cratons of North America because all three cratons contain mafic magmatic events that fall between 2.23-2.21 Ga, 2.19-2.17 Ga, and 1.89-1.88 Ga. These similarities in Paleoproterozoic crustal evolution place the Dharwar, Slave, and Superior cratons in a similar class, the significance of which is currently debatable. In Chapter 3, it is outlined that coeval mafic magmatism at 1.9 Ga in the Kalahari, Bastar, Dharwar, and Superior cratons took place in contrasting tectonic settings and during a time of global crustal amalgamation and orogenesis, and that this global record of mafic magmatism therefore reflects a period of enhanced mantle plume activity or significant asthenospheric up-welling on Earth at 1.9 Ga. This newly recognized 1.9 Ga global mafic magmatism is analogous to widespread mafic magmatic events that took place at 1.1 Ga during Rodinia assembly (Hanson et al., 2004). Chapter 4 explores the possibility that global mafic magmatism at 2.2 Ga might be linked with mantle plume-defined continental break-up events involving the Dharwar, Slave, and Superior cratons. In this interpretation, the relative ages and geometries of 2.23-2.17 Ga dyke swarms in these cratons may shed light on possible plate reconstructions at 2.2 Ga (Fig. 5-4), but robust correlations will require paleomagnetic studies on Dharwar dykes and further U-Pb dating to define regional dyke patterns more clearly. Correlation of 2.2 Ga mafic

igneous provinces in this study provides a valuable hint that the ancient continents Ur (Rogers, 1993; 1996) and Kenorland (Williams et al., 1991; Pesonen et al., 2003) may have been connected as a single supercontinent (Kurnorland) that underwent break-up at this time (Fig. 5-4). At any rate, the correlations indicate unequivocally that fragments of both putative paleocontinents shared a similar history of intracontinental mafic dyke swarm emplacement during this time, and this mafic magmatism may have been linked with an increase in global mantle plume activity at ~2.2 Ga.

References

- Anand, M., Gibson, S.A., Subbarao, K.V., Kelly, S.P., & Dickin, A.P. (2003). Early Proterozoic melt generation processes beneath the intracratonic Cuddapah Basin, southern India. *Journal of Petrology* **44**, 2139-2171.
- Bhaskar Rao, Y.J., Pantulu, G.V.C., Damodara Reddy, V., Gopalan, V. (1995). Time of early sedimentation and volcanism in the Proterozoic Cuddapah Basin, South India: Evidence from the Rb-Sr age of Pulivendla mafic sill. In: *Devaraju, T.C., ed., Mafic Dyke Swarms of Peninsular India, Geological Society of India Memoir* **33**, 329-338.
- Biswal, T.K. & Sinha, S. (2003). Deformation history of the NW salient of the Eastern Ghats mobile belt, India. *Journal of Asian Earth Sciences* **22**, 157-169.
- Crowe, W.A., Nash, C.R., Harris, L.B., Leeming, P.M., & Rankin, L.R. (2003). The geology of the Rengali Province: implications for the tectonic development of north Orissa, India. *Journal of Asian Earth Sciences* **21**, 697-710.
- Doehler, J.S., and Heaman, L.M. (1998). 2.41 Ga U-Pb baddeleyite ages for two gabbroic dykes from the Widgiemooltha swarm, western Australia: A Yilgarn-Lewisian connection? *Geological Society of America Abstracts with Programs* **30**, A291-292.
- Ernst, R.E., Head, J.W., Parfitt, E., Grosfils, E., & Wilson, L. (1995). Giant radiating dyke swarms on Earth and Venus. *Earth-Science Reviews* **39**, 1-58.
- Ernst, R.E. & Buchan, K.L. (2001a). The use of mafic dike swarms in identifying and locating mantle plumes. In: *Ernst, R.E. & Buchan, K.L., eds., Mantle Plumes: Their Identification Through Time – Geological Society of America Special Paper* **352**, 247-265.
- Ernst, R.E. & Buchan, K.L. (2001b). Large mafic magmatic events through time and links to mantle-plume heads. In: *Ernst, R.E. & Buchan, K.L., eds., Mantle Plumes: Their*

Identification Through Time – Geological Society of America Special Paper 352, 483-566.

Fahrig, W.F. (1987). The tectonic settings of continental mafic dyke swarms: failed arm and early passive margin, *In: Halls, H.C. and Fahrig, W.F., eds., Mafic Dyke Swarms, Geological Association of Canada Special Paper 34*, 331-348.

Féraud, G., Giannérini, G., & Campredon. (1987). Dyke Swarms as Paleostress Indicators in Areas Adjacent to Continental Collision Zones: Examples from the European and Northwest Arabian Plates. *In: Halls, H.C. and Fahrig, W.F., (eds.), Mafic Dyke Swarms, Geological Association of Canada Special Paper 34*, 273-278.

French, J.E., Heaman, L.M., Chacko, T. (2002a). Feasibility of chemical U-Th-total Pb baddeleyite dating by electron microprobe. *Chemical Geology 188*, 85-104.

French, J.E., Heaman, L.M., Chacko, T., Armstrong, J. & Cairns, S. (2002b). Electron Microprobe dating of mafic to ultramafic igneous rocks. *Abstract Volume, 30th Yellowknife Geoscience Forum*.

French, J.E., Atkinson, B., Heaman, L.M., Chacko, T., Armstrong, J., Cairns, S. & Hartlaub, R. (2004). Application of electron microprobe chemical baddeleyite dating to reconnaissance geochronological investigations of mafic dyke swarms. *Joint Annual GAC/MAC Meeting, St. Catharines, Ontario, Abstracts Volume 29*, 442 (digital volume).

Geisler, T. & Schleicher, H. (2000). Improved U-Th-total Pb dating of zircons by electron microprobe using a simple new background modelling procedure and Ca as a chemical criterion of fluid-induced U-Th-Pb discordance in zircon. *Chemical Geology 163*, 269-285.

Halls, H.C. (1978). The structural relationship between Archean granite-greenstone terrains and late Archean mafic dikes. *Canadian Journal of Earth Sciences 15*, 1665-1668.

Halls, H.C. (1982). The importance and potential of mafic dyke swarms in studies of geodynamic processes. *Geoscience Canada 9*, 145-153.

Hanson, R.E., Crowley, J.L., Bowring, S.A., Ramezani, J., Gose, W.A., Dalziel, I.W.D., Pancake, J.A., Seidel, E.K., Blenkinsop, T.G., & Mukwakwami, J. (2004a). Coeval large-scale magmatism in the Kalahari and Laurentian cratons during Rodinia assembly. *Science 304*, 1126-1129.

Harlan, S.S., Heaman, L., LeCheminant, A.N., & Premo, W.R. (2003). Gunbarrel mafic magmatic event: A key 780 Ma time marker for Rodinia plate reconstructions. *Geology 31*, 1053-1056.

Heaman, L.M. (1997). Global mafic magmatism at 2.45 Ga: Remnants of an ancient

large igneous province? *Geology* **25**, 299-302.

Heaman, L.M. (2004). 2.5-2.4 Ga Global magmatism: remnants of supercontinents or products of superplumes? *Geological Society of America Abstracts with Programs* **36**, 255.

Heaman, L. & Parrish, R. (1991). U-Pb geochronology of accessory minerals. In: *MAC short course handbook* **19**, Heaman, L. & Ludden, J.N. (eds.), on applications of radiogenic isotope systems to problems in geology, 59-102.

Heaman, L.M. & Machado, N. (1992). Timing and origin of midcontinent rift alkaline magmatism, North America: evidence from the Coldwell Complex. *Contributions to Mineralogy and Petrology* **110**, 289-303.

Heaman, L.M. & LeCheminant, A.N. (1993). Paragenesis and U-Pb systematics of baddeleyite (ZrO₂). *Chemical Geology* **110**, 95-126.

Krogh, T.E., Corfu, F., Davis, D.W., Dunning, G.R., Heaman, L.M., Kamo, S.L., Machado, N., Greenough, J.D., & Nakamura, E. (1987). Precise U-Pb isotopic ages of diabase dykes and mafic to ultramafic rocks using trace amounts of baddeleyite and zircon. In: *Halls, H.C. and Fahrig, W.F., eds., Mafic Dyke Swarms, Geological Association of Canada Special Paper* **34**, 147-152.

LeCheminant, A.N. & Heaman, L.M. (1989). Mackenzie igneous events, Canada: Middle Proterozoic hotspot magmatism associated with ocean opening. *Earth and Planetary Science Letters* **96**, 38-48.

Mallikarjuna Rao, J., Bhattacharji, S., Rao, M.N., & Hermes, O.D. (1995). ⁴⁰Ar-³⁹Ar Ages and Geochemical Characteristics of Dolerite Dykes Around the Proterozoic Cuddapah Basin, South India. In: *Devaraju, T.C., ed., Mafic Dyke Swarms of Peninsular India, Geological Society of India Memoir* **33**, 307-328.

Manyeruke, T.D., Blenkinsop, T.G., Buchholz, P., Love, D., Oberthür, T., Vetter, U.K., & Davis, D.W. (2004). The age and petrology of the Chimbadzi Hill Intrusion, NW Zimbabwe: first evidence for early Paleoproterozoic magmatism in Zimbabwe. *Journal of African Earth Sciences* **40**, 281-292.

Mertanen, S., Halls, H.C., Vuollo, J.I., Pesonen, L.J., & Stepanov, V.S. (1999). Paleomagnetism of 2.44 Ga mafic dykes in Russian Karelia, eastern Fennoscandian Shield – implications for continental reconstructions. *Precambrian Research* **98**, 197-221.

Murty, Y.G.K., Babu Rao, V., Guptasarma, D., Rao, J.M., Rao, M.N., & Bhattacharji, S. (1987). Tectonic, petrochemical and geophysical studies of mafic dyke swarms around the Proterozoic Cuddapah basin, South India. In: *Halls, H.C. & Fahrig, W.F., eds., Mafic Dyke Swarms, Geological Association of Canada Special Paper* **34**, p.303-316.

- Naqvi, S.M. & Rogers, J.J.W. (1987). Precambrian Geology of India, *Oxford monographs on geology and geophysics* **6**, 233p.
- Nash, C.R., Rankin, L.R., Leeming, P.M., and Harris, L.B. (1996). Delineation of lithostructural domains in northern Orissa (India) from Landsat Thematic Mapper imagery. *Tectonophysics* **260**, 245-257.
- Nemchin, A.A. & Pidgeon, R.T. (1998). Precise conventional and SHRIMP baddeleyite U-Pb age for the Binneringie Dyke, near Narrogin, Western Australia. *Australian Journal of Earth Sciences* **45**, 673-675.
- Padmukari, V.M. & Dayal, A.M. (1987). Geochronological studies of some mafic dykes around the Cuddapah basin, south India. In: Radhakrishna, B.P., ed., *Purana basins of peninsular India (Middle to Late Proterozoic)*, Geological Society of India Memoir **6**, 369-373.
- Pesonen, L.J., Elming, S.-Å., Mertanen, S., Pisarevsky, S., D'Agrella-Filho, M.S., Meert, J.G., Schmidt, P.W., Abrahamsen, N. & Bylund, G. (2003). Paleomagnetic configuration of continents during the Proterozoic. *Tectonophysics* **375**, 289-324.
- Rasmussen, B. & Fletcher, I.R. (2004). Zirconolite: A new U-Pb geochronometer for mafic igneous rocks. *Geology* **32**, 785-788.
- Rogers, J.J.W. (1993). India and Ur. *Journal of the Geological Society of India* **42**, 217-222.
- Rogers, J.J.W. (1996). A history of continents in the past three billion years. *The Journal of Geology* **104**, 91-107.
- Santosh, M., Yokoyama, K., & Acharyya, S.K. (2004). Geochronology and tectonic evolution of Karimnagar and Bhopalpatnam Granulite Belts, central India. *Gondwana Research* **7**, 501-518.
- Simonetti, A., Heaman, L.M., Hartlaub, R.P., Creaser, R.A., MacHattie, T., & Böhm, C. (2005). Rapid and precise U-Pb zircon dating by laser ablation MC-ICP-MS using a new multiple ion counting-faraday collector array. *Journal of Analytical Atomic Spectroscopy* **20**, 677-686.
- Simonetti, A., Heaman, L.M., Chacko, T., & Banerjee, N.R. (2006). In situ petrographic thin section dating of zircon, monazite, and titanite using laser ablation-MC-ICP-MS. *International Journal of Mass Spectrometry* **253**, 87-97.
- Söderlund, U. & Johansson, L. (2002). A simple way to extract baddeleyite (ZrO₂). *Geochemistry Geophysics Geosystems* **3**(2), 1-7.

Stern, R.A., Fletcher, I.R., Rasmussen, B., McNaughton, N.J., & Griffin, B.J. (2005). Ion microprobe (NanoSIMS 50) Pb-isotope geochronology at <5 μm scale. *International Journal of Mass Spectrometry* **244**, 125-134.

Suzuki, K. & Adachi, M. (1991). Precambrian provenance and Silurian metamorphism of the Tsubonosawa paragneiss in the South Kitakami terrane, Northeast Japan, revealed by the chemical Th-U-total Pb isochron ages of monazite, zircon, and xenotime. *Geochemical Journal* **25**, 357-376.

Williams, H., Hoffman, P.F., Lewry, J.F., Monger, J.W.H., & Rivers, T. (1991). Anatomy of North America: Thematic geologic portrayals of the continent. In: Hilde, T.W.G. and Carlson, R.L., eds., *Silver anniversary of plate tectonics: Tectonophysics* **187**, 117-134.

Wingate, M.T.D., Campbell, I.H., Compston, W., Gibson, & G.M. (1998). Ion microprobe U-Pb ages for Neoproterozoic basaltic magmatism in south-central Australia and implications for the breakup of Rodinia. *Precambrian Research* **87**, 135-159.

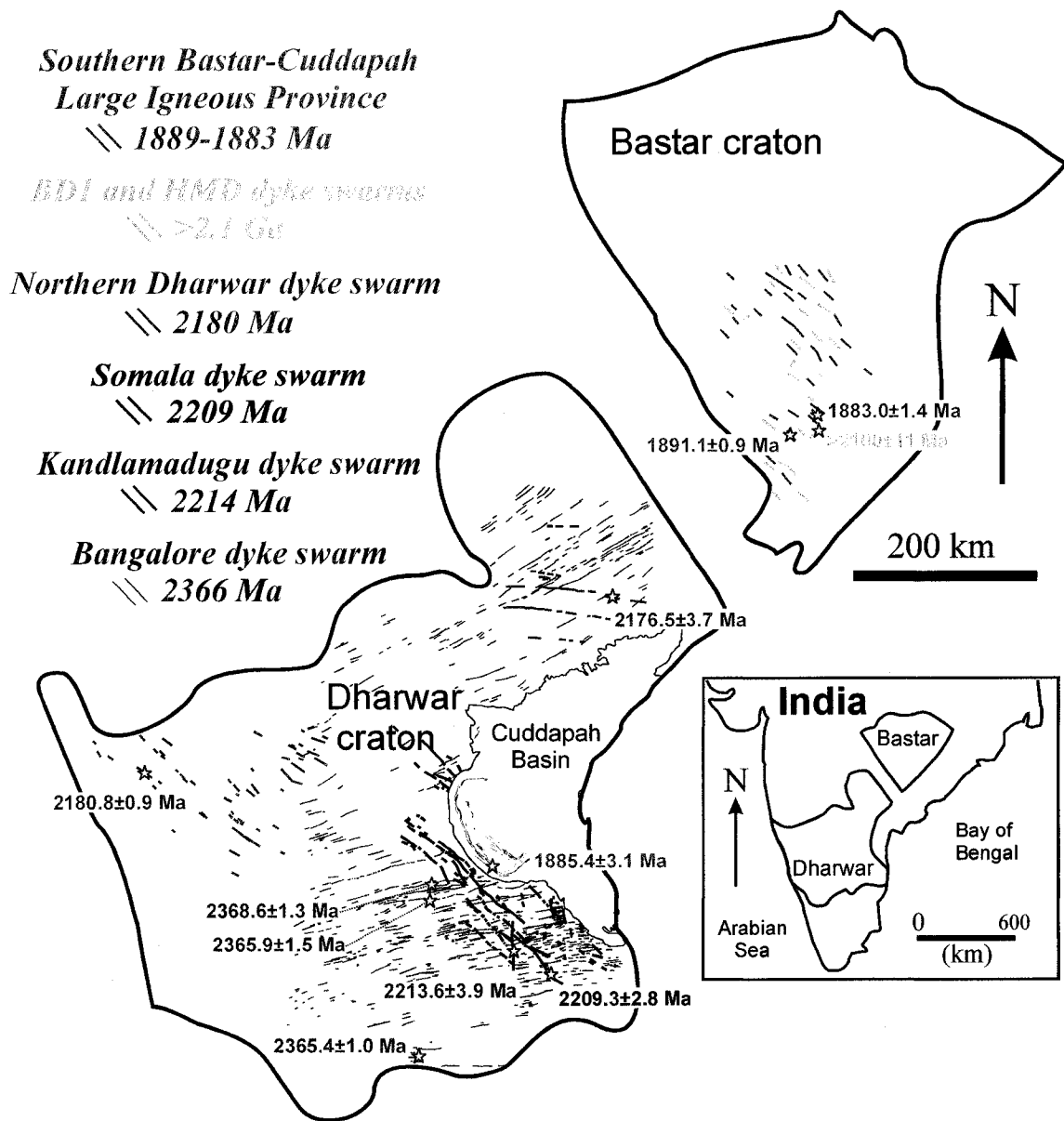


Fig. 5-1. Overview of Paleoproterozoic mafic igneous provinces of the south Indian shield dated by U-Pb IDTIMS in this study.

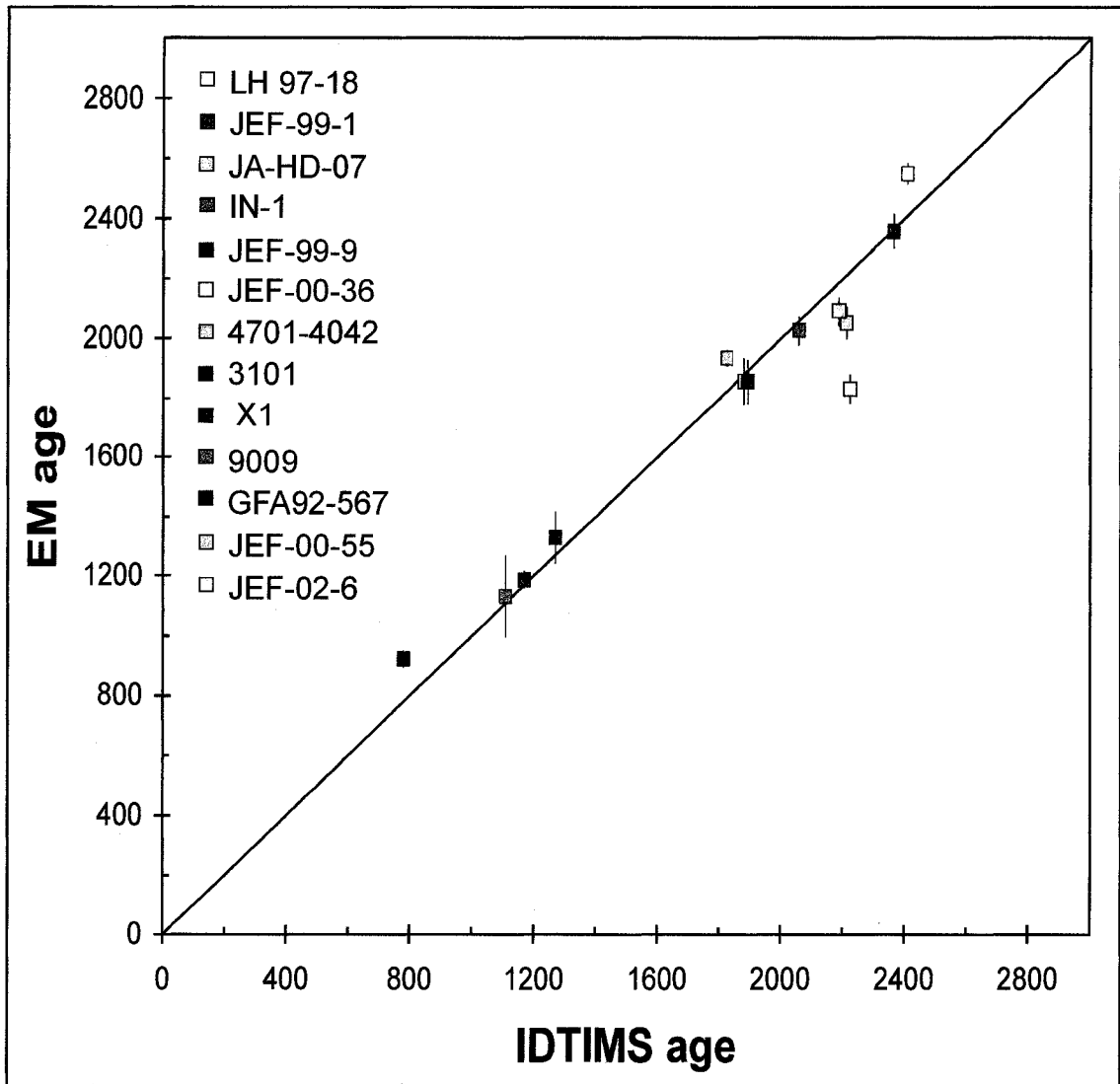
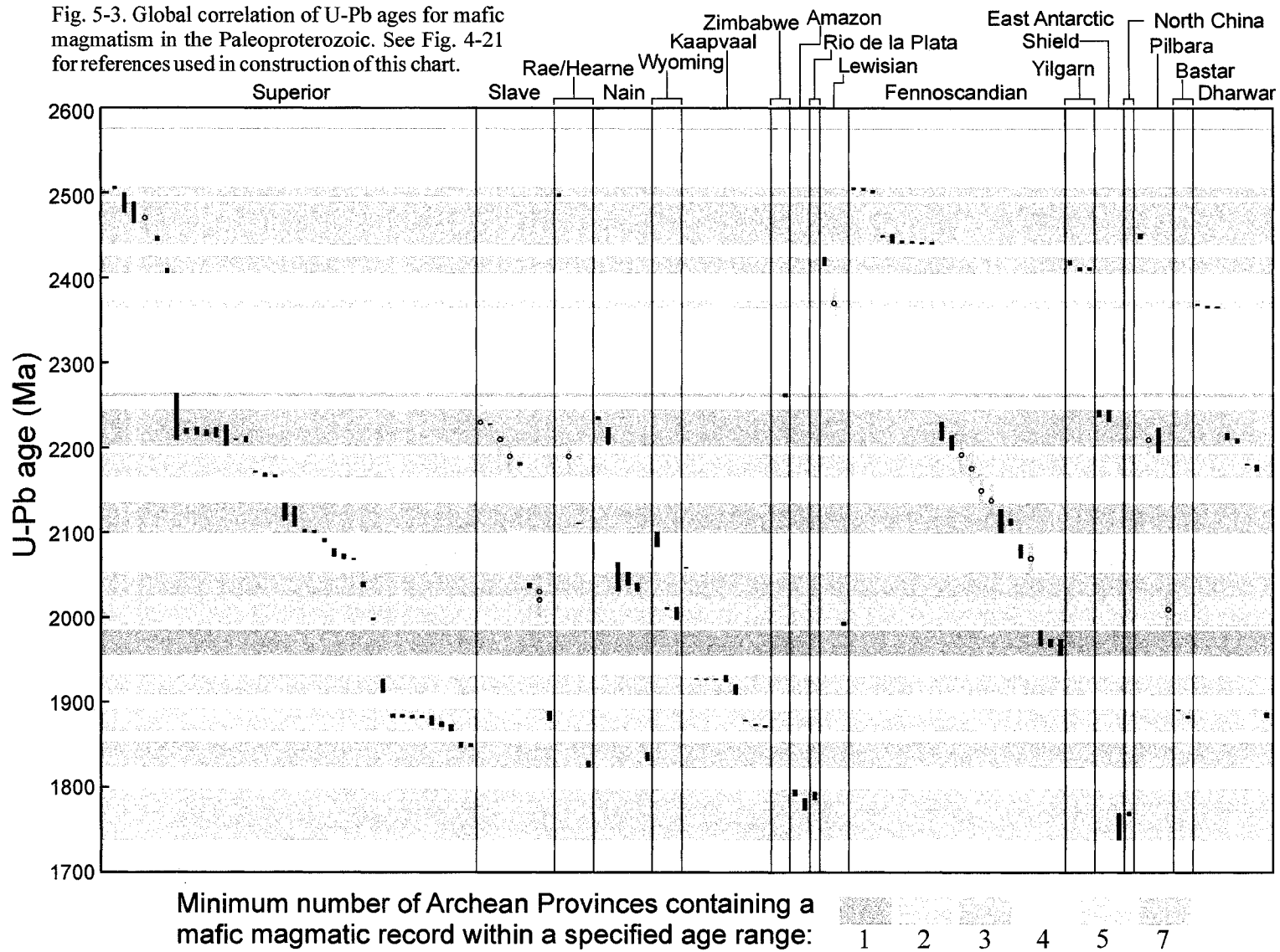


Fig. 5-2. Comparison of electron microprobe (EM) chemical U-Th-total Pb ages with isotopic (IDTIMS) ages for thirteen baddeleyite samples analysed in this study. The line represents 1:1 correspondence in ages obtained with the two techniques.



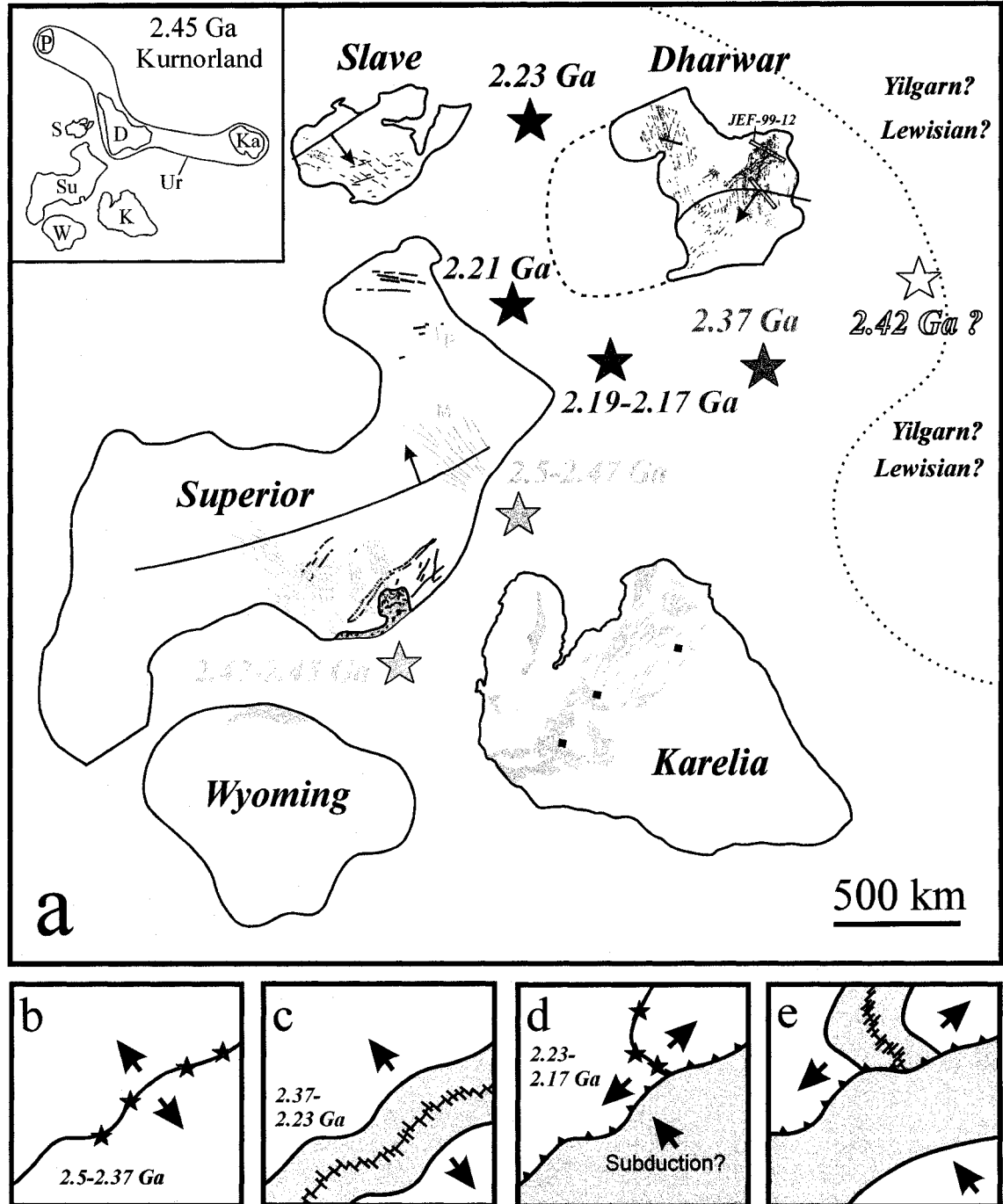


Fig. 5-4. Paleocontinental reconstruction of Kurnorland showing break-up in two separate stages at 2.5-2.37 Ga, and 2.23-2.17 Ga. See Fig. 4-25 for references, abbreviations, previous correlations and the details used in making this reconstruction.

APPENDIX A

Morphological and geochemical characterization, and electron microprobe chemical U-Th-total Pb dating of zircon from the BD2 mafic dyke swarm, Bastar craton, India

Summary

This appendix presents the results of a detailed chemical U-Th-total Pb dating study carried out on zircon in polished thin section from the BD2 mafic dyke swarm (petrology and IDTIMS geochronology outlined in Chapter 3). In this study it was discovered that zircon in BD2 mafic dykes shows a richness and variety of zircon morphologies and textures that has not been described before (descriptions of petrographic textures of zircon from mafic rocks in the literature are rare but include: Krogh et al., 1982; Bossart et al., 1986; Corfu et al., 2003), and on account of this a detailed description of several types of igneous zircon in BD2 dykes is also presented. In the spirit of Black et al. (1991), the geochronological data presented in this appendix demonstrates how *not* to date mafic dykes (which was the original goal), because as will be shown, zircon in mafic dykes is not a very good chemical U-Th-total Pb geochronometer for dating the timing of dyke emplacement. The chemical data presented are similar in nature to the complex geochronological datasets observed in chemical dating of zircons from granitic rocks (Geisler and Schleicher, 2000), and are probably a reflection of complex Pb-loss behaviour in association with varying degrees of hydrothermal alteration and subsequent weathering of zircon. It is shown that for very high Th and U domains in zircon, the chemical ages date precisely to the timing of hydrothermal alteration determined independently by IDTIMS dating of zircon (Chapter 3). These data indicate for the first time, that specific types of zircon in mafic dykes show great promise as a chemical U-Th-total Pb geochronometer for dating the timing of hydrothermal alteration of mafic dykes by electron microprobe.

Analytical set-up during electron microprobe analysis of zircon

The instrument employed during back-scattered electron (BSE) imaging and quantitative chemical analysis in this study is a JEOL 8900 electron microprobe (EM) equipped with five wavelength dispersive spectrometers (WDS) and one energy dispersive spectrometer (EDS). During quantitative analysis of zircon, operating conditions were set at an accelerating voltage of 20 kV, a beam current of 150 nA, and a beam diameter of $\sim 1\mu\text{m}$. However, during acquisition of BSE images for the contextual information (Figs. A-1, A-2, and A-4), the probe current was dropped to $\sim 10\text{-}30$ nA in order to allow for identification of more subtle features such as fracturing, inclusions, overgrowths and zoning which tend to be faded out due to the more intense signal at higher currents. In some cases, the absolute petrographic context of the WDS spot analyses could be verified unequivocally, because for the more metamict and hydrothermally altered zircons investigated there was apparently a significant quantity of light elements (presumably including H_2O ; Geisler and Schleicher, 2000) that moved away from the excitation volume during the analysis, imparting a relatively higher average atomic number to those regions that was visible during BSE imaging after the analysis (Fig. A-2a), and in addition translated to a $\sim 1\%$ deficit in total oxides for those spots. A comparison of the coordinates for 65 originally programmed WDS analysis spot locations to these apparently newly dehydrated bright spots in BSE images of the altered zircon showed that the originally chosen spot locations are all accurate to within $\sim 2\mu\text{m}$, and so all other spot locations shown in petrographic context (indicated as dots in Fig.'s A-2 and A-4) are inferred to be accurate to within $\sim 2\mu\text{m}$.

A synthetic Pb-silicate glass (National Bureau of Standards K-456) was used as a standard for quantitative measurement of Pb, and synthetic oxides of UO_2 and ThO_2

were used as standards for U and Th measurements. Other standards included synthetic YPO_4 (for Y and P) and ZrO_2 (for Zr), natural zircon (for Si), and suite of natural minerals were used as standards for measurement of all other elements. The X-ray lines chosen for quantitative analysis were $\text{M}\alpha$ for measurement of Pb and Th, and $\text{M}\beta$ for measurement of U, and an overlap correction was employed to account for the overlap of the Y $\text{L}\gamma$ peak on Pb $\text{M}\alpha$ (Suzuki and Adachi, 1991). Count times were set at 300s on the peak measurements and 150s on the background measurements for U and Pb, and for measurement of Th the peak and background measurements were set at 180s and 90s, respectively. For measurement of Ca in zircon count times were 40 s on the peak measurement and 20 s on the background measurement, and these times corresponded to 20 s and 10 s on the peak and background, respectively for all other trace elements. All quantitative chemical data determined in this study on zircon in polished thin sections of samples JEF-00-36, JEF-00-39, and JEF-00-37 are listed in Tables A-1, A-2, and A-3, respectively.

ZIRCON MORPHOLOGIES

On the basis of appearance in back-scattered electron (BSE) images of polished thin sections (and observations of zircon grains isolated by mineral separation: Chapter 3), igneous zircon from this study has been classified into three principal morphological types including polyhedral (Fig. A-2a), bladed (Fig. A-2b), and dendritic crystals (Fig. A-2c). These morphological types (and their interrelationships) are similar to some of the different crystal morphologies and textures observed for olivine and plagioclase in quenched basalts, and have been linked to different styles of crystal growth during varied conditions of undercooling (Lofgren, 1974; Faure et al., 2003).

Polyhedral zircon

Isolated crystals of euhedral zircon showing well defined crystal faces, and occurring commonly as square or rectangular/diamond/triangular shapes in cross sections interpreted to be perpendicular to, and oblique to the c-axis, respectively, are referred to as polyhedral zircons. Based on texture and relative brightness in BSE images and geochemical criteria, polyhedral zircon has been divided into three sub-domains including overgrowth rims, hydrothermally altered cores, and corroded regions (Fig. A-2a). The altered cores of polyhedral crystals appear as a medium grey in BSE, in contrast to the much brighter rims, and darker corroded regions. A distinctive feature of the overgrowth rims on the polyhedral zircons are the occurrence of projections of the rims out past the main body and apparently parallel to the crystallographic axes of the zircon being overgrown (Figs. A-1b, A-1e and A-2a), and in places where two polyhedral crystals are in close proximity there is a marked thinning of their outer rims (Fig. A-1e). Overgrowths of this type have been documented in plagioclase during experimental crystallization studies (compare overgrowths on polyhedral zircon in Figs. A-1e and A-2a to overgrowths on polyhedral plagioclase in Figs. 3b and 3c of Lofgren, 1974), whereby plagioclase was allowed to crystallize under equilibrium conditions for a certain length of time, followed by a rapid drop in temperature and continued crystallization at conditions of significant undercooling. For instance the crystallization sequence of run #50 (Lofgren, 1974) is initial polyhedral plagioclase followed by a thin overgrowth rim of optically continuous, more Na-rich plagioclase which extends past the main polyhedral body as branches parallel to its edges (i.e. crystallographic axes). It is not possible to evaluate whether or not the cores of polyhedral zircons are optically

continuous with the rims because the cores are now metamict and hydrothermally altered, but they are interpreted to represent igneous overgrowths based on their precursor relationship to dendritic and bladed zircon (Figs. A-1c and e) and this is also supported by trace element concentrations in the rims in that they have a Th/U range of 0.6-1.0 (Fig. A-5), which is typical for igneous zircon (Heaman et al., 1990; Hoskin et al., 2000). These geochemical and textural observations provide unequivocal evidence that the overgrowth rims on polyhedral crystals (Figs. A-1 and A-2) are igneous and not metamorphic in origin.

Bladed zircon

Bladed zircons comprise elongate flat crystals with sharp edges and usually display a needle-like habit in cross section (Fig. A-2b). This morphological type has been subdivided into two sub-domains based on relative brightness and texture in BSE images, and trace element geochemistry, comprising rims of blades, in addition to altered cores of blades, which appear relatively darker in BSE images. In thin section the blades appear to be overgrowing polyhedral zircons (Fig. A-1c), and also appear to branch off each other (Figs. A-1c and A-2b), as observed in some of the blades with t-junctions recovered by mineral separation (Chapter 3).

Dendritic zircon

The most common morphological variety of zircon encountered in thin sections of BD2 dykes was a cross-shaped form of dendritic zircon, with branches that have distinctive narrow (<2 μm) axial zones that are characteristically darker in BSE (Fig. A-2c). For sample JEF-00-39, dendritic zircon shows more pronounced regions up to ~10 μm across which are relatively darker in BSE, and occur commonly along axial zones or

as thin oscillatory bands, and consequently dendritic zircon from this sample is subdivided into altered and unaltered varieties (Fig. A-2d). This morphological variety of zircon is similar in nature to skeletal zircons described from a norite from the Sudbury Nickel Irruption, which are thought to have formed through rapid crystallization (Krogh et al., 1982; Corfu et al., 2003). A cross shape occurs in a section perpendicular to the c-axis because the prism faces of the crystals are highly concave surfaces. Such skeletal crystals develop because in conditions where the melt concentration of the species being added is relatively low, and under conditions of inefficient stirring, the edges of crystals will grow preferentially fast as a result of depletion gradients which develop around the grains, whereby the central portions of growing crystal faces are exposed to more depleted regions of the melt (Bossart et al., 1986). There is evidence from some zircon crystals in sample JEF-00-36 that some of the branch tips were shedding a wake of side branches as they grew (Fig. A-1d), which is a characteristic feature of dendritic crystals precipitating out of supercooled melts (Glicksman and Lupulescu, 2004; Yoshioka et al., 2004), and this is one reason why we have classified this morphological type as dendritic as opposed to skeletal. Analogous minute ripple-like structures occurring on the concave faces of skeletal zircons from the Saedelhorn diorite in Switzerland, have also been described by Bossart et al (1986) and were interpreted to represent evidence for supersaturation triggered by intrusion of the magma into cooler levels of the crust. One of the most remarkable features of this morphological class of zircons in BD2 dyke thin sections is the tendency for the zircon crosses to occur in dense clusters and in linear to grid-like arrays, where the orientation of all of the crosses is virtually identical and their relative spacing is quite constant. One explanation for the orderly spatial distribution of

the zircons might be that they grew from a highly dense cluster of nucleation sites in the magma, and their spacing was a function of a uniform distribution of local Zr-enrichment. This seems unlikely however, because the zircons are not randomly oriented. The most reasonable interpretation of the orderly arrangement of the crosses is that they are crystallographically aligned because they comprise a composite cross section through a complex array of branches from a single zircon dendrite. Three-dimensional modelling of the zircon tree represented by the parallel rows of zircon crosses in the BSE image (i.e.: two-dimensional cross-section) of thin section JEF-00-36 (Fig. A-1a), is carried out in Appendix B.

ZIRCON GEOCHEMISTRY AND IN SITU CHEMICAL DATING

Polished thin sections of three BD2 mafic dyke samples (JEF-00-36, JEF-00-37, and JEF-00-39) were selected for a textural EM chemical dating study of zircon, and the petrographic context of all of the analyses from sample JEF-00-36 is shown in Fig. A-2. Quantitative chemical data for all samples was divided into sub-domains on the basis of morphological type of zircon and degree of alteration. Individual apparent ages were calculated according to the method of Suzuki and Adachi (1991), and the isochrons in Fig. A-3f are forced through the origin by including a fictive data-point in the regression that has no associated data-point error. In a companion study, U-Pb IDTIMS dating of baddeleyite and zircon from sample JEF-00-36 yielded a high precision crystallization age of 1883.0 ± 1.4 Ma (Chapter 3). It is expected that a large number of WDS spot analyses in the present study should yield chemical ages much younger than the crystallization age of the zircon, because all of the conventional U-Pb zircon data from sample JEF-00-36 determined by IDTIMS are discordant (Chapter 3). Calcium

concentration can be used as a chemical proxy for fluid induced discordance during EM U-Th-total Pb dating of zircon (Geisler and Schleicher, 2000), and because these BD2 dykes have clearly been affected by a major episode of deuteritic alteration, the data for all zircons are shown on plots of CaO concentration versus apparent age t (Figs. A-3a to e). The P_2O_5 content of the zircons was also monitored to evaluate the potential for association of CaO with possible tiny inclusions of apatite in the zircon, and this was ruled out for most of the data as the zircons either contained negligible P_2O_5 or the P-Ca oxide ratio was extremely variable and deviated strongly (0.0 to 10) from that for stoichiometric fluorapatite which is 0.76 (Geisler and Schleicher, 2000). It is notable however that for the sub-domain of overgrowth rims on polyhedral zircon from samples JEF-00-36 ($n=10$) and JEF-00-39 ($n=5$), the range in P-Ca oxide ratios (0.51-1.05) was similar to the stoichiometric ratio of 0.76, although the data still plots along the expected exponential trends in Fig. A-3. Incorporation of Ca into radiation damaged zircon during low temperature hydrothermal alteration is thought to occur as zircon hydration is accompanied by an ion exchange process involving replacement of Zr^{4+} , Si^{4+} , as well as radiogenic Pb^{2+} , by Ca^{2+} in addition to other ions (Geisler and Schleicher, 2000).

For all samples there is a remarkable spread of individual apparent ages ranging from ~1.5-2.0 Ga down to 0.0 Ga, with a predicted exponential decrease in apparent age t with increasing concentration of CaO in zircon. Unfortunately because the most Ca-poor regions of zircon are also associated with the most U- and Th-poor regions (i.e.: least radiation damaged regions), the uncertainty in apparent age for these analyses is the highest, and is mostly limited by the low total radiogenic Pb content in those domains. Very few individual apparent ages overlap within analytical uncertainty of the

emplacement ages for the dykes determined by IDTIMS (1883.0 ± 1.4 Ma and 1891.1 ± 0.9 Ma) and the apparent disturbance of the U-Th-Pb system for all samples prevents straightforward calculation of crystallization ages. Any individual apparent age theoretically represents a reliable minimum age of crystallization of the zircon, but many of the ages are otherwise geologically meaningless as they probably represent for the most part zircon domains that have lost part of their radiogenic Pb, and which would likely plot as discordant points along a discordia line (as do the U-Pb zircon data for BD2 dykes in Chapter 3). Geisler and Schlicher (2000) proposed a threshold CaO content of $<0.2\text{wt}\%$ below which zircon domains have corresponding apparent ages that agree well with previously known isotopic crystallization ages, and this holds true to some degree for zircon from the BD2 dykes. However, the datasets for zircon from samples JEF-00-36 and JEF-00-39 are the most comprehensive, and for the data with $<0.2\text{wt}\%$ CaO, many of the apparent ages do not overlap the IDTIMS ages for BD2 dykes within analytical uncertainty and are anomalously young. This may be an indication that the relationship between apparent age t and CaO is truly exponential down to zircon domains containing effectively no CaO. If this relationship holds true, then regressions of the data on plots of CaO versus apparent age t for progressively CaO-exclusive datasets should yield y-intercept dates that systematically approach the crystallization age of the zircon, and this possibility was tested for unaltered dendritic zircon from sample JEF-00-39 which comprises the largest geochemical dataset for any sub-domain of zircon in this study. The regressions (Fig. A-3d) do not yield y-intercept dates that overlap within analytical uncertainty of the IDTIMS ages of BD2 dykes until exclusion of data containing >0.075 wt% CaO which yields a model age of 1865 ± 310

Ma (MSWD=0.80) that is interpreted to represent the best estimate for a minimum crystallization age of dendritic zircon from sample JEF-00-39 by chemical dating of zircon in this study. As a manner of direct comparison to a sample with a known U-Pb IDTIMS age, a similar series of regressions was constructed for the more limited dataset of dendritic zircon data from sample JEF-00-36 (Fig. A-3c), and yielded somewhat less-precise estimates for the minimum age of crystallization of the zircon of 1790 ± 140 Ma (MSWD=0.71), 1914 ± 230 Ma (MSWD=0.49), and 2056 ± 370 Ma (MSWD=0.36), for data with CaO concentrations of $<0.6\text{wt}\%$, $<0.3\text{wt}\%$, and $<0.2\text{wt}\%$, respectively. In contrast, the weighted mean of individual apparent ages for the same datasets are 1367 ± 170 Ma (MSWD=4.7), 1534 ± 130 Ma (MSWD=1.6), and 1633 ± 110 Ma (MSWD=0.99) for data with corresponding CaO concentrations of $<0.6\text{wt}\%$, $<0.3\text{wt}\%$, and $<0.2\text{wt}\%$, respectively, none of which overlap within analytical uncertainty of the known IDTIMS age of 1883.0 ± 1.4 Ma. This suggests that the y-intercept method of minimum apparent age calculation although generally less precise, seems to be more accurate, especially for datasets where the age information is limited to domains relatively higher in CaO. Weighted mean ages are typically similar to UO_2^* versus PbO chemical isochron ages in which the isochron is forced through the origin with a fictive data point that has zero associated data-point errors (as in this study), and so y-intercept ages also appear to be more accurate than ages based on this type of regression as well. Regardless of which style of age calculation is used, chemical ages should always be regarded as minimum estimates for the crystallization age of the zircon, because for some zircon domains, despite an association with extremely low CaO concentrations, the apparent ages may be anomalously young. For instance, application of the y-intercept

method of age calculation to strictly the bladed morphological zircon variety (sample JEF-00-36) which generally has CaO concentrations of <0.100wt%, yields a minimum crystallization age of 1436 ± 230 Ma (MSWD=0.46), and a weighted mean apparent age of 1440 ± 100 Ma (MSWD=0.43) (regressions not shown).

Thin (<10 μm) zircon overgrowths on baddeleyite blades in polished thin section were also selected for chemical dating, and analogous to many of the other zircon domains the individual apparent ages span a wide range from ~ 1.9 Ga down to ~ 350 Ma. It is clear from isotopic data for sample JEF-00-36 that zircon overgrowths are the main cause of discordance for the most discordant baddeleyite analyses and that they contribute to generating the observed mixing line in the data from 1883 Ma down to ~ 370 Ma (Chapter 3). One interpretation of the isotopic data is that the zircon overgrowth on baddeleyite is related to crystallization of new zircon during hydrothermal alteration of the baddeleyite at ~ 370 Ma. However, the model Th/U of the zircon rim fragments analysed in fraction #9 (Chapter 3) is quite high (0.762, but probably higher because the analysis includes a small portion of baddeleyite that should have characteristically low Th/U of <0.1), which is a hallmark of zircon crystallizing from a mafic magma (Heaman et al., 1990). Accordingly, another plausible interpretation is that the zircon overgrowths represent magmatic rims/intergrowths on baddeleyite that were susceptible to Pb-loss during hydrothermal alteration of the rock at ~ 370 Ma. Textural evidence to support this idea (Fig. A-4b) includes baddeleyite intergrown with high Th/U zircon, which forms a composite grain that is rimmed by a late, very thin (<2 μm) coating of zircon that appears slightly brighter in BSE images than the early zircon intergrowth. An analogous case where baddeleyite and inter-grown

magmatic zircon form a composite grain, and which together are overgrown by metamorphic zircon was reported from a coronitic metagabbro from the Grenville Province, Ontario, Canada (Heaman and LeCheminant, 1993).

Zircon data from sample JEF-00-37 originate from a single subhedral zircon crystal (not shown) and also from high Th/U zircon (0.3-1.2) inter-grown with baddeleyite (Fig. A-4d), but estimation of an accurate crystallization age for the zircon is hindered because only a very limited amount of low-CaO data was acquired (Fig. A-3e). A series of regressions of the data yield y-intercept dates of 1319 ± 550 Ma (MSWD=17) for subhedral zircon with $\text{CaO} < 1.5\text{wt}\%$, 1543 ± 450 Ma (MSWD=3.4) for zircon inter-grown with baddeleyite ($\text{CaO} < 1.0\text{ wt}\%$), and a composite regression of both domains with $\text{CaO} < 0.6\text{wt}\%$ yields a y-intercept date of 1601 ± 280 Ma (MSWD=0.71) which we interpret as the best estimate for a minimum age of zircon crystallization.

The most Th- and U- rich zircon domains in this study, which appear to be relatively homogeneous in BSE images, and which have a very limited spread of individual apparent ages are the cores of polyhedral zircons and the zircon intergrowth with baddeleyite grain A from sample JEF-00-36 (Figs. A-2a and A-4b). One interpretation of the consistency of apparent ages in these high CaO domains is that because of the relatively high U and Th contents (i.e.: high degree of radiation damage), these regions of zircon were completely isotopically reset in terms of U-Th-total Pb chemical dating during a hydrothermal alteration event. Chemical isochrons for these hydrothermally altered cores of polyhedral zircons from samples JEF-00-36 (excluding the corroded zone) and JEF-00-39, yield apparent hydrothermal alteration ages of 353 ± 15 Ma (MSWD=3.1) and 365 ± 20 Ma (MSWD=1.9), respectively. The Th- and U- rich zircon

intergrowth on baddeleyite grain A (JEF-00-36, Fig. A-4b) yields a similar chemical isochron age of 375 ± 32 Ma (MSWD=2.4). A weighted mean of all three isochron ages yields a composite age of 359 ± 11 Ma (MSWD=1.00), which is interpreted to represent the best estimate for the timing of hydrothermal alteration of the BD2 dykes by the EM chemical dating method. The chemical age of 359 ± 11 Ma overlaps well within analytical uncertainty of the lower intercept date of 370 ± 14 Ma determined by IDTIMS (Chapter 3), which is interpreted to represent the timing of major resetting of the U-Pb isotopic system in zircon from sample JEF-00-36. The lower intercept date of 370 ± 14 Ma determined for baddeleyite and zircon from dolerite dyke JEF-00-36 (Fig. 3-7a, Chapter 3) probably represents the timing of regional hydrothermal alteration of the BD2 mafic dyke swarm, and the independent EM chemical age data determined here for two BD2 dykes supports this conclusion. The origin of this Devonian hydrothermal activity in the southern Bastar region is currently unknown, but it is notable that extensive deformation, plutonism, and hydrothermal activity associated with gold mineralization was taking place in the Australian fragment of east Gondwanaland at that time (Arne et al., 1998; Foster et al., 1998). On the basis of this very tenuous correlation, the identification of similar aged hydrothermal activity by two independent geochronological techniques in this thesis could have remote economic implications in terms of an increased potential for gold exploration in the southern Bastar craton.

For reference a number of plots of trace element geochemical data for the igneous zircon dated by EM are also shown (Fig. A-5), and correspond to the same zircon spot analyses and textural domains as per the chemical dating studies (data in Table A-1).

However, a comprehensive interpretation and discussion of the significance of these geochemical data is beyond the scope of this appendix.

References

- Arne, D.C., Bierlein, F.P., McNaughton, N., Wilson, C.J.L., & Morand, V.J. (1998). Timing of gold mineralization in western and central Victoria, Australia: new constraints from SHRIMP II analysis of zircon grains from felsic intrusive rocks. *Ore Geology Reviews* **13**, 251-273.
- Black, L.P., Kinny, P.D., & Sheraton, J.W. (1991). The difficulties of dating mafic dykes: an Antarctic example. *Contributions to Mineralogy and Petrology* **109**, 183-194.
- Bossart, P.J., Meier, M., Oberli, F., & Steiger, R.H. (1986). Morphology versus U-Pb systematics in zircon: a high-resolution isotopic study of a zircon population from a Variscan dike in the central Alps. *Earth and Planetary Science Letters* **78**, 339-354.
- Corfu, F., Hanchar, J.M., Hoskin, P.W.O., & Kinny, P. (2003). Atlas of zircon textures. *Reviews in Mineralogy and Geochemistry* **53**, 469-500.
- Faure, F., Trolliard, G., Nicollet, C., & Montel, J-M. (2003). A developmental model of olivine morphology as a function of the cooling rate and the degree of undercooling. *Contributions to Mineralogy and Petrology* **145**, 251-263.
- Foster, D.A., Gray, D.A., Kwak, T.A.P., & Bucher, M. (1998). Chronology and tectonic framework of turbidite-hosted gold deposits in the western Lachlan Fold Belt, Victoria: ^{40}Ar - ^{39}Ar results. *Ore Geology Reviews* **13**, 229-250.
- Geisler, T. & Schleicher, H. (2000). Improved U-Th-total Pb dating of zircons by electron microprobe using a simple new background modelling procedure and Ca as a chemical criterion of fluid-induced U-Th-Pb discordance in zircon. *Chemical Geology* **163**, 269-285.
- Glicksman, M.E. & Lupulescu, A.O. (2004). Dendritic crystal growth in pure materials. *Journal of Crystal Growth* **264**, 541-549.
- Heaman, L.M., Bowins, R., & Crocket, J. (1990). The chemical composition of igneous zircon suites: Implications for geochemical tracer studies. *Geochimica et Cosmochimica Acta* **54**, 1597-1607.
- Heaman, L.M. & LeCheminant, A.N. (1993). Paragenesis and U-Pb systematics of baddeleyite (ZrO_2). *Chemical Geology* **110**, 95-126.

Hoskin, P.W.O., Kinny, P.D., Wyborn, D., & Chappell, B.W. (2000). Identifying accessory mineral saturation during differentiation in granitoid magmas: an integrated approach. *Journal of Petrology* **41**, 1365-1396.

Krogh, T.E, McNutt, R.H, & Davis, G.L. (1982). Two high precision U-Pb zircon ages for the Sudbury Nickel Irruptive. *Canadian Journal of Earth Sciences* **19**, 723-728.

Lofgren, G. (1974). An experimental study of plagioclase crystal morphology: isothermal crystallization. *American Journal of Science* **274**, 243-273.

Suzuki, K. & Adachi, M. (1991). Precambrian provenance and Silurian metamorphism of the Tsubonosawa paragneiss in the South Kitakami terrane, Northeast Japan, revealed by the chemical Th-U-total Pb isochron ages of monazite, zircon, and xenotime. *Geochemical Journal* **25**, 357-376.

Yoshioka, H., Tada, Y., & Hayashi, Y. (2004). Crystal growth and its morphology in the mushy zone. *Acta Materialia* **52**, 1515-1523.

Table A-1. Chemical data (wt%) for zircon from sample JEF-00-36 of the BD2 mafic dyke swarm (Basaltic craton), determined by electron microprobe WDS spot analysis. (FeO represents total Fe oxide, uncorrected for Fe₂O₃ content).

No.	SiO ₂	FeO	UO ₂	PbO	P ₂ O ₅	HfO ₂	Y ₂ O ₃	ZrO ₂	Nb ₂ O ₅	TiO ₂	CaO	TiO ₂	Total	Comment	spot #	Crystal morphology/context	t (Ma)
370	33.912	0.5	0.112	0.033	0.118	0.401	0.417	66.373	0.028	0.083	0.112	0	102.089	JEF-00-36	56	Overgrowth rim on polyhedral crystal	1554
371	33.566	0.657	0.112	0.03	0.112	0.422	0.476	65.954	0	0.091	0.154	0.004	101.477	JEF-00-36	57	Overgrowth rim on polyhedral crystal	1411
372	33.564	0.655	0.114	0.028	0.12	0.437	0.463	65.082	0	0.072	0.196	0	100.691	JEF-00-36	58	Overgrowth rim on polyhedral crystal	1358
373	33.368	0.745	0.123	0.03	0.138	0.413	0.746	65.047	0	0.106	0.224	0	100.94	JEF-00-36	59	Overgrowth rim on polyhedral crystal	1287
374	33.56	0.738	0.113	0.03	0.112	0.381	0.6	65.939	0.016	0.104	0.157	0	101.75	JEF-00-36	60	Overgrowth rim on polyhedral crystal	1371
375	34.087	0.843	0.134	0.031	0.122	0.392	0.68	65.999	0	0.105	0.175	0	101.968	JEF-00-36	61	Overgrowth rim on polyhedral crystal	1248
376	32.447	0.888	0.136	0.026	0.13	0.382	0.752	65.07	0	0.138	0.263	0	100.232	JEF-00-36	62	Overgrowth rim on polyhedral crystal	1002
377	32.644	0.82	0.143	0.033	0.148	0.371	0.751	64.475	0	0.117	0.285	0.001	98.788	JEF-00-36	63	Overgrowth rim on polyhedral crystal	1236
378	32.682	0.761	0.117	0.035	0.144	0.396	0.695	64.777	0	0.114	0.287	0.009	100.01	JEF-00-36	64	Overgrowth rim on polyhedral crystal	1505
379	33.728	0.878	0.147	0.036	0.14	0.368	0.746	65.537	0	0.133	0.248	0.002	101.963	JEF-00-36	65	Overgrowth rim on polyhedral crystal	1281
380	33.163	0.47	0.419	0.026	0	0.311	1.322	63.163	0	0.644	1.495	0	101.013	JEF-00-36	66	Core of polyhedral crystal	309
381	31.91	0.43	0.428	0.025	0.001	0.301	1.296	62.544	0	0.823	1.267	0	98.825	JEF-00-36	67	Core of polyhedral crystal	295
382	32.664	0.4	0.423	0.029	0	0.318	1.33	62.174	0.03	0.599	1.277	0	99.244	JEF-00-36	68	Core of polyhedral crystal	348
383	32.026	0.429	0.452	0.032	0	0.312	1.333	61.872	0.059	0.595	1.28	0.004	98.394	JEF-00-36	69	Core of polyhedral crystal	366
384	32.019	0.458	0.454	0.033	0	0.32	1.324	62.478	0	0.63	1.404	0.009	98.129	JEF-00-36	70	Core of polyhedral crystal	370
385	33.086	0.468	0.432	0.027	0	0.284	1.354	62.486	0.023	0.811	1.453	0.012	100.236	JEF-00-36	71	Core of polyhedral crystal	318
386	32.548	0.434	0.422	0.03	0	0.321	1.267	62.032	0	0.601	1.232	0.001	98.888	JEF-00-36	72	Core of polyhedral crystal	360
387	32.389	0.436	0.407	0.029	0	0.366	1.22	62.502	0.016	0.53	1.38	0.008	98.263	JEF-00-36	73	Core of polyhedral crystal	370
388	33.359	0.377	0.44	0.03	0	0.329	1.274	62.783	0	0.606	1.214	0.003	100.415	JEF-00-36	74	Core of polyhedral crystal	349
389	32.205	0.418	0.429	0.026	0.35	0.328	1.32	61.872	0	0.963	1.807	0.001	98.119	JEF-00-36	75	Core of polyhedral crystal	315
390	32.35	0.417	0.435	0.039	0	0.315	1.238	62.387	0.017	0.596	1.314	0.007	99.115	JEF-00-36	76	Core of polyhedral crystal	315
391	32.839	0.451	0.424	0.032	0	0.341	1.267	62.343	0.058	0.573	1.363	0.009	99.7	JEF-00-36	77	Core of polyhedral crystal	455
392	32.404	0.432	0.416	0.027	0	0.318	1.279	61.169	0	0.565	1.308	0.018	97.923	JEF-00-36	78	Core of polyhedral crystal	387
393	32.164	0.442	0.435	0.029	0	0.328	1.376	61.091	0	0.601	1.276	0.001	97.743	JEF-00-36	79	Core of polyhedral crystal	334
394	33.026	0.453	0.427	0.026	0	0.31	1.302	61.442	0.013	0.599	1.351	0.001	98.99	JEF-00-36	80	Core of polyhedral crystal	341
395	33.169	0.466	0.461	0.035	0	0.319	1.349	62.451	0	0.849	1.45	0.002	100.351	JEF-00-36	81	Core of polyhedral crystal	311
396	32.489	0.446	0.447	0.038	0	0.301	1.353	62.421	0.044	0.642	1.274	0.004	98.459	JEF-00-36	82	Core of polyhedral crystal	385
397	32.862	0.483	0.452	0.033	0	0.306	1.354	62.57	0	0.811	1.342	0.009	100.022	JEF-00-36	83	Core of polyhedral crystal	427
398	32.481	0.454	0.426	0.029	0	0.306	1.298	61.823	0	0.569	1.369	0.005	98.76	JEF-00-36	84	Core of polyhedral crystal	375
399	32.364	0.472	0.422	0.027	0	0.324	1.209	62.838	0	0.567	1.463	0.002	98.716	JEF-00-36	85	Core of polyhedral crystal	351
400	32.006	0.599	0.446	0.032	0	0.338	1.241	62.413	0.027	0.636	1.24	0	98.778	JEF-00-36	86	Core of polyhedral crystal	330
401	31.265	0.41	0.431	0.03	0	0.337	1.238	61.525	0	0.606	1.416	0	97.258	JEF-00-36	87	Core of polyhedral crystal	363
402	33.002	0.385	0.413	0.024	0	0.346	1.096	62.616	0	0.518	1.328	0	98.728	JEF-00-36	88	Core of polyhedral crystal	354
403	33.711	0.402	0.428	0.035	0	0.306	1.225	62.777	0.02	0.579	1.146	0.001	100.63	JEF-00-36	89	Core of polyhedral crystal	406
404	33.195	0.411	0.389	0.022	0.051	0.342	1.161	62.261	0.003	0.51	1.528	0.002	98.875	JEF-00-36	90	Core of polyhedral crystal	418
405	32.337	0.414	0.366	0.027	0.003	0.311	1.231	62.275	0.048	0.544	1.226	0.01	98.822	JEF-00-36	91	Core of polyhedral crystal	295
406	31.973	0.381	0.432	0.029	0	0.34	1.201	62.46	0.017	0.478	1.264	0	98.675	JEF-00-36	92	Core of polyhedral crystal	349
407	32.169	0.372	0.405	0.027	0	0.307	1.1	62.727	0	0.478	1.242	0	98.827	JEF-00-36	93	Core of polyhedral crystal	346
408	32.492	0.413	0.444	0.025	0	0.29	1.186	62.305	0	0.519	1.254	0.004	98.932	JEF-00-36	94	Core of polyhedral crystal	356
409	32.709	0.432	0.411	0.031	0	0.323	1.206	61.818	0.016	0.555	1.34	0.001	98.842	JEF-00-36	95	Core of polyhedral crystal	303
																Core of polyhedral crystal	387

Table A-1 continued. Chemical data (wt%) for zircon from sample JEF-00-36 of the BD2 mafic dyke swarm (Bastar craton), determined by electron microprobe WDS spot analysis. (FeO represents total Fe oxide, uncorrected for Fe₂O₃ content).

No.	SiO ₂	FeO	UO ₂	PbO	P ₂ O ₅	HfO ₂	Y ₂ O ₃	ZrO ₂	Nb ₂ O ₅	ThO ₂	CaO	TiO ₂	Total	Comment	spot #	Crystal morphology/context	t (Ma)
410	32.229	1.634	0.465	0.019	0.188	0.289	1.115	57.943	0.059	0.485	2.899	0.015	97.34	JEF-00-36	96	Corroded core of polyhedral crystal	228
411	32.718	1.371	0.457	0.014	0.158	0.285	1.13	58.582	0.004	0.503	2.972	0.009	98.203	JEF-00-36	97	Corroded core of polyhedral crystal	169
412	32.838	1.299	0.457	0.024	0.06	0.306	1.087	60.258	0.026	0.458	2.088	0.004	98.905	JEF-00-36	98	Corroded core of polyhedral crystal	294
413	31.796	1.157	0.464	0.021	0.117	0.288	1.124	59.071	0	0.577	2.12	0.006	96.741	JEF-00-36	99	Corroded core of polyhedral crystal	240
414	32.172	0.651	0.426	0	0	0.3	1.044	58.319	0	0.45	3.309	0.007	96.678	JEF-00-36	100	Corroded core of polyhedral crystal	0
415	32.306	0.707	0.441	0	0.477	0.328	1.139	59.35	0.001	0.509	2.83	0.008	98.096	JEF-00-36	101	Corroded core of polyhedral crystal	0
416	33.169	0.743	0.441	0	0	0.308	1.12	59.738	0	0.456	2.635	0.018	98.628	JEF-00-36	102	Corroded core of polyhedral crystal	0
417	33.144	0.958	0.463	0	0.003	0.303	1.149	58.302	0.009	0.465	1.918	0.005	96.719	JEF-00-36	103	Corroded core of polyhedral crystal	0
418	33.062	1.165	0.452	0	0	0.314	1.182	58.281	0.018	0.47	2.338	0.012	97.294	JEF-00-36	104	Corroded core of polyhedral crystal	0
419	33.127	1.058	0.442	0.009	0	0.279	1.092	58.59	0	0.481	2.276	0.357	97.711	JEF-00-36	105	Corroded core of polyhedral crystal	113
420	34.279	0.043	0.071	0.014	0.102	0.464	0.151	65.512	0.011	0.051	0.017	0	100.715	Line 1	JEF-00-36-LINEQ	bladed zircon	1097
421	32.521	0.06	0.027	0.009	0.067	0.52	0.135	64.554	0	0.024	0.007	0	97.924	Line 2	JEF-00-36-LINEQ	bladed zircon	1677
422	33.421	0.046	0.041	0.012	0.074	0.482	0.087	65.192	0	0.015	0.02	0.002	99.392	Line 3	JEF-00-36-LINEQ	bladed zircon	1667
423	33.013	0.068	0.052	0.015	0.084	0.519	0.118	64.459	0	0.036	0.017	0.004	98.385	Line 4	JEF-00-36-LINEQ	bladed zircon	1541
424	33.753	0.075	0.052	0.014	0.11	0.473	0.205	64.383	0.01	0.047	0.039	0	99.161	Line 5	JEF-00-36-LINEQ	bladed zircon	1392
425	32.856	0.123	0.062	0.02	0.119	0.478	0.231	64.897	0.025	0.058	0.05	0	98.919	Line 6	JEF-00-36-LINEQ	bladed zircon	1617
426	33.122	0.156	0.077	0.02	0.158	0.461	0.322	65.146	0	0.049	0.051	0	99.56	Line 7	JEF-00-36-LINEQ	bladed zircon	1424
427	33.945	0.221	0.103	0.027	0.209	0.44	0.438	65.015	0	0.082	0.079	0.004	100.563	Line 8	JEF-00-36-LINEQ	bladed zircon	1390
428	33.2	0.4	0.119	0.034	0.171	0.443	0.569	64.158	0.007	0.118	0.102	0.001	99.322	Line 9	JEF-00-36-LINEQ	bladed zircon	1442
429	33.337	0.355	0.105	0.033	0.127	0.456	0.512	63.882	0	0.08	0.088	0	98.975	Line 10	JEF-00-36-LINEQ	bladed zircon	1635
430	33.75	0.248	0.106	0.027	0.089	0.477	0.408	64.476	0	0.054	0.036	0	99.671	Line 11	JEF-00-36-LINEQ	bladed zircon	1438
444	34.245	0.321	0.111	0.031	0.152	0.444	0.481	65.177	0	0.08	0.099	0	101.141	JEF-00-36-111		bladed zircon	1490
445	33.624	0.302	0.107	0.029	0.115	0.46	0.474	64.393	0	0.076	0.061	0	99.641	JEF-00-36-112		bladed zircon	1455
436	33.832	0.259	0.078	0.018	0.055	0.507	0.309	65.131	0	0.076	0.132	0	100.397	Line 1	JEF-00-36-LINES	bladed zircon	1498
438	33.611	0.216	0.085	0.025	0.07	0.507	0.381	64.743	0	0.091	0.166	0	99.895	Line 3	JEF-00-36-LINES	bladed zircon	1456
431	33.205	0.432	0.233	0.027	0.179	0.42	1.417	61.093	0	0.308	1.466	0.009	98.789	Line 1	JEF-00-36-LINER	altered core of bladed zircon	588
432	33.316	0.459	0.227	0.032	0.173	0.417	1.393	60.98	0.011	0.305	1.333	0.007	98.653	Line 2	JEF-00-36-LINER	altered core of bladed zircon	706
433	33.421	0.401	0.229	0.027	0.148	0.405	1.456	60.506	0.053	0.293	1.443	0.012	98.394	Line 3	JEF-00-36-LINER	altered core of bladed zircon	603
434	33.242	0.413	0.246	0.031	0.175	0.419	1.494	60.457	0	0.322	1.471	0	98.27	Line 4	JEF-00-36-LINER	altered core of bladed zircon	639
435	33.578	0.421	0.24	0.024	0.188	0.374	1.606	60.812	0.021	0.331	1.56	0.017	99.172	Line 5	JEF-00-36-LINER	altered core of bladed zircon	505
447	32.716	0.427	0.529	0.052	0	0.337	1.532	59.969	0	0.91	1.9	0.008	98.38	JEF-00-36-114		altered core of bladed zircon	464
448	32.573	0.406	0.441	0.044	0.026	0.351	1.54	61.18	0	0.67	1.6	0.011	98.842	JEF-00-36-115		altered core of bladed zircon	490
449	32.929	0.31	0.479	0.044	0.005	0.367	1.557	59.919	0	0.751	1.521	0.014	97.896	JEF-00-36-116		altered core of bladed zircon	448
450	32.286	0.371	0.46	0.039	0.009	0.37	1.441	60.75	0	0.394	1.43	0.015	97.565	JEF-00-36-117		altered core of bladed zircon	483
451	33.167	0.93	0.106	0.032	0.119	0.42	0.717	64.641	0	0.11	0.114	0	100.356	JEF-00-36-118		dendritic zircon	1499
452	33.308	1.148	0.17	0.033	0.223	0.372	1.142	62.897	0	0.177	0.57	0	100.04	JEF-00-36-119		dendritic zircon	1010
453	35.917	0.804	0.065	0.027	0.123	0.37	0.433	63.129	0.005	0.063	0.022	0	100.958	JEF-00-36-120		dendritic zircon	1983
455	34.418	0.923	0.123	0.03	0.275	0.396	0.523	64.714	0	0.072	0.167	0.001	101.642	JEF-00-36-122		dendritic zircon	1363
456	34.532	0.712	0.094	0.031	0.269	0.404	0.451	65.687	0	0.06	0.061	0.01	102.311	JEF-00-36-123		dendritic zircon	1743
457	33.762	1.209	0.141	0.032	0.194	0.392	0.771	63.354	0	0.104	0.261	0.006	100.226	JEF-00-36-124		dendritic zircon	1239
458	33.349	1.02	0.13	0.042	0.124	0.377	0.566	64.572	0.001	0.073	0.121	0	100.375	JEF-00-36-125		dendritic zircon	1739
459	33.784	1.221	0.126	0.036	0.125	0.392	0.685	64.54	0	0.094	0.227	0.012	101.242	JEF-00-36-126		dendritic zircon	1512
460	34.552	1.054	0.085	0.026	0.095	0.424	0.424	66.127	0.013	0.068	0.118	0.008	102.994	JEF-00-36-127		dendritic zircon	1586
461	33.169	1.039	0.095	0.03	0.122	0.367	0.54	65.141	0	0.057	0.12	0.006	100.686	JEF-00-36-128		dendritic zircon	1694
462	34.065	1.039	0.099	0.035	0.115	0.39	0.606	64.837	0	0.08	0.079	0.015	101.36	JEF-00-36-129		dendritic zircon	1788
463	34.316	1.183	0.09	0.029	0.102	0.39	0.565	65.491	0	0.078	0.133	0.008	102.385	JEF-00-36-130		dendritic zircon	1637
464	33.791	1.302	0.141	0.038	0.162	0.349	0.714	64.343	0	0.11	0.241	0.022	101.213	JEF-00-36-131		dendritic zircon	1428
465	32.175	1.18	0.156	0.029	0.156	0.35	0.883	63.346	0	0.137	0.446	0.012	98.87	JEF-00-36-132		dendritic zircon	1005

Table A-2. Chemical data (wt%) for zircon from sample JEF-00-39 of the BD2 mafic dyke swarm (Basalt craton), determined by electron microprobe WDS spot analysis. (FeO represents total Fe oxide, uncorrected for Fe₂O₃ content).

No.	SiO ₂	FeO	UO ₂	PbO	P ₂ O ₅	HfO ₂	Y ₂ O ₃	ZrO ₂	Nb ₂ O ₅	ThO ₂	CaO	TiO ₂	Total	Comment	Crystal morphology/context	f (Ma)
26	32.277	0.883	0.136	0.023	0.172	0.366	0.88	63.308	0	0.122	0.31	0	98.457	JEF-00-39-1	Overgrowth rim on polyhedral crystal	917
27	34.257	1.171	0.114	0.021	0.15	0.405	0.524	63.917	0	0.074	0.195	0	100.804	JEF-00-39-2	Overgrowth rim on polyhedral crystal	1047
28	33.592	1.016	0.116	0.026	0.15	0.434	0.787	63.113	0.006	0.12	0.313	0	99.657	JEF-00-39-3	Overgrowth rim on polyhedral crystal	1152
29	32.552	0.403	0.136	0.029	0.083	0.244	0.438	61.52	0	0.057	0.051	0.006	100.157	JEF-00-39-4	dendritic zircon	1259
30	32.851	0.574	0.081	0.023	0.184	0.398	0.617	65.307	0.013	0.049	0.058	0	100.157	JEF-00-39-5	dendritic zircon	1539
31	33.969	0.791	0.082	0.029	0.185	0.28	0.551	65.12	0.003	0.049	0.095	0	101.154	JEF-00-39-6	dendritic zircon	1860
32	33.789	1.054	0.082	0.028	0.124	0.257	0.658	64.006	0	0.055	0.09	0	100.143	JEF-00-39-7	dendritic zircon	1782
33	31.447	0.597	0.103	0.029	0.128	0.204	0.588	61.022	0	0.048	0.071	0	94.207	JEF-00-39-8	dendritic zircon	1560
34	33.723	0.523	0.082	0.021	0.129	0.364	0.487	65.721	0.016	0.054	0.114	0	101.214	JEF-00-39-9	dendritic zircon	1400
35	33.305	0.861	0.077	0.021	0.12	0.431	0.549	65.358	0.009	0.064	0.068	0	100.863	JEF-00-39-10	dendritic zircon	1428
36	32.447	0.708	0.338	0.024	0	0.313	0.826	63.309	0	0.321	0.632	0	98.922	Line	Core of polyhedral crystal	398
37	32.64	0.772	0.319	0.021	0	0.349	0.845	62.882	0.04	0.293	0.652	0	98.813	Line	Core of polyhedral crystal	373
38	33.557	0.651	0.336	0.022	0	0.352	0.773	62.76	0.021	0.33	0.736	0	99.538	Line	Core of polyhedral crystal	366
39	32.976	0.97	0.317	0.023	0	0.312	0.787	62.952	0	0.319	0.721	0	98.377	Line	Core of polyhedral crystal	402
40	32.936	0.604	0.326	0.019	0	0.339	0.824	62.476	0	0.33	0.675	0	98.729	Line	Core of polyhedral crystal	324
41	32.813	0.633	0.317	0.022	0	0.334	0.766	63.244	0.004	0.282	0.601	0.003	99.034	Line	Core of polyhedral crystal	395
42	32.869	0.591	0.294	0.017	0	0.368	0.713	63.526	0.019	0.256	0.626	0	99.264	Line	Core of polyhedral crystal	333
43	32.777	0.746	0.31	0.025	0	0.313	0.734	62.054	0	0.292	0.66	0.005	97.916	Line	Core of polyhedral crystal	451
44	32.629	0.696	0.328	0.026	0	0.345	0.787	63.179	0	0.303	0.634	0	98.927	Line	Core of polyhedral crystal	446
45	32.45	1.045	0.328	0.024	0	0.343	0.855	62.602	0	0.341	0.763	0	98.731	Line	Core of polyhedral crystal	402
46	32.245	2.592	0.333	0.022	0	0.312	0.783	60.461	0.019	0.336	0.724	0.003	97.85	Line	Core of polyhedral crystal	366
47	32.343	1.701	0.33	0.019	0	0.342	0.724	62.279	0	0.281	0.624	0.003	98.616	Line	Core of polyhedral crystal	358
48	31.719	0.761	0.311	0.019	0	0.303	0.718	55.51	0	0.312	1.08	0	98.896	Line	Core of polyhedral crystal	368
49	33.28	0.618	0.351	0.023	0	0.324	0.854	63.219	0.027	0.399	0.744	0	99.839	Line	Core of polyhedral crystal	340
50	32.554	0.774	0.312	0.017	0	0.326	0.754	62.665	0	0.305	0.701	0	98.408	Line	Core of polyhedral crystal	353
51	32.031	1.217	0.289	0.013	0	0.338	0.741	61.758	0	0.283	0.743	0	97.432	Line	Core of polyhedral crystal	306
52	33.716	1.368	0.289	0.019	0	0.319	0.681	61.694	0.013	0.265	0.605	0	98.969	Line	Core of polyhedral crystal	252
53	34.262	0.88	0.275	0.016	0	0.344	0.685	62.686	0	0.257	0.658	0	100.063	Line	Core of polyhedral crystal	330
54	32.693	0.643	0.307	0.022	0	0.319	0.718	62.971	0	0.296	0.639	0.005	98.613	Line	Core of polyhedral crystal	330
55	32.694	0.858	0.305	0.02	0	0.317	0.751	62.804	0.009	0.288	0.645	0	98.691	Line	Core of polyhedral crystal	401
56	33.166	1.011	0.297	0.036	0	0.333	0.689	63.75	0.027	0.26	0.704	0	100.273	Line	Core of polyhedral crystal	369
57	32.917	1.009	0.293	0.091	0	0.353	0.714	61.834	0.002	0.258	0.716	0.003	98.19	Line	Core of polyhedral crystal	676
58	32.856	0.801	0.34	0.024	0	0.309	0.824	63.22	0.016	0.357	0.735	0.009	99.491	Line	Core of polyhedral crystal	1582
59	33.125	1	0.303	0.019	0	0.355	0.785	63.168	0	0.3	0.716	0	99.771	Line	Core of polyhedral crystal	387
60	33.161	0.83	0.322	0.018	0	0.318	0.834	62.439	0.002	0.321	0.713	0	98.858	Line	Core of polyhedral crystal	350
61	32.883	0.875	0.087	0.027	0.171	0.395	0.711	64.673	0.003	0.067	0.129	0	100.029	JEF-00-39-11	Core of polyhedral crystal	312
62	32.891	0.931	0.11	0.03	0.172	0.385	0.703	64.681	0	0.093	0.129	0	100.144	JEF-00-39-12	dendritic zircon	1614
63	33.94	0.754	0.067	0.021	0.15	0.417	0.425	64.818	0	0.055	0.026	0	100.673	JEF-00-39-13	dendritic zircon	1424
64	33.124	1.14	0.091	0.024	0.128	0.397	0.454	65.704	0.006	0.05	0.11	0.001	101.229	JEF-00-39-14	dendritic zircon	1612
65	23.283	0.884	0.115	0.011	0	0.35	0.109	46.109	0	0.038	0.316	0	71.215	JEF-00-39-15	altered dendritic zircon	1469
75	33.027	0.691	0.085	0.024	0.241	0.399	0.563	65.084	0.089	0.058	0.086	0	100.347	JEF-00-39-16	dendritic zircon	616
76	33.096	1.005	0.158	0.022	0.26	0.367	0.969	61.702	0.019	0.118	0.495	0	98.211	JEF-00-39-17	dendritic zircon	1515
77	35.114	1.091	0.09	0.025	0.141	0.506	0.597	66.562	0	0.06	0.179	0	104.365	JEF-00-39-18	dendritic zircon	792
78	35.75	1.759	0.34	0.025	0.068	0.358	0.91	58.12	0.034	0.393	0.831	0.005	98.593	JEF-00-39-19	altered dendritic zircon	393
79	33.49	1.349	0.26	0.027	0.182	0.346	0.916	63.089	0.033	0.115	0.254	0	98.927	JEF-00-39-20	dendritic zircon	1134
80	34.212	0.874	0.13	0.031	0.184	0.397	0.925	64.477	0.02	0.132	0.22	0	101.602	JEF-00-39-21	dendritic zircon	1223
81	33.901	0.782	0.376	0.02	0.042	0.337	0.967	60.44	0.006	0.424	1.016	0.01	98.321	JEF-00-39-22	altered dendritic zircon	289
82	36.09	1.36	0.103	0.023	0.185	0.408	0.564	66.979	0	0.06	0.194	0	105.966	JEF-00-39-23	dendritic zircon	1262
83	34.378	1.156	0.103	0.026	0.214	0.391	0.666	65.987	0	0.075	0.154	0	103.15	JEF-00-39-24	dendritic zircon	1363
84	34.466	1.063	0.105	0.022	0.203	0.36	0.631	65.846	0	0.062	0.121	0.01	102.889	JEF-00-39-25	dendritic zircon	1191

Table A-2 continued. Chemical data (wt%) for zircon from sample JEF-00-39 of the BDZ mafic dyke swarm (Bastar craton), determined by electron microprobe WDS spot analysis. (FeO represents total Fe oxide, uncorrected for Fe₂O₃ content).

No.	SiO ₂	FeO	UO ₂	PbO	P ₂ O ₅	HfO ₂	Y ₂ O ₃	ZrO ₂	Nb ₂ O ₅	TiO ₂	CaO	TiO ₂	Total	Comment	Crystal morphology/context	t (Ma)
85	35.86	0.97	0.089	0.027	0.12	0.453	0.466	65.664	0	0.034	0.108	0	103.791	JEF-00-39-26	dendritic zircon	1711
86	36.629	1.319	0.224	0.026	0.066	0.39	0.677	63.327	0	0.241	0.449	0	103.353	JEF-00-39-27	altered dendritic zircon	621
87	36.649	1.278	0.104	0.03	0.156	0.46	0.542	66.189	0.034	0.055	0.185	0	105.682	JEF-00-39-28	dendritic zircon	1592
88	34.818	1.114	0.092	0.021	0.155	0.406	0.548	65.799	0.036	0.059	0.145	0.004	103.197	JEF-00-39-29	dendritic zircon	1270
89	36.087	0.965	0.105	0.033	0.19	0.384	0.572	66.558	0	0.084	0.111	0	105.06	JEF-00-39-30	dendritic zircon	1683
90	36.551	0.782	0.072	0.023	0.137	0.433	0.459	67.066	0	0.041	0.022	0	105.59	JEF-00-39-31	dendritic zircon	1720
91	23.392	0.4	0.085	0.019	0.168	0.174	0.724	48.507	0	0.073	0.115	0	73.857	JEF-00-39-32	dendritic zircon	1191
92	29.718	0.384	0.097	0.024	0.132	0.297	0.62	58.635	0	0.074	0.039	0.002	90.022	JEF-00-39-33	dendritic zircon	1330
93	34.3	0.587	0.101	0.023	0.153	0.427	0.342	63.501	0.004	0.069	0.168	0	101.143	JEF-00-39-34	dendritic zircon	1206
94	33.364	0.868	0.262	0.026	0.079	0.361	0.682	63.501	0.014	0.173	0.732	0	100.062	JEF-00-39-35	altered dendritic zircon	588
95	35.188	0.517	0.137	0.029	0.065	0.368	0.331	61.487	0.009	0.075	0.256	0.003	98.445	JEF-00-39-36	dendritic zircon	1213
96	35.9	1.075	0.098	0.031	0.284	0.361	0.688	64.581	0	0.069	0.245	0	103.292	JEF-00-39-37	dendritic zircon	1662
97	36.114	1.017	0.304	0.018	0.02	0.374	0.851	65.872	0.044	0.278	0.718	0.009	103.619	JEF-00-39-38	altered dendritic zircon	337
98	34.157	0.531	0.114	0.029	0.181	0.395	0.638	65.435	0.031	0.093	0.193	0.001	101.798	JEF-00-39-39	dendritic zircon	1348
99	32.546	3.245	0.321	0.027	0	0.327	0.784	58.805	0.046	0.175	0.745	0.004	97.025	JEF-00-39-40	altered dendritic zircon	517
100	31.916	0.615	0.113	0.03	0.156	0.321	0.691	64.378	0.01	0.072	0.105	0	98.407	JEF-00-39-41	dendritic zircon	1451
101	33.761	0.777	0.089	0.021	0.139	0.43	0.717	63.878	0	0.108	0.155	0.002	100.075	JEF-00-39-42	Oyegrowth rim on polyhedral crystal	1170
102	36.187	0.449	0.071	0.025	0.114	0	0.255	63.333	0	0.377	0.891	0	101.451	JEF-00-39-43	Oyegrowth rim on polyhedral crystal	1880
103	29.324	0.906	0.338	0	0	0	0.255	63.333	0	0.377	0.891	0	86.341	JEF-00-39-44	altered dendritic zircon	0
104	34.587	0.813	0.097	0.034	0.14	0.484	0.785	65.658	0	0.079	0.139	0	102.776	JEF-00-39-45	dendritic zircon	1773
105	23.161	0.629	0.278	0.016	0	0.187	0.896	49.627	0.035	0.258	0.505	0.001	75.593	JEF-00-39-46	altered dendritic zircon	327
106	36.242	0.36	0.051	0.022	0.113	0.364	0.348	65.818	0.009	0.025	0.01	0	103.36	JEF-00-39-47	dendritic zircon	2218
107	28.091	0.46	0.025	0.013	0.117	0.253	0.493	57.108	0.051	0.031	0.05	0.028	86.69	JEF-00-39-48	dendritic zircon	2269
108	34.348	0.673	0.114	0.027	0.269	0.452	0.527	65.271	0.036	0.076	0.117	0	101.885	JEF-00-39-49	dendritic zircon	1368
109	36.807	0.651	0.089	0.03	0.167	0.463	0.695	67.174	0.003	0.071	0.071	0	106.226	JEF-00-39-50	dendritic zircon	1704
110	32.847	1.043	0.32	0.017	0.003	0.353	0.939	57.946	0.012	0.432	1.167	0.01	95.089	JEF-00-39-51	altered dendritic zircon	275
111	32.226	0.853	0.147	0.027	0.434	0.361	0.666	63.32	0.002	0.066	0.442	0	96.584	JEF-00-39-52	dendritic zircon	1059
112	34.19	0.173	0.078	0.024	0.284	0.435	0.865	64.977	0.016	0.042	0.078	0	100.742	JEF-00-39-53	dendritic zircon	1677
113	33.567	0.464	0.122	0.031	0.294	0.415	0.72	64.443	0.009	0.095	0.272	0.004	100.436	JEF-00-39-54	dendritic zircon	1357
114	33.294	0.192	0.07	0.017	0.108	0.409	0.342	65.006	0	0.045	0.091	0	99.574	JEF-00-39-55	dendritic zircon	1341
130	34.228	3.05	0.124	0.032	0.086	0.435	0.426	65.672	0	0.063	0.163	0	101.554	JEF-00-39-71	dendritic zircon	1406
131	33.46	0.525	0.164	0.036	0.175	0.412	0.967	63.713	0.019	0.159	0.37	0.001	100.001	JEF-00-39-72	dendritic zircon	1146
132	32.732	0.53	0.112	0.03	0.148	0.413	0.749	64.557	0.029	0.11	0.104	0	99.514	JEF-00-39-73	dendritic zircon	1364
133	32.813	0.281	0.094	0.024	0.167	0.376	0.468	66.479	0	0.047	0.051	0.003	100.613	JEF-00-39-74	dendritic zircon	1443
135	34.238	0.251	0.118	0.026	0.195	0.443	0.519	66.172	0.031	0.062	0.107	0	102.162	JEF-00-39-76	dendritic zircon	1263
136	32.593	0.854	0.376	0.019	0	0.375	0.996	60.579	0	0.386	1.178	0.005	97.361	JEF-00-39-77	altered dendritic zircon	281
137	33.769	0.62	0.344	0	0	0.405	0.896	61.857	0	0.338	1.084	0.009	99.322	JEF-00-39-78	altered dendritic zircon	1231
138	32.674	2.704	0.289	0.069	0.07	0.361	0.855	58.969	0	0.286	1.108	0	97.386	JEF-00-39-79	altered dendritic zircon	503
139	32.775	0.627	0.323	0.019	0.022	0.384	0.817	60.878	0	0.367	1.257	0.011	97.48	JEF-00-39-80	altered dendritic zircon	318
140	32.26	0.696	0.277	0.026	0.16	0.394	1.088	61.553	0.004	0.308	0.994	0	97.76	JEF-00-39-81	altered dendritic zircon	503
141	33.862	1.121	0.322	0.013	0.024	0.411	0.792	61.133	0	0.234	1.077	0.021	99.01	JEF-00-39-82	altered dendritic zircon	242
142	33.339	0.633	0.266	0.026	0.11	0.375	0.86	62.737	0	0.209	0.937	0.008	99.5	JEF-00-39-83	altered dendritic zircon	562
143	33.075	0.552	0.147	0.034	0.174	0.395	0.887	64.301	0	0.114	0.137	0.032	99.848	JEF-00-39-84	dendritic zircon	1250
144	33.23	0.569	0.152	0.036	0.151	0.459	0.786	65.793	0	0.113	0.115	0	101.384	JEF-00-39-85	dendritic zircon	1285
145	33.005	0.506	0.12	0.03	0.154	0.39	0.711	66.151	0.01	0.075	0.07	0	101.222	JEF-00-39-86	dendritic zircon	1380
146	33.715	0.42	0.107	0.028	0.165	0.394	0.604	66.069	0	0.061	0.051	0	101.614	JEF-00-39-87	dendritic zircon	1453
147	33.319	0.626	0.214	0.03	0.043	0.395	0.543	64.512	0.013	0.137	0.437	0	100.268	JEF-00-39-88	dendritic zircon	817
148	32.966	0.424	0.275	0.026	0	0.46	0.156	64.847	0.051	0.077	0.649	0.006	99.937	JEF-00-39-89	altered dendritic zircon	618
149	33.794	0.524	0.245	0.028	0.012	0.475	0.217	65.651	0.006	0.084	0.733	0.004	101.773	JEF-00-39-90	altered dendritic zircon	726
150	32.662	0.512	0.244	0.038	0.347	0.367	0.912	63.4	0	0.231	0.871	0	99.584	JEF-00-39-91	altered dendritic zircon	841
151	33.077	0.548	0.254	0.027	0	0.447	0.997	64.933	0.01	0.069	0.553	0	100.015	JEF-00-39-92	altered dendritic zircon	691
152	32.744	0.218	0.056	0.019	0.048	0.445	0.234	65.756	0	0.006	0.022	0.001	99.549	JEF-00-39-93	dendritic zircon	1979
153	33.236	0.184	0.069	0.023	0.054	0.403	0.222	67.69	0.014	0.033	0.006	0	101.934	JEF-00-39-94	dendritic zircon	1813
154	33.56	0.181	0.058	0.021	0.058	0.444	0.226	67.832	0.002	0.031	0.006	0	102.419	JEF-00-39-95	dendritic zircon	1918
155	33.236	0.684	0.129	0.027	0.139	0.387	0.79	64.681	0	0.111	0.212	0	100.378	JEF-00-39-96	dendritic zircon	1123
156	33.801	0.626	0.13	0.033	0.14	0.424	0.679	65.555	0.003	0.087	0.157	0	101.635	JEF-00-39-97	dendritic zircon	1386
157	33.528	0.625	0.115	0.028	0.128	0.444	0.647	65.793	0	0.072	0.163	0	101.563	JEF-00-39-98	dendritic zircon	1221
158	33.279	0.621	0.162	0.028	0.121	0.367	0.823	64.317	0.016	0.151	0.428	0	100.313	JEF-00-39-99	dendritic zircon	929
159	32.757	0.638	0.153	0.028	0.088	0.383	0.586	65.229	0	0.108	0.398	0	100.368	JEF-00-39-100	dendritic zircon	1028

Table A-3. Chemical data (wt%) for zircon from sample JEF-00-37 of the BD2 mafic dyke swarm (Bastar craton), determined by electron microprobe WDS spot analysis. (FeO represents total Fe oxide, uncorrected for Fe₂O₃ content).

No.	SiO ₂	FeO	UO ₂	PbO	P ₂ O ₅	HfO ₂	Y ₂ O ₃	ZrO ₂	Nb ₂ O ₅	ThO ₂	CaO	TiO ₂	Total	Comment	Crystal morphology/context	t (Ma)	
166	32.2	0.746	0.064	0.023	0.102	0.338	0.533	59.226	0.061	0.012	0.275	0.032	93.612	JEF-00-37-7	overgrowth on baddeleyite A	Domain I	2038
167	31.916	1.383	0.085	0.024	0.065	0.345	0.443	59.027	0.082	0.019	0.299	0.042	93.73	JEF-00-37-8	overgrowth on baddeleyite A	Domain I	1667
168	32.705	0.702	0.08	0.023	0.087	0.366	0.361	60.19	0.054	0.005	0.33	0.045	94.948	JEF-00-37-9	overgrowth on baddeleyite A	Domain I	1751
169	31.465	0.687	0.069	0.018	0.093	0.367	0.412	60.595	0.039	0.013	0.318	0.047	94.093	JEF-00-37-10	overgrowth on baddeleyite A	Domain I	1573
170	33	0.76	0.075	0.024	0.092	0.372	0.382	59.491	0.041	0.011	0.342	0.043	94.633	JEF-00-37-11	overgrowth on baddeleyite A	Domain I	1875
171	40.535	1.536	0.124	0.042	0	0.372	0.017	59.525	0.111	0.028	0.301	0.209	102.8	JEF-00-37-12	overgrowth on baddeleyite A	Domain II	1931
172	40.167	1.512	0.095	0.032	0	0.388	0.035	63.091	0.125	0	0.471	0.357	106.273	JEF-00-37-13	overgrowth on baddeleyite A	Domain II	2012
173	35.098	1.279	0.116	0.03	0	0.38	0.045	58.787	0.109	0	0.441	0.254	96.539	JEF-00-37-14	overgrowth on baddeleyite A	Domain II	1629
182	32.951	0.92	0.192	0.031	0	0.27	0.241	65.115	0.033	0.059	0.571	0.071	100.454	JEF-00-37-23	overgrowth on baddeleyite B	Domain I	1006
183	30.096	0.924	0.138	0.026	0	0.298	0.169	70.189	0.04	0.079	0.334	0.191	102.484	JEF-00-37-24	overgrowth on baddeleyite B	Domain I	1087
184	33.299	0.882	0.207	0.039	0	0.225	0.137	63.483	0.01	0.138	0.891	0.048	99.357	JEF-00-37-25	overgrowth on baddeleyite B	Domain I	1087
185	32.58	0.982	0.147	0.025	0	0.286	0.106	65.171	0	0.066	0.485	0.057	99.875	JEF-00-37-26	overgrowth on baddeleyite B	Domain I	1020
186	30.571	0.995	0.136	0.029	0	0.296	0.087	68.498	0.032	0.035	0.209	0.157	101.045	JEF-00-37-27	overgrowth on baddeleyite B	Domain I	1303
187	33.919	0.984	0.14	0.03	0	0.287	0.135	65.273	0	0.075	0.462	0.123	101.428	JEF-00-37-28	overgrowth on baddeleyite B	Domain I	1230
188	29.937	0.966	0.131	0.029	0	0.308	0.093	70.512	0.023	0.043	0.337	0.312	102.691	JEF-00-37-29	overgrowth on baddeleyite B	Domain I	1325
189	31.379	1.165	0.159	0.027	0	0.282	0.117	66.388	0.037	0.047	0.523	0.253	100.377	JEF-00-37-30	overgrowth on baddeleyite B	Domain I	1056
190	33.455	0.862	0.208	0.021	0	0.26	0.275	63.088	0	0.26	0.923	0.074	99.426	JEF-00-37-31	overgrowth on baddeleyite B	Domain I	524
203	32.584	0.739	0.702	0.078	0.269	0.25	1.846	60.658	0.015	0.702	1.989	0.015	99.847	JEF-00-37-32	subhedral zircon crystal	Domain I	605
204	32.85	1.078	0.355	0.07	0.075	0.331	0.752	61.547	0	0.477	1.12	0	98.655	JEF-00-37-33	subhedral zircon crystal	Domain I	965
205	32.353	1.161	0.324	0.041	0.07	0.427	0.648	60.128	0	0.308	1.404	0.02	96.884	JEF-00-37-34	subhedral zircon crystal	Domain I	692
206	33.785	1.174	0.154	0.035	0.028	0.248	0.596	63.718	0.084	0.051	0.336	0	100.147	JEF-00-37-35	subhedral zircon crystal	Domain I	1355
207	33.892	1.111	0.125	0.033	0.01	0.271	0.509	63.519	0.027	0.045	0.294	0	99.836	JEF-00-37-36	subhedral zircon crystal	Domain I	1530
208	33.479	1.082	0.367	0.039	0.027	0.409	0.931	59.428	0	0.392	1.571	0.029	97.774	JEF-00-37-37	subhedral zircon crystal	Domain I	550
209	33.127	1.075	0.338	0.06	0.082	0.295	0.778	61.662	0.009	0.537	1.298	0.006	98.267	JEF-00-37-38	subhedral zircon crystal	Domain I	835
210	32.466	0.762	0.705	0.041	0.164	0.258	1.821	57.126	0.007	0.712	2.578	0.031	96.669	JEF-00-37-39	subhedral zircon crystal	Domain I	324
211	32.955	0.894	0.601	0.044	0.473	0.253	1.962	57.951	0	0.684	1.945	0.027	97.419	JEF-00-37-40	subhedral zircon crystal	Domain I	393
212	32.484	1.174	0.312	0.04	0.086	0.312	1.016	59.596	0.036	0.451	1.544	0.015	97.066	JEF-00-37-41	subhedral zircon crystal	Domain I	632
213	33.102	1.101	0.413	0.041	0.024	0.427	1.165	59.387	0.005	0.428	1.619	0.035	97.747	JEF-00-37-42	subhedral zircon crystal	Domain I	540
214	33.531	1.335	0.43	0.067	0.074	0.441	1.009	59.268	0	0.608	1.769	0.012	98.544	JEF-00-37-43	subhedral zircon crystal	Domain I	765
215	33.771	1.11	0.131	0.027	0.028	0.217	0.522	63.782	0.005	0.047	0.276	0	99.914	JEF-00-37-44	subhedral zircon crystal	Domain I	1236
216	33.773	1.178	0.156	0.03	0.031	0.272	0.565	63.303	0	0.051	0.366	0	98.725	JEF-00-37-45	subhedral zircon crystal	Domain I	1171
217	33.92	1.128	0.141	0.031	0.034	0.274	0.498	63.929	0.017	0.059	0.306	0	100.337	JEF-00-37-46	subhedral zircon crystal	Domain I	1291
218	33.605	0.965	0.535	0.052	0.407	0.27	2.291	59.692	0.008	0.585	1.877	0.02	100.307	JEF-00-37-47	subhedral zircon crystal	Domain I	522
219	32.313	1.141	0.258	0.031	0.102	0.264	1.277	60.088	0.003	0.443	1.306	0.01	97.236	JEF-00-37-48	subhedral zircon crystal	Domain I	563
220	33.036	1.164	0.464	0.048	0.105	0.419	1.273	60.039	0.022	0.581	1.726	0.034	98.911	JEF-00-37-49	subhedral zircon crystal	Domain I	536
221	33.922	1.338	0.263	0.039	0.076	0.378	1.17	60.604	0.011	0.478	1.394	0.006	98.708	JEF-00-37-50	subhedral zircon crystal	Domain I	631
222	33.389	0.985	0.601	0.054	0.176	0.285	2.232	59.769	0.013	0.723	1.492	0.013	99.732	JEF-00-37-51	subhedral zircon crystal	Domain I	473
223	32.373	0.895	0.64	0.056	0.184	0.252	2.345	58.574	0	0.63	1.286	0.018	97.253	JEF-00-37-52	subhedral zircon crystal	Domain I	484
224	31.856	0.997	0.69	0.062	0.249	0.243	2.269	59.206	0	0.651	1.223	0.006	97.452	JEF-00-37-53	subhedral zircon crystal	Domain I	501
225	31.993	1.368	0.479	0.065	0.202	0.361	2.052	58.073	0.006	0.709	1.485	0.012	96.805	JEF-00-37-54	subhedral zircon crystal	Domain I	662
226	32.876	1.168	0.55	0.058	0.169	0.319	2.14	58.65	0.014	0.784	1.379	0.031	98.138	JEF-00-37-55	subhedral zircon crystal	Domain I	526
227	32.958	1.132	0.478	0.062	0.214	0.363	1.987	59.041	0.012	0.687	1.437	0.022	98.393	JEF-00-37-56	subhedral zircon crystal	Domain I	640
228	32.87	1.565	0.569	0.05	0.156	0.301	1.622	59.769	0	0.714	1.906	0.039	99.561	JEF-00-37-57	subhedral zircon crystal	Domain I	463
229	32.978	1.254	0.86	0.03	0.177	0.234	1.927	54.323	0	1.368	4.173	0.023	97.937	JEF-00-37-58	subhedral zircon crystal	Domain I	174
230	35.997	4.706	0.422	0.039	0.055	0.31	1.311	55.972	0	0.548	2.818	0.096	102.274	JEF-00-37-59	subhedral zircon crystal	Domain I	476
231	31.245	1.261	0.657	0	0.991	0.271	1.877	55.15	0	1.29	4.871	0.025	97.639	JEF-00-37-60	subhedral zircon crystal	Domain I	0
232	31.617	1.482	0.633	0.016	0.537	0.239	1.669	52.37	0.017	2.275	4.793	0.028	95.676	JEF-00-37-61	subhedral zircon crystal	Domain I	89

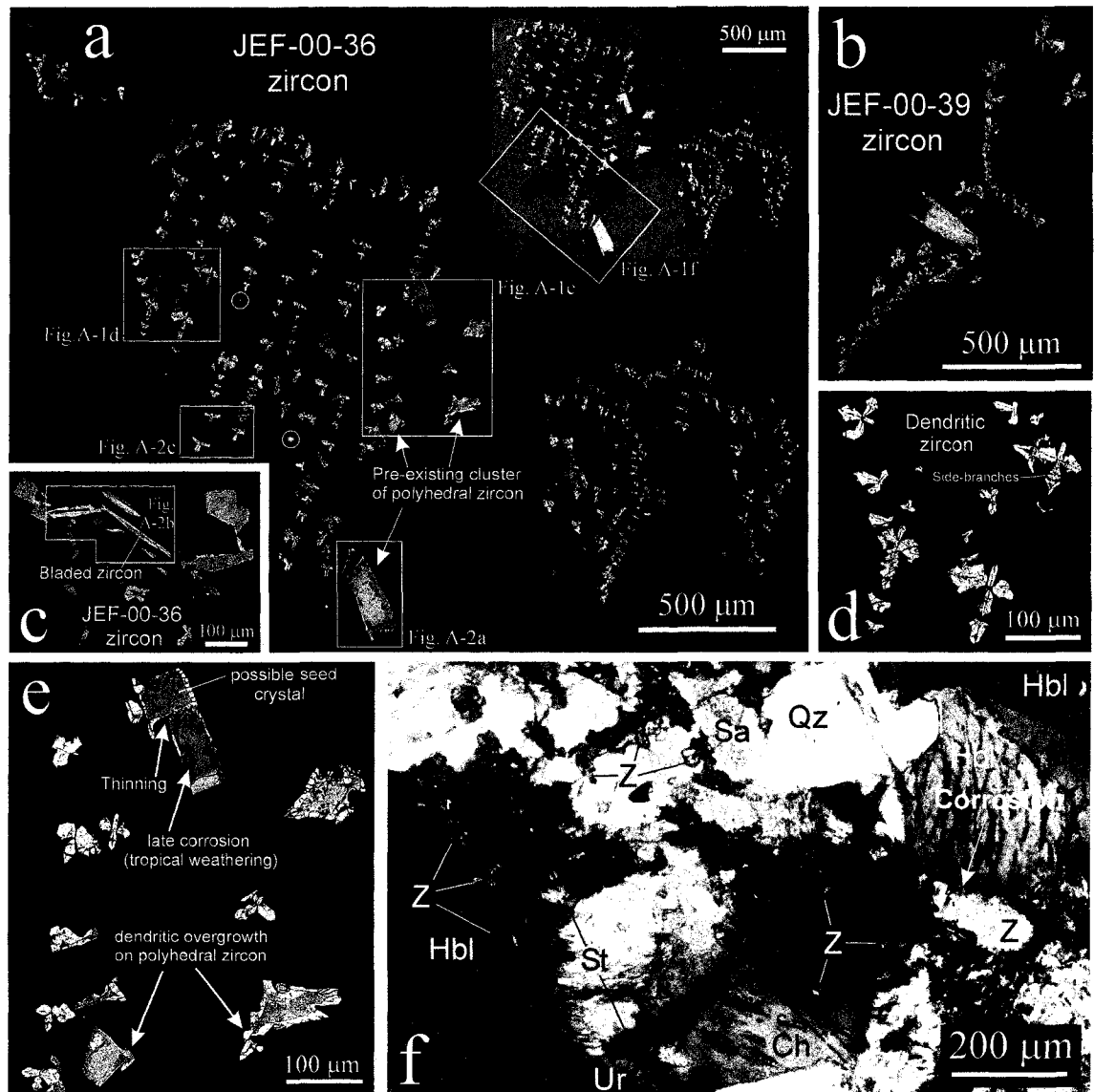


Fig. A-1. a-e) BSE images of igneous zircon in polished thin sections of the BD2 mafic dyke swarm, Bastar craton, south India. The inset in figure in a) is a BSE image of the same region at lower contrast showing the petrographic context of the photomicrograph (plain light) in f). The bright minerals in all of the high contrast BSE images are igneous zircon, except for the two circled bright spots in a) which are thorite. For both JEF-00-36 (a) and JEF-00-39 (b), the majority of dendritic zircons exposed in the BSE images are interpreted to be interconnected in 3-dimensions as a single complex tree that nucleated on earlier formed polyhedral zircon. Fractal growth modelling of a large part of the structure in a) is carried out in Appendix B, and a possible seed crystal onto which the structure grew is shown in e). Abbreviations in f): Bi - biotite; Ch - chlorite; Hbl - hornblende; Qz - quartz; Sa - saussurite; St - stilpnomelane; Ur - uralite; Z - zircon.

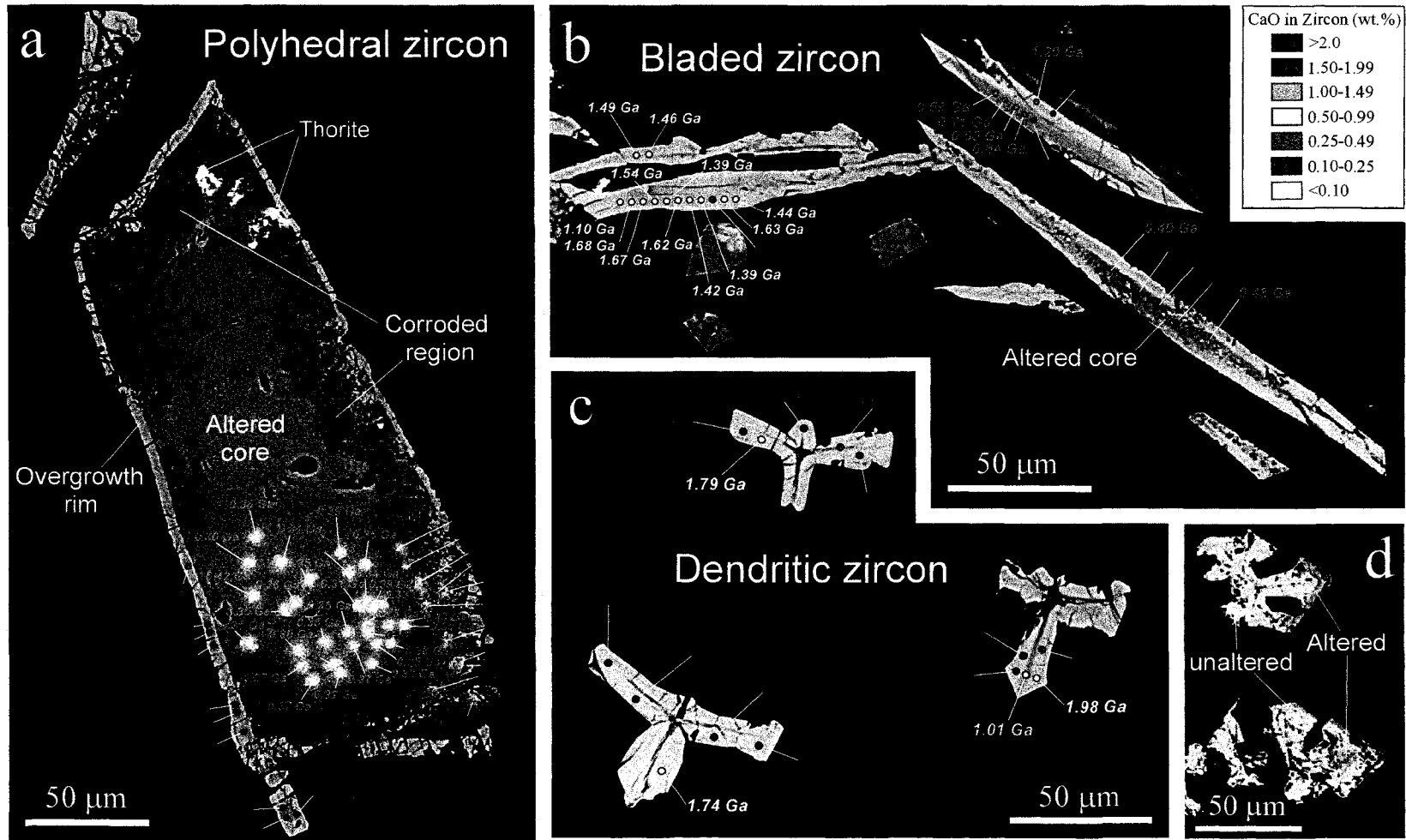


Fig. A-2. Close-up BSE images (from Fig. A-1) of zircon from BD2 dyke samples JEF-00-36 (a-c) and JEF-00-39 (d), highlighting three morphological types of igneous zircon. The context of the quantitative (WDS) spot analyses carried out during electron microprobe chemical U-Th-total Pb chemical dating is shown and the individual apparent age for each spot is labelled and colour coded to CaO (wt.%) content.

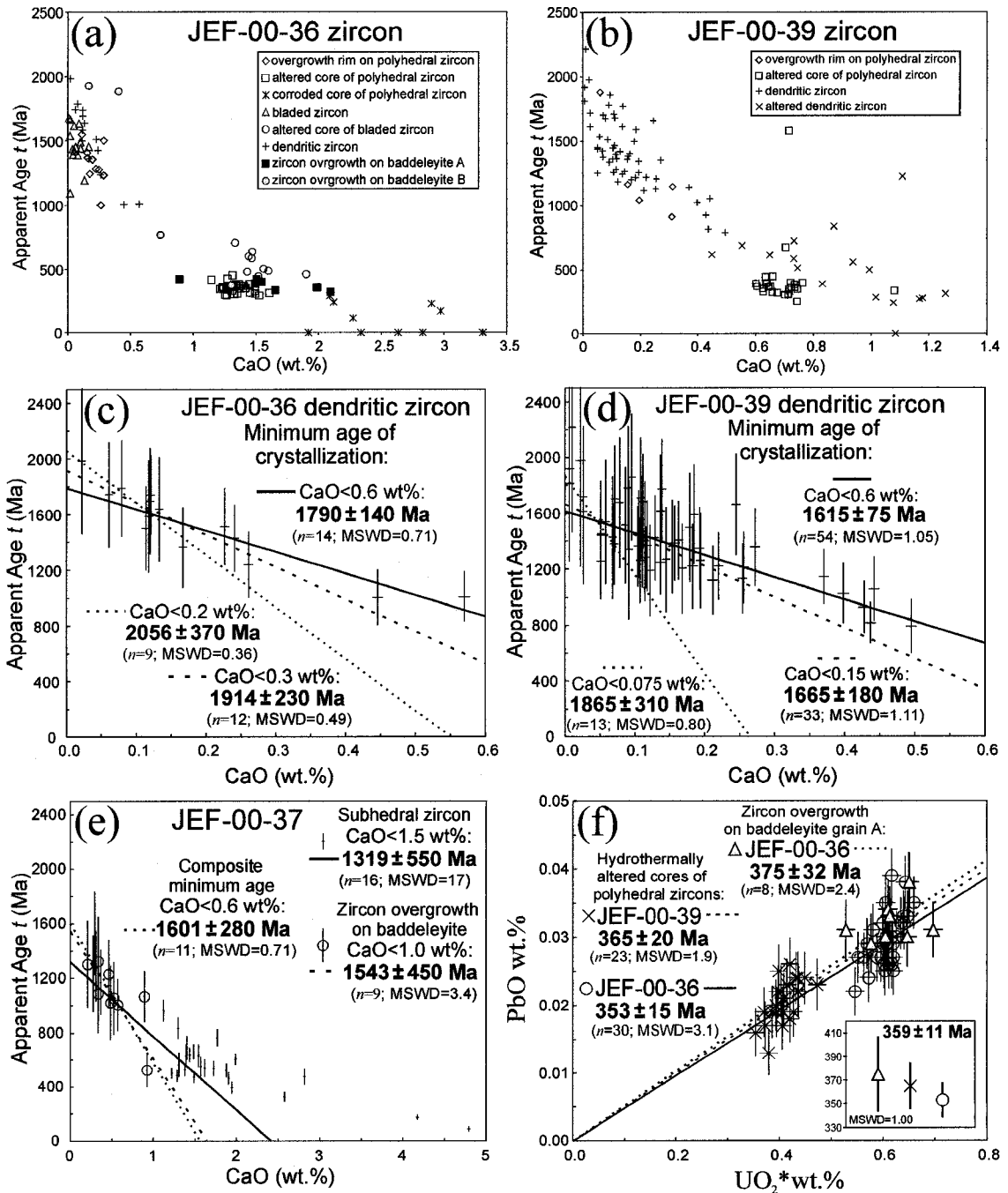


Fig. A-3. a-e) Plots of CaO (wt%) versus apparent age (t) for zircon spot analyses determined by electron microprobe (WDS) from BD2 mafic dykes. Ages were calculated using the y-intercept method described in the text. c) and d) are close-ups of the data shown in a) and b), respectively, with the exclusion of all data except that for dendritic zircon. Petrographic context of the data for JEF-00-36 is shown in Fig. A-2, and the petrographic context of data for zircon overgrowths on baddeleyite (e and f) is shown in Fig. A-4.

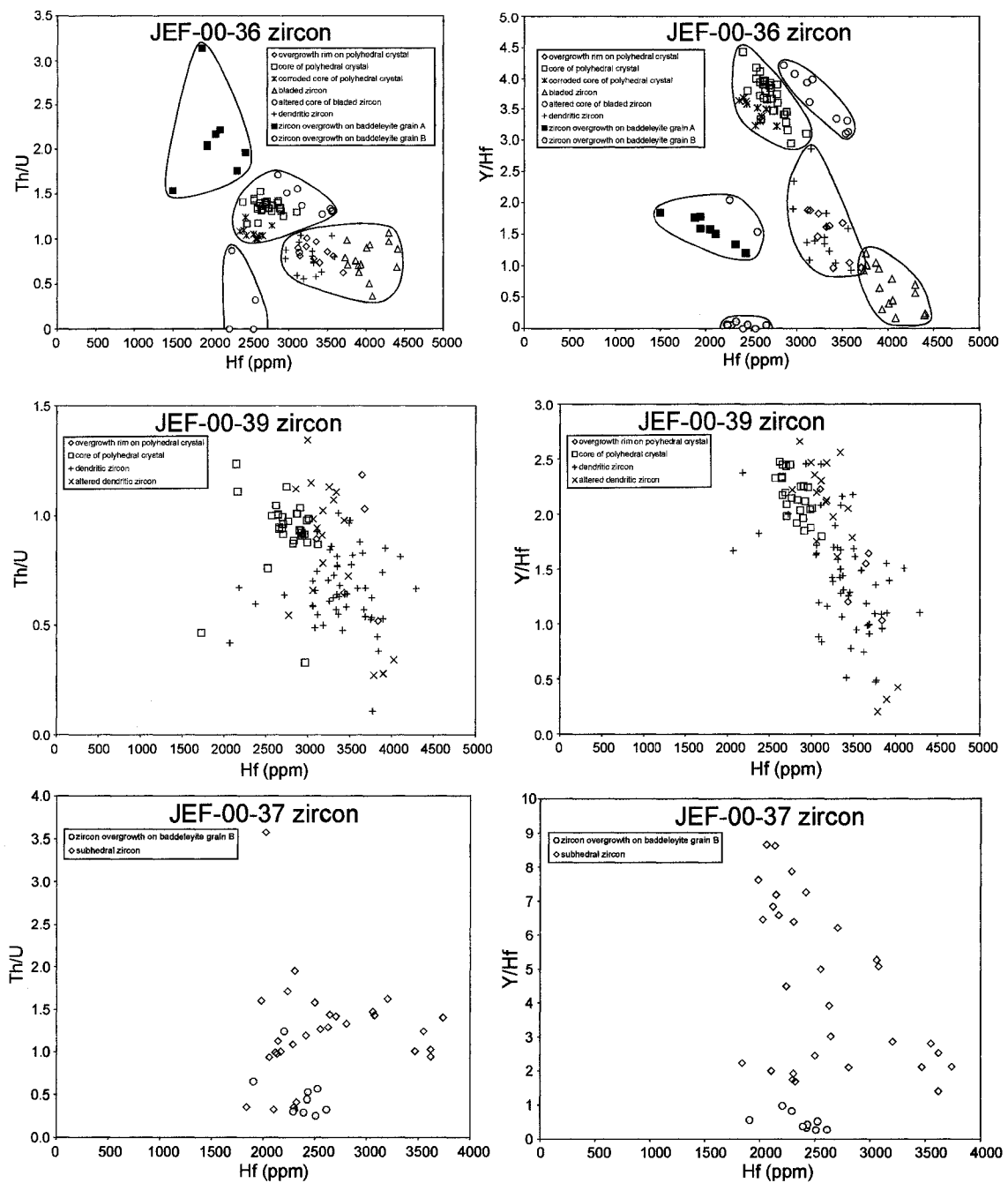


Fig. A-5. Selected plots of geochemical data for zircon from BD2 mafic dykes. The data points correspond to the same analyses acquired during electron microprobe chemical U-Th-total Pb dating.

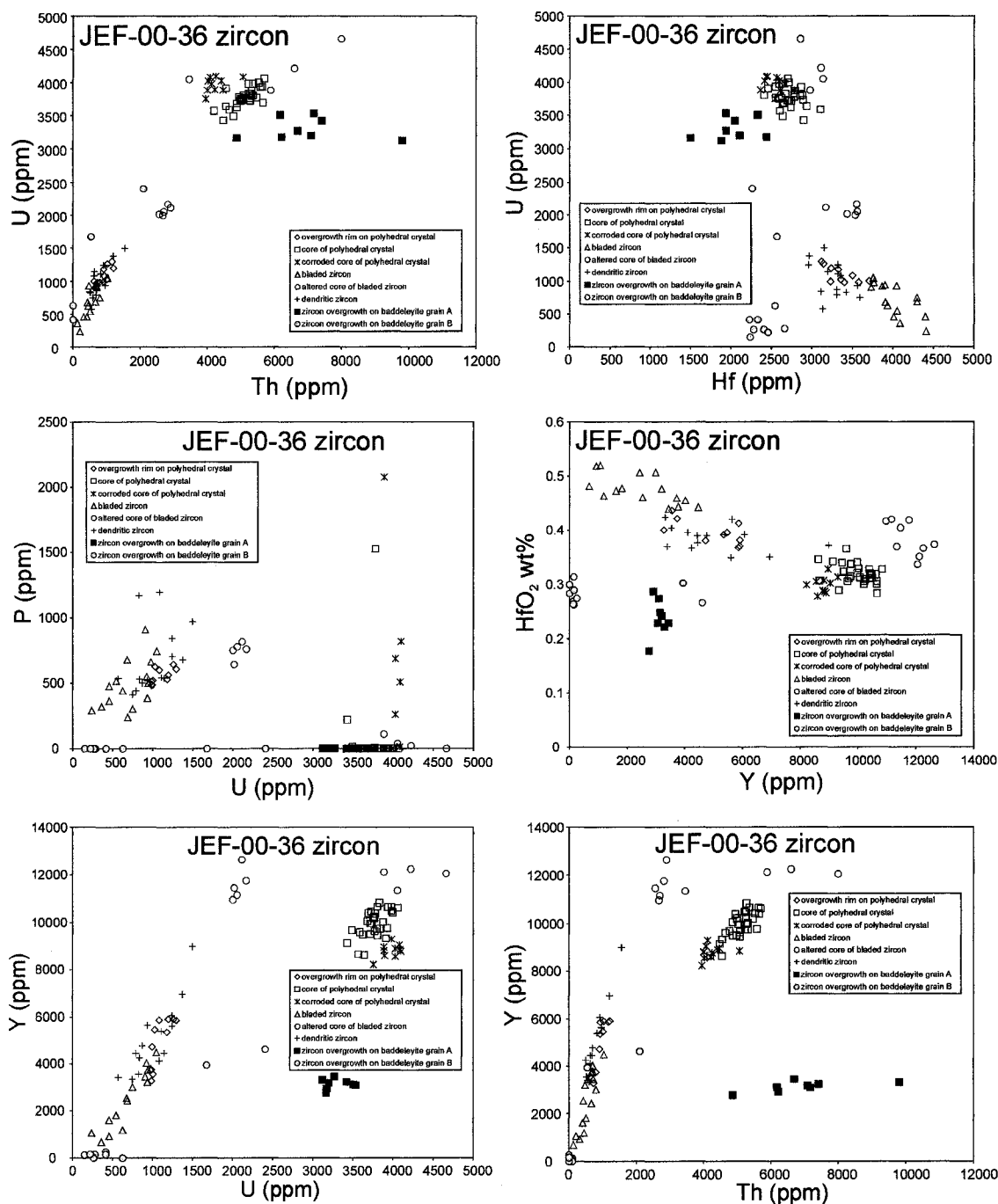


Fig. A-5 continued. Selected plots of geochemical data for zircon from BD2 mafic dykes. The data points correspond to the same analyses acquired during electron microprobe chemical U-Th-total Pb dating.

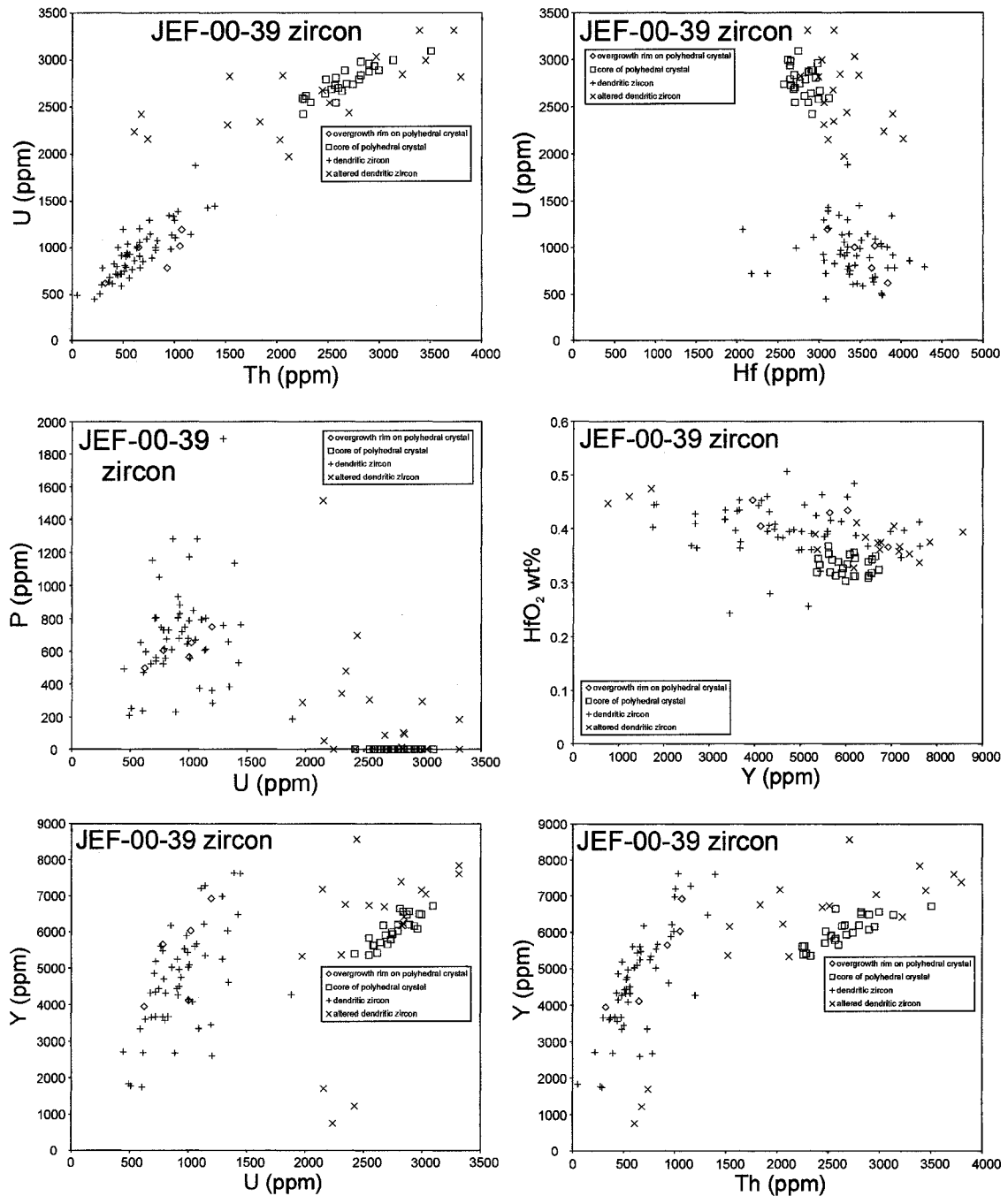


Fig. A-5 continued. Selected plots of geochemical data for zircon from BD2 mafic dykes. The data points correspond to the same analyses acquired during electron microprobe chemical U-Th-total Pb dating.

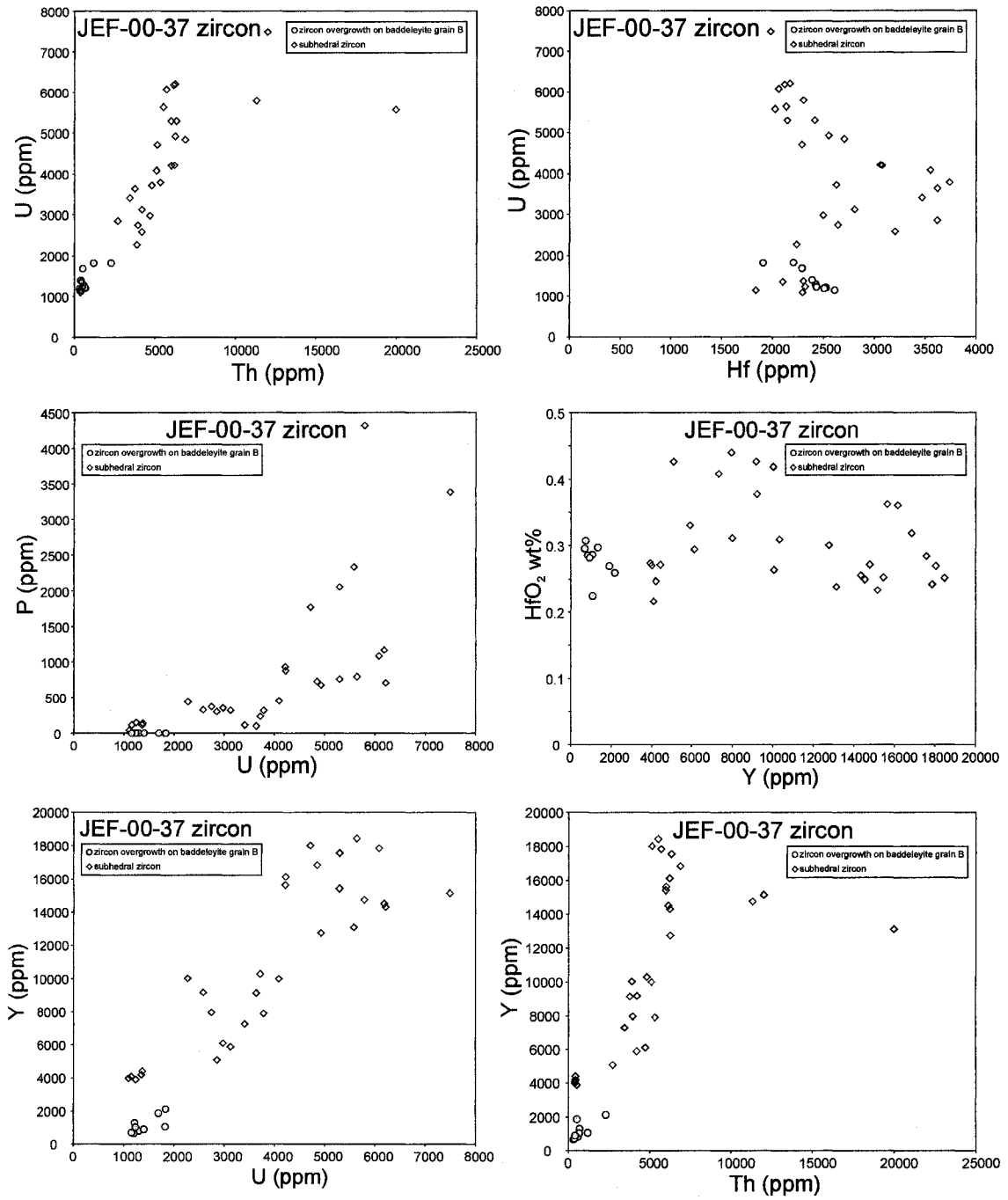


Fig. A-5 continued. Selected plots of geochemical data for zircon from BD2 mafic dykes. The data points correspond to the same analyses acquired during electron microprobe chemical U-Th-total Pb dating.

APPENDIX B

Modelling of dendritic zircon formation by deterministic volume filling fractal growth

Modelling of dendritic zircon formation by deterministic volume filling fractal growth

Dendritic silicate minerals in magmatic systems represent a form of disequilibrium crystal growth whereby the growth rate of the crystal is very large but the rate of diffusion of the species being added is very limited, and this type of crystal growth may be triggered when a system is subjected to rapid undercooling (Lofgren, 1974; Faure et al., 2003). In impure melts, dendritic crystals grow as they reject impurities, which flow away by diffusion through the melt, but the latent heat of fusion must also dissipate away from the crystal-melt interface, and during dendritic crystal growth in pure melts this process is the fundamental rate-controlling mechanism and is coupled with two other kinetic effects including molecular attachment at the crystal-melt interface and the creation of interfacial area (Langer, 1989; Glicksman and Lupulescu, 2004). Here it is shown that several structural features observed in 2-dimensional images of natural dendritic zircon, which crystallized from a mafic magma in a dyke from south India (BD2 dyke sample JEF-00-36; see Fig. A-1a in Appendix A), can be modelled by a simple mechanism of deterministic volume filling fractal growth. This simple growth mechanism for dendritic crystals is an ideal way to generate infinite surface area at the crystal-melt interface during rapid crystallization, and the modelling reveals that natural dendritic zircon crystallizing in mafic dykes displays a complexity in structure that rivals that of snowflakes precipitating out of the atmosphere (e.g.: Reiter, 2005).

Newman et al. (1997) introduced area and volume filling fractal trees with and without side branching, and outlined potential applications to a number of fields

including diffusion-limited aggregation (DLA). The concept of DLA was first developed by Witten and Sander (1981), and variations of DLA have been used to model a wide diversity of natural growth phenomena including viscous fingering (Daccord et al., 1986), dendritic drainage networks (Masek and Turcotte, 1993), bacterial colony growth (Matsuyama and Matsushita, 1996), neuronal networks (Schierwagen, 1990), and dielectric breakdown (Irurzun et al., 2002) to name a few. It has been shown that DLA clusters exhibit fractal statistics (Vicsek, 1992) and that variations of DLA can be used to model the growth (in two-dimensions) of natural mineral dendrites (Fowler et al., 1989; Chopard et al., 1991; Schoeny and Saunders, 1993).

Dendritic zircon showing complex ordered structure was discovered in a BD2 mafic dyke (JEF-00-36: see Chapter 3 and Appendix A for more details about this sample) from south India (Fig. B-1). As a model for the three-dimensional growth of this zircon, a theoretical dendritic crystal is developed in this study by deterministic volume filling fractal growth without side branches (Newman et al., 1997), but with two additional constraints: 1) that the tree is forced to fill out a tetragonal prism, and 2) that branches perpendicular to the long axis of the structure extend at angles of 45° to the prism faces.

Zircon is a tetragonal mineral which commonly displays a prismatic habit (Finch and Hanchar, 2003), and in igneous rocks exhibits an incredibly wide diversity of morphological types, which may to some degree be classified according to melt parameters (e.g. temperature) and composition (Pupin, 1980). The simplest type of zircon morphology exhibits the $\{010\}$ prismatic and $\{011\}$ pyramidal crystal forms, and corresponds suitably to zircon crystallizing from high temperature tholeiitic magma

(Corfu et al., 2003), and so this was chosen as the prototype for modelling. As a reflection of the underlying tetragonal nature of zircon and the tendency for it to grow preferentially fast along the c-axis in hypabyssal rocks (Corfu et al., 2003), growth modelling of the zircon branches was carried out with the assumption that tip propagation occurs fastest parallel to the c-axis, and at equal rates in two mutually perpendicular directions that are at 45° to the prism faces and 90° to the c-axis. Length-to-width ratios of zircon most commonly range from 1 to 5 and are thought to reflect crystallization velocity, and in rapidly crystallizing rocks such as high level granites and gabbros (e.g. mafic dykes) this ratio tends to be much higher resulting in very elongate needle-like zircon crystals (Corfu et al., 2003). Because polyhedral zircons in mafic dykes are typically quite elongate, we have excluded volume filling of the pyramidal terminations as they comprise only a small portion of the crystal, but also because they are not actually expected to take shape during dendritic crystal growth. For clarity in the construction we have chosen a 2:1 tetragonal prism, but note that this type of modelling is directly applicable to any aspect ratio and to other crystal systems. Because dendritic zircon appears to be nucleating on earlier formed polyhedral zircon in the mafic dyke sample chosen (Fig. B-1c), we have anchored the model fractal tree to the corner of intersection of two prism faces of a hypothetical previously existing polyhedral crystal of arbitrary size (Fig. B-2a), such that the dendrite is crystallographically aligned with the polyhedral crystal.

During the first growth stage (Iteration A in Fig. B-2), a solitary branch (labelled 1, representing a first-order branch of the fractal set that is perpendicular to the c-axis) extends out from the seed crystal to the center of the tetragonal prism being filled where

it forms a node that undergoes a tip-splitting event. This coincides with the formation of two additional branches (labelled 2, representing first-order branches of the fractal set that is parallel to the c-axis), which extend outward from the node along the c-axis of the crystal to the center points of two half-volumes and form the sites of two additional tip nodes. From each of these tip nodes, four additional branches (labelled 3, representing second-order branches of the fractal set that is perpendicular to the c-axis) extend outwards in directions that are perpendicular to the c-axis and that head towards the four lines of intersection of the prism faces and terminate at each of the mid points of a subset of eight equal divisions of the volume being filled. This composite branching structure (Fig. B-2a) is chosen as iteration A of the deterministic volume filling fractal tree being modelled because the directions for continued growth have been fully specified (deterministic). With each subsequent iteration (B through D), the order of each fractal set increases by one. When considering all branches as a part of a single fractal set, the structure does not fulfill Horton's Laws that the bifurcation (R_b) and length-order (R_r) ratios of the tree remain constant (Newman et al., 1997), where:

$$R_b = N_i / (N_{i+1}) \quad \text{(Equation 1)}$$

$$R_r = (r_{i+1}) / r_i \quad \text{(Equation 2)}$$

and where N_i is equal to the total number of branches of a given order, and r_i is equal to the average branch length in a given order. This complicates calculation of the fractal dimension (D) of this tree by the method of Newman et al (1997), where:

$$D = \ln(R_b) / \ln(R_r) \quad \text{(Equation 3)}$$

This problem is the reason for considering the two subsets of branches as individual fractal sets (either branches parallel to, or perpendicular to the c-axis), and appropriately

mapping each new generation of linear objects to their respective coordinates as outlined in the construction (Fig. B-2a). By solving the more general equation (Turcotte, 1997) for the fractal dimension (D) in the present case:

$$D = \ln(N_{i+1}/N_i)/\ln(r_i/r_{i+1}) \quad (\text{Equation 4})$$

where for a given order, N_i is the number of objects, and r_i is the characteristic linear dimension, we find that D is equal to 3 for both subsets. In other words either fractal set when considered in isolation, is enough to fill out the entire volume of the tetragonal prism without overlap. But both subsets are required in the construction because if the structure is a part of a single zircon crystal oriented in a particular way, all branches must be connected in three dimensions, and so in this growth model both fractal sets co-emerge in a synergistic way. Taken to infinite order, it can be shown that the tree in Fig. B-2 will become completely volume filling without overlap, and in the interest of zircon dendrite formation, will generate infinite surface area at the crystal-melt interface.

In order to compare the model fractal tree to the natural zircon array observed in thin section, a series of cross sections was constructed through Iteration D of the model (Figs. B-3 and B-4a). Because the c -axis of the zircon array exposed in thin section (Fig. B-1) appears to be oriented at a high angle to the surface of the thin section, resulting in cross shapes (Fig. B-1b) analogous to a grain documented by Krogh et al (1982), we have oriented the model cross sections perpendicular to the c -axis of the model zircon tree. A sequence of four parallel cross sections passing through the model spaced at slightly different positions along the tree demonstrates that the apparent density of branches in a cross section changes drastically depending on where the cross section passes through the tree. The blue cross section passes through only a single

branch of the tree, while moving slightly further along, the green, orange and red cross sections pass through large but varying numbers of branches. The blue and orange cross-sections pass only through branches that are perpendicular to the c-axis (only one fractal set), while the green and red cross sections pass through both fractal sets, including varying numbers of branches parallel and perpendicular to the c-axis. That only one branch is intersected by the blue cross section demonstrates the presence of significant gaps in the structure, and there are many such gaps along the structure where very few branches occur in c-axis perpendicular cross sections. It is clear from these four cross-sections that there are myriad possible model cross-sections that could be produced from the tree in Fig. B-3, and generating cross-sections at slightly oblique angles to the c-axis (which would produce more complex patterns allowing for more realistic comparisons) is beyond the scope of this appendix.

Comparison of the model deterministic volume filling fractal tree to natural dendritic zircon, was done by isolating a negative (Fig. B-4b) of a back-scattered electron image (BSE) of the main body of the large zircon array in Fig. B-1a, and then scaling the red cross-section from Figs. B-3 and B-4a to the approximate size and best visual fit to the BSE image. The model cross-section was fitted to the BSE image of zircon visually by: i) orienting it so that model zircon cross orientations matched the natural ones; ii) by positioning the model seed crystal in the appropriate corner of the image; and iii) by sizing it to cover the entire natural zircon grid. A direct overlay of the model cross section onto the BSE image of natural zircon (Fig. B-4c), reveals many interesting similarities. Approximately the same number of diagonal rows exist in both the real zircon array and the model, and the number and density of branch intersections

is similar. In addition, the spacing between diagonal rows is similar for the model and natural zircon, and for the bottom horizontal row and central diagonal row (top right to bottom left) many branch intersections coincide closely in the comparison. Furthermore, the angles between the edges of a ~square shaped cross section of a polyhedral zircon grain in the BSE image (seed crystal in Fig. B-4b), and the rows of cross-shaped zircons (one of which the natural polyhedral grain appears to be attached to), are similar as the respective relative orientations for these features displayed by the model section. A significant difference between the model cross-section and the natural zircon array is that the overall shape of the main body of the natural array is diamond shaped as opposed to square shaped. One explanation for this is that the natural cross-section could be slightly oblique to the c-axis, passing from a region dense with branches (encompassing the diamond shaped grid in Fig. B-4b) into one of the aforementioned gaps in the structure (triangular region devoid of zircon in the top right corner of Fig. B-4b). Some of the significant discrepancies in exact positions of branch intersections in the comparison are probably due to the natural cross-section not being precisely perpendicular to the c-axis as in the model, but also because there may have been a significant amount of side-branching in the natural structure (e.g.: Fig. B-1b) that was not included in the fractal growth modelling. An additional smaller grid-like array of zircon (lower right in Fig. B-1a) also has diagonal rows that seem to be parallel to rows in the larger structure, which indicates that they are a part of the same crystallographically aligned network of branches and that the natural zircon tree has an overall more complex shape than just a simple tetragonal prism. This feature could be

explained by the occurrence of two fractal zircon trees anchored to opposite sides of a single polyhedral seed crystal from the central cluster (Fig. B-1a).

All natural, self-similar fractals are only self-similar over a limited range of scales of observation, but commonly across several orders of magnitude of length scale (Turcotte, 1997). The fractal sets comprising the model tree that is shown to approximate the structure of natural dendritic zircon in this study (Fig. B-3), are self-similar across ~ 1 order of magnitude of length scale. Although the theoretical model (Figs. B-2 and B-3) when taken to infinite order generates a structure with infinite surface area, the natural zircon tree (Fig. B-1a) can only be said to have a *very large* surface area in comparison to polyhedral zircon of similar volume. One interesting question that arises however is why does the natural dendritic zircon appear to encompass a fractal tree of a specific order? In other words why did the natural structure appear to stop deterministic volume filling fractal growth at Iteration D (Fig. B-3), as opposed to Iteration C (Fig. B-2)? There is potential for this information to represent a petrogenetic indicator of possible use (such as degree of undercooling), and this is something that needs to be explored with experimental studies of dendritic zircon formation in magmatic systems.

References

- Chopard, B., Herrmann, H.J., & Vicsek, T. (1991). Structure and growth mechanism of mineral dendrites. *Nature* **353**, 409-412.
- Corfu, F., Hanchar, J.M., Hoskin, P.W.O., & Kinny, P. (2003). Atlas of zircon textures. In: John M. Hanchar and Paul W.O. Hoskin, (eds.), *Zircon, Reviews in Mineralogy and Geochemistry* **53**, 469-500.

- Daccord, G., Nittmann, J., & Stanley, H.E. (1986). Radial viscous fingers and diffusion-limited aggregation: fractal dimension and growth sites. *Physical Review Letters* **56**, 336-339.
- Faure, F., Trolliard, G., Nicollet, C., & Montel, J-M. (2003). A developmental model of olivine morphology as a function of the cooling rate and the degree of undercooling. *Contributions to Mineralogy and Petrology* **145**, 251-263.
- Finch, R.J. & Hanchar, J.M. (2003). Structure and Chemistry of Zircon-Group Minerals. In: *John M. Hanchar and Paul W.O. Hoskin, (eds.), Zircon, Reviews in Mineralogy and Geochemistry* **53**, 1-25.
- Fowler, A.D., Stanley, H.E., & Daccord, G. (1989). Disequilibrium silicate mineral textures: fractal and non-fractal features. *Nature* **341**, 134-138.
- Glicksman, M.E. & Lupulescu, A.O. (2004). Dendritic crystal growth in pure materials. *Journal of Crystal Growth* **264**, 541-549.
- Irurzun, I.M., Bergero, P., Mola, V., Cordero, M.C., Vicente, J.L., & Mola, E.E. (2002). Dielectric breakdown in solids modelled by DBM and DLA. *Chaos, Solitons and Fractals* **13**, 1333-1343.
- Krogh, T.E, McNutt, R.H, & Davis, G.L. (1982). Two high precision U-Pb zircon ages for the Sudbury Nickel Irruptive. *Canadian Journal of Earth Sciences* **19**, 723-728.
- Langer, J.S. (1989). Dendrites, viscous fingers, and the theory of pattern formation. *Science* **243**, 1150-1156.
- Lofgren, G. (1974). An experimental study of plagioclase crystal morphology: isothermal crystallization. *American Journal of Science* **274**, 243-273.
- Masek, J.G. & Turcotte, D.L. (1993). A diffusion-limited aggregation model for the evolution of drainage networks. *Earth and Planetary Science Letters* **119**, 379-386.
- Matsuyama, M. & Matsushita, M. (1996). Morphogenesis by bacterial cells. In: *Fractal geometry in biological systems, an analytical approach*, 127-171.
- Newman, W.I., Turcotte, D.L., & Gabrielov, A.M. (1997). Fractal trees with side branching. *Fractals* **5**(4), 603-614.
- Pupin, J.P. (1980). Zircon and granite petrology. *Contributions to Mineralogy and Petrology* **73**, 207-220.
- Reiter, C.A. (2005). A local cellular model for snow crystal growth. *Chaos, Solitons and Fractals* **23**, 1111-1119.

Schierwagen, A.K. (1990). Scale-invariant diffusive growth: A dissipative principle relating neuronal form to function. *In: Organizational constraints on the dynamics of evolution*, 167-189.

Schoeny, P.A. & Saunders, J.A. (1993). Natural gold dendrites from hydrothermal Au-Ag deposits: characteristics and computer simulation. *Fractals* **1**, 585-593.

Turcotte, D.L. (1997). *Fractals and Chaos in Geology and Geophysics (2nd Ed.)*, Cambridge University Press, Cambridge, 398 pp.

Vicsek, T. (1992). *Fractal Growth Phenomena*, 2nd ed., World Scientific, Singapore, 488 pp.

Witten, T.A. & Sander, L.M. (1981). Diffusion-limited aggregation: a kinetic critical phenomenon. *Physical Review Letters* **47**(19), 1400-1403.

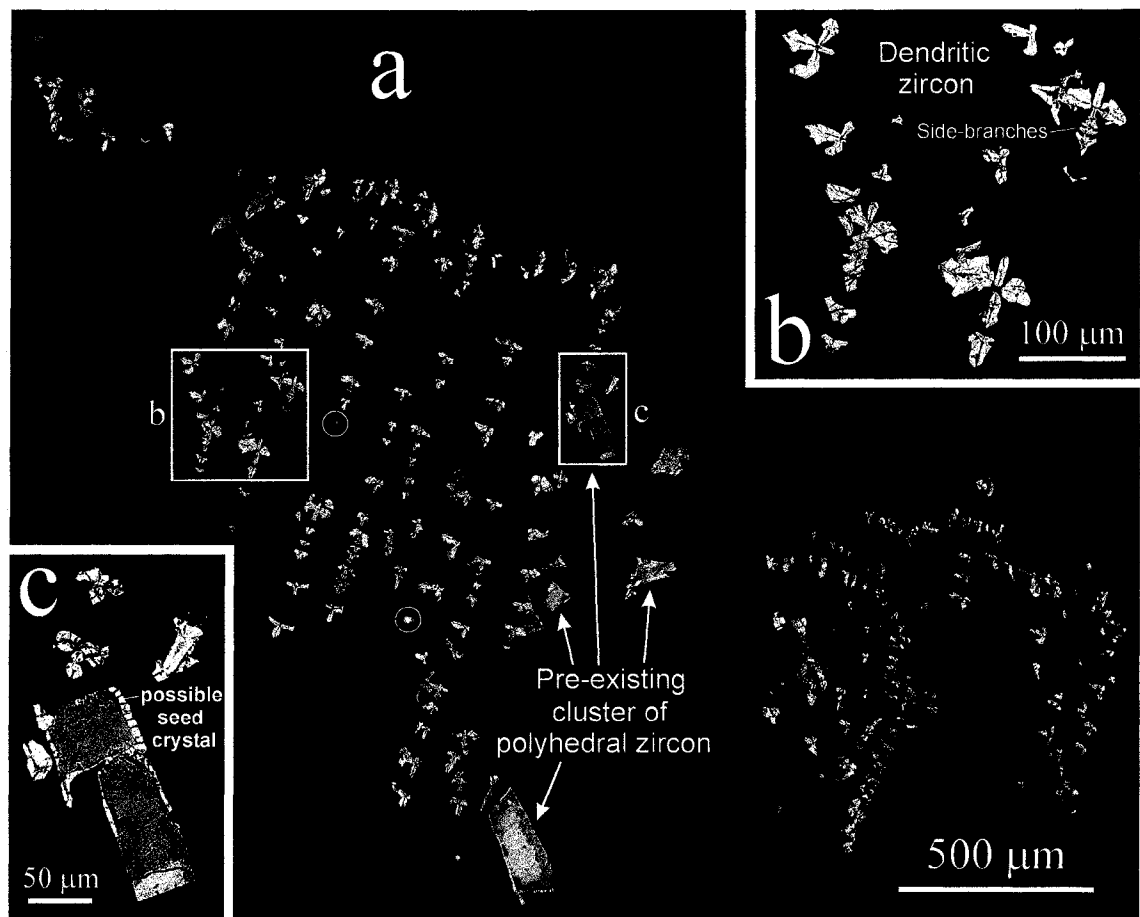


Fig. B-1. Backscattered electron images of igneous zircon (and rare thorite - circled) from a polished thin section of BD2 mafic dyke sample JEF-00-36 (see Appendix A for quantitative chemical data for this zircon). Most of the individual zircon images in this dense array are interpreted to be a part of a single dendritic crystal, and probably represent intersections of individual branches from this single zircon tree. A close-up of dendritic zircon with side-branches is shown in (b). The dendritic zircon appears to have nucleated onto earlier formed polyhedral zircon, and a possible seed crystal is shown in (c).

Fig. B-2. Three successive iterations of deterministic volume filling fractal growth, simulating rapid crystallization of zircon. Tree generation is anchored to a hypothetical previously existing polyhedral zircon seed crystal with which it is crystallographically aligned. The model dendritic crystal takes shape as two mutually perpendicular, co-emerging fractal sets develop (one that is parallel to the c-axis, and one that is perpendicular to the c-axis), each of which is volume-filling without overlap (has a fractal dimension of 3). The sequence of branch development is numbered in Iteration A. With each successive iteration, the order of each fractal set increases by one.

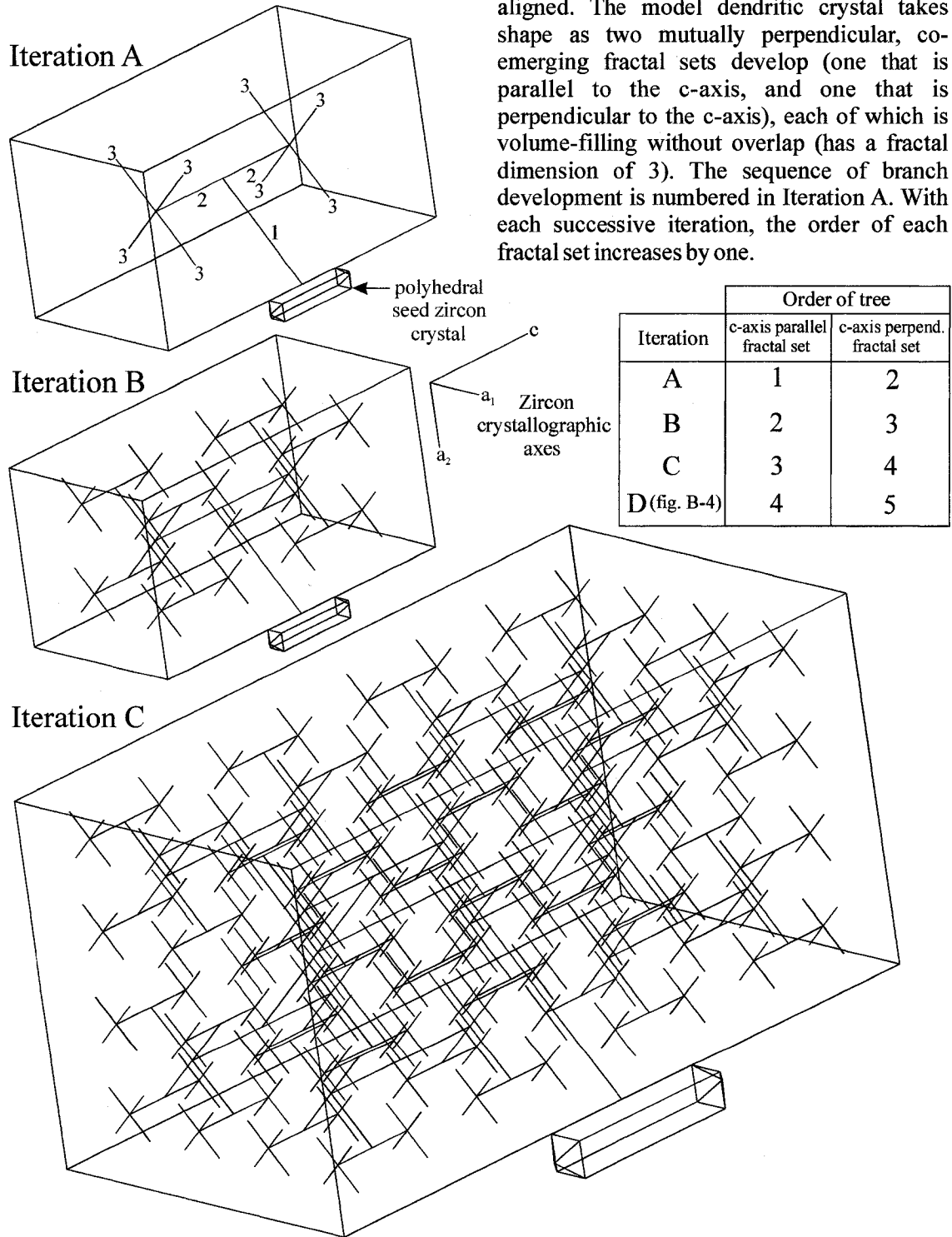
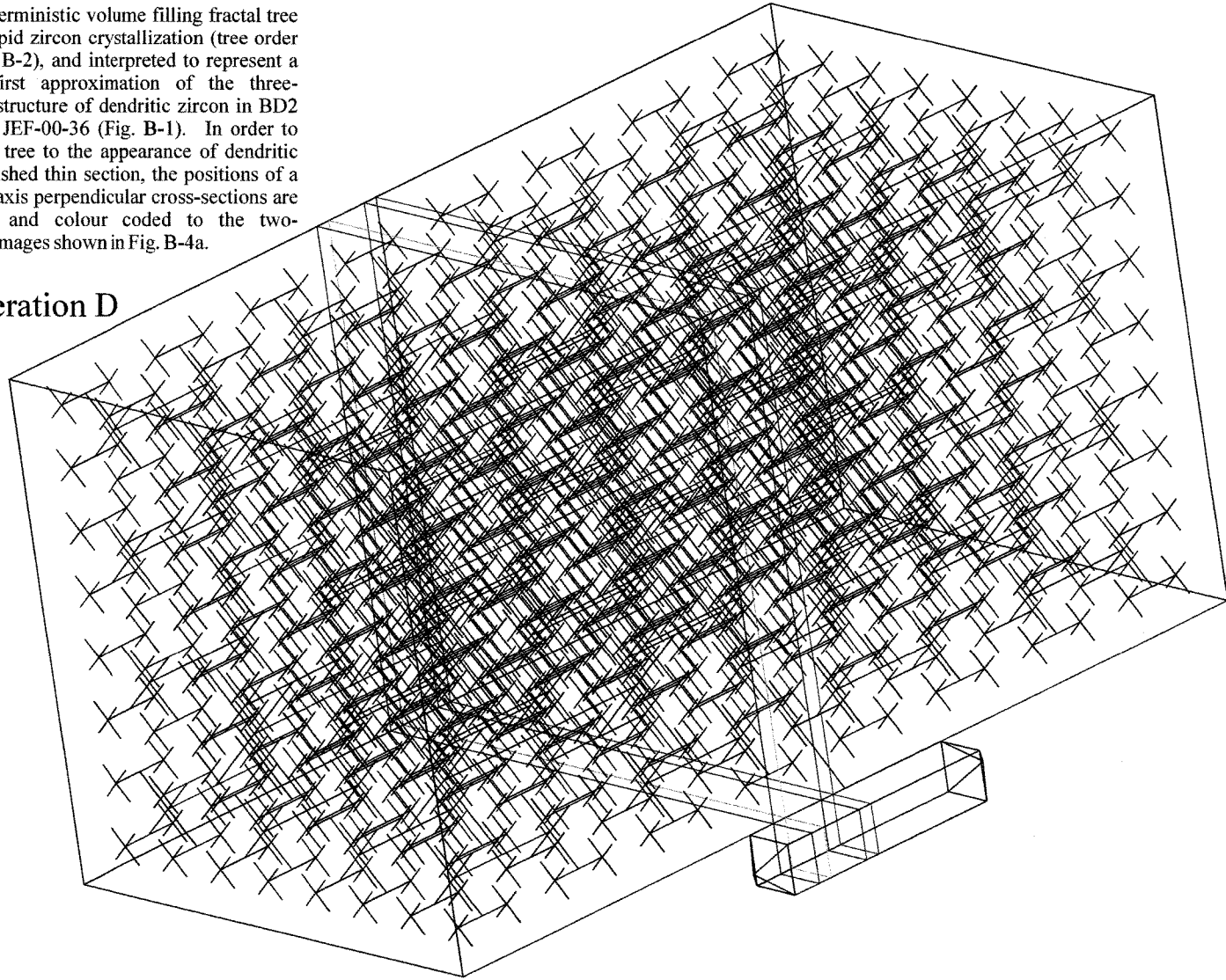


Fig. B-3. Deterministic volume filling fractal tree simulating rapid zircon crystallization (tree order listed in Fig. B-2), and interpreted to represent a reasonable first approximation of the three-dimensional structure of dendritic zircon in BD2 dyke sample JEF-00-36 (Fig. B-1). In order to compare this tree to the appearance of dendritic zircon in polished thin section, the positions of a number of c-axis perpendicular cross-sections are shown here and colour coded to the two-dimensional images shown in Fig. B-4a.

Iteration D



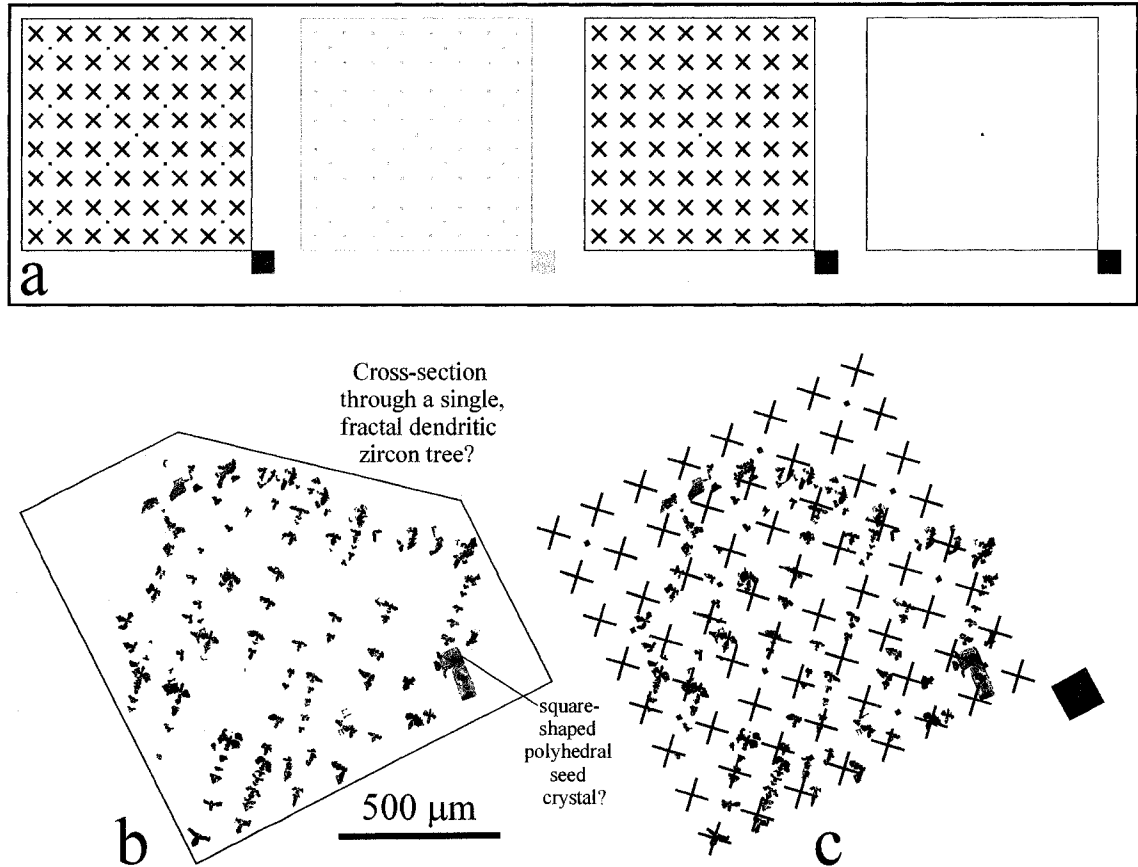


Fig. B-4. a) Four cross-sections through the model zircon tree shown in Fig. B-3 (colours of the cross-sections are coded to those in Fig. B-3). All model cross-sections are oriented perpendicular to the c-axis of zircon for direct comparison to the zircon in thin section. This orientation was chosen because skeletal zircons take on a cross shape in sections perpendicular to the c-axis (Krogh, 1982), and this appears to be the case for the thin section to which the model is being compared (see Fig. B-1b). b) Negative BSE image of a large portion of a grid-like array of zircons from a polished thin section of BD2 dyke sample JEF-00-36 (from Fig. B-1a). c) Overlay of a model cross-section through the tree shown in Fig. B-3 onto the negative BSE image from b).

APPENDIX C

Electron microprobe chemical U-Th-total Pb dating of baddeleyite (ZrO_2) and zircon (ZrSiO_4) from mafic dyke swarms of the south Indian shield

Summary

It was shown in Chapter 2 (French et al., 2002) that electron microprobe (EM) chemical U-Th-total Pb dating of the mineral baddeleyite (ZrO_2) is a useful tool for rapidly and cost-effectively determining first-order reconnaissance age information in geochronological studies of Precambrian mafic dyke swarms. Since that study, this technique has been used in this thesis to determine reconnaissance age information from a large number of mafic dyke samples collected from the Dharwar and Bastar cratons of the south Indian shield. This appendix presents the results of EM baddeleyite (and zircon in two cases) dating of nine mafic dykes and one mafic sill from the Dharwar craton (sample locations in Fig. C-1), in addition to five mafic dykes from the BD2 dyke swarm of the Bastar craton (see Fig. 3-4 in Chapter 3 for BD2 sample locations). A detailed interpretation of the data is presented here for six samples of the 1.9 Ga, Southern Bastar-Cuddapah large igneous province (identified in Chapter 3). Although EM chemical age data for nine mafic dykes from the Dharwar craton is included here, detailed interpretations of the data are beyond the scope of this appendix. For several samples dated by EM baddeleyite or zircon in this study (JEF-99-1; JEF-99-9; JEF-00-1; JEF-00-30; JEF-00-36; JEF-00-43; JEF-00-55), U-Pb IDTIMS ages have also been determined on baddeleyite±zircon from the same sample (Chapters 3 and 4), allowing for an evaluation of the accuracy of the EM ages presented in some cases. Overall, the EM baddeleyite ages correlate well with the IDTIMS ages determined for the same samples and support the main conclusions of French et al. (2002). For the five EM baddeleyite age determinations presented for the BD2 mafic dyke swarm, a detailed evaluation of the possibility that excess Nb in baddeleyite may generate anomalously

young chemical ages is also presented. The interpretation of the wide range EM zircon apparent ages (Fig. C-5) determined from zircon in a polished thin section of JEF-00-1 (Dandeli dyke dated at 2176 Ma, Chapter 4) is analogous to that outlined for zircon from the BD2 dykes (Appendix A). One simple but important conclusion which may be drawn from the chemical ages presented in this appendix is that based on the dyke samples studied (excluding the Pulivendla sill), dyke swarm emplacement generally appears to have occurred earlier in the Dharwar craton (2.4-2.0 Ga) than in the Bastar craton (2.0-1.8 Ga).

Analytical set-up during EM baddeleyite dating

The instrument employed was a JEOL 8900 Electron Microprobe housed in the Department of Earth and Atmospheric Sciences (University of Alberta), equipped with five wavelength dispersive spectrometers (WDS). Analysis of all minerals was conducted at 20kV accelerating voltage, 150nA beam current, and a 1 μ m beam diameter.

For quantitative analysis of baddeleyite, the instrumental set-up followed closely that outlined in Chapter 2 (French et al., 2002). As detailed in that paper, baddeleyite crystals with high Nb content commonly return spuriously young ages because of an overlap between the Nb L β 4 peak position and the Pb M α background positions. As a consequence, baddeleyite analyses with >0.5wt.% Nb₂O₅ were removed from consideration in the final age calculations for the BD2 mafic dyke swarm as indicated. For all of the Dharwar samples this was not generally a problem because all baddeleyite samples contained <0.5wt.% Nb₂O₅ (except for JEF-00-55 baddeleyite and JEF-00-43 zircon which had moderate Nb₂O₅ concentrations of 0.5-1.0wt.%, and this might also

explain the anomalously young chemical isochron age reported for JEF-00-55, Fig. C-4d). Analytical conditions for JEF-00-43 and JEF-00-1 zircon analyses were similar to those for baddeleyite, but in addition, the zircon analyses were corrected for the overlap of $Y\ L\gamma$ on $Pb\ M\alpha$ (Suzuki and Adachi, 1991), and for JEF-00-1 zircon (Fig. C-5), Ca content was used as a crude monitor of fluid induced discordance (Geisler and Schleicher, 2000). Data reduction and age calculations were carried out following the method outlined in Chapter 2, and one of two baddeleyite samples with known U-Pb IDTIMS ages including JEF-00-36 and JEF-99-1 were used as age standards during all EM chemical dating studies in this thesis (see summaries of age standard results in Figs. C-2a and C-4a).

EM baddeleyite dating: Southern Bastar-Cuddapah Large Igneous Province (LIP)

The results of EM chemical dating of baddeleyite from polished thin sections of five mafic dykes from the BD2 dyke swarm and one mafic sill from the Cuddapah basin (see Chapter 3 for discussion of this LIP) are presented in UO_2^* versus PbO diagrams in Fig. C-2, where UO_2^* is the sum of the measured UO_2 concentration plus the amount of fictive ThO_2 needed to account for the amount of radiogenic Pb produced by Th decay in baddeleyite. For each thin section, baddeleyite age data were collected during one of two analytical sessions, but in one case (sample JEF-00-37) the dataset was collected during both sessions to evaluate the reproducibility of the results. As a further test of the analytical reproducibility, and to allow for a more direct comparison of the EM chemical dating results to the U-Pb isotopic results for sample JEF-00-36, mechanically separated baddeleyite blades picked from the same populations analysed by IDTIMS were incorporated into a polished epoxy resin grain mount, and analysed over three additional

analytical sessions (Fig. C-2a). For all regressions, the data sets originate from analysis of multiple baddeleyite grains (ranging from two to nineteen) from the same thin section or grain mount. Data reduction and age calculation was carried out following the method of French et al. (2002), and the data for any given sample was regressed separately for each analytical session.

A regression of 28 analyses obtained from two baddeleyite grains in a thin section from sample JEF-00-36 yields a well-defined chemical isochron age of 1856^{+77}_{-79} Ma with a MSWD of 1.0 (Fig. C-2a), and the spatial context of the analyses is shown in Figs. A-4a and A-4b of Appendix A. This isochron age overlaps within analytical uncertainty the baddeleyite crystallization age of 1883.0 ± 1.4 Ma obtained by IDTIMS (Chapter 3, Fig. 3-7a), and reinforces the reliability of the other chemical baddeleyite ages obtained for BD2 dykes in this study. EM data for a suite of 19 grains from the polished grain mount of JEF-00-36 baddeleyite, yields a similar chemical isochron age for each analytical session of 1903^{+62}_{-63} Ma (session 1), 2018^{+77}_{-79} Ma (session 2), and 1999^{+96}_{-99} Ma (session 3), all of which overlap within analytical uncertainty (Fig. C-2a). The regression of data from the first analytical session of the grain mount yields a chemical isochron age that overlaps within error the baddeleyite crystallization age of 1883.0 ± 1.4 Ma obtained by IDTIMS, but for the other two sessions (sessions 2 and 3), the ages are slightly too old. A weighted mean of all isochron ages for JEF-00-36 baddeleyite yields a composite age of 1933 ± 120 Ma with a relatively high MSWD of 3.8, which is interpreted as the best objective estimate for the age of emplacement of this dyke by EM baddeleyite dating. This is a further indication that the accuracy of the technique is relatively low (~ 140 m.y.), and as noted by French

et al. (2002) this relates to the low (<500 ppm) concentrations of radiogenic Pb in baddeleyite typically found in Precambrian mafic dykes, and the possibility that very minor X-ray line interferences from other contaminating elements may be slightly compromising the accuracy of some of the results.

Chemical U-Th-total Pb isochron plots obtained for baddeleyite from a thin section of sample JEF-00-37 are shown in Fig. C-2b and regressions of the datasets acquired during two separate analytical sessions yield similar ages of 1911^{+85}_{-87} Ma (MSWD=0.52) and 1937^{+149}_{-156} Ma (MSWD=1.8). The composite weighted mean age of 1916 ± 73 Ma for the two sessions is interpreted to represent a reasonable first-order estimate for the emplacement age of the dyke. A relatively modest number of WDS spot analyses (10 to 13) were acquired from baddeleyite in polished thin sections of samples JEF-00-34 and JEF-00-18, and the apparent radiogenic Pb content for the grains was significantly low (typically <250ppm). Nevertheless, relatively low precision chemical isochron ages of 1831^{+116}_{-120} Ma (MSWD=4.5) and 1932^{+153}_{-161} Ma (MSWD=0.93), for samples JEF-00-34 (Fig. C-2c) and JEF-00-18 (Fig. C-2d), respectively, are in good agreement with the chemical and isotopic ages reported for other BD2 dykes in this study and provide compelling independent evidence that these two dykes were also emplaced in the late Paleoproterozoic. An isochron plot for baddeleyite from a polished thin section of sample JEF-00-30 (Fig. C-2e) shows a significant amount of scatter relative to the datasets for the other samples, and yields a relatively low precision age of 1685^{+155}_{-163} Ma and a high MSWD of 6.7. The anomalously young chemical isochron age and associated high MSWD for JEF-00-30 baddeleyite might be related to the presence of localized regions of baddeleyite that were

partially affected by recent Pb-loss because some of the U-Pb analyses for baddeleyite separates (Chapter 3, Fig. 3-7c) yielded slightly discordant results, despite the absence of visible incipient zircon. Alternatively, the young ages and significant scatter of the data for this sample might be attributable to possible unexplored complexities pertaining to accurate measurements of the peak and background of the Pb $M\alpha$ X-ray line for chemically impure baddeleyite. It is possible, under the operating conditions used in this study, that X-ray lines from other contaminating trace elements including Hf ($L\lambda$) and especially Nb ($L\beta_4$) might be contributing in tandem to variability of the background intensity at locations typically chosen for the upper Pb $M\alpha$ background position (near 171.138 mm, in the present case). On UO_2^* versus PbO diagrams, baddeleyite data from samples JEF-00-30 and JEF-00-34 showed the most scatter and the regressions yielded correspondingly high values for the MSWD (4.5 to 6.7), and both of these baddeleyite populations were significantly more chemically impure than baddeleyite from all other BD2 dykes. For example, baddeleyite from BD2 dykes JEF-00-18, JEF-00-36, and JEF-00-37 all had Nb_2O_5 concentrations that were quite low (0.0-0.4 wt%), but for samples JEF-00-30 and JEF-00-34, Nb_2O_5 ranged from 0.5-1.6 wt% and 0.1-0.9 wt%, respectively, and these two samples yield distinct negative correlations on plots of Nb_2O_5 versus apparent age t (Fig. C-3a). Moreover, a plot of the Nb_2O_5 concentration in baddeleyite versus the background intensity measured at 171.138 mm (near the Pb $M\alpha$ peak) shows a strong positive correlation (Fig. C-3b), which further supports the idea that the Nb $L\beta_4$ X-ray line centered at 171.2 mm, is contributing to a significant underestimation of the Pb $M\alpha$ peak intensity for these two samples, resulting in anomalously young ages. Below $Nb_2O_5 < 0.5$ wt% there is no positive correlation between Nb_2O_5

concentration and background intensity at 171.138 mm for the baddeleyite analyses, and so this was chosen as a cut-off for the age calculations. Using this constraint, a recalculated chemical isochron age for sample JEF-00-34 yields a result with an improved MSWD of 0.30, and a more precise age of $1902 \pm 52 / -53$ Ma, which is interpreted to represent the best estimate for the age of baddeleyite crystallization and dyke emplacement. The baddeleyite data for sample JEF-00-30 are completely eliminated because all data have $\text{Nb}_2\text{O}_5 > 0.5\text{wt}\%$, and the chemical isochron age of $1685 \pm 155 / -163$ Ma is therefore interpreted to be geologically meaningless. A more detailed evaluation of all possible X-ray line interferences could potentially improve upon the apparently low accuracy of EM chemical dating of baddeleyite, but the data from this study nevertheless confirms the conclusion by French et al. (2002) that the technique can still provide useful first-order reconnaissance age information for mafic dyke swarms, particularly when the technique is used in combination with conventional isotopic methods.

Chemical dating of baddeleyite from the Pulivendla sill (JEF-99-9) was conducted over two sessions, one of which included analysis of the baddeleyite grain mount of JEF-00-36, and all of the data is shown on a UO_2^* versus PbO diagram in Fig. C-2f. Two high Nb analyses (Nb_2O_5 of 0.6 wt%) were excluded from the plots. A regression of 20 analyses from one session yields a chemical isochron age of $1738 \pm 104 / -107$ Ma with an MSWD of 1.8. Most of the data from that session yielded PbO concentrations less than 0.05wt% except for a single data point which plots farther away from the origin and has $\sim 0.08\text{wt}\%$ PbO. This anomalous data point was not discarded during data reduction because it is not a 2σ outlier (French et al., 2002), but nevertheless

yields an anomalously young apparent age of 1549 Ma. Because of its high PbO content, this point more than any other controls the slope of the regression line. A second regression of that dataset which excludes this data point yields an age of $1845+101/-104$ Ma with an MSWD of 1.4. The high PbO concentration data-point is interpreted to be either an anomalous partially reset point, or an analytical artefact, and the age of $1845+101/-104$ Ma is interpreted as a better estimate for the time of baddeleyite crystallization. A modest amount of data was collected during another analytical session (Fig. C-2f) and a regression of 6 data points yields a similar, albeit low precision chemical age of $1823+209/-224$ Ma. A composite weighted mean age for the two sessions yields an age of 1838 ± 91 Ma (MSWD=0.053), which is interpreted to represent the best estimate for the crystallization age of the baddeleyite and the timing of emplacement of the Pulivendla sill.

References

- French, J.E., Heaman, L.M., Chacko, T. (2002). Feasibility of chemical U-Th-total Pb baddeleyite dating by electron microprobe. *Chemical Geology* **188**, 85-104.
- Geisler, T. & Schleicher, H. (2000). Improved U-Th-total Pb dating of zircons by electron microprobe using a simple new background modelling procedure and Ca as a chemical criterion of fluid-induced U-Th-Pb discordance in zircon. *Chemical Geology* **163**, 269-285.
- Suzuki, K. & Adachi, M. (1991). Precambrian provenance and Silurian metamorphism of the Tsubonosawa paragneiss in the South Kitakami terrane, Northeast Japan, revealed by the chemical Th-U-total Pb isochron ages of monazite, zircon, and xenotime. *Geochemical Journal* **25**, 357-376.

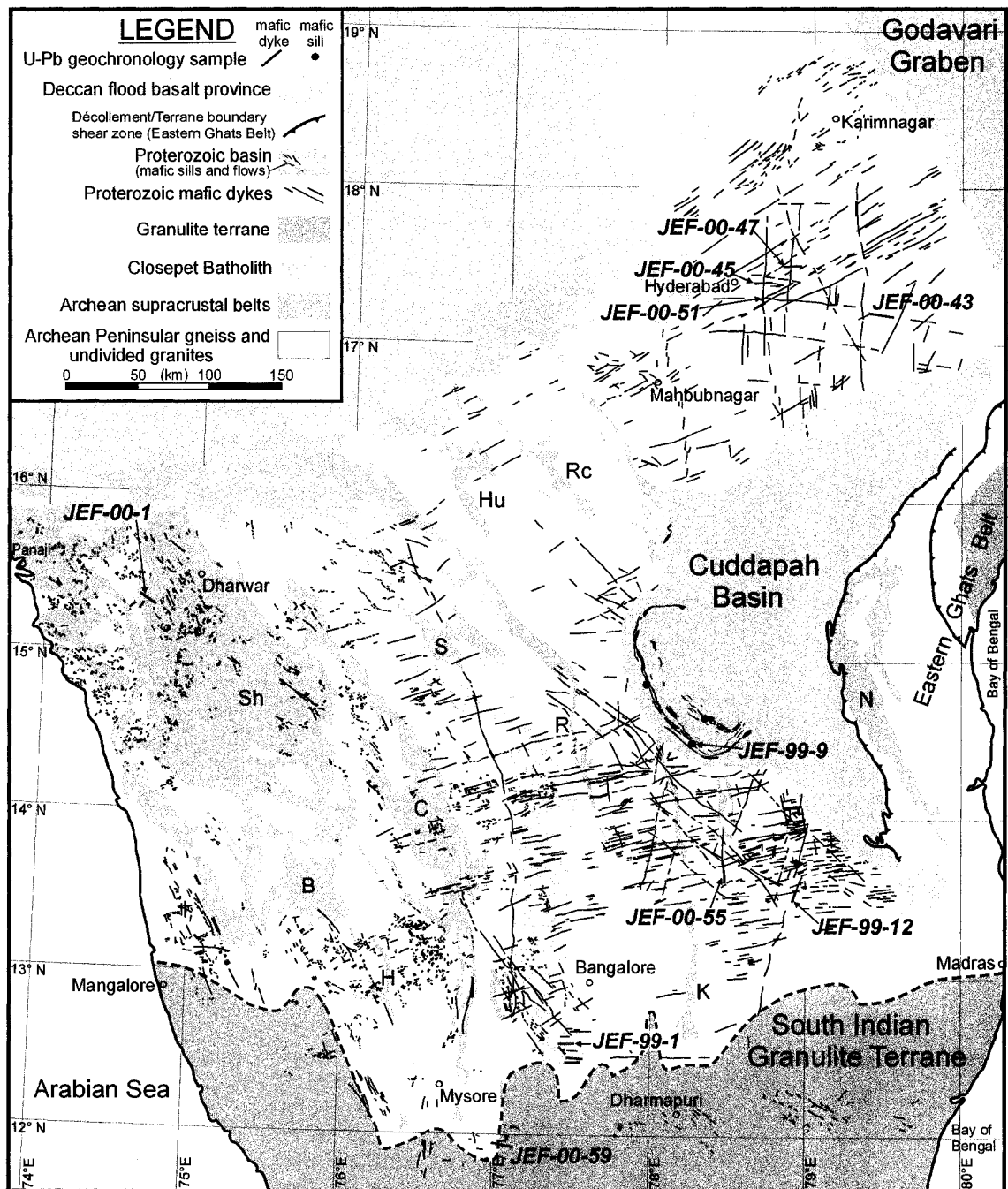


Fig. C-1. Geological map of the Dharwar craton showing the locations (labelled) of mafic dyke samples dated by electron microprobe chemical U-Th-total Pb baddeleyite and zircon analysis. Abbreviations and references for this map are outlined in Fig. 4-2.

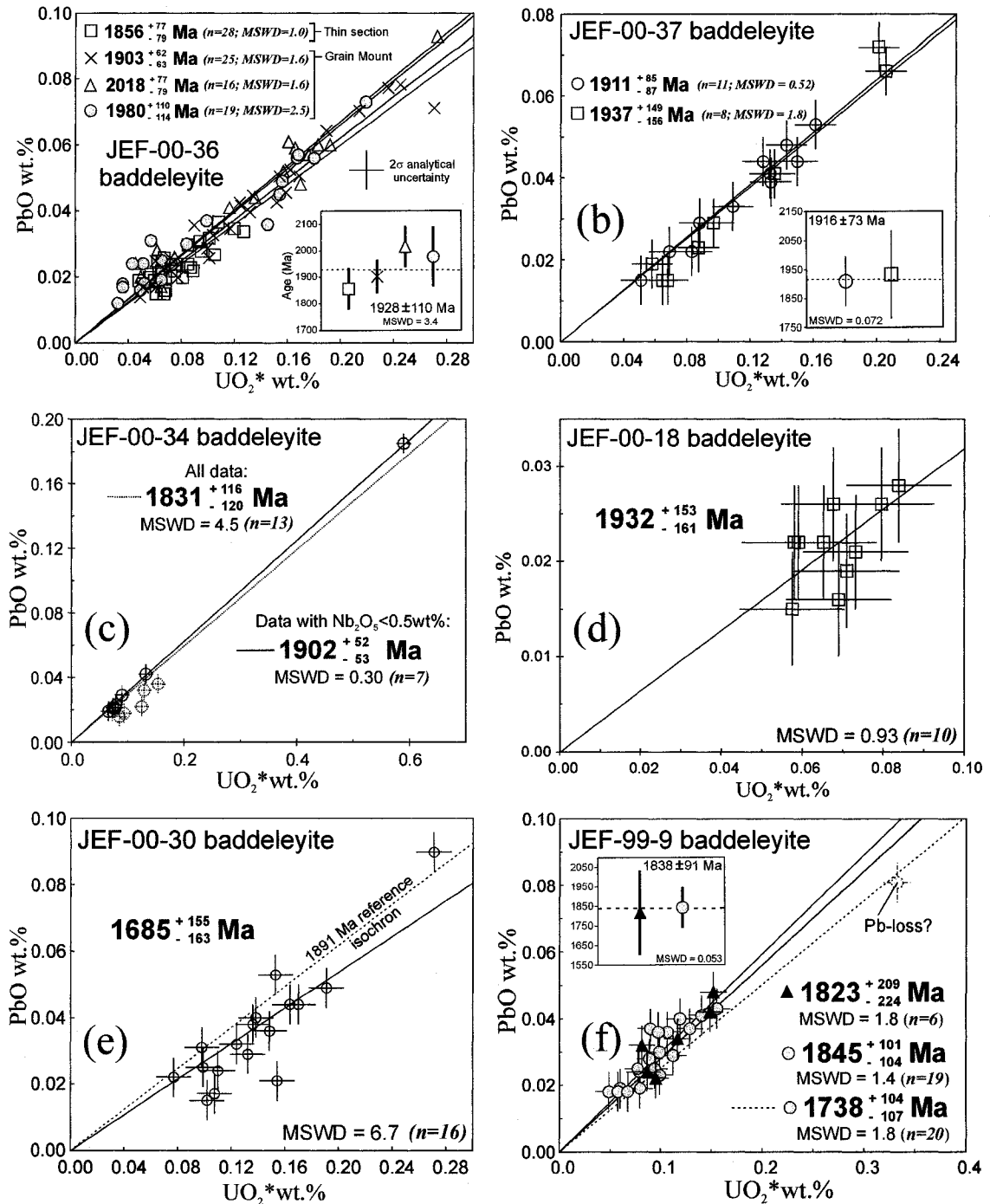


Fig. C-2. a-f) UO_2^* versus PbO diagrams, showing EM chemical data for baddeleyite from Southern Bastar - Cuddapah LIP. Error bars represent 2σ analytical uncertainty, and errors reported for the final ages represent 2σ . Except as noted in (a), all data was determined from *in situ* baddeleyite in polished thin sections. Any given style of data point label (e.g. open square, filled triangle, etc.) represents a unique analytical session, and the data for all plots is categorized collectively in this manner. All chemical isochrons are anchored to the origin with a fictive data point that has no associated error. Inset Figs., show weighted mean plots of multiple chemical isochron ages determined independently for a given dyke/sill sample.

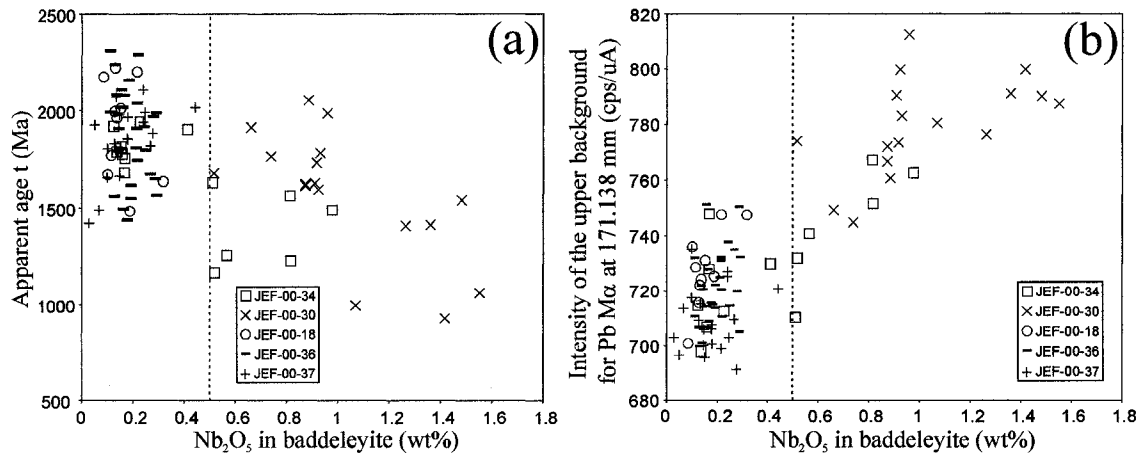


Fig. C-3. a) Plot of Nb₂O₅ content in baddeleyite versus apparent age *t*, for baddeleyite from BD2 mafic dykes. The dashed lines in a (and b) represent the cut-off line for data used in the age calculations, whereby anomalously young chemical ages determined for baddeleyite with Nb₂O₅ > 0.5wt% are discarded because the baddeleyite is deemed to be chemically impure. b) Plot of background intensity (X-ray counts per second/μA) at a spectrometer position of 171.138 mm (the upper background position chosen in this study for measuring the PbMα X-ray line) versus Nb₂O₅ content in baddeleyite. The pronounced positive correlation of background intensity at 171.138 mm and Nb₂O₅ content in baddeleyite, is consistent with elevation of the upper background for PbMα by the Nb Lβ₄ X-ray line, and provides an explanation for why chemically impure baddeleyite can yield anomalously young EM chemical U-Th-total Pb ages by over-subtraction of X-ray counts from the PbMα peak.

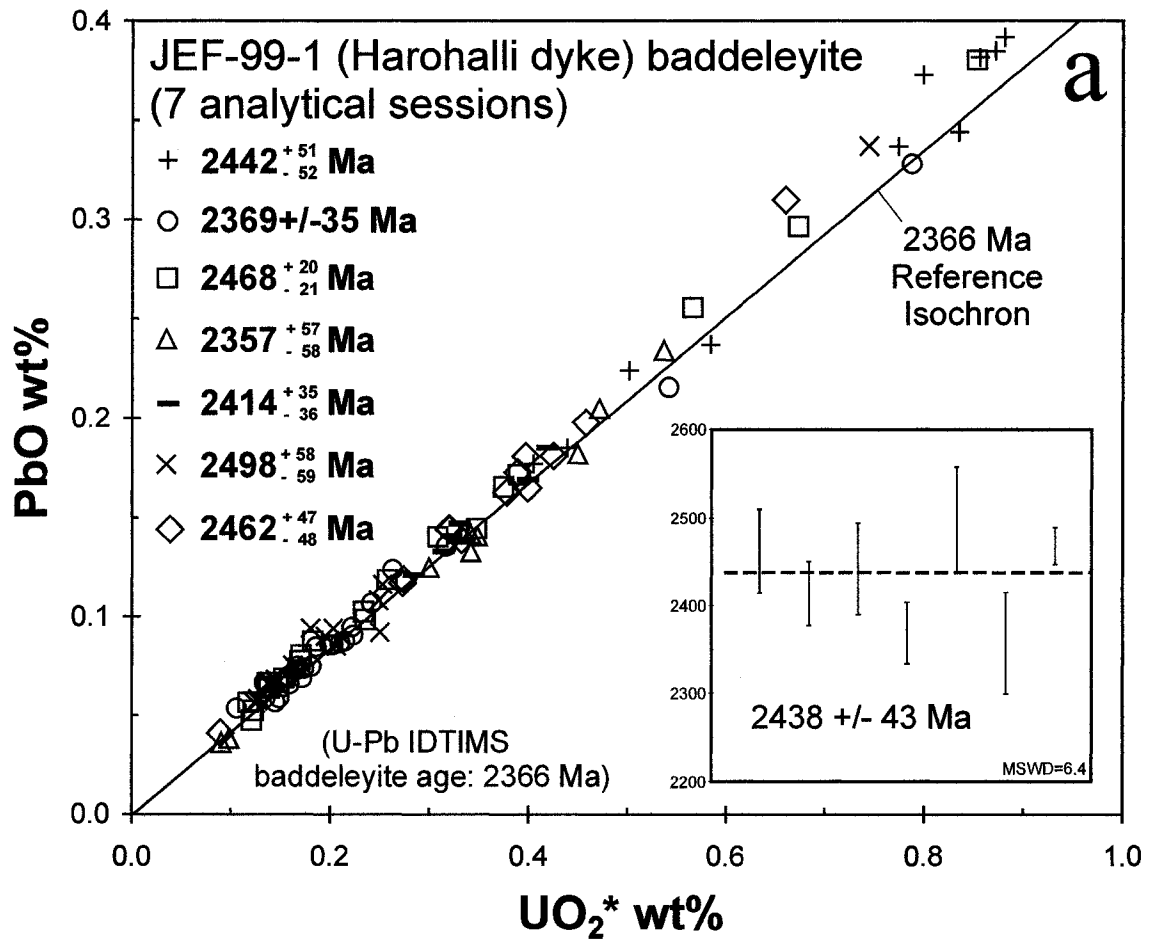
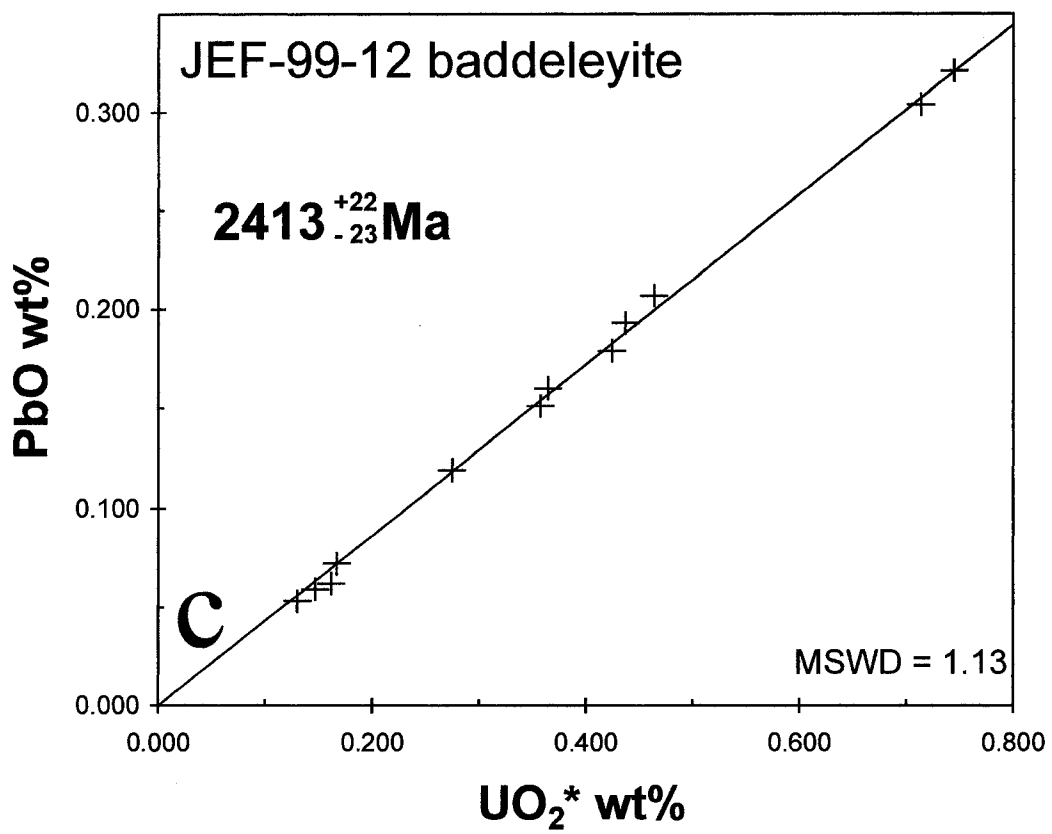
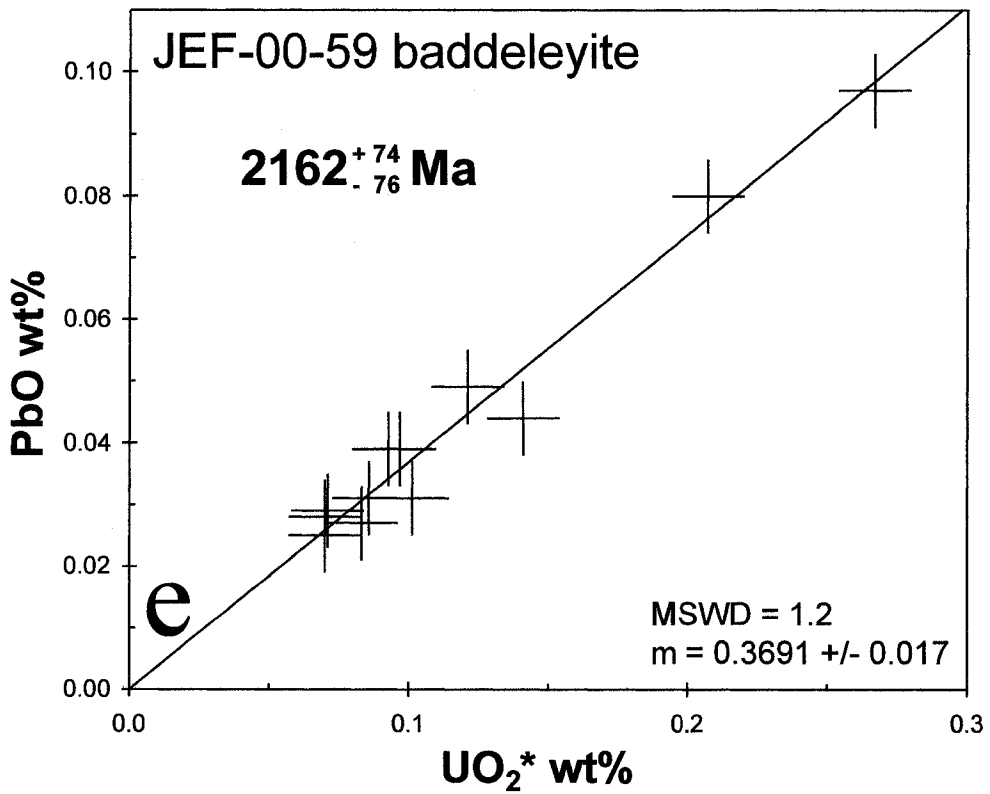
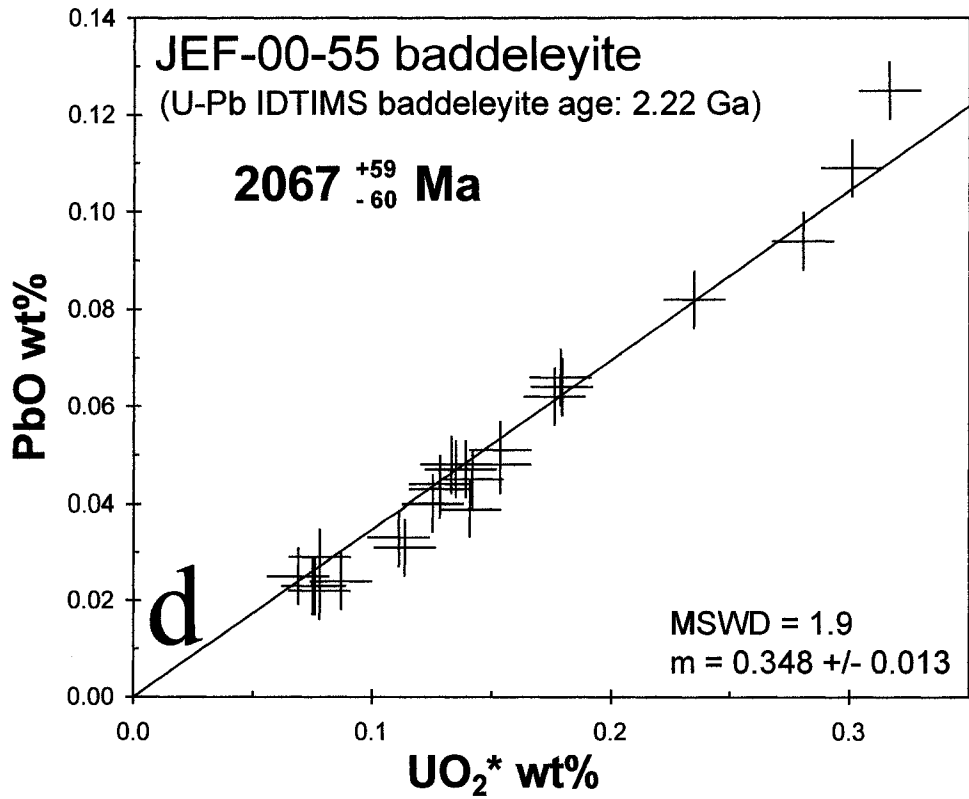


Fig. C-4. a-i). Chemical isochron diagrams for baddelyite and zircon from mafic dykes of the Dharwar craton, south India. In Fig. C-4(b-i) the data-point error bars represent 2σ analytical uncertainty, the error on all of the final ages is reported at 2σ , and the isochrons are anchored to the origin with a fictive data-point with no associated error. Inset in Fig. C-4a shows a weighted mean plot of seven chemical isochron ages determined during individual analytical sessions of JEF-99-1 baddeleyite (each plotted as a separate symbol), which was used as an age standard during EM chemical dating in this thesis.



(Fig. C-4 continued.)



(Fig. C-4 continued.)

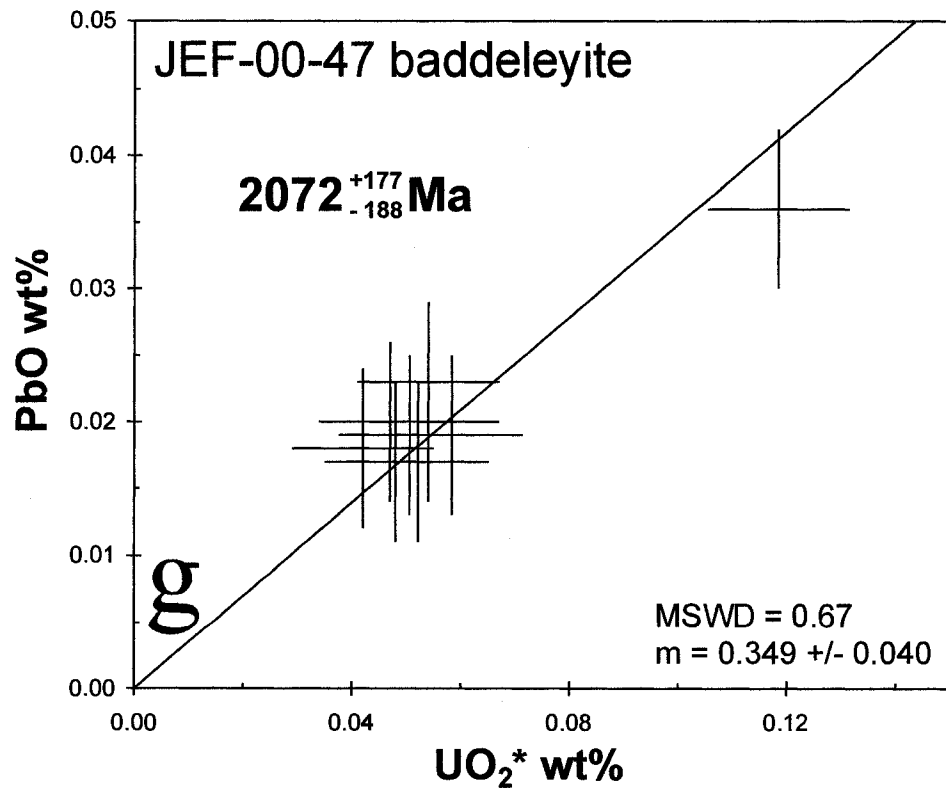
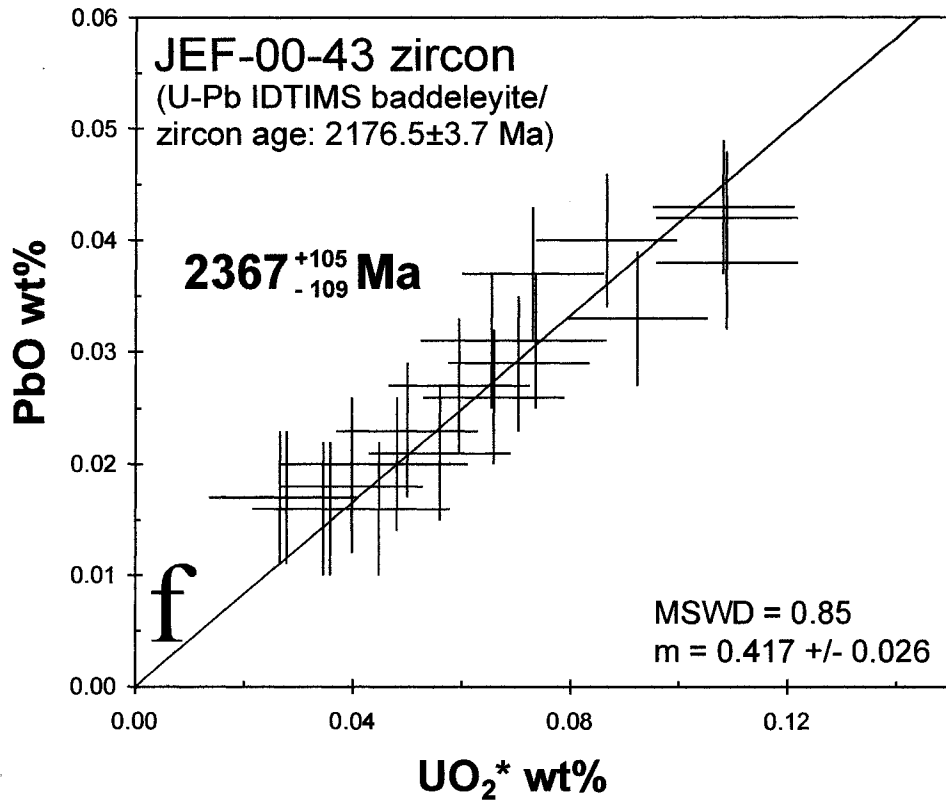


(Fig. C-4 continued.)

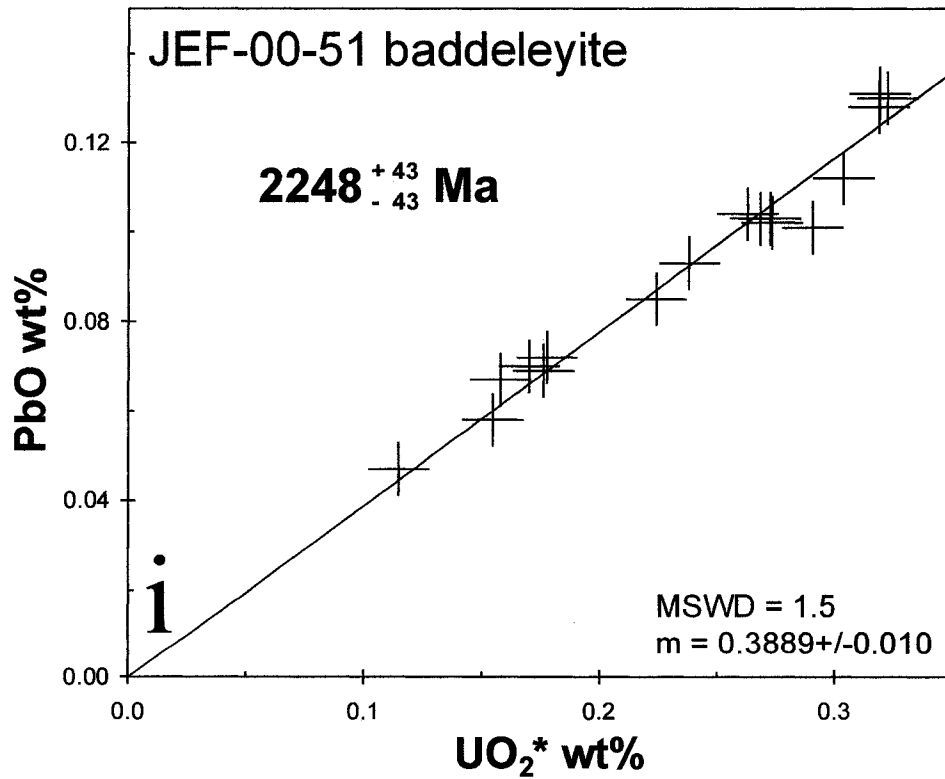
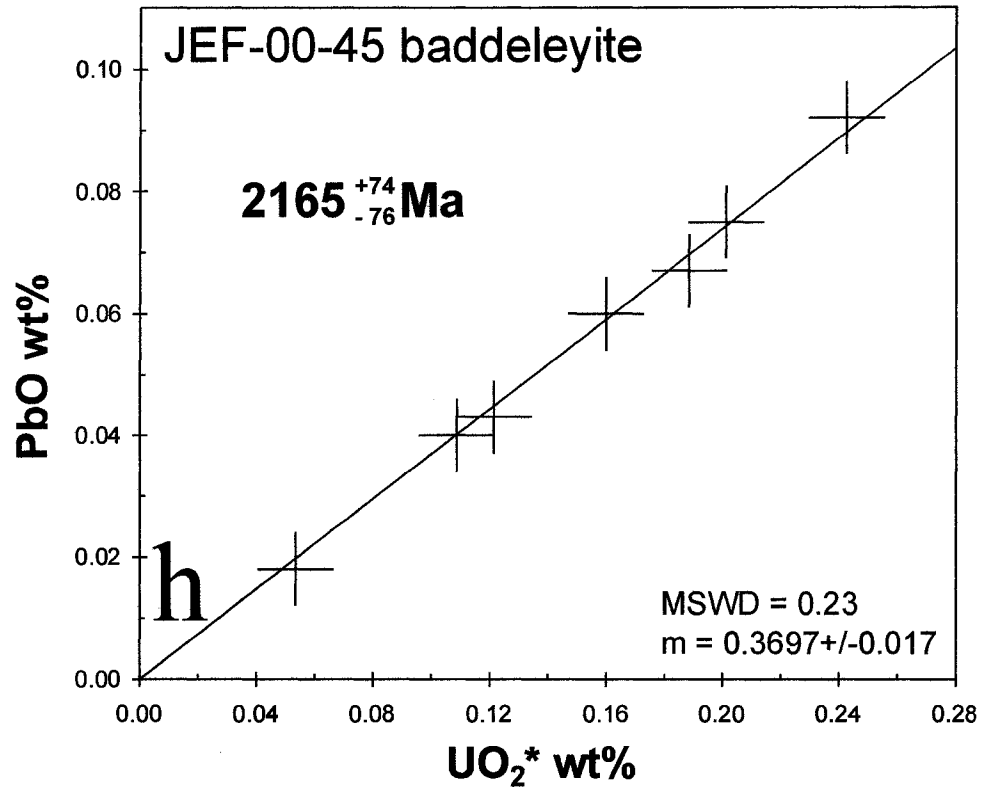
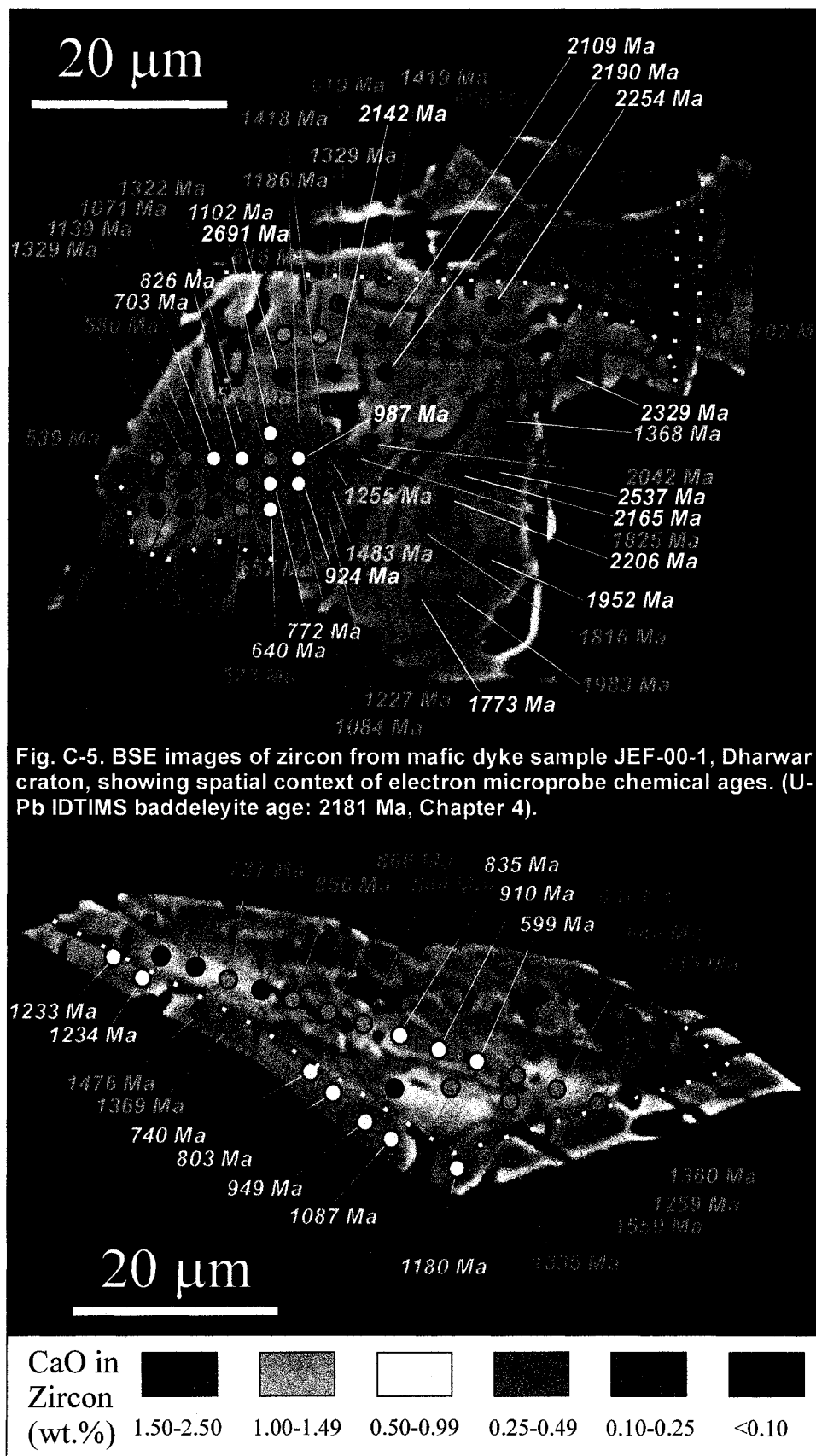


(Fig. C-4 continued.)



APPENDIX D

Whole rock geochemistry (major, trace, and rare earth elements) for representative samples of the BD2 and HMD dyke swarms, Bastar craton

Summary

This appendix presents whole rock geochemical data including major and trace elements (including the rare Earth elements - REE) for samples JEF-00-36 (BD2 mafic dyke swarm) and JEF-00-14 (HMD mafic dyke swarm), which were also the subject of a U-Pb IDTIMS dating study (see Chapter 3 for petrographic descriptions and geological setting). A representative portion of each of these samples were selected for whole-rock geochemical analysis, and only fresh rock fragments devoid of any visible signs of weathering were included in these aliquots. Samples were crushed using a jaw crusher equipped with hardened steel plates and pulverized with a tungsten carbide puck mill at the University of Alberta Radiogenic Isotope Facility. These rock powders were sent to Activation Laboratories Ltd. (Ancaster, ON, Canada) and analysed by ICP-MS methods in accordance with their code 4LithoResearch package for major, trace and rare earth element (REE) compositions, and the geochemical data for both samples is presented in Table D-1. The data for both samples, along with previously published data for Bastar mafic dyke swarms, are plotted on the total-alkalis versus silica (TAS) diagram (Irvine and Baragar, 1971; Le Maitre, 2002) and on three variation diagrams (Figs. D-1 and D-2), and the association of samples JEF-00-36 and JEF-00-14 with the BD2 (diorite) and HMD geochemical fields, respectively, is clear on all diagrams. A discussion of the data presented in Figs. D-1 and D-2 is provided below, and addresses the possibility of correlating southern Bastar dyke swarms (BD1, BD2 and HMD swarms of Srivastava and Singh, 2003; Srivastava and Singh, 2004) with the parallel Bhanupratappur-Keskal (BK) swarm which occurs ~150 km to the north (Ramachandra et al., 1995) on the basis of the available major element geochemistry. Detailed petrographic descriptions,

geochemical classification, and petrogenetic interpretations of the HMD, BD1 and BD2 mafic dyke swarms are provided by Srivastava et al. (1996), Srivastava and Singh (2003), and Srivastava and Singh (2004). Although the HMD dyke analysed in this thesis (sample JEF-00-14) was observed in the field to outcrop along a bearing of ~050°, the majority of HMD dykes (along with BD1 and BD2 dykes) appear to trend NW-SE to WNW-ESE (Srivastava and Singh, 2003; Srivastava and Singh, 2004).

Geochemical comparisons of the BD1, BD2, HMD, and BK dyke swarms

Some whole rock major element data is available for parallel dolerite dykes from the BK dyke swarm (Ramachandra et al., 1995; see Fig. 3-2 in Chapter 3) and is shown in Figs. D-1 and D-2 for comparison with previously published data for the BD1, BD2, and HMD dykes from the present study area (from: Srivastava and Singh, 2003; Srivastava and Singh, 2004; including samples JEF-00-36 and JEF-00-14 from Table D-1). We highlight however, that in the absence of more trace element data from the BK swarm it is difficult to rule out the possible effects of secondary weathering, alteration, or crustal contamination, especially because all BK dykes are altered to some degree and secondary carbonate and epidote have been identified in some BK dykes (Ramachandra et al., 1995). Nevertheless, some first-order geochemical comparisons can presently be made between the BK swarm and dykes from the present study area. NW-SE trending dykes from the BK swarm (~150km north, Fig. 3-2, Chapter 3) plot predominantly within the subalkaline series on a TAS diagram (Ramachandra et al., 1995) and range in composition from basaltic andesites to basalts (Fig. D-1), and within the fields for the BD1, BD2, and HMD swarms. In contrast to the HMD and BD1 dyke swarms however, none of the BK dykes are metamorphosed (Ramachandra et al., 1995). Representative

variation diagrams for the BK, BD1, BD2, and HMD dyke swarms of the SBC, including plots of MgO versus TiO₂, P₂O₅, and CaO, are shown in Fig. D-2. Overall, many BK dykes show a similar range of whole-rock major element compositions as dykes from the present study area, but one notable difference is that for a given MgO content, the BK dykes seem to be more calcic. On plots of MgO versus TiO₂ and P₂O₅, many BK dykes plot within the fields for the BD1 dyke swarm, and a few plot very close to the fields for the BD2 mafic dyke swarm (labelled as 1, 2, and 3 in Figs. D-1 and D-2). An important geochemical feature useful in discriminating BD1 and BD2 mafic dykes is the observed contrast in whole-rock P₂O₅ and TiO₂ concentrations for samples with overlapping MgO concentrations (BD2 dykes show distinctly higher values: Srivastava and Singh, 2004). In the present comparison, the BK dyke with the highest Ti content (labelled 1) can likely be ruled out as a BD2 candidate because it plots well within the trachy-basalt field on a TAS diagram (Fig. D-1). However, the BK dyke with the second highest Ti content (labelled 2) also has the highest P₂O₅ concentration of all dykes in the BK area, plots close to the BD2 fields on all plots in Figs. D-1 and D-2, and like most BD2 dykes is CIPW quartz normative (Ramachandra et al., 1995; Srivastava and Singh, 2004). One BK dyke (labelled 4) plots near the field for the HMD dykes on the variation diagrams, but on the TAS diagram this sample is classified as basalt, rather than basaltic andesite so a direct correlation with the HMD swarm seems unlikely. Seven BK dykes (labelled as 5 to 11) plot directly within the BD1 fields on plots of MgO versus P₂O₅ and TiO₂ (Fig. D-2), and all but one plot within the subalkaline basalt field on the TAS diagram (Fig. D-1). These BK dykes range from quartz to olivine normative (Ramachandra et al., 1995), which is another characteristic

of the BD1 dyke swarm (Srivastava and Singh, 2004). In summary, the available whole-rock major element geochemical data suggest that no HMD dykes occur in the BK area, but that BD1 and BD2 dykes could be present. If this proves to be the case, then BD1 dykes appear to be more common and they are not metamorphosed (Ramachandra et al., 1995).

References

Irvine, T.N. & Baragar, W.R.A. (1971). A guide to the Chemical Classification of the Common Volcanic Rocks. *Canadian Journal of Earth Sciences* **8**, 523-548.

Le Maitre, R.W. & International Union of Geological Sciences. (2002). *Igneous Rocks: A Classification and Glossary of Terms* (Editor: Le Maitre), 252p.

Ramachandra, H.M., Mishra, V.P., & Deshmukh, S.S. (1995). Mafic dykes in the Bastar Precambrian: study of the Bhanupratappur-Keskal mafic dyke swarm. In: Devaraju, T.C., ed., *Mafic Dyke Swarms of Peninsular, Geological Society of India Memoir* **33**, 183-207.

Srivastava, R.K., Hall, R.P., Verma, R., & Singh, R.K. (1996). Contrasting Precambrian mafic dykes of the Bastar craton, central India: petrological and geochemical characteristics. *Journal of the Geological Society of India* **48**, 537-546.

Srivastava, R.K., & Singh, R.K. (2003). Geochemistry of high-Mg mafic dykes from the Bastar craton: evidence of late Archean boninite-like rocks in an intracratonic setting. *Current Science* **85**, 808-812.

Srivastava, R.K. & Singh, R.K. (2004). Trace element geochemistry and genesis of Precambrian sub-alkaline mafic dikes from the central Indian craton: evidence for mantle metasomatism. *Journal of Asian Earth Sciences* **23**, 373-389.

Table D-1. Major and trace element geochemistry for representative mafic dykes from the BD2 and HMD dyke swarms, Baster craton. Both dykes were dated by U-Pb in this thesis (Chapter 3).

Sample ID:	JEF-00-36	JEF-00-14
Dyke swarm:	BD2	HMD
Dyke trend:	NW-SE	NE-SW
Latitude:	18° 58.42' N	18° 49.37' N
Longitude:	81° 33.85' E	81° 34.71' E
wt%		
SiO ₂	53.22	53.46
TiO ₂	2.033	0.446
Al ₂ O ₃	13.11	9.98
Fe ₂ O ₃ *	16.37	10.48
MnO	0.202	0.172
MgO	1.71	14.44
CaO	7.01	6.11
Na ₂ O	2.65	1.33
K ₂ O	1.34	0.98
P ₂ O ₅	0.71	0.07
LOI	1.11	1.97
TOTAL	99.46	99.44
ppm		
V	96	183
Cr	-	1,030
Co	55	63
Ni	-	220
Cu	42	48
Zn	144	77
Ga	21	9
Ge	1.4	1.4
Rb	43	53
Sr	168	74
Y	98.8	13.1
Zr	454	60
Nb	20.7	3.5
Sn	6	4
Cs	-	-
Ba	363	192
La	36.8	8.59
Ce	81.2	17.0
Pr	10.5	1.87
Nd	47.5	7.44
Sm	12.72	1.65
Eu	3.55	0.463
Gd	14.5	1.80
Tb	2.60	0.32
Dy	15.1	1.83
Ho	3.01	0.39
Er	9.39	1.23
Tm	1.39	0.184
Yb	8.35	1.14
Lu	1.27	0.181
Hf	10.5	1.5
Ta	2.06	0.55
W	300	135
Tl	0.20	0.31
Th	9.70	4.04
U	2.58	1.47

(* the Fe₂O₃ represents total Fe-oxide and has not been adjusted for FeO)

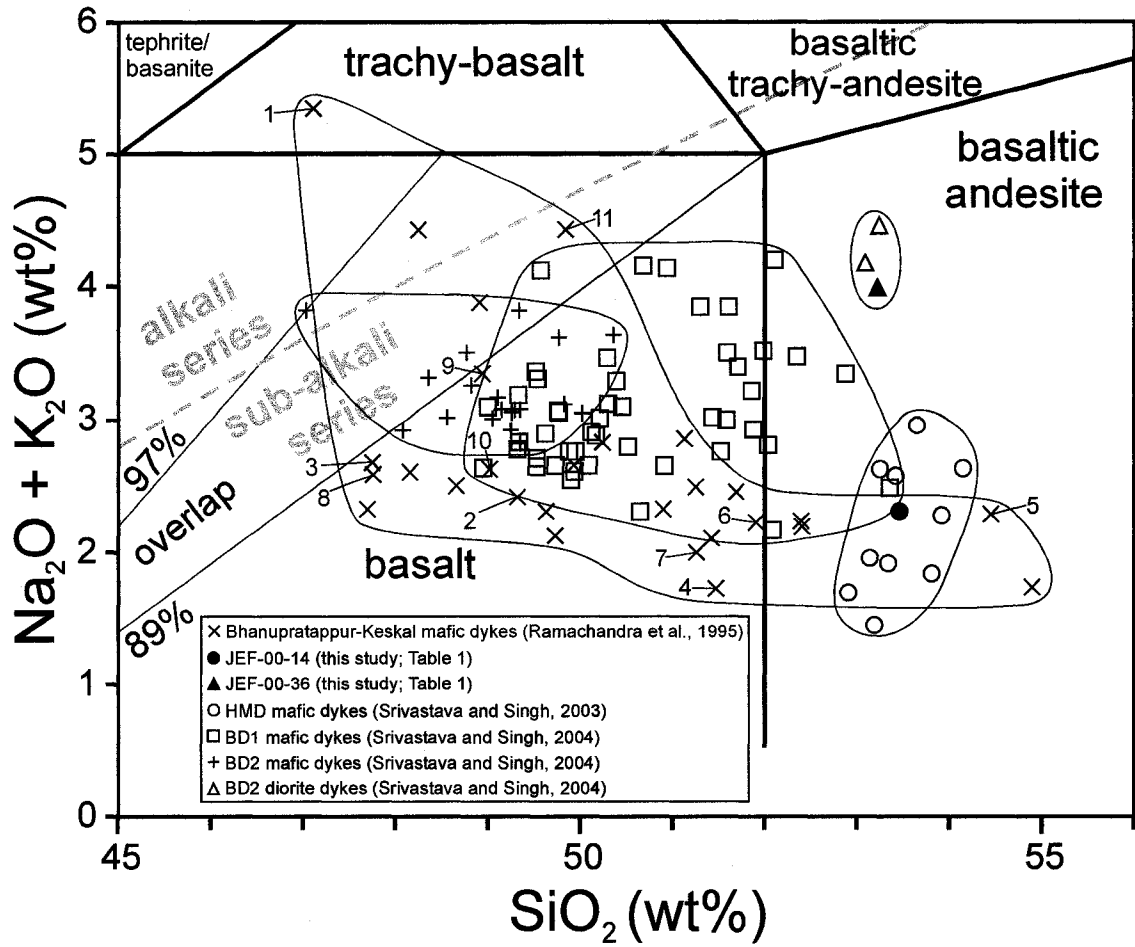


Fig. D-1. Total alkalis versus silica diagram (Le Maitre, 2002) showing geochemical data for mafic dyke swarms of the Bastar craton.

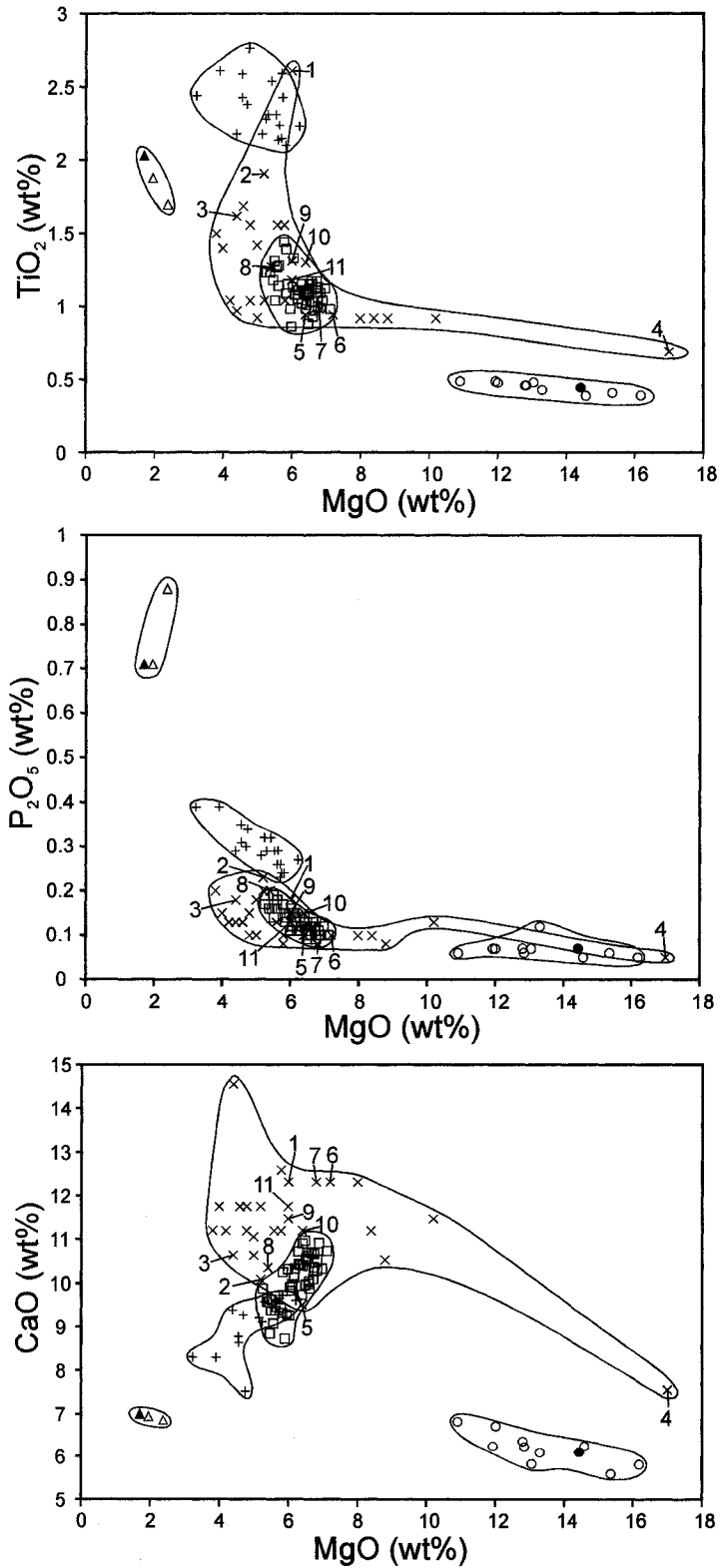


Fig. D-2. Three representative variation diagrams showing geochemical data for mafic dyke swarms of the Bastar craton. Symbols as in Fig. D-1.

APPENDIX E

Electron microprobe chemical U-Th-total Pb dating of zirconolite ($\text{CaZrTi}_2\text{O}_7$)

Summary

The mineral zirconolite ($\text{CaZrTi}_2\text{O}_7$) is known to occur in a wide diversity of rock types and displays a wide range of chemical compositions (Williams and Gieré, 1996), and until very recently has been overlooked as a geochronometer for dating the timing of crystallization of mafic igneous rocks (French et al., 2002; Rasmussen and Fletcher, 2004). Because this mineral has been identified in a large number of Indian mafic dyke samples in this project (JEF-99-2, JEF-99-6, JEF-99-7, JEF-00-3, and JEF-00-30), and typically occurs as thin ($<10 \mu\text{m}$) blades with high concentrations of UO_2 (typically 0.5-1.5 wt%), ThO_2 (typically 1-3 wt%), and PbO (typically 0-1 wt%) in these dykes, zirconolite may be ideally suited for electron microprobe chemical U-Th-total Pb (EM) dating studies of Precambrian mafic dyke swarms. This Appendix presents the preliminary results of a detailed electron microprobe (EM) chemical U-Th-total Pb dating study of a suite of two zirconolite samples, including zirconolite from a polished thin section of the Duck Lake sill, Slave craton, and zirconolite in polished grain mount, originating from the Phalaborwa carbonatite, South Africa. Because there are complexities in the data that are still not clearly understood, and because much of the data is considered to be preliminary and a work in progress, only brief interpretations are presented for each dataset. The principal conclusion from this data is that EM zirconolite dating shows excellent promise in geochronological studies of igneous rocks; especially contextural dating studies of Precambrian mafic sills or dykes. On account of the wide range in chemical compositions displayed by zirconolite, a comprehensive survey of all possible X-ray line interferences which pertain to chemical U-Th-total Pb zirconolite dating needs to be carried out in order to ensure the accuracy of the chemical

age information. Although isotopic dating of zirconolite has been carried out recently by sensitive high resolution ion microprobe (SHRIMP: Rasmussen and Fletcher, 2004) and NanoSIMS (Stern et al., 2005), questions remain as to the ability of this mineral to incorporate common Pb (especially on account of the large range of cation substitutions that is demonstrated for this mineral: Williams and Gieré, 1996), closure temperature of the U-Th-total Pb system in zirconolite, and susceptibility of zirconolite to alteration, metamictization (and ability or inability to self anneal) and Pb-loss. Exploring some of these major questions is far beyond the scope of this preliminary study, but it is important to note that this needs be done in the future in order to evaluate the accuracy of the EM zirconolite dating technique, and this would probably help to explain some of the complexity in chemical age results and conflicting datasets presented in this appendix.

Analytical set-up during EM zirconolite dating

The instrument employed in this study was a JEOL 8900 Electron Microprobe equipped with five wavelength dispersive spectrometers (WDS) and housed in the Department of Earth and Atmospheric Sciences (University of Alberta). Analysis of all minerals (zirconolite and baddeleyite in this appendix) was conducted at 20kV accelerating voltage, 150nA beam current (100nA for the Phalaborwa sample), and a 1 μ m beam diameter (though a 5 μ m beam was used for some analyses of the Phalaborwa carbonatite - see Fig. E-8).

The U M β , Th M α , and Pb M α X-ray lines were chosen during analysis of zirconolite and baddeleyite (with the exception that Pb M β was chosen during analysis of the Phalaborwa sample), and an overlap correction was employed to account for

interference of the Y $L\gamma$ peak on Pb $M\alpha$ (Suzuki and Adachi, 1991). For analysis of the Duck Lake sample, count times were set at 300s (peak) and 150s (background) for U, 120-180s (peak) and 60-90s (background) for Th, and 300s (peak) and 150s (background) for Pb. During analysis of the Phalaborwa zirconolite, count times were set at 120s (peak) and 60s (background), 40s (peak) and 20s (background) for Th, and 200s (peak) and 100s (background) for Pb. A Pb-silicate glass (NBS-K 456) was used for analysis of Pb, synthetic oxide standards for analysis of Th, U, and Zr, synthetic phosphate standards for analysis of the REE, and natural mineral standards for measurement of all other elements. The data were collected over three analytical sessions (1: Duck Lake session 1; 2: Duck Lake session 2, and 3: Phalaborwa session), and all of the chemical data are listed in Tables E-1 to E-3. During analysis of the Duck Lake zirconolite in session 1 (Table E-1), the chemical totals are significantly low (~80%) because quantitative analysis of some additional trace elements in this zirconolite was not carried out, but these totals were improved upon (typically 96-98%) during session 2 (Table E-2) which included analysis of several additional trace elements. Ages were calculated after the chemical isochron method of Suzuki and Adachi (1991), except that in some cases where noted, the regression lines were anchored to the origin with a fictive data-point containing no associated data-point errors, and data reduction was identical to the method outlined in Chapter 2.

EM dating of *in-situ* zirconolite and baddeleyite: Duck Lake sill, Slave craton

A polished thin section (JA HD-07) of the Duck Lake sill, which intrudes the Late Archean Burwash Formation of the Slave craton near Yellowknife, Canada, was kindly provided by John Armstrong for this reconnaissance EM dating study. A large

number of baddeleyite crystals of substantial size (up to 20 x 100 μm in cross section) were identified in thin section JA HD-07 in addition to three relatively small (<20 μm in the longest dimension) zirconolite crystals, and in one case these two minerals were inter-grown (Figs. E-1 to E-3). EM chemical dating was carried out on both minerals in this study and the results of this research (data from Figs. E-1 to E-6) were presented at the 2002 Yellowknife Geoscience Forum (abstract included at the end of the text section of this appendix). The petrographic context of all baddeleyite and zirconolite analyses from session 1 is shown in Figs. E-1 to E-3, and the data plotted on UO_2^* versus PbO (wt.%) diagrams (Suzuki and Adachi, 1991) in Figs. E-4 to E-6 (session 1) and Fig. E-7 (session 2).

EM baddeleyite dating yielded a relatively well-defined 48-point isochron age of 2080 ± 50 Ma (Fig. E-4), which is interpreted to represent a reasonable first-order estimate for the age of emplacement of the Duck Lake sill. EM analysis of three zirconolite crystals from the Duck Lake sill yielded slightly different chemical compositions (Grains A, B, and E: Tables E-1 and E-2), and in all cases very high concentrations of UO_2 (0.6-1.5 wt.%), ThO_2 (3.0-4.5wt.%), and PbO (0.5-1.0 wt.%) in relation to baddeleyite. Despite remarkably different chemical compositions and contrasting UO_2 , ThO_2 , and PbO concentrations, most of the data for grains A and B from session 1 plot along a single isochron yielding an age of $2193 \pm 31/-32$ Ma (Fig. E-5). Another regression line (not shown) constructed to pass through these same data points, but anchored to the origin yields a more precise isochron age of 2162 ± 8 Ma (equivalent to the average of the *blue* individual spot ages in Fig. E-1), and is considered to represent the best estimate of the age of zirconolite crystallization from session 1.

When considered individually the datasets for grains A and B (Fig. E-5) yield significantly less precise isochron ages of $2318 \pm 281 / -312$ Ma (grain A) and $2224 \pm 163 / -173$ Ma (grain B). A significant number of individual spot ages determined from grain B are anomalously young and were excluded from the aforementioned isochron diagrams because of their association with fractures (and localized Pb-loss?) visible in back-scattered electron images (BSE) of that crystal (Fig. E-1). A separate isochron plot showing all of the data from grain B (Fig. E-6) demonstrates the pronounced scatter of the data when these anomalous data are included on the plot.

Two zirconolite crystals (grains A and E) were analysed from this same thin section of the Duck Lake sill in a second analytical session (Table E-2), including repeat analysis of the aforementioned grain A, and the data are shown on chemical isochron plots in Fig. E-7. The EM chemical ages determined on zirconolite grains A and E in session 2 are distinctly different, yielding precise but contrasting isochron ages (anchored regressions) of 2191 ± 8.7 Ma EM (grain A) and 1849 ± 17 Ma (grain E). The isochron age of 2191 ± 8.7 Ma determined in session 2 is significantly older than the anchored regression from session one (2162 ± 8 Ma). The analytical set-up was essentially the same during analysis of U, Th, and Pb in zirconolite for both Duck Lake sessions, but a significantly larger number of elements were analysed in session 2 (22 oxides versus 11 in session 1), which yielded much better chemical totals (~97% versus ~80%). One reasonable interpretation for the discrepancy in ages of Grain A between sessions is that ZAF matrix corrections on the U, Th, and Pb measurements were different because of the contrasting estimates of the bulk zirconolite composition. For that reason, it is concluded that the isochron age of 2191 ± 8.7 Ma is considered to be the

more accurate EM chemical age for zirconolite grain A, and the best estimate for the age of emplacement of the Duck Lake sill by EM zirconolite dating. The anomalously young age of 1849 Ma determined for zirconolite grain E might be related to Pb-loss from that crystal, as it was a very thin (~6 μm wide) blade, although there was no evidence for fracturing or alteration in BSE images of that grain (images not shown).

The Duck Lake sill has also been the subject of a more recent geochronological study, which yielded a highly precise U-Pb IDTIMS (baddeleyite and zircon) age of 2181 ± 2 Ma (Bleeker and Kamo, 2003). A comparison of this U-Pb age to the EM chemical ages determined on baddeleyite and zirconolite from this same igneous intrusion, indicates that the EM baddeleyite age of 2080 ± 50 Ma determined in this study is slightly too young, but still a reasonable first-order estimate for the age of emplacement of the Duck Lake sill. The EM zirconolite age of 2191 ± 8.7 Ma determined for the Duck Lake sill in this study overlaps within error of the U-Pb IDTIMS age of 2181 ± 2 Ma determined for this intrusion (Bleeker and Kamo, 2003), which suggests that the EM zirconolite dating routine employed in this study may be correct (see a marked contradiction to this conclusion in the discussion of the dataset for the Somala dyke below however). It is concluded from the dataset determined on zirconolite from the Duck Lake sill that this mineral shows great promise as a geochronometer for the determining the crystallization age of mafic igneous rocks by EM chemical dating, but that localized Pb-loss is anticipated to be a significant problem for some zirconolite crystals in such studies.

EM dating of zirconolite: Phalaborwa carbonatite, South Africa

A large zirconolite crystal originating from the Phalaborwa carbonatite, South Africa, was generously donated by Tony Mariano for this EM dating study. Three small (<0.5 mm) fragments were broken off and made into a polished grain mount for EM analysis, and two of these zirconolite fragments were analysed in this study (Fig. E-8). These zirconolite fragments contained a diversity of other mineral inclusions, including baddeleyite, calcite, ilmenite, hematite, and rare sulfides, but significantly large (>100x100µm) domains of pure zirconolite existed, allowing for quantitative chemical analysis of 78 spots (Fig. E-8; Table E-3). The Phalaborwa zirconolite has a remarkably mottled appearance in BSE images, and this appears to be the result of compositional variations associated with both oscillatory zoning and secondary fracturing and alteration (Fig. E-8). Some relatively small (10-50µm across) domains within this zirconolite however, show a very smooth appearance in BSE images, and the EM dating results were generally the most consistent in these domains (Fig. E-8). Overall, there was a very wide range in apparent ages from 261 Ma to 7154 Ma, but a probability density plot of all of the age data shows a significant peak in apparent ages at ~2050 Ma (Fig. E-9). It is clear that most of the anomalous ages are associated with the most mottled and fractured areas in BSE images (Fig. E-8), which indicates that the U-Th-total Pb system is disturbed in these areas, possibly in association with localized secondary fracturing and alteration. The prominent peak in chemical ages at c. 2050 Ma corresponds closely with $^{207}\text{Pb}/^{206}\text{Pb}$ ages (2048-2051 Ma: concordant to 4.5% normally discordant analyses) determined in a preliminary U-Pb IDTIMS study (conducted by Larry M. Heaman) on this same zirconolite sample. EM dating of the Phalaborwa zirconolite in this study provides further evidence that for some zirconolite samples,

localized secondary alteration may result in anomalous chemical ages, but that detailed BSE imaging can help to circumvent this problem. 50 out of 78 EM zirconolite spot ages (Fig. E-8) are within 50 m.y. of the preliminary U-Pb IDTIMS age determinations, which suggests that the EM zirconolite dating routine being used for this sample is correct, and that the Pb M β X-ray line may be a better choice than Pb M α for analysis of Pb in EM zirconolite dating studies.

References

Bleeker, W. & Kamo, S. (2003). A precise age for the Duck Lake sill and its relevance for fitting the Slave in a global Archean context. *Abstract Volume, 31st Yellowknife Geoscience Forum*.

French, J.E., Heaman, L.M., Chacko, T., Armstrong, J. & Cairns, S. (2002). Electron Microprobe dating of mafic to ultramafic igneous rocks. *Abstract Volume, 30th Yellowknife Geoscience Forum*.

Rasmussen, B. & Fletcher, I.R. (2004). Zirconolite: A new U-Pb geochronometer for mafic igneous rocks. *Geology* **32**, 785-788.

Stern, R.A., Fletcher, I.R., Rasmussen, B., McNaughton, N.J., & Griffin, B.J. (2005). Ion microprobe (NanoSIMS 50) Pb-isotope geochronology at <5 μm scale. *International Journal of Mass Spectrometry* **244**, 125-134.

Suzuki, K. & Adachi, M. (1991). Precambrian provenance and Silurian metamorphism of the Tsubonosawa paragneiss in the South Kitakami terrane, Northeast Japan, revealed by the chemical Th-U-total Pb isochron ages of monazite, zircon, and xenotime. *Geochemical Journal* **25**, 357-376.

Williams, C.T. & Gieré, R. (1996). Zirconolite: a review of localities worldwide, and a compilation of its chemical compositions. *Bulletin of the Natural History Museum of London* **52**, 1-24.

Electron Microprobe dating of mafic to ultramafic igneous rocks (Presented at the 30th annual Yellowknife Geoscience Forum, 2002)

¹French, J. E., ¹Heaman, L. M., ¹Chacko, T., ²Armstrong, J., and ²Cairns, S.

1) Department of Earth and Atmospheric Sciences, University of Alberta, Edmonton, AB, Canada, T6G 2E3

2) NWT GEOLOGY Division DIAND, Box 1500, Yellowknife, NT, Canada, X1A 2R3

The Electron Microprobe (EM) chemical U-Th-total Pb dating technique is now well established as a valuable contextual tool in reconnaissance geochronological investigations of monazite-bearing igneous and metamorphic rocks (e.g. Cocherie et al., 1998). The main advantages of the technique are tied to the excellent spatial resolution of the EM (~1 μm), but also to the fact that it is relatively rapid and inexpensive when compared to conventional isotopic methods. As most EM chemical dating studies have focussed on the mineral monazite (and to a lesser extent zircon and xenotime), the technique has been used almost exclusively to obtain contextual age information from metasedimentary and granitoid rocks. Recent studies have shown that reliable first-order chemical age information can successfully be obtained by EM from the mineral baddeleyite (ZrO_2) (French et al., 2002), a mineral used commonly in conventional U-Pb dating of mafic dykes and sills. As such, there is great potential for incorporating this technique in geochronological investigations of mafic rocks, particularly in reconnaissance dating of crustal-scale mafic dyke swarms. Here we review tactics for EM chemical dating of mafic to ultramafic rocks, outline some fields of application, the advantages and limitations of the technique, and discuss case studies from the Slave Province.

The Zr-rich, U-bearing minerals baddeleyite (ZrO_2), zircon (ZrSiO_4), and zirconolite ($\sim\text{CaZrTi}_2\text{O}_7$), commonly occur in trace amounts in many gabbro dykes and sills, and in the ultramafic cumulates of layered mafic intrusions (Heaman and LeCheminant, 1993). Of these accessory phases, zircon and baddeleyite are now well-established geochronometers in conventional U-Pb geochronological studies of mafic to ultramafic rocks (Krogh et al., 1987). In-situ chemical dating of baddeleyite by EM was recently carried out by French et al. (2002), and Geisler and Schleicher (2000) have evaluated in detail, methods for improving the accuracy and precision of EM chemical ages determined from discordant zircon grains. Although zirconolite is known to occur in a wide range of rock types and geological environments and has been reported from a number of terrestrial and lunar mafic to ultramafic samples (Williams and Giere, 1996), the U-Pb systematics and typical common Pb contents of this mineral have not yet been evaluated. As the combined U + Th content in zirconolite from terrestrial mafic to ultramafic rocks is typically >5000 ppm (Williams and Giere, 1996), there may be potential for development of this mineral as a new geochronometer for mafic to ultramafic rocks.

In one case study, EM chemical data are presented for baddeleyite and spatially associated zirconolite, originating from a shallow-dipping, ultramafic sheet (the Hay Duck sill*) which intrudes the Burwash Formation near Yellowknife. The baddeleyite data yield a well-defined, 48 point U-Th-total Pb isochron age of 2080 ± 50 Ma, which coincides closely with the upper limit of K-Ar ages determined by Leech (1966) for that intrusive body (1925-2090 Ma). Preliminary EM analyses indicate that zirconolite from this sample contains >4.0 wt% ThO_2 , and 0.7-1.6 wt% UO_2 , and high PbO concentrations (>0.5 wt%), and may also have retained meaningful, and comparable chemical U-Th-total Pb age information. Refs: Cocherie et al. (1998), GCA 62, p.2475-2497; French et al. (2002), Chem.Geol.188, p.85-104; Geisler and Schleicher(2000), Chem.Geol. 163, p.269-285; Heaman and LeCheminant (1993), Chem.Geol. 110, p.95-

126; Krogh et al.(1987), In: Mafic Dyke Swarms, p. 147-152; Leech(1966), CJES 3, p.389-412; Williams and Giere(1996), Bull.Nat.Hist.Mus.Lond.(Geol.) 52, p.1-24.

* The Hay Duck sill in this abstract refers to a composite mafic-ultramafic intrusion that extends along the Hay-Duck Fault east of Yellowknife that has also been referred to as the Duck Lake Intrusive Sheet (Gibbons, W.A. 1987. The Duck Lake Intrusive Sheet. *Yellowknife Guide Book, A guide to the geology of the Yellowknife Volcanic belt and its bordering rocks.* Ed. Padgham, W.A., 135-136) and the Duck Lake sill (Bleeker, 2003).

Table E-1. Electron Microprobe data (wt%) for baddeleyite and zirconolite from sample JA HD-07 of the Duck Lake (Hayduck) sill, Slave craton - Analytical session 1.

No.	ZrO ₂	*FeO	UO ₂	PbO	ThO ₂	HfO ₂	Y ₂ O ₃	Nb ₂ O ₅	TiO ₂	SiO ₂	CaO	Total	Comment
355	98.889	0.406	0.02	0.006	0.003	0.518	0	0.156	0.396	0.112	0.078	100.564	Hayduck-1
356	99.558	0.459	0.044	0.009	0.004	0.509	0	0.157	0.427	0.126	0.067	101.36	Hayduck-2
357	99.88	0.492	0.01	0.001	0.014	0.509	0	0.135	0.402	0.096	0.058	101.597	Hayduck-3
358	99.167	0.552	0.012	0.011	0.006	0.53	0	0.17	0.411	0.09	0.071	101.02	Hayduck-4
359	97.247	0.141	0.009	0.009	0.006	0.968	0	0.253	0.817	0.208	0.012	99.67	Hayduck-5
360	95.727	0.112	0.035	0.014	0.001	1.032	0	0.249	0.385	0.414	0.014	97.983	Hayduck-6
361	97.137	0.124	0.013	0.003	0.001	0.938	0	0.252	0.854	0.169	0.012	99.503	Hayduck-7
362	92.696	0.071	0.038	0.002	0	1.018	0	0.137	0.27	3.752	0.012	97.996	Hayduck-8
363	27.148	8.941	1.438	0.915	4.269	0.174	4.466	1.42	29.218	0.127	4.404	82.52	Hayduck-9 (zirconolite)
364	27.331	8.906	1.614	0.966	4.188	0.155	4.551	1.473	29.204	0.095	4.427	82.91	Hayduck-10 (zirconolite)
365	27.499	8.927	1.7	0.997	4.069	0.15	4.67	1.553	29.107	0.1	4.376	83.148	Hayduck-11 (zirconolite)
366	27.435	8.788	1.826	1.054	4.213	0.159	4.659	1.648	29.037	0.092	4.299	83.21	Hayduck-12 (zirconolite)
367	99.77	1.033	0.034	0.009	0.011	0.595	0	0.162	0.962	0.183	0.13	102.889	Hayduck-13
368	94.701	1.26	0.876	0.286	0.162	0.311	0.655	0.6	2.793	0.292	0.144	101.88	Hayduck-14
369	95.676	1.329	0.486	0.195	0.103	0.359	0.442	0.446	2.985	0.313	0.133	102.467	Hayduck-15
370	96.815	0.505	0.155	0.051	0.036	0.438	0.143	1.168	2.685	0.112	0.018	102.126	Hayduck-16
371	98.287	0.493	0.111	0.039	0.018	0.483	0.064	0.826	1.733	0.381	0.027	102.462	Hayduck-17
372	27.627	8.489	0.577	0.548	4.006	0.214	2.91	2.553	27.78	0.082	4.672	79.458	Hayduck-18 (zirconolite)
373	27.686	8.712	0.573	0.556	4.069	0.211	2.928	2.461	27.796	0.087	4.678	79.757	Hayduck-19 (zirconolite)
374	27.794	8.501	0.579	0.575	4.238	0.195	2.947	2.522	27.785	0.069	4.673	79.878	Hayduck-20 (zirconolite)
375	27.809	8.354	0.542	0.537	4.005	0.239	2.904	2.651	27.891	0.091	4.645	79.668	Hayduck-21 (zirconolite)
376	99.125	0.107	0.015	0.004	0.003	0.572	0.029	0.363	0.505	0.096	0.001	100.82	Hayduck-22
377	98.867	0.088	0.027	0.007	0	0.585	0.006	0.38	0.58	0.113	0.016	100.669	Hayduck-23
378	97.839	0.083	0.009	0.003	0.012	0.555	0.012	0.379	0.55	0.143	0.004	99.589	Hayduck-24
379	99.953	0.047	0.022	0.005	0.004	0.515	0.021	0.223	0.355	0.095	0	101.24	Hayduck-25
380	99.344	0.067	0.004	0.003	0.011	0.496	0	0.165	0.333	0.084	0.008	100.515	Hayduck-26
381	98.507	0.117	0.055	0.02	0.008	0.439	0.031	0.558	0.631	0.09	0.001	100.457	Hayduck-27
382	98.499	0.155	0.072	0.026	0.009	0.437	0.055	0.533	0.694	0.117	0.006	100.603	Hayduck-28
383	99.115	0.136	0.039	0.015	0	0.466	0.029	0.405	0.519	0.142	0.002	100.868	Hayduck-29
384	97.566	0.144	0.047	0.012	0	0.425	0.028	0.4	0.511	0.176	0	99.309	Hayduck-30
385	99.83	0.076	0.008	0.007	0.01	0.799	0.008	0.199	0.272	0.076	0.007	101.292	Line
386	100.42	0.119	0.02	0.004	0.009	0.696	0	0.203	0.327	0.061	0.014	101.873	Line
387	98.612	0.134	0.046	0.02	0	0.468	0.025	0.481	0.723	0.068	0.03	100.807	Line
388	98.464	0.156	0.045	0.012	0	0.428	0.012	0.465	0.702	0.1	0.043	100.427	LineA
389	99.71	0.303	0.065	0.028	0.004	0.43	0.023	0.65	0.805	0.042	0.118	102.178	Hayduck-31
390	98.735	0.445	0.021	0.019	0.003	0.479	0.032	0.651	0.795	0.031	0.128	101.339	Hayduck-33
391	99.85	0.382	0.067	0.021	0.028	0.448	0.004	0.571	0.771	0.052	0.125	102.319	Hayduck-34
392	96.234	0.231	0.057	0.009	0.011	0.469	0.015	0.696	1.371	0.094	0.038	99.225	Hayduck-35
393	96.555	0.261	0.06	0.015	0.013	0.461	0.048	0.95	1.812	0.043	0.037	100.255	Hayduck-36
394	97.317	0.232	0.033	0.01	0	0.455	0.004	0.761	1.478	0.077	0.027	100.394	Hayduck-37
395	99.03	0.153	0.017	0	0.006	0.586	0	0.351	0.741	0.139	0.023	101.046	Hayduck-38
396	98.054	0.154	0.021	0.007	0	0.4	0	0.256	0.579	0.14	0.042	99.653	Hayduck-39
397	99.919	0.117	0.015	0.002	0.012	0.441	0.03	0.24	0.546	0.161	0.041	101.524	Hayduck-40
398	96.798	0.489	0.016	0.002	0	0.441	0	0.249	0.539	0.05	0.046	98.63	Hayduck-41
399	98.198	0.29	0.011	0	0	0.392	0.018	0.314	0.627	0.099	0.033	99.982	Hayduck-42
400	98.254	0.139	0.032	0.004	0	0.509	0.015	0.425	0.52	0.065	0.009	99.972	Hayduck-43
401	97.696	0.105	0.01	0	0	0.695	0.001	0.363	0.387	0.109	0.012	99.378	Hayduck-45
402	98.416	0.113	0.039	0.009	0	0.464	0.037	0.495	0.568	0.049	0.012	100.202	Hayduck-47
403	96.538	0.08	0.009	0	0.009	0.827	0.006	0.227	0.248	0.042	0.017	98.003	Hayduck-49
404	98.527	0.065	0.017	0	0.007	0.526	0.002	0.231	0.382	0.194	0.024	99.975	Hayduck-51
405	92.84	0.204	0.006	0.006	0.003	0.828	0	0.171	0.231	5.51	0.068	99.867	Hayduck-53
406	92.761	0.245	0.014	0.011	0	0.528	0	0.286	0.433	7.328	0.07	101.676	Hayduck-55
407	97.155	0.108	0.014	0.002	0.005	0.536	0.006	0.346	0.463	0.438	0.085	99.158	Hayduck-57
408	98.037	0.126	0.032	0.005	0	0.524	0.033	0.405	0.519	0.594	0.095	100.37	Hayduck-59
409	95.461	0.127	0.003	0	0.007	0.679	0.008	0.338	0.382	0.69	0.093	97.768	Hayduck-60
410	98.42	0.555	0.11	0.039	0.01	0.45	0.042	0.106	0.43	0	0.079	100.241	Line
411	97.636	0.521	0.104	0.041	0	0.423	0.049	0.163	0.425	0.001	0.072	99.435	Line
412	96.699	0.5	0.109	0.036	0	0.422	0.027	0.128	0.427	0	0.046	98.394	Line
413	98.222	0.439	0.115	0.048	0	0.434	0.026	0.088	0.42	0.002	0.026	99.82	Line
414	97.275	0.375	0.132	0.046	0	0.464	0.015	0.094	0.42	0.004	0.025	98.85	Line
415	97.315	0.288	0.118	0.046	0	0.47	0.019	0.121	0.423	0	0.019	98.819	Line
416	97.487	0.187	0.112	0.04	0	0.455	0.03	0.079	0.385	0.018	0.005	98.798	Line
417	96.486	0.721	0.078	0.034	0.002	0.474	0.021	0.09	0.377	0	0.128	98.411	Line
418	98.061	0.692	0.1	0.031	0	0.448	0.017	0.121	0.399	0.016	0.119	100.004	Line
419	98.435	0.627	0.083	0.04	0.007	0.437	0.044	0.133	0.401	0.014	0.078	100.299	Line
420	98.789	0.63	0.112	0.036	0.001	0.485	0.026	0.134	0.406	0.014	0.072	98.705	Line
421	97.695	0.609	0.114	0.039	0	0.472	0	0.122	0.408	0.007	0.073	99.539	Line
422	97.342	0.605	0.156	0.05	0.02	0.316	0.009	0.142	0.404	0.015	0.068	99.127	Line
423	96.042	0.595	0.138	0.047	0.004	0.429	0.028	0.083	0.419	0.017	0.05	97.852	Line
424	97.712	0.47	0.071	0.025	0.008	0.431	0.017	0.085	0.409	0.022	0.041	99.291	Line
425	95.918	0.423	0.07	0.025	0.01	0.394	0.019	0.099	0.396	0.006	0.025	97.385	Line
426	96.963	0.34	0.083	0.026	0.006	0.421	0.011	0.091	0.404	0.01	0.031	98.386	Line
427	97.409	0.29	0.071	0.027	0.009	0.425	0.033	0.124	0.404	0.021	0.017	98.83	Line
428	96.544	0.265	0.084	0.025	0	0.437	0.002	0.115	0.414	0.026	0.014	97.926	Line
429	97.543	0.235	0.078	0.027	0.007	0.444	0.035	0.135	0.41	0.015	0.018	98.947	Line
430	97.604	0.206	0.083	0.032	0.001	0.455	0.043	0.15	0.402	0.032	0.011	99.019	Line
431	97.66	0.158	0.13	0.038	0	0.456	0.042	0.134	0.423	0.034	0.007	99.082	Line
432	94.934	0.177	0.115	0.037	0	0.452	0.027	0.126	0.392	0.058	0.013	96.331	Line
433	96.201	0.172	0.059	0.017	0	0.486	0	0.046	0.318	0.097	0.007	97.403	Line
434	96.466	0.214	0.098	0.033	0.007	0.464	0.002	0.128	0.33	0.072	0.005	97.819	Line
435	96.18	0.21	0.126	0.05	0.007	0.462	0.04	0.117	0.377	0.044	0.03	97.643	Line
436	95.776	0.288	0.129	0.045	0	0.458	0.029	0.104	0.397	0.054	0.022	97.302	Line
437	96.581	0.326	0.126	0.047	0	0.476	0.032	0.11	0.386	0.039	0.021	98.144	Line
438	96.95	0.369	0.131	0.051	0.016	0.467	0.025	0.08	0.388	0.049	0.024	98.55	Line
439	96.617	0.446	0.125	0.046	0.006	0.458	0.039	0.124	0.399	0.032	0.036	98.328	Line

(*FeO represents total Fe oxide concentration, uncorrected for Fe₂O₃)

Table E-1 cont'd. Electron Microprobe data (wt%) for baddeleyite and zirconolite from sample JA HD-07 of the Duck Lake (Hayduck) sill, Slave craton - Analytical session 1.

No.	ZrO ₂	*FeO	UO ₂	PbO	ThO ₂	HfO ₂	Y ₂ O ₃	Nb ₂ O ₅	TiO ₂	SiO ₂	CaO	Total	Comment	
440	96.265	0.511	0.129	0.045	0.007	0.458	0.035	0.09	0.404	0.036	0.039	98.019	Line	8 Hayduck Sill
441	95.733	0.589	0.133	0.048	0.001	0.466	0.025	0.113	0.398	0.016	0.054	97.576	Line	9 Hayduck Sill
442	96.379	0.554	0.119	0.045	0.013	0.472	0.006	0.123	0.388	0.016	0.075	98.19	Line	10 Hayduck Sill
443	96.019	0.554	0.123	0.044	0.008	0.442	0.024	0.131	0.392	0.022	0.102	97.861	Line	11 Hayduck Sill
444	96.625	0.545	0.097	0.038	0.009	0.505	0.014	0.107	0.348	0.018	0.156	98.462	Line	12 Hayduck Sill
445	96.609	0.505	0.062	0.033	0.006	0.525	0	0.122	0.299	0.026	0.193	98.38	Line	13 Hayduck Sill
446	96.625	0.497	0.034	0.012	0.001	0.514	0.003	0.085	0.269	0.028	0.244	98.312	Line	14 Hayduck Sill
447	96.041	0.522	0.056	0.022	0	0.461	0	0.083	0.336	0.016	0.111	97.648	Hayduck	61
448	94.711	0.517	0.117	0.04	0.009	0.451	0.055	0.109	0.407	0.028	0.052	96.496	Hayduck	62
449	96.799	0.322	0.128	0.039	0	0.473	0.026	0.118	0.423	0.033	0.023	98.384	Hayduck	63
450	26.561	8.474	0.586	0.54	3.824	0.21	3.005	2.687	27.167	0.092	4.634	77.78	Hayduck	64
451	26.811	8.412	0.588	0.551	4.104	0.186	2.999	2.741	27.338	0.097	4.636	78.463	Hayduck	65
452	26.193	8.382	0.589	0.578	4.15	0.228	2.999	2.598	27.404	0.088	4.654	77.863	Hayduck	66
453	26.819	7.892	0.617	0.597	4.244	0.206	2.972	2.623	27.519	0.122	4.511	78.122	Hayduck	67
454	26.957	7.66	0.77	0.674	4.448	0.195	3.268	2.674	27.598	0.109	4.499	78.852	Hayduck	68
455	27.83	5.42	0.615	0.554	4.429	0.224	3.146	2.722	28.691	0.785	2.458	76.874	Hayduck	69
456	27.434	5.384	0.621	0.515	4.336	0.202	3.134	2.742	28.766	0.759	2.474	76.367	Hayduck	70
457	28.206	5.31	0.611	0.504	4.279	0.21	3.183	2.656	28.644	0.748	2.462	76.813	Hayduck	71
458	27.965	5.497	0.616	0.51	4.106	0.21	3.191	2.899	28.715	0.545	2.281	76.535	Hayduck	72
459	28.853	8.243	0.587	0.536	3.904	0.176	2.917	2.753	27.398	0.094	4.637	78.098	Hayduck	73
460	26.998	8.333	0.573	0.532	3.836	0.172	2.872	2.827	27.035	0.114	4.61	77.902	Hayduck	74
461	27.048	8.58	0.581	0.529	3.852	0.213	2.896	2.749	27.202	0.102	4.632	78.384	Hayduck	75
462	26.671	8.354	0.59	0.538	3.822	0.201	2.921	2.681	26.983	0.094	4.586	77.441	Hayduck	76
463	26.105	8.477	1.57	0.976	4.222	0.167	4.609	1.562	28.629	0.305	4.335	80.957	Hayduck	77 (zirconolite)
464	26.772	8.669	1.593	0.959	4.202	0.167	4.729	1.57	28.73	0.15	4.369	81.91	Hayduck	(zirconolite) 78
465	26.272	8.601	1.601	0.966	4.042	0.154	4.709	1.563	28.773	0.154	4.383	81.218	Hayduck	(zirconolite) 79
466	26.442	8.928	1.56	0.953	4.131	0.14	4.675	1.645	28.919	0.155	4.357	81.905	Hayduck	(zirconolite) 80
467	26.184	8.663	1.54	0.959	4.109	0.137	4.644	1.536	28.739	0.156	4.354	81.221	Hayduck	(zirconolite) 81
468	26.207	8.835	1.47	0.933	4.247	0.142	4.648	1.432	28.776	0.193	4.414	81.297	Hayduck	(zirconolite) 82
469	26.404	8.784	1.417	0.913	4.269	0.168	4.592	1.322	29.159	0.154	4.412	81.594	Hayduck	(zirconolite) 83
470	26.448	9.178	1.484	0.941	3.984	0.156	4.715	1.463	28.718	0.147	4.329	81.563	Hayduck	(zirconolite) 84
471	26.623	9.169	1.665	0.983	4.01	0.131	4.689	1.581	28.809	0.113	4.309	82.082	Hayduck	(zirconolite) 85
472	26.74	8.853	1.824	1.06	4.188	0.159	4.681	1.782	28.226	0.123	4.276	81.912	Hayduck	(zirconolite) 86
473	26.111	8.326	1.585	0.958	4.182	0.182	4.567	1.587	28.526	0.127	4.298	80.449	Hayduck	(zirconolite) 87
474	26.356	8.463	1.638	1.001	4.264	0.149	4.614	1.672	28.509	0.303	4.285	81.254	Hayduck	(zirconolite) 88
475	25.727	8.717	1.67	1.014	4.285	0.151	4.709	1.577	28.272	0.723	4.194	81.039	Hayduck	(zirconolite) 89
478	26	7.24	0.584	0.572	4.013	0.219	2.969	2.682	27.548	0.686	3.953	76.486	Hayduck	(zirconolite grain B) 90
479	26.903	8.808	0.583	0.594	3.961	0.216	2.918	2.672	27.482	0.108	4.637	78.882	Hayduck	(zirconolite grain B) 91
480	26.796	8.428	0.581	0.608	4.097	0.193	2.961	2.672	27.435	0.123	4.626	78.52	Hayduck	(zirconolite grain B) 92
481	26.403	8.42	0.598	0.617	4.14	0.233	2.954	2.682	27.459	0.133	4.612	78.251	Hayduck	(zirconolite grain B) 93
482	27.044	8.718	0.569	0.577	3.939	0.2	3.002	2.727	27.335	0.115	4.628	78.854	Hayduck	(zirconolite grain B) 94
483	26.73	8.534	0.581	0.582	3.854	0.185	2.99	2.739	27.27	0.142	4.619	78.226	Hayduck	(zirconolite grain B) 95
484	27.006	8.446	0.607	0.593	4.003	0.205	3.035	2.775	27.463	0.142	4.626	78.903	Hayduck	(zirconolite grain B) 96
485	27.187	8.503	0.587	0.6	4.128	0.205	2.959	2.707	27.464	0.158	4.641	79.139	Hayduck	(zirconolite grain B) 97
486	27.082	8.942	0.833	0.734	4.467	0.214	3.401	2.773	27.762	0.196	4.095	78.499	Hayduck	(zirconolite grain B) 98
487	26.448	7.103	0.618	0.608	4.235	0.215	3.04	2.684	27.259	0.416	4.457	77.083	Hayduck	(zirconolite grain B) 99
488	27.752	5.399	0.615	0.564	4.314	0.22	3.142	2.9	28.823	0.776	2.468	76.973	Hayduck	(zirconolite grain B) 100
489	26.688	4.255	1.584	0.728	5.969	0.385	5.186	2.669	26.993	4.376	2.266	81.099	Hayduck	(zirconolite grain B) 101
490	27.018	5.269	0.619	0.537	4.092	0.202	3.24	2.859	28.381	0.772	2.396	75.385	Hayduck	(zirconolite grain B) 102
491	23.277	7.237	1.034	0.37	3.616	0.224	3.712	1.796	22.534	10.457	1.699	75.956	Hayduck	(zirconolite grain B) 103
492	27.615	5.356	0.62	0.559	4.103	0.205	3.114	2.862	28.519	0.942	2.409	76.304	Hayduck	(zirconolite grain B) 104
493	26.708	6.549	0.586	0.52	3.89	0.204	2.989	2.774	27.791	1.067	3.121	76.199	Hayduck	(zirconolite grain B) 105
494	24.695	4.499	1.207	0.469	4.101	0.234	3.507	3.227	29.865	4.661	1.981	78.446	Hayduck	(zirconolite grain B) 106
495	28.195	5.411	0.621	0.525	4.105	0.219	3.185	2.921	28.931	0.581	2.274	76.968	Hayduck	(zirconolite grain B) 107
496	26.261	7.623	0.597	0.556	3.784	0.211	2.873	2.736	26.938	1.007	3.787	76.373	Hayduck	(zirconolite grain B) 108
497	26.169	8.044	0.582	0.552	3.751	0.222	2.876	2.797	26.815	0.748	4.319	76.875	Hayduck	(zirconolite grain B) 109
498	26.576	7.398	0.608	0.564	3.861	0.186	2.908	2.773	27.284	0.269	4.442	76.869	Hayduck	(zirconolite grain B) 110
499	27.007	8.58	0.583	0.576	3.8	0.217	2.983	2.878	26.954	0.137	4.583	78.298	Hayduck	(zirconolite grain B) 111
500	26.49	8.586	0.587	0.577	3.743	0.191	2.95	2.766	27.189	0.115	4.601	77.795	Hayduck	(zirconolite grain B) 112
501	27.14	7.572	0.58	0.574	3.869	0.216	2.954	2.817	27.604	0.201	4.565	78.092	Hayduck	(zirconolite grain B) 113
502	27.123	8.518	0.595	0.578	3.896	0.2	2.957	2.793	26.911	0.124	4.584	78.279	Hayduck	(zirconolite grain B) 114
503	26.809	8.756	0.59	0.598	3.965	0.206	2.983	2.731	27.203	0.17	4.626	78.637	Hayduck	(zirconolite grain B) 115
504	26.313	8.654	1.572	0.984	4.184	0.174	4.665	1.645	28.355	0.282	4.36	81.188	Hayduck	(zirconolite grain A) 116
505	26.424	8.852	1.579	0.981	4.123	0.182	4.594	1.674	28.653	0.193	4.357	81.612	Hayduck	(zirconolite grain A) 117
506	26.028	8.862	1.568	0.99	4.164	0.158	4.647	1.482	28.494	0.197	4.319	80.929	Hayduck	(zirconolite grain A) 118
507	26.295	8.876	1.446	0.94	4.291	0.157	4.577	1.36	29.023	0.182	4.427	81.574	Hayduck	(zirconolite grain A) 119
508	26.411	8.967	1.453	0.939	4.25	0.168	4.554	1.499	28.452	0.175	4.306	81.174	Hayduck	(zirconolite grain A) 120
509	26.057	8.921	1.531	0.974	4.103	0.16	4.592	1.538	28.637	0.16	4.357	81.03	Hayduck	(zirconolite grain A) 121
510	26.621	8.951	1.639	0.998	4.017	0.155	4.689	1.531	28.699	0.124	4.403	81.827	Hayduck	(zirconolite grain A) 122
511	26.61	8.775	1.694	1.022	3.942	0.154	4.674	1.462	28.703	0.146	4.344	81.526	Hayduck	(zirconolite grain A) 123
512	25.893	8.599	1.541	0.979	4.232	0.142	4.667	1.631	28.729	0.166	4.347	80.926	Hayduck	(zirconolite grain A) 124
513	28.269	8.478	1.616	0.984	4.213	0.154	4.535	1.576	27.82	0.171	4.147	81.963	Hayduck	(zirconolite grain A) 125
514	26.067	8.598	1.762	1.082	4.281	0.154	4.627	1.797	27.702	0.321	4.118	80.499	Hayduck	(zirconolite grain A) 126
515	25.679	8.699	1.773	1.069	4.371	0.148	4.689	1.881	27.589	1.019	4.015	80.922	Hayduck	(zirconolite grain A) 127
516	24.898	8.497	1.675	1.032	4.352	0.155	4.356	1.795	26.876	2.813	3.941	80.39	Hayduck	(zirconolite grain A) 128
517	24.341	8.618	1.542	0.969	4.054	0.163	4.282	1.667	27.1	3.225	3.994	79.955	Hayduck	(zirconolite grain A) 129
518	24.574	8.462	1.577	0.965	4.201	0.136	4.374	1.591	26.78	3.887	3.953	80.5	Hayduck	(zirconolite grain A) 130

(*FeO represents total Fe oxide concentration, uncorrected for Fe₂O₃)

Table E-2. Electron Microprobe data (wt%) for zirconolite from sample JA HD-07 of the Duck Lake (Hayduck) sill, Slave craton - Analytical session 2.

No.	SiO ₂	*FeO	UO ₂	PtO	P ₂ O ₅	HfO ₂	Y ₂ O ₃	ZrO ₂	CaO	Sm ₂ O ₃	La ₂ O ₃	Dy ₂ O ₃	TiO ₂	Gd ₂ O ₃	Er ₂ O ₃	Yb ₂ O ₃	Ta ₂ O ₅	Total	Comment	UO ₂ *	t (Ma)					
52	0.227	8.602	1.566	0.998	0	0.174	4.686	26.28	3.257	1.508	4.148	4.351	0.677	4.372	0.44	0.342	28.33	1.534	0.241	0.364	0.151	96.781	JA-HD-07-3	2.685	2166	
53	0.214	8.92	1.584	1.014	0	0.155	4.647	29.22	3.291	1.414	4.125	4.243	0.714	4.472	0.451	0.366	28.34	1.559	0.224	0.363	0.128	96.766	JA-HD-07-4	2.67	2201	
54	0.189	9.172	1.637	1.026	0	0.148	4.869	29.62	3.301	1.535	4.122	4.153	0.665	4.426	0.421	0.4	28.55	1.621	0.267	0.283	0.118	97.903	JA-HD-07-5	2.7	2202	
55	0.329	9.223	1.54	0.983	0	0.158	4.704	29.34	3.345	1.409	4.244	4.444	0.814	4.444	0.334	0.461	0.307	28.48	1.471	0.263	0.429	0.134	97.686	JA-HD-07-6	2.637	2170
56	0.231	8.979	1.449	0.976	0	0.171	4.548	29.3	3.49	1.174	4.369	4.328	0.706	4.444	0.353	0.483	0.382	28.55	1.373	0.272	0.354	0.121	97.042	JA-HD-07-7	2.565	2210
57	0.385	8.978	1.515	1.01	0	0.161	4.665	28.85	3.54	1.192	4.171	4.498	0.793	4.306	0.466	0.336	0.26	28.21	1.537	0.248	0.386	0.094	96.675	JA-HD-07-8	2.667	2186
58	23.86	7.193	1.072	0.71	0	0.143	3.344	23.36	2.606	0.892	3.062	3.632	0.467	2.759	0.37	0.33	0.286	20.26	1.537	0.295	0.168	0.037	96.278	JA-HD-07-9	2.016	2078
59	8.279	8.477	1.369	0.886	0	0.168	4.398	27.58	3.194	1.149	3.966	4.209	0.639	3.823	1.278	0.463	0.353	26.08	1.342	0.293	0.381	0.037	98.393	JA-HD-07-10	2.458	2115
60	1.387	9.204	1.519	0.991	0	0.168	4.702	28.93	3.473	1.528	4.169	4.425	0.802	4.27	1.32	0.474	0.38	28.12	1.527	0.275	0.352	0.156	98.168	JA-HD-07-11	2.458	2115
61	30.31	7.338	0.959	0.642	0	0.135	3.612	21.69	2.463	0.99	2.942	3.249	0.466	2.99	0.882	0.325	0.254	20.9	1.089	0.201	0.266	0.227	101.92	JA-HD-07-12	2.686	2172
62	67.8	7.314	0.238	0.141	0	0.035	0.729	5.878	0.599	0.296	0.611	0.791	0.117	0.92	0.18	0.086	0.057	4.953	0.179	0.031	0.092	0.009	91.058	JA-HD-07-13	1.801	2097
63	70.04	3.539	0.313	0.196	0	0.03	1.08	7.945	0.713	0.334	0.87	1.115	0.144	0.876	0.268	0.084	0.068	6.577	0.187	0.064	0.052	0.06	94.537	JA-HD-07-14	Stage drifted	
64	75.74	2.409	0.245	0.14	0	0.03	0.881	6.177	0.562	0.254	0.626	0.837	0.079	0.596	0.136	0.07	0.058	4.63	0.177	0.054	0.024	0.052	93.775	JA-HD-07-15	Stage drifted	
141	0.288	8.976	1.587	1.012	0	0.164	4.702	29.95	3.286	1.261	4.26	4.27	0.717	4.447	1.295	0.449	0.758	28.51	1.616	0.592	0.348	0.076	98.569	JA-HD-07(A)-1	2.681	2191
142	0.268	8.713	1.655	1.036	0	0.135	4.833	29.83	3.326	1.156	4.172	4.193	0.56	4.379	1.301	0.461	0.758	28.43	1.631	0.671	0.416	0.171	97.99	JA-HD-07(A)-2	2.728	2201
143	0.228	8.897	1.757	1.064	0	0.15	4.862	29.89	3.355	1.316	4.097	4.206	0.743	4.408	1.362	0.422	0.919	28.48	1.639	0.636	0.404	0.128	98.962	JA-HD-07(A)-3	2.636	2181
144	0.25	9.127	1.7	1.036	0	0.156	4.691	29.88	3.333	1.232	4.154	4.114	0.653	4.391	1.328	0.418	0.954	28.65	1.524	0.582	0.327	0.148	98.649	JA-HD-07(A)-4	2.765	2185
145	0.253	8.954	1.641	1.025	0	0.139	4.721	29.98	3.276	1.041	4.308	4.243	0.71	4.447	1.378	0.431	0.813	28.58	1.55	0.595	0.414	0.166	98.665	JA-HD-07(A)-5	2.759	2182
147	0.371	8.933	1.482	0.992	0	0.176	4.799	29.87	3.56	0.915	4.186	4.385	0.748	4.482	1.416	0.478	0.793	28.6	1.497	0.602	0.313	0.199	98.789	JA-HD-07(A)-7	2.604	2206
148	0.424	9.265	1.522	0.98	0	0.155	4.669	29.83	3.348	0.909	4.28	4.26	0.705	4.441	1.394	0.47	0.806	28.58	1.42	0.555	0.364	0.129	98.609	JA-HD-07(A)-8	2.615	2179
149	0.137	8.307	1.202	0.632	0	0.129	4.903	30.81	3.202	1.516	4.205	3.26	0.767	4.034	1.399	0.412	0.933	28.11	1.418	0.591	0.378	0.065	96.407	JA-HD-07(E)-1	2.071	1858
150	0.186	8.437	1.34	0.692	0	0.131	4.797	30.97	3.28	1.449	4.216	3.385	0.558	3.887	1.365	0.398	0.926	28.1	1.638	0.634	0.357	0.185	96.964	JA-HD-07(E)-2	2.241	1876
151	0.213	8.673	1.256	0.643	0	0.136	4.908	30.77	3.199	1.84	4.17	3.301	0.778	3.706	1.442	0.408	0.962	27.84	1.499	0.543	0.388	0.195	96.868	JA-HD-07(E)-3	2.198	1837
152	0.15	8.083	1.095	0.571	0	0.137	4.641	31.1	3.262	1.757	4.202	3.072	0.659	3.599	1.402	0.398	0.938	27.81	1.469	0.656	0.381	0.098	96.469	JA-HD-07(E)-4	1.917	1822
153	0.15	8.93	1.181	0.621	0	0.122	4.946	30.94	3.214	1.829	4.16	3.222	0.767	3.622	1.333	0.435	0.892	28.11	1.521	0.5	0.463	0.122	97.068	JA-HD-07(E)-5	2.043	1826
154	0.165	8.823	1.216	0.621	0	0.137	4.827	30.7	3.12	1.652	4.2	3.186	0.611	3.668	1.366	0.43	0.917	28.38	1.428	0.508	0.443	0	96.4	JA-HD-07(E)-6	2.068	1835
155	0.165	8.331	1.32	0.68	0	0.123	4.928	30.4	3.2	1.7	4.225	3.277	0.706	3.762	1.336	0.409	0.965	28.23	1.574	0.6	0.381	0.093	96.418	JA-HD-07(E)-7	2.191	1884
156	0.17	9.054	1.334	0.679	0	0.144	4.829	31.05	3.284	1.662	4.279	3.345	0.865	3.698	1.39	0.44	0.957	28.08	1.61	0.565	0.428	0.233	98.085	JA-HD-07(E)-8	2.226	1858
157	0.217	8.896	1.374	0.678	0	0.162	4.961	30.81	3.318	1.518	4.324	3.381	0.837	3.588	1.374	0.46	1.004	28.04	1.576	0.564	0.417	0.135	97.634	JA-HD-07(E)-9	2.279	1821
158	0.254	8.748	1.38	0.662	0	0.16	5.009	30.78	3.325	1.457	4.324	3.443	0.691	3.584	1.347	0.441	0.913	28.22	1.434	0.57	0.451	0.125	97.338	JA-HD-07(E)-10	2.302	1815
159	0.419	8.39	1.455	0.728	0	0.131	5.095	30.86	3.247	1.552	4.306	3.616	0.714	3.745	1.374	0.415	0.963	28.23	1.682	0.627	0.438	0.259	98.244	JA-HD-07(E)-11	2.421	1837
160	0.374	8.608	1.44	0.743	0	0.146	4.768	31.25	3.377	1.689	4.246	3.528	0.665	3.928	1.411	0.393	0.944	28.32	1.388	0.617	0.373	0.047	98.232	JA-HD-07(E)-12	2.377	1894

(*FeO represents total Fe oxide concentration, uncorrected for Fe₂O₃)

Table E-3. Electron Microprobe chemical data (wt%) for zirconolite from the Phalaborwa carbonate, South Africa.

No.	NiO	SiO ₂	ZrO ₂	HfO ₂	MO ₂	La ₂ O ₃	CeO ₂	Pr ₂ O ₃	Nd ₂ O ₃	Sm ₂ O ₃	Gd ₂ O ₃	Er ₂ O ₃	Dy ₂ O ₃	Y ₂ O ₃	Yb ₂ O ₃	K ₂ O	K ₂ O	ThO ₂	UO ₂	PaO	Total	Comment	(Mg)
44	0.05	0.82	34.32	0.135	33.477	6.263	0.003	0.003	0.003	0.003	0.003	0.003	0.003	0.003	0.003	0.003	0.003	0.003	0.003	0.003	0.003	0.003	2042
45	0.684	0.045	33.888	0.2	33.32	7.066	0.137	1.902	0.211	1.531	0.419	0.399	0.066	0.468	0.10	10.64	6.336	1.824	1.824	1.824	1.824	96.114	Phalaborwa zircono 1
46	0.741	0.046	33.48	0.126	33.27	7.066	0.002	0.176	0.263	1.145	0.372	0.449	0.044	0.068	0.423	0	0.165	0.115	6.416	1.26	1.353	96.656	Line 3 LINEA Phala zircono
47	0.655	0.026	33.086	0.137	33.329	7.203	0.02	0.65	0.176	1.086	0.453	0.257	0.065	0.426	0	10.203	0.104	6.441	2.206	2.206	2.206	96.396	Line 4 LINEA Phala zircono
48	0.815	0.054	33.194	0.172	32.998	6.916	0.028	0.083	0.075	1.199	0.451	0.437	0.147	0.023	0.847	0	10.203	0.104	6.441	2.206	2.206	96.396	Line 6 LINEA Phala zircono
49	0.719	0.054	33.194	0.172	32.998	6.916	0.028	0.083	0.075	1.199	0.451	0.437	0.147	0.023	0.847	0	10.203	0.104	6.441	2.206	2.206	96.396	Line 8 LINEA Phala zircono
50	0.684	0.033	33.411	0.18	33.269	7.947	0.023	0.927	0.222	1.321	0.45	0.413	0.201	0.056	0.979	0	9.934	0.153	6.13	2.142	1.73	96.516	Line 9 LINEA Phala zircono
51	0.684	0.033	33.411	0.18	33.269	7.947	0.023	0.927	0.222	1.321	0.45	0.413	0.201	0.056	0.979	0	9.934	0.153	6.13	2.142	1.73	96.516	Line 11 LINEA Phala zircono
52	0.684	0.033	33.411	0.18	33.269	7.947	0.023	0.927	0.222	1.321	0.45	0.413	0.201	0.056	0.979	0	9.934	0.153	6.13	2.142	1.73	96.516	Line 12 LINEA Phala zircono
53	0.684	0.033	33.411	0.18	33.269	7.947	0.023	0.927	0.222	1.321	0.45	0.413	0.201	0.056	0.979	0	9.934	0.153	6.13	2.142	1.73	96.516	Line 14 LINEA Phala zircono
54	0.684	0.033	33.411	0.18	33.269	7.947	0.023	0.927	0.222	1.321	0.45	0.413	0.201	0.056	0.979	0	9.934	0.153	6.13	2.142	1.73	96.516	Line 16 LINEA Phala zircono
55	0.684	0.033	33.411	0.18	33.269	7.947	0.023	0.927	0.222	1.321	0.45	0.413	0.201	0.056	0.979	0	9.934	0.153	6.13	2.142	1.73	96.516	Line 18 LINEA Phala zircono
56	0.684	0.033	33.411	0.18	33.269	7.947	0.023	0.927	0.222	1.321	0.45	0.413	0.201	0.056	0.979	0	9.934	0.153	6.13	2.142	1.73	96.516	Line 20 LINEA Phala zircono
57	0.684	0.033	33.411	0.18	33.269	7.947	0.023	0.927	0.222	1.321	0.45	0.413	0.201	0.056	0.979	0	9.934	0.153	6.13	2.142	1.73	96.516	Line 22 LINEA Phala zircono
58	0.684	0.033	33.411	0.18	33.269	7.947	0.023	0.927	0.222	1.321	0.45	0.413	0.201	0.056	0.979	0	9.934	0.153	6.13	2.142	1.73	96.516	Line 24 LINEA Phala zircono
59	0.684	0.033	33.411	0.18	33.269	7.947	0.023	0.927	0.222	1.321	0.45	0.413	0.201	0.056	0.979	0	9.934	0.153	6.13	2.142	1.73	96.516	Line 26 LINEA Phala zircono
60	0.684	0.033	33.411	0.18	33.269	7.947	0.023	0.927	0.222	1.321	0.45	0.413	0.201	0.056	0.979	0	9.934	0.153	6.13	2.142	1.73	96.516	Line 28 LINEA Phala zircono
61	0.684	0.033	33.411	0.18	33.269	7.947	0.023	0.927	0.222	1.321	0.45	0.413	0.201	0.056	0.979	0	9.934	0.153	6.13	2.142	1.73	96.516	Phalaborwa zircono 2
62	0.571	0.035	34.036	0.151	33.173	6.311	0.074	0.885	0.259	1.247	0.439	0.364	0.06	0.027	0.469	0	10.24	0.07	6.288	2.771	1.29	96.261	Phalaborwa zircono 3
63	0.571	0.035	34.036	0.151	33.173	6.311	0.074	0.885	0.259	1.247	0.439	0.364	0.06	0.027	0.469	0	10.24	0.07	6.288	2.771	1.29	96.261	Phalaborwa zircono 4
64	0.571	0.035	34.036	0.151	33.173	6.311	0.074	0.885	0.259	1.247	0.439	0.364	0.06	0.027	0.469	0	10.24	0.07	6.288	2.771	1.29	96.261	Phalaborwa zircono 5
65	0.571	0.035	34.036	0.151	33.173	6.311	0.074	0.885	0.259	1.247	0.439	0.364	0.06	0.027	0.469	0	10.24	0.07	6.288	2.771	1.29	96.261	Phalaborwa zircono 6
66	0.571	0.035	34.036	0.151	33.173	6.311	0.074	0.885	0.259	1.247	0.439	0.364	0.06	0.027	0.469	0	10.24	0.07	6.288	2.771	1.29	96.261	Phalaborwa zircono 7
67	0.571	0.035	34.036	0.151	33.173	6.311	0.074	0.885	0.259	1.247	0.439	0.364	0.06	0.027	0.469	0	10.24	0.07	6.288	2.771	1.29	96.261	Phalaborwa zircono 8
68	0.571	0.035	34.036	0.151	33.173	6.311	0.074	0.885	0.259	1.247	0.439	0.364	0.06	0.027	0.469	0	10.24	0.07	6.288	2.771	1.29	96.261	Phalaborwa zircono 9
69	0.571	0.035	34.036	0.151	33.173	6.311	0.074	0.885	0.259	1.247	0.439	0.364	0.06	0.027	0.469	0	10.24	0.07	6.288	2.771	1.29	96.261	Phalaborwa zircono 10
70	0.571	0.035	34.036	0.151	33.173	6.311	0.074	0.885	0.259	1.247	0.439	0.364	0.06	0.027	0.469	0	10.24	0.07	6.288	2.771	1.29	96.261	Phalaborwa zircono 11
71	0.571	0.035	34.036	0.151	33.173	6.311	0.074	0.885	0.259	1.247	0.439	0.364	0.06	0.027	0.469	0	10.24	0.07	6.288	2.771	1.29	96.261	Phalaborwa zircono 12
72	0.571	0.035	34.036	0.151	33.173	6.311	0.074	0.885	0.259	1.247	0.439	0.364	0.06	0.027	0.469	0	10.24	0.07	6.288	2.771	1.29	96.261	Phalaborwa zircono 13
73	0.571	0.035	34.036	0.151	33.173	6.311	0.074	0.885	0.259	1.247	0.439	0.364	0.06	0.027	0.469	0	10.24	0.07	6.288	2.771	1.29	96.261	Phalaborwa zircono 14
74	0.571	0.035	34.036	0.151	33.173	6.311	0.074	0.885	0.259	1.247	0.439	0.364	0.06	0.027	0.469	0	10.24	0.07	6.288	2.771	1.29	96.261	Phalaborwa zircono 15
75	0.571	0.035	34.036	0.151	33.173	6.311	0.074	0.885	0.259	1.247	0.439	0.364	0.06	0.027	0.469	0	10.24	0.07	6.288	2.771	1.29	96.261	Phalaborwa zircono 16
76	0.571	0.035	34.036	0.151	33.173	6.311	0.074	0.885	0.259	1.247	0.439	0.364	0.06	0.027	0.469	0	10.24	0.07	6.288	2.771	1.29	96.261	Phalaborwa zircono 17
77	0.571	0.035	34.036	0.151	33.173	6.311	0.074	0.885	0.259	1.247	0.439	0.364	0.06	0.027	0.469	0	10.24	0.07	6.288	2.771	1.29	96.261	Phalaborwa zircono 18
78	0.571	0.035	34.036	0.151	33.173	6.311	0.074	0.885	0.259	1.247	0.439	0.364	0.06	0.027	0.469	0	10.24	0.07	6.288	2.771	1.29	96.261	Phalaborwa zircono 19
79	0.571	0.035	34.036	0.151	33.173	6.311	0.074	0.885	0.259	1.247	0.439	0.364	0.06	0.027	0.469	0	10.24	0.07	6.288	2.771	1.29	96.261	Phalaborwa zircono 20
80	0.571	0.035	34.036	0.151	33.173	6.311	0.074	0.885	0.259	1.247	0.439	0.364	0.06	0.027	0.469	0	10.24	0.07	6.288	2.771	1.29	96.261	Phalaborwa zircono 21
81	0.571	0.035	34.036	0.151	33.173	6.311	0.074	0.885	0.259	1.247	0.439	0.364	0.06	0.027	0.469	0	10.24	0.07	6.288	2.771	1.29	96.261	Phalaborwa zircono 22
82	0.571	0.035	34.036	0.151	33.173	6.311	0.074	0.885	0.259	1.247	0.439	0.364	0.06	0.027	0.469	0	10.24	0.07	6.288	2.771	1.29	96.261	Phalaborwa zircono 23
83	0.571	0.035	34.036	0.151	33.173	6.311	0.074	0.885	0.259	1.247	0.439	0.364	0.06	0.027	0.469	0	10.24	0.07	6.288	2.771	1.29	96.261	Phalaborwa zircono 24
84	0.571	0.035	34.036	0.151	33.173	6.311	0.074	0.885	0.259	1.247	0.439	0.364	0.06	0.027	0.469	0	10.24	0.07	6.288	2.771	1.29	96.261	Phalaborwa zircono 25
85	0.571	0.035	34.036	0.151	33.173	6.311	0.074	0.885	0.259	1.247	0.439	0.364	0.06	0.027	0.469	0	10.24	0.07	6.288	2.771	1.29	96.261	Phalaborwa zircono 26
86	0.571	0.035	34.036	0.151	33.173	6.311	0.074	0.885	0.259	1.247	0.439	0.364	0.06	0.027	0.469	0	10.24	0.07	6.288	2.771	1.29	96.261	Phalaborwa zircono 27
87	0.571	0.035	34.036	0.151	33.173	6.311	0.074	0.885	0.259	1.247	0.439	0.364	0.06	0.027	0.469	0	10.24	0.07	6.288	2.771	1.29	96.261	Phalaborwa zircono 28
88	0.571	0.035	34.036	0.151	33.173	6.311	0.074	0.885	0.259	1.247	0.439	0.364	0.06	0.027	0.469	0	10.24	0.07	6.288	2.771	1.29	96.261	Phalaborwa zircono 29
89	0.571	0.035	34.036	0.151	33.173	6.311	0.074	0.885	0.259	1.247	0.439	0.364	0.06	0.027	0.469	0	10.24	0.07	6.288	2.771	1.29	96.261	Phalaborwa zircono 30
90	0.571	0.035	34.036	0.151	33.173	6.311	0.074	0.885	0.259	1.247	0.439	0.364	0.06	0.027	0.469	0	10.24	0.07	6.288	2.771	1.29	96.261	Phalaborwa zircono 31
91	0.571	0.035	34.036	0.151	33.173	6.311	0.074	0.885	0.259	1.247	0.439	0.364	0.06	0.027	0.469	0	10.24	0.07	6.288	2.771	1.29	96.261	Phalaborwa zircono 32
92	0.571	0.035	34.036	0.151	33.173	6.311	0.074	0.885	0.259	1.247	0.439	0.364	0.06	0.027	0.469	0	10.24	0.07	6.288	2.771	1.29	96.261	Phalaborwa zircono 33
93	0.571	0.035	34.036	0																			

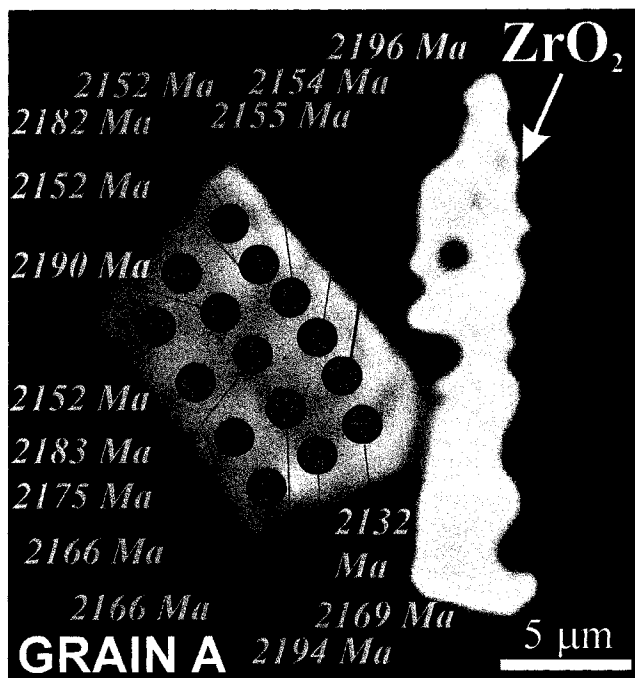
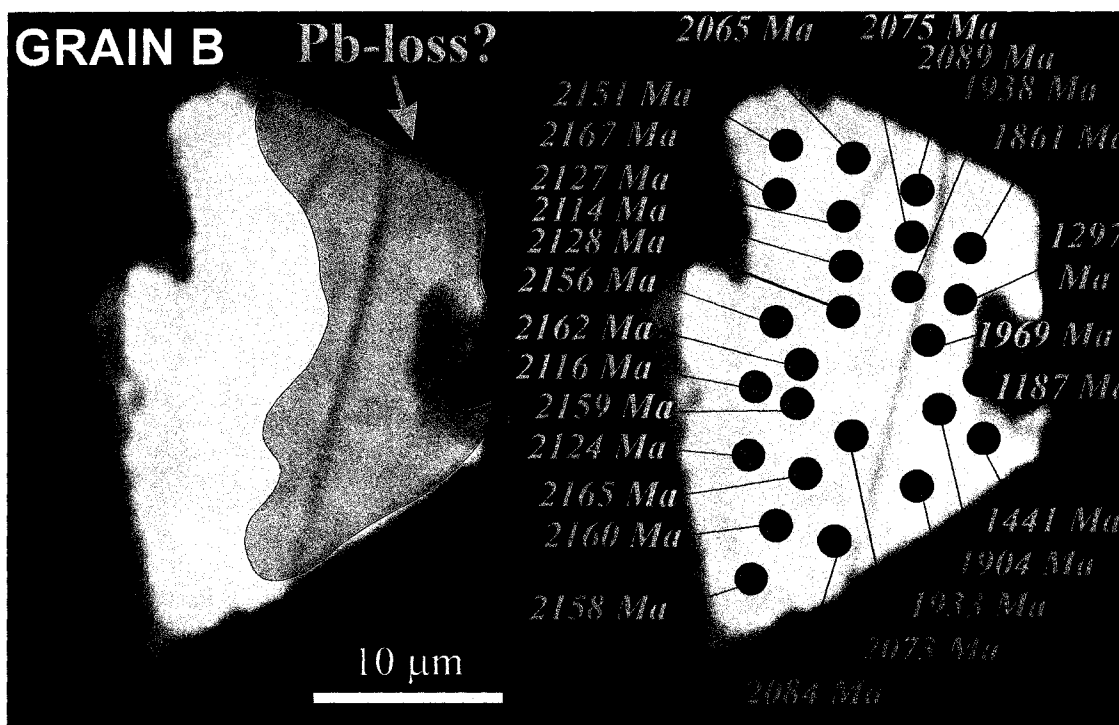


Fig. E-1. Context of EM apparent ages determined on zirconolite from the Duck Lake sill (JA HD-07) during analytical session 1. Notable features are the spatial association of zirconolite with baddeleyite (see petrographic context of these crystals in Fig. E-2), and a significant decrease in apparent ages for Grain B in the vicinity of visible fractures suggesting associated localized Pb-loss. See plots of UO_2^* (wt.%) versus PbO (wt.%) and chemical isochron ages for these grains in Figs. E-5 to E-7.



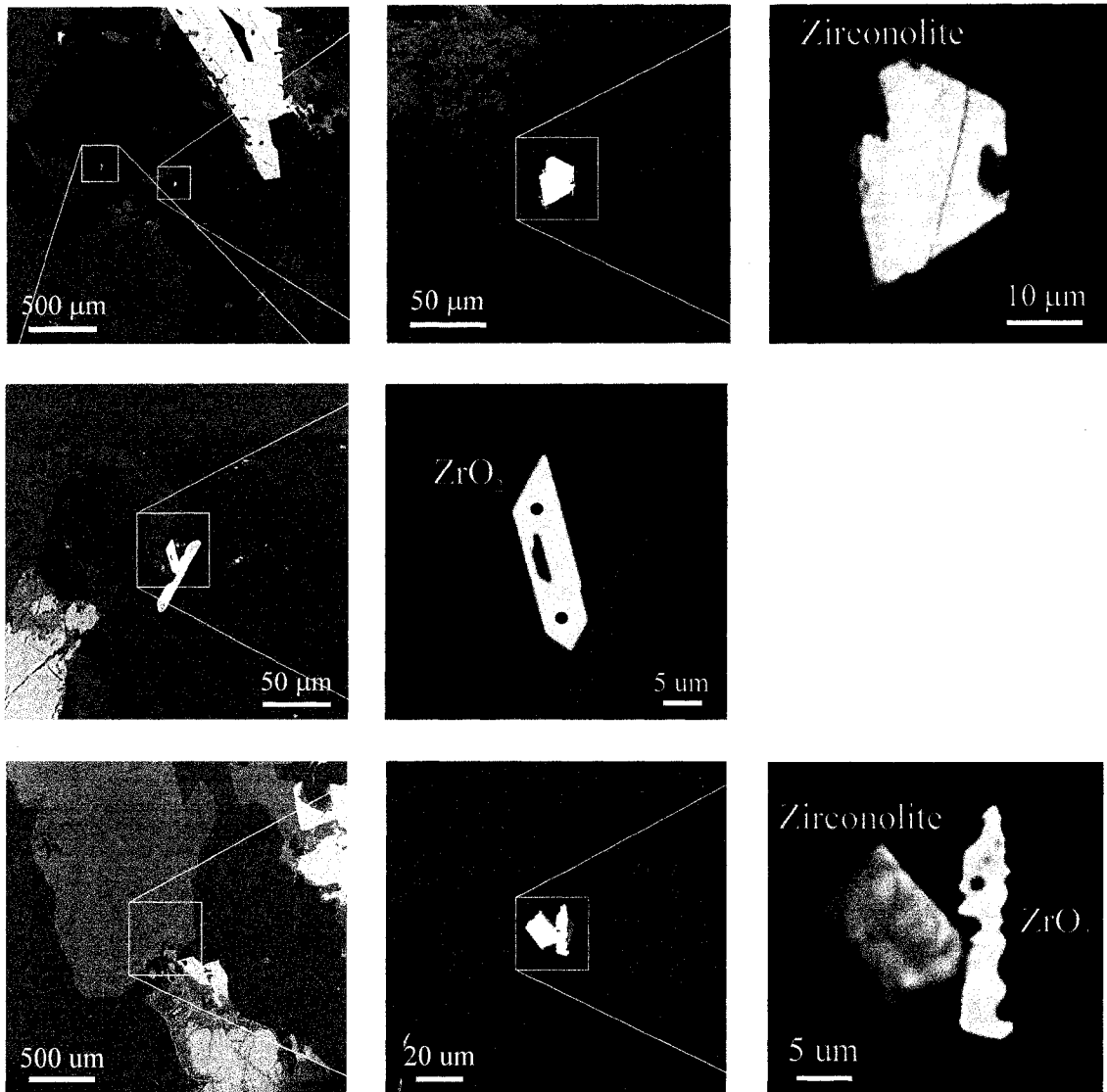


Fig. E-2. BSE images of zirconolite and baddeleyite from sample JA HD-07 of the Duck Lake sill. Blue dots correspond to the locations of EM baddeleyite analyses used in construction of the chemical isochron plot (Fig. E-4).

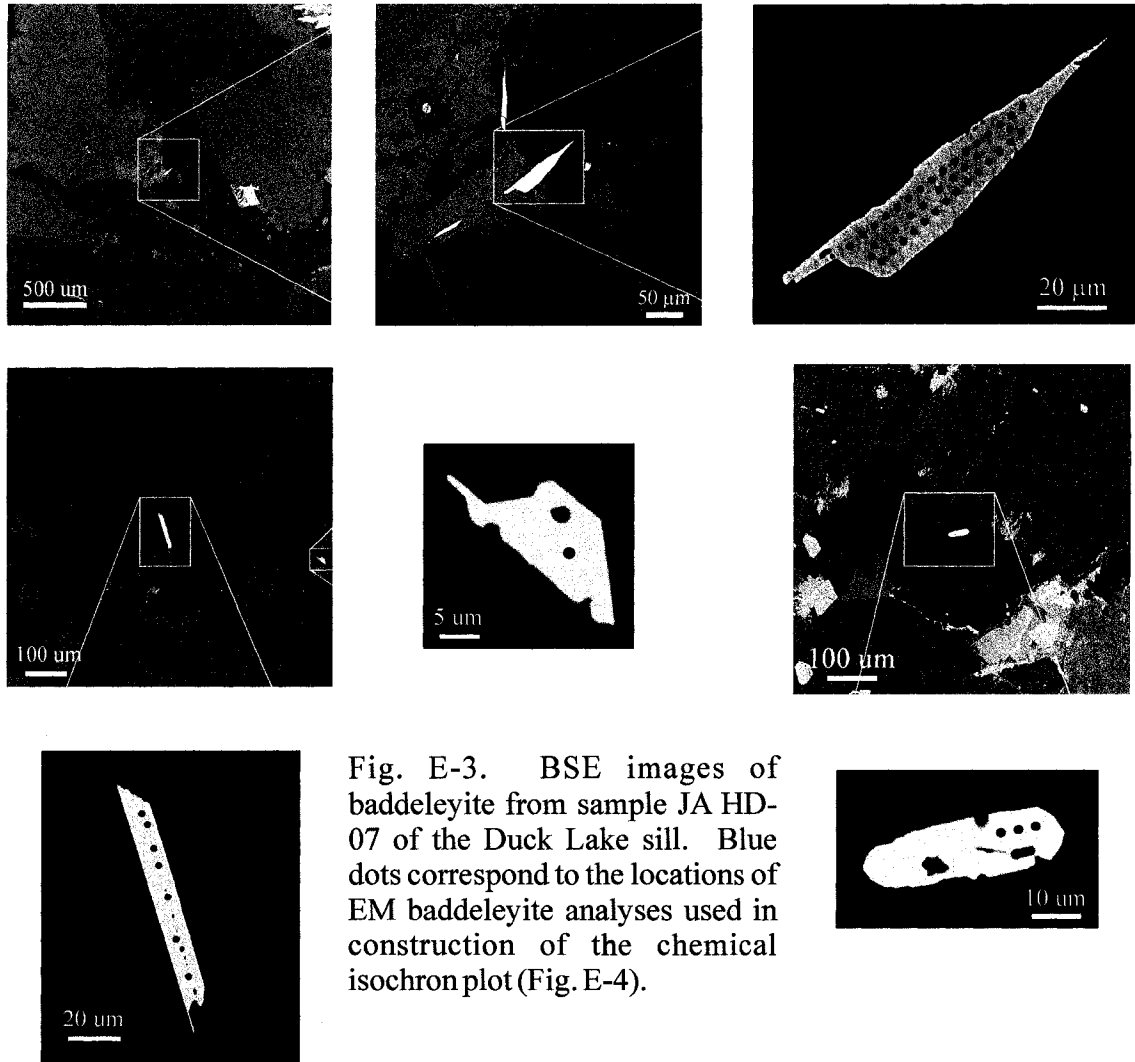


Fig. E-3. BSE images of baddeleyite from sample JA HD-07 of the Duck Lake sill. Blue dots correspond to the locations of EM baddeleyite analyses used in construction of the chemical isochron plot (Fig. E-4).

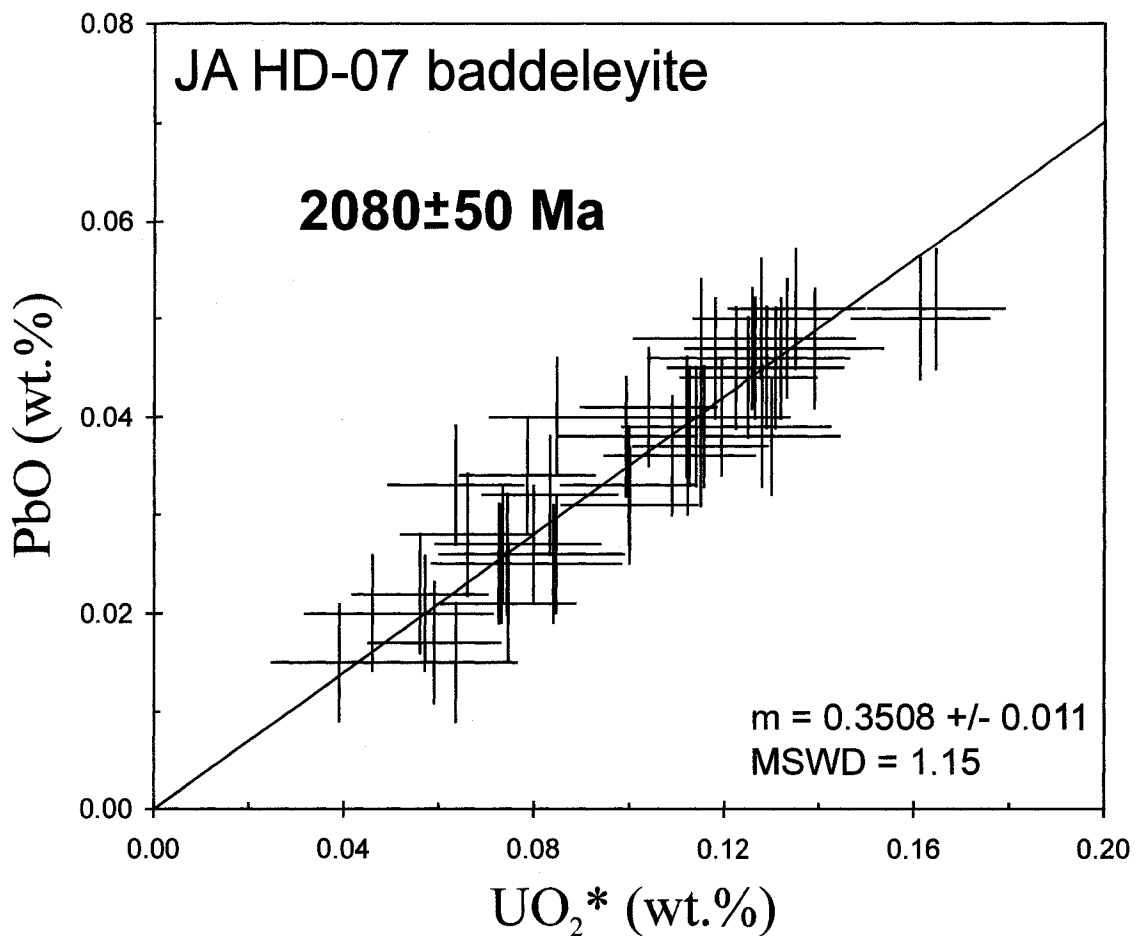


Fig. E-4. Chemical isochron plot showing EM baddeleyite data (session 1) for the Duck Lake sill. Error bars correspond to 2σ analytical uncertainty and the error on the final age is reported at 2σ . The isochron is anchored to the origin using a fictive data point with no associated data-point errors. Chemical data listed in Table E-1.

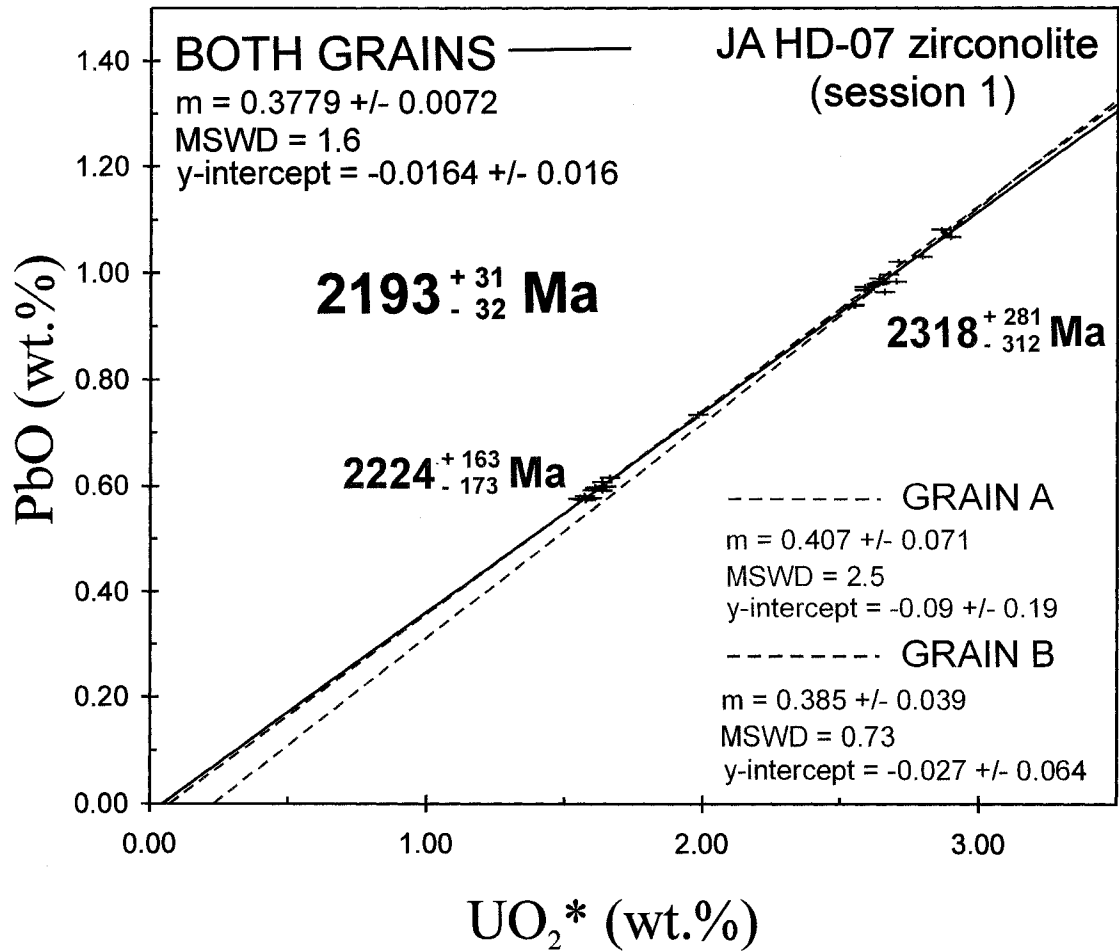


Fig. E-5. Chemical isochron plot showing EM zirconolite data (session 1) for the Duck Lake sill. Anomalously young ages for Grain B (Fig. E-1) are excluded (see Fig. E-6 for all Grain B data). Error bars correspond to 2σ analytical uncertainty and the error on the final ages are reported at 2σ . The isochrons are not anchored to the origin. Chemical data listed in Table E-1.

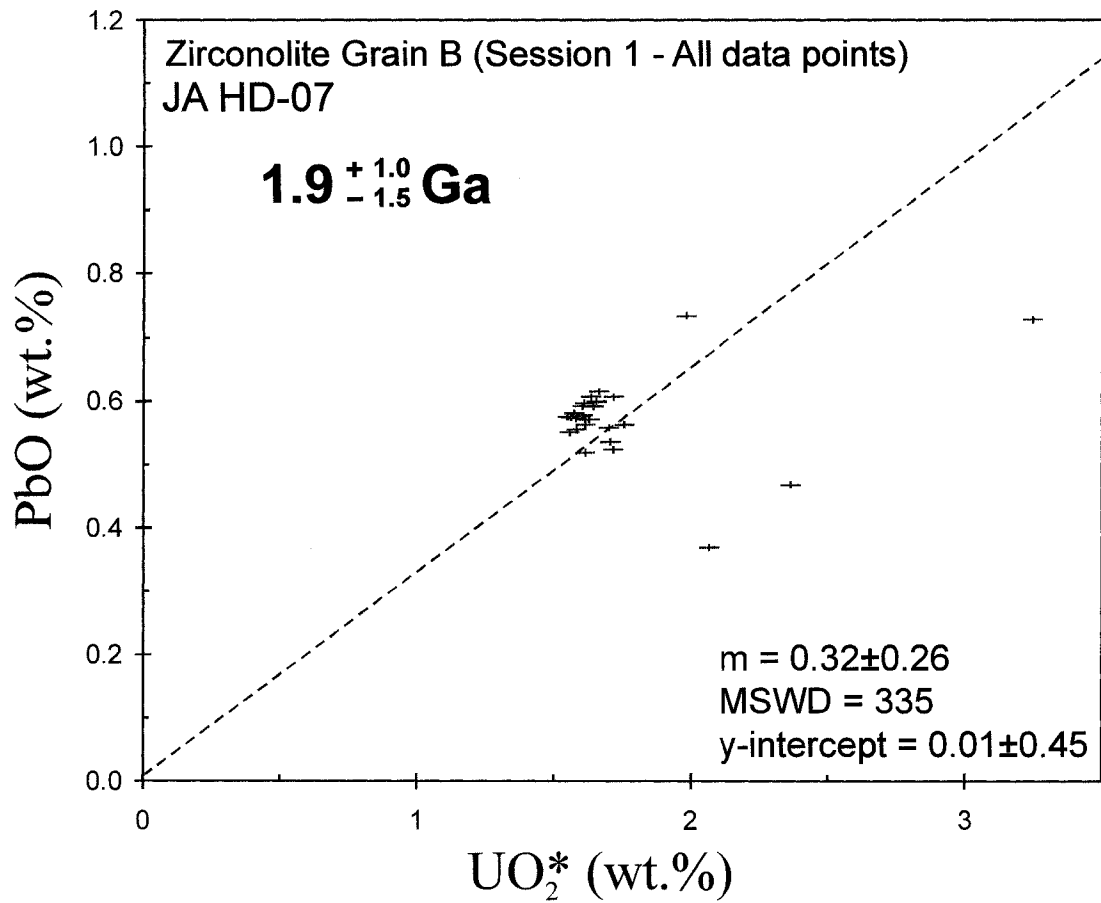


Fig. E-6. Chemical isochron (errorchron) plot showing all EM zirconolite data (session 1) for zirconolite Grain B (Fig. E-1) of the Duck Lake sill. Error bars correspond to 2σ analytical uncertainty and the error on the final age is reported at 2σ . The isochron is not anchored to the origin. Chemical data listed in Table E-1.

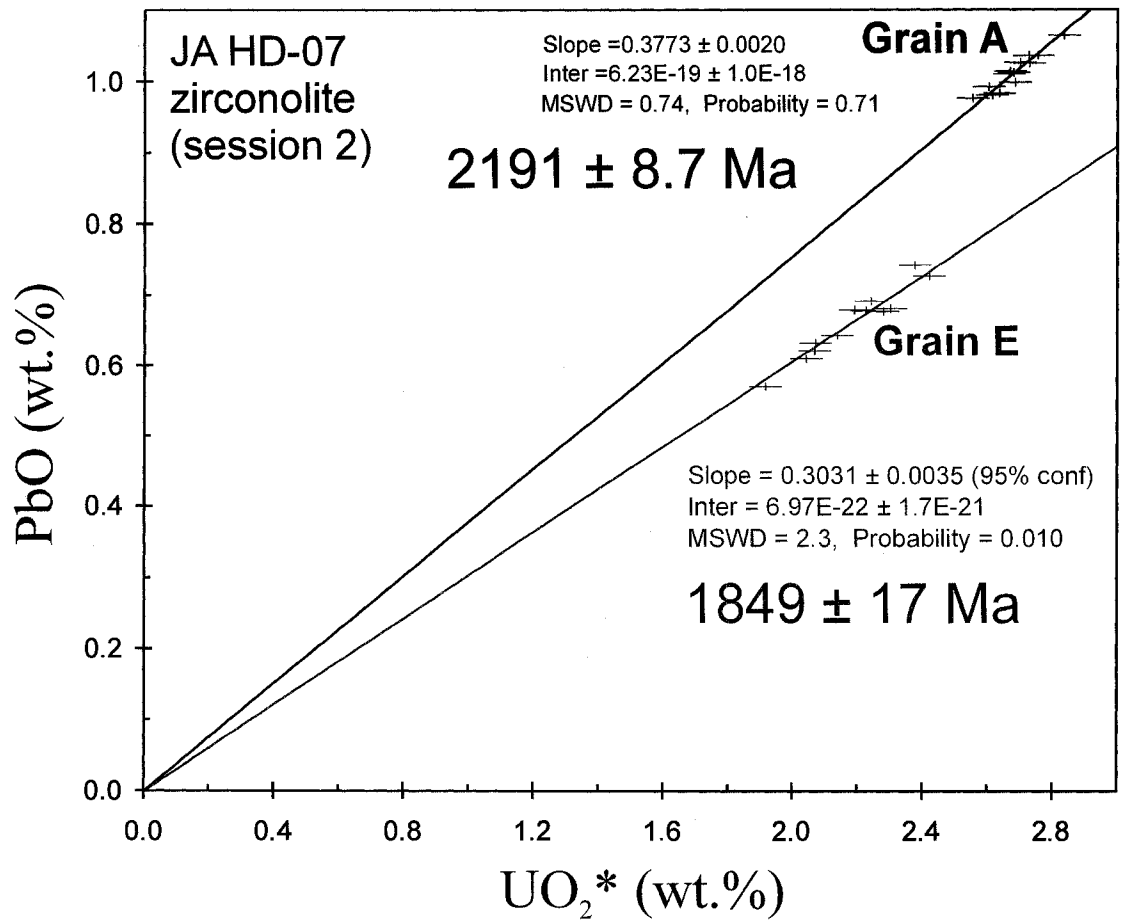


Fig. E-7. Chemical isochron plot showing EM zirconolite data (session 2) for the Duck Lake sill. Error bars correspond to 2σ analytical uncertainty and the error on the final ages are reported at 2σ . The isochrons are anchored to the origin using a fictive data-point with no associated data-point error. Chemical data listed in Table E-2. Grain A corresponds to the same Grain A analysed during session 1 (Fig. E-1).

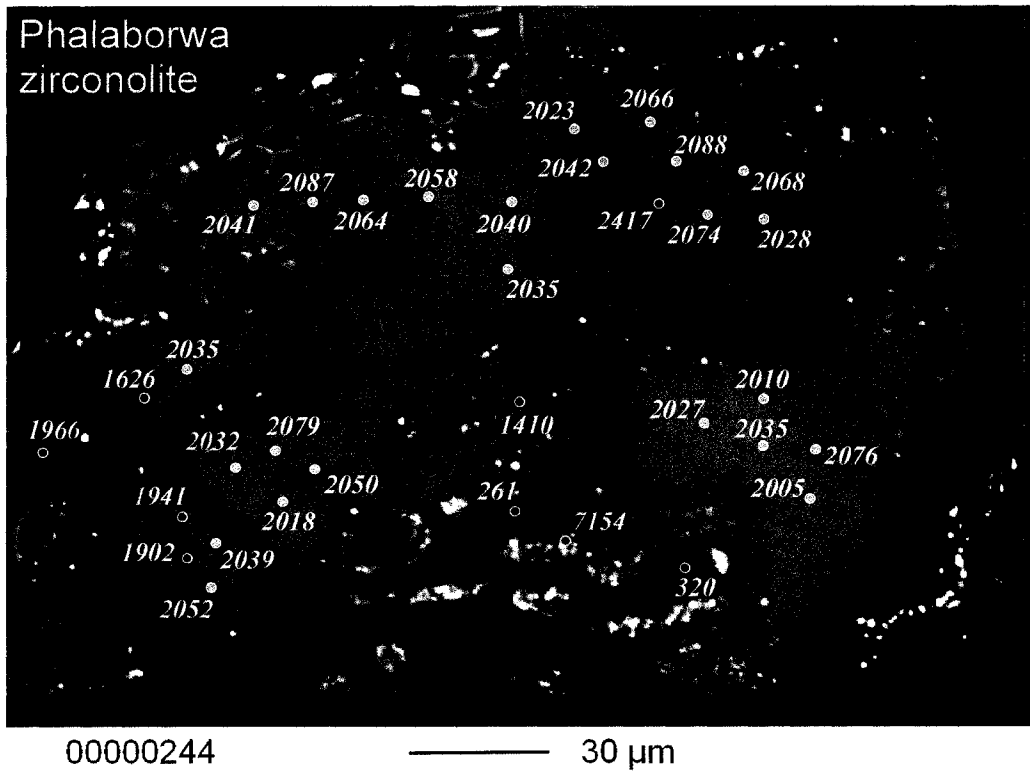
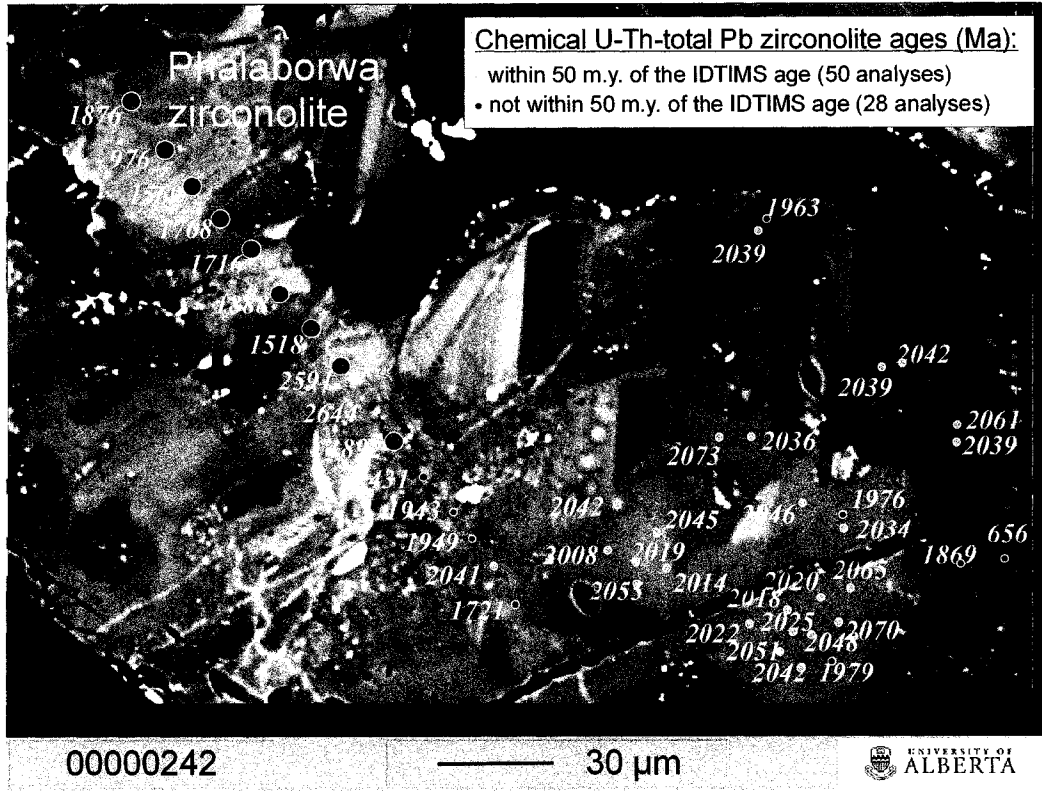


Fig. E-8. Context of electron microprobe chemical U-Th-total Pb ages for zirconolite from the Phalaborwa carbonatite, south Africa. Note: beam diameter varied between 1-5µm as shown.

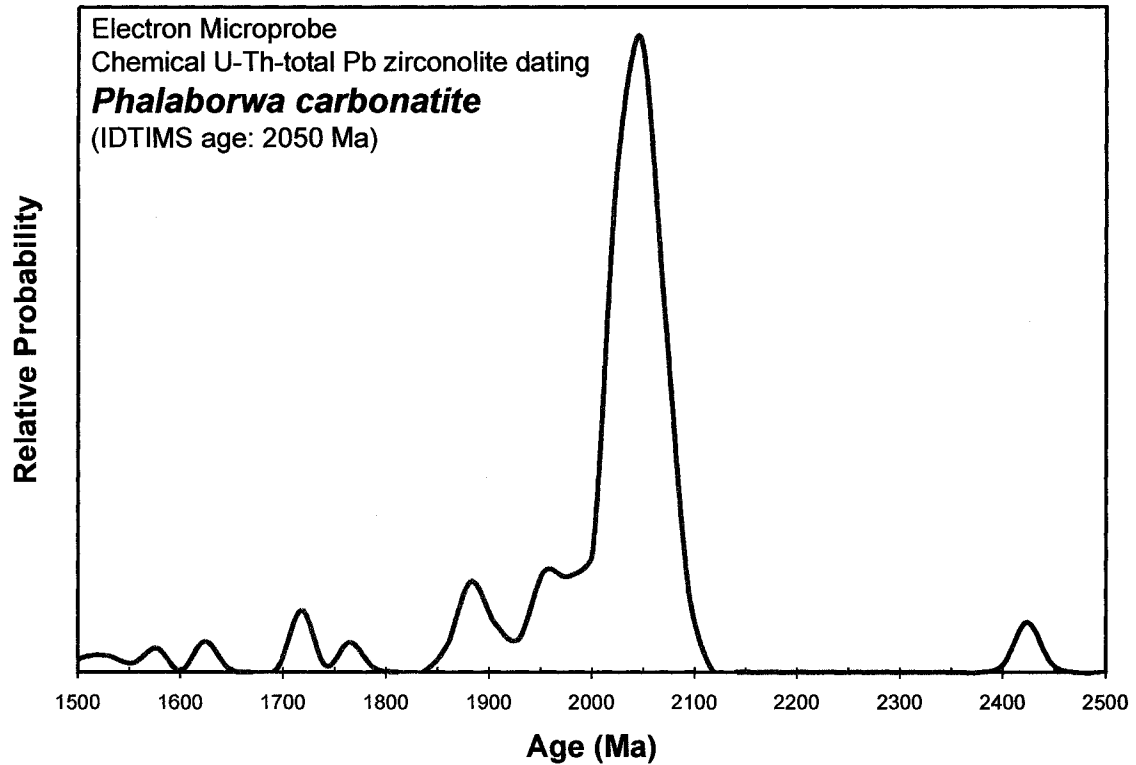


Fig. E-9. Probability density plot for electron microprobe chemical U-Th-total Pb ages for zirconolite from the Phalaborwa carbonatite, South Africa. The spatial context of these ages is shown in Fig. E-8. The prominent peak in chemical ages at c. 2050 Ma corresponds closely with $^{207}\text{Pb}/^{206}\text{Pb}$ ages (2048-2051 Ma: concordant to 4.5% normally discordant analyses) determined in a preliminary U-Pb IDTIMS study (conducted by Larry M. Heaman) on the same zirconolite sample. Chemical data used in the age calculations are listed in Table E-4.

APPENDIX F

Description of samples collected during fieldwork in south India (Dec. 7, 1999 to March 5, 2000), and included in the thesis collection for this project

Table F-1. Samples collected during fieldwork in south India (Dec. 7, 1999 to March 5, 2000), comprising the thesis collection for this project.

SAMPLE NAME	Rock Type	Locality	GPS Location	Dyke Width	Dyke Trend	Comments/Geological Setting	Thin Section	Hand Sample
JEF-99-1	Gabbro	Harohalli, Karnataka	12° 36.92' N 77° 29.80' E	100m	E-W	Intrudes Dharwar basement rocks, Eastern Dharwar craton (EDC)	yes	yes
JEF-99-2	Dolerite	Huchega, Karnataka	12° 36.99' N 77° 28.08' E	40m	NW-SE	Intrudes Dharwar basement rocks, EDC	no	yes
JEF-99-3	Dolerite	Hevandyapannalli, Karnataka	12° 28.20' N 77° 32.09' E	~35m	E-W	Intrudes Dharwar basement rocks, EDC	no	yes
JEF-99-4	Gabbro	Hevandyapannalli, Karnataka	12° 28.68' N 77° 32.77' E	>15m	WNW-ESE	Intrudes Dharwar basement rocks, EDC	yes	yes
JEF-99-5	Dolerite	Hevandyapannalli, Karnataka	12° 28.68' N 77° 32.77' E	>15m	WNW-ESE	Intrudes Dharwar basement rocks, EDC	yes	yes
JEF-99-6	Dolerite	Penukonda, Andhra Pradesh	14° 08.06' N 77° 36.03' E	~50m	E-W (090°)	Intrudes Dharwar basement rocks, EDC	yes	yes
JEF-99-7	Gabbro	Cheneko, Andhra Pradesh	14° 15.06' N 77° 37.33' E	~50m	E-W	Intrudes Dharwar basement rocks, EDC	yes	yes
JEF-99-8	Dolerite	Tadimari, Andhra Pradesh	14° 32.99' N 77° 49.74' E	30m	NW-SE	Intrudes Dharwar basement rocks, EDC	yes	yes
JEF-99-9	Dolerite	Pulivendla, Andhra Pradesh	14° 25.83' N 78° 12.85' E	-	-	Intrudes the Cuddapah Basin, near its base, probably a shallow mafic sill based on grain size, EDC	yes	yes
JEF-99-10	Dolerite	Chaudepalle, Andhra Pradesh	13° 22.51' N 78° 41.77' E	50m	E-W (085°)	Intrudes Dharwar basement rocks, EDC	yes	yes
JEF-99-11	Dolerite	Somala, Andhra Pradesh	13° 29.29' N 78° 49.86' E	30m	NW-SE (150°)	Intrudes Dharwar basement rocks, EDC	yes	yes
JEF-99-12	Dolerite	Tradum, Andhra Pradesh	13° 32.80' N 78° 55.21' E	40m	NNE-SSW (025°)	Intrudes Dharwar basement rocks, EDC	yes	yes
JEF-99-13	Kimberlite	Himalapura, Yadagiri Taluk, Gulberga District, Karnataka	-	-	-	Donated by P.H. Babu, Geological Survey of India, (Dharwar craton)	yes	yes
JEF-00-1	Dolerite	Dandeli, Karnataka	15° 19.49' N 74° 36.06' E	12m	NW-SE (120°)	NW corner of the Shimoga supracrustal belt, Western Dharwar craton (WDC)	yes	yes
JEF-00-2	Dolerite	Badagund, Karnataka	15° 15.49' N 74° 34.77' E	>15m	NNE-SSW (210°)	NW corner of the Shimoga supracrustal belt, WDC	no	yes
JEF-00-3	Dolerite	Dandeli, Karnataka	15° 15.75' N 74° 32.46' E	~35m	NE-SW (050°)	NW corner of the Shimoga supracrustal belt, WDC	yes	yes
JEF-00-4	Syenite	Gokarna	14° 31.10' N 74° 19.89' E	-	-	Intrudes JEF-00-5/JEF-00-8 amphibolite succession, WDC	yes	yes
JEF-00-5	Amphibolite Gneiss	Gokarna	14° 31.11' N 74° 20.22' E	-	-	Amphibolite Succession (Mafic Metavolcanics?), WDC	yes	yes
JEF-00-6	Syenite	Gokarna	14° 31.11' N 74° 20.22' E	-	-	Intrudes JEF-00-5/JEF-00-8 amphibolite succession, WDC	yes	yes
JEF-00-7	Labradorite Monzonite	Gokarna	14° 31.11' N 74° 20.22' E	-	-	Intrudes JEF-00-5/JEF-00-8 amphibolite succession, WDC	yes	yes
JEF-00-8	Amphibolite Gneiss	Gokarna	14° 31.11' N 74° 20.22' E	-	-	Amphibolite Succession (Mafic Metavolcanics?), WDC	yes	yes
JEF-00-9	Mafic Volcanics	Katekalyan, Bastar District, Madhya Pradesh	18° 48.28' N 81° 39.28' E	-	-	Southern Bastar craton (SBC), one of many 2km by 10-20km, NW-SE trending belts	yes	yes
JEF-00-10	Dolerite	Katekalyan, Bastar District, Madhya Pradesh	18 48.02 N 81 38.60 E	30m	-	Intrudes the basement rocks of the SBC	yes	yes
JEF-00-11	Granitoid Gneiss	Katekalyan, Madhya Pradesh	18° 48.02' N 81° 38.60' E	-	-	Part of the SBC basement assemblage	yes	yes
JEF-00-12	Andalucite Muscovite Schist	Gatam, Bastar District, Madhya Pradesh	18° 49.03' N 81° 35.10' E	-	-	Part of the Bengpal Series Schist Belts, SBC	yes	yes
JEF-00-13	Dolerite	Gatam, Bastar District, Madhya Pradesh	18° 49.03' N 81° 35.10' E	15m	-	Intrudes the Bengpal Series Schist Belts, SBC	yes	yes
JEF-00-14	Dolerite	Gatam, Bastar District, Madhya Pradesh	18° 49.37' N 81° 34.71' E	25m	-	Intrudes the basement rocks of the SBC	yes	yes
JEF-00-15	Metadolerite (greenschist facies)	Kaklur, Bastar District, Madhya Pradesh	18° 53.46' N 81° 30.76' E	20m	NNE-SSW (202°)	Intrudes the basement rocks of the SBC	yes	yes
JEF-00-16	Gabbro	Kaklur, Bastar District, Madhya Pradesh	18° 53.39' N 81° 30.69' E	30m	NW-SE (~310°)	Intrudes the basement rocks of the SBC	yes	yes
JEF-00-17	Gabbro	Pondum, Bastar District, Madhya Pradesh	18° 53.10' N 81° 26.56' E	30m	NW-SE (145°)	Intrudes the basement rocks of the SBC	yes	yes
JEF-00-18	Dolerite	Matenar, Bastar District, Madhya Pradesh	18° 50.39' N 81° 26.59' E	25m	NNW-SSE (345°)	Intrudes the basement rocks of the SBC	yes	yes
JEF-00-19	Red siliceous intrusive dyke	Matenar, Bastar District, Madhya Pradesh	18° 50.39' N 81° 26.59' E	30cm	NE-SW	Intrudes the basement rocks of the SBC	yes	yes

Table F-1 cont'd. Samples collected during fieldwork in south India (Dec. 7, 1999 to March 5, 2000), comprising the thesis collection for this project.

SAMPLE NAME	Rock Type	Locality	GPS Location	Dyke Width	Dyke Trend	Comments/Geological Setting	Thin Section	Hand Sample
JEF-00-20	Dolerite	Matenar, Bastar District, Madhya Pradesh	18° 51.14' N 81° 26.23' E	25m	NW-SE (315°)	Intrudes the basement rocks of the SBC	yes	yes
JEF-00-21	Porphyritic Mafic Metavolcanics	Dantewarra, Bastar District, Madhya Pradesh	18° 50.65' N 81° 21.54' E	-	-	SBC, one of many 2km by 10-20km, NW-SE trending belts	yes	yes
JEF-00-22	Mafic Volcanics	Chandenar, Bastar District, Madhya Pradesh	18° 49.63' N 81° 20.24' E	-	-	SBC, one of many 2km by 10-20km, NW-SE trending belts	yes	yes
JEF-00-23	Tourmaline Pegmatite	Chandenar, Bastar District, Madhya Pradesh	18° 48.51' N 81° 20.84' E	~5m	-	Intrudes the basement rocks of the SBC	yes	yes
JEF-00-24	Muscovite Granite	Chandenar, Bastar District, Madhya Pradesh	18° 48.51' N 81° 20.84' E	-	-	Part of the SBC basement assemblage	yes	yes
JEF-00-25	Dolerite	Masenar, Bastar District, Madhya Pradesh	18° 47.71' N 81° 21.69' E	25m	NNE-SSW (~200°)	Intrudes the basement rocks of the SBC	yes	yes
JEF-00-26	Meta-rhyolite?	Bhansi, Bastar District, Madhya Pradesh	18° 44.95' N 81° 15.65' E	-	-	Context unclear	yes	yes
JEF-00-27	Pegmatite	Bhansi, Bastar District, Madhya Pradesh	18° 46.87' N 81° 17.12' E	-	-	Presumably intrude the basement rocks of the SBC, fresh quarry pile sampled	yes	yes
JEF-00-28	Granite	Bhansi, Bastar District, Madhya Pradesh	18° 46.87' N 81° 17.12' E	-	-	Part of the SBC basement assemblage	yes	yes
JEF-00-29	Meta-dolerite (greenschist facies)	Ganawada, Bastar District, Madhya Pradesh	18° 48.79' N 81° 18.85' E	~20m	-	Intrudes the basement rocks of the SBC	yes	yes
JEF-00-30	Dolerite	Satdhar, Bastar District, Madhya Pradesh	18° 49.18' N 81° 19.87' E	20m	~NW-SE	Intrudes the basement rocks of the SBC	yes	yes
JEF-00-31	Granite	Gidam, Bastar District, Madhya Pradesh	18° 57.97' N 81° 30.16' E	-	-	Part of the SBC basement assemblage	yes	yes
JEF-00-32	Mafic Enclave	Gidam, Bastar District, Madhya Pradesh	18° 57.94' N 81° 30.70' E	-	-	Part of the SBC basement assemblage	yes	yes
JEF-00-33	Granite, Granite Gneiss, Mafic Enclave	Gidam, Bastar District, Madhya Pradesh	18° 57.94' N 81° 30.70' E	-	-	Part of the SBC basement assemblage	yes	yes
JEF-00-34	Dolerite	Gidam, Bastar District, Madhya Pradesh	18° 58.47' N 81° 33.62' E	~25m	-	Intrudes the basement rocks of the SBC	yes	yes
JEF-00-35	Porphyritic Granodiorite	Gidam, Bastar District, Madhya Pradesh	18° 58.42' N 81° 33.85' E	-	-	Part of the SBC basement assemblage	yes	yes
JEF-00-36	Gabbro	Gidam, Bastar District, Madhya Pradesh	18° 58.42' N 81° 33.85' E	>30m	-	Intrudes the basement rocks of the SBC	yes	yes
JEF-0037	Dolerite	Gidam, Bastar District, Madhya Pradesh	18° 58.41' N 81° 34.17' E	~30m	NW-SE (155°)	Intrudes the basement rocks of the SBC	yes	yes
JEF-00-38	Dolerite	Suldapara, Bastar District, Madhya Pradesh	18° 58.48' N 81° 35.23' E	~25m	NW-SE (124°)	Intrudes the basement rocks of the SBC	yes	yes
JEF-00-39	Dolerite	Suldapara, Bastar District, Madhya Pradesh	18° 58.92' N 81° 36.75' E	~40m	NW-SE (140°)	Intrudes the basement rocks of the SBC	yes	yes
JEF-00-40	Dolerite	Suldapara, Bastar District, Madhya Pradesh	18° 59.78' N 81° 40.65' E	~20m	NW-SE (138°)	Intrudes the basement rocks of the SBC	yes	yes
JEF-00-41	Granulite (Khondalite?)	Visakapatnam, Andhra Pradesh	17° 43.15' N 83° 20.06' E	-	-	Eastern Ghats Belt	yes	yes
JEF-00-42	Granite	Inpamia, Nalgonda District, Andhra Pradesh	17° 09.42' N 79° 27.63' E	-	-	Part of the EDC basement assemblage	yes	yes
JEF-00-43	Gabbro	Inpamia, Nalgonda District, Andhra Pradesh	17° 08.63' N 79° 27.50' E	40m	E-W (090°)	Intrudes the basement rocks of the EDC, North of Cuddapah basin	yes	yes
JEF-00-44	Granite Gneiss	Inpamia, Nalgonda District, Andhra Pradesh	17° 08.63' N 79° 27.50' E	-	-	Part of the EDC basement assemblage	yes	yes
JEF-00-45	Dolerite	Narapalli, Warangal District, Andhra Pradesh	17° 25.35' N 78° 37.54' E	40m	E-W (265°)	Intrudes the basement rocks of the EDC, North of Cuddapah basin	yes	yes
JEF-00-46	Biotite Granite	Gatkesar, Warangal District, Andhra	17° 26.59' N 78° 39.92' E	-	-	Part of the EDC basement assemblage	yes	yes

Table F-1 cont'd. Samples collected during fieldwork in south India (Dec. 7, 1999 to March 5, 2000), comprising the thesis collection for this project.

SAMPLE NAME	Rock Type	Locality	GPS Location	Dyke Width	Dyke Trend	Comments/Geological Setting	Thin Section	Hand Sample
JEF-00-47	Dolerite	2km west of Wongin Fort near a small ghost town	17° 30.03' N 78° 51.57' E	30m	E-W (085°)	Intrudes the basement rocks of the EDC, North of Cuddapah basin	yes	yes
JEF-00-48	Granite	Granite quarry at Haziped village	17° 58.35' N 79° 29.82' E			Megacrystic granite (>5cm twinned feldspars), EDC	yes	yes
JEF-00-49	dolerite	Ganpur Village	17° 51.02' N 79° 22.10' E	15-20m	N-S (004°)	Intrudes the basement rocks of the EDC, North of Cuddapah basin	yes	yes
JEF-00-50 Sample V5-V5 of Dr. Kumar	Dolerite	Khammam District Eastern Dharwar craton				Donated by Dr. A.P. Siva Kumar, Dept. of Geology University College of Science, Osmania University	yes	yes
JEF-00-51	Dolerite	~20 km E of Hyderabad	17° 18.19' N 78° 40.81' E	35m	N-S	intrudes the basement rocks of the EDC, North of Cuddapah basin	yes	yes
JEF-00-52	Dolerite		16° 14.85' N 77° 57.57' E	~20m	(115°)	Intrudes the basement rocks of the EDC, West of Cuddapah basin	yes	yes
JEF-00-53	Gabbro	~10 km SW of Tadpatri	14° 52.40' N 77° 55.19' E			EDC, Intrudes lower shales of the Tadpatri Formation, Cuddapah basin, 250m x >1km long x 30m high	yes	yes
JEF-00-54	Gabbro		14° 37.06' N 78° 20.00' E			Intrudes upper shale of the Tadpatri Formation, Cuddapah basin, EDC, outcrops several 100m ²	yes	yes
JEF-00-55	Dolerite	Sampled at Kandlamadugu	13° 40.20' N 78° 25.78' E	~18m	(345°) N-S at a regional scale of obs.	Intrudes the basement rocks of the EDC, South of Cuddapah basin	yes	yes
JEF-00-56	Grey Granite	~2km W of Bidadi, quarry of Closepet granite	12° 46.82' N 77° 21.94' E			Probably represents grey anatectic phase of the Closepet granite occurring at the periphery, EDC	yes	yes
JEF-00-57	Mafic enclave from within JEF- 00-56	~2km W of Bidadi, quarry of Closepet granite	12° 46.82' N 77° 21.94' E			Enclave within the grey anatectic Closepet granite	yes	yes
JEF-00-58	Dolerite	Melamala village, quarry no. CHMM 6155	11° 56.84' N 77° 05.12' E	45m		Dyke intrudes peninsular gneiss, WDC, extends into granulite terrain, probably same dyke as JEF-00-59	yes	yes
JEF-00-59	Dolerite	Jyothigowdanapura village (quarry ID: CH.JP.2 MML Q.L.)	11° 57.71' N 77° 03.01' E	45m		Dyke intrudes peninsular gneiss, WDC, extends into granulite terrain, probably same dyke as JEF-00-58	yes	yes
JEF-00-60	Banded Iron Formation		12° 52.35' N 76° 59.20' E			Part of the Kunigal schist belt, 50m x 10m outcrop, strongly laminated, folded, minor faulting, WDC	yes	yes
JEF-00-61	Felsic sill		12° 52.35' N 76° 59.20' E			5-m-wide bedding parallel sill within JEF-00-60 BIF of the Kunigal Schist belt, WDC	yes	yes
JEF-00-62	Mafic Amphibolite	~1km NE Hegedahalli	12° 54.95' N 76° 58.82' E			Mafic amphibolite unit within the Kunigal schist belt (metavolcanic?), WDC	yes	yes
JEF-00-63	Mafic enclave from within JEF- 00-65	near Wasnijgul village	13° 14.67' N 77° 13.76' E			Mafic enclave in Closepet (beautiful outcrop here), same spot as next two samples, EDC	yes	yes
JEF-00-64	Syenite body within JEF-00-65	near Wasnijgul village	13° 14.67' N 77° 13.76' E			Evidence for magma mingling with JEF-00-65, EDC	yes	yes
JEF-00-65	K-feldspar porphyritic granite	near Wasnijgul village	13° 14.67' N 77° 13.76' E			Megacrystic porphyritic variety of the Closepet granite - main intrusive phase, EDC	yes	yes